ISTITUTO NAZIONALE DI FISICA NUCLEARE

LABORATORI NAZIONALI DEL SUD

INFN LNS

ACTIVITY REPORT 2013/2014

LNS Director
Giacomo Cuttone

Editor
Gaetano Agnello

Assistant
Virginia Potenza

Cover design e layout
Mauro Felice
Stefania Rifuggiato
Dueterzi Graphic Design
Unoseinovetre General Contractor

INFN
LNS

Foreword

The INFN Laboratori Nazionali del Sud is going through an intense period of renovation in terms of the scientific lines of research as well as of the infrastructure itself. Indeed, thanks to the recent improvement in scientific and technological activities the LNS have achieved a leading role in the international scientific community, in the fields of nuclear physics, nuclear and particle astrophysics, application of nuclear physics to medicine and cultural heritage, development of systems for acceleration and ion sources. This is confirmed by the long list of contributions here included, which are spread in a wide scientific basis.

The next future will see the LNS putting effort into the consolidation of such scientific activities. In particular, the LNS will be strongly involved in a new physics case, the double beta decay, which has triggered a wide path of upgrade of the LNS facilities.

Finally, it is a pleasure for me to remark the fundamental contribution of the LNS staff to all the activities above mentioned. Without the administration support, the continuous and professional operation of all the technical divisions, our research would not be so varied and so intense.

Thank you very much.

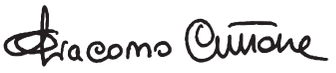

Giacomo Cuttone
INFN -LNS DIRECTOR
Phone: +39 095 54 23 25
Mobile:+39 329 83 12 280
E-mail: cuttone@lns.infn.it

ISTITUTO NAZIONALE DI FISICA NUCLEARE
LABORATORI NAZIONALI DEL SUD
ACTIVITY REPORT 2013/2014

INDEX

21 EXPERIMENTAL NUCLEAR PHYSICS AND ASTROPHYSICS

97 THEORETICAL NUCLEAR PHYSICS

113 INSTRUMENTATION AND RELATED TECHNIQUES

145 ASTROPARTICLE PHYSICS

157 ION SOURCES AND ACCELERATORS

195 INTERDISCIPLINARY PHYSICS

237 GENERAL INFORMATION

259 LNS ACTIVITY PHOTO GALLERY

EXPERIMENTAL NUCLEAR PHYSICS AND ASTROPHYSICS

23 The NUMEN Project @ LNS
C. Agodi, F. Cappuzzello, D.L.Bonanno, D.G. Bongiovanni, V. Branchina, L. Calabretta, A. Calanna, D. Carbone, M. Cavallaro, M. Colonna, G. Cuttone, A. Foti, P. Finocchiaro, V. Greco, G. Lanzalone, D. Lo Presti, F. Longhitano, A. Muoio, L. Pandola, D. Rifuggiato, S. Tudisco

26 Double charge-exchange reactions with MAGNEX: a tool towards the $0\nu\beta\beta$ nuclear matrix elements
M. Cavallaro, F. Cappuzzello, C. Agodi, M. Bondì, D. Carbone, A. Cunsolo, A. Foti, M. De Napoli

28 Signatures of the Giant Pairing Vibration in the ^{14}C and ^{15}C nuclei
D. Carbone, F. Cappuzzello, M. Cavallaro, M. Bondì, C. Agodi, F. Azaiez, A. Bonaccorso, A. Cunsolo, L. Fortunato, A. Foti, S. Franchoo, E. Khan, R. Linares, J. Lubian, J. A. Scarpaci, A. Vitturi

30 Elastic scattering for the system ^{6}Li + p at near barrier energies with MAGNEX
V. Soukeras, A. Pakou, F. Cappuzzello, L. Acosta, C. Agodi, N. Alamanos, M. Bondi, D. Carbone, M. Cavallaro, A. Cunsolo, M. De Napoli, A. Di Pietro, J.P. Fernandez-Garcia, P. Figuera, M. Fisichella, A. Foti, N. Keeley, G. Marquinez-Duran, I. Martel, M. Mazzocco, D. Nicolosi, D. Pierroutsakou, K. Rusek, O. Sgouros, E. Stiliaris, E. Strano, D. Torresi

32 Measurement of the 10 keV resonance in the ^{10}B(p,α_0)^{7}Be reaction via the Trojan Horse Method
C. Spitaleri, L.Lamia, S.M.R.Puglia, S. Romano, M. La Cognata, V. Crucillà, R.G. Pizzone, G.G. Rapisarda, M.L. Sergi, M. Gimenez Del Santo, N. Carlin, M.G. Munhoz, F.A. Souza, A. Szanto de Toledo, B. Irgaziev, A. Mukhamedzhanov, G. Tabacaru, V. Burjan, V. Kroha, Z. Hons, J. Mrazek, Shu-Hua Zhou, Chengbo Li, Qungang Wen, Y. Wakabayashi, H. Yamaguchi, E. Somorjai

34 Astrophysical factor and reaction rate of the ^{13}C(α,n)^{16}O reactions under astrophysical conditions
M. La Cognata, C. Spitaleri, O. Trippella, G. G. Kiss, G. V. Rogachev, A. M. Mukhamedzhanov, M. Avila, G.L. Guardo, E. Koshchiy, A. Kuchera, L. Lamia, S.M.R. Puglia, S. Romano, D. Santiago, R. Spartà

36 The ^{18}F(p,α)^{15}O reaction studied via THM
R.G. Pizzone, B.T. Roeder, L. Trache, C. Spitaleri, C. Bertulani, S. Cherubini, V.Z. Goldberg, M. Gulino, M. Kurokawa, I. Indelicato, M. La Cognata, L. Lamia, M. McCluskey, G.G. Rapisarda, E. Simmons, R. Spartà, A. Spiridon, R.E. Tribble

38 Big Bang nucleosynthesis revisited via Trojan Horse Method measurements
R.G. Pizzone, R. Spartà, C. Bertulani, C. Spitaleri, A. Mukhamedzhanov, M. La Cognata, L. Lamia, A. Tumino

40 Recents developments on the THM ^{17}O(p,α) ^{14}N study
M.L. Sergi, C. Spitaleri, B. Bucher, M. Couder, P. Davies, R. deBoer, X. Fang, B. Irgaziev, V. Kroha, M. La Cognata, L. Lamia, C. Ma, J. Mrazek, A. Mukhamedzhanov, M. Notani, S.O' Brien, R.G. Pizzone, G.G. Rapisarda, S. Robertson, W. Tan, X.D. Tang, M. Wischer

42 Asymptotic normalization coefficients from the $^{6}Li(^{3}He,d)^{7}Be$ reaction
G.G. Kiss, M. La Cognata, C. Spitaleri, M. Lattuada, L. Lamia, S. Palmerini, R.G. Pizzone, G.G. Rapisarda, R. Sparta, O. Tripella, I. Wiedenhöver, L.T. Baby

44 Indirect measurement of the $^{10}B(n,\alpha)^{7}Li$ to discern the α_0 e α_1 contribution to the total cross section
R. Spartà, C. Spitaleri, L. Lamia, S. Cherubini, G.L. Guardo, M. Gulino, S. Romano, M.L. Sergi

46 $^{18}F(p,\alpha)^{15}O$ and $^{18}F(n,\alpha)^{15}N$ reactions studied by Trojan Horse
M. Gulino, S. Cherubini, G. G. Rapisarda, L. Lamia, M. La Cognata, S. Kubono, H. Yamaguchi, S. Hayakawa, Y. Wakabayashi, N. Iwasa, S. Kato, H. Komatsubara, T. Teranishi, A. Coc, N. De Sèrèville, F. Hammache, C. Spitaleri

58 The $^{2}H(d,p)^{3}H$ and $^{2}H(d,n)^{3}He$ reactions at astrophysical energies
A. Tumino, R. Spartà, C. Spitaleri, A.M. Mukhamedzhanov, S. Typel, R.G. Pizzone, E. Tognelli, S. Degl'Innocenti, V. Burjan, V. Kroha, Z. Hons, M. La Cognata, L. Lamia, J. Mrazek, S. Piskor, P.G. Prada Moroni, G.G. Rapisarda, S. Romano, M.L. Sergi

50 New improved experimental measurement of the $^{19}F(p,\alpha 0)^{16}O$ S(E)-factor at energies of astrophysical interest
I. Indelicato, M. La Cognata, V. Burjan, S. Cherubini, M. Gulino, S. Hayakawa, Z. Hons, V. Kroha, L. Lamia, M. Mazzocco, J. Mrazek, R.G. Pizzone, S. Romano, E. Strano, D. Torresi, A. Tumino, C. Spitaleri

52 Indirect study of the $^{12}C(^{12}C,\alpha)^{20}Ne$ and $^{12}C(^{12}C,p)^{23}Na$ reactions via the Trojan Horse Method applied to the $^{12}C(^{16}O,\alpha\,^{20}Ne)^{4}He$ and $^{12}C(^{16}O,p^{23}Na)^{4}He$ three-body reactions
G.G. Rapisarda, C. Spitaleri, S. Cherubini, D. Filipescu, I. Gheorghe, D. Ghita, S. Hayakawa, I. Indelicato, M. La Cognata, J. Mrazek, H. Petrascu, R.G. Pizzone, R. Spartà, O. Tesileanu, L. Trache

54 Measurement of the astrophysical S(E)-factor for the $^{19}F(p,\alpha)^{16}O$ reaction through the Trojan Horse method
O. Trippella, M. La Cognata, C. Spitaleri, S. Ayakawa, G.L. Guardo, I. Indelicato, L. Lamia, S. Palmerini, G.R. Pizzone, S.M.R. Puglia, G. Rapisarda, S. Romano, M.L. Sergi, R. Spart, A. Tumino

56 The ELI-NP facility: nuclear astrophysics with gamma-ray beams
M. La Cognata, A. Anzalone, V. Crucillà, D. Lattuada, C. Spitaleri, A. Taffara

58 GEANT 4 simulations of electromagnetic background for photonuclear reactions at the ELI-NP facility
D. Lattuada, A. Anzalone, G.A.P. Cirrone, V. Crucillà, M. La Cognata, C. Spitaleri, A.Taffara, A. Tramontana

60 The determination of the $^{17}O(p,\alpha)^{14}N$ and $^{18}O(p,\alpha)^{15}N$ reaction rate through the THM and the composition of oxide grains of AGB origin
S. Palmerini, M.L. Sergi, M. La Cognata, L. Lamia, R.G. Pizzone, C. Spitaleri

62 The updated $^{6}Li(p,\alpha)^{3}He$ reaction rate as deduced by THM measurements
L. Lamia, C. Spitaleri, R.G. Pizzone, E. Tognelli, S. Degl'Innocenti, M. La Cognata, P.G. Prada Moroni, M.L. Sergi, A. Tumino

64 Study of the $^{19}F(\alpha,p)\ ^{22}Ne$ reaction under astrophysical conditions via Trojan Horse Method
G. D'Agata, C. Spitaleri, R.G. Pizzone, P. Figuera, G.L. Guardo, S. Hayakawa, I. Indelicato, R. Kshetri, M. La Cognata, L. Lamia, M. Lattuada, L. Sergi, M. Gulino, A. Tumino, S. Blagus, L.M. Grassi,M. Milin, D. Miljanic, N. Skukan, N. Soic, V. Tokic

66 βDelayed α decay of ^{16}N and the $^{12}C(\alpha,\gamma)\ ^{16}O$ cross section atastrophysical energies: a new experimental approaches
S. Sanfilippo, S. Cherubini, S. Hayakawa, A. Di Pietro, P. Figuera, M. Gulino, M. La Cognata, M. Lattuada, C. Spitaleri, H. Yamaguchi, D. Kahl, T. Nakao, S. Kubono, Y. Wakabayashi, T. Hashimoto, N. Iwasa, Y. Okoda, K. Ushio, T. Teranishi, M. Mazzocco, C. Signorini, D. Torresi, J.Y. Moon, T. Komatsubara, P.S. Lee, K.Y.Chae, M.S. Gwak

68 Neutron yield from the absorption of 62 MeV protons on a thick Beryllium target: final results
R. Alba, M. Barbagallo, P. Boccaccio, N. Colonna, L. Cosentino, A. Celentano, A. Del Zoppo, A. Di Pietro, J. Esposito, P. Figuera, P. Finocchiaro, A. Kostyukov, C. Maiolino, M. Osipenko, G. Ricco, M. Ripani, D. Santonocito, M.C. Schillaci, C. M. Viberti

70 Effects of coupling to the continuum states in the $^{6,7}Li+^{64}Zn$ reactions at energies around the Coulomb barrier
J.P. Fernandez-Garcia , M. Zadro, A. Di Pietro, P. Figuera, M. Fisichella, O. Goryunov, M. Lattuada, A. M.Moro, A. Musumarra, V. Ostashko, M. G. Pellegriti, V. Scuderi, E. Strano, D. Torresi

72 Effects of Coulomb and nuclear couplings in the $^{6}He+^{64}Zn$ reactions at energies around the Coulomb barrier
J.P. Fernandez-Garcia , A. Di Pietro , P. Figuera, M. Fisichella , M. Lattuada, A. M. Moro, A. Musumarra, M. G. Pellegriti, V. Scuderi, and D. Torresi, M. Zadro

74 Ion recombination correctionfactorsfor parallel-plate ionization chambers in a 62 MeV/n carbon ion beam
S. Rossomme, R. Thomas, N. Lee, S. Vynckier, H. Palmans

76 The InKiIsSy experiment: competition between statistical and dynamical fission in projectile break-up of isobaric systems
E. De Filippo, A. Pagano, P. Russotto, L. Acosta, L. Auditore, V. Baran, T. Cap, G. Cardella, M. Colonna, L. Francalanza, B. Gnoffo, G. Lanzalone, I. Lombardo, G. Marquínez-Durán, C. Maiolino, T. Minniti, S. Norella, E.V. Pagano, M. Papa, E. Piasecki, S. Pirrone, G. Politi, F. Porto, L. Quattrocchi, F. Rizzo, E. Rosato, A. Trifirò, M. Trimarchi, G. Verde, M. Vigilante, K. Siwek-Wilczynska, J. Wilczynski

78 The ASY-EOS experiment at GSI:constraining the symmetry energy at supra-saturation densities
P. Russotto for ASY-EOS and NewCHIM collaborations

80 Study of cluster structures in ^{10}Be and ^{16}C via projectile break-up reactions with the CHIMERA multi-detector

D. Dell'Aquila, L. Acosta, F.Amorini, R. Andolina, L. Auditore, I. Berceanu, G. Cardella, M.B. Chatterjiee, E. De Filippo, L. Francalanza, B. Gnoffo, A. Grzeszczuk, G. Lanzalone, I. Lombardo, N.S. Martorana, T. Minniti, A. Pagano, E.V. Pagano, M. Papa, S. Pirrone, G. Politi, A. Pop, F. Porto, L. Quattrocchi, F. Rizzo, E. Rosato†, P. Russotto, A. Trifirò, M. Trimarchi, G.Verde, M.Vigilante

82 Decay competition in IMF production in the collisions ^{78}Kr+^{40}Ca and ^{86}Kr+^{48}Ca at 10 A.MeV

G. Politi, S. Pirrone, M. La Commara, J.P. Wieleczko, E. De Filippo, B. Gnoffo, M. Trimarchi, M. Vigilante, G. Ademard, F. Amorini, L. Auditore, C. Beck, I. Berceanu, E. Bonnet, B. Borderie, G. Cardella, A. Chbihi, M. Colonna, Antonio D'Onofrio, J.D. Frankland, E. Geraci, E. Henry, E. La Guidara, G. Lanzalone, P. Lautesse, D. Lebhertz, N. Le Neindre, I. Lombardo, K. Mazurek, A. Pagano, M. Papa, E. Piasecki, F. Porto, M. Quinlann, F. Rizzo, E. Rosato, P. Russotto, W.U. Schroeder, G. Spadaccini, A. Trifirò, J. Toke, G. Verde

84 Study of two and multi-particle correlations in ^{12}C+ ^{24}Mg, ^{208}Pb reactions

L. Quattrocchi, L. Acosta, F. Amorini, A. Anzalone, L. Auditore, G. Cardella, A. Chbihi, E. De Filippo, Francalanza, G. Lanzalone, I. Lombardo, I. Martel, T. Minniti, S. Norella, A. Pagano, E.V. Pagano, M. Papa, S. Pirrone, G. Politi, F. Porto, F. Rizzo, E. Rosato, P. Russotto, A. Trifiro, M. Trimarchi, G. Verde, M. Veselsky, M. Vigilante

86 Dipolar degrees of freedom and isospin equilibration processes in heavy ion collisions - I

M. Papa, I. Berceanu, L. Acosta, F. Amorini, C. Agodi, A. Anzalone, L. Auditore, G. Cardella, M.B. Chatterjee, E. De Filippo, L. Francalanza, E. Geraci, L. Grassi, B. Gnoffo, J. Han, E. La Guidara, G. Lanzalone, I. Lombardo, C. Maiolino, T. Minniti, A. Pagano, E.V. Pagano, S. Pirrone, G. Politi, F. Porto, L. Quattrocchi, F. Rizzo, P. Russotto, A.Trifirò, M. Trimarchi, G. Verde, M.Vigilante

88 Dipolar degrees of freedom and isospin equilibration processes in heavy ion collisions - II

M. Papa, I. Berceanu, L. Acosta, F. Amorini, C. Agodi, A. Anzalone, L. Auditore, G. Cardella, M.B. Chatterjee, E. De Filippo, L. Francalanza, E. Geraci, L. Grassi, B. Gnoffo, J. Han, E. La Guidara, G. Lanzalone, I. Lombardo, C. Maiolino, T. Minniti, A. Pagano, E.V. Pagano, S. Pirrone, G. Politi, F. Porto, L. Quattrocchi, F. Rizzo, P. Russotto, A. Trifirò, M. Trimarchi, G. Verde, M. Vigilante

90 Dynamical Dipole mode in heavy-ion fusion reactions in the ^{192}Pb mass region

C. Parascandolo, D. Pierroutsakou, R. Alba, A. Del Zoppo, C. Maiolino, D. Santonocito, C. Agodi, V. Baran, A. Boiano, M. Colonna, R. Coniglione, E. De Filippo, M. Di Toro, U. Emanuele, F. Farinon, A. Guglielmetti, M. La Commara, B. Martin, C. Mazzocchi, M. Mazzocco, C. Rizzo, M. Romoli, M. Sandoli, C. Signorini, R. Silvestri, F. Soramel, E. Strano, D. Torresi, A.Trifirò, M.Trimarchi

92 Hot GDR evolution at high E*in nuclei of mass A ~ 120-132
D. Santonocito, Y. Blumenfeld, C. Agodi, R. Alba, G. Bellia, R. Coniglione, F. Delaunay, A. Del Zoppo, P. Finocchiaro, V. Lima, C. Maiolino, E. Migneco, P. Piattelli, P. Sapienza, J. A. Scarpaci, O.Wieland

94 Studying RIB induced fusion reactions with stacked targets
M. Fisichella, A.C. Shotter, A. Di Pietro, P. Figuera, M. Lattuada,V. Privitera, L.Romano, C. Ruiz, M. Zadro

THEORETICAL NUCLEAR PHYSICS

99 Shear viscosity of the quark-gluon plasma in a kinetic theory approach
A. Puglisi, S. Plumari, F. Scardina, V. Greco

101 Energy density fluctuation in early universe
G.L. Guardo, V. Greco, M. Ruggieri

103 Signals of Bose Einstein condensation and Fermi quenching in the decay of hot nuclear systems
P. Marini, H. Zheng, G. Verde, A. Chbihi, A. Bonasera

105 Exotic break-up in low energy reactions
M. Colonna, V. Baran, C. Rizzo

107 Heavy Quark Dynamics in QGP:Boltzmann vs Langevin
F. Scardina, S. K. Das, S. Plumari, V. Greco

110 Neutron stars and supernova explosions in the framework of Landau's theory
H. Zheng, J. Sahagun, A. Bonasera

INSTRUMENTATION AND RELATED TECHNIQUES

115 4π γ-ray detection with CsI(Tl) scintillators of the CHIMERA array
G. Cardella, L. Acosta, F. Amorini, L. Auditore, I. Berceanu, A. Castoldi, E. De Filippo, L. Francalanza, B. Gnoffo, C. Guazzoni, G. Lanzalone, I. Lombardo, T. Minniti, E. Morgana, S. Norella, A. Pagano, E.V. Pagano, M. Papa, S. Pirrone, G. Politi, A. Pop, L. Quattrocchi, F. Rizzo, E. Rosato, P. Russotto, A. Trifirò, M. Trimarchi, G. Verde, M. Vigilante

117 A note on light particle calibration with CsI(Tl) scintillators of the CHIMERA array
L. Acosta, F. Amorini, L. Auditore, I. Berceanu, G. Cardella, A. Castoldi, S. De Luca, E. De Filippo, L. Francalanza, B. Gnoffo, C. Guazzoni, G. Lanzalone, I. Lombardo, N. Martorana, T. Minniti,E. Morgana, S. Norella, A.Pagano, E.V. Pagano, M. Papa, S. Pirrone, G. Politi, A. Pop, L. Quattrocchi, F. Rizzo, E. Rosato, P. Russotto, A. Trifirò, M. Trimarchi, G. Verde, M. Vigilante

119 First test with beam of the FARCOS Correlator
E.V. Pagano, L. Acosta, R. Andolina, L. Auditore, C. Boiano, G. Cardella, A. Castoldi, M. Dandrea, E. De Filippo, S. De Luca, D. Dell'Aquila, L. Francalanza, E. Geraci, B. Gnoffo, C. Guazzoni, G. Lanzalone, I. Lombardo, N. Martorana, T. Minniti, S. Norella, A. Pagano, M. Papa, S. Pirrone, G. Politi, F. Porto, L. Quattrocchi, F. Rizzo, P. Russotto, G. Sacca', A. Trifiro', M. Trimarchi, G. Verde, M. Vigilante

121 Performance qualification of a FARCOS telescope by means of Digital Data Acquisition
L. Acosta, L. Auditore, C. Boiano, G. Cardella, A. Castoldi, E. De Filippo, L. Francalanza, C. Guazzoni, G. Lanzalone, I. Lombardo, T. Minniti, E. Morgana, S. Norella, A. Pagano, E. V. Pagano, M. Papa, T. Parsani, S. Pirrone, G. Politi, L. Quattrocchi, F. Riccio, F. Rizzo, P. Russotto, M. Trimarchi, A. Trifirò, G. Verde, P. Zambon

123 FAZIA demonstrator: a significant step forward
S. Barlini, D. Gruyer, N. LeNeindre, G. Pastore, S.Valdrè for the FAZIA

125 The ELI-NP facility: design of a large area silicon array detector and of the vacuum chamber for nuclear astrophysics at ELI-NP
V. Crucillà, A. Anzalone, M. La Cognata, D. Lattuada, C. Spitaleri, A. Taffara

127 The ELI-NP facility: Electronic readout of silicon strip detector
A.Taffara, A. Anzalone, V. Crucillà, M. La Cognata, D. Lattuada, C. Spitaleri

129 Thomson Spectrometer for ionic acceleration study
C. Altana, G. Lanzalone, A. Muoio, S. Tudisco A. Anzalone, G.A.P. Cirrone, F. Musumeci, F. Schillaci, M. Castro, S. Salamone

131 Calibration and characteriation of a Thomson parabola spectrometer
F. Schillaci, G.A.P. Cirrone, G. Cuttone, M. Maggiore, D. Margarone, G. Parasiliti Palumbo, P. Pisciotta, D. Rifuggiato, F. Romano, G. Russo, V. Scuderi, A. Tramontana, A. Velyhan, A. Amato, G.F. Caruso, S. Salamone

133 Medium resolution mass separator for SPES project at LNL
D. Russo, L. Calabretta, M. Comunian, L. Bellan

135 HELNED: Helium-3-free low-cost neutron detectors
M. Barbagallo, Luigi Cosentino, Carmelo Marchetta, Alfio Pappalardo, Carlotta Scirè, Sergio Scirè, Gianfranco Vecchio, Paolo Finocchiaro

137 Mapping the inter-strip response of the silicon layers of the FARCOS telescopes
L. Acosta, L. Auditore, C. Boiano, G. Cardella, L. Carraresi, A. Castoldi, E. De Filippo, L. Francalanza, C. Guazzoni, G. Lanzalone, I. Lombardo, T. Minniti[1,3], E. Morgana[3], S. Norella, A. Pagano, E. V. Pagano, M. Papa[1], T. Parsani, S. Pirrone, G. Politi, L. Quattrocchi, F. Riccio, F. Rizzo, P. Russotto, F. Taccetti, M. Trimarchi, A. Trifirò, G. Verde, P. Zambon

139 New spectrometer for cluster ion beam induced luminescence
H. Ryuto, F. Musumeci, A. Sakata, M. Takeuchi, G.H. Takaoka

141 A Multiaxis Motion Control System based on an FPGA
G. De Luca, G. Limoli

ASTROPARTICLE PHYSICS

147 The acoustic detectors network in the central Mediterranean sea
G. Larosa, S. Viola (for the KM3NeT-Italia, EMSO-Italia and SMO Teams)

149 First results on underwater acoustic background in Capo Passero: towards monitoring station for the European Marine Strategy
R. Grasso, G. Larosa for SMO, KM3NeT Italia, EMSO Collaborations

151 Deep-Sea multidisciplinary observatories: SMO & EMSO infrastructures for the long term acoustic monitoring of cetaceans
V. Sciacca, F. Caruso, E. De Domenico G. Bellia, G. Larosa, G. Pavan, E. Papale, C. Pellegrino, S. Pulvirenti, G. Riccobene, F. Simeone, S. Viola for the SN, EMSO and SMO Collaborations

153 Hydrophone calibration of the SMO acoustic antenna
R. Grasso, S. Viola for SMO, KM3NeT Italia and EMSO Collaborations

ION SOURCES AND ACCELERATORS

Accelerators status and developments
D. Rifuggiato on behalf of the Accelerator Division
159

Proposal to upgrade the LNS Superconducting Cyclotron
A.Calanna, L. Calabretta, D. Rifuggiato, G. Cuttone, G. D'Agostino, M. Maggiore, A. Radovinsky
161

Injection tests of high-intensity H2+ beam for IsoDAR cyclotron
J. R. Alonso, S. Axani, L. Calabretta, L. Celona, D. Campo, G. Castro, J. M. Conrad, F. Labrecque, R. Gutierrez-Martinez, G. Messina, B.F. Milton, M. Sedita, D. Winklener, L. Winslow, E. Zappalà
163

Superconducting ring cyclotron for DAEδALUS experiment
A. Calanna, J.R. Alonso, L. Calabretta, J.M. Conrad, F. Meot, M. Haj Tahar, J. Minervini
165

Injection and extraction from the superconducting ring cyclotron for DAEδALUS experiment
Calanna, J.R. Alonso, L. Calabretta, J.M. Conrad, F. Meot, M. Haj Tahar, M.Shaevitz
167

Update of the ECR ion sources
S. Marletta, M. Castro, M. Cafici, F. Chines, F. Speziale, S. Vinciguerra, L. Andò, G. Castro, L. Celona, L. G. Cosentino, S. Gammino, O. Leonardi, D. Mascali, D. Nicolosi, S. Pulvirenti, F. Noto, G. Torrisi
169

Plasma heating studies in Electron Cyclotron Resonance Ion Sources in the framework of the ENSAR-ARES activities
D. Mascali, S. Biri, R. Racz, C. Caliri, G. Castro, L. Celona, L. Neri, G. Torrisi, C. Altana, G. Sorbello, A. Galatà, S. Gammino, G. Ciavola
171

Test of the first equipment developed for the ESS accelerator
S. Gammino, L. Celona, L. Neri, D. Mascali, G. Castro, G. Torrisi, L. Andò, O. Leonardi, D. Nicolosi, L. Allegra, N. Amato, A. Caruso, F. Chines, G. Gallo, A. Longhitano, G. Manno, S. Marletta, E.G. Messina, S.M. Passarello, E. Zappalà
173

Design of the AISHa ion source for hadrontherapy facilities
L. Celona, L. Allegra, G. Castro, G. Costa, F. Chines, G. Cuttone, G. Gallo, S. Gammino, O. Leonardi, S. Marletta, D. Mascali, L. Neri, D. Nicolosi, F. Noto, G. Torrisi, G. Ciavola, L. Andò, F. Romano, G. Costa, A. Galatà
175

3D-full wave and kinetics numerical modelling of Electron Cyclotron Resonance Ion Sources plasma
G. Torrisi, D. Mascali, L. Neri, G. Sorbello, L. Celona, G. Castro, L. Di Donato, T. Isernia, S. Gammino
177

The Flexible Plasma Trap (FPT) for the production of overdense plasmas
S. Gammino, L. Celona, D. Mascali, G. Castro, L. Neri, G. Torrisi, G. Sorbello, O. Leonardi, C. Altana, C. Caliri, L. Allegra, F. Chines, L. D'Antoni, S. Di Modica, G. Gallo, G. Manno, S. Marletta, A. Maugeri, E. Messina, A. Seminara, B. Trovato, M. Tringale, G. Vasta, E. Zappalà
179

181 Conceptual design and simulation of a microwave interferometer for plasma density measurements in ion sources
G. Torrisi, V. Finocchiaro, D. Mascali, G. Sorbello, R. Agnello, G. Castro, L. Celona, L. Neri, S. Gammino

183 Upgrade of the Versatile Ion Source for H_2^+ generation at the BEST test-stand
L. Celona, G. Castro, S. Gammino, D. Mascali, L. Neri, G. Torrisi, G. Castorina, O. Leonardi, G. Patti, L. Allegra, G. Gallo, E. Zappalà, G. Messina, A. Maugeri, A. Seminara

185 Waveguide DC-break design at 2.45 GHz
O. Leonardi, L. Celona, G. Torrisi, L. Allegra, S. Gammino

187 The new axial buncher at INFN-LNS
A. Caruso, G. Gallo, A. Longhitano, A. Spartà, E. Zappalà, G.F. Caruso, G. Manno, E.G. Messina, J. Sura, F. Consoli, Li Pengzhan

189 Management software for the INFN-LNS accelerators beamlines
G. Vecchio, L. Cosentino, S. Pulvirenti, E. Furia, S. Cavallaro, B. Diana

191 Data exchange protocol for the INFN-LNS accelerators beamlines
G. Vecchio, L. Cosentino, S. Pulvirenti, E. Furia, S. Cavallaro, B. Diana

INTERDISCIPLINARY NUCLEAR PHYSICS

197 Transport and dosimetry solutions for laser driven beams: the ELIMED beam line
G.A.P. Cirrone, G. Cuttone, F. Romano, V. Scuderi, A. Amato, L. Andò, A. Attili, M. Borghesi, G. Candiano, L. Cosentino, M. Costa, F. Costanzo, C. D'Amato, G. De Luca, D. Doria, G. Gallo, S. Gammino, G. Korn, T. Germek, G. La Rosa, R. Leanza, R. Manna, M. Maggiore, V. Marchese, D. Margarone, A. Maugeri, G. Milluzzo, A. Musumarra, L. Pandola, G. Petringa, S. Pulvirenti, D. Rifuggiato, D. Rizzo, R. Sacchi, S. Salamone, F. Schillaci, M. Sedita, A. Tramontana, B. Trovato, C. Vaglianisi

199 GEANT 4 Monte Carlo simulations and applications in medical physics
F. Romano, R. Calcagno, G.A.P. Cirrone, G. Cuttone, S.E. Mazzaglia, G. Milluzzo, M.G. Sabini, V. Scuderi, A. Tramontana, A. Varisano

201 Dosimetric approaches for laser-driven ion beams: an innovative Faraday cup
V. Scuderi, G.A.P. Cirrone, F. Romano, A. Amato, G. Candiano, G. Cuttone, R. Leanza, R. Manna, V. Marchese, G. Milluzzo, G. Petringa, F. Schillaci, A. Tramontana

203 Monte Carlo simulation of neutrons flux and ambient dose equivalent in 0° experimental room at Laboratori Nazionali del Sud
S. Russo, R. Leanza, G. Russo, G.A.P. Cirrone, G. Cuttone

205 LENS - Laser Energy for Nuclear Science
G. Lanzalone, S. Tudisco, A. Anzalone, C. Altana, A. Muoio, F. Musumeci, C. Caliri, G.A.P. Cirrone, D. Mascali, F.P. Romano, G. De Luca, S. Salamone, F. Schillaci, A. Scordino

207 Test at ENEA ABC laser to study some nuclear fusion reactions in plasma
A. Anzalone, A. Bonasera, P.L. Andreoli, M. Cipriani, F. Consoli, V. Crucillà, R. De Angelis, G. Di Giorgio, F. Ingenito, M. La Cognata, D. Lattuada, R. Manna, S. Romano, V. Scuderi, A. Spitaleri, C. Spitaleri, S. Tudisco, A. Tumino

209 Advanced targets preparation for proton acceleration by laser-plasma using TNSA regime
L. Torrisi, M. Cutroneo, L. Calcagno, P. Musumeci, G. Ceccio, A. Cannavò, A. Italiano, S. Cavallaro, C. Marchetta, J. Ullschmied, J. Wolowski, J. Badziak, A. Torrisi

211 Stabilisation/solidification of radionuclide-polluted soils: application of a performance testing protocol and assessment of γ-radiation shielding index as a function of emission energy
P.P. Falciglia, S. Romano, V. Puccio, F.G.A. Vagliasindi Collaboration

213 PIXE-α non destructive and in situ compositional investigation of black gloss on ancient pottery
L. Pappalardo, S. Barresi, G. Biondi, C. Caliri, F. Caruso, R. Catalano, G. Lamagna, A. Manenti, A. Orlando, F. Rizzo, F.P. Romano, H.C. Santos

215 The improved XPIXE-α spectrometer: calibration of the system by using fused petrological standard materials
L. Pappalardo, R. Catalano, C. Caliri, A. Orlando, F. Rizzo, H.C. Santos, F.P. Romano

217 Elemental and imaging X-ray based techniques for the investigation of Attic black gloss and its imitation in the Mediterranean area
C. Caliri, R. Catalano, A. Orlando, L. Pappalardo, F. Rizzo, H.C. Santos, F.P. Romano

219 In-situ compositional investigation of silver coins by means of X-ray fluorescence portable technique
R. Catalano, R. Amato, C. Caliri, G. Lamagna, A.M. Manenti, A. Orlando, L. Pappalardo, F. Rizzo, S. Santangelo, H.C. Santos, and F.P. Romano

221 Non-destructive compositional investigation of historical enamels by using XRF imaging techniques
H.C. Santos, C. Caliri, R. Catalano, G. Mascali, A. Orlando, L. Pappalardo F. Rizzo, F.P. Romano

223 On-line remote monitoring of radioactive waste repositories
C. Calì, L. Cosentino, P. Litrico, A. Pappalardo, G. Passaro, C. Scirè, S. Scirè, G. Vecchio, P. Finocchiaro

225 The DMNR system hardware setup
S. Scirè, G. Vecchio, C.Scirè, S. Grillo, C. Greco, A. Pappalardo, L. Cosentino, C. Calì, P. Litrico, G. Passaro, P. Finocchiaro

227 Functional characterization of mitochondrial respiratory complex I by delayed luminescence spectroscopy
I. Baran, A. Scordino, D. Ionescu, S. Privitera, R. Grasso, M. Gulino, F. Musumeci, I.T. Tofolean, C. Ganea

229 Apoptotic pathway induced by Berberine on thyroid cancer cell lines monitored by delayed Luminescence
A. Scordino, A. Campisi, R. Grasso, R. Bonfanti, M. Gulino, R. Parenti, F. Musumeci

231 Radiobiological analysis of human lung adenocarcinoma cells after irradiations with protons and carbon ions
O. Keta, T. Bulat, D. Todorović, V. Petković, G.A.P. Cirrone, F. Romano, V. Marchese, G. Cuttone, A. Ristić-Fira, I. Petrović

233 Analyses of apoptotic and cell cycle protein expression in non-small lung cancer cells: effects of proton and carbon ion irradiations
V. Petković, O. Keta, T. Bulat, D. Todorović, G.A.P. Cirrone, F. Romano, V. Marchese, G. Cuttone, I. Petrović, A. Ristić-Fira

GENERAL INFORMATION

238 Organization and Personnel

241 Scientific guests and Users

246 Seminars at LNS

252 Degrees theses

256 Events

LNS ACTIVITY PHOTO GALLERY

260 LNS activity photo gallery

ISTITUTO NAZIONALE DI FISICA NUCLEARE
LABORATORI NAZIONALI DEL SUD
ACTIVITY REPORT 2013/2014

EXPERIMENTAL NUCLEAR PHYSICS AND ASTROPHYSICS

The NUMEN Project @ LNS

C. Agodi[1)], F. Cappuzzello[1),2)], D. L.Bonanno[3)], D. G.Bongiovanni[3)], V. Branchina[2)], L. Calabretta[1)], A.Calanna[1)], D. Carbone[1)], M. Cavallaro[1)], M. Colonna[1)], G. Cuttone[1)], A. Foti[2),3)], P. Finocchiaro[1)], V. Greco[1),2)], G.Lanzalone[5)], D. Lo Presti[2),3)], F.Longhitano[3)], A.Muoio[4)],L. Pandola[1)], D. Rifuggiato[1)], S. Tudisco[1)]

1) INFN - Laboratori Nazionali del Sud, Catania, Italy
2) Dipartimento di Fisica e Astronomia, Università di Catania, Catania, Italy
3) INFN - Sezione di Catania, Catania, Italy
4) Università di Messina, Messina, Italy
5) Università di Enna, Enna, Italy

Abstract - An innovative technique to access the nuclear matrix elements entering the expression of the life time of the double beta decay by relevant cross sections of double charge exchange reactions is proposed. A key aspect of the project is the use of the MAGNEX large acceptance magnetic spectrometer, for the detection of the ejectiles, and of the LNS K800 Superconducting Cyclotron (CS), for the acceleration of the required high resolution and low emittance heavy-ion beams.

INTRODUCTION

Neutrinoless double beta decay, $0\nu\beta\beta$, is at the present time strongly pursued both experimentally and theoretically [1]. Its observation will determine whether the neutrino is a Dirac or Majorana particle and will provide a measurement of the average neutrino mass, which is one of the most fundamental problems in physics. Extraction of the neutrino mass from $0\nu\beta\beta$ decay rate measurements requires the knowledge of the Nuclear Matrix Elements (NME), $M_{0\nu}$, which appear in the expression for the inverse half-life:

$$[T_{1/2}]^{-1} = G_{0\nu}|M_{0\nu}|^2|f(m_i,U_{ei})|^2 \qquad (1)$$

where $G_{0\nu}$ is a phase-space factor, $f(m_i,U_{ei})$, a term that contains the masses m_i and the mixing coefficients U_{ei} of the neutrino species, and $|M_{0\nu}|^2$ is the transition amplitude from the initial to the final nuclear state of the $\beta\beta$ process, throught the $0\nu\beta\beta$ operator:

$$|M_{0\nu}|^2 = \left|\langle\varphi_f|O^{0\nu\beta\beta}|\varphi_i\rangle\right|^2 \qquad (2)$$

Thus, if NME are known with sufficient precision, neutrino masses and the mixing coefficients of neutrino species will be extracted from (1) by $0\nu\beta\beta$ decay rate measurements. The evaluation of the NMEs is presently limited to state of the art model calculations. The framework used for estimating the matrix elements has been largely that provided by the proton–neutron quasiparticle random phase approximation (QRPA) [2] which is successful in describing overall features of nuclear properties. QRPA depends on some rather drastic simplifying assumptions and is thus often not quantitatively accurate in describing the details of nuclear structure. On the other hand, large model spaces can easily be accommodated. Shell- model calculations are also used [3]. The shell model can generally describe most features of nuclear structure more quantitatively, but there are limits on the range of orbitals that can be included in the calculations. This restricted model space requires renormalization of transition operators and the closure approximation [4] is invoked for the virtual intermediate states in neutrinoless double beta decay. Detailed aspects of nuclear structure can also be described using so-called algebraic approaches, where the interacting boson approximation (IBA) has been found to be very useful. It is therefore not surprising that double beta decay matrix elements have also been calculated using the IBA model [5], again utilizing the closure approximation. Despite all the effort in the model calculations, discrepancy factors higher than two are presently reported in literature [6]. From an experimentalist's perspective, the dominant question is to understand which readily measurable nuclear properties probe aspects of the nuclear Hamiltonian that are important for the nuclear matrix elements. These properties can then be measured and the results used to investigate the extent to which the theoretical models used for the matrix element calculations reproduce them [7].

In this picture, we suggest an innovative technique in the NUMEN (Nuclear Matrix Elements of Neutrinoless Double Beta Decay) Project, where we propose for the first time Heavy-Ions Double Charge Exchange (HI-DCE) cross section measurements towards the $0\nu\beta\beta$ NME determination [8].

DCE REACTIONS AND NEUTRINOLESS DOUBLE BETA DECAYS

There are a number of important similarities among DCE and 0νββ decay processes, despite they are mediated by different interactions. The basic point is the coincidence of the initial and final state wave-functions in the two classes of processes, and the similarity of the transition operators, which in both cases present a superposition of Fermi, Gamow-Teller and rank-two tensor component.

Moreover a large linear momentum (~100 MeV/c) is available in the virtual intermediate channel in both processes; the two processes are non-local and are characterized by two vertices localized in a pair of valence nucleons; both processes take place in the same nuclear medium; a relevant off-shell propagation through virtual intermediate channels is present in the two cases. The description of NMEs extracted from DCE and $0\nu\beta\beta$ presents the same degree of complexity, with the advantage for DCE to be "accessible" in laboratory. However a simple relation between DCE cross sections and $\beta\beta$-decay half-lives is not trivial and needs to be explored.

The use of modern high resolution and large acceptance spectrometers, like MAGNEX, togheter with high resolution and low emittance heavy-ion beams, like that produced at LNS K800 Superconducting Cyclotron (CS), are crucial for the experimental challenges, looking forward to extract quantitative information from DCE reactions. Moreover the measurement of DCE high resolution energy spectra and accurate cross sections at very forward angles are key points to identify the transitions of interest [9]. The concurrent measurement of the other relevant reaction channels allows to isolate the direct DCE mechanism from the competing transfer processes. These are at least of 4^{th}-order and can be effectively minimized by the choice of the proper projectile-target system and incident energy [10].

First experimental results, obtained at the INFN-LNS laboratory in Catania, for the $^{40}Ca(^{18}O,^{18}Ne)^{40}Ar$ reaction at 270 MeV, in a wide range of transferred momenta, give encouraging indication on the capability to access quantitative information towards the determination of the Nuclear Matrix Elements for $0\nu\beta\beta$ decay. These experimental results are described in a separate contribution in the present Report Volume.

On the basis of the above mentined ground-breaking achievement, we propose an ambitious project, NUMEN, with the aim to go deep inshight in the HI-DCE studies on nuclei of interest in $0\nu\beta\beta$ decay, looking forward at the $0\nu\beta\beta$ NME dermination.

TOWARD THE " HOT " CASES

The availability of the MAGNEX spectrometer [11] for high resolution measurements of very suppressed reaction channels was essential for the first pilot experiment [12]. However with the present set-up it is difficult to suitably extend this research to the "hot" cases, where ββ decay studies are and will be concentrated. We consider that about one order of magnitude more yield would have been necessary for the reaction studied; the (^{18}O,^{18}Ne) reaction is particularly advantageous, due to the large value of both the $B[GT;^{18}O_{gs}(0^+) \rightarrow {}^{18}F_{gs}(1^+)]$ and $B[GT;^{18}F_{gs}(1^+) \rightarrow {}^{18}Ne_{gs}(0^+)]$ strengths and to the concentration of the GT strength in the $^{18}F(1^+)$ ground state. However this reaction is of $\beta^+\beta^+$ kind, while most of the research on 0νββ is on the opposite side; none of the reactions of $\beta^-\beta^-$ kind looks like as favorable as the (^{18}O,^{18}Ne), so a sensible reduction of the yield is foreseen in these cases. Moreover in some cases gas target will be necessary, e.g. ^{136}Xe or ^{130}Xe, which are normally much thinner than solid state ones, with a consequent reduction of the collected yield; in other cases the energy resolution we can provide (about half MeV) is not enough to separate the ground state from the excited states in the final nucleus. In these cases the coincident detection of γ-rays from the de-excitation of the populated states is necessary; a strong fragmentation is kown in the nuclei of interest compared to the ^{40}Ca.

So the present limit of low beam current we have experienced both for the CS accelerator and for the MAGNEX focal plane detector must be sensibly overcome. For a systematic study of the many "hot" cases of ββ decays an upgraded set-up, able to work with two orders of magnitude more current than the present, is thus necessary. This goal can be achieved by a substantial change in the technologies used in the beam extraction and in the detection of the ejectiles. For the accelerator the use of a stripper induced extraction is an adequate choice. More details about that are in the technical part of this project. For the spectrometer the main foreseen upgrades are:

1. The substitution of the present Focal Plane Detector (FPD) [13] gas tracker with a GEM tracker system;
2. The substitution of the wall of silicon pad stopping detectors with a wall of telescopes based on SiC-CsI detectors;
3. The enhancement of the maximum magnetic rigidity;
4. The introduction of an array of detectors for measuring the coincident γ-rays.

THE FOUR PHASES OF NUMEN PROJECT

In this framework we propose four phases in the NUMEN project, looking forward to do in the same time both the experimental and the up-grade activity, as indicated in the following Phases of the project.

Phase1: the experiment feasibility

The pilot experiment :$^{40}Ca(^{18}O,^{18}Ne)^{40}Ar$ reaction at 270 MeV, with the first experimental data on heavy-ion double charge-exchange reactions in a wide range of transferred momenta, was already done. The results demostrate the technique feasibility.

Phase2: toward "hot" cases optimizing experimental conditions and getting first results

The necessary work for the upgrading of both the accelerator and MAGNEX will be carried out still preserving the access to the present facility. Due to the relevant technological challenges connected, in which test, with and without beam will be crucial, the Phase2 is foreseen to have a duration of a 3-4 years. In the

meanwhile, experiments with integrated charge of tens of mC (about one order of magnitude more than that collected in the pilot experiment) will be performed. These will require several weeks (4-8 depending on the case) data taking for each reaction, since thin targets (a few 10^{18} atoms/cm^2) are mandatory in order to achieve enough energy and angular resolution in the energy spectra and angular distributions. The attention will be focused on a few favorable cases, with the goal to achieve conclusive results for them.

Phase3: the facility upgrade

Once all the building block for the upgrade of the accelerator and spectrometer facility will be ready at the LNS a Phase3, connected to the disassembling of the old set-up and re-assembling of the new will start. An estimate of about 18-24 months is considered.

Phase4: the experimental campaign

The Phase4 will consist of a series of experimental campaigns at high beam intensities (some pμA) and long experimental runs in order to reach in each experiment integrated charge of hundreds of mC up to C, for the experiments in coincidences, spanning all the variety of candidate isotopes for $0\nu\beta\beta$ decay.

CONCLUSIONS

Once selected the optimal experimental condition for the different cases in the Phase2, with the upgrades, both of CS and the MAGNEX array, the Phase4 will be devoted to collect data addressed to give, with an accurate analysis, a rigorous determination of the absolute cross sections values and their uncertainties for all the system of interest, to the challenging determination of the $0\nu\beta\beta$ decay nuclear matrix elements, that is the ambitious goal

REFERENCES

[1] Report to the Nuclear Science Advisory Committee, Neutrinoless Double Beta Decay, 2014

[2] Elliot S. R. and Vogel P 2002 Ann.Rev.Nucl.Part.Sci. 52 115.

[3] Caurier E.,Nowacki F.,Poves A. and Retamosa J. 1954

[4] Primakov H. 1952 Phys.Rev.85 888

[5] Barea J. and Iachello F2009 Phys.Rev.C79 044301

[6] J. Barea, et al., PRL 109 (2012) 042501

[7] D. Frekers, Prog. Part. Nucl. Phys. 64 (2010) 281; D. Frekers, et al., Nucl. Phys. A 916 (2013) 219

[8] C. Agodi et al., Nuclear Physics B in print

[9] H. Matsubara, et al., Few-Body Systems 54 (2013) 1433.

[10] D. M. Brink, Phys. Lett. B 40 (1972) 37

[11] F. Cappuzzello et al., MAGNEX: an innovative large acceptance spectrometer for nuclear reaction studies in: Magnets: Types, Uses and Safety, Nova Publisher Inc., New York, 2011, pp 1-63.

[12] F.Cappuzzello et al., submitted to Phys. Lett. B

[13] M. Cavallaro, et al., Eur. Phys. J. A (2012) 48: 59.

[14] D. Carbone, et al., Eur. Phys. J. A (2012) 48: 60

Double charge-exchange reactions with MAGNEX: a tool towards the 0νββ nuclear matrix elements

M. Cavallaro[1], F. Cappuzzello[1,2], C. Agodi[1], M. Bondì[1,2], D. Carbone[1], A. Cunsolo[1], A. Foti[2,3], M. De Napoli[3]

1) INFN - Laboratori Nazionali del Sud, Catania, Italy
2) Dipartimento di Fisica e Astronomia, Università di Catania, Catania, Italy
3) INFN - Sezione di Catania, Catania, Italy

Abstract – A first pioneering experiment to measure the ^{40}Ca(^{18}O,^{18}Ne)^{40}Ar double charge exchange reaction has been performed at INFN – LNS. The aim of such a measurement is to investigate on the relationship between the measured cross-sections and the nuclear matrix elements for the neutrinoless double beta decay.

INTRODUCTION

Double charge-exchange reactions (DCE) are processes characterized by the transfer of two units of the isospin third component ($\Delta T_z = \pm 2$), leaving the mass number unchanged.

Several features make the study of DCE interesting. One of these is the capability to reach nuclei far from the line of stability, especially for light systems, thus allowing spectroscopic studies of neutron-rich or proton-rich nuclei. Another very ambitious goal, which is the guide line of the DCE experiments discussed in the present report, is related to the connection to the neutrinoless double beta decay (0νββ). Since the 0νββ decay process involves transitions in atomic nuclei, issues concerning the nuclear structure must be accounted for.

In particular, the 0νββ decay rate $[T_{1/2}]^{-1}$ can be factorized as a phase-space factor $G_{0\nu}$, the nuclear matrix element (NME) $M_{0\nu}$ and a term $f(m_i,U_{ei})$ containing the masses m_i and the mixing coefficients U_{ei} of the neutrino species:

$$[T_{1/2}]^{-1} = G_{0\nu}|M_{0\nu}|^2|f(m_i,U_{ei})|^2$$

The NME is defined as the transition amplitude from the initial to the final nuclear state of the ββ process through the 0νββ decay operator. Thus, if the NMEs are established with sufficient precision, the neutrino masses and the mixing coefficients can be extracted from 0νββ decay rate measurements.

The evaluation of the NMEs is presently limited to calculations based on different methods (QRPA, shell-model, IBM etc.) [1], [2], [3], [4]. However the ambiguities in the models are still too large and the constraints too loose to reach accurate values of the NMEs. [5].

The experimental study of other nuclear transitions as the double charge-exchange reactions (DCE) where the nuclear charge is changed by two units leaving the mass number unvaried, similarly to the 0νββ decay, could give important information. In the two cases in fact (DCE and 0νββ decay) the initial and final states (wave functions) are the same.

Early studies of heavy-ion induced DCE reactions were not conclusive because of the lack of zero-degree data and the poor yields in the measured energy spectra and angular distributions, due to the very low cross-sections involved [6], [7], [8]. An additional complication in the interpretation of the data was due to possible contributions of multi-nucleon transfer reactions leading to the same final.

The use of the high resolution and large acceptance spectrometer MAGNEX allows to face the experimental challenges and to extract quantitative information from DCE reactions. The measurement of DCE high resolution energy spectra and accurate cross-sections for the first time at very forward angles (including zero degree) is crucial to identify the transitions of interest. The concurrent measurement of the other relevant reaction channels allows to isolate the direct DCE mechanism from the competing transfer processes.

THE EXPERIMENT

The ^{40}Ca(^{18}O,^{18}Ne)^{40}Ar DCE reaction has been measured at INFN - LNS in Catania together with the competing processes:

- ^{40}Ca(^{18}O,^{18}F)^{40}K single charge-exchange reaction,
- ^{40}Ca(^{18}O,^{20}Ne)^{38}Ar two-proton transfer reaction,
- ^{40}Ca(^{18}O,^{16}O)^{42}Ca two-neutron transfer reaction.

A beam of $^{18}O^{4+}$ ions, extracted by the K800 Superconducting Cyclotron accelerator, bombarded a 279 ± 30 μg/cm^2 Ca target at 270 MeV incident energy.

The ejectiles produced in the collisions were momentum-analysed by the MAGNEX large acceptance spectrometer [9] and detected by its focal plane detector [10], [11]. An angular range of $-1.2° < \theta_{lab} < +8°$ in the laboratory reference was explored, corresponding to scattering angles in the center of mass $0° < \theta_{CM} < 12°$. The ejectiles identification was achieved as described in refs. [12] [13]. The positions and angles of the selected ions measured at the focal plane were used as input for a 10th order ray-reconstruction of the scattering angle θ_{CM} and excitation energy [14], [15].

Figure 1 shows examples of energy spectra. An energy resolution of ~500 keV (FWHM) is obtained consistently with ref. [16]. The absolute cross-section was extracted

from measured yields according to ref. [14]. A systematic error of ~10% was estimated from the uncertainty in the target thickness and beam collection.

RESULTS

In the ^{40}Ca(^{18}O,^{20}Ne)^{38}Ar two-proton-transfer energy spectrum of Figure 1a, the cross-section tends to increase with excitation energy as a consequence of the kinematical Q-matching conditions (Q_{opt} = 32 MeV). Known low-lying states are identified indicating the suppression of low multipolarity transitions due to L-matching conditions (L_{opt} = 6). The L- and Q-optimum for the second step 2n-transfer ^{38}Ar(^{20}Ne,^{18}Ne)^{40}Ar are similar. Thus multistep transfer reactions are expected to be strongly suppressed in the population of the mismatched (L = 0, Q = -2.9 MeV) ^{40}Ar ground state. In addition the required condition of a total L = 0 in the transfer to the ^{40}Arg.s. gives a supplementary reduction due to the vanishing Clebsh-Gordan coefficients, especially for the high-spin intermediate states. The cross-section for the ^{40}Ca(^{18}O,^{20}Ne)^{38}Ar$_{gs}$ is ~3 μb/sr, not larger than the ^{40}Ca(^{18}O,^{18}Ne)^{40}Ar$_{gs}$ (11 μb/sr). Assuming a similar scaling between 2p-transfer and DCE for the present data, an upper limit of 30 nb/sr in the (^{18}O,^{18}Ne) reaction channel is estimated for the ^{18}O+^{40}Ca → ^{20}Ne+^{38}Ar → ^{18}Ne$_{gs}$+^{40}Ar$_{gs}$ multi-step route. This will not give a contribution at least at very forward angles.

The 2n-pickup 2p-stripping channel ^{18}O+^{40}Ca → ^{16}O+^{42}Ca → ^{18}Ne$_{gs}$+^{40}Ar$_{gs}$ is unlikely to contribute significantly since the first step is already very suppressed in our experiments, with cross-sections which are about half of the 2p-transfer.

The ^{40}Ca(^{18}O,^{18}F)^{40}K single charge-exchange spectrum is shown in Figure 1b. The strongest transition is to the 2$^-$ state at 800 keV, even if higher multipolarities are visible (4$^-$ g.s. and 3$^-$ 30 keV state). The group of 1$^+$ states at 2.27 and 2.73 MeV is also populated even if other high spin states could hide them. The cross-section for these GT transitions is about 500 times larger than the DCE transition to the ^{40}Ar ground state. This is an expected result, since in the single charge-exchange both the square of volume integral and the B(GT) strengths are larger than the DCE.

In the DCE energy spectrum of Figure 1c, the ^{40}Ar ground state is clearly separated from the group of ^{40}Ar 2$^+$ at 1.460 MeV and ^{18}Ne 2$^+$ at 1.887 MeV. At higher excitation energy the measured yield is spread over many overlapping states.

CONCLUSIONS

The measurement of the absolute cross-section of the DCE transition to the ^{40}Ar ground state at zero-degree is a crucial milestone, not available before the present measurement at LNS. It allows to investigate whether and under which conditions the factorization of the DCE cross-section in a structure part (proportional to the NMEs) and a dynamical part holds.

One should stress that, in the case of single charge exchange reactions, a proportionality relationship between the nuclear reaction cross-sections and the single beta decay NMEs is well known since long time. An accurate study of the proportionality relation validity is presently under progress.

The pioneering measurement of DCE cross-sections on ^{40}Ca has represented the starting point of the NUMEN project, which is described in a separate contribution in the present report volume.

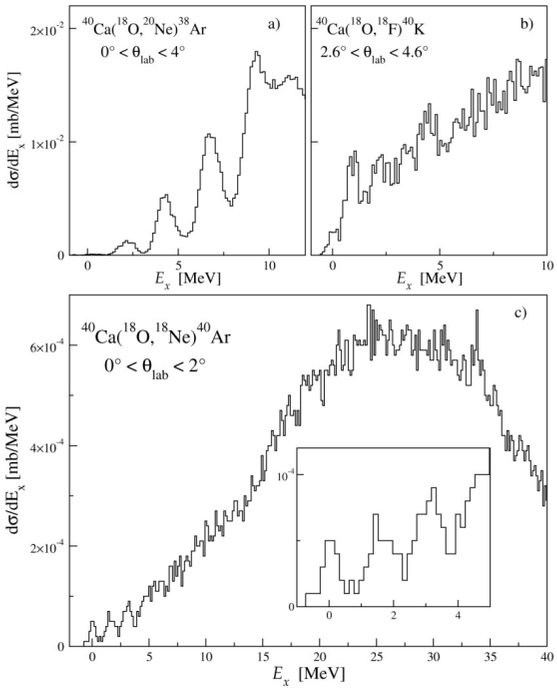

Figure 1: (a) ^{38}Ar energy spectrum populated in the ^{40}Ca(^{18}O,^{20}Ne)^{38}Ar 2p-transfer. (b) ^{40}K energy spectrum from ^{40}Ca(^{18}O,^{18}F)^{40}K single charge-exchange. (c) ^{40}Ar energy spectrum from ^{40}Ca(^{18}O,^{18}Ne)^{40}Ar DCE.

REFERENCES

[1] E. Caurier, et al., PRL 100 (2008) 052503.
[2] J. Suhonen and M.Kortelainen, Int. Journ. of Mod. Phys. E 17 (2008) 1.
[3] N. L. Vaquero, et al., PRL 111 (2013) 142501.
[4] J. Barea, et al., PRC 87 (2013) 014315.
[5] J. Barea, et al., PRL 109 (2012) 042501.
[6] D. M. Drake, et al., PRL 45 (1980) 1765.
[7] F. Naulin, et al., PRC 25 (1982) 1074.
[8] J. Blomgren, et al., PLB 362 (1995) 34.
[9] F. Cappuzzello et al., MAGNEX: an innovative large acceptance spectrometer for nuclear reaction studies, Nova Publisher Inc., New York, 2011, pp 1-63.
[10] M. Cavallaro, et al., Eur. Phys. J. A (2012) 48: 59.
[11] D. Carbone, et al., Eur. Phys. J. A (2012) 48: 60.
[12] M. Bondì, et al., AIP Conf. Proc. 1595 (2014) 245.
[13] F. Cappuzzello, et al., NIM A 621 (2010) 419.
[14] M. Cavallaro, et al., NIM A 648 (2011) 46.
[15] F. Cappuzzello, et al., NIM A 638 (2011) 74.
[16] F. Cappuzzello, et al., NIM A 763 (2014) 314.

Signatures of the Giant Pairing Vibration in the ^{14}C and ^{15}C nuclei

D. Carbone[1], F. Cappuzzello[1,2], M. Cavallaro[1], M. Bondì[1,2], C. Agodi[1], F. Azaiez[3], A. Bonaccorso[4], A. Cunsolo[1], L. Fortunato[5,6], A. Foti[2,7], S. Franchoo[3], E. Khan[3], R. Linares[8], J. Lubian[8], J. A. Scarpaci[9], A. Vitturi[5,6]

1) INFN – Laboratori Nazionali del Sud, Catania, Italy
2) Dipartimento di Fisica e Astronomia, Università di Catania, Catania, Italy
3) Institut de Physique Nucléaire, Université Paris-Sud-11-CNRS/IN2P3, Orsay, France
4) INFN – Sezione di Pisa, Pisa, Italy
4) Dipartimento di Fisica e Astronomia, Università di Padova, Padova, Italy
5) INFN – Sezione di Padova, Padova, Italy
6) INFN – Sezione di Catania, Catania, Italy
7) Instituto de Física da Universidade Federal Fluminense, Niterói, Brazil
8) Centre de Sciences Nucléaires et de Sciences de la Matières - Université Paris-Sud-11-CNRS/IN2P3, Orsay, France

Abstract - The ^{12}C(^{18}O,^{16}O)^{14}C and ^{13}C(^{18}O,^{16}O)^{15}C reactions have been studied at 84 MeV incident energy and the ejectiles have been detected at forward angles by the MAGNEX spectrometer. The presence of broad resonances at high excitation energy in the ^{14}C and ^{15}C energy spectra are observed. This is associated for the first time with the observation of the Giant Pairing Vibration.

INTRODUCTION

The elementary excitation mode known as Giant Pairing Vibration (GPV) was predicted by the theory in the 70's [1], in analogy with the Giant Resonances (GR) observed in almost all nuclei. The link between GPV and GR is the symmetry between single-particle states above (particle) and below (hole) the Fermi level. Both of them are collective states, manifestation of a coherence mechanism of the particle-hole (GR) or particle-particle/hole-hole (GPV) excitations connecting major shells of the harmonic oscillator like nuclear mean field. The excitation of the GPV should be induced by two-nucleon transfer reactions with $L = 0$ angular momentum transfer.

Despite the strong theoretical indications in favour of the existence of the GPV [2][3] and many experimental attempts [4][5], a clear identification of it was missing up to now. The first clear signature of the GPV has been achieved only by studying the ^{12}C(^{18}O,^{16}O)^{14}C and ^{13}C(^{18}O,^{16}O)^{15}C reactions at 84 MeV incident energy [6]. This result represents a significant progress in this research field.

THE EXPERIMENT

The experiment was performed at the INFN-LNS laboratory in Catania. The ^{14}C and ^{15}C nuclei were populated through the (^{18}O,^{16}O) two-neutron transfer reaction. A 49 ± 3 μg/cm^2 self-supporting ^{12}C and a 50 ± 3 μg/cm^2 self-supporting 99% enriched ^{13}C targets were used. The $^{18}O^{6+}$ beam at 84 MeV incident energy was produced and accelerated by the Tandem Van de Graaff facility. The ^{16}O ejectiles produced in the collisions were momentum analysed by the MAGNEX spectrometer [7], The ejectiles were identified event by event in atomic number (Z), atomic mass (A) and charge (q) [8]. The trajectories of the $^{16}O^{8+}$ ejectiles were reconstructed and the momentum vector was deduced at the target position [9].

EXPERIMENTAL RESULTS

The reaction Q-values or, equivalently, the excitation energies $E_x = Q_0 - Q$ (where Q_0 is the ground to ground state Q-value) were obtained by the missing mass determination based on relativistic kinematic transformations. An overall energy resolution of ~160 keV full width at half maximum (FWHM) is obtained. Examples of the reconstructed energy spectra for the two experiments are shown in Fig. 1. Several narrow peaks corresponding to well-known low-lying bound and resonant states are observed in both case. A sudden increase of the yield is also found just above the two-neutron separation energy (S_{2n}= 13.123 MeV for ^{14}C and S_{2n}= 9.394 MeV for ^{15}C). This observation is discussed in ref.s [10][11], in which an extreme model assuming the removal of two independent neutrons from the projectile is applied for describing the energy region above S_{2n} in the energy spectra.

A large bump, superimposed to the continuum background, is observed in both spectra. A best fit procedure with Gaussian shapes and a locally adjusted linear background model (see Fig. 1) gives an energy of E_x = 16.9 ± 0.1 MeV (FWHM 1.2 ± 0.3 MeV) in ^{14}C and E_x = 13.7 ± 0.1 MeV (FWHM 1.9 ± 0.3 MeV) in ^{15}C. In the ^{14}C case two known narrow resonances at 16.43 and 16.72 MeV are weakly populated in the lower energy region of the bump and accounted for in the fit.

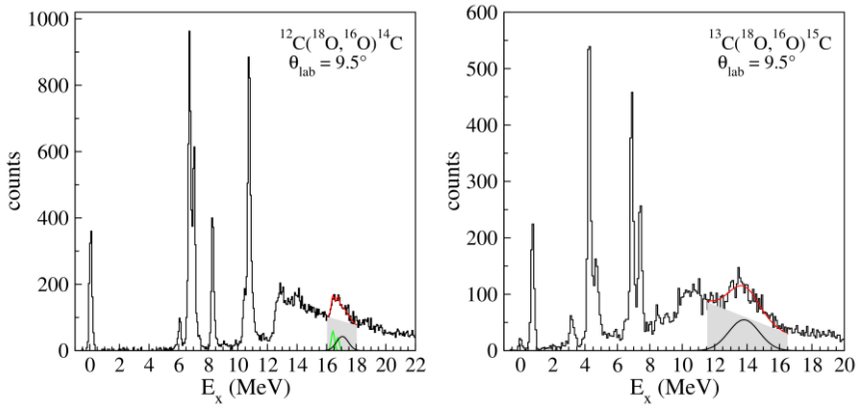

Figure 1: Energy spectra for the $^{12}C(^{18}O,^{16}O)$ and the $^{13}C(^{18}O,^{16}O)$ reactions at 84 MeV at forward angles. The linear background models, the fitted bumps and their sum are shown as the grey area, the black Gaussian and the red continuous line, respectively. In the ^{14}C case, the known resonances at 16.43 and 16.72 MeV are also indicated (green Gaussians).

The absolute cross section angular distributions were extracted, according to the procedure described in ref. [12]. For transitions to bound states of the residual nuclei, exact finite range coupled reaction channels calculations based on a parameter free double-folding potential were performed in ref. [13]. They accurately described the measured cross sections without the need of any scaling factor.

The experimental angular distributions for the transitions to the ^{14}C and ^{15}C bumps are shown in Fig. 2. The contribution to the angular distribution of the bumps due to the continuous background in the spectra was estimated at each angle by a least-squared approach, assuming the model shown in Fig.1. A clear indication of an oscillating pattern is present. This behaviour reveals the dominance of a resonant state in that energy region, characterized by a well-defined angular momentum.

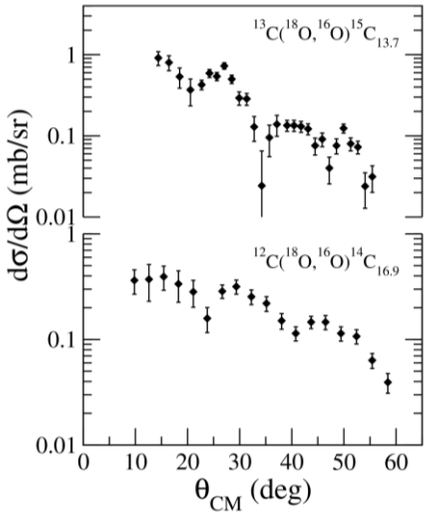

Figure 2: Angular distributions for the $^{12}C(^{18}O,^{16}O)^{14}C$ and $^{13}C(^{18}O,^{16}O)^{15}C$ reactions at 84 MeV.

The properties of such resonances, such as the energy, width, strength and angular momentum transfer, were analysed and were found to be compatible with those expected for the GPV [6].

CONCLUSIONS

The data presented in this report show the clearest signal compatible with the long searched GPV so far. The experimental observation of GPV confirm the foundation of the particle-hole quantum symmetry in a system of interacting fermions.

AKNOWLEDGMENTS

The work of D. C. was supported by the Italian Ministry of Education, Universities and Research (MIUR) under the grant “LNS-Astrofisica Nucleare (fondi premiali)”.

REFERENCES

[1] R. A. Broglia and D. R. Bes, Phys. Lett. B 69 (1977) 129.
[2] P. Lotti et al., Phys. Rev. C 40 (1989) 1791.
[3] G. Potel et al., Rep. Prog. Phys. 76 (2013) 106301.
[4] G. M. Crawley et al., Phys. Rev. C 22 (1980) 316.
[5] B. Mouginot et al., Phys. Rev. C 83 (2011) 037302.
[6] F. Cappuzzello et al., Nature Communications (in press).
[7] F. Cappuzzello et al., in Magnets: Types, Uses and Safety (Nova Publisher Inc., New York, 2011) 1-63.
[8] F. Cappuzzello et al., Nucl. Instr. and Meth. A 621 (2010) 419.
[9] F. Cappuzzello et al., Nucl. Instr. and Meth A 638 (2011) 74.
[10] F. Cappuzzello et al., Phys. Lett. B 711 (2012) 347.
[11] D. Carbone et al., EPJ Web Conf. 66 (2014) 03015.
[12] M. Cavallaro et al., Nucl. Instr. And Meth. 648 (2011) 46.
[13] M. Cavallaro et al., Phys. Rev. C 88 (2013) 054601.

Elastic scattering for the system ^{6}Li + p at near barrier energies with MAGNEX

V. Soukeras[1], A. Pakou[1], F. Cappuzzello[2], L. Acosta[3], C. Agodi[4], N. Alamanos[5], M. Bondi[2], D. Carbone[4], M. Cavallaro[4], A. Cunsolo[4], M. De Napoli[6], A. Di Pietro[4], J. P. Fernandez-Garcia[4], P. Figuera[4], M. Fisichella[4], A. Foti[7], N. Keeley[8], G. Marquinez-Duran[3], I. Martel[3], M. Mazzocco[9], D. Nicolosi[4], D. Pierroutsakou[10], K. Rusek[11], O. Sgouros[1], E. Stiliaris[12], E. Strano[9], D. Torresi[9]

1) Department of Physics and HINP, The University of Ioannina, 45110 Ioannina, Greece
2) INFN Laboratory Nazionali del Sud, via S. Sofia 62, 95125, Catania, Italy and Dipartimento di Fisica e Astronomia, Universita di Catania, via S. Sofia 64, 95125, Catania, Italy
3) Departamento di Fisica Aplicada, Universidad de Huelva, E-21071, Huelva, Spain
4) INFN Laboratory Nazionali del Sud, via S. Sofia 62, 95125, Catania, Italy
5) CEA-Saclay, DAPNIA-SPhN, 91191, Gif-sur-Yvette, France
6) INFN - Sezione di Catania, via S. Sofia 64, 95125, Catania, Italy
7) Dipartimento di Fisica e Astronomia, Universita di Catania, via S. Sofia 64, 95125, Catania, Italy
8) National Center for Nuclear Research, A. Soltana 7, 05-400, Otwock Warsaw, Poland
9) Departimento di Fisica and INFN - Sezione di Padova, via Marzolo 8, I-35131, Padova, Italy
10) INFN - Sezione di Napoli, via Cinthia, I-80126, Napoli, Italy
11) Heavy Ion Laboratory, University of Warsaw, Pasteura 5a, 02-093, Warsaw, Poland
12) Institute of Accelerating Systems and Applications and Department of Physics, University of Athens, Greece

Abstract - Elastic scattering measurements have been performed for the ^{6}Li + p system in inverse kinematics at the energies of 16, 20, 25 and 29 MeV. The heavy ejectile was detected by the large acceptance MAGNEX spectrometer at the Laboratori Nazionali del Sud (LNS) in Catania, in the angular range between ~ 2^{0} and 12^{0} in the laboratory system, giving us the possibility to span almost a full angular range in the center of mass system.

The analysis is under progress and preliminary results will be presented here for one of the energies.

INTRODUCTION

In a long term plan, we have undertaken systematic work [1-9] concerning the optical potential or/and the structure of nuclei via proton elastic scattering and reactions on weakly bound stable or radioactive nuclei in inverse kinematics. All these studies but the [9] were performed at energies well above 10MeV/u. In [9] we have performed measurements with the radioactive nucleus ^{17}F at E ~ 4MeV/u putting on stake the validity of the microscopic JLM potential [10], which is applied for medium and heavy mass stable nuclei and for energies above 10MeV/u, with slight adjustments only on the imaginary part. Going a step forward, herewith, the elastic scattering and reactions were studied for ^{6}Li+p in inverse kinematics at near barrier energies, by using a weakly bound projectile with a lower mass than before and at energies on resonance exploring further the case of compound versus direct couplings to continuum.

The reactions of nucleons and light nuclei with ^{6}Li are of great practical and theoretical importance, with serious consequences on astrophysical problems. As the ^{6}Li nucleus exhibits a pronounced cluster structure with a very small binding energy in the α-d channel and a low density of its excited states up to excitation energy of 16 MeV, the choice of a global optical potential is inapplicable. Therefore, elastic scattering measurements and induced reaction measurements at low energies for a detailed CRC approach could be very useful.

In the LIPMAGNEX experiment we have proposed the study of ^{6}Li+p, in a full angular distribution measurement to probe the elastic scattering in a precise way as previous measurements in direct kinematics (Ref. [11-13] and Ref. therein) seem to present inconsistencies due to normalization problems. Moreover, the elastic scattering measurement will be the first step for obtaining the optical potential and subsequently for describing the various reaction processes. In this point we should underline that our final goal, will be the measurement of direct (breakup) and compound reactions, which will give us the opportunity to explore coupling effects on the compound as well as to direct contributions in a more detailed way.

We have planned our experiment in the MAGNEX facility [14-16] which is a powerful tool for detecting both heavy and light ejectiles with a very good angular and energy resolution. This measurement is planned to be a predecessor measurement on MAGNEX with radioactive projectiles where both elastic scattering and breakup are channels of vital importance.

In the present article we present a preliminary analysis of the first part of this study, referring to the elastic scattering at the highest energy at 29MeV.

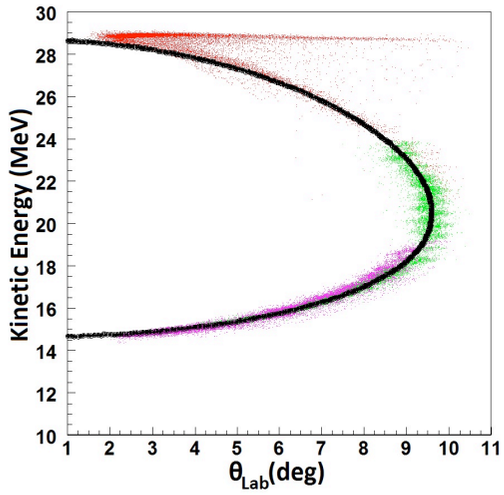

Figure 1: A reconstructed ^{6}Li+p spectrum. The two kinematical solutions of the reaction were obtained in 3 different runs with 3 sets of magnetic fields. The plot shows the superposition of these runs, designated with different colors. The black solid line represents the theoretical prediction which seems to describe perfectly well the data, giving further support to the accurate spectrum reconstruction.

EXPERIMENTAL DETAILS AND RESULTS

The experiment was performed at LNS-INFN-Italy. Beams of $^{6}Li^{+3}$ were accelerated at the energies 16, 20, 25 and 29MeV and impinged on a 240 μg/cm^2 CH_2 target. Measurements were repeated with a ^{12}C target of similar thickness, for estimating the carbon background. The beam charge was collected by a Faraday cup, set at the entrance of MAGNEX and its absolute value was re-confirmed via the measurement at the very forward angles, where the elastic scattering is Rutherford. In this way our measurements can considered as absolute and can be used to clarify possible inconsistencies of previous data. The elastically scattered lithium ions were momentum analyzed by the MAGNEX spectrometer [14-16] set at $\theta_{opt}=4^0$, working in a full horizontal angular acceptance and detected by its focal plane detector [17]. The vertical acceptance of MAGNEX was reduced for protecting the focal plane detectors from the elastic high counting rate. Our data reduction technique, based on a differential algebraic method [18] and the performances of the whole system are described in Refs [19-20].

The two kinematical solutions of the ejectiles were measured by the application of three different magnetic fields. A typical reconstructed spectrum at projectile energy of 29 MeV, obtained with the superposition of the three different sets, is displayed in Figure 1. For an angular step of 0.5^0 the counts were integrated and the solid angle, defined by 4 slits located at 250mm from the target, was calculated taking into account the contour of the reconstructed (θ_i-φ_i) locus [21]. The solid angle uncertainty is estimated to be ~2%. The differential cross sections, obtained at the projectile energy of 29 MeV are compared in Figure 2 with previous measurements as well as with JLM calculations. It is obvious that our data are in very good consistency with previous results, while the JLM calculations fail to reproduce the data. Continuum Discretized Coupled Channel calculations are in progress and will be presented in a fourth coming article. Further data analysis is also in progress.

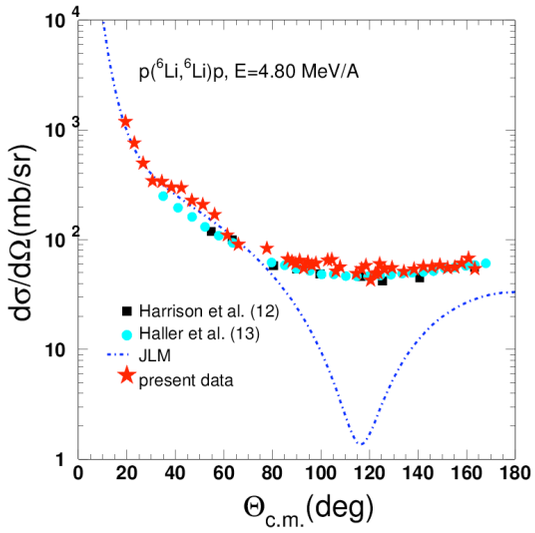

Figure 2: Present elastic scattering data for ^{6}Li+p at 29MeV are compared with previous values [12, 13] as well as with JLM calculations.

REFERENCES

[1] N. Alamanos et al., Nucl. Phys. A 660 (1999) 406.
[2] A. Pakou et al., Nucl. Phys. A 691 (2001) 661.
[3] N. Alamanos et al., J. Phys. G24 (1998) 541.
[4] A. de Vismes et al.,Phys. Lett. B 505 (2001) 15.
[5] A. Lagoyiannis et al., Phys. Lett. B518 (2001) 27.
[6] V. Lapoux et al., Nucl. Phys. A722 (2003) 49c.
[7] F. Skaza et al., Phys. Lett. B 619 (2005) 82.
[8] A. Gillibert et al., Nucl. Phys. A787 (2007) 423c.
[9] N. Patronis et al., Phys. Rev. C 85 (2012) 024609.
[10] J. P. Jeukenne, A. Lejeune, C. Mahaux; Phys. Rev. C 16 (1977) 80.
[11] M. Skill et al., Nucl. Phys. A581 (1995) 93.
[12] W. D. Harisson and A. B. Writehead; Phys. Rev 132 (1963) 2607.
[13] M. Haller et al., Nucl. Phys. A496 (1989) 189.
[14] A. Cunsolo et al., Eur. Phys. J. Special Topics 150 (2007) 343.
[15] A. Cunsolo et al., NIM A 484 (2002)56.
[16] A. Cunsolo et al., NIM A 481 (2002) 48.
[17] M. Cavallaro et al., Eur. Phys. J. A 48 (2012) 59.
[18] F. Cappuzzello et al., NIM A 638 (2011) 74.
[19] F. Cappuzzello et al., NIM A 621 (2010) 419.
[20] M. Cavallaro et al., NIM A 648 (2011) 46.
[21] M. Cavallaro et al., NIM A 637 (2011) 77.

Measurement of the 10 keV resonance in the ^{10}B(p,α_0)^{7}Be reaction via the Trojan Horse method

C. Spitaleri[1,2], L.Lamia[1], S.M.R.Puglia[2], S. Romano[1,2], M. La Cognata[2], V. Crucillà[12], R.G. Pizzone[2], G. G. Rapisarda[12], M. L. Sergi[2] , M. Gimenez Del Santo[3] , N. Carlin[3], M. G. Munhoz[3], F. A. Souza[3], A. Szanto de Toledo[3], B. Irgaziev[4], A. Mukhamedzhanov[5], G. Tabacaru[5], V. Burjan[6], V. Kroha[6], Z. Hons[6], J. Mrazek[6], Shu-Hua Zhou[7], Chengbo Li[8], Qungang Wen[9], Y. Wakabayashi[10], H. Yamaguchi[10] and E. Somorjai[11]

1) Dipartimento di Fisica e Astronomia, Universita` di Catania, Catania, Italy
2) INFN, Laboratori Nazionali del Sud, Catania, Italy
3) Departamento de Fisica Nuclear, Universitade de Sao Paulo, Sao Paulo, Brasil
4) GIK Institute of Engineering Sciences and Technology, Topi, Districti Swabi, Khyber Pakhtunkhwa, Pakistan
5) Cyclotron Institute, Texas A&M University, College Station, Texas 77843, USA
6) Nuclear Physics Institute of ASCR, Rez, Czech Republic
7) China Institute of Atomic Energy, Beijing, China
8) Beijing Radiation Center, 100875 Beijing
9) China Auhui University, 23060 Hefei, China
10) Center for Nuclear Study, University of Tokyo, RIKEN Campus, 2-1 Hirosawa, Wako, Saitama 351-0198, Japan
11) Institute for Nuclear Research (ATOMKI), Debrecen, Hungary

Abstract - Nuclear reaction rates are among the most important input for understanding the primordial nucleosynthesis and therefore for a quantitative description of the early Universe. An up-to-date compilation of direct cross sections of reactions is given. These are among the most uncertain cross sections used and input for Big Bang nucleosynthesis calculations. Their measurements through the Trojan Horse Method (THM) are also reviewed and compared with direct data. The reaction rates and the corresponding recommended errors in this work were used as input for primordial nucleosynthesis calculations to evaluate their impact on the primordial abundances, which are then compared with observations.

INTRODUCTION

Boron-depleting reactions play an important role in understanding different scenarios, ranging from astrophysics to applied nuclear physics. In particular, the measurements of (p,α) reactions on boron, beryllium, and lithium isotopes are of particular interest to determine light element abundances in stars. These elements are destroyed at different depths in stellar interiors, and residual (atmospheric) abundances can be used to constrain mixing phenomena occurring in such stars [1]. Boron burning is triggered at temperatures $T \geq 5\times10^6$ K and takes place mainly through the (p,α) processes, with a Gamow peak centered at about 10 keV. In this context, the ^{10}B(p,α_0)^{7}Be reaction, for which the ^{7}Be nucleus is left in its ground state, has special interest.

However, direct cross section measurements at ultralow energies are extremely difficult to perform, mainly because of the Coulomb barrier penetrability [2] and of the electron screening effects [3,4]. To remove the strong energy dependence due to Coulomb barrier penetration, the astrophysical S(E) factor is introduced via the relation $S(E) = E\,\sigma(E)\,\exp(2\pi\eta)$, where E is the center-of-mass energy, η is the Sommerfeld parameter.

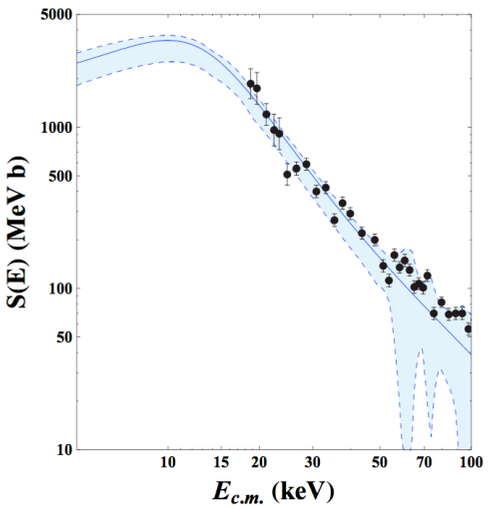

Figure 1: (Color online) The TH ^{10}B(p,α_0)^{7}Be S(E) factor at infinite resolution, together with its allowed upper and lower limits as given by the corresponding uncertainties,.

To overcome the difficulties related to the suppression of the cross section at ultralow energies, indirect techniques have proven to be effective. In particular, the Trojan Horse method (THM, [5-8], and references therein) provides, at present, one of the most powerful techniques for measuring the energy dependence of the bare nucleus cross section down to astrophysically relevant energies. The THM allows one to extract the low-energy S(E) range where the electron screening effects are negligible

to reduce systematic errors. The THM has been successfully applied to measure the bare nucleus cross sections of several reactions related to fundamental astrophysical and nuclear physics problems [] (participant) and the cluster S acting as a spectator to the x + B → C + D virtual reaction. The nucleus A should have a strong x + S cluster structure to maximize the QF breakup yield. When this reaction mechanism is present, it can be distinguishable from others in a region of the three body phase space where the intercluster momentum (p_{x-S}) of the spectator S is small, i.e., for QF conditions. The THM has its background in the theory of direct reactions (see, e.g., []), and in particular in the studies of

RESULTS

By following then the typical THM data analysis procedure, we have firstly determined the QF-contribution to the total ^{2}H(^{10}B,α^{7}Be)n experimental yield and then extracted the THM S(E)-factor by means of PWIA (see details in [7,8]). Thus, to determine the bare nucleus THM S_b(E) factor in absolute units, the direct data of [10-12] have been used, as shown in Fig.2. However, low-energy direct measurements are strongly affected by the electron screening effects [12], thus the absolute scale on the S_b(E) factor needs to be obtained by normalizing the TH data to the OES one in an energy

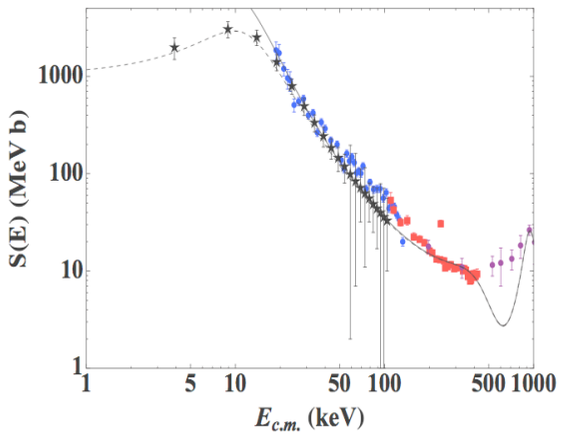

Figure 2: Color online) The THM S(E) factor (black stars), as given in Table IV, compared with the R-matrix calculation (dashed line) and with the one including electron screening (full line). Red symbols mark the direct data.

Figure 1 shows the comparison between the direct data of and the THM S(E) factor at infinite resolution (full blue line) together with its allowed upper and lower values (dashed blue lines). The 10 keV THM S(E) factor is S(10 keV)TH = 3127 ± 583 MeV b, with the error including statistical, subthreshold subtraction, channel radius, and normalization uncertainties. The THM value is in agreement with the extrapolated 2870 ± 500 MeV b [12].

Table I lists the S(E) factor values in the literature and the ones obtained in this work, while in Fig. 2 we compare our THM S(E) factor with the R-matrix calculation previously described. Figure 2 shows a very good agreement between two independent approaches, namely, the experimental THM (stars) and the R-matrix calculation performed taking the resonance parameters in the literature (dashed and solidlines for bare-nucleus and screened astrophysical factors, respectively).

Table I: The 10B(p,α)7Be S(E) factor values as given in the literature and as obtained in the present work.

S(0) (MeV b)	S(10 keV) (MeV b)	Approach	Ref.
	2200 ± 600	Direct exp.	[11]
	2870 ± 500	Direct exp.	[12]
800	3480	DWBA	[13]
1116	3105	R-matrix	
1247 ± 312	3147 ± 583	THM	[2]

The present THM investigation of the ^{10}B(p,α_0)^{7}Be reaction leads to S(10 keV)$_{TH}$ = 3127 ± 583 MeV b for the S(E) factor value in correspondence with the 10 keV resonance, in which the quoted error accounts for statistical, subthreshold subtraction, normalization, and channel radius uncertainties. By using the measured bare-nucleus TH S(E) factor, a value of 240 ± 200 eV has been deduced for the electron screening potential value, where the large error takes into account the uncertainties on the TH S(E) factor.

The authors acknowledge the support of the Italian Ministry of Education, University and Research under grant Progetto Premiale ASTROF.MIUR PFE, CD 19/12/2012 n. 12609'

REFERENCES

[1] C. Rolfs and W. Rodney, in *Cauldrons in the Cosmos* (The University of Chicago Press, Chicago, 1988), p.561
[2] C.Spitaleri et al. Phys. Rev. C **9,** 035801 (2013)
[3] H. Assenbaum et al., Z. Phys. A **327**, 461 (1987).
[4] F. Strieder et al. Naturwissenschaften **88**, 461 (2001).
[5] G. Baur *et al.*, Nucl. Phys. A **458**, 188 (1986).
[6] C. Spitaleri et al. Phys. At. Nucl. **74**, 1725 (2011).
[7] C. Spitaleri, International School of Physics "Enrico Fermi" edited by A. Bracco and E. Nappi (Academic, New York, 2011), p. 210.
[8] R.Tribble, C.Bertulani, A.M.Mukamedzhanov, M.La Cognata, C.Spitaleri, Rep. Progr. Phys. 77, 106901 (2014)
[9] L. Lamia *et al.*, Il Nuovo Cimento C **31**, 423 (2008).
[10] M. G. Del Santo *et al.*, Proc. Sci. **53**, 2496 (2008).
[11] M. Youn *et al.*, Nucl. Phys. A **533**, 321 (1991)
[12] C. Angulo *et al.*, Z. Phys. A **187**, 345 (1993).
[13] T. Rauscher and G. Raimann, Phys. Rev. C **53**, 2496 (1996).

Astrophysical factor and reaction rate of the $^{13}C(\alpha,n)^{16}O$ reactions under astrophysical conditions

M. La Cognata[1], C. Spitaleri[1,2], O. Trippella[1,3], G. G. Kiss[1,4], G. V. Rogachev[5], A. M. Mukhamedzhanov[6], M. Avila[5], G. L. Guardo[1,2], E. Koshchiy[5], A. Kuchera[5], L. Lamia[2], S. M. R. Puglia[1,2], S. Romano[1,2], D. Santiago[5], R. Spartà[1,2]

1) Istituto Nazionale di Fisica Nucleare - Laboratori Nazionali del Sud, Catania, Italy
2) Dipartimento di Fisica e Astronomia, University of Catania, Catania, Italy
3) INFN - Sezione di Perugia & Dipartimento di Fisica, University of Perugia, Perugia, Italy
4) Institute of Nuclear Research (ATOMKI), Debrecen, Hungary
5) Department of Physics, Florida State University, Tallahassee, FL, USA
6) Cyclotron Institute, Texas A&M University, College Station, TX, USA

Abstract - The $^{13}C(\alpha,n)^{16}O$ reaction is the neutron source for the main component of the s-process, responsible for the production of most of the nuclei in the mass range $90 \leq A \leq 208$. This reaction takes place inside the helium-burning shell of asymptotic giant branch stars, at temperatures $\sim 10^8$ K, corresponding to an energy interval where the $^{13}C(\alpha,n)^{16}O$ reaction is effective of 140–230 keV. In this regime, the astrophysical S(E)-factor is dominated by the −3 keV sub-threshold resonance due to the 6.356 MeV level in ^{17}O. To provide a more accurate S-factor at these energies, we have applied the Trojan horse method (THM) to the $^{13}C(^6Li,n^{16}O)d$ quasi-free reaction, leading to an unprecedented accuracy in the determination of the reaction rate for astrophysical applications.

BACKGROUND

The origin of the chemical elements has been subject of quantitative investigations since the born of modern physics. Regarding $90 \leq A \leq 204$ nuclei, a major nucleosynthesis site has been identified in low-mass ($< 3M_\odot$) asymptotic giant branch (AGB) stars [1], responsible for the production of heavy elements along the stability valley through slow neutron captures (s-process) [2]. In these stars, protons mixed downward following the quenching of the H-burning shell are quickly captured by carbon nuclei, eventually lead- ing to the formation of a ^{13}C pocket [3]. Then, ^{13}C nuclei give up their excess neutrons to heavier nuclei through the $^{13}C(\alpha,n)^{16}O$ reaction, at temperatures varying between 0.8 10^8 K and 1 10^8 K [4]. At 0.9 10^8 K, the energy range where the 13C(α,n)16O reaction is most effective, the Gamow window [5], is $\sim 140 - 230$ keV.

In such region, its direct measurement is exceedingly challenging because of the Coulomb barrier, exponentially suppressing the cross section, and the interplay between the rise of the cross section due to the sub threshold resonance at -3 keV due to the 6.356 MeV ^{17}O level and atomic electron screening. Indeed, discrepancies between extrapolations [6], advanced theoretical calculations, such as the microscopic two-cluster model [7], and indirect measurements proceeding through the determination of the ^{13}C-α spectroscopic factor [8,9] and ANC [10] for the 6.356 MeV ^{17}O state suggest an incomplete knowledge of the low-energy $^{13}C(\alpha,n)^{16}O$ S(E)-factor.

ASTROPHYSICAL FACTOR AND REACTION RATE

The Trojan horse method (THM) allowed us to study the $^{13}C(\alpha,n)^{16}O$ reaction free of Coulomb suppression and electron screening with no need of extrapolation (see [11] for a review on the method). In the THM, the low-energy cross section of a *A(x,c)C* reaction is obtained by extracting the quasi-free (QF) contribution to a suitable *A(a,cC)s* reaction. Particle *x* is virtual so the *A(x,c)C* THM cross section is half-off-energy-shell (HOES) and cannot be right juxtaposed to the direct (on-energy-shell, OES) cross section. In the case of resonance reactions, the modified R-matrix approach has been devised ([12,13] and references therein) to extract the reduced γ-widths, which are the parameters of interest as they appear in both the HOES and in OES astrophysical factor, and can be used then to reproduce the $^{13}C(\alpha,n)^{16}O$ astrophysical factor down to zero energy with no need of extrapolation, devoid of HOES effects.

The experiment was performed at the John D. Fox Superconducting Linear Accelerator Facility at Florida State University, which delivered a 7.82 MeV, 1 mm spot ^6Li beam impinging onto a 99% ^{13}C enriched foil 53 μg/cm2 thick. Therefore, we used ^6Li, having a well known α+*d* structure, to transfer an α-particle to ^{13}C while *d* was emitted without interacting in QF kinematics. ^{16}O from the $^{13}C(\alpha,n)^{16}O$ sub reaction and deuterons were detected, to maximize the detection efficiency and reduce systematic uncertainties. Details on the experiment and the data analysis are given in [12,13].

The $^{13}C(\alpha,n)^{16}O$ astrophysical factor

Figure 1 shows the comparison of the THM S(E)-factor of the $^{13}C(\alpha,n)^{16}O$ reaction with the available direct data. Our result is given as a red band; the middle line is the best fit curve and the upper and lower red lines delineate the recommended range allowed by the statistical, normalization, and data reduction uncertainties. Only the uncertainty due to the −3 keV resonance is displayed; the error due to the accuracy of the R-matrix fit of Heil et al. [6], which is used for normalization, is smaller than 5%. For comparison, the S-factor omitting the contribution of the 6.356 MeV ^{17}O level is also shown in this figure as a blue line. The black points represent the available direct $^{13}C(\alpha,n)^{16}O$ data from [6] and references therein, namely, scaled to match the high-precision data reported in this work. A very good agreement is found between the THM S(E)-factor and experimental data, as should be expected since no electron screening significantly alters yet the low-energy trend at the measured energies.

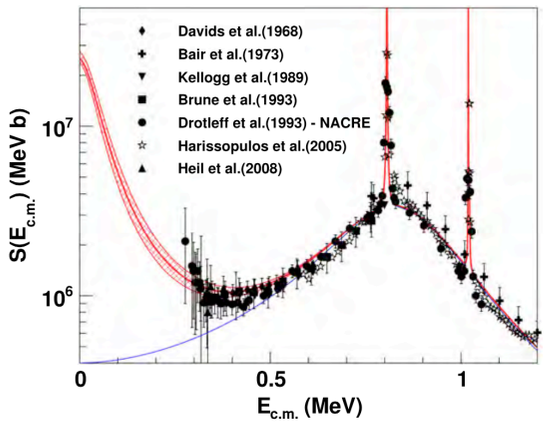

Figure 1: THM astrophysical factor of the $^{13}C(\alpha,n)^{16}O$ reaction (red), compared with direct data (symbols). The blue line shows its trend in the case no resonance at -3 keV is present. THM data are from Ref. [13].

The $^{13}C(\alpha,n)^{16}O$ reaction rate

Figure Figure 2(a) shows the reaction rate R calculated from the S(E)-factor using the standard formula [5]. Upper and lower limits are also given, but they are barely visible because of the steep decrease of R with decreasing temperature and the small errors, adding up to about 16%. In Figure 2(b), we compare the present $^{13}C(\alpha,n)^{16}O$ reaction rate with the one reported in [6] (R_{Heil}). For ease of comparison, the quantity R/R_{Heil} is given. In this way, the strong temperature dependence is divided out. The ratio of the THM rate to the one obtained by [6] is given by the red band, delimiting the interval allowed by the uncertainties. Other rates available in the literature are also shown in Figure 18(b), divided by the rate in [6]. In particular, the black hatched area indicates the NACRE rate [14] divided by the one in [6]. The solid black line highlights the ratio of the rate [15] to R_{Heil} and, finally, the brown line is obtained from the ratio of the rate based on the preliminary results of [12] to R_{Heil}.

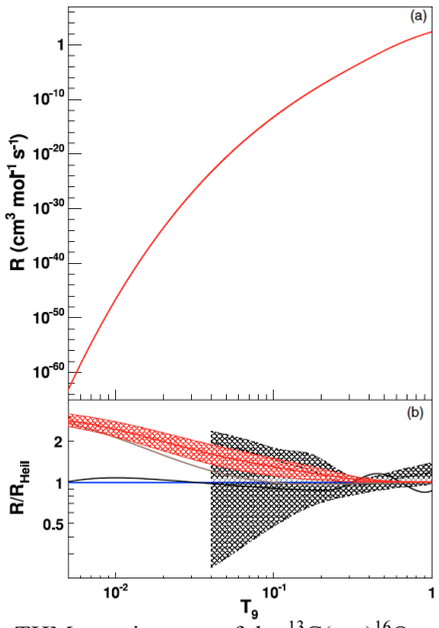

Figure 2: THM reaction rate of the $^{13}C(\alpha,n)^{16}O$ reaction (red band), compared with other rates in the literature (see text for details), in log- and linear scales, panel (a) and (b), respectively. In the latter case, ratios of the reaction rates are shown. THM data are from Ref. [13].

This work has been supported in part by MIUR under grant RBFR082838

REFERENCES

[1] B. Meyer, Annu. Rev. Astron. Astrophys. 32 (1994) 153.
[2] F. Käppeler et al., Reviews of Modern Physics 83 (2011) 157.
[3] R. Gallino, et al., Astrophys. J. 497 (1998) 388.
[4] M. Busso et al., Annu. Rev. Astron. Astrophys. 37 (1999) 239.
[5] C. Iliadis, Nuclear Physics of Stars, Wiley-VCH Verlag, 2007.
[6] M. Heil et al., Phys. Rev. C 78 (2008) 025803.
[7] M. Dufour, and P. Descouvemont, Phys. Rev. C 72 (2005) 015801.
[8] S. Kubono et al., Phys. Rev. Lett. 90 (2003) 062501.
[9] M. G. Pellegriti et al., Phys. Rev. C 77 (2008) 042801.
[10] E.D. Johnson et al., Phys. Rev. Lett. 97 (2006) 192701.
[11] R.E. Tribble et al., Rep. Prog. Phys. 77 (2014) 106901.
[12] M. La Cognata et al., Phys. Rev. Lett. 109 (2012) 232701.
[13] M. La Cognata et al., Astrophys. J. 777 (2013) 143.
[14] C. Angulo et al., Nuclear Physics A 656 (1999) 3.
[15] H. W. Drotleff et al., Astrophys. J. 414 (1993) 735

The $^{18}F(p,\alpha)^{15}O$ reaction studied via THM

R.G. Pizzone[1*], B.T.Roeder[2], L. Trache[2], C.Spitaleri[1,3], C. Bertulani[4], S. Cherubini[3], V.Z. Goldberg[2], M.Gulino[1,5], M. Kurokawa[2], I.Indelicato[1,3], M. La Cognata[1], L. Lamia[1], M.McCluskey[2], G.G.Rapisarda[1], E. Simmons[2], R.Spartà[1,3], A.Spiridon[2], R.E.Tribble[2]

1)INFN Laboratori Nazionali del Sud, Catania, Italy
2) Cyclotron Institute, Texas A&M University, College Station, USA
3) Dipartimento di Fisica e Astronomia, Università di Catania Italy
4) Physics and Astronomy department, Taxas A&M University, Commerce, USA
5)Università KORE, Enna, Italy

INTRODUCTION

Classical Novae Gamma-ray emission is dominated, during the first hours of the explosion, by positron annihilation resulting from the beta decay of radioactive nuclei. The main contribute to this process arises from the decay of the ^{18}F [1]. Therefore it is directly related to ^{18}F production and destruction during the outburst. Among the physical inputs, which are necessary to uncover the 18F nucleosinthesis a crucial role is played by the proton captures. The abundance of ^{18}F depends largely on few reaction rated among which the $^{18}F(p,\alpha)^{15}O$ is present.

Measuring cross sections at astrophysical energies (in the case of novae nucleosynthesis few hundreds keV) in the case of charged particle induced reactions is very difficult and this becomes an almost impossible task in the case of radioactive ion beams induced reactions. In order to by-pass these problems indirect methods are usually applied and among them one of the most powerful in the case of charged particle induced reactions is the Trojan Horse Method (THM) [2,3,4].

In particular, the THM selects the quasi-free (QF) contribution of an appropriate three-body reaction performed at energies well above the Coulomb barrier to extract a charged particle two-body cross section. The idea of the THM is to extract the cross section of an astrophysically relevant two-body reaction A(x,c)C at low energies from a suitable chosen three-body quasifree reaction A(a,cC)S. This is done with the help of direct theory assuming that the nucleus a has a strong x,S cluster structure. In many applications this assumption is trivially fulfilled e.g. a = deuteron, x = proton, S=neutron. This three-body reaction can be described by a Pseudo-Feynmam diagram, where only the first term of the Feynman series is retained.

The upper pole describes the virtual break-up of the target nucleus a into the clusters x and S; S is then considered to be spectator to the A(x,c)C reaction which takes place in the lower pole. In the present case we plan to study the $^{18}F(p,\alpha)^{15}O$ through the $^{18}F(d,\alpha^{15}O)n$ (see figure 1 for the present case); thus the deuteron will act like Trojan Horse nucleus, p as participant and neutron as spectator.

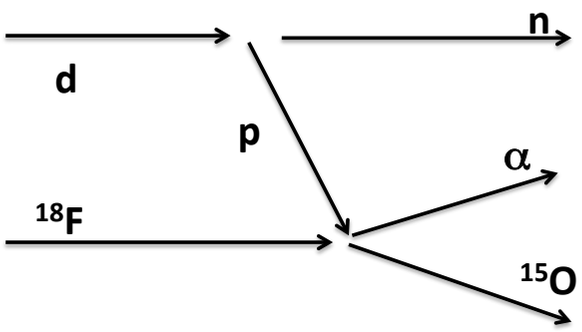

Figure 1: Schematic skets of the quasi-free reaction studied in the present experiment

Once the three body reaction cross section is determined (by means of ^{15}O and α detection in coincidence) it is possible to extract the binary reaction cross section of interest (in our case the $^{18}F(p,\alpha)^{15}O$) at the energies of astrophysical interest.

In the simplest approach, the plane wave impulse approximation, the three body cross section can be factorized as:

$$d\sigma/dE_a\, d\Omega_a\, d\Omega_{15O} \propto (KF)\, |\Phi(p_s)|^2\, d\sigma^N/d\Omega$$

where KF is a kinematical factor containing the final state phase space factor, $|\Phi(p_s)|^2$ is the momentum distribution of the spectator *neutron* inside *deuteron*, and $d\sigma^N/d\Omega$ is the differential nuclear cross section for the two body reaction $^{18}F(p,\alpha)^{15}O$ [5,6].

The experiment was performed at the Cyclotron Institute of the Texas A&M University where the K500 cyclotron provided an ^{18}O beam as a primary beam at 9 A MeV. The K150 cyclotron was used in the beginning of the run for the same purpose, but problems to the injection line prevented to use this machine for the entire

[1] Visiting Scientist, Cyclotron Institute, TAMU, College Station USA

run. The MARS spectrometer was then used to get a ^{18}F beam via the p(18O,18F)n reaction, after energy degrading of the primary beam by means of 1.25 mils Al degrader. The obtained secondary beam was tuned through MARS with a final energy of 56,7 MeV and then the beam-spot was tuned at the TECSA target position on a position sensitive detector. A beam-spot of 3 x 5 mm was obtained after the tuning was completed. The energy spread of the beam was around 2%. The isotopic purity of the beam was checked during the tuning and it was found that the beam was 94% pure and the intensity of the beam was about 3-4 x 10^5 ions/sec. All these beam characteristics are clear from figure 2 where the energy is reported as a function of y position in the target detector.

The beam impinged on an isotopically enriched deuterated polyethylene target (98% purity) around 800 $\mu g/cm^2$ thick. The experimental set-up consisted of two detector arrays working in coincidence. The TECSA array (TExas Edinburgh Catania Silicon Array) [7], made up of 8 YY-1-300 Micron detectors (each one with 16 strips), was set at 190 mm from target covering angles in the range $\theta=15^o$-40^o. Closer to the beam axis a second detector array, the CROSS, is placed, consisting of two position sensitive detectors (16 strips each), placed at 340 mm and covering angles from 3 to 12 degrees. The TECSA array was devoted to the detection of the alpha particles while the CROSS was used to detect the ^{15}O in coincidence. The experimental set-up is sketched in figure 3. The displacement of the experimental setup was chosen in order to cover the whole Quasi-Free angular range, known "a priori" from a Monte Carlo simulation. A scintillator was used to improve the definition of the timing of the experiment.

The detectors were calibrated in energy by means of standard alpha sources and ^{18}F scattering off the CD_2 target. The CROSS detector was also calibrated in position by means of an a mask which was used during the calibration runs. The measurement of the energy and position of the two ejectiles will give the possibility to calculate all the kinematic variables regarding the third, undetected, particle as well as other variables of interest for the following data analysis (e.g. Q-value, relative energy α-^{15}O, spectator momentum).

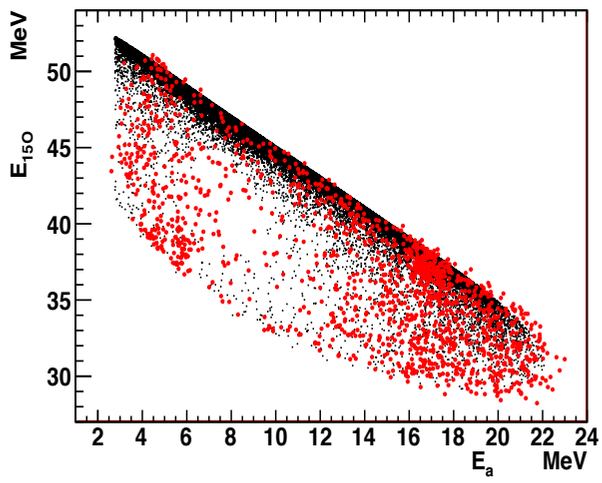

Figure 2: Typical kinematic locus for the α-^{15}O coincidence for one strip of detector #4 of TECSA and the bottom detector of the CROSS. The red curve marks the region where the three body reaction of interest is expected.

After calibration (and taking into account the energy loss of beam and ejectiles in the target) the kinematic locus of α-^{15}O energy is studied and plotted in figure 2. The experimental data are compared with a Montecarlo simulation taking into account the geometrical and physical conditions of the present experimental run. After selecting the relevant data arising from the the $^{18}F(d,\alpha^{15}O)n$ by means of a graphical cut the data analysis under the THM stander prescriptions will be carried on aiming at extracting the astrophysical S(E)-factor at the novae nucleosynthesys energy range.

This work was supported by the Italian Ministry of the University under Grant No. RBFR082838 and by the Italian Ministry of University MIUR under the grant "LNS Astrofisica Nucleare (fondi premiali)".

REFERENCES

[[1] A. Coc et al., A.& A. 357, 561 (2000)

[2] S. Cherubini et al., Ap. J. 457, 855 (1996)

[3] C. Spitaleri et al., Phys. Rev. C 60, 055802 (1999)

[4] R.G. Pizzone et al., Phys. Rev C 71, 058801 (2005)

[5] C. Spitaleri et al., Phys. Rev. C 63, 055806 (2004)

[6] C. Spitaleri et al., Phys. Rev. C 63, 005801 (2001)

[7] B.T. Roeder et al., Nucl. Instr. and Meths. A634 (2011) 71-76.

Big Bang nucleosynthesis revisited via Trojan Horse Method measurements

R.G. Pizzone[1], R. Spartà[1], C. Bertulani, C. Spitaleri[1,2], A. Mukhamedzhanov[4], M. La Cognata[1], L. Lamia[2], A. Tumino[1,5]

1 INFN - Laboratori Nazionali del Sud, Catania, Italy

2 Dipartimento di Fisica e Astronomia, Università degli Studi di Catania, Catania, Italy

3 Department of Physics and Astronomy, Texas A\&M University, Commerce, TX 75025, USA

4 Cyclotron Institute, Texas A\& M University, College Station, TX, USA

5 Universita' degli Studi di Enna ``Kore", Enna, Italy

Abstract - Nuclear reaction rates are among the most important input for understanding the primordial nucleosynthesis and therefore for a quantitative description of the early Universe. An up-to-date compilation of direct cross sections of reactions is given. These are among the most uncertain cross sections used and input for Big Bang nucleosynthesis calculations. Their measurements through the Trojan Horse Method (THM) are also reviewed and compared with direct data.

The reaction rates and the corresponding recommended errors in this work were used as input for primordial nucleosynthesis calculations to evaluate their impact on the primordial abundances, which are then compared with observations.

INTRODUCTION

Over the last decades Big Bang Nucleosynthesis (BBN) has emerged as one of the pillars of the Big Bang model, together with the Hubble expansion and the Cosmic Microwave Background (CMB) radiation. BBN probes the Universe to the earliest times, from a fraction of second to few minutes.

It involves events that occurred at temperatures below 1 MeV, and naturally plays a key role in forging the connection between cosmology and nuclear physics. Focusing only on the products of the BBN, according to the Standard Big Bang Nucleosynthesis model (SBBN), only the formation of light nuclei (^{2}H,^{3,4}He,^{7}Li) is predicted in observable quantities, starting from protons and neutrons. Today, with the only exception of lithium, the abundances of these isotopes in the appropriate astrophysical environments are rather consistent with SBBN predictions. A comparison between the primordial abundances from WMAP observations and the calculated ones constrains the baryon-to-photon ratio, η, which is the only free parameter in the presently accepted model of the SBBN. BBN nucleosynthesis requires several nuclear physics inputs and, among them, an important role is played by nuclear reaction rates. Due to the relatively small amount of key nuclear species involved in the BBN nuclear reaction network, only 12 reactions play a major role[1,2]. The reaction rates are calculated from the available low-energy cross sections for reactions which are also a fundamental information for a number of other still unsolved astrophysical problems, e.g. the so called ``lithium depletion" either in the Sun or in other galactic stars. Cross sections should be measured in the astrophysically relevant Gamow window, of the order of few hundreds keV. In the last decades these reactions have been widely studied and, in particular, great efforts have been devoted to their study by means of direct measurements at the relevant astrophysical energies, sometimes in underground laboratories or improved detection systems.

An experimental program has been carried out during the last decade to apply the THM to study reactions of relevance for the SBBN. In the next sections, we will first discuss the available direct data for these 4 reactions in order to calculate their rate. We will show the calculations of the reaction rates based also on the THM measurements of the cross sections. Such studies are necessary, as the Trojan Horse method has become one of the major tools for the investigation of reactions of astrophysical interest. Thus, the method can be regarded as a powerful indirect technique to get information about bare nucleus cross section for reactions of astrophysical interest, which leads to new reaction rates determination [3].

The reactions of interest for the SBBN i.e. ^{7}Li(p,a)^{4}He, ^{2}H(d,p)^{3}H, ^{2}H(d,n)^{3}He, ^{3}He(d,p)^{4}He, were studied by means of the THM in the energy range of interest and their measurements were performed in an experimental campaign which took place in the last decade

RESULTS

The reaction rates for the the four reactions mentioned above (from a compilation of direct and THM data, as reported in the sections above) have been carried out numerically introducing the R-matrix results. Thus, we fitted the rates with the parametrization displayed in [1]. For the 4 reactions of interest, we have included the experimental errors from measurements, allowing us to evaluate the respective errors in the reaction rates.

The SBBN is sensitive to certain parameters, including the baryon-to-photon ratio, the number of neutrino families, and the neutron decay lifetime. We use the values $\eta = 6.16\ 10^{-10}$ for the baryon-photon ratio, the number of neutrino families N = 3, and the neutron lifetime τ_n = 878.5 s, respectively [1] and references therein). Our BBN abundances were calculated with a modified version of the standard BBN code derived from the pioneering work of Kawano.

In Figure 1 we show the results for the abundances as a function of time The uncertainties in the experimental nuclear data are reflected in the width of the predicted abundances. In Table 1 the first column is the result obtained with our own fit to the world data from direct measurements. The column labelled ``all" uses all four reaction rates calculated in this paper. Finally, the last column lists the observed abundances. The uncertainties in the experimental data are reflected in the errors for the predicted abundances. As expected, the abundance of ^{4}He is barely affected by the new measurements. Also, some of the abundances are not affected by changes in reactions not directly related to the production or destruction of the element. Some appreciable changes in the abundances of d, ^{3}He and ^{7}Li are visible.

The present work gives an exhaustive and updated review of the rate reaction evaluation for some of the relevant reactions for nuclear astrophysics (arising both from direct and indirect methods). We can point out that the discrepancy calculated-to-observed is still evident, as seen in many other investigations [2] and it seems to not be due to nuclear reaction rates uncertainties.

This work was supported by the Italian Ministry of the University under Grant No. RBFR082838 and by the Italian Ministry of University MIUR under the grant "LNS Astrofisica Nucleare (fondi premiali)".

Table 1: Comparison of the abundances calculated in this paper with observed value (see [1] for references)

Isotope	**Calculated in present paper**	**Observation**
He/H	0,2485±0,002	0,256 ±0006
D/H (10^{-5})	2,692±0,2	2,82± 0,26
^{3}He/H (10^{-6})	9,441±0,5	>11 ±2
^{7}Li/H (10^{-10})	4,683 ±0,3	1,58± 0.3
Left	20 mm	20 mm (0.79 in)
Right	20 mm	26 mm (1.0 in)

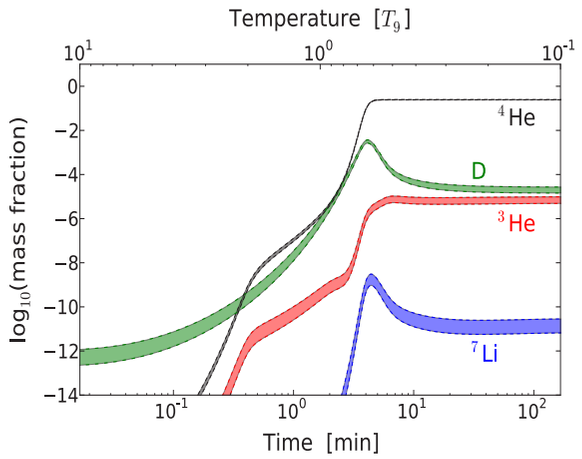

Figure 1: Calculated BBN abundance of primordial elements as a function of time and temperature. Black line represents ^{4}He mass fraction, green the deuterium abundance, red the ^{3}He abundance and blue the ^{7}Li abundance. The error band represents the uncertainty in the THM measurements and their influence on the abundances.

REFERENCES

[1] R.G. Pizzone et al., Ap. J. 786 (2014) 112
[2] G.Steigman,Ann.Rev.Nucl.Part. Sci.,57(2007) 463
[3] R.E.Tribble et al., Rep. Progr. Phys., 77 (2014) 106901

Recent developments on the THM $^{17}O(p,\alpha)^{14}N$ study

M.L. Sergi[1], C. Spitaleri[1,2], B. Bucher[3], M. Couder[3], P. Davies[3], R. deBoer[3], X. Fang[3], B. Irgaziev[4], V. Kroha[5], M. La Cognata[1], L. Lamia[2], C. Ma[3], J. Mrazek[5], A. Mukhamedzhanov[6], M. Notani[3], S. O' Brien[3], R.G. Pizzone[1], G.G. Rapisarda[2], S. Robertson[3], W. Tan[3], X.D. Tang[3], M. Wischer[3]

1) INFN, Laboratori Nazionali del Sud, Catania, Italy
2) Dipartimento di Fisica e Astronomia, Univerità degli Studi di Catania, Catania, Italy
3) Department of Physic, Joint Institute for Nuclear Astrophysics, University of Notre Dame, Indiana, USA
4) GIK Institute of Engineering Sciences and Technology, Topi District, Swabi NWFP, Pakistan
5) Nuclear Physics Institute of ASCR, Rez, Czech Republic
6) Cyclotron Institute, Texas A&M University, College Station, TX 77843, USA

Abstract - In recent years, the Trojan Horse Method (THM) has been used to investigate the low-energy cross sections of proton-induced reactions on ^{17}O nuclei, overcoming extrapolation procedures and enhancement e_ects due to electron screening. We will report on the indirect study of the $^{17}O(p,\alpha)^{14}N$ reaction via the THM by applying the approach recently developed for extracting the resonance strength of narrow resonance in the ultra-low energy region. Two measurements will be discussed and the experimental THM cross sections will be shown for both experiments.

INTRODUCTION

The ^{17}O+p reactions are of paramount importance for the nucleosynthesis in a number of stellar sites, including red giants (RG), asymptotic giant branch (AGB) stars, massive stars and classical novae [1, 2]. In particular the $^{17}O(p,\alpha)^{14}N$ and $^{17}O(p,\gamma)^{18}F$ reaction govern the destruction of ^{17}O and the formation of the short-live radio-isotope ^{18}F which is of special interest for gamma ray astronomy [1, 2]. At temperatures typical of the above mentioned astrophysical scenario, T=0.01-0.1 GK for RG, AGB and massive stars and T=0.1-0.4 GK for classical nova explosion, the $^{17}O(p,\alpha)^{14}N$ reaction cross section is dominated by two resonances: one at about $E_{c.m.}^{R}$ =65 keV above the ^{18}F proton threshold energy, corresponding to the E_X=5.673 MeV level in ^{18}F, and another one at $E_{c.m.}^{R}$=183 keV (E_X=5.786 MeV). While, in the last years, several measurements [2-6] of the $E_{c.m.}^{R}$=183 keV resonance for both (p,α) and (p,γ) channels have drastically reduced the uncertainties on both $^{17}O(p,\alpha)^{14}N$ and $^{17}O(p,\gamma)^{18}F$ rates in the context of explosive H-burning, only one direct measurement for the $E_{c.m.}^{R}$=65 keV resonance was performed [7]. In fact, direct measurements of low-lying resonance strengths such that of the 65 keV resonant level, are very difficult because the Coulomb barrier and large uncertainties are still present on the available direct data. In addition, some sub-threshold levels could contribute to the total reaction rate and then a further study of this reaction in the energy region relevant for astrophysics is necessary. In the present work we report on the indirect measurement of $^{17}O(p,\alpha)^{14}N$ reaction at energies below 300 keV by using the Trojan Horse Method [8-10].

THE EXPERIMENTS

The study of the $^{17}O(p,\alpha)^{14}N$ via the THM application was made via two experiments: the first one at the Laboratori Nazionali del Sud (LNS) in Catania (Italy) and the second one at the Nuclear Science Laboratory (NSL) of the University of Notre Dame (USA). In the LNS experiment, the SMP Tandem Van de Graaf accelerator provided a 41 MeV ^{17}O beam, with a spot size on target of about 1.5 mm and intensities up to 2-3 nA, impinging on a deuterated polyethylene target (CD_2) of about 150 μg/cm^2 placed at 90° with respect to the beam axis. In the NSL experiment, a beam energy of 43.5 MeV and a target thickness of 170 μg/cm^2 were used. The angles and the energies of the ejected α and ^{14}N were detected in coincidence by using an experimental setup, symmetric with respect to the beam axis, which consisted of six single-area, resistive-readout position-sensitive silicon detectors (PSDs) with spatial resolution of 0.5 mm. The neutron was not detected in these experiments, and its energy and emission angle were reconstructed from the momenta of the detected particles. The PSD detectors covered the angular ranges in the laboratory reference system 5.1°-10.1° ($PSD_{1,4}$), 13.8°-21.2° ($PSD_{2,5}$) and 21.3° -28.7° ($PSD_{3,6}$) in the LNS experiment and 5.0°-10.0° ($PSD_{1,4}$), 13.1°- 8.1° ($PSD_{2,5}$), and 23.8°- 28.8°

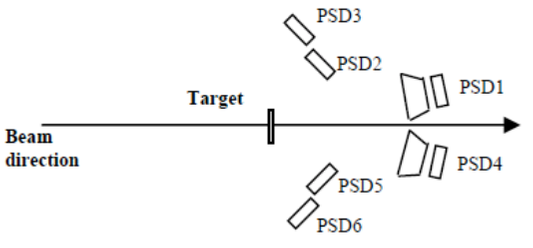

Figure 1: Schematic representing of experimental setup.

(PSD3,6), in the NSL experiment. In Fig. 1, a schematic drawing of the detection set-up is shown. In front of the two forward PSDs, two ionization chambers (IC) were further used as ΔE detectors to discriminate the impinging ^{14}N reaction products from ^{14}C coming from the ^{2}H(^{17}O,α^{14}C)p reaction. The ionization chambers were filled with 60 mbar of isobuthane gas and were closed on both sides by 1.5 μm thick mylar foil windows. The gas pressure inside the ionization chambers was selected to yield an high enough signal-to-noise ratio. The angular ranges were chosen in order to cover momentum values p_s of the undetected neutron ranging from -100 MeV/c to 100 MeV/c. This allows us to select the kinematical region where a strong contribution of the Quasi Free (QF) mechanism is expected.

RESULTS

The THM was successfully applied to study several reactions relevant to astrophysics ([9] and reference therein). The method has proven particularly suited for acquiring information on charged as well as neutral-particle-induced reaction cross sections at astrophysical energies.

The basic idea of the THM is to extract the cross section in the low-energy region of a two-body reaction with significant astrophysical impact,

$$A + x \rightarrow b + B$$

from a suitable three-body reaction,

$$a + A \rightarrow s + b + B$$

by properly selecting the contribution to the total reaction yield coming from the quasi-free (QF) direct reaction mechanism, where the Trojan Horse (TH) nucleus a, which has a strong x+s cluster structure, breaks up inside the nuclear field of nucleus A.

For resonant cases the ^{17}O +^{2}H →^{14}N +α +n reaction can be regarded as a two-step process, namely the stripping ^{17}O +^{2}H → ^{18}F+n to a resonant state in the compound system ^{18}F* , which later decays to the ^{14}N +α channel [11]. Correspondingly, the cross section of such process can be factorized and the resonance parameters can be deduced from the experimental TH data (see [11] for more details).

The resulting ^{2}H(^{17}O,α^{14}N)n reaction cross section is shown in Fig. 2 as full dots for both the LNS (a) and the NSL experiments (b). Here, the vertical error bars arise from the statistical uncertainty (about 20% on the average) while the horizontal one represents the integration energy bin.

energy bin. The quoted energy resolution of about 20 keV is the result of the propagation of the energy and angular straggling, affecting the measured quantities, on the $E_{14N-\alpha}$ variable intervening in the calculation of $E_{c.m.}= E_{14N-\alpha}- Q_2$, where Q_2 = 1.192 MeV is the Q-value of the ^{17}O(p, α)^{14}N. Thus, the experimental width reflects the effects of the energy resolution that can be considered the same for all the observed resonances inthe 0-250 keV energy range.

The detailed data analysis as well as the main results and the astrophysical implications of LNS results will already pubblished in [8] while the NSL data are the subject of a forthcoming dedicated paper [12].

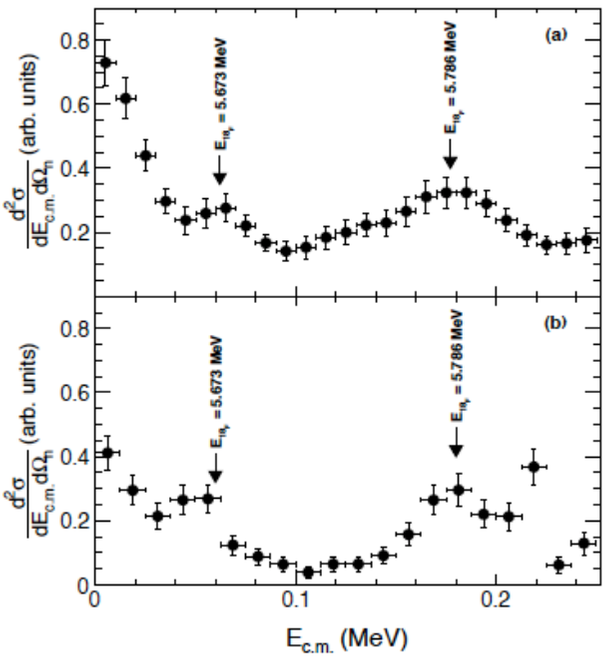

Figure 2: Cross section of the ^{2}H(^{17}O,α^{14}N)n for the LNS (a) and NSL (b) experiments.

ACKNOWLEDGEMENTS

This work has been partially supported by the Italian Ministry of University MIUR under the grants RFBR082838 (FIRB2008) and `LNS-Astrofisica Nucleare (fondi premiali)'. It has been partially supported also by the grant LC 07050 of the Czech MSMT, grant M10480902 of the Czech Academy of Science, grant LH1101 of the AMVIS project. A. M. M. acknowledges the support by U.S. Department of Energy under Grants No. DE-FG52-09NA29467, No. DE-FG02-93ER40773, and No. DE-SC0004958 and by NSF under Grant No.PHY-0852653.

REFERENCES

[1] A. Coc et al. AA 357 (2000) 561.
[2] A. Chafa et al., Phys. Rev. C 75, (2007), 035810.
[3] J. Newton et al., Phys. Rev. C 75, (2007), 055808.
[4] B. Moazen et al., Phys. Rev C 75, (2007), 065801.
[5] D. Scott et al., Phys. Rev. Lett. 109, (2012), 202501.
[6] A. Di Leva et al., Phys. Rev. C. 89, (2014), 015803.
[7] J. Blackmon et al., Phys. Rev. Lett. 74, (1995), 2642.
[8] M. L. Sergi et al., Phys. Rev.C.82, (2010), 032801(R).
[9] R. Tribble et al., Rep. Prog. Phys. 77, (2014), 106901.
[10] C. Spitaleri et al., Phys. Rev. C 69, (2004), 055806.
[11] M. La Cognata et al., Astrophys. J. 708, (2010), 796.
[12] M.L. Sergi et al., Phys. Rev. C (2015), (Submitted)

Asymptotic normalization coefficients from the ^{6}Li(^{3}He,d)^{7}Be reaction

G.G. Kiss[1,*], M. La Cognata[2], C. Spitaleri[2,3], M. Lattuada[2], L. Lamia[3], S. Palmerini[2], R. G. Pizzone[2], G. G. Rapisarda[2,3], R. Sparta[2,3], O. Tripella[4,5], I. Wiedenhöver[6], L. T. Baby[6]

1) MTA Atomki, H-4001 Debrecen, Hungary
2) Laboratori Nazionali del Sud, INFN, Catania, Italy
3) Dipartimento di Fisica e Astronomia, Università degli Studi di Catania, Italy
4) Istituto Nazionale di Fisica Nucleare, Sezione di Perugia,
5) Dipartimento di Fisica, Università di Perugia, Perugia, Italy
6) Department of Physics, Florida State University, Tallahassee, Florida, USA
**) present address: RIKEN Nishina Center, Wako, Saitama, Japan*

Abstract - The ^{3}He(α,γ)^{7}Be reaction plays an important role in several astrophysical scenarios ranging from stellar hydrogen burning to Big Bang nucleosynthesis. Contrary to its importance, the knowledge on the reaction cross section at the relevant energies is still limited. By the study of the angular distribution of the deuterons emitted in the ^{6}Li(^{3}He,d)^{7}Be alpha transfer reaction we can gain an insight into the low energy behaviour of the ^{3}He(α,γ)^{7}Be radiative capture reaction.

ASTROPHYSICAL MOTIVATION

The ^{3}He(α,γ)^{7}Be reaction is an excellent example of those reactions which preserve their importance over several decades despite many experimental and theoretical studies devoted to them [1].

The crucial role played by the ^{3}He(α,γ)^{7}Be reaction in solar hydrogen burning was realized more than 50 years ago [2]. The ^{3}He(α,γ)^{7}Be and ^{3}He(^{3}He,2p)^{4}He reactions compete in the proton-proton (pp) chain of solar hydrogen burning. The ratio of their rates at the temperature of the solar center determines how much the ^{7}Be and ^{8}B branches of the pp chain contribute to solar hydrogen-burning. Moreover, around the turn of the century the detection of solar neutrinos entered a precision era, the measured fluxes can be used to probe the solar core and test solar models as soon the underlying nuclear physics input (cross sections of the pp chain reactions) is known with sufficient precision [3]. Finally, the need for a more precise ^{3}He(α,γ)^{7}Be cross section arose also from the big-bang nucleosynthesis. Owing to the high precision measurement of the baryon-to-photon ratio of the universe primordial abundances of the light nuclei can be compared to observation with high accuracy. While good agreement is found between model predictions and observations for most of the nuclei produced in the big-bang, ^{7}Li is significantly overproduced in the models. The precise knowledge of the ^{3}He(α,γ)^{7}Be reaction rate is crucial in order to exclude a solution of the so-called ^{7}Li problem based on this reaction rate [4].

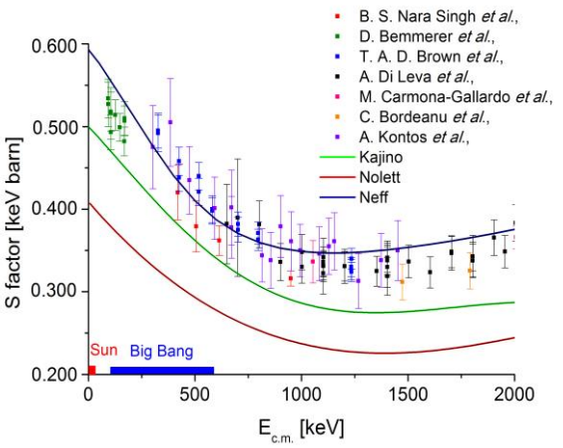

Figure 1: The modern experimental data for the ^{3}He(α,γ)^{7}Be reaction and cross-section predictions based on microscopic calculations [1,5 and reference therein]. The discrepancy between different experimental datasets and different calculations is clearly seen and this gives the motivation of the present work. The energy ranges important in the Sun (red) and at the Big Bang (blue) is marked.

Several experimental studies aiming at the determination of the ^{3}He(α,γ)^{7}Be cross section at energies as low as possible in order to approach the astrophysically relevant energy range were carried out [1,6 and references therein]. This energy range, the so-called Gamow window, lies between about 15 and 30 keV at 15 MK temperature relevant for the solar core. The cross section at these energies is too small to be measured directly, theory-based extrapolations are therefore necessary to obtain the cross section at solar energies and hence the reaction rate. The available "modern" experimental database together with the most recent extrapolations based on different theoretical models is shown on Fig. 1.

As can be seen, the data is scattered and none of the theoretical models can provide precise description for the experimental results and therefore the uncertainty of the extrapolated S_0 astrophysical S factor is above the required 5% precision [1,5]. An independent experiment utilize an approach never used to study this reaction can help understanding better the low energy behaviour of this important reaction.

THE ASYMPTOTIC NORMALIZATION COEFFICIENT TECHNIQUE

An external direct-capture process at low / stellar energies essentially proceeds through the tail of the nuclear overlap function. The shape of the overlap function in the tail region is determined by the Coulomb interaction, so the amplitude of the overlap function alone dictates the rate of the capture reaction [7,8].

The direct capture cross-sections are directly proportional to the squares of the ANCs, which are found from transfer reactions. In fact, for the transfer reaction a + A → c + B, where particle p is transferred from a cluster to a bound system B (that is a = c + p, B = A + p) the DWBA cross-section can be written in the form:

$$\frac{\partial\sigma}{\partial x} = \sum_{j_B j_a} (C^B_{Ap l_B j_B})^2 (C^a_{cp l_a j_a})^2 \frac{\sigma^{DW}_{l_B j_B l_a j_a}}{b^2_{Ap l_B j_B} b^2_{cp l_a j_a}}$$

where σ^{DW} is the reduced DWBA cross-section, j_i and l_i are the total and orbital angular momentum of the transferred particle p in nucleus i and the b factors are the ANCs of the bound-state wave functions of particle p in nuclei a and B. If the reaction under consideration is peripheral, the previous ratio is independent of the b parameters and the ANCs for the B = A + p and a = c + p vertexes provides the normalization of the DWBA cross-section.

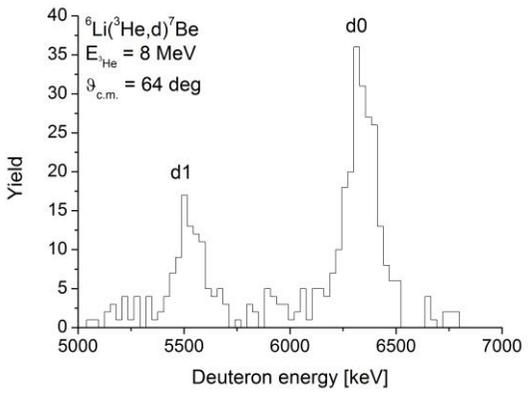

Figure 2: Deuteron spectrum measured with a ΔE-E telescope positioned at $\vartheta_{c.m.}$ = 64°. The peaks used for the analysis are indicated.

In our case, the ^{6}Li → α+d ANC is well known, the ANC for the ^{7}Be → ^{3}He+α will be extracted from the angular distribution of the ^{6}Li+^{3}He → d+^{7}Be reaction (Q=0.112 MeV), where ^{6}Li=α+d is used to transfer an α particle to form the ^{7}Be bound system. In turn, this ANC fixes the normalization of the cross-section. The main scope of the experiment is therefore, to determine the angular distribution of the ^{6}Li+^{3}He→d+^{7}Be reaction by measuring the yield of the emitted deuterons.

EXPERIMENTAL TECHNIQUE

The experiment was carried out at the John D. Fox Superconducting Accelerator Laboratory, Florida State University, Tallahassee, USA. A ~50μg/cm^2 pure ^{6}Li target was bombarded with 8 MeV ^{3}He particles provided by FN tandem accelerator.

Altogether 6 silicon ΔE-E telescopes and 3 monitor detectors were mounted in the large scattering chamber. The monitor detectors placed at ϑ_{lab} = ±15° respect the beam direction were used to monitor the target thickness during the irradiations. An additional detector was mounted at fixed ϑ_{lab} = 150° angle, this detector played a crucial role in absolute normalization. Namely, the cross section of the ^{6}Li(^{3}He,p)^{8}Be (Q=16.79 MeV) reaction is well known, by measuring the yield of the emitted high energy protons (and taking into account the known solid angle) it was possible to extract the multiplication of the number of target atoms and the number of impinging ^{3}He particles for every angular setting.

The six ΔE-E telescopes were used to measure the deuteron angular distribution between ϑ_{lab} = 21.34° - 158.97° using ~5° steps. The detector solid angles were determined from the known geometry and the ratio of the solid angles were cross checked by measuring elastic scattering on Au at overlapping angles. The signals of the ΔE detectors were used to discriminate between elastically scattered ^{3}He particles and the deuterons of our interest. A typical 1D spectrum, measured at $\vartheta_{c.m.}$ = 64° is shown in figure 2, the peaks corresponding to deuterons emitted in the ^{6}Li(^{3}He,d)^{7}Be reaction are indicated. The data analysis is in progress.

This work has been supported by MIUR under grants RBFR082838 and "Premiale Astrofisica Nucleare" and by OTKA PD104664.

REFERENCES

[1] E. G. Adelberger et al., Rev. Mod. Phys. 83 (2011) 195
[2] H.D. Holmgrenet al., Phys. Rev. 113 (1959) 1556
[3] J. Bahcall et al., Astrophys. J. Suppl. 165 (2006) 400
[4] F. Iocco, et al., Phys. Rep. 472 (2009) 1
[5] R. J. deBoer et al, Phys. Rev. C 90 (2014) 035804
[6] A. Kontos et al., Phys. Rev. C 87 (2013) 065804
[7] A.M. Mukhamedzhanov et al., JETP. Lett. 51 (1990) 282
[8] H. M. Xu el al., Phys. Rev. Lett., 73 (1994) 2027

Indirect measurement of the $^{10}B(n,\alpha)^{7}Li$ to discern the α_0 e α_1 contribution to the total cross section

R. Spartà[1], C. Spitaleri[1,2], L. Lamia[2], S. Cherubini[1,2], G.L. Guardo[1], M. Gulino[1,3], S. Romano[2], M.L. Sergi[1]

1) INFN Laboratori Nazionali del Sud, Catania, Italy
2) Dipartimento di Fisica e Astronomia - Università di Catania, Catania, Italy
3) Università degli Studi di Enna "Kore", Enna, Italy

Abstract – A new Trojan Horse measurement of the $^{10}B(n,\alpha)^{7}Li$ reaction has been performed, in order to discern the α_1 contribution (coming from the first ^{7}Li excited level) to the cross section from the ground state. Preliminary results are encouraging.

INTRODUCTION

The $^{10}B(n,\alpha)^{7}Li$ standard cross section have received considerable attention in recent years, because of their relatively poor database available at incident neutron energies above 100 keV [1]. This cross section is mainly dominated by the α emission, through two channels, α_0 and α_1, the latter coming by the eccitation of the ^{7}Li (its first excited level has an energy of 478 keV).

This reaction have already been approached via the Trojan Horse Method [2] [3], using the deuteron as a virtual source of neutrons, continuing the experimental Trojan Horse campaign for neutron involving reactions [3] [4] [5].

To gain more statystics and to investigate the presence of the α_1 contribution, a new experiment has been performed at LNS in March 2014.

EXPERIMENT

Experimental setup

A 28 MeV ^{10}B beam, coming from the Tandem Accelerator, was impinging in Camera2000 on very thin CD_2 target (50 μg/cm^2), to perform the 3-body reaction $^{10}B(d,p\ \alpha_{0,1})^{7}Li$, in order to obtain the $^{10}B(n,\alpha)^{7}Li$ cross section, via the quasi-free channel selection, as shown in Fig. 1.

The experimental setup is shown in Fig.2. The products of reaction (α and ^{7}Li) were collected by four detectors, whose positions are listed in Table 1.

Detector	Distance [cm]	Angle range [°]
PSD1	20	21.5-35.5
PSD2	20	21.5-35.5
PSD3	45	11.5-17.5
PSD4	45	11.5-17.5

Table 1: Detectors position features.

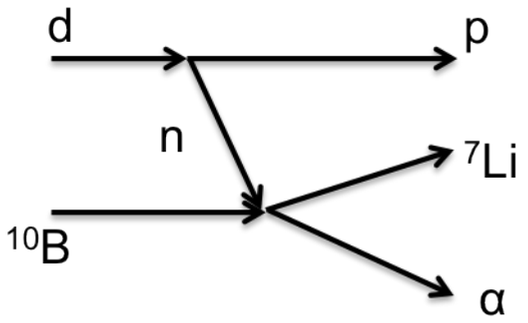

Figure 1: Diagram of the performed 3-body reaction, to obtain the $^{10}B(n,\alpha)^{7}Li$ cross section, via the quasi-free channel selection.

Two Ionization Chambers, filled with isobutane gas, were placed in front of the two central Position Sensitive Detectors (PSD), to obtain telescopes so as to select the ejectiles, as shown in Fig. 3.

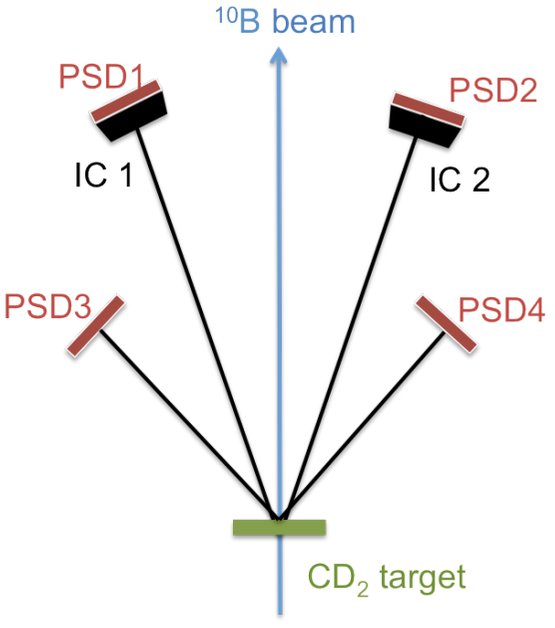

Figure 2: Scheme of the experimental setup, as was set in Camera2000.

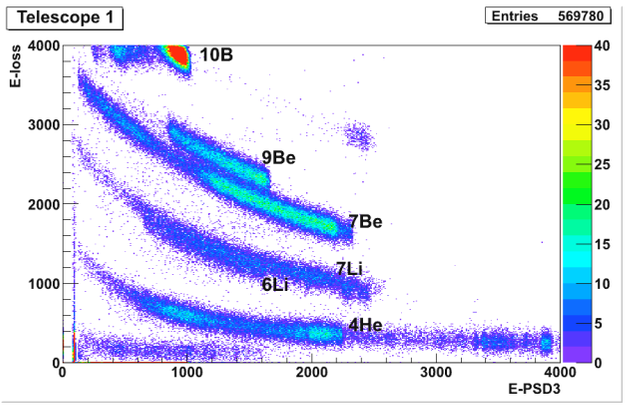

Figure 3: Different ions are selected through graphical cut on the energy loss vs. energy remaining matrix. Here is shown the case of the first telescope (PSD3 and IC1).

DATA ANALYSIS AND RESULTS

The 3-body reaction selection

Once the ^{7}Li and α particles have been selected by a graphical cut on Fig. 3, the kinematical locus shows the agreement between the Montecarlo simulations and the obtained data. In Fig. 4 the locus for the quasi free angular couple (taken as example) θ_1=14.5° - θ_2 = 25° is shown. The presence of the two different levels is evident: data coming from α_0 contribution (black dots) perfectly match the red α_0 simulation dots, while black stars (data from α_1) occupy the green zone of the α_1 simulation.

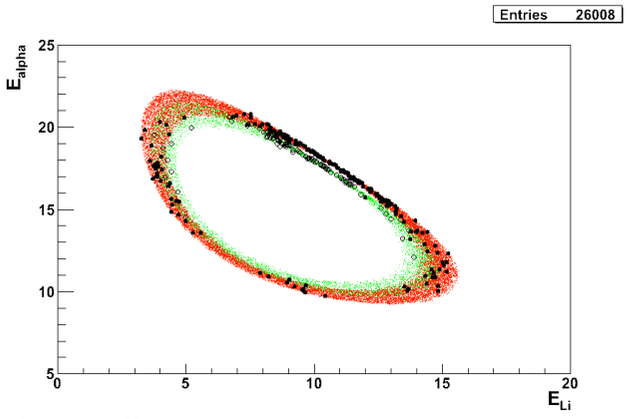

Figure 4: Kinematical locus for the quasi-free angular couple θ_1=14.5° - θ_2 = 25°. Black dots are data coming from α_0 contribution, black stars from α_1, red and green zone respectively indicate α_0 and α_1 simulation.

The levels separation is also evident in the Q-value spectrum in Fig. 5. It shows clear peaks around the theoretical values 0.565 MeV (α_0) and 0.88 MeV (α_1), coming from the difference between the α_0 Q-value and the energy level of the first excited state.

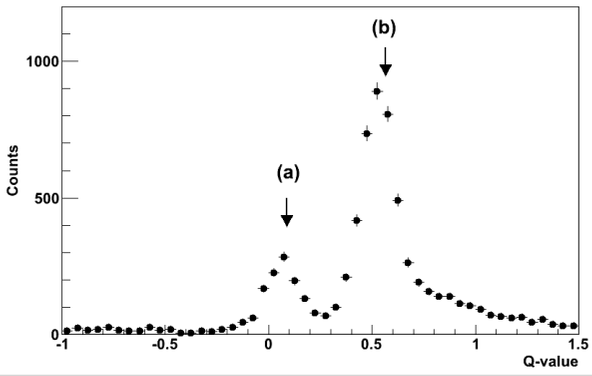

Figure 5: Q-value spectrum for data analysed. Data are peaked just around the theoretical values for excited (a) and ground state (b), indicated by the arrows.

CONCLUSIONS

Results obtained for this partial and preliminary analysis make us confident that the experimental run will be fruitful to obtain an accurate cross section estimation, for both α_0 e α_1 contribution.

ACKNOWLEDGMENTS

The authors acknowledge the support of the Italian Ministry of Education, University and Research under grant Progetto Premiale ASTROF.MIUR PFE, CD 19/12/2012 n. 12609.

REFERENCES

[1] F.J. Hambsch et al., Journal of Physics: Conference Series 205 (2010) 012049
[2] R.E. Tribble et al., Rep. Prog. Phys. 77 (2014)
[3] Lamia et al., Nuovo Cimento C31, 423 (2008)
[4] M. Gulino et al., J. Phys. G37, 125105 (2010)
[5] M. Gulino et al. Phys Rev C87 (2013) 012801(R)

$^{18}F(p,\alpha)^{15}O$ and $^{18}F(n,\alpha)^{15}N$ reactions studied by Trojan Horse.

M. Gulino[1,2], S. Cherubini[1,3], G. G. Rapisarda[1,3], L. Lamia[3], M. La Cognata[1], S. Kubono[4], H. Yamaguchi[5], S. Hayakawa[2], Y. Wakabayashi[5], N. Iwasa[6], S. Kato[7], H. Komatsubara[8], T. Teranishi[9], A. Coc[10], N. De Sèrèville[10], F. Hammache[10], C. Spitaleri[1,3]

1) INFN-LNS, Catania, Italy
2) Università di Enna KORE, Enna, Italy
3) Dipartimento di Fisica ed Astronomia, Università di Catania, Catania, Italy
4) Riken, Wako, Tokyo, Japan
5) Center for Nuclear Study, The University of Tokyo, Japan
6) Department of Physics, Tohoku University, Sendai, Japan
7) Department of Physics, Yamagata University, Yamagata, Japan
8) Department of Physics, Tsukuba University, Tsukuba, Japan
9) Department of Physics, Kyushu University, Fukuoka, Japan
10) Centre de Spectromètrie Nuclèaire et de Spectromètrie de Masse, IN2P3, F-91405 Orsay, France

Abstract - The Trojan Horse Method (THM) has been applied to study reactions induced by a radioactive ion beam (RIB) for the first time. The experiment was performed at RIKEN by using a ^{18}F beam produced at the CRIB facility of the CNS of The Tokyo University. The ^{18}F+d reaction has been studied, and pieces of information about both the $^{18}F(p,\alpha)^{16}O$ and $^{18}F(n,\alpha)^{15}N$ reactions have been obtained. To overcome the experimental problems coming from the radioactive nature of the beam, a new detection set-up has been especially designed for the experiment.

INTRODUCTION

The reactions involving ^{18}F nucleus have great interest in nuclear astrophysics for the Novae explosion phenomena. Indeed, the first signal after the explosion comes from the γ-ray emission following the e^+-e^- annihilation, which gives a clear signature line at 511 keV. The positrons mostly come from the β decay of ^{18}F, as its production is abundant and its lifetime (~158 min) matches well the timescale for the Novae ejects to become transparent to γ-ray emission. It is then important to known the cross sections of the reactions producing and destroying the ^{18}F at astrophysical energies [1].

The radioactive nature of the ^{18}F makes even worse the already difficult measurement of reactions at the low energies of interest for astrophysics [2]. The THM [3] has been applied to a RIB induced reaction for the first time, and the obtained results are shown in the following [4].

THE EXPERIMENT

The $^{18}F(p,\alpha)^{16}O$ and $^{18}F(n,\alpha)^{15}N$ reactions have been studied at RIKEN, Wako, Japan, by using the ^{18}F beam, provided by the CRIB facility, impinging on a CD_2 target. Among the other possible reactions, the $^{18}F(d,n\alpha)^{15}O$ and $^{18}F(d,p\alpha)^{15}N$ ones have been identified. Figure 1 shows the experimental set-up as it is described in a Monte Carlo simulation used for the data analysis. Two doubled sided silicon strips detectors (DSSD), green squares in fig.1, 50x50 mm, 3 mm per strip, cover the geometrical angular range from 2° to 12° and detect heavier particles. A safety disk, (pink cylinder in fig. 1) covers the smaller angles, from 2° to 4°, and prevents the break down of the detectors. Eight bi-dimensional position sensitive detectors (DPSD), blue plane in fig. 1, 45x45 mm, resolution of 1 mm, placed all around the beam line, cover the geometrical angular range from 11.5° to 31.5° and detect α particles. All the detector set-up is arranged in a mechanical structure, especially designed and implemented at the Laboratori Nazionali del Sud, assuring a self-consistent alignment of the set-up. To achieve the angular resolution requested by the THM, the beam was tracked event by event by using two proportional parallel plate avalanche chambers (PPAC), red planes, placed before the target at a relative distance of 50 cm, and the real track was used for the reconstruction of the emission angle of each detected particle. An overall angular uncertainty of 0.2° was achieved. In fig.1 the target position is showed as a yellow spot.

Figure 1: Experimental set-up as described in the simulation.

DATA ANALYSIS AND RESULTS

The experimental set-up does not allow for particle identification, and kinematical conditions are used to discriminate among the occurring reactions. The following conditions are imposed to experimental data: only one of the strips of the DSSD and one of the 8 DPSD is crossed; only in plane events are considered. Moreover

a graphical cut on the correlation plot between the energies of the two detected ejectiles allows discriminating the reactions induced on C from that coming from ^{18}F+d. As only two particles are detected, the energy and angle of the third one is reconstructed assuming the masses of the other two particles. The q-value spectra show the presence of the processes:
1) ^{18}F+d→^{15}N+α+p, q=4.194 MeV;
2) ^{18}F+d→^{15}O+α+n, q=0.658 MeV;
3) ^{18}F+d→^{18}O+p+p, q=0.213 MeV;
4) ^{18}F+d→^{18}F+p+n, q=-2.225 MeV.

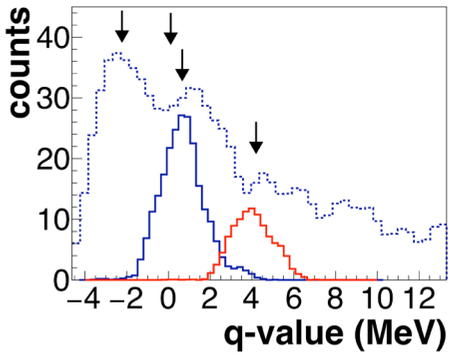

Figure 2: q-value spectra. All the events are reported as dotted line. The blue and red solid line are obtained by using the condition on the relative energies respectively for the ^{18}F+d→^{15}N+a+n and for the ^{18}F+d→^{15}O+a+n reaction. The arrows represent the theoretical q values for the four reactions discussed in the text.

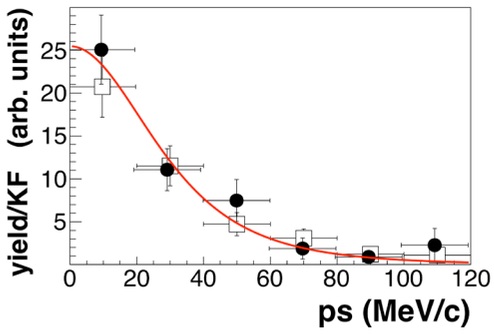

Figure 3: Distribution of the spectator momentum. The open squares are obtained for the ^{18}F+d→^{15}N+α+n reaction. The full dots come from the ^{18}F+d→^{15}O+α+p reaction. The red line is the Hultén function calculated using the standard parameters and normalized to the data.

In order to discriminate among these reactions, a constraint on the relative energies of two among the three reaction products is used. In figure 2, the q-value is reported without any condition and selecting the first and the second three body reactions in the list above.

The correspondence between the obtained q-value and the theoretical value, shown by the arrows in the figure, proves the correct selection of the events and the goodness of the calibration of the detectors.

If the events proceeding through a Quasi-free (QF) reaction mechanism are selected, the three body reactions ^{18}F(d,pα)^{15}N and ^{18}F(d,nα)^{15}O can give information about the two body reactions ^{18}F(n,α)^{15}N and ^{18}F(p,α)^{15}O, respectively. The strongest signature of the predominance of QF mechanism is given by the momentum distribution of the particle that acts as a spectator. Here d is the used as TH nucleus. As the spectator (p or n) does not take part in the reaction, its momentum distribution remains unchanged in the reaction and should follow the Hultén function. In figure 3 the momentum distribution obtained for ^{18}F(d,pα)^{15}N (open squares) and ^{18}F(d,nα)^{15}O (full dots) are reported. The line represents the Hultèn function that is in agreement with the data.

The cross section for the two body reactions ^{18}F(p,α)^{15}O and ^{18}F(n,α)^{15}N is shown in figure 4. Both distributions are characterized by the presence of several resonances, which can be associated to excited states of the compound nucleus, ^{19}Ne and ^{19}F. To disentangle the contribution of different excited states, a fit has been performed using an incoherent sum of Gaussian having a fixed sigma of 53 keV. This value, corresponding to the experimental resolution, has been provided both by the simulation and by fitting isolate resonances.

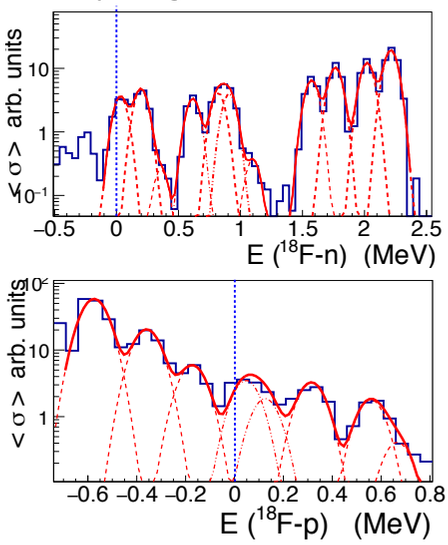

Figure 3: Cross section for the two studied reactions.

CONCLUSIONS

For the first time the THM was applied to study a reaction induced by radioactive beam. The experiment succeeded to infer information about the cross section of both the studied reactions and a second experimental run aimed to increase the statistic has been approved.

In particular, we derived pieces of information about ^{18}F(p,α) reaction of astrophysical interest and demonstrated the possibility of using the THM to study neutron-induced reaction on a radioactive nucleus, even when its lifetime would prevent the use of direct measurements.

REFERENCES

[1] A Coc et al., A.&A., 357 (2000) 561 and ref. therein
[2] AM Laird et al., PRL110,032502(2013) and ref. in
[3] RE Tribble et al., Rep. Prog. Phys. 77 (2014) 106901
[4] S Cherubini et al., AIP Conf. Proc.1594 (2014)184

The $^{2}H(d,p)^{3}H$ and $^{2}H(d,n)^{3}He$ reactions at astrophysical energies

A. Tumino[1,2], R. Spartà[1,3], C. Spitaleri[1,3], A.M. Mukhamedzhanov[4], S. Typel[5], R.G. Pizzone[5], E. Tognelli[6], S. Degl'Innocenti[6], V. Burjan[7], V. Kroha[7], Z. Hons[7], M. La Cognata[1], L. Lamia[3], J. Mrazek[7], S. Piskor[7], P.G. Prada Moroni[6], G.G. Rapisarda[1,3], S. Romano[1,3], M.L. Sergi[1,]

1) Laboratori Nazionali del Sud - INFN, Catania, Italy
2) Facoltà di Ingegneria e Architettura, Università degli Studi di Enna "Kore", Enna, Italy
3) Dipartimento di Fisica e Astronomia, Università degli Studi di Catania, Catania, Italy
4) Cyclotron Institute Texas A&M University - College Station, Texas, USA
5) GSI Helmholtzzentrum fuer Schwerionenforschung GmbH - Theorie Darmstadt Germany
6) Dipartimento di Fisica, Università di Pisa, and INFN-Sezione di Pisa, Pisa, Italy
7) Nuclear Physics Institute of ASCR - Rez near Prague, Czech Republic

Abstract - The $^{2}H(d,p)^{2}H$ and $^{2}H(d,n)^{3}He$ reactions have been recently investigated from E_{dd}=1.5 MeV down to 2 keV, by means of the Trojan Horse Method applied to the quasi free $^{3}He+d$ interaction at 18 MeV. The knowledge of their fusion cross section at low energies is of interest for pure and applied physics. Providing experimental data for both channels from a single experiment and over the entire energy range of interest is crucial for an accurate calculation of the reaction rates. This is what has been obtained from the present TH investigation with new reaction rates which deviate by more than 20% from available direct data. This represents also the first pioneering experiment in quasi free regime where the charged spectator is detected.

Low energy $^{2}H(d,p)^{2}H$ and $^{2}H(d,n)^{3}He$ reactions belong to the Standard Big Bang Nucleosynthesis (SBBN) network, synthesizing D,^{3}He,^{4}He and ^{7}Li in the early universe. They are the most important and still critical points at the SBBN relevant energies (d-d relative energies E_{dd} from 50 to 350 keV). All published measurements for both channels have been mainly focused either on the E_{dd} region below 200 keV [1] or at E_{dd} above 1 MeV [1], while an accurate calculation of the reaction rate needs the cross section to be known from E_{dd}=30 keV to at least 1 MeV. All the reaction rates quoted so far rely either on polynomial [1] or in the best case on R-Matrix fits [1], whose different slopes bring inside the calculations deviations of more than 15%. For this reason, a new experimental campaign was recommended by the astrophysical community, to provide new data in the SBBN energy range of interest. Moreover, the importance of the $^{2}H(d,p)^{2}H$ and $^{2}H(d,n)^{3}He$ reactions in the ultra- low energy region below 30 keV is twofold: it overlaps with the burning temperatures (0-10 keV) of deuterium in Pre Main Sequence (PMS) stars and corresponds to the thermal energy range of future fusion power plants. However, the measured cross section below 10 keV, available only for the $^{2}H(d,p)^{2}H$ channel with a gas target, has shown a clear enhancement attributed to electron screening. The deduced electron screening potential of U_e= 25±5 eV is significantly larger than the adiabatic limit (14 eV) provided by atomic physics. Unfortunately, nuclear reactions in the laboratory are affected by a different mechanism of electron screening than in a plasma, either astrophysical or laboratory fusion with inertial confinement. Hence, the laboratory screening effects of the bound electrons should be removed from the data to assess the reaction rate correctly. This makes the knowledge of the bare nucleus cross section essential for several purposes, from basic to applied research. Usually, a simple extrapolation of available unscreened higher energy data is taken as an approximation of the bare nucleus cross section, and compared to measured low-energy data to extract the electron screening potential. However, this approach can lead to large uncertainties. One can consider that available theoretical extrapolations of the bare nucleus $^{2}H(d,p)^{2}H$ and $^{2}H(d,n)^{3}He$ cross sections provide quite different S(0) values wich vary by 10-15%. A valid alternative approach is represented by the Trojan Horse Method (THM) ([2,3] and references therein) , that provides at present the only way to measure the energy dependence of the bare nucleus cross section down to the relevant ultra-low energies, overcoming the main problems of direct measurements. The THM has already been applied several times to reactions connected with fundamental astrophysical problems. In the present paper we report on a novel investigation of the deuterium depletion reactions $^{2}H(d,p)^{2}H$ and $^{2}H(d,n)^{3}He$ throughout the energy range relevant for pure and applied physics by means of the THM. The method was applied by choosing the $H(^{3}He,p^{3}H)^{1}H$ and $^{2}H(^{3}He,n^{3}He)^{1}H$ reactions in QF kinematics a 17 and 18 MeV of beam energy and with ^{3}He as the Trojan horse. For the first time in the application of the THM, we have detected the particle that acts as a spectator to both $^{2}H(d,p)^{2}H$ and $^{2}H(d,n)^{3}He$ binary processes, namely the proton. This technique was mandatory for the $^{3}He+n$ fusion channel to avoid the limitation of standard neutron detectors. However, it was well suited also for the $^{3}H+p$ channel, preventing unwanted quasi free events from target break-up to be detected. A detailed account of the measurement and

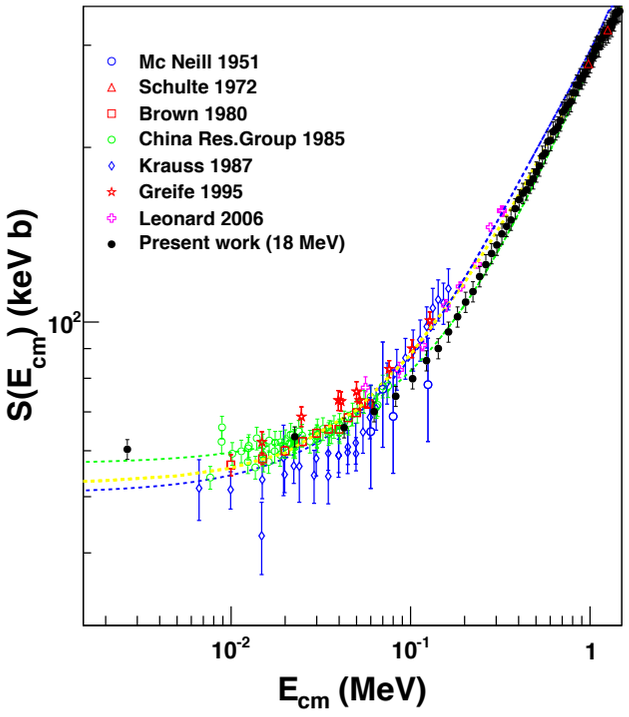

Fig. 1. S (E) factor for the ^{2}H(d,p)^{3}H reaction: black solid squares and circles=THM data (17 and 18 MeV respectively); colored symbols=direct data. Green, blue and yellow dashed lines represent the polynomial/R-matrix fits on direct data from [1].

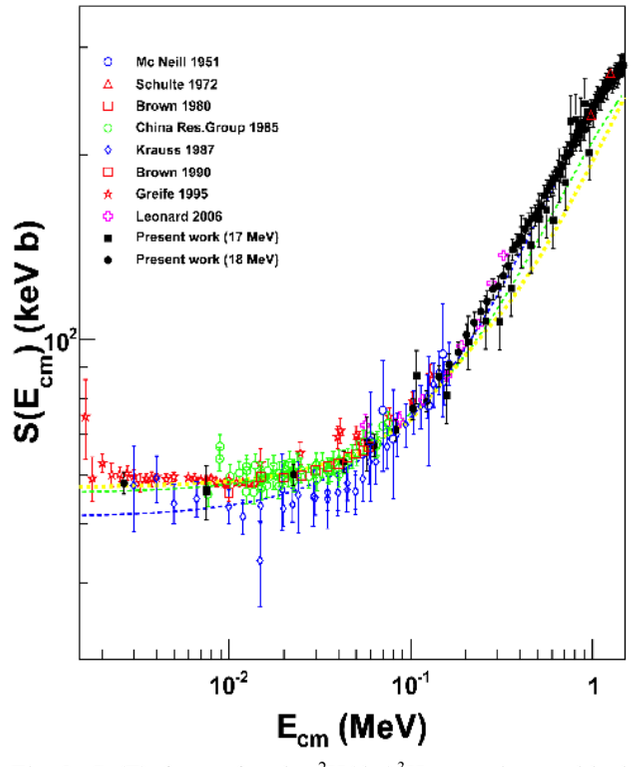

Fig. 2. S (E) factor for the ^{2}H(d,n)^{3}He reaction as black solid circles. Same meaning for symbols and lines as in Fig.1.

related data analysis is given in [4,5]. Here, we briefly report on the main final results. The TH S(E) factors of the ^{2}H(d,p)^{2}H and ^{2}H(d,n)^{3}He reactions are shown as black full dots in Figs. 1 and 2, respectively, with uncertainties accounting for statistical and normalization errors. We provide a new parameterization of the THM S(E) factor (black solid line in both figures) as a sum of the theoretical l = 0 and l = 1 contributions as reported in [6] with relative weight fixed from the fit to the measured three-body coincidence yield. Direct data from [1] are shown as colored symbols in (the legend in both figures associates a symbol and a color to each refefernce), with the black TH solid line superimposed on them. The very regular trend of TH data contrasts with that of direct data taken as a whole, both in energy dependence and absolute values, with deviations of more than 15%. The polynomial/R-matrix fits to direct data, usually taken as reference, are shown as green, blue and yellow dashed lines [1]. They barely overlap with most of the direct low-energy data, in particular in the case of the ^{3}He+n channel, probably due to their larger scatter. Conversely, the green line seems to agree with low-energy TH data, while for E_{cm} >200 keV they seem to be better reproduced by the blue line. However, none of them correctly reproduces the slope of the THM S(E)-factor in the entire energy region investigated, thus calling for a revision of the previous theoretical descriptions based on these new high quality data. The THM parameterizations of the S(E) factors lead to new values of S(0) = 57.7±1.8 keVb for ^{3}H+p and 60.1±1.9 keVb for ^{3}He+n, with uncertainties including the 1% normalization error and 3% coming from the theory, combined in quadrature. These new experimental data for both channels available over a wide energy range allows for an accurate calculation of the reaction rate. Both the deduced ^{2}H(d,p)^{2}H and ^{2}H(d,n)^{3}He reaction rates experience relevant changes. At the SBBN temperature, the rate for the ^{3}H+p (^{3}He+n) channel increases (decreases) by up to 15% with respect to previous studies [1] while at the temperatures relevant for PMS and future fusion power plants it undergoes a stronger increase by up to 20% for both channels.

REFERENCES

[1] C. Angulo et al., Nucl. Phys. A, 656, 3 (1999)

[2] C. Spitaleri et al., Phys. At. Nucl., 74, 1763 (2011)

[3] R.E. Tribble et al., Rep. Prog. Phys. 76, 106901 (2014)

[4] A. Tumino et al., Phys. Lett.B, 700(2), 111 (2011) and A. Tumino et al., Phys. Lett.B, 705(5), 546 (2011)

[5] A. Tumino et al., Astrophys. Journ., 785, 96 (2014)

New improved experimental measurement of the $^{19}F(p,\alpha_0)^{16}O$ S(E)-factor at energies of astrophysical interest.

I. Indelicato[1,2], M. La Cognata[2], V. Burjan[3], S. Cherubini[1], M. Gulino[4], S. Hayakawa[2], Z. Hons[3], V. Kroha[3], L. Lamia[1], M. Mazzocco[5,6], J. Mrazek[3], R.G. Pizzone[2], S. Romano[1,2], E. Strano[5,6], D. Torresi[5,6], A. Tumino[4], C. Spitaleri[1,2]

1) Dipartimento di Fisica e Astronomia dell'Università degli studi di Catania, Catania, Italy.
2) INFN,Laboratori Nazionali del Sud, Catania, Italy.
3) Nuclear Physics Institute of ASCR, Rez near Prague, Czech Republic.
4) Università degli studi di Enna "Kore", Enna, Italy.
5) INFN, Sezione di Padova, Padova, Italy.
6) Dipartimento di Fisica dell'Università di Padova, Padova, Italy.
7) INFN, Laboratori Nazionali di Legnaro, Legnaro (Padova), Italy.

Introduction - The $^{19}F(p,\alpha)^{16}O$ reaction is the main destruction channel of fluorine at the bottom of the convective envelope in AGB stars [1].

Because of the Coulomb barrier, measurements in the literature do not have access to the energy region of astrophysical interest, which is the Gamow peak (E=38 keV). In particular, at present direct measurement of the cross section stop about 500 keV [2]. Therefore, only extrapolations are actually available in the energy region for fluorine nucleosynthesis in AGB stars. A measurement of the low energy cross section is extremely important to evaluate the contribution of possible resonances which could significantly enhance the reaction rate at low temperatures. So, a new experimental study throught the Trojan Horse method (THM) is important because the method is particulary suited for the study of low-energy resonances. In particular, the THM [3,4] is an experimental indirect technique which selects the quasi-free (QF) contribution of an appropriate three-body reaction performed at energies above the Coulomb barrier to extract a charged particle two-body cross section.

THE EXPERIMENT

A first run was performed in Catania at the Laboratori Nazionali del Sud in 2008 using the THM, extracting the quasi-free contribution to the $^2H(^{19}F,\alpha^{16}O)n$ reaction at E_{beam}=50 MeV. The measurement of the α_0 channel showed the presence of resonance groups not observed before that cause a significant increase in the reaction rate at astrophysical temperatures, with important consequences for stellar nucleosynthesis [5]. Statistics turned out to be scarce as the α1 channel was dominant, preventing one to draw accurate quantitative conclusion from the data for the α_0 channel. Anyway the promising result motivate the request of a second run.

The new measurement was performed at the Laboratori Nazionali di Legnaro in July 2013 where the Tandem-XTU accelerator provided a 55 MeV ^{19}F beam impinging onto deuterated polyethylene targets. The energy beam and angular condition were selected in order to reduce the contribution of the α_1 channel and maximize the expected QF contribution.

A schematic view of the QF three-body reaction proceeding through deuteron break-up is reported in Fig.1, while a drawing of the experimental setup is given in Fig.2. It consisted of a telescope optimized for ^{16}O detection to discriminate oxygen nuclei via the ΔE-E technique, made up of an ionization chamber (IC) and a silicon position sensitive detector (PSD1) on one side with respect to the beam direction an additional silicon PSD on the opposite side of the beam axis optimized for coincident detection of the alfa particles (PSD2). A symmetric setup was adopted to double the statistics.

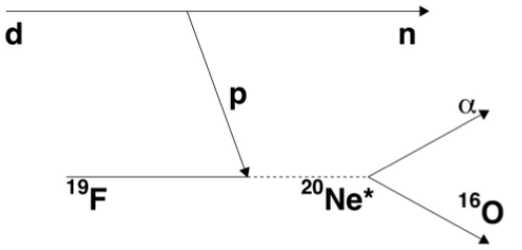

Figure 1: Sketch of the QF reaction.

The IC was filled with 50 mbar butane gas that provided an energy resolution of about 10%, which was enough to discriminate the impinging particles according to their nuclear charge but not their mass. The two 1000-micron PSD (5.0 cm^2) having energy and position resolution 0.5% and 0.3 mm respectively and covering the 8°-21° and 38°-54° angular range.

SELECTION OF THE REACTION CHANNEL

After detector energy and position calibration, the $^2H(^{19}F,\alpha_0{}^{16}O)n$ channel has been selected by gating on the ΔE-E spectra. Fig.3 shows that the contribution from

scattered ^{19}F beam particles is separated from the oxygen locus. However, by means of the standard ΔE-E approach no isotopic separation has been possible, as it is displayed in figure.

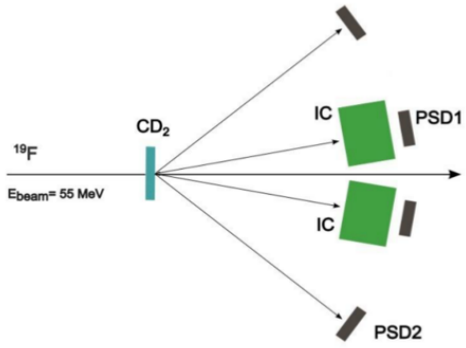

Figure 2: Sketch of the experimental setup.

Even if no isotopic discrimination is possible, we can disclose the presence of reactions having other oxygen isotopes in the exit channel by analyzing the reaction kinematics. Therefore, energy correlation spectra have been deduced and compared with the simulated ones to single out the kinematic locus for the ^{2}H(^{19}F,α_0^{16}O)n reaction.

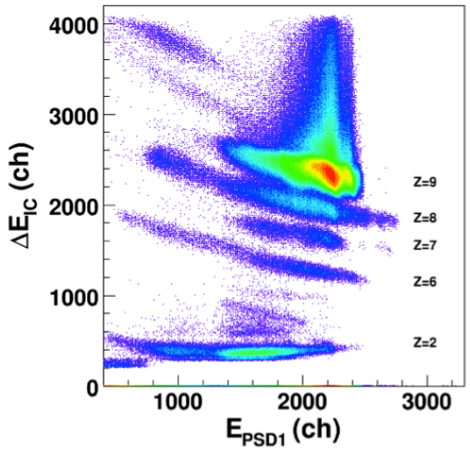

Figure 3: Particle ID with the standard DE-E technique.

From Fig. 4 it turns out that several reaction channels contribute in the explored phase space region. From its analysis (3) is recognized as the locus of the ^{2}H(^{19}F,α_0^{16}O)n reaction while (1) and (2) are attributable to binary reactions, such as the ^{19}F(d,α)^{17}O one. By means of a graphical cut the events corresponding to the loci marked as (1) and (2) have been excluded from the following analysis.

To check for the presence of further background and to evaluate the accuracy of the performed calibrations, the experimental Q-value has been extracted for the selected events by imposing energy balance for the three-body reaction. It is shown in Fig.5 where the arrow demonstrate the theoretical Q-value for the ^{2}H(^{19}F,α_0^{16}O)n reaction. The presence of a single and symmetric peak, centered at expected Q-value, rules out the occurence of significant systematic errors and confirms the identification of the reaction channel.

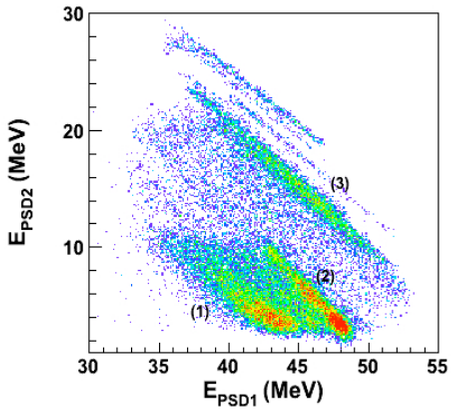

Figure 4: Kinematic locus from the PSD1-2 coincidence.

Similar result are deduced from the symmetric pair.

The data analysis is still going on and the next step is the evaluation the presence of the QF mechanism and the study of the ^{16}O-α relative energy spectrum. Then, the modified R-matrix approach [6] will be applied to extract information on resonance parameters and calculate the reaction rate that is the input quantity for astrophysical nucleosynthesis codes.

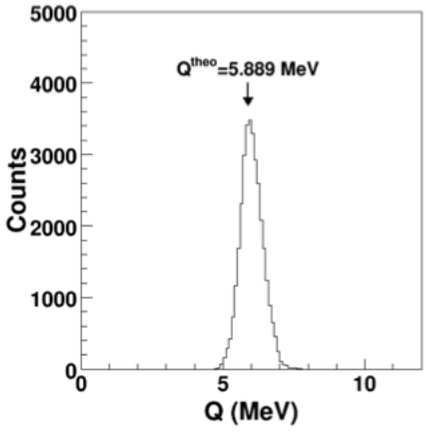

Figure 5: Q-value from the PSD1-2 coincidence.

The authors acknowledge the support of the Italian Ministry of Education, University and Research under grant Progetto Premiale ASTROF.MIUR PFE, CD 19/12/2012 n. 12609.

REFERENCES

[1] M. Lugaro et al., Ap. J. 615 (2004) 934.
[2] C. Angulo et al., Nucl. Phys. A656 (1999) 3.
[3] C. Spitaleri et al., Phys. Rev C 63, (2001) 055801.
[4] A.M. Mukhamedzhanov et al., J. Phys. G: Nucl. Part. Phys.35 (2008) 014016.
[5] M. La Cognata et al., Ap. J. 739 (2011) L54.
[6] M.La Cognata et al.,Ap. J. 723 (2010) 1512.

Indirect study of the $^{12}C(^{12}C,\alpha)^{20}Ne$ and $^{12}C\,(^{12}C,p)^{23}Na$ reactions via the Trojan Horse Method applied to the $^{12}C\,(^{16}O,\alpha\,^{20}Ne)^{4}He$ and $^{12}C\,(^{16}O,p^{23}Na)^{4}He$ three-body reactions

G.G. Rapisarda[1,2], C. Spitaleri[1,2], S. Cherubini[1,2], D. Filipescu[3], I. Gheorghe[3], D. Ghita[3], S. Hayakawa[1], I. Indelicato[1,2], M. La Cognata[1], J. Mrazek[4], H. Petrascu[3], R.G. Pizzone[1], R. Spartà[1], O. Tesileanu[3], L. Trache[3]

1) INFN Laboratori Nazionali del Sud, Catania, Italy
2) Dipartimento di Fisica e Astronomia Università di Catania, Italy
3) NIPNE, Bucharest, Romania
4) Nuclear Physics Institute of ASCR, Rez near Prague, Czech Republic

Abstract - We report about a new experimental run where the Trojan Horse Method (THM) was applied to study carbon-carbon fusion reaction at astrophysical energy. The set-up was optimized to investigate the $^{16}O(^{12}C,\alpha\,^{20}Ne)\alpha$ and $^{16}O(^{12}C,p\,^{23}Na)\alpha$ three-body processes in order to study, via THM, two of the possible carbon-carbon fusion reaction channels, that is: $^{12}C(^{12}C,\alpha)^{20}Ne$ and $^{12}C(^{12}C,p)^{23}Na$.

The experiment was performed at the Horia Hulubei National Institute of Physics and Nuclear Engineering - IFIN HH (Bucharest, Romania). Preliminary results will be presented in this paper.

ASTROPHYSICAL FRAMEWORK

When helium is consumed in the center of the star, the core mainly consists of ^{12}C and ^{16}O. In stars with mass $M > 8\ M_{\odot}$ the gravitational contraction increases the central temperature up to trigger ^{12}C burning. The first activated process is the $^{12}C+^{12}C$ fusion due to the lowest Coulomb barrier. The most likely reaction channels are: $^{12}C(^{12}C,\alpha)^{20}Ne$,$^{12}C(^{12}C,p)^{23}Na$,$^{12}C(^{12}C,n)^{23}Mg$ [1].

These reactions are involved in the ^{20}Ne, ^{23}Ne and ^{23}Mg nucleosynthesis, but, most important thing, they determine the successive stellar evolution. Carbon burning reaction rate is a fundamental parameter to determine the so-called $M_{up.}$ Stars with $M < M_{up}$ cannot burn carbon and evolve into CO white dwarf, while stars with $M > M_{up}$ can trigger carbon burning and conclude their life as core-collapse Supernovae [2].

The core carbon burning takes place in a temperature range of T = 0.5 - 1.0 GK. For a temperature of 0.5 GK, the corresponding Gamow energy for the $^{12}C+^{12}C$ fusion is $E_G = 1.5 \pm 0.3$ MeV (well below the Coulomb barrier about 8 MeV).

Although carbon fusion reactions take a key role in understanding stellar evolution, its reaction rate is not very well determined right at the energies relevant for astrophysics. Experiments performed so far ([3] and references therein), involving both charged particle and gamma ray spectroscopy, have measured excitation function down to carbon-carbon center of mass energy $E_{cm} = 2$ MeV, that is at the higher edge of the Gamow peak. Nevertheless, experimental data below $E_{cm} = 3$ MeV are rather uncertain [2]. For instance, a recent paper [4] questions the presence of the claimed resonance at $E_{cm} = 2.14$ MeV [3].

Because of the experimental data uncertainty, up to now the only way to obtain the carbon-carbon fusion reaction rate at astrophysical energies has been the extrapolation from experimental data at higher energy [5].

The presence of possible resonant structures in the astrophysical energy range as well, like the already mentioned 2.14 MeV or a theoretically predicted resonance at $E_{cm} = 1.5$ MeV [6], makes the extrapolation a dangerous procedure that can be source of possible systematic uncertainties.

For these reasons new and accurate experimental data, down to the astrophysical energies, are strongly required.
In this paper, we report on the study of the $^{12}C(^{12}C,\alpha)^{20}Ne$ and $^{12}C(^{12}C,p)^{23}Na$ reaction carried out applying the Trojan Horse Method (THM) ([8-9] and references therein) to the three-body reactions $^{16}O(^{12}C,\alpha\,^{20}Ne)\alpha$ and $^{16}O(^{12}C,p\,^{23}Na)\alpha$.

THE EXPERIMENT

The experiment was performed at the Horia Hulubei National Institute of Physics and Nuclear Engineering - IFIN HH. The 9 MV Tandem accelerator provided a 26.5 MeV ^{16}O beam with a spot size on the target of about 1.5 mm and an intensity of about 5 enA. A CH_2 target, 100 $\mu g/cm^2$ thick, was used to induce the $^{16}O + {}^{12}C$ reaction.
^{16}O was used as TH nucleus since it can be described in terms of a $^{12}C \oplus \alpha$ configuration [10]. In the quasi-free breakup framework the interaction between ^{16}O and ^{12}C produces the oxygen breakup in to ^{12}C and α, then ^{12}C interacts with the ^{12}C target giving the two-boy reaction of astrophysical interest, while α is the so-called spectator since does not interfere with the two-body process.
Energy and position of the outgoing particles were detected using five position sensitive silicon detectors (PSD) 1000 μm tick (figure 1). To avoid the problems related to the heavy outgoing particles (^{20}Ne and ^{23}Na)

detection, mainly energy and angular straggling, the experimental set-up of this new measure was defined to detect only the light particles that is alphas and protons. PSD1 covered the 4.5°-18.5° angular range where the alpha spectator detection is highly probable. A 8 μm tick gold foil was put in front of PSD1 to preserve this detector from the elastic scattering.

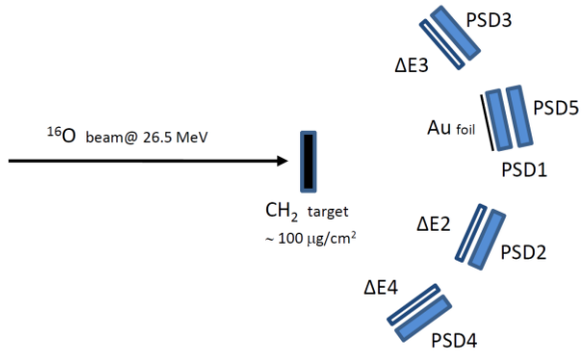

Figure 1: Experimental set-up

PSD2, PSD3 and PSD4 covering the angular range 17.5° - 31.5°, 33.5° - 47° and 47° - 61° respectively, were dedicated to alpha and proton detection. In order to identify these two particles the ΔE-E technique was employed. For this aim 20 μm silicon detector (ΔE2, ΔE3, ΔE4 in figure1) were placed in front of PSD2-3-4. PSD5 was put behind PSD1 in order to catch protons of higher energy. The trigger to the ACQ system was generated setting multiplicity two between PSD1-2-3-4. This experimental set-up allowed us to measure $^{12}C(^{12}C,\alpha)^{20}Ne$ and $^{12}C(^{12}C,p)^{23}Na$ excitation functions in a wide range including the Gamow energy ($E_G = 1.5 \pm 0.3$).
In figure 2 typical ΔE-E 2D plot is shown. It is clear the presence of the proton and alpha loci.

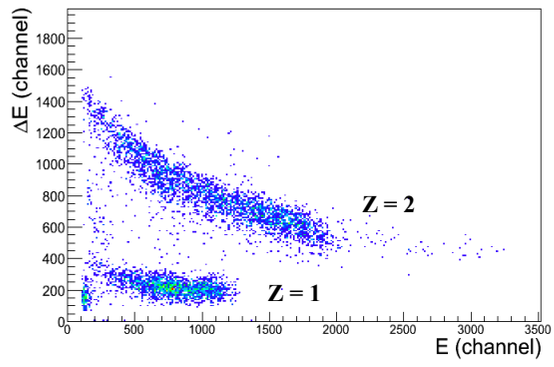

Figure 2: ΔE-E 2D plot for alpha and proton identification.

In figure 3 the experimental Q-value for the three-body process is shown. This experimental variable has been calculated selecting on the ΔE-E matrix the events populating the alpha locus, considering alpha particles detected on PSD1 and assuming that the third undetected particle is a ^{20}Ne. The two peaks are centered at -2.53 MeV and -4.25 MeV corresponding to the Q-value of the three-body reaction $^{16}O(^{12}C,\alpha^{20}Ne)\alpha$ with ^{20}Ne at ground state ad first excited state respectively.

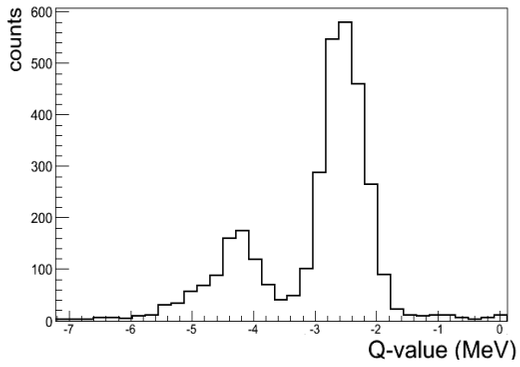

Figure 3: Experimental Q-value for the three-body process $^{16}O(^{12}C,\alpha^{20}Ne)\alpha$. Details in the text.

The good agreement between experimental values and the theoretical ones (-2.545 MeV and -4.175 MeV) makes us confident on the calibration performed and on the correct selection of the reaction channel. Similar result has been obtained for the $^{16}O(^{12}C,p\,^{23}Na)\alpha$ reaction channel.
Next step of the analysis will be the selection of the quasi-free break-up mechanism and the study of the ^{20}Ne-α and ^{23}Na+p relative energy spectrum.

This work was supported by the Italian Ministry of the University under Grant No. RBFR082838 and by the Italian Ministry of University MIUR under the grant "LNS Astrofisica Nucleare (fondi premiali)".

REFERENCES

[1] C. Iliadis *Nuclear Physics of the Stars* WILEY-VCH Verlag GmbH & Co. KGaA (2007).

[2] F. Strieder J. Phys.: Conf. Ser. 202 012025 (2010).

[3] T. Spillane *et al.* Phys. Rev. Lett. 98 122501-4 (2007)

[4] X.D. Tang *et al.* J. Phys.: Conf. Ser. 337 012016 (2012)

[5] G.R. Caughlan and W.A. Fowler *At. Nucl.Data Tables* 40 283-334 (1988).

[6] R.L. Cooper, A.W. Steiner and E.F. Brown *Astroph. J* 702 660-671 (2009).

[8] C. Spitaleri, Proceedings of the 5th Winter School on Hadronic Physics, Folgaria, Italy, (1990)

[9] R. Tribble et al., Rep. Prog. Phys. 77, 106901 (2014).

[10] A. Guichard *et al.* Phys. Rev. C 4 700 (1971).

Measurement of the astrophysical S(E)-factor for the $^{19}F(p,\alpha_1)^{16}O$ reaction through the Trojan Horse method

O. Trippella[1], M. La Cognata[2], C. Spitaleri[2,3], S. Ayakawa[2], G. L. Guardo[2,3], I. Indelicato[2,3], L. Lamia[3], S. Palmerini[2], G. R. Pizzone[2], S. M. R. Puglia[2], G. Rapisarda[2], S. Romano[2], M. L. Sergi[2], R. Spartà[2], A. Tumino[4]

1) Dipartimento di Fisica e Geologia, Università degli Studi di Perugia e INFN, Sezione di Perugia, Perugia, Italy

2) Istituto Nazionale di Fisica Nucleare, Laboratori Nazionali del Sud, Catania, Italy

3) Dipartimento di Fisica e Astronomia, Università di Catania, Catania, Italy

4) Facoltà di Ingegneria e Architettura, Università degli Studi di Enna "Kore", Enna, Italy

Abstract - One of the most important fluorine destruction channel in the hydrogen-rich outer layers of asymptotic giant branch (AGB) stars is the $^{19}F(p,\alpha)^{16}O$. Since the direct measurements in literature do not cover the energy range of astrophysical interest, a new experiment was performed in order to extract the quasi-free (QF) contribution of the $^{19}F(^2H,\alpha^{16}O)n$ through the Trojan Horse Method (THM). The TH measurement has been devoted to the investigation of the α_1 channel, which is often ignored. Here, we describe the experimental technique and present the preliminary results of detectors calibration.

INTRODUCTION

In astrophysics, fluorine, whose the only stable isotope is ^{19}F, is a crucial element of particular interest, because it is extremely sensitive to the physical conditions within stars [1]. Since ^{19}F can be created and destroyed in several different astrophysical sites and conditions, its dominant source is not yet clear [1]. The most likely environments indicated as responsible of its production are: core collapse of Type II supernovae [2]; Wolf–Rayet stars through the ν-process [3]; the convective zone generated by a thermal pulse in the AGB stars [4]. It might also play a fundamental role in hydrogen-deficient post-AGB star nucleosynthesis.

Concerning the AGB phase, the ^{19}F abundance is a consequence of nucleosynthesis processes in both He- and H-rich shells. Specifically, fluorine is produced during the convective thermal pulses and also during the interpulse periods if protons from the envelope are partially mixed in the top layers of the He intershell [5]. On the other hand, the main destruction channels of fluorine are the $^{19}F(\alpha,p)^{22}Ne$ reaction and the neutron captures inside layers enriched in helium, while proton captures $^{19}F(p,\alpha)^{16}O$ and $^{19}F(p,\gamma)^{20}Ne$ are the typical processes occurring in the hydrogen-rich shell.

In this particular environment, deep mixing phenomena in AGB stars can alter the stellar outer-layer isotopic composition due to proton captures at low temperatures (< 0.04 GK), affecting the transported material [6,7,8].

We focused our attention on the $^{19}F(p,\alpha)^{16}O$ reaction, one of the destruction channel in the proton-rich outer layers of AGB stage mentioned in the small list above. So far, available direct measurements do not reach the energy region of astrophysical interest ($E_{c.m.}$ < 300 keV), because of the hindrance effect of the Coulomb barrier. In this context, the measurement of the α_0 channel via the indirect TH technique allowed to observe the presence of resonant structures not observed before [9]. The direct measurements of [10] seem to confirm the results. These caused an increase of the reaction rate at astrophysical temperatures up to a factor of 1.7, with potential consequences for stellar nucleosynthesis [9,10].

Now, we are mostly interested on the α_1 channel investigated with a new measurement using the TH approach This reaction, leading to the first excited state of ^{16}O after feeding virtual levels of ^{20}Ne, is followed by the decay of it to the ground state through the emission of an electron-positron pair. In literature, the astrophysical factor for the (p,α_1) channel is obtained from [11,12,13,14] and then collected in the European Compilation of Reaction Rates (NACRE) by [15]. A non-resonant extrapolation of the S(E)-factor is assumed for the energies below about 600 keV.

MEASUREMENT AND DETECTORS CALIBRATION

In this context, a new experiment was performed by the ASFIN collaboration at the INFN - Laboratori Nazionali del Sud, in Catania with the aim to indirectly investigate the $^{19}F(p,\alpha_1)^{16}O$ reaction (Q value = 8.11361 MeV) via the THM [16]. This technique was used to access the most relevant energy region for astrophysics, by extracting the QF contribution of the $^{19}F(^2H,\alpha^{16}O)n$ reaction (Q value = 5.88904 MeV), from the interaction between a ^{19}F beam and a deuterated polyethylene (CD_2) targets (∼ 100 μg/cm^{-2} thick). The 15 MV Tandem provided a 1 mm collimated ^{19}F beam at the energy of 55 MeV well above the Coulomb barrier of the three body reaction. The deuteron, characterizing the enriched target up to about 99%, is the TH nucleus because it is considered to be composed by two nuclear clusters, a proton and a neutron, with large probability. The QF kinematic conditions were studied so that the fluorine only interacts with protons. A sketch of the experimental setup is schematically represented in Figure 1.

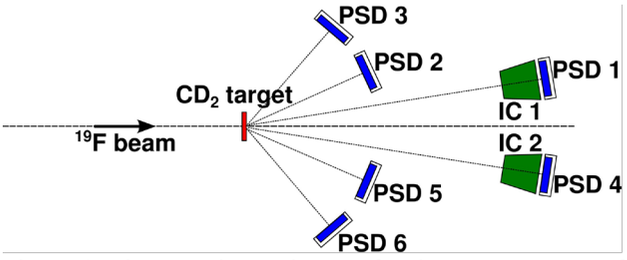

Figure 1. The experimental setup for the measurement of the $^{19}F(^{2}H,\alpha^{16}O)d$ reaction in order to extract the contribution for the two body $^{19}F(p,\alpha_1)^{16}O$ interaction.

Six position-sensitive detectors (PSDs) and two ionization chambers, placed in front of the most forward detectors were used for particles identification. Three PSDs are located on the positive semi-plane of the experimental chamber (diameter of 2 m), while other ones are on the opposite side with respect to the beam line. The distances and the angular position of each detector are listed in Table 1. The experimental setup is essentially symmetric.

Table1. Linear distance from the CD_2 target and angular position for each detector in the case of the $^{19}F(^{2}H,\alpha^{16}O)n$ reaction. The two ionization chambers are placed at 5.9 and 6.1 cm from the corresponding PSD.

PSD	Distance	Angular position
1	36.2 cm	+9.00 deg
2	18.0 cm	+24.45 deg
3	17.8 cm	+49.95 deg
4	35.8 cm	-9.00 deg
5	18.0 cm	-23.65 deg
6	18.0 cm	-49.7 deg

The ΔE − E telescopes was optimized for the detection of ^{16}O recoils, while the PSDs for coincident detection of the α-particles with the oxygen. Angular conditions were selected to optimize the QF contribution. In our case, neutrons are not detected because they would represent a further major source of uncertainty. Their physical quantities, such as energy and angular position, are then reconstructed during the off-line data analysis using standard equation for both momentum and energy conservation.

The first step of data analysis is represented by the calibration on the detectors. For this purpose, grids with eighteen equally spaced vertical slits were placed in front of each PSD at the initial stage of the measurement. This is a fundamental phase in order to establish an unique correspondence between the recorded channel and physical angular position of a signal. A typical and preliminary calibrated angle-energy matrix for PSD2 is shown in Figure 2. At this point, the highly populated kinematic loci in the calibrated matrix should represents the physical signal resulting from the ejectile particles of reactions used for calibration runs.

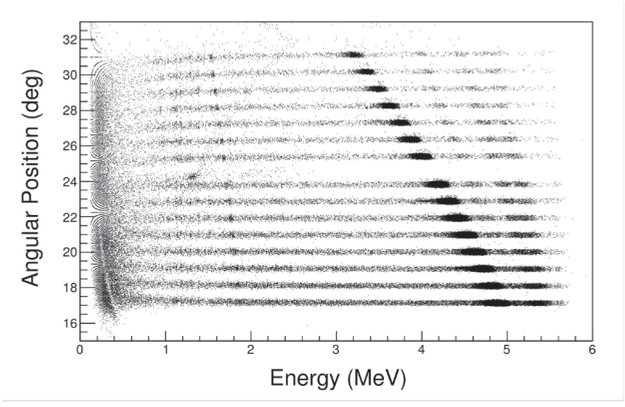

Figure 2. Calibrated position-energy matrix for the PSD2 during the calibration run involving a ^{19}F beam at 30 MeV impinging on a ^{2}H enriched target.

Calibration runs were performed by using several reactions with different targets and/or sources, such as the ^{228}Th 6-peaks alpha-source, elastic scattering of $^{16}O+^{197}Au$ reaction and $^{16}O+^{12}C$, $^{19}F+^{2}H$ and $^{19}F+^{12}C$ reactions at different energies (55, 45, 37, 30 MeV). Specifically, Figure 2 represents the interaction between the ^{19}F beam at 30 MeV and the CD_2 target.

After the procedure of channel and mechanism selection the resulting energy spectrum, representing the three-body excitation function, will be used for the extraction of the $d_2\sigma/dE_{c.m.}d\Omega_n$ cross section of the reaction of astrophysical interest.

As a consequence, the experimental TH data will be analyzed using the modified R-matrix approach [18] and then scaled to the measurements available in literature in the overlap region between direct and indirect data [15].

Then, the astrophysical S(E)-factor and the rate for the $^{19}F(p,\alpha_1)^{16}O$ reaction can be calculated by means of standard formulas and compared to the previous investigations.

REFERENCES

[1] S. Lucatello et al., ApJ 729 (2011) 40.
[2] S. E. Woosley & W. C. Haxton, Nature 334 (1988) 45.
[3] G. Meynet & M. Arnould, A&A 355 (2000) 176.
[4] A. Jorissen et al., A&A 261 (1992) 164.
[5] M. Lugaro et al., ApJ 615 (2004) 934.
[6] M. L. Sergi et al., Ph. Rev. C 82 (2010) 032801.
[7] M. Busso et al., ApJ 717 (2010) L47.
[8] S. Palmerini et al., ApJ 741 (2011) 26.
[9] M. La Cognata et al., ApJ 739 (2011) L54.
[10] I. Lombardo et al., J. Phys. G: Nucl. Part. Phys. 40 (2013) 125102.
[11] R. W. Devons et al., Proc. Phy. Soc. A67 (1954) 134.
[12] W. A. Ranken et al., Ph. Rev. 109 (1958) 1646.
[13] R. Caracciolo et al., Lett. Nuovo Cim. 11 (1974) 33.
[14] P. Cuzzocrea et al., Lett. Nuovo Cim. 28 (1980) 515.
[15] C. Angulo et al., Nuc. Ph. A 656 (1999).
[16] C. Spitaleri et al., Ph. Atomic Nuclei 74 (2011) 1725.

The ELI-NP facility: nuclear astrophysics with gamma-ray beams

M. La Cognata[1], A. Anzalone[1], V. Crucillà[1], D. Lattuada[1,2], C. Spitaleri[1,3], A. Taffara[3]

1) Laboratori Nazionali del Sud – Instituto Nazionale di Fisica Nucleare, Catania, Italy
2) Kore University, Enna, Italy
3) Dipartimento di Fisica & Astronomia, University of Catania, Catania, Italy

Abstract - The ELI-NP facility will supply high intensity and high resolution gamma ray beams at a maximum energy of 20 MeV. Owing to the features of the beam, several nuclear reactions of astrophysical interest can be measured, with unprecedented accuracy

THE ELI-NP FACILITY. A BRIEF DESCRIPTION

The ELI-NP project aims at establishing an European Research Infrastructure Center for ultra-high intensity lasers, laser-matter interactions, nuclear and material science, using laser-driven radiation sources [1]. This multidisciplinary facility will provide new opportunities to study fundamental processes that occur in ultra-intense laser fields during laser–matter interactions. It will also open new dimensions in nuclear research with intense γ beams, produced in Compton back-scattering, and in material research with intense positron beams.

One of the main research tools at the ELI-NP laboratory is the brilliant γ-ray beam. The γ beam is produced through Compton back-scattering of laser light off an accelerated electron beam. Laser photons with energy E_0 are exploited to generate photon beams with high energies E_γ via Compton back-scattering at a small angle θ from a counter-propagating fast electron beam, characterized by its relativistic factor γ according to

$$E_\gamma = 4\gamma^2 \frac{1}{1+(\theta\gamma)^2+\frac{4\gamma E_0}{mc^2}} E_0 \approx 4\gamma^2 E_0 \,.$$

The ELI-NP γ-beam system will enable the production of a brilliant, highly collimated beam of γ rays with a narrow bandwidth. Such a facility will open new experimental perspectives for studies in the field of photonuclear physics. Compared to the existing γ-beam facilities, ELI-NP will provide beams which are about two orders of magnitude more intense with an order of magnitude narrower bandwidth and a smaller beam spot. The expected parameters of the ELI-NP gamma beam system are presented in Table 1.

Advanced γ-ray beams, based on Compton back-scattering between electron bunches and counter-propagating laser pulses, are considered to be the new roadmap to open the field of nuclear photonics. By varying the energy of the accelerated electrons, the energy of the γ beam will be tuned with a very high precision.

Table 1: Parameters of the ELI-NP γ-beam system

Parameter	**Range**
γ-ray energy [MeV]	0.2–19.5
γ-beam divergence [rad]	$\leq 2 \times 10^{-4}$
Average relative bandwidth of the γ-ray beam	$\leq 5 \times 10^{-3}$
Average spectral density at peak energy [$s^{-1}eV^{-1}$]	$\geq 5 \times 10^{3}$

PHYSICS CASE: TWO EXAMPLES

The ELI-NP facility provides unique opportunities for nuclear astrophysics research. For example, the γ-induced nuclear reactions of astrophysical interest were extensively studied during the years but still represent a challenge for the experimental and theoretical work. The difficulty arises from the very small cross sections due to the fact that the reactions occur deep below the Coulomb barrier especially for the case of (γ,α) reactions. Therefore, a very intense γ beam would be of interest for such investigations.

Understanding core-collapse supernovae

Silicon burning sets the chemical composition, and hence the neutron excess, of the star right before the core collapse and the subsequent supernova explosion. This demonstrates the importance of silicon burning in the understanding of core-collapse supernovae [2,3,4].

When ^{16}O is depleted at the conclusion of core oxygen burning, the most abundant nuclei are ^{28}Si and ^{32}S. The stellar core contracts and the temperature increases, reaching values as large as T = 2.8 - 4.1 GK, depending on the stellar mass. Fusion reactions such as $^{28}Si + {}^{28}Si$ or $^{28}Si + {}^{32}S$ are too unlikely to occur owing to the Coulomb barrier between interacting nuclei, even at such high temperatures [5]. Instead, nucleosynthesis takes place through photodisintegration of less bound nuclei and radiative captures of the dissociated light particles (protons, neutrons, and α-particles) to create gradually heavier and more tightly bound nuclei [6]. In detail, since α-particle captures on ^{20}Ne are less likely to occur than the competing (γ,α) reactions, the $^{24}Mg(\gamma,\alpha)^{20}Ne$ reaction governs the downward flow from ^{24}Mg to ^{4}He. It means that the effective rate of ^{28}Si destruction is established by the photodisintegration of ^{24}Mg, making its reaction rate critically important to stellar models of silicon burning [4].

The $^{24}Mg(\gamma,\alpha)^{20}Ne$ reaction rate has been calculated from the $^{20}Ne(\alpha,\gamma)^{24}Mg$ rate. Near T ≈ 3.6 GK, the $^{20}Ne(\alpha,\gamma)^{24}Mg$ reaction rate may be subject to systematic errors of the order of a factor of ≈ 2, as can be seen from the different results reported by Caughlan and Fowler [7], Angulo et al. [8] and Rauscher and Thielemann [9].

A direct ^{24}Mg photodissociation measurement using gamma beams of energies 10.4 - 12 MeV will allow us to determine a much more accurate cross section to be used in nuclear reaction network calculations to improve the knowledge of the pre-supernova chemical composition. Performing Hauser-Feshbach calculations of the $^{20}Ne(\alpha,\gamma)^{24}Mg$ cross section [10] a value of approximately 0.5 mb is obtained for the reverse process in this gamma-ray energy region, corresponding to about 3×10^4 reaction events per day, using the conservative beam intensity of $5x10^3$ γ/s/eV. The estimated $^{24}Mg(\gamma,\alpha)^{20}Ne$ cross section is displayed in Fig. 1.

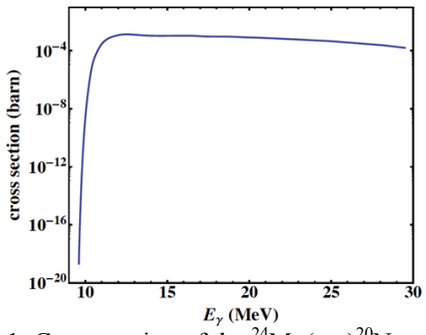

Figure 1: Cross section of the $^{24}Mg(\gamma,\alpha)^{20}Ne$ reaction estimated by the applying the detailed balance principle to the $^{20}Ne(\alpha,\gamma)^{24}Mg$ cross section, calculated using the Hauser-Feshbach approach [10].

Investigation of the p-process

The very neutron-deficient, stable nuclides with mass numbers of A ≥ 74 (between ^{74}Se and ^{196}Hg) are bypassed by the s- and r-process. These species are referred to as p-nuclei, where the letter p designates the fact that they contain more protons relative to other stable isotopes of the same element. As a group, the p-nuclei are the rarest among the stable nuclides. Their synthesis is still very uncertain; one of the most likely scenarios is type II supernova. Indeed, when the shockwave passes through the O–Ne-rich layer of a massive star the temperature, density and composition might be suited for the production of p-nuclei [4].

With few exceptions, no data are available on photodissociation reactions leading to the production of p-nuclei, and Hauser–Feshbach calculations have to be performed. However, different prescriptions of the Hauser–Feshbach model influence sensitively the final p-nuclei abundances obtained from type II supernovae. Therefore, large systematic errors might be present, leading to inaccurate and misleading comparison of models with observational data, making it very difficult to identify the correct p-process site and understand the p-process nucleosynthesis.

A common feature of p-process calculations is the underproduction of species such as ^{92}Mo, ^{94}Mo, ^{113}In and ^{115}Sn, pointing at an unsolved problem of current p-process computations [4]. A critical process, among many others, is the $^{96}Ru(\gamma,\alpha)^{92}Mo$ reaction, whose cross section changes the final abundance of ^{96}Ru by a factor of 2 if the reaction rate is changed by a factor of 3, which is a very realistic modification at present [4]. It is worth noting that most the reactions above involve nuclear species that are unavailable in gaseous form, making the use of a silicon strip detector mandatory for the investigation of the corresponding photodissociation reactions.

Hauser-Feshbach calculations of the $^{92}Mo(\alpha,\gamma)^{96}Ru$ cross section [10] yield a value of approximately 18 mb for the reverse process at a gamma-ray energy of 9.3 MeV, that is, the energy at which such photodissociation reaction is most effective in type II supernovae. Using this cross section would yield about 6.6×10^5 reaction events per day, using the conservative beam intensity of 5x103 γ/s/eV onto a 100 μg/cm^2 target. The estimated $^{96}Ru(\gamma,\alpha)^{92}Mo$ cross section is displayed in Fig. 2

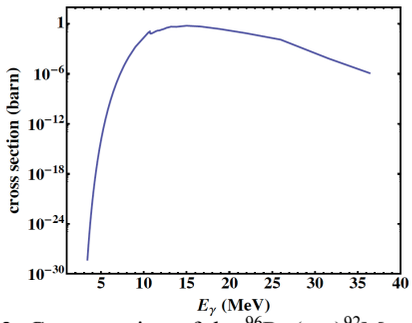

Figure 2: Cross section of the $^{96}Ru(\gamma,\alpha)^{92}Mo$ reaction estimated by the applying the detailed balance principle to the $^{92}Mo(\alpha,\gamma)^{96}Ru$ cross section, calculated using the Hauser-Feshbach approach [10].

REFERENCES

[1] ELI — Extreme Light Infrastructure Science and Technology with Ultra-Intense Lasers Whitebook, eds. G.A. Mourou et al., THOSS Media, 2011.

[2] Bodansky, D., Clayton, D.D., Fowler, W.A., Astrophys. J. Suppl. 148 (1968) 299.

[3] S.E. Woosley, W.D. Arnett, D.D. Clayton, Astrophys. J. Suppl. 26 (1973) 231.

[4] Iliadis, C., Nuclear Physics of Stars (Weinheim: Wiley-VCH Verlag, 2007).

[5] A.J. Howard, H.B. Jensen, M. Rios, W.A. Fowler, B.A. Zimmerman, Astrophys. J. 188 (1974) 131.

[6] Hix, W.R. & Thielemann, F.-K., Astrophys. J. 460 (1996)869.

[7] G.R. Caughlan and W.A. Fowler, At. Dat. Nucl. Dat. Tab. 40 (1988) 283.

[8] C. Angulo et al., Nucl. Phys. A656 (1999) 3.

[9] Rauscher, T. & Thielemann, F.-K., At. Data Nucl. Dat. Tab. 75 (2000) 1.

[10] Rauscher, T., At. Data Nucl. Dat. Tab. 79 (2001) 47.

GEANT4 simulations of electromagnetic background for photonuclear reactions at the ELI-NP facility

D. Lattuada[1,2], A. Anzalone[1], G. A. P. Cirrone[1], V. Crucillà[1], M. La Cognata[1], C. Spitaleri[1,3], A. Taffara[3], A. Tramontana[1]

1) Laboratori Nazionali del Sud – Instituto Nazionale di Fisica Nucleare, Catania, Italy

2) Dipartimento di Ingegneria e Architettura, Università degli Studi KORE, Enna, Italy

3) Dipartimento di Fisica & Astronomia, University of Catania, Catania, Italy

Abstract - The ELI-NP facility will supply high intensity and high resolution gamma ray beams at a maximum energy of 20 MeV. A study of the electromagnetic and hadronic background produced by photonuclear reactions of astrophysical interest by means of GEANT4-based Monte Carlo simulations is ongoing.

THE ELI-NP FACILITY. A BRIEF DESCRIPTION

ELI-NP will be one of the three pillars of ELI - THE EXTREME LIGHT INFRASTRUCTURE and aims at establishing an European Research Infrastructure Center for ultra-high intensity lasers, laser-matter interactions, nuclear and material science, using laser-driven radiation sources [1]. One of the main research tools at the ELI-NP laboratory is the brilliant γ-ray beam, produced through Compton back-scattering of laser light off an accelerated electron beam. Compared to the existing γ-beam facilities, ELI-NP will provide beams which are about two orders of magnitude more intense with an order of magnitude narrower bandwidth and a smaller beam spot [2].

MONTE CARLO SIMULATION

The ELI-NP facility provides unique opportunities for nuclear astrophysics research. In order to study γ-induced nuclear reactions of astrophysical interest an experiment is proposed to use Silicon Strip Detectors (SSDs) to detect alpha particles in (γ,α) reactions of astrophysical interest [2,3].

For example, the $^{24}Mg(\gamma,\alpha)^{20}Ne$ reaction has great astrophysical importance in stellar evolution [2] and a direct measurement of the photonuclear cross section would set a milestone in the development of core-collapse supernova models.

Since many silicon strip detector assemblies to detect charged particles off photodissociation events at ELI-NP are possible (for instance, a silicon ball or a barrel of double sided silicon strip detectros), we have performed GEANT4 [4] simulations of the experimental setup to optimize resolution, detection efficiency , compactness, granularity, costs and possibility of particle identification. According to our simulations, the barrel configuration (Fig. 1) represents the best configuration, both on the technical point of view and for its cost [3].

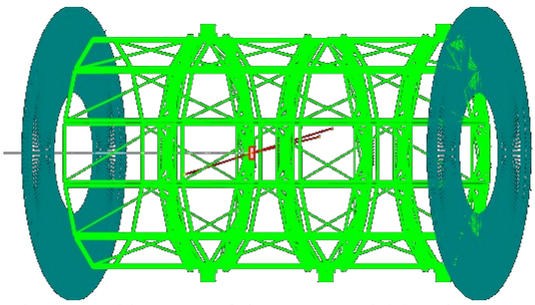

Figure 1: Close up of the proposed SSD detector, the ^{24}Mg target and the ^{12}C backing is shown. A γ photon (grey) coming from the left and producing 3 alpha tracks (red) by interacting with the carbon backing.

Electromagnetic Background

Beam induced background plays a key role especially because low detection thresholds are needed to fully reconstruct the reaction kinematics. A major source of background might be ascribed to electrons, positrons and5 gamma rays from Compton and photoelectric effects and pair production in the target. Of course, at ≈ 11 MeV the -photoelectric contribution is negligible. Assuming a solid ^{24}Mg target, 100 μg/cm^2 thick to reduce energy straggling of the outgoing alphas, deposited onto a 60 μg/cm^2 thick carbon backing, a GEANT4 (version 4.10.01) simulation code has been used to estimate such background, to confirm that a silicon array can be used under typical ELI-NP gamma-beam conditions.

In first instance, the detector geometry has been built using GEANT4 standard geometry objects and a CAD model (STEP) was eventually imported through STL format using FreeCAD and CADMesh [6]. Tests on this procedure are still ongoing in order to reduce geometry overlaps due to tessellation in the conversion procedure (STEP to STL) and to optimize the simulation to save

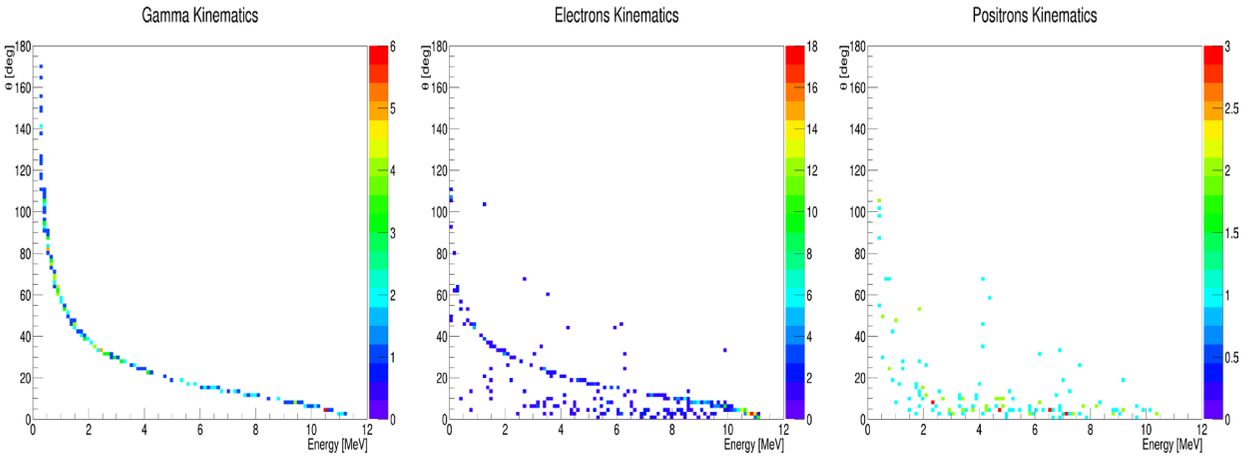

Figure 2: Kinematics of emitted photons, electrons and positrons after the gamma beam interaction with the target plus backing system.

CPU time.

We simulated a gamma beam of 10^8 photons at 11.40 MeV, approximately equal to the amount of gammas hitting the target in 0.1 seconds and want to evaluate the electromagnetic background due to Compton scattering (mainly), photoelectric effect and electron-positron couple annihilation-creation. We look for electrons, positrons and gamma rays reaching the target and produced by the interaction of the beam with the magnesium target, the carbon backing and the chamber.

We used GEANT4 standard electromagnetic *physics list* with *G4EmStandardPhysics_option3* and tested different cuts for secondary particles tracking up the energies of interest in order to boost the simulation without losing important information and particle production.

As shown in Fig. 2 the expected electromagnetic background of gammas, electrons and positrons is rather small and it isn't an issue for particle identification or detector damage. In particular the fraction of photons whose energies exceed a typical particle emission threshold (4 MeV) and reaching the detector ($\theta > 15°$) is absolutely negligible. Moreover, the energy deposited by electrons in the silicon detectors (e.g. 150 μm thick), is well below 100 keV, making the electronic threshold necessary to cut background events significantly smaller than the energies of the alpha particles from the reaction of interest.

Photonuclear Reactions

We also investigated the possibility to use kinematics to disentangle the channel of interest from background processes, evaluating the particle yield from gamma interaction with a ^{24}Mg target and other nuclei that may be present in the chamber. Unfortunately, photonuclear models aren't yet validated in GEANT4 at energy close to the threshold (i.e. they don't provide correct physics) [7] .

So we used a simple but efficient Monte Carlo simulation to show that particle identification and background suppression due to reactions on impurities and especially on the target backing can be effectively achieved if the reaction kinematics is recorded, since the ^{24}Mg(γ,α)^{20}Ne reaction is a binary process. This is possible because at a known fixed angle alphas are emitted with a well-determined energy, making it possible to gate on this region to determine the differential cross section. The analysis is still ongoing.

REFERENCES

[1] ELI — Extreme Light Infrastructure Science and Technology with Ultra-Intense Lasers Whitebook, eds. G.A. Mourou et al., THOSS Media, 2011.

[2] The ELI-NP facility: nuclear astrophysics with gamma-ray beams, La Cognata et al., LNS Activity Report 2013-2014.

[3] The ELI-NP facility: design of a large area silicon array detector and of the vacuum chamber for nuclear astrophysics at ELI-NP, Crucilllà et al., LNS Activity Report 2013-2014.

[4] GEANT4 – a simulation toolkit, GEANT4 Collaboration, Nuclear Instruments and Methods in Physics Research Section A: Accelerators, Spectrometers, Detectors and Associated Equipment, Volume 506, Issue 3, 1 July 2003, Pages 250–303.

[5] A. Anzalone, et al. Charged Particle Detection at ELI-NP, Technical Design Report RA4 – TDR 4.

[6] A CAD Interface for GEANT4, Poole, C. M. and Cornelius, I. and Trapp, J. V. and Langton, C. M., Australasian Physical & Engineering Science in Medicine, September 2012.

[7] GEANT4 User Forum, Hadronic Interactions section: http://hypernews.slac.stanford.edu/HyperNews/geant4/get/hadronprocess.html

The determination of the $^{17}O(p,\alpha)^{14}N$ and $^{18}O(p,\alpha)^{15}N$ reaction rate trough the THM and the composition of oxide grains of AGB origin

S. Palmerini[1], M. L. Sergi[1], M. La Cognata[1], L. Lamia[2], R.G. Pizzone[1], C. Spitaleri[1,2]

1) INFN-Laboratori Nazionali del Sud, Catania, Italy.
2) Dipartimento di Fisica e Astronomia, Università degli Studi di Catania, Italy.

Abstract - The $^{17}O(p,\alpha)^{14}N$ and $^{18}O(p,\alpha)^{15}N$ reaction rate determined by the Trojan Horse Method (THM) have been introduced into calculations of Asymptotic Giant Branch (AGB) star nucleosynthesis. Results compared with geochemical analysis of oxygen rich meteorite grains strengthen the hypothesis that they formed in very low mass stars.

INTRODUCTION

Asymptotic Giant Branch phase (AGB) is the last stage of evolution for low mass stars ($M \leq 6M_{\odot}$). Since the small is the mass the large is the number of objects in a galaxy, AGB stars contribute to the chemical evolution of the interstellar medium as well as more massive but less frequent supernovae.

The main energy source for AGB stars is the H-burning, which radiatively takes place in a thin shell placed below an extended and cold convective envelope. In this environment products of stellar nucleosynthesis might condensate in grains. Part of these solids, which came to us as inclusions in meteorites felt on the Earth, provide very precise hints of the nucleosynthesis of stars where they formed. Indeed, geochemical analysis can determine the isotopic composition of these solids with an extremely high precision, which is not allowed to stellar spectroscopy.

Meteorites grains have been classified on the base of their composition and the possible stellar progenitor [1]. In particular, group 1 and 2 oxide grains are considered to be born in the envelope of Red Giant Branch (RGB)[1] and AGB stars, respectively [2]. Indeed the oxygen isotopic mix they show provide stringent constraints to the nucleosynthesis of the progenitor stars, because of the fragility of ^{18}O and the sensitivity of ^{17}O abundance to temperature. In particular, the excess of $^{17}O/^{16}O$ and the large $^{18}O/^{16}O$ depletion with respect to the solar values found in group 2 grains cannot be accounted by the nuclesynthesis of star more massive than $2M_{\odot}$ [3].

However, this abundances remain far also from the predictions of the standard models of low mass star nuclosynthesis. As an explanation for the reported anomalies of O isotopic ratios in presolar grains, [4] suggested a non convective transport mechanism called 'Cool Bottom Process' (CBP) linking the stellar convective envelope to deeper layers where H-burning takes place. In this context, the ^{18}O is burnt through the $^{18}O(p,\alpha)^{15}N$ reaction, by mixing phenomena, while the maximum temperature experienced by the circulating material determines the $^{17}O/^{16}O$ isotopic ratio [5,6,7].

THM REACTION RATES AND AGB NUCLEOSYNTHESIS

The $^{17}O(p,\alpha)^{14}N$ and $^{18}O(p,\alpha)^{15}N$ reaction cross section have been measured by the THM in the energy region of interest for AGB nucleosynthesis, where they are dominate by the 65keV, and 20keV and 70keV respectively [8]. In the temperature range of our interest the 65 keV resonance tail is also dominant in determining the $^{17}O(p,\gamma)^{18}F$ reaction rate, for this reason a modified $^{17}O(p,\gamma)^{18}F$ reaction rate including the THM-scaled strength of the 65 keV resonance has been also estimated [7]. The comparisons between the THM reaction rates and other data in literature are shown by figure 1.

The THM rates of the three reaction of our interest have been introduced into the models for proton-capture nucleosynthesis coupled with CBP episodes presented by [9]. To safely analyze the consequences on stellar nucleosynthesis of the new nuclear physics inputs and to avoid uncertainties due to the hypothesis about physical cause of CBP (which are still subject of debate), the studied rates have been introduced into the parametric model presented by [5,6].

RESULTS

In Figure 2, we present a comparison between our results and ones obtained by [6] adopting in calculation the reaction rates reported in literature [10]. In the figure the black squares along the almost horizontal dashed line report the oxygen isotopic abundances in the envelope of RGB stars with different mass (from 1 to $2M_{\odot}$ as indicated by the labels) and solar composition. These values, which have been taken as initial ones for our CBP calculations, do not result to be sensitive to the $^{17}O+p$ or the $^{18}O+p$ reaction rates employed in calculations. Instead, it is clearly shown that, for the same CBP cases during the AGB phase, models considering TH data (red curves) are in better agreement with the $^{18}O/^{16}O$ versus $^{17}O/^{16}O$ values found in group 2 grains (solid points).

[1] The evolutionary stage that foregoes the AGB phase.

The temporal evolution of chemical abundances under the effect of CBP is actually shown by the downward red and black curves, which deal with calculations employing

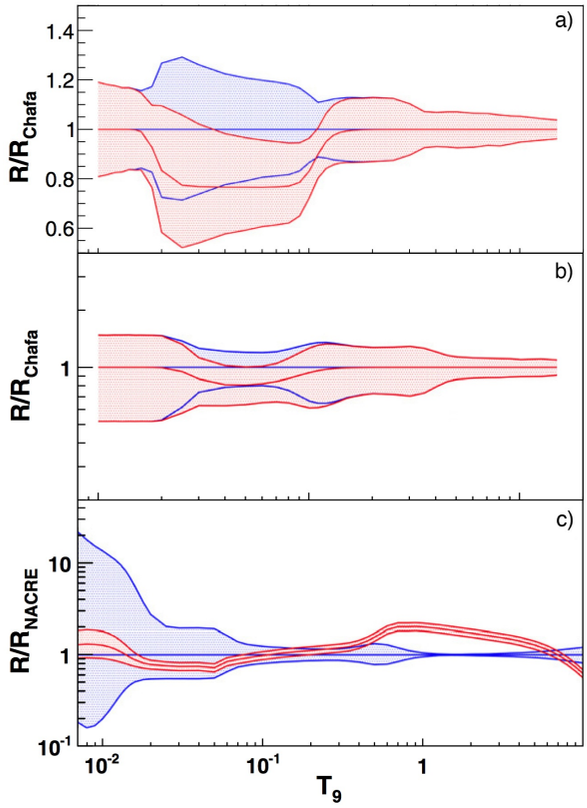

Figura 1. Ratios between the $^{17}O(p,\alpha)^{14}N$ (a), $^{17}O(p,\gamma)^{18}F$ (b) and $^{18}O(p,\alpha)^{15}N$ (c) reaction rates including resonance strengths measured by the THM (red lines), and the reaction rates reported in literature (blue lines)[10].

THM measurements and data from [23], respectively. The lowest $^{18}O/^{16}O$ values exhibited by group 2 grains can be explained by the most efficient CBP case applied to a $1.2M_{\odot}$ AGB model. Since the THM determinations of the $^{17}O+p$ reaction rates increase the $^{17}O/^{16}O$ equilibrium values in the CNO burning by about 30%, predictions for oxygen isotopic mix better agree with "observational" constraints retrieved from oxide grains and points with $^{17}O/^{16}O \leq 0.001$ can be better accounted. This finding strengthens the idea that group 2 grains were formed in the envelope of low-mass AGB stars. According to the present work, the upper limit for the progenitor mass should be reduced to 1.2-1.5 $M_{\odot}$ from 1.5-2$M_{\odot}$, $^{17}O/^{16}O \leq 0.0013$ being well reproduced by CBP models applied to an AGB star of 1.2 $M_{\odot}$ and solar metallicity.

Finally, the composition of grains most poor in ^{17}O is accounted for by models assuming that CBP has occurred in a $1M_{\odot}$ star during the AGB stage and also during previous longer RGB phase. Notice that in the study by [7], where nuclear physics input from [25] were considered, these grains were retined to belong to a 'forbidden' region, which could not be accounted for by nucleosynthesis models.

Conversely, no significant changes in the AGB nucleosynthesis predictions arise from the investigation of $^{18}O(p,\alpha)^{15}N$ fusion reaction by means of THM.

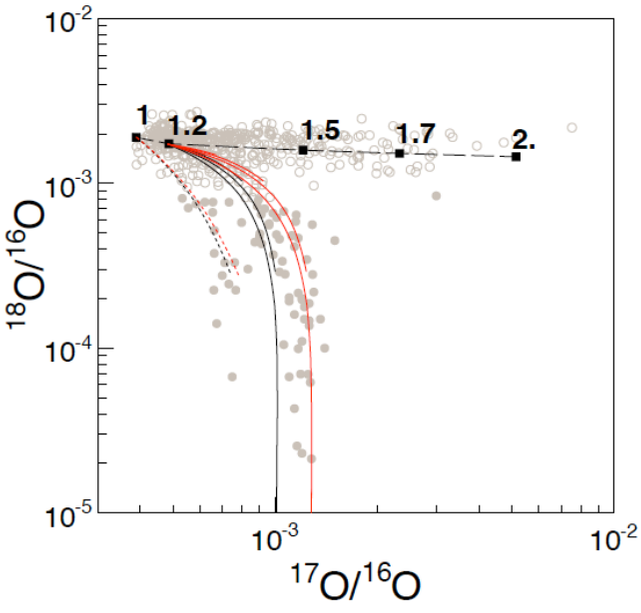

Figura 2: Comparison between the oxygen isotopic mix meassured in a sample of oxide grains and nucleosynthesis calculations for AGB stars with mass from a $1M_{\odot}$ and a $1.2M_{\odot}$ and solar composition. Different lines refer to different mixing parameters, see the text and [7] for details. Grain data from WUSTL Presolar Database (http://presolar.wustl.edu/~pgd/welcome.html)

The authors acknowledge the support of the Italian Ministry of Education, University and Research under grant Progetto Premiale ASTROF.MIUR PFE, CD 19/12/2012 n. 12609'.

REFERENCES

[1] E. Zinner, Treatise of Geochemistry I. Meteorites, Comets, and Planets, Annu. Rev. Astron. Astrophys. (2005) Amsterdam: Elsevier, 17.
[2] L. R. Nittler, et al., ApJ, 483 (1997) 475.
[3] C. Iliadis, et al., PhRvC, 77 (2008) 045802.
[4] A. I. Boothroyd, I. J. Sackmann, G. J. Wasserburg, ApJL , 442 (1995) 21.
[5] K. M. Nollett, M. Busso, G. J.Wasserburg, ApJ, 582 (2004) 1036.
[6] S. Palmerini, et al., ApJ , 729 (2011) 3.
[7] S. Palmerini, et al., ApJ , 764 (2013) 128.
[8] M. L. Sergi, et al., PhRvC., submitted.
[9] M. La Cognata, et al. ApJ , 708 (2010) 796.
[10] E. G. Adelberger, et al., Rev.Mod.Phys., 83 (2011) 195.

The updated ^{6}Li(p,α)^{3}He reaction rate as deduced by THM measurements

L. Lamia[a], C. Spitaleri[a,b], R.G. Pizzone[b], E. Tognelli[c,d], S. Degl'Innocenti[c,d], M. La Cognata[b], P.G. Prada Moroni[c,d], M.L. Sergi[a,b], A. Tumino[b,e],

a) Dipartimento di Fisica e Astronomia, Università di Catania, Italy
b) INFN Laboratori Nazionali del Sud, Catania, Italy
c) Università di Pisa, Pisa, Italy
d) INFN-Sezione di Pisa, Pisa, Italy
e) Università "Kore" di Enna, Enna, Italy

Abstract - Lithium problem is among one of the most interesting and unsolved issues in astrophysics, being its interest connected with both primordial and stellar nucleosynthesis. The ^{6}Li-case is of importance in pre-main-sequence (PMS) and the most recent THM ^{6}Li investigation is here discussed together its impact on PMS phase as evaluated via the updated FRANEC evolutionary code.

FRAMEWORK

In the stellar physics domain the "light elements", deuteron, lithium, beryllium and boron mainly experience (p,α) burning at different temperatures, corresponding to different depths of stellar interior. Due to their different fragility against (p,α) reaction, these are mainly destroyed in stars at temperatures of few millions of kelvin, increasing from T_6>2 for those induced on lithium up to T_6>4.5 for the one induced on boron isotopes. Thus during the Pre-main sequence (PMS) phase, light lements are completely burned in the stellar interiors; however light elements can still be present at the stellar surface where they can be spectroscopically observed. Pre-main sequence (PMS) stars show really deep convective envelopes at the bottom of whose the temperature reach the ignition values for nuclear burning. Deuteron and lithium are usually strongly depleted in such environments, while the Be and B depletion is less efficient, strongly depending on the depth of the convective envelope. This is in turn related to the stellar mass and its metallicity; as well known the extension of the convective envelope increases with the decrease of the mass and with the increase of the metallicity. Since the burning efficiency depends on the extension of the convective envelope, the light elements can be then used as tracers of stellar mixing phenomena, possibly induced by stellar rotation. In order to complement the still open questions for astrophysical models (i.e. opacity evaluation, stellar mass determination, convection mechanisms description, etc.), nuclear cross section reaction rates need to be precisely known in the astrophysical range of interest for the Li, Be, and B burning, which corresponds to Gamow peak ranges from few keV's up to 10 keV [1]. Here, the lithium-6 depleting channel has been discussed, by means of the investigation performed at energies of few keV's very close to the Gamow peak for PMS stars.

THE THM APPROACH: EXPERIMENTAL RESULTS

The main lithium-6 depleting channel, namely the ^{6}Li(p,α)^{3}He nuclear reaction, has been studied via two different experiments in which the Trojan Horse Method (THM) has been applied to the ^{2}H(^{6}Li, α^{3}He)n quasi-free (QF) reaction, using a deuteron as the TH nucleus due to its obvious p–n structure. The full details of the experimental set-up and data analysis can be found in the works of [2,3]. Thanks to the lowest energy range explored, the TH data of [3] have been re-studied in [4] because of the ^{6}Li(p, α)^{3}He cross section measurements of [5,6], thus allowing us to perform a new normalization procedure taking into account the most recent direct measurements. In particular, the more accurate high-energy data of [5,6] affected by an overall error of about 6%, together with the direct measurements proposed in the NACRE compilation [7], constitute a single set of experimental results to which the TH data have been normalized. The result of this procedure is shown in Fig.1, where the TH data discussed here are shown as solid red squares, while the direct measurements of [5,6] are shown as open diamonds (blue and red, respectively). The other direct measurements, as given in the NACRE compilation [7] are also shown. Solid black points represent the data of the previous TH experiment discussed in [3].

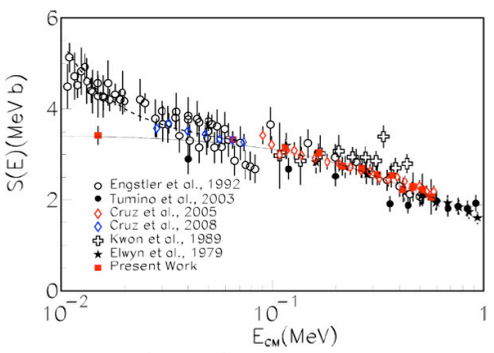

Figure 1: The THM ^{6}Li(p,α)^{3}He measurements (red squares) discussed in [4] together with their experimental fit (solid black line). The dashed line corresponds to the enhanced THM S(E)-factor with U_e=355 eV.

The black solid line in Fig.1 represents the fit on the THM experimental data (red squares), thus returning the value of S(0)=3.44±0.44 MeV b for the zero-energy S(E)-factor (see [4] for details). By using the bare-nucleus THM S(E)-factor (S_b), the "shielded" low-energy data of [8] (namely S_{sh}) have been finally used for extracting the electron screening potential U_e by means of the standard formula $S_{sh}(E)=S_b(E)\times\exp(\pi\eta U_e/E)$ [8]. Here, η and E are the Sommerfeld parameter and the center of mass energy in the entry ^{6}Li-p channel, respectively. This returns the value of U_e=355±100 eV in agreement with the available direct measurements, although it largely exceeds the value of about 180 eV predicted by the available theoretical predictions. The disagreement, already detected in several low-energy S(E)-factor determinations, strongly confirms the need of more accurate theoretical approach for solving the long-standing electron screening problem.

REACTION RATE CALCULATION AND ITS IMPACT

By using the measured THM S(E)-factor, namely S_b(E), we have then calculated the corresponding thermonuclear reaction rate via the standard formula

$$N_A<\sigma v>=\left(\frac{8}{\pi\mu}\right)^{1/2}\frac{N_A}{(kT)^{3/2}}\int_0^\infty S_b(E)e^{-2\pi\eta-\frac{E}{kT}}dE \quad (cm^3mol^{-1}s^{-1})$$

where μ is the ^{6}Li-p reduced mass, N_A the Avogadro's number and k the Boltzmann constant. The integration of the THM reaction rate has been performed in the energy range cover by the experiment, i.e. E<300 keV. Thus, the adopted reaction rate has been finally expressed by means of the analytical form given in the JINA REACLIB [9], as

$$N_A<\sigma v>^{THM}=N_A<\sigma v>^{REACLIB}\cdot f_{corr}$$

where f_{corr} is a correction factor given in terms of billions of Kelvin, T_9, as

$$f_{\rm corr}(T_9)=1.09-0.48\times10^{-1}\cdot\ln T_9 -0.50\times10^{-2}\cdot(\ln T_9)^2+0.38\times10^{-2}\cdot(\ln T_9)^3 +0.99\times10^{-3}\cdot(\ln T_9)^4+0.68\times10^{-4}\cdot(\ln T_9)^5$$

Thus, the adopted-to-fitted THM reaction rate evaluation has been also performed, returning a maximum difference of less than 2%, as shown in Fig. 2.

The obtained THM reaction rate deviates of about 15% from the REACLIB one at temperatures of about T_9=0.001, thus possibly intervening in modifying our present understanding of lithium-6 fate in PMS stars.

For such a reason, the THM reaction rate has been then adopted for evaluating its astrophysical implications by using the FRANEC code for PMS models since the surface ^{6}Li is essentially burned in this stellar phase [1].

Fig. 3 shows the relative ^{6}Li abundance evolution for a given stellar metallicity of [Fe/H]=-0.5 for the labeled stellar masses. From the figure it's evident the well known

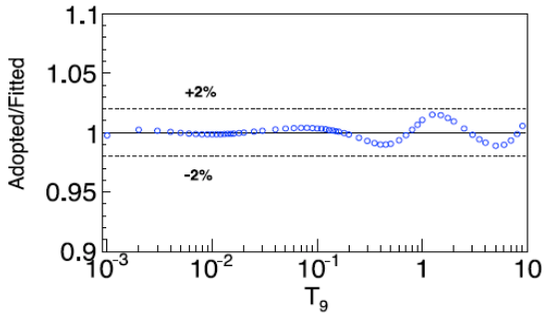

Figure 2: Deviation between the adopted and the fitted THM THM ^{6}Li(p,α)^{3}He reaction rate.

dependence of lithium depletion on the stellar mass and thus on the temperature at the bottom of the convective envelope. In addition, for each stellar mass, we have also reported the ^{6}Li evolution by using three different reaction rates, in order to evaluate the impact of the nuclear physics on the adopted stellar models. For such a reason, the NACRE reaction rate (dotted line), the JINA reaction rate (dashed line), and the TH reaction rate extracted in [4] (full line) have been used in our calculation. The evaluated ^{6}Li time evolution for the TH case tends to lowering the lithium abundance at about 15% of that one given by the NACRE calculation. However, we strongly underline that, while the NACRE result relies on an extrapolation procedure from about 50 keV down to zero, the TH reaction rate has been performed by using the measurement at about 10keV, without any extrapolation. The present results represent then a further assessment of the ^{6}Li+p reaction rate evaluation without the need of any extrapolation and, additionally, underlines its effects on stellar lithium burning.

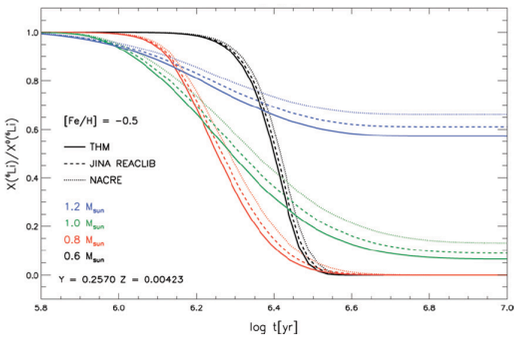

Figure 3: The ^{6}Li time evolution for a [Fe/H]=-0.5 metallicity star and for the labeled mass values. Different line styles refer to different adopted reaction rates, as given in the text.

REFERENCES

[1] E. Tognelli et al., A&A, 548, A41 (2012)
[2] A. Tumino et al., Phys. Rev. C, 67, 065803 (2003)
[3] A. Tumino et al., PThPs, 154, 341 (2004)
[4] L. Lamia et al., The Astroph. Journ., 768, 65 (2013)
[5] J. Cruz et al., PLB, 624, 181 (2005)
[6] J. Cruz et al., JPhG, 35, 014004 (2008)
[7] NACRE, Angulo et al., NuPhA, 656, 3 (1999)
[8] S. Engstler, ZPhA, 342, 471 (1992)
[9] R. Cyburt et al., ApJS, 189, 240 (2010)

Study of the $^{19}F(\alpha,p)^{22}Ne$ reaction under astrophysical conditions via THM method

G.D'Agata[1,2], C. Spitaleri[1,2], R.G.Pizzone[1], P. Figuera[1,2], , G. L. Guardo[1,2], S. Hayakawa[1], I. Indelicato[1,2], R. Kshetri[1], M. La Cognata[1],L. Lamia[1,2], M. Lattuada[1,2], L. Sergi[1], M,Gulino[1,3], A. Tumino[1,3], S. Blagus[4], L. M. Grassi[4], M. Milin[4], D. Miljanic[4], N. Skukan[4], N. Soic[4], V. Tokic[4]

1) Istituto Nazionale di Fisica Nucleare - Laboratori Nazionali del Sud, Catania, Italy

2) Dipartimento di Fisica e Astronomia, University of Catania, Catania, Italy

3)Kore University, Enna, Italy

4)Rudjer Boskovic Institut,Zagreb,Croatia

Abstract - $^{19}F(\alpha,p)^{22}Ne$ is one of the key reaction in the destruction of fluorine in AGB stars. The Coulomb barrier, at astrophysical energies, is a hindrance for such reaction: in our case, in fact, the so-called Gamow peak (E_{CM} ≈430 keV), is far below (E_{CM} ≈3.81 MeV). The cross section was therefore measured using the Trojan Horse Method (THM), that consist in extracting a two-body cross section from the quasi-free contribution of a three-body reaction in the exit channel. This measurement shows the presence of resonant structures that could cause an increase in the reaction rate at typical temperatures for AGB stars at about $T=2\cdot10^8$ K, with great consequences for stellar nucleosynthesis.

INTRODUCTION

In AGB stars, the ways in which ^{19}F is created and destroyed is crucial: the understanding of fluorine abundances, in fact, can constitute a strong constraint, since this element is connected to standard and extra-mixing processes taking place inside AGB stars, and given the fact that AGB stars are considered to be the main source of fluorine in galactic environment [1]. Models do not fit the experimental abundances, overestimating them: it is therefore clear that further investigations are needed, from an astrophysical and a "nuclear" point of view. Those uncertainties are, in most part, the result of a not-so-good treatment of mixing phenomena [2], but a better knowledge about the reaction rate at such low energies is also important [3]. In this work we will focus on the $^{19}F(\alpha,p)^{22}Ne$, representing the main destruction channel in the He-rich environment of AGB stars, at $T\approx2\cdot10^8$ K. As for now, the lowest energies at which this reaction has been seen and studied with direct methods are at E_{Beam} = 1100 keV [9][10], corresponding at 660 keV in the C.M. system , while the Gamow window is between 390 and 800 keV, far below the Coulomb barrier.

THE EXPERIMENT

The $^{19}F(\alpha,p)^{22}Ne$ reaction has been measured at the Rujder Boskovic Institute (Zagreb) applying the THM. Following this method we selected the quasi-free contribution coming from $^6Li(^{19}F, p^{22}Ne)d$ 2➔3 reaction at $E_{Beam}=6MeV$. The experimental Set-up (Fig.1) consist of two telescopes (placed at 32° and 12.3°), made up from a thin silicon detector (9μm thick) (DE1 and DE2) and a thick Position Sensitive Detector (500μm thick) (PSD1 and PSD2) in the region between 0° and 90° with respect to the beam, and three PSD (PSD3 PSD4 and PSD5)(*500μm* thick), on the other side. In the two telescopes, the thin silicon detector was used to discriminate d particles (spectator particle) coming from the reaction, realized using a ^6Li beam impinging on a ^7LiF target (approximately $150\mu g/cm^2$ thick and oriented at 45° in respect of the beam direction), using the ΔE-E technique. Regarding the PSDs 3-5, they are meant to detect protons.

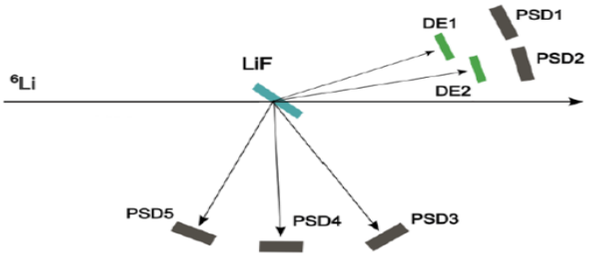

Figure 1: Experimental set-up

Angular conditions were selected in order to maximize QF contributions, and were chosen to cover the momentum region of the deuteron between *0* and *70MeV/c*, in which the momentum distribution for the α-d system is expected to have a maximum *at* $p_s=0$ *MeV/c*. In this case the spectator is detected, so the distribution is not complete and symmetric. The experiment allows us to distinguish particles hitting PSD1 and PSD2 using the ΔE-E identification technique. Our apparatus is able to discern particles in charge and in mass: we are therefore able to select only the particle we are interested in, in this case deuterium (Z=1, A=2 spectator particle). After this operation we cannot be sure from which reaction this particles are coming. Studying the Q-value spectrum of

the selected events, we try to find a peak corresponding to the expected theoretical Q-value (*Q=0.199MeV*). In our region of interest (i.e. *-1÷2MeV*) a shallow peak corresponding to the expected Q-value and a stronger one at negative energies are present, with the last one that could disturb our reaction channel. The Q-value must be independent from other kinematic variables (i.e. angle), as ascertained for this case. The experimental set-up, as said before, allows us to experimentally determine only two out of three particle angles and energies. Energies and angles of the third particle (in our case ^{22}Ne) are evaluated using the conservation principles. In this way we have selected the events coming from the reaction of interest only. It is now crucial to understand if the events selected so far derive from QF processes or from sequential decay. If the events come from a QF process, the coincidence yield must vary following the impulse distribution. Yield variation must be therefore an index of the correlation between the relative energy and, assuming slowly varying with $E_{p\text{-}Ne}$ and p_s. To strengthen the idea that the selected particles actually came from QF-processes, we also analyzed the impulse distribution of the spectator particle (deuterium) in ^{6}Li, that is well known and given by [5]. This result to be true for our case, and FWHM will result to be *50 MeV/c*. Following THM prescriptions, we reduced our attention to $30<p_s<55MeV/c$ for further analysis.

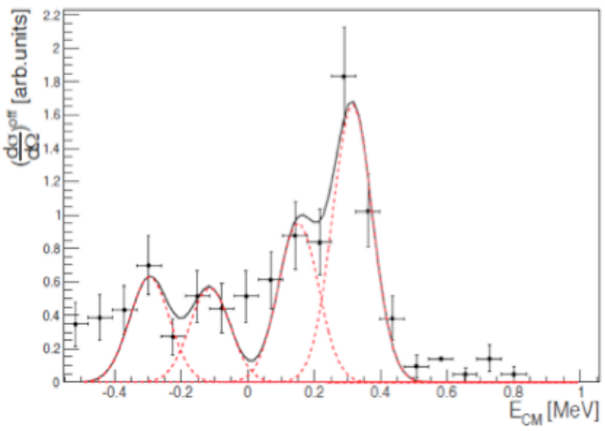

Figure 2: off-energy-shell cross-section, fitted with four gaussians calculations, in arbitrary units

The next step is to calculate the triple-differential cross section. To do so is necessary to define E_{CM} in *post collision prescription* [6] as $E_{CM} = E_{p\text{-}Ne} - Q^{2B}$. It is therefore important to know the proton emission angle in the CM system between ^{22}Ne and p. It results to be $120°<\vartheta<160°$. Unfortunately it is impossible to gain angular distribution due to the low rate of events for this coincidence. Off-shell differential cross section is calculated in PWIA following [7]. Using Monte-Carlo simulation is possible to calculate KF, and then have the off-energy-shell cross section. Selecting only the above-threshold resonances, penetrability factors were calculated (imposing $l_{max}=0$ and $l_{max}=2$ [8]) to take in account the effects coming from Coulomb and centrifugal barriers. In this way we were able to extract the bare nucleus cross section, measured in arbitrary units (Fig.2). Such a cross section was in the end normalized with R-Matrix calculations to obtain a cross section, in barn, at astrophysical energies (Fig.3).

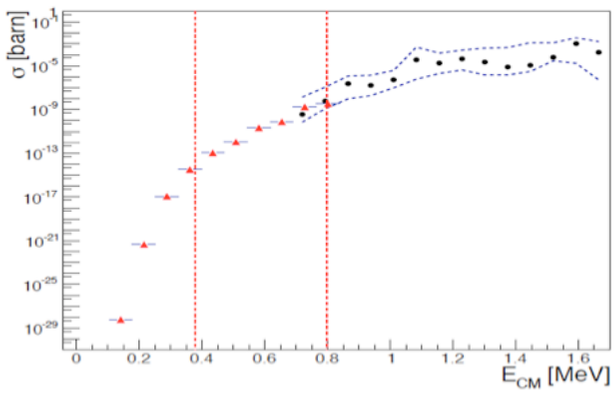

Figure 3: Cross-section normalized to the Ugalde R-Matrix [9][10][11]

CONCLUSIONS

In this paper the study conducted on the reaction $^{19}F(\alpha,p)^{22}Ne$ using the Trojan Horse Method at astrophysical energies was briefly exposed. It is important to underline that, until today, no experimental cross-section at astrophysical energies (*390 ÷ 800 keV*) are reported in literature. On this experiment, further analysis are necessary: in particular we have to study the coincidences PSD1-PSD3, PSD1-PSD4 and PSD1- PSD5 and PSD2-PSD4 and PSD-5. These could be useful to strengthen or nullify the measurement obtained so far. This work was supported by the Italian Ministry of the University under Grant No. RBFR082838 and by the Italian Ministry of University MIUR under the grant "LNS Astrofisica Nucleare (fondi premiali)".

REFERENCES

[1] Abia et al., *The Astrophysical Journal* 649 (2009) 971.
[2] Cristallo et al., The Astrophysical Journal Supplement Series 197 (2011) 17.
[3] Forestini et al., *Astronomy and Astrophysics*, 261(1) (1992) 157.
[4] Rolfs and Rodney, *Cauldron in the Cosmos*, University of Chicago Press.
[5] Pizzone et al., *Physical Review C*, 71 (2005).
[6] Cew and Wick, *Physical Review* 85 (1952) 636.
[7] Jain et al., *Nuclear Physics A* 153 (1970) 49.
[8] Firestone (2007), *Nuclear Data Sheets*.
[9] Lane and Thomas, *Review of Modern Physics*, 20(2) (1958) 257.
[10] Ugalde et al., *Physical Review C*, 77 (3) (2008).
[11] Ugalde et al., *Nuclear Physics A*, 758 (2005) 577.

β-Delayed α decay of ^{16}N and the ^{12}C(α,γ)^{16}O cross section at astrophysical energies: a new experimental approach

S. Sanfilippo[1)], S. Cherubini[1, 2)], S. Hayakawa[2)], A. Di Pietro[2)], P. Figuera[2)], M. Gulino[2,3)], M. La Cognata[2)], M. Lattuada[1,2)], C. Spitaleri[1,2)], H. Yamaguchi[4)], D. Kahl[4)], T. Nakao[4)], S. Kubono[5)], Y. Wakabayashi[5)], T. Hashimoto[6)], N. Iwasa[7)], Y. Okoda[7)], K. Ushio[7)], T. Teranishi[8)], M. Mazzocco [9)], C. Signorini[9)], D. Torresi[9)], J.Y. Moon[10)], T. Komatsubara[10)], P.S. Lee[11)], K.Y. Chae[12)], M.S. Gwak[12)].

1) Dipartimento di Fisica e Astronomia, Università degli Studi di Catania, Via S.Sofia 64, 95123 Catania, Italy;
2) INFN – Laboratori Nazionali del Sud, Catania, Italy;
3) Università Kore, Enna, Italy;
4) Center for Nuclear Study, University of Tokyo, Wako Branch, Saitama, Japan;
5) RIKEN Nishina Center, Wako, Saitama, Japan;
6) RCNP, Osaka University, Osaka, Japan;
7) Department of Physics, Tohoku University, Sendai, Japan;
8) Department of Physics, Kyushu University, Fukuoka, Japan;
9) Dipartimento di Fisica e Astronomia, Università di Padova and INFN-Sez. Padova, Padova, Italy;
10) Institute for Basic Science, Daejeon, Korea;
11) Department of Physics, Chung Ang University, Seoul, Korea;
12 Department of Physics, Sungkyunkwan University, Seoul, Korea.

Abstract - The ^{12}C(α,γ)^{16}O reaction at energies corresponding to the quiescent helium burning in massive stars is regarded as one of the most important processes in nuclear astrophysics. Although this process has been studied for over four decades, our knowledge of its cross section at the energies of interest is still widely unsatisfactory. Indeed, in the energy region of astrophysical interest extrapolations are performed using some theoretical approaches, usually R-matrix calculations. To improve the reliability of these extrapolations, data from complementary experiments, such as elastic and quasi-elastic α scattering on ^{12}C, α-transfer reactions to ^{16}O, and ^{16}N β-delayed α decay are usually included in the analysis. Here a new experimental technique has been used to study the ^{16}N β-delayed α decay of ^{16}N is used to infer information on the ^{12}C(α,γ)^{16}O reaction.

INTRODUCTION

^{12}C(α,γ)^{16}O and the 3-α process are the most important reactions that occur during the helium burning stage in red giants. This begins with the 3-α reaction among helium nuclei to form ^{12}C that can radiatively capture another helium nucleus producing ^{16}O. In principle, this process can produce heavier elements but, because of the increase in the Coulomb barriers and the properties of the resonances in the critical energy region for the first relevant reaction, ^{16}O(α,γ)^{20}Ne, the helium is mainly converted into ^{12}C and ^{16}O. Carbon and oxygen abundance depends on the relative cross section of the reaction and on stellar temperature and density.

Despite the simultaneous interaction of 3-α nuclei to form ^{12}C is energetically possible, the probability for this direct process is too small to account for observed abundance in stars. To overcome this problem, Salpeter [1] and Öpik [2] proposed that carbon was created via a two step process: two alphas produce ^{8}Be in its ground state, and then, in the second step, ^{8}Be can capture another helium nucleus producing ^{12}C. Hoyle [3] showed that the amount of carbon produced in this way is insufficient to explain the observed abundance in red giants. So, he proposed that a proper carbon quantity could be synthesized if the ^{8}Be+α reaction took place through an s-wave resonance near the threshold at about 7.65 MeV, as the existence of such a resonance would greatly accelerate the rate of the 3-α process. This was later verified and a narrow resonance near the Q-value (7.68 MeV) of the reaction was found.

As just mentioned, the ^{12}C(α,γ)^{16}O reaction near the Gamow energy corresponding to helium burning temperatures ($T_9 \sim 0.2$) represents one of the most important reactions in nuclear astrophysics, but the measurement of its cross section is extremely complicated. Indeed, its cross section is extremely low (10^{-17} b). Moreover, two resonant processes contribute to the total cross section. One is the E_1 capture mode proceeding through the f-resonance at E* = 9.632 MeV and the subthreshold state 1^- at E* = 7.117 MeV, and the other one is the E_2 capture mode that includes the contribution of direct capture and the tail of the subthreshold state 2^+ at E* = 6.917 MeV.

Information about the total cross section at stellar energy is then obtained through extrapolation using theoretical models, such as R-matrix calculations, leading to a wide range of values for the calculated astrophysical factor S(E). Indeed, at $E_{c.m.}$ = 300 keV it varies from 1 keVb to 288 keVb for the E_1 component, and from 7 keVb to 120 keVb for the E_2 [4,5].

Since direct measurements of the cross section under $E_{c.m.}$ = 0.9 MeV are presently not possible, indirect approaches are used to get complementary informations.

STATE OF THE ART

Barker [6] proposed an experimental method to investigate the $^{12}C+\alpha$ reaction cross section based on the β-delayed α decay of ^{16}N. The decay of ^{16}N into $^{12}C+\alpha$ proceeds through a first step governed by the beta decay of ^{16}N (τ = 10.24 s, Q = 10.42 MeV) into $^{16}O^*$, which can in turn decay to $^{12}C+\alpha$. Information about the E_1 component of the astrophysical factor can be extracted from the height of the peak located at roughly $E_{c.m.}$ = 1.1 MeV in the spectrum of the $^{12}C+\alpha$. This peak originates from the interference of the high-lying 1^- state of ^{16}O at E* = 9.632 MeV with the subthreshold one at E* = 7.117 MeV. This is presently considered the best method to investigate the value of $S(E_1)$.

Tang et al. [7] performed an experiment using an intense in-flight produced beam of ^{16}N sent into a gas cell chamber and implanted on a thin carbon foil. In order to detect in coincidence ^{12}C-α pairs, after 15 s of implantation time, the foil was rotated between two ionization chambers, decay products were collected and their spectrum measured. The obtained results are shown in [7]. Data were collected down to 450 keV and the percentage of ^{16}N ions captured in the foil, was only 6%.

Here we present a new experimental method based on the use of a TPC thus preventing implantation techniques.

A new experimental approach: Time Projection Chamber based experiment

The idea is to avoid implantation techniques using a Time Projection Chamber as an active target, in order to increase detection efficiency to about 19%. The experiment was performed using the Multi Sampling TPC and the CNS Radioacive Ion Beam (CRIB) of the Center for Nuclear Study of the University of Tokyo based at RIKEN campus in Wako, Japan.

A beam of ^{15}N was used to bombard a nitrogen cooled deuterium gas target at about 400 Torr pressure. The ^{16}N beam was selected by means of CRIB and sent into the scattering chamber. The produced ^{16}N beam had a purity of 90% and a maximum intensity of 10^6 pps. During the experiment the average beam intensity was 10^5 pps. A TPC detector was installed in the scattering chamber, and the whole scattering chamber was filled with P10 gas. The gas pressure was tuned to stop the ^{16}N beam in the middle of the TPC active volume. This pressure of 150 Torr was kept during the measurement.

The TPC was used as an active target to detect in coincidence the ^{12}C and the α particles coming from the decay of ^{16}O, produced by the beta decay of ^{16}N. It must be stressed that a gas detector like the MSTPC is practically insensitive to beta background. The TPC was equipped in the bottom plane with two Gas Electron Multipliers (GEMs) that multiply the ionization electrons that then were collected into a backgammon-shaped pad detector plane. The ^{16}N ions were implanted inside the TPC for 50 ms and the ^{12}C-α back to back decays were collected for the next 50 ms and then the cycle started over again. The TPC is equipped with a Gating Grid used for switching off the TPC during the beam implantation to prevent the GEMs to be destroyed by too high currents.

The tracks produced by the decay particles are reconstructed in the three directions. Since the charge collected at the pads is proportional to the energy loss of the particles, the signal amplitude from the anode provides information on this energy loss along with position one. This piece of information can be used to identify the particles.

The configuration of the TPC allowed for a sensitive volume of 2000 cm^3, with an active length of 20 cm along the beam axis and 10 cm along the other two directions. The TPC spatial resolution is 2 mm along the beam axis and 1 mm in the other directions.

The data analysis is still in progress.

ACKNOWLEDGEMENTS

The authors acknowledge the support of the Italian Ministry of Education, University and Research under grant Progetto Premiale ASTROF.MIUR PFE, CD 19/12/2012 n. 12609.

REFERENCES

[1] E. E. Salpeter, Phys. Rev. **88**, 547 (1952); Ap. J. **115**, 326 (1952);
[2] E. J. Öpik, Proc. Roy. Irish Acad. **A54**, 49 (1951);
[3] F. Hoyle, D. N. F. Dunbar, W. A. Wenzel and W. Whaling, Phys. Rev. **92**, 1095 (1953);
[4] R. Kunz et al., Astrophys. J. **576**, 643 (2002);
[5] X. D. Tang et al., Phys. Rev. Lett.**99**, 052502 (2007);
[6] F. C. Barker, Aust. J. Phys. **24**, 777 (1971);
[7] X. D. Tang et al., Phys. Rev. **C81**, 045809 (2010).

Neutron yield from the absorption of 62 MeV protons on a thick Beryllium target: final results

R. Alba[2], M. Barbagallo[4], P. Boccaccio[5], N. Colonna[4], L. Cosentino[2], A. Celentano[1], A. Del Zoppo[2], A. Di Pietro[2], J. Esposito[5], P. Figuera[2], P. Finocchiaro[2], A. Kostyukov[3], C. Maiolino[2], M. Osipenko[1], G. Ricco[1], M. Ripani[1], D. Santonocito[2], M.C. Schillaci[2], C. M. Viberti[1]

1) INFN and University of Genova – Genova, Italy
2) INFN – Laboratori Nazionali del Sud – Catania, Italy
3)Moscow State University – Mosca, Russia
4) INFN – Bari, Italy
5) INFN – Laboratori Nazionali di Legnaro, Italy

Abstract – For the design of the low power neutron amplifier that was proposed in [1] detailed data on the neutron yield from a thick Beryllium target by a proton beam of about 70 MeV were necessary. To this end, a comprehensive measurement of the neutron yield from Beryllium, induced by 62 MeV protons delivered by the Superconducting Cyclotron (SC), was performed at LNS.

MOTIVATION

Alternative systems for producing energy via nuclear reactions, the so-called Accelerator Driven Systems (ADS), are subject for intensive research. In this system a subcritical fission reactor core is coupled to an external neutron source. Such a system presents several advantages, among which one can mention the intrinsic safety due to the fact that the reactor core power will automatically vanish by switching off the neutron source, i.e. the primary beam. Moreover, the fast neutron spectrum allows to study radioactive waste burn-out by fission.

Based on this perspective, a subcritical fast reactor core based on Uranium Oxide rods enriched with 20 % ^{235}U, with solid lead as diffusing medium and helium gas as a coolant, coupled to a 70 MeV proton beam at current of about 1 mA produced by a commercial cyclotron, has been proposed in [1]. For this project, a Beryllium target was envisaged as a proton-to-neutron converter. Preliminary simulations performed with the MCNPX code resulted in a thermal power of about 200 kW. In order to validate these calculations accurate data on the neutron yield from a thick Beryllium target in the 70 MeV proton energy region were needed.

EXPERIMENT

The 62 MeV SC proton beam with operating current of 30-50 pA was delivered on the target. The 40 MHz beam structure was modified by suppression of four bunches out of five providing 1.5 ns wide beam bunches separated by 125 ns intervals. The target consisted of a solid 3 cm thick ^{9}Be cylinder with 3.5 cm diameter. The neutrons produced in the target were measured by the ToF technique. To this end, the RF signal from the cyclotron was used as the reference time. Eight neutron detectors were installed simultaneously around the target at different angles and at two different distances (150 cm and 75 cm). Many separate runs were taken during the experiment moving the detectors simultaneously to different angles for a total of 16 angular settings for both distances.

To reduce γ production from surrounding materials induced by the emitted neutrons, the beamline components downstream of the target were removed and a new, lightweight, final segment of the beamline was installed. It consisted of 100 cm long carbon fiber tube with 3 mm thick walls. Such a solution allowed to reduce the background by more than a factor of 2, maintaining the vacuum quality better than 10^{-5} mbar.

The charge deposited by the proton beam on the Beryllium target was read out via direct electrical contact using a high precision current digitizer. This total charge was used in the absolute normalization of the yields.

Neutron detectors were 4 cm long Aluminum cylindrical cells filled with liquid scintillator EJ301. In order to measure neutron yields at two different distances from the target, keeping the same solid angle, two different diameters were chosen: 4.6 cm and 2.3 cm.

Neutrons with energy lower than about 0.5 MeV were measured by a 50 cm long, 5 cm in diameter, 2 bar ^{3}He tube (Canberra 150NH50/5A).

Neutrons scattered from surrounding materials, like beamline or detector supports, experimental hall floor or walls and other installations nearby were measured in dedicated runs. These special runs were taken by screening the target direct view from the detector with a shadow bar. The shadow bar consisted of a 50 cm long 4.6 cm diameter steel cylinder.

Few examples of measured neutron yields are shown in Fig.1 together with a comparison to MCNP, FLUKA and Geant4 simulations performed using different physics libraries. MCNP simulations underestimate significantly the low energy part of the spectra. Very similar distributions were obtained with FLUKA. Five physics models of Geant4 were considered: PreCompound model,

Binary Cascade, Bertini Cascade, LEProtonInelastic and INCLXX. The PreCompound model, mostly used to describe final state emission, was proposed also as stand-alone model. Although it manages to form a sufficient number of ^{10}B compound nuclei in the p+^{9}Be interaction, the excess energy, instead of going into nucleus excitation, gets lost via emission of few high energy γs. As a result the simulated yield is two orders of magnitude lower than the data. LEProtonInelastic does not generate two major channels: ^{8}Be and 2α. It also frequently releases the excess energy through a high energy γ. Binary Cascade has too high threshold (of about 30MeV) for ^{8}Be production. INCLXX model does not have this problem, but shows similar results. The best Geant4 model for our kinematics, Bertini Cascade, gives results similar to MCNP and FLUKA, and also underestimates significantly the yield at low neutron energy.

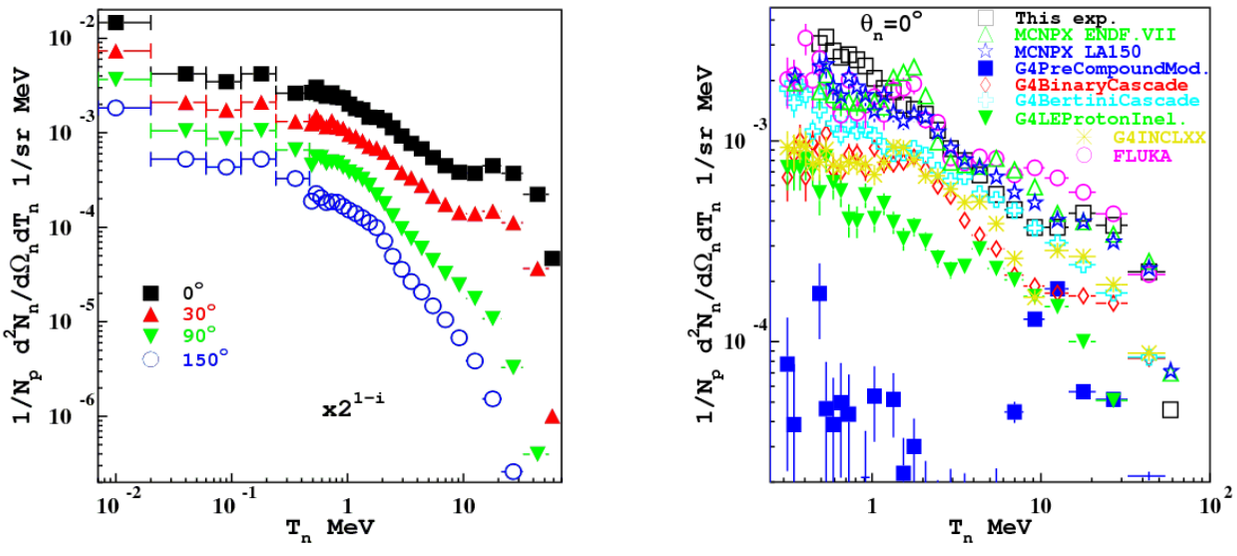

Figure 1: Measured neutron yields at different angles (left plot) and the comparison with various Monte Carlo models at 0 degrees (right plot). Each successive angle distribution was rescaled by a factor of 2 for visibility.

CONCLUSIONS

Differential neutron yields produced by a 62 MeV proton beam impinging on a thick, fully absorbing ^{9}Be target were measured in almost complete energy and angular ranges, published in [2] and discussed in [4,5,6,7,8,9]. The systematic uncertainties of the yields due to the detector efficiency and the absolute normalization are of the order of 10%. The obtained data are in agreement with previous experiments in the 60-70 MeV beam energy range, extending considerably the kinematic coverage. By integrating over neutron energy and angle, an overall yield of $0.0987 \pm 0.0003_{stat} \pm 0.0053_{sys}$ n/p is obtained. This value is in good agreement with the measurement based on thermalization and capture of produced neutrons [10]. The comparison of our data to MCNP and FLUKA simulations showed some deviations in angular and neutron energy behaviors, although the integrated yield values were found to be consistent. The comparison to various Geant4 models exhibited their limitations in the low beam energy domain. The presented data were used in the design of the ADS core [1,3] to describe its neutron source. These data can also be useful for the development of the neutrino source proposed recently in [11]. The whole data set is available in the EXFOR database.

REFERENCES

[1] L. Mansani et al., EPJ Plus, 129 4 (2014), 64.
[2] M. Osipenko et al., NIM A723 (2013), 8.
[3] M. Osipenko et al., EPJ Plus, 129 4 (2014), 68.
[4] R. Alba et al., J.Phys.Conf.Ser. 420 (2013), 012162.
[5] M. Osipenko et al., IEEE Advancements in Nuclear Instrumentation Measurement Methods and their Applications, 1293 (2013), 1.
[6] M. Schillaci et al., EPJ Web of Conferences 66 (2014), 10015.
[7] A. Celentano et al., LNS Report 2011/2012, 127.
[8] A. Celentano et al., LNS Report 2010, 56.
[9] A. Celentano, Master Thesis, University of Genova 2010.
[10] I. Tilquin et al., NIM, A545 (2005), 339.
[11] A. Bungau et al., PRL 109 (2012), 141802.

Effects of coupling to the continuum states in the ^{6,7}Li+^{64}Zn reactions at energies around the Coulomb barrier

J.P. Fernández-García[1], M. Zadro[2], A. Di Pietro[1], P. Figuera[1], M. Fisichella[1], O. Goryunov[3], M. Lattuada[1, 4], A. M. Moro[5], A. Musumarra[1, 4], V. Ostashko[3], M. G. Pellegriti[1, 4], V. Scuderi[1, 4], E. Strano[1, 4] and D. Torresi[1, 4]

1) INFN, Laboratori Nazionali del Sud, via S. Sofia 62, 1-95123 Catania, Italy

2)Ruđer Bošković Institute, Bijenička cesta 54, HR-10000 Zagreb, Croatia

3)Institute for Nuclear Research, Prospekt Nauki, UA-03680 Kiev, Ukraine

4)Dipartamento di Fisica e Astronomia, via S. Sofia 64, I-95123 Catania, Italy

5)Departamento de FAMN, Universidad de Sevilla, Apartado 1065, E-41080 Seville, Spain

Abstract - The experimental elastic scattering angular distributions for the weakly bound nuclei ^{6,7}Li on ^{64}Zn at several energies around the Coulomb barrier were measured at the Laboratori Nazionali del Sud (LNS). The measured elastic scattering angular distributions and the barrier distributions obtained from the experimental backscattering excitation functions were analyzed within the Continuum-Discretized Coupled-Channels (CDCC) framework.

INTRODUCTION

The study of collisions induced by halo and weakly bound nuclei had a considerable interest in the last decade. In fact, due to the coupling to breakup channels, strong effects on the elastic scattering and fusion have been predicted and observed [1-5].

In the case of the two stable lithium isotopes, ^{6,7}Li, elastic scattering angular distributions on different targets have been extensively measured and analyzed within the CDCC method, showing that the couplings to the breakup process have a significant effect on the elastic scattering [6].

The barrier distribution is considered as a powerful method to study the effects of the couplings to different reaction channels [7]. A description of the barrier distribution can be obtained from the quasielastic scattering [8], using the following equation,

$$D_{qel} = -\frac{d}{dE}\left(\frac{d\sigma_{qel}}{d\sigma_{Ruth}}\right),$$

where $d\sigma_{qel}/d\sigma_{Ruth}$ correspond to the ratio between the quasielastic scattering and the Rutherford cross section at a fixed backward angle. Quasielastic scattering is defined as the sum of elastic and inelastic scattering, and all other direct reaction processes.

Recently, a systematic study of ^{6,7}Li + ^{64}Zn reactions at energies around the Coulomb barrier was carried out at LNS. The elastic scattering angular distribution and the barrier distribution extracted from the elastic excitation function at backward angles were obtained for both systems[9,10]. In this report, we present results concerning the elastic scattering for the ^{6,7}Li+^{64}Zn reactions at the same center of mass energy and the experimental barrier distributions. These experimental data are compared with CDCC calculations.

EXPERIMENTAL SETUP

The ^{6,7}Li beams were produced by the SMP Tandem Van de Graaff accelerator and transported to the CT2000 scattering chamber at center of mass energies of 11.7, 12.4, 13.5, 15.0, 16.3 and 18.1 MeV.

The experimental setup was composed by five silicon telescopes situated on a rotating plate, in order to cover a wide angular range. The telescope systems consisted in a 10 μm detector plus a 200 μm detector. A ^{64}Zn target of 400 μg/cm^2 was used for the ^{6}Li+^{64}Zn reactions, while a 70 μg/cm^2 target for the ^{7}Li+^{64}Zn collisions. The measurements of the quasielastic scattering for both reactions were performed at the same laboratory energy range E_{lab}=9-20 MeV in steps of 0.5 MeV. For these measurements, the telescopes were positioned at ±160º and ±170º with respect to the beam direction [9,10].

As an example, the experimental elastic scattering differential cross sections at $E_{c.m.}$=15.0 MeV for the systems ^{6,7}Li+^{64}Zn are presented in Fig. 1. In the same figure, the barrier distributions for both systems are also represented.

THEORETICAL CALCULATIONS

In the CDCC framework, three-body models of the systems ^{6,7}Li+^{64}Zn were considered. The ^{6}Li nucleus was described as an α+d structure, with a break-up threshold at 1.47 MeV above the ground state. The resonances 3^+, 2^+, 1^+, corresponding to the coupling between the angular momentum l=2 and the spin of the deuteron s=1, and the non-resonant states were included in the calculations. On the other hand, the ^{7}Li isotope was understood as an α+t

system, with a break-up threshold at 2.47 MeV. The excited state $1/2^-$, the resonances $7/2^-$, $5/2^-$ (l=3 coupled to the tritium spin s=1/2) and the non-resonant states were considered. These calculations were performed using the code FRESCO.

In Fig. 1, the solid red lines represent the full CDCC calculations, while the dashed green lines correspond to those calculations without couplings to the continuum states of the projectile. A good agreement between the predictions of the CDCC calculations and the experimental data was observed. In the case of the ^{6}Li reaction, it was necessary to include the couplings to the breakup channels to reproduce the experimental data, while for the ^{7}Li reactions these couplings were less important. Similar results were observed at the other bombarding energies. The barrier distributions were also well reproduced by the CDCC calculations. In the case of 6Li, note that the couplings to the continuum states of the projectile produces a widening of the barrier distribution and increase the average barrier.

From the comparison of both systems, ^{6}Li+^{64}Zn and ^{7}Li+^{64}Zn, the results suggest that the coupling to the breakup channels is more relevant in the ^{6}Li induced collisions than that reactions induced by ^{7}Li. This behavior could be linked to the fact that the break-up threshold of ^{6}Li (S_α=1.47 MeV) is smaller than the one of ^{7}Li (S_α =2.47 MeV).

REFERENCES

[1] A. Di Pietro et al. Phys. Rev. Lett. 105,022701(2010)
[2] J. P. Fernández-García et al., Nucl. Phys. A 840 19 (2010)
[3] M. Cubero et al., Phys. Rev. Lett. 109 262701 (2012)
[4] V. Scuderi et al., Phys. Rev. C 84 064604(2011)
[5] L .F. Canto et al., Nucl. Phys. A 821 51 (2009)
[6] L. F. Canto et al., Phys. Rep. 424 1 (2006)
[7] M. Dasgupta et al., Annu. Rev. Nucl. Sci. 48 40(1998)
[8] T. Himmers et al., Nucl. Phys. A 584, 190 (1995)
[9] M. Zadro et al., Phys. Rev. C 80, 064610 (2009)
[10] M. Zadro et al., Phys. Rev. C 87, 054606 (2013)

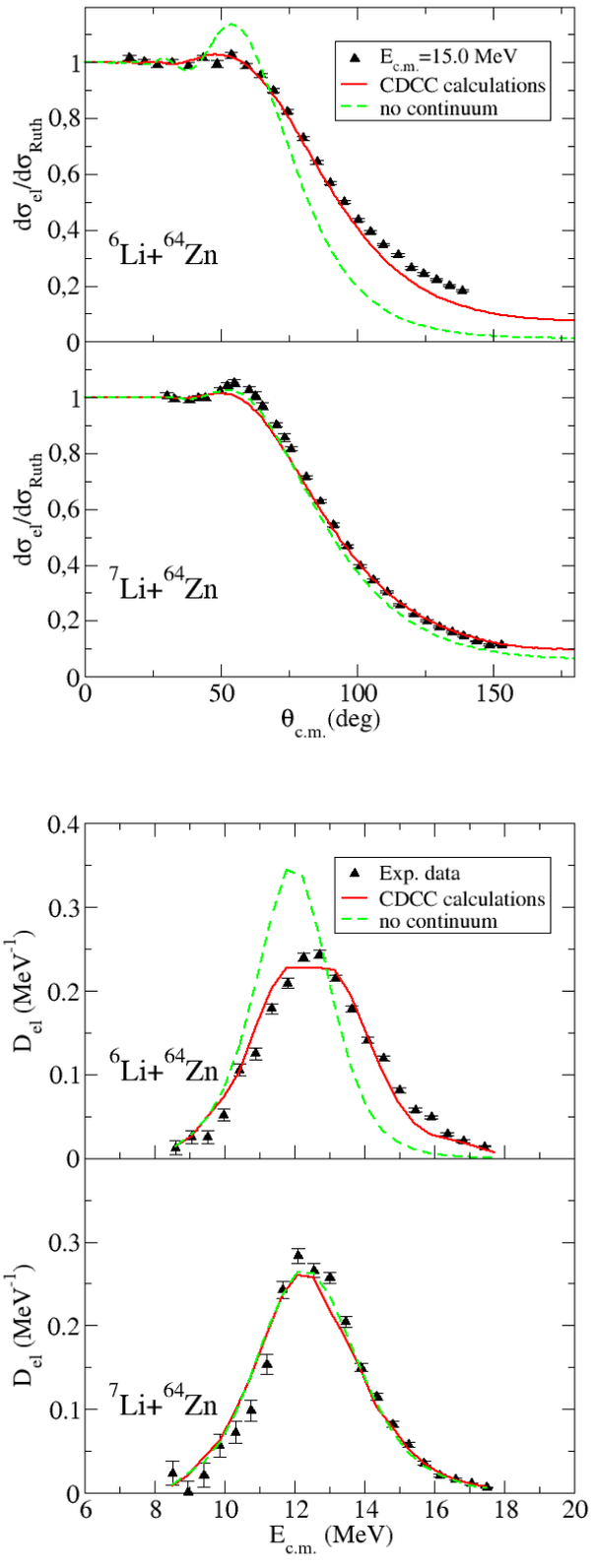

Figure 1. (Up) Elastic scattering angular distributions for the systems ^{6,7}Li at the c.m. energy of 15.0 MeV. (Bottom) Barrier distributions for both sistems. See text for details.

Effects of Coulomb and nuclear couplings in the ^{6}He+^{64}Zn reactions at energies around the Coulomb barrier

J.P. Fernández-García[1], A. Di Pietro[1], P. Figuera[1], M. Fisichella[1], M. Lattuada[1, 2], A. M. Moro[3], A. Musumarra[1, 2], M. G. Pellegriti[1], V. Scuderi[1], and D. Torresi[1, 2] M. Zadro[4]

1) INFN, Laboratori Nazionali del Sud, via S. Sofia 62, 1-95123 Catania, Italy

2)Dipartamento di Fisica e Astronomia, via S. Sofia 64, I-95123 Catania, Italy

3)Departamento de FAMN, Universidad de Sevilla, Apartado 1065, E-41080 Seville, Spain

4)Ruđer Bošković Institute, Bijenička cesta 54, HR-10000 Zagreb, Croatia

Abstract - New experimental elastic scattering angular distributions for the halo nucleus ^{6}He on ^{64}Zn at different energies around the Coulomb barrier were measured at the Cyclotron Research Center (CRC), Louvain La Neuve, Belgium. The measured elastic scattering angular distributions were analyzed within the Optical Model (OM). In addition, Continuum-Discretized Coupled-Channels (CDCC) have been performed.

INTRODUCTION

In the last decade, many studies have been performed concerning collisions induced by exotic weakly bound nuclei. These studies have theoretically predicted and experimentally observed strong effects on elastic scattering and fusion owing to the coupling to breakup channels [1-5].

One of the most used exotic nuclei for such studies was ^{6}He [6-13] since intense beams of such isotope are available at different RIB facilities. This nucleus can be understood as a bound core (α particle) and two loosely bound neutrons (S_{2n}=0.97 MeV). These two neutrons have a large probability to be far away from the core, producing the so-called nuclear halo. The ^{6}He nucleus constitutes an archetype of Borromean nucleus, since the α-neutron and neutron-neutron interactions are well known. In Refs. [8-13], it was demonstrated that, as a consequence of the weakly bound structure, this nucleus can be easily polarizable, and eventually, broken up in the presence of a strong electric field produced by heavy targets. Furthermore, a long range effect on the optical potential was observed. This effect is evidenced by the large value of the diffuseness of the imaginary part of the phenomenological optical potential needed to reproduce the data.

In this work, new experimental data for the collision ^{6}He+^{64}Zn are presented. We discuss an optical model study of these ^{6}He data, using the Woods-Saxon parametrization. Moreover, three-body CDCC calculations have been performed in order to complement the optical model analysis.

EXPERIMENTAL SETUP

The experiment was performed at the CRC of Louvain La Neuve, Belgium. The reactions ^{6,4}He+^{64}Zn at center of mass energies of 13.7 and 16.5 MeV were measured to complement old measurements performed by the group on the same systems at different energies [4,6].

The experimental setup was composed by half-LAMP detector [14], one covering the angular range 0º<φ<180º and 15º<θ<50º. Moreover, four double sided silicon strips detectors were covering the angular range between 70º and 100º. A ^{64}Zn target of 0.5 mg/cm^2 was used and rotated 45º with respect to the beam direction. For additional details see Refs. [4,15].

The experimental elastic scattering differential cross sections for the system ^{6}He+^{64}Zn are presented in Fig. 1.

THEORETICAL CALCULATIONS

We have performed OM calculations, in which the ^{6}He+^{64}Zn potential is parametrized according to the following expression:

$$U_{opt}(R) = U_{bare}(R) + W_{d}(R),$$

where for the complex bare potential, $U_{bare}(R)$, the α-target interactions of Refs. [15,16] were considered, while the long range effects were taken into account by a derivative Woods-Saxon form, $W_d(R)$.

The parameters of the potential are obtained by means of a χ^2 minimization. The results are represented by blue dashed lines in Fig. 1. Good quality data fits have been observed. In this case a large imaginary diffuseness of 1.05 fm was required to reproduce the experimental data, which is related with the long range effects.

These results are compared with the three-body CDCC calculations, where a simple di-neutron model for the ^{6}He

nucleus (2n+α) has been considered [17]. These calculations were performed using the code FRESCO.

In Fig. 1, the same CDCC calculations have been performed considering only Coulomb or nuclear couplings to all orders, represented by black dotted lines and green dashed lines, respectively. The results show a large contribution of the nuclear couplings, displayed by red lines unlike Coulomb couplings.

This effect can be also observed in the OM calculations when an analytical formula for the complex Coulomb Dipole Polarization (CDP) potential, based on a semiclassical approximation, is included. The inclusion of the CDP potential in the OM analysis produces a small reduction of the imaginary diffuseness (a=0.99 fm) with respect to the calculations without the CDP potential (a=1.05 fm), which confirms that the long range effect observed is mainly due to nuclear couplings.

The results obtained in this work differ from the OM analysis performed in Ref. [10] for the reaction ^{6}He+^{208}Pb. In this case, a reduction of the imaginary diffuseness from 1.9 fm to 1.1 fm was observed when the CDP potential is included. Contrary to the ^{6}He+^{64}Zn case , the long range found in the OM analysis for the heavier target is partially due to the effect of dipole Coulomb couplings.

To conclude, the comparison between the collisions induced by ^{6}He on the medium and heavy targets ^{64}Zn and ^{208}Pb, confirms the strong dependence of the dipole Coulomb breakup on the electric field generated by the target, which depend on its atomic number.

REFERENCES

[1] A. Di Pietro et al. Phys. Rev. Lett. 105, 022701(2010)
[2] J. P. Fernández-García et al., Phys. Rev. Lett. 110, 142701 (2013).
[3] M. Cubero et al., Phys. Rev. Lett. 109 262701 (2012)
[4] V. Scuderi et al., Phys. Rev. C 84 064604(2011)
[5] L .F. Canto et al., Nucl. Phys. A 821 51 (2009)
[6] A. Di Pietro et al,. Phys. Rev. C 69, 044613 (2004)
[7] E.A. Benjamim, et al., Phys. Lett. B 647 (2007) 30–35.
[8] A.M. Sánchez-Benítez, et al., Nucl. Phys. A 803 (2008) 30–45.
[9] L. Acosta et al., Phys. Rev. C 84, 044604 (2011)
[10] J. P. Fernández-García et al., Nucl. Phys. A 840, 19 (2010).
[11] P.N. de Faria et al., Phys. Rev. C 81 , 044605 (2010)
[12] E.F. Aguilera et al., Phys. Rev. Lett. 84 , 5058 (2000)
[13] O.R. Kakuee et al., Nucl. Phys. A728 , 339 (2003)
[14] T. Davinson et al., Nucl. Instrum. Methods A, 454 (2000) 350.
[15] A. Di Pietro et al,. Europhys. Lett., 64 (3), pp. 309–315 (2003).
[16] T. B. Robinson and V. R. W Edwards, Nucl. Phys. A 301, 36 (1978).
[17] A.M. Moro, K. Rusek, J.M. Arias, J. Gómez-Camacho, M. Rodríguez-Gallardo, Phys. Rev. C 75 (2007) 064607.

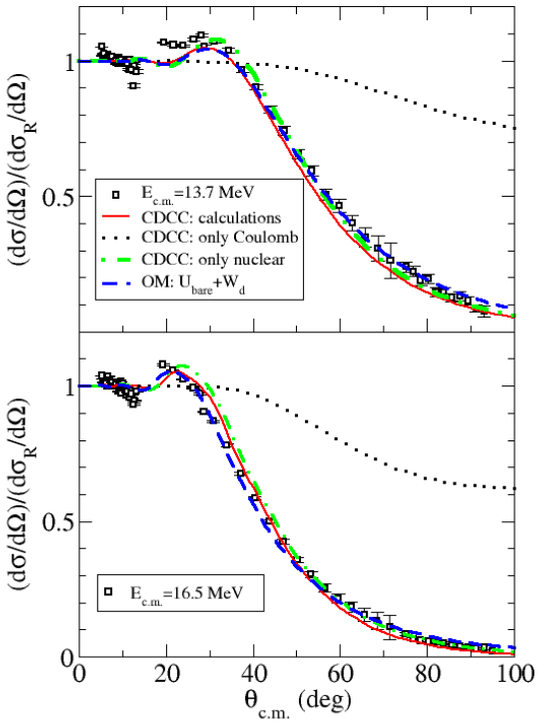

Figure 1. Elastic scattering angular distributions for the system ^{6}He+^{64}Zn at the c.m. energies of 13.7 and 16.5 MeV.

Ion recombination correction factors for parallel-plate ionization chambers in a 62 MeV/n carbon ion beam

S. Rossomme[(1)], R. Thomas[(2)], N. Lee[(2)], S. Vynckier[(1,3)] and H. Palmans[(2,4)]

[(1)] Molecular Imaging and Experimental Radiotherapy, Université catholique de Louvain, Brussels, Belgium
[(2)] National Physical Laboratory, Teddington, UK
[(3)] Cliniques univ. Saint-Luc, Brussels, Belgium
[(4)] EBG MedAustron GmbH, Wiener Neustadt, Austria

Abstract – The objective of this work was to measure the ion recombination correction for parallel-plate ionization chambers in carbon ion beams. As confirmed by the literature, due to the high LET of the beams, we have shown that the ion recombination mechanism is dominated by initial recombination. Significant differences appear depending on the orientation of the chamber.

INTRODUCTION

In external beam radiotherapy, the absorbed dose is measured daily using an ionization chamber (IC). An IC is a detector that measures a current produced by radiation induced ionization in a gas, such as air using two electrodes (an anode and a cathode). However, there is always a certain lack of collection of charge due to the recombination of positive and negative charges before they arrive at the electrodes. A correction has to be applied to the response of the IC for this effect. Two main recombination mechanisms have to be distinguished: initial recombination and volume recombination. Initial recombination occurs between the ions created in the same ionization track (see figure 1.A). This mechanism is independent of the ionization current, but it depends on the ion density within the track, i.e. the beam quality. On the contrary, volume recombination occurs when ions created in different ionization tracks recombine together (see figure 1.B). This mechanism depends on the ionization current, thus the dose rate. Different theoretical models have been published to describe the recombination process, but it's a complex phenomenon which depends on various properties: the LET of the beam, the type of radiation (continuous, pulsed or pulsed-swept radiation) and the dose rate. Among the different theories, there are the theories of Onsager [1], Kara-Michailova [2] or Jaffé [3] for initial recombination and the theory of Boag for volume recombination [4,5,6], from which the 2 voltage method is derived which is used in IAEA Code of Practice TRS-398 [7]. For ion beams, due to the high ionization density, the recombination process is dominated by diffusion and initial recombination, as described by Jaffé's theory, and volume recombination is often negligible in comparison [8].

This work aimed at measuring the ion recombination correction (k_s) for parallel-plate IC in carbon ion beams from a slow cycle synchrotron. Our goals were to study:

* the variation of the current with the voltage
* the contribution of the volume recombination
* the influence of orientation of the IC.

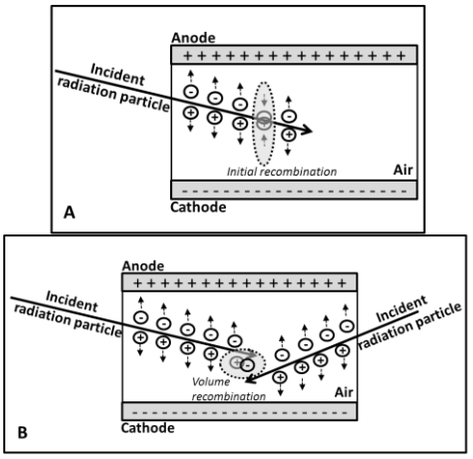

Figure 1. Recombination mechanisms: (A) initial recombination and (B) volume recombination.

This report included preliminary results. Future investigations have to be made. More details concerning the method and results will be published soon.

ACTIVITIES AND RESULTS

The recombination correction is defined as the inverse of the ion collection efficiency, which is the ratio of the ionization current produced in the IC measured at a voltage V, *I(V)*, and the saturation current, I_{sat}. The experimental method to determine the recombination correction used in this study was based on the following equation, which derived from a procedure explained in Palmans *et al.* [6]:

$$k_s \approx 1 + \frac{A}{V} + \frac{m^2 g}{V^2} I_V \quad (1).$$

The second term and the third term on the right-hand side of the equation represent initial recombination and volume recombination, respectively. Measurements were performed with plane parallel ICs. Two ICs are positioned face to face in a phantom. One of the two IC is used as monitor and the second IC as the IC under test. To check the influence of the position and the orientation of the ICs, the role of the ICs is changed. To reach our goals, we changed:

* the voltage of the IC under test, to derive the saturation curve;
* the dose rate of the beam, to evaluate the contribution of volume recombination;

* the orientation of the IC, to evaluate the influence of the angle between the ion tracks and the electric field.

In these analyses, the value of I_{sat} has been determined by linear extrapolation of the variation of ($I_{sat}/I(V)$) versus (1/V) from V = 400 V until V = 66 V. Figure 2 shows the variation of the recombination correction factors, i.e. the ratio of the ionization current produced (the saturation current) and the measured current as a function of the inverse of the voltage, for three different dose rates (DR), for a PTW Ross chamber (serial number 1684). The non-filled circles represent data obtained with the third dose rate, but when the value of I_{sat} has been determined by linear extrapolation excluding the point at 400 V. This example shows the disadvantage of the method: the dependence of the value of I_{sat} to the extreme points. Figure 3 shows a comparison between the experimental results (solid squares), the Jaffé's theory (continuous line) and equation (1) (dot-dashed line). Choosing an adapted value of the free parameter in the Jaffé theory (b = 0.00345), we observe a good agreement between the theory and experimental results. Based on the analyses of experimental data, we found that the volume recombination term in equation (1) can be neglected and a find the value of the parameter A (A = 1.23). Then, the behaviour of ion recombination correction factors is considered as linear. In figure 3, we see a good agreement for high voltages, until V = 50 V. Figure 4 shows the influence of the orientation of the ionization chamber. As expected by Jaffé's theory the initial ion recombination depends on the angle between the ion path and the electric field. With an angle of 45 degrees (solid circles), ion recombination correction factors was found to decrease strongly.

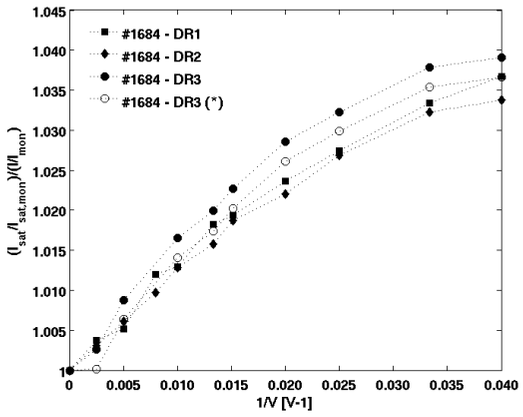

Figure 2. Variation of $I_{sat}/I(V)$ as a function of the inverse of the voltage, for different dose rates, for a Roos chamber.

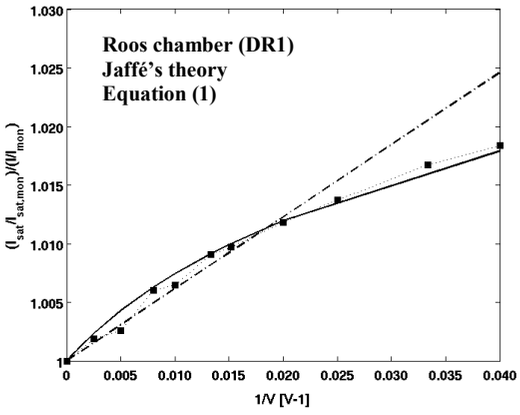

Figure 3. Variation of $I_{sat}/I(V)$ as a function of the inverse of the voltage: comparison between experimental results (solid squares), the theory of Jaffé (continuous line) and equation (1) (dot-dashed line).

CONCLUSIONS

We have determined ion recombination correction factors for different parallel-plate ICs. Due to the high LET of the beams, the mechanism is dominated by initial recombination consistent with other findings in the literature. Significant differences in recombination correction factors appear depending on the orientation of the chamber.

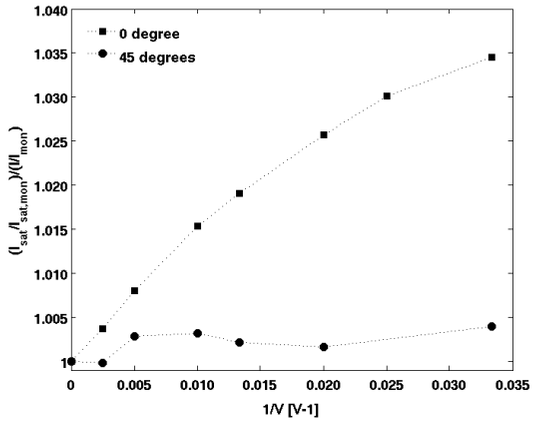

Figure 4. Influence of the orientation of the ionization chamber on the ion recombination correction factors, measured with the PTW Roos #711 chamber. The squares represent data obtained when the ionization chamber is perpendicular to the ion tracks and the circles represent data obtained when the ionization chamber is tilted of 45 degrees compared to the ion tracks.

REFERENCES

[1] Onsager L, Phys Rev. 54(8):554 (1938)
[2] Kara-Michailova E and Lea DE, Proceedings of the Cambridge Phil. Soc., 36(1): 101 (1940)
[3] Jaffé G, Ann Phys, 343: 303 (1913)
[4] Boag JW, Chapter 9: *Ionization Chambers*, Attix FH et al., *Radiation dosimetry*, Second Edition, Volume II: Instrumentation, Academic Press, New York (1966)
[5] Boutillon M, Phys Med Biol 43(8):2061 (1998)
[6] Palmans H *et al.*, Phys Med Biol, 51: 903 (2006)
[7] Andreo P *et al.*, IAEA TRS 398, Vienna (2000).
[8] Kanai T *et al.*, Phys Med Biol, 43(12): 3549 (1998).

The InKiIsSy experiment: competition between statistical and dynamical fission in projectile break-up of isobaric systems

E. De Filippo[1*], A. Pagano[1], P. Russotto[1], L. Acosta[3,10], L. Auditore[4], V. Baran[5], T. Cap[9], G. Cardella[1], M. Colonna[3], L. Francalanza[2,3], B. Gnoffo[1,2], G. Lanzalone[3,6], I. Lombardo[7], G. Marquínez-Durán[3,10], C. Maiolino[3], T. Minniti[3], S. Norella[4], E.V. Pagano[2,3], M. Papa[1], E. Piasecki[8,9], S. Pirrone[1], G. Politi[2,1], F. Porto[2,3], L. Quattrocchi[4], F. Rizzo[2,3], E. Rosato[7], A. Trifirò[4], M. Trimarchi[4], G. Verde[1], M. Vigilante[7], K. Siwek-Wilczynska[8], J. Wilczynski[9]

1) INFN, Sezione di Catania, Italy
2) Dipartimento di Fisica e Astronomia, Università di Catania, Italy
3) *INFN, Laboratori Nazionali del Sud, Catania, Italy*
4) INFN, Gruppo collegato di Messina and Dip. Fisica, Univ. Messina, Italy
5) Physics Faculty, University of Bucharest, Romania
6) Università Kore, Enna, Italy
7) INFN, Sezione di Napoli and Dip. Fisica, Università di Napoli, Italy
8) Heavy Ion Laboratory, University of Warsaw, Poland
9) National Centre for Nuclear Research, Otwock-Swierk, Poland
10) Departamento de Fisica Aplicada, Huelva, Spain

**Corresponding author, e-mail:* defilippo@ct.infn.it

Abstract – We present preliminary results of the reactions ^{124}Xe + ^{64}Zn and ^{64}Ni at 35 A.MeV beam incident energy (InKiIsSy experiment) performed at LNS with the 4π CHIMERA detector coupled with one cluster (four telescopes) of the prototype FARCOS array.

INTRODUCTION

In mid-peripheral heavy ion collisions the reaction dynamics can result in binary products such as excited projectile-like (PLF*) and target-like residues (TLF*) accompanied by the emission of light charged particles and/or intermediate mass fragments (IMF), these last generally detected in the midrapidity velocity region ranging between the PLF and TLF velocities. Experimental results on the reactions ^{124,112}Sn + ^{64,58}Ni and ^{64,58}Ni + ^{124,112}Sn at 35 A.MeV beam incident energy, essentially based on the analysis of ternary emission, have shown a well-defined chronology: light IMFs ($Z < 9$) are likely to be emitted either dynamically on a short time scale (within 50 fm/*c*) with a prompt neck rupture mechanism or statistically in the sequential decay of the PLF* and/or TLF* primary fragments. In contrast, heavier fragments ($Z \geq 9$) are predominantly emitted on a longer time scale (>120 fm/c) and they have been associated either with a massive binary splitting of deformed PLF* or TLF* ("dynamical fission") or a statistical equilibrated fission decay. Slower processes of statistical de-excitations also contribute to a thermal background of IMFs and light particles cross section emission. In the study of the reactions ^{124}Sn+^{64}Ni and ^{112}Sn+^{58}Ni at 35 A.MeV [1-3] it has been shown that while the statistical-sequential emission assumes the same cross section for the two systems as a function of the IMF charge *Z* of the emitted fragments, the dynamical IMF emission cross section is enhanced for the neutron rich system, pointing to an isospin effects related to the neutron richness of the entrance channel. Using the 4π detector CHIMERA, the reactions ^{124}Xe+^{64}Zn and ^{64}Ni at 35 A.MeV (InKiIsSy, Inverse Kinematic Isobaric Systems), have been carried recently at LNS. Our goal was to extend the study using a projectile/target combination having the same mass of the neutron rich ^{124}Sn+^{64}Ni system and a N/Z close to the value of the neutron poor ^{112}Sn+^{58}Ni one, at the same bombarding energy of the previous experiments, in order to disentangle the effects related to isospin from the ones related upon the initial different mass (size) of the entrance channel.

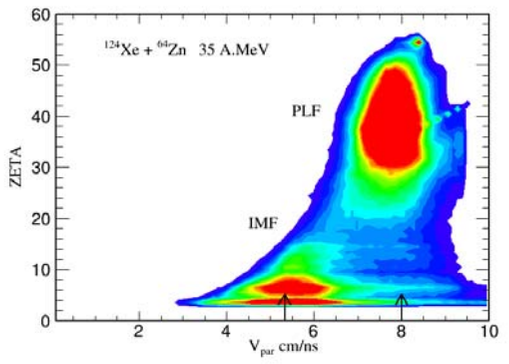

Fig. 1: Yield distribution for particles punching-through the Silicon detectors as a function of their charge Z and parallel velocity for the ^{124}Xe+^{64}Zn reaction.

RESULTS

The experiment was performed using the ^{124}Xe beam at 35 A.MeV from the LNS Cyclotron incident on targets of

^{64}Zn (308 μg/cm^2) and ^{64}Ni (370 μg/cm^2) in the CHIMERA 4π detector. The FARCOS telescopes were placed at 25 cm from the target and covering the angular region (Δθ = 15°-45°, Δφ=90°) in a 2x2 configuration. The main goal of the FARCOS array was to measure with high angular and energy resolution IMF-IMF and proton-proton correlation functions with the event characterization provided by the CHIMERA array. Data acquisition was triggered by at least three or two silicon detectors were fired. Fig. 1 shows a 2-dimensional plot of charge fragments v.s. their parallel velocity along the beam axis as a function of their charge for the ^{124}Xe+^{64}Zn reaction, limited to particles well identified in ΔE-E in Si-CsI CHIMERA telescopes. The figure shows the regions of PLF and IMF very well detected around or above the c.m. velocity. Future progresses in data analysis will permit to add slower particles stopped in the Si detectors and identified by Time-of-Flight and/or Pulse-Shape techniques.

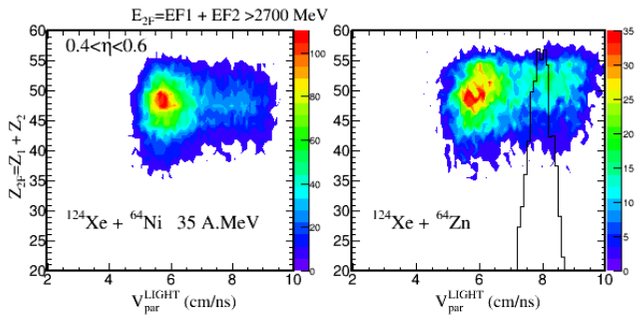

Fig. 2: Distribution of the sum of charges of the two heaviest fragments (Z_{2F}) vs. the parallel velocity of the lighter fragment for ^{64}Ni (left) and ^{64}Zn (right) targets.

In order to examine the binary decay of the PLF produced in peripheral reactions, we considered events in which the sum of the charge of the two heaviest fragments Z_{2F} is larger than the value of 70% of the projectile charge. Fig 2. shows the distribution of Z_{2F} vs. the parallel velocity of the lighter fragment for the reactions ^{124}Xe+^{64}Ni (left) and ^{124}Xe+^{64}Zn (right) for large asymmetric splitting, $0.4< \eta=(Z_1-Z_2)/(Z_1+Z_2)<0.6$, of quasi-projectiles and for a window of the total kinetic energy of the two fragments E_{2F}> 2700 MeV, so removing in this way the more dissipative collisions. The velocity distribution of the heaviest fragment is shown for comparison in the right panel. We see that the light fragment velocity has two components characteristic of "forward" and "backward" emission in the PLF frame as compared with the projectile heavy residue velocity distribution centered around the beam velocity, consistent with the scenario of the scattering of the PLF followed by its splitting into two fragments [2,4]. In order to examine this aspect in more detail we construct for three different values of the asymmetry η the θ_{prox} angle, defined as the angle between the PLF* flight direction in the c.m. frame and the relative velocity between Z_1 and Z_2. In case of an equilibrated, statistical process of binary PLF splitting, it is expected a $cos(\theta_{prox})$ distribution that is symmetric around $cos(\theta_{prox})$=0.

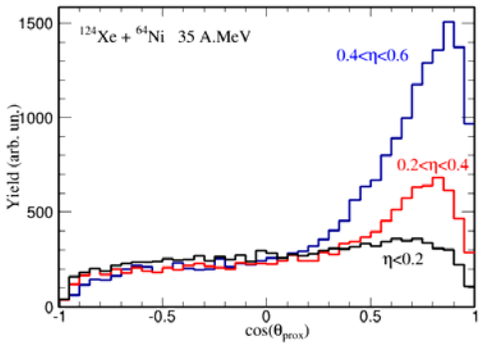

Fig. 3: $cos(\theta_{prox})$ distribution for three different asymmetries η in the binary splitting of the PLF* in the ^{124}Xe + ^{64}Ni reaction.

Fig. 3 shows the $\cos(\theta_{prox})$ distribution. From the figure we notice that it results from the superposition of a symmetric component and a peaked distribution increasing with the charge asymmetry. This last component, around $\cos(\theta_{prox})$=1 is a signature of a backward emission along the PLF direction in an aligned configuration. This anisotropy is the main signature of a "dynamical fission" process. As shown in Ref. [1], we can use this observable in order to disentangle the statistical and dynamical fission decay as a function of the emitted IMFs charge. Preliminary results [5], for the two different targets ^{64}Ni and ^{64}Zn in the isobaric systems studied here, show that dynamical IMF emission is enhanced when the neutron rich target ^{64}Ni is used. More detailed and careful analysis (including the achievement of data analysis for particles stopping in the Si detectors) and absolute cross sections determination for the statistical and dynamical components, will permit the comparison with results of the previous experiment ^{124}Sn+^{64}Ni that was one of the main goals of the InKiIsSy experiment. The dynamical IMF emission can be a good probe in order to constraint the density dependence of the symmetry energy but this need calculations that are able to follow the largest possible reaction time-scales of the IMF emission involved in PLF binary splitting. Finally the merging of the CHIMERA and FARCOS data will certainly extends our experimental capabilities, due to their isotopic resolving power of IMFs and light charged particles, providing also the first set of data available in order to characterize the FARCOS performances.

REFERENCES

[1] P. Russotto et al., Phys. Rev C**91**, 014610 (2015).

[2] P. Russotto et al., Phys. Rev C**81**, 064605 (2010).

[3] E. De Filippo et al., Phys. Rev. C**86**, 014610 (2012); *ibid.* Phys. Rev. C**71**, 064604 (2005).

[4] A.B. McIntosh et al., Phys. Rev. C**81**, 034603 (2010).

[5] *Asy-Eos 2015 Int. Workshop*, 3-6 March 2015.

The ASY-EOS Experiment at GSI: Constraining the Symmetry Energy at Supra-Saturation Densities

P. Russotto[1] for ***ASY-EOS*** and ***NewCHIM*** collaborations

1) INFN-Sezione di Catania,Catania, Italy

Abstract - The elliptic-flow ratio of neutrons with respect to protons or light complex particles in reactions of heavy ions at pre-relativistic energies has been proposed as an observable sensitive to the strength of the symmetry term of the nuclear equation of state at supra-saturation densities. In the ASY-EOS experiment at the GSI laboratory, flows of neutrons and light charged particles were measured for ^{197}Au+^{197}Au, ^{96}Zr+^{96}Zr and ^{96}Ru+^{96}Ru collisions at 400 MeV/nucleon. Flow results obtained for the Au+Au system have been compared with predictions of the UrQMD transport model to constrain the density dependence of the symmetry energy.

INTRODUCTION

The neutron-proton elliptic flow ratio and difference have been proposed as effective probes of the high-density behavior of the nuclear symmetry energy [1, 2, 3]. The comparison of existing data from the FOPI-LAND experiment [4] with calculations performed with the UrQMD transport model [5] suggests a moderately soft to linear symmetry term. The result suffers, however, from the considerable statistical uncertainty of the experimental data [1,3]. The same data set was also compared to calculations performed with the Tübingen QMD model and a constraint compatible with the UrQMD result was obtained [6]. At the same time, a thorough study of the parameter dependence of the model predictions was performed in order to devise a route towards a model independent constraint of the high-density symmetry energy [6]. It was, in particular, found that different parameterizations of the isovector part of the equation of state, the Gogny inspired (momentum dependent) vs. the power law (momentum independent) potential, lead to very similar results.

In order to improve the statistical accuracy of the experimental flow parameters for the Au+Au reaction and to extend the flow measurements to other systems, the symmetric collision systems ^{197}Au+^{197}Au, ^{96}Zr+^{96}Zr and ^{96}Ru+^{96}Ru at 400 MeV/nucleon incident energies have been chosen for the ASY-EOS experiment, conducted at the GSI laboratory in May 2011 (S394 experiment). As in the previous experiment, the Large Area Neutron Detector LAND [7] was used for the detection and identification of neutrons and light charged particles. By including the KRATTA telescope array [8] in the setup, the study of isospin effects in these reactions was extended to additional observables as, e.g., the yield ratios of light isobar pairs ^{3}H/^{3}He and ^{7}Li/^{7}Be.

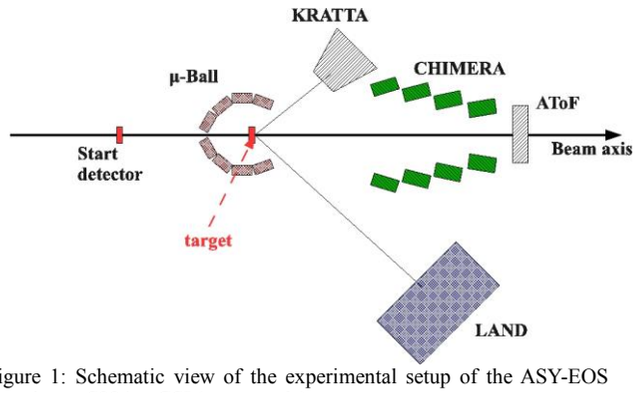

Figure 1: Schematic view of the experimental setup of the ASY-EOS experiment S394 at GSI (not to scale).

ASY-EOS EXPERIMENT AT GSI

A schematic view of the experimental set-up is shown in Fig. 1. The Large Area Neutron Detector (LAND) [7] was positioned to cover laboratory angles around 45° with respect to the beam direction, at a distance of about 5 m from the target. A veto-wall of plastic scintillators in front of LAND allowed discriminating neutrons and charged particles. In this configuration, it was possible to measure the direct and elliptic flows of neutrons and charged particles at mid-rapidity with high precision in the same angular acceptance. In addition, the Krakow Triple Telescope Array, KRATTA [8], was installed to measure the energy, emission angles and isotopic composition of light charged reaction products. The 35 modules of KRATTA, were placed opposite to LAND at a distance of 40 cm from the target at polar angles between 20° and 64° [9]. The determination of the impact parameter and the orientation of the reaction plane required the use of several devices: i) the ALADIN Time-of-Flight (AToF) wall [10] was used to detect charged particles at polar angles smaller than 7°; two walls (front and rear) of 2.5*100 cm^2 plastic scintillators, read by two photo-multipliers at both ends, gave information on emission angle, atomic number and velocity of forward-emitted ions; ii) 50 thin (between 3.6 and 5.6 mm) CsI(Tl) elements, read out by photo-diodes and arranged in 4 rings, of the Washington-University μBall array [11], surrounded the target at polar angles between 60° and 147° with the aim of measuring the multiplicity and angular distribution of backward emitted particles in order to discriminate against background reactions on non-target material; iii) 352 CsI(Tl) scintillators, 12 cm thick, of the CHIMERA multi-detector [12], arranged in 8 rings with

2π azimuthal coverage around the beam axis and covering polar angles between 7° and 20°, were used to detect light charged particles from mid-rapidity emissions. With beam intensities of about 10^5 pps and targets of 1-2% interaction probability, about $5*10^6$ events were collected for each system. Special runs were performed with and without target, in order to measure the background from interaction of projectile ions with air, and with iron shadow bars in front of LAND or the neutron background measurement.

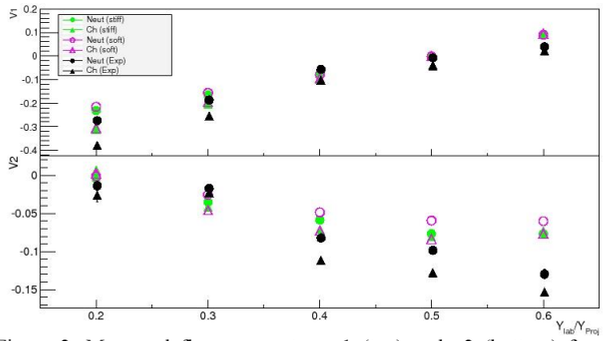

Figure 2: Measured flow parameters v1 (top) and v2 (bottom) for b<7.5 fm Au+Au collisions at 400 MeV/nucleon for neutrons (black full dots) and charged particles (black full triangles) as a function of the normalized rapidity Y_{lab}/Y_{proj} . The UrQMD predictions for neutrons and charged particles obtained with a stiff (γ=1.5, green full symbols) and a soft (γ=0.5, purple empty symbols) density dependence of the symmetry term have been filtered to correspond to the geometrical acceptance of the experiment. The experimental data have been corrected for the dispersion of the reaction plane.

Elliptic neutron and charged-particle flows

Firstly we have rejected background reactions due to the interaction of Au projectiles with non-target material (mainly air), by using the correlation of the two reaction plane orientations given by CHIMERA and by the μBall detectors, and characterized collision centrality by using global variables [13]. Then, azimuthal distributions of neutrons and light charged particles measured with LAND with respect to the reaction plane given by CHIMERA have been extracted for Au+Au reactions from runs with and without the shadow bar. After subtracting the background, the obtained distributions have been fitted with formula (1) of Ref. [1] in order to determine the direct (v1) and elliptic (v2) flow coefficients. The results for neutrons and for all recorded charged particles (Ch) are here presented. The v1 and v2 parameters for Ch and neutrons as functions of the reduced rapidity Y_{lab}/Y_{proj} are shown in the upper and lower panels of Fig. 2, respectively. In the same figure, also the UrQMD predictions for a soft (γ=0.5) and a stiff (γ=1.5) symmetry energy potential [1] are given. Constraints for the symmetry energy were determined as in Ref. [1] by comparing the ratios of the elliptic flows of neutrons and Ch, $v2^n/v2^{Ch}$, with the corresponding UrQMD predictions for the soft and stiff cases. The results obtained as functions of the reduced rapidity and of the transverse momentum p_t/A are shown in Fig. 3. A preliminary value for the power-law coefficient γ, deduced by linearly interpolating between the predictions, is γ = 0.76 ± 0.12. The new constraint is compatible with the previous one presented in Ref. [1] by using FOPI-LAND data and the same UrQMD model but the statistical error has been significantly reduced by a factor of ~ 2. The determination of systematic uncertainties is still on-going; a preliminary analysis indicates an overall final uncertainty of the order of γ ≈ ±0.25.

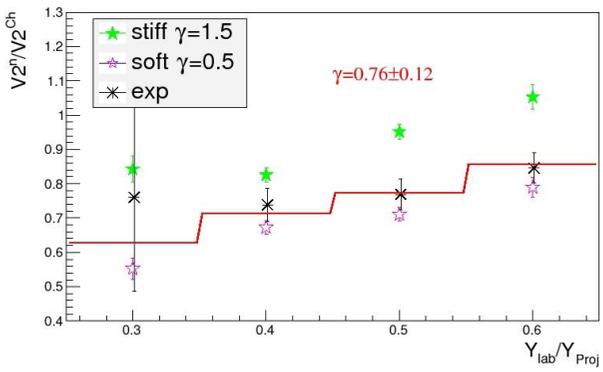

Figure 5: Elliptic flow ratio of neutrons and charged particles for moderately central (b < 7.5 fm) collisions of Au+Au at 400 MeV/nucleon, as a function of the normalized rapidity Y_{lab}/Y_{proj}. The black symbols represent the experimental data. The UrQMD predictions for stiff (γ=1.5, green symbols) and soft (γ=0.5, purple symbols) are shown. The red line in each panel is the result of a linear interpolation between the predictions; the obtained gamma values and their uncertainties are indicated.

OUTLOOKS

Comparisons of the experimental data with other theoretical transport models will be useful in order to pursue the route towards a model-independent constraint of the high-density symmetry energy initiated in Ref. [6]. The promising preliminary results of the present experiment may also be seen as an encouragement for extending the measurement of neutron and charged particle flows to other reaction systems and energies. Future experiments may thereby benefit from the unique possibilities offered by the NeuLAND detector presently constructed as part of the R^3B experimental set-up [14] and from the availability of radioactive ion beams for reaction studies at FAIR.

REFERENCES

[1] P. Russotto et al., Phys. Lett. B697 (2011) 471.
[2] M.D. Cozma, Phys. Lett. **B700** (2011) 139.
[3] P. Russotto et al., Eur. Phys. Jour. **A50** (2014) 38.
[4] Y. Leifels et al. Phys. Rev. Lett. **71** (1993) 963.
[5] Q. Li et al., J. Phys **G 31** (2005) 1359.
[6] M.D. Cozma et al., Phys. Rev. **C88** (2013) 044912.
[7] Th. Blaich et al., NIM **A314** (1992) 136.
[8] J. Lukasik et al., NIM. **A709** (2013) 120.
[9] J. Lukasik et al., Procs of IWM-EC 2014.
[10] A. Schüttauf et al., Nucl. Phys. **A607** (1996) 457.
[11] D.G. Sarantites et al., NIM. **381** (1996) 418.
[12] A. Pagano et al., Nucl. Phys. **A734** (2004) 504.
[13] P. Russotto et al. et al., Procs of IWM-EC 2014.
[14] https://www.gsi.de/r3b

Study of cluster structures in ^{10}Be and ^{16}C via projectile break-up reactions with the CHIMERA multi-detector

D.Dell'Aquila[4], L.Acosta[11], F.Amorini[2], R.Andolina[3], L.Auditore[5], I.Berceanu[8], G.Cardella[1], M.B.Chatterjiee[9], E.DeFilippo[1], L.Francalanza[2,3], B.Gnoffo[1], A.Grzeszczuk[10], G.Lanzalone[2,6], I.Lombardo[4], N.S. Martorana[2,3], T.Minniti[5], A.Pagano[1] E.V.Pagano[2,3], M.Papa[1], S.Pirrone[1], G.Politi[1,3], A.Pop[8], F.Porto[2], L.Quattrocchi[5], F.Rizzo[2,3], E.Rosato[4†], P.Russotto[1], A.Trifirò[5], M.Trimarchi[5], G.Verde[1,7], M.Vigilante[4]

1) INFN—Sezione di Catania, Via S. Sofia, 95123 Catania, Italy
2) INFN—Laboratori Nazionali del Sud, Via S. Sofia, Catania, Italy
3) Dipartimento di Fisica e Astronomia, Università di Catania, Via S. Sofia, Catania, Italy
4) Dipartimento di Fisica, Università di Napoli Federico II and INFN Sezione di Napoli, Italy
5) INFN Gruppo Collegato di Messina and Dipartimento di Fisica e Scienze della Terra, Università di Messina, Italy
6) Facoltà di Ingegneria e Architettura, Università Kore, Enna, Italy
7) Institute de Physique Nucléaire d'Orsay, Orsay, France
8) Institute for Physics and Nuclear Engineering, Bucharest, Romania
9) Saha Institute for Nuclear Physics, Kolkata, India
10) Institut of Physics, University of Silesia, Katowice, Poland
11) National Autonomous University of Mexico, Mexico City, Mexico
† *Deceased*

INTRODUCTION

The study of the structure of light nuclei is considered a very important topic in modern Nuclear Physics. Indeed, the presence of nucleon-nucleon correlations inside nuclei may strongly affect the spatial organization of nucleons, leading to clustering phenomena. Their investigation is therefore a crucial point in the understanding of nuclear forces. Typical examples of α-clustering in light systems are represented by ground and excited states of the self-conjugated nuclei (as ^{8}Be, ^{12}C, ^{16}O, ^{20}Ne) [1].

However, clustering phenomena may play an important role not only in self-conjugated systems but also in neutron-rich nuclei. The effect of the neutron excess on α-clustering in light nuclei can lead to very exotic structures, characterized by high deformation or neutron halo. As pointed out in several works [2,3], in the case of even *Z* systems, the extra neutrons can act as covalent particles between α-clusters, increasing the stability of the structure. A classic example is the ^{9}Be nucleus, for which the existence of rotational bands built on large deformation states has been discussed in the literature. The case of ^{10}Be is not still definitely understood. Near the ^{4}He+^{6}He energy threshold the existence of a 0^+ state is reported. This state can be described as a α:2n:α linear dimer with a super-deformed structure. The existence of a 2^+ state at 7.54 MeV reflects the rotational excitation of this molecular structure [4]. The subsequent 4^+ member is the 10.5 MeV state, while the 6^+ member is still missing, and it is predicted to be at about 13.5 MeV excitation energy. Other interesting examples of α-cluster phenomena in presence of neutron excess are represented by carbon isotopes, for which the existence of exotic chain structures has been theoretically predicted [3].

For the ^{16}C isotope, the presence of two couple of valence neutrons may lead to possible iper-deformed chain states (e.g. ^{10}Be+α+2n like configurations), as predicted by very recent Antisymmetrized Molecular Dynamics (AMD) calculations [8]. Unfortunately, no experimental evidence of the presence of such structure in ^{16}C has still been reported because of the lack of data on ^{16}C spectroscopy at large value of excitation energy.

In this paper we report a new experimental investigation of ^{10}Be and ^{16}C spectroscopy via sequential break-up reactions, that allows to explore the structure of these nuclei in energy regions where molecular states are expected (i.e. above the ^{4}He and ^{6}He decay thresholds).

EXPERIMENTAL DETAILS

The experiment was performed at the FRIBs facility of INFN - Laboratori Nazionali del Sud (LNS). The fragmentation beam was produced starting from a 55 MeV/u ^{18}O primary beam accelerated by the LNS K-800 superconductive cyclotron. It impinged on a 1.5 mm thick ^{9}Be target. Fragmentation products are selected in magnetic rigidity (Bρ ≈2.8Tm) via the LNS-Fragment Separator (LNS-FRS), with a momentum acceptance of $\Delta p/p \approx 0.01$. In this way, a cocktail beam with high intensity of ^{16}C at 49.4MeV/u (≈10^5 pps), ^{13}B (≈5×10^4 pps) and ^{10}Be at 54MeV/u (≈4×10^4 pps) is produced. The identification of the exotic beam particles was obtained by the ΔE-TOF technique, by using the Chimera tagging system [9]. To induce sequential projectile break-up reactions we used mainly polyethylene $(CH_2)_n$ target. For some runs deuterated polyethylene $(CD_2)_n$ was also used.

The break-up products from the $^{1}H,^{2}H,^{12}C(^{10}Be,^{4}He+^{6}He)$ and $^{1}H,^{2}H,^{12}C(^{16}C,^{6}He+^{10}Be)$ reactions were detected by using the 4π multi-detector Chimera [10, 11]. In the present experiment we used the first three forward rings of the Chimera array ($2° \leq \theta \leq 6.4°$). Si and CsI(Tl) detectors of the Chimera array were calibrated via elastic scattering of various light beams impinging on CH_2 target. The dependence of CsI(Tl) light response on the mass and charge of incident particles [12] was taken into account [13].

DATA ANALYSIS

The spectroscopy of ^{10}Be and ^{16}C nuclei was investigated by reconstructing the relative energy of couple of break-up fragments.

From the clusters decomposition of ^{10}Be in $^{4}He+^{6}He$, we obtained the excitation energy spectrum reported in Fig. 1. The dashed curve represents the detection efficiency, evaluated by a MonteCarlo simulation. As is clearly visible from the figure, the detection efficiency has a flat contribution, while the excitation energy shows peaks corresponding to known states, indicated by arrows. The bump at about 13.5 MeV suggest the presence of a possible new state in ^{10}Be. This state is energetically compatible with a possible 6^{+} state, member of the ^{10}Be rotational molecular band. Our suggestion seems in agreement with the findings of a recent resonant elastic scattering experiment $^{6}He+^{4}He$ [15].

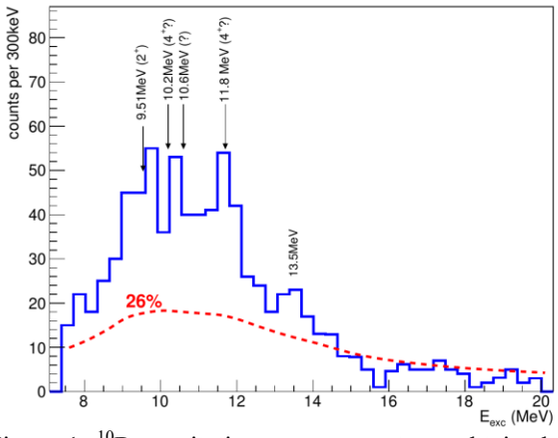

Figure 1: ^{10}Be excitation energy spectrum obtained from the $^{4}He+^{6}He$ break-up channel. Dashed curve indicates the detection efficiency. Arrows indicate ^{10}Be known states.

The excitation energy of ^{16}C was obtained from the relative energy analysis of the $^{10}Be+^{6}He$ break-up channel. The result is shown in Fig. 2. In this case the statistics is very low but the spectrum exhibits a peak at about 20.6 MeV that doesn't match with an effect due to the efficiency (dashed curve). The possible evidence of a state at about 20.6 MeV could be in agreement with previous works reported in the literature (with statistics lower or similar compared to the present analysis) [6,7].

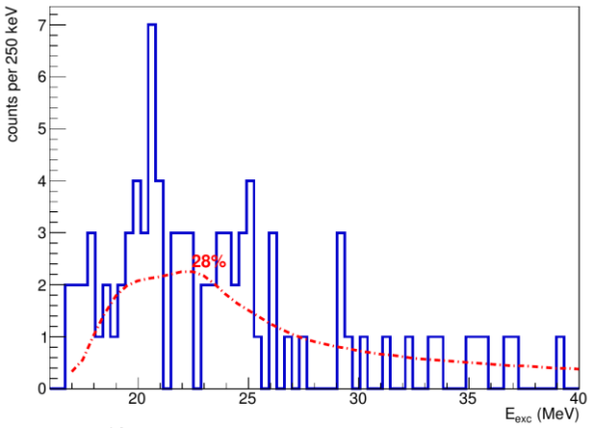

Figure 2: ^{16}C energy spectrum obtained from the relative energy analysis of the $^{10}Be+^{6}He$ break-up channel. The dashed curve is the result of a detection efficiency estimate via MonteCarlo calculations.

CONCLUSIONS

A new experimental investigation of ^{10}Be and ^{16}C neutron-rich nuclei was performed at LNS using the CHIMERA multi-detector and FRIBs beams. The spectroscopy of ^{10}Be and ^{16}C was studied respectively via the cluster break-up channels $^{4}He+^{6}He$ and $^{10}Be+^{6}He$. From these analyses we suggest the existence of a new state at 13.5 MeV in ^{10}Be, that could be the further member of the known ^{10}Be molecular band. To determine the J^{π} of this state an angular correlation analysis is in progress. Finally, the excitation energy spectrum of ^{16}C, reconstructed starting from $^{6}He+^{10}Be$ correlation, shows a peak at about 20.6 MeV, possibly related to the existence of an high-lying molecular excited state in this nucleus.

REFERENCES

[1] K. Ikeda, N. Tagikawa, and H. Horiuchi., Prog. Theo. Phys. Suppl. (1968) 464.
[2] C. Beck, Clusters in Nuclei (Springer, Heidelberg, 2013), Vol. 1,2,3.
[3] W. Von Oertzen, M. Freer, and Y. Kanada-En'yo, Phys. Rep. 432 (2006) 43.
[4] M. Freer et al., Phys. Rev. Lett. 96, 042501 (2006).
[5] Y. Chiba T. Baba and M. Kimura, Phys. Rev. C 90 (2014) 064319.
[6] P.J. Leask, Jour. Phys. G: Nucl. Part. Phys. 27 (2001) B9.
[7] N. I. Ashwood et al., Phys. Rev. C 70 (2004) 0644607.
[9] I. Lombardo et al., Nuc. Phys. B 215 (2011) 272.
[10] A. Pagano et al., Nucl. Phys. A 734 (2004) 504.
[11] A. Pagano et al., Nucl. Phys. News 22 (2012) 25.
[13] D. Horn et al., Nucl. Instr. and Meth. A 320 (1992) 273.
[14] L. Acosta et al., Nucl. Instr. and Meth. A 715 (2013) 56.
[15] G.V. Rogachev et al., J. Phys.: Conf. Ser. 569 (2014).

Decay competition in IMF production in the collisions ^{78}Kr+^{40}Ca and ^{86}Kr+^{48}Ca at 10 A.MeV

G. Politi[1,2], S. Pirrone[2], M. La Commara[3,4], J. P. Wieleczko[5], E. De Filippo[2], B. Gnoffo[1,2], M. Trimarchi[7], M. Vigilante[3,4], G. Ademard[11] , F. Amorini[6], L. Auditore[7,8], C. Beck[9], I. Berceanu[10], E. Bonnet[5], B. Borderie[11], G. Cardella[2], A. Chbihi[5], M. Colonna[6], Antonio D'Onofrio[4,12], J. D. Frankland[5], E. Geraci[1,2], E. Henry[13], E. La Guidara[1,14], G. Lanzalone[15,6], P. Lautesse[16], D. Lebhertz[5], N. Le Neindre[17], I. Lombardo[3], K. Mazurek[5], A. Pagano[2], M. Papa[2], E. Piasecki[18], F. Porto[1,6], M. Quinlann[13], F. Rizzo[1,6], E. Rosato[3,4], P. Russotto[1,2], W. U. Schroeder[13], G. Spadaccini[3,4], A. Trifirò[7,8], J. Toke[13], G. Verde[2].

1) Dipartimento di Fisica e Astronomia, Università di Catania, Italy 2) INFN Sezione di Catania, Italy
3) Dipartimento di Fisica, Università Federico II Napoli, Italy 4) INFN Sezione di Napoli, Italy
5) GANIL Caen,France 6) INFN Laboratori Nazionali del Sud, Italy
7) Dipartimento di Fisica, Università di Messina, Italy 8) INFN Gruppo collegato di Messina, Italy
9) IN2P3 - IPHC Strasbourg, France 10) IPNE, Bucharest, Romania 11) IN2P3 - IPN Orsay, France
12) Dipartimento di Matematica e Fisica - Seconda Università di Napoli,Caserta, Italy
13) University of Rochester, USA 14) Centro Siciliano Fisica Nucleare e Struttura della Materia, Catania, Italy
15) Università Kore, Enna, Italy 16) IN2P3 - IPN Lyon, France
17) IN2P3 - LPC Caen, France 18) University of Warsaw, Poland

Abstract - De-excitation modes of compound systems ^{118}Ba and ^{134}Ba, produced respectively in the ^{78}Kr+^{40}Ca and ^{86}Kr+^{48}Ca collisions at 10 AMeV, are investigated. In particular, the competition among the various disintegration decay paths and the neutron richness dependence of the decay process are studied. Global decay patterns and fragment emission characteristics are presented for the two systems.

INTRODUCTION

The neutron richness of a compound nucleus is expected to play a crucial role in the competition among various de-excitation channels, thus providing information about fundamental nuclear quantities such as level density, fission barrier and viscosity in the exotic domain of the nuclear chart. Novel information on these nuclear properties can be gained from the study of the decay modes across long isotopic chains of compound nuclei, extending from the neutron rich side to the neutron poor one. Formation and decay modes of composite systems were studied in the reactions ^{78}Kr+^{40}Ca and ^{86}Kr+^{48}Ca at 10 AMeV at INFN-LNS in Catania [1-4]. The two experiments complement the data already obtained at 5.5 AMeV for ^{78,82}Kr+^{40}Ca reactions studied at GANIL by using the INDRA detector [5].

EXPERIMENTAL PROCEDURE

The experiment needs the measurements of several key quantities such as the production cross sections, multiplicities, angular and kinetic energy distributions of the reaction products, i.e. Intermediate Mass Fragments (IMFs), Light Charge Particles (LCPs) and Fission Fragments (FFs), with a low energy thresholds, high granularity and large angular acceptance. The experiment was performed at INFN-LNS with the 4π multidetector for charged particle CHIMERA [6], consisting of 1192 ΔE-E detection telescopes, each one consisting of a silicon detector (thickness 300 μm) followed by a Cesium Iodine Thallium doped crystal (with a thickness ranging from 12 cm for forward laboratory direction to 3 cm for backward direction) coupled to a read-out photodiode. This device combines different identification methods as ΔE-E, TOF and Pulse Shape Discrimination for Silicon and CsI(Tl) signals, providing a complete discrimination in charge and/or mass of the main reaction products [7,8].

RESULTS

IMF Characteristics

The energy and velocity spectra of IMFs in CM frame slightly change with the detection angle in both systems, showing thus a strong relaxation of relative kinetic energy. IMFs yields in the range θ_{lab} = 10°-16° plotted in figure 1 present a strong odd-even staggering for detected light fragments with Z<10. The effect persists for fragments having higher Z but with a smaller amplitude. Besides, comparing the two systems, the even-odd staggering is more pronounced for the neutron poor system than for the neutron rich one, as also reported by other examples in the literature [9,10,11].

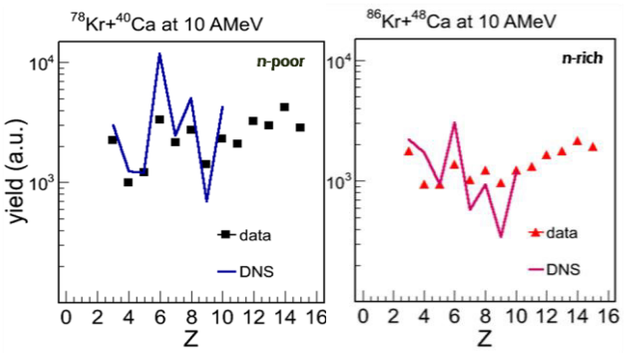

Figure 1: IMF yields for θ_{lab} = 10°-16° in the two systems compared to DNS calculations

In figure 1 the lines are the preliminary results obtained by calculations with the dynamical Di-Nuclear-System model (DNS) [12] for Z<10. Following this model a dinuclear system is formed in the beginning of the reaction, which evolves either towards a fast-fission configuration without fully equilibration, or towards a compound nucleus that subsequently undergoes to fission.

Global decay patterns

Global decay patterns are studied by examining spectra of complete events, selected by imposing a total detected mass M_{tot}>90 and a total detected momentum P_{tot}>0.7P_{beam}. Figure 2 shows for example the correlations between the mass and the parallel velocity with respect to the beam direction for each reaction product, while the correlations between masses M1 and M2 of the two heaviest fragments, are presented in figure 3.

Different reaction products as fragments coming from Fusion-Fission (FF) and Quasi-Fission (QF) or Evaporation Residue (ER) can be easily localized in these plots, giving a qualitative first evaluation of the ratio among the different reaction mechanism contributions.

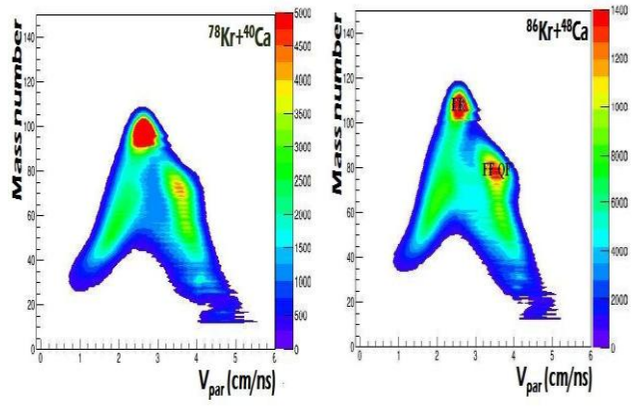

Figure 2: Correlation between fragment mass and parallel velocity Vpar for the two systems

This preliminary analysis, in particular the results of figure 2, suggest that that the fusion-evaporation process is relatively more favoured in the neutron poor system.

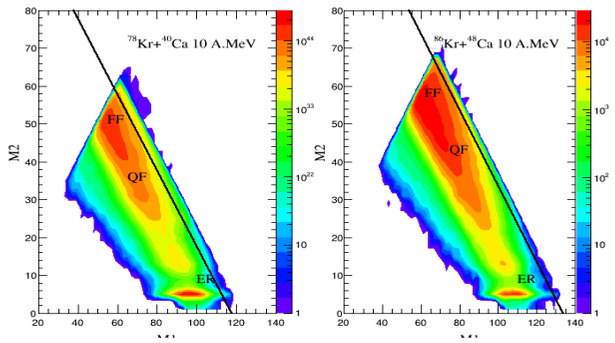

Figure 3: Correlation between the masses M1 and M2 of the two heaviest fragments for the two systems

CONCLUSIONS

Results of the study of the ^{78,86}Kr+^{40,48}Ca reactions at 10 AMeV incident energy are presented. Kinematical characteristics of the IMFs seem to indicate an high degree of kinetic energy relaxation before the breakup, as expected in typical fusion-fission like reaction mechanism. Staggering effects are evident in the IMF charge distributions. Global feature analysis seems to show differences for the two systems in the contribution arising from the different reaction mechanisms. The observed effects could be due to the different neutron richness and thus to the role of the isospin degree of freedom on the decay channels. Data analysis and more refined comparisons with theoretical models are in progress. A Letter of Intent has been presented for an experiment at radioactive ion beam facility SPES at INFN-LNL, with $^{88-94}$Kr + $^{40-48}$Ca at 10 MeV/A, in order to study these effects in neutron richer systems.

REFERENCES

[1] S. Pirrone et al., EPJ WOC **17** (2011) 16010
[2] G. Politi et al., EPJ WOC **21** (2012) 02003
[3] S. Pirrone et al., AIP Conf. Proc. (2013) **1524** 7
[4] M. La Commara et al., EPJ WOC **66** (2014) 03052
[5] G. Ademard et al., Phys. Rev. **C 83** (2011) 054619
[6] A. Pagano et al., Nucl. Phys. **A734** (2004) 504
[7] G. Politi et al., IEEE NSS Conference Record **N28** (2006) 1140
[8] G. Lanzalone et al., INFN-LNS Activity Report (2004) 125
[9] I. Lombardo et al., Phys. Rev. **C 84** (2011) 024613
[10] G. Casini et al., Phys. Rev. **C 86** (2012) 011602(R)
[11] M. D'Agostino et al., Nucl. Phys. **A 861** (2011) 47
[12] Sh. A. Kalandarov et al., Phys. Rev. **C 82** (2010) 044603

Study of two and multi-particle correlations in $^{12}C+^{24}Mg,^{208}Pb$ reactions

L. Quattrocchi[1,2], L. Acosta[3,13] , F. Amorini[7] , A. Anzalone[7] , L. Auditore[1,2] , G. Cardella[3] , A. Chbihi[5], E. De Filippo[3] , Francalanza[7,9] , G. Lanzalone[7,10] , I. Lombardo[8,11], I. Martel[6] , T. Minniti[9] , S. Norella[1,2] , A. Pagano[3] , E.V. Pagano[7,9] , M. Papa[3] , S. Pirrone[3] , G. Politi[3,9] , F. Porto[7,9] , F. Rizzo[7,9] , E. Rosato[8,11†] , P. Russotto[3] , A. Trifiro[1,2], M. Trimarchi[1,2] G. Verde[3,4] , M. Veselsky[12] , M. Vigilante[8,11]

1) Università di Messina, Dip. di Fisica e Scienze della Terra, Messina, Italy
2) INFN, Gruppo Collegato di Messina, Messina Italy
3) INFN, Sezione di Catania, Catania Italy
4) IPN Orsay, Orsay, France
5) GANIL, CEA-IN2P-CNRS, Caen, France
6) Departamento de Fìsica Aplicada, Universitad de Huelva, Huelva, Spain
7) INFN, Laboratori Nazionali del Sud , Catania Italy
8) INFN, Sezione di Napoli, Napoli Italy
9) Università di Catania, Dip. di Fisica e Astronomia, Catania, Italy
10) Università Kore, Enna, Italy
11) Università di Napoli Federico II, Dipartimento di Fisica, Napoli, Italy
12)Slovak Academy of Sciences, Bratislava, Slovakia
13) Instituto de Física, Universidad Nacional Autónoma de México, Apartado Postal 20-364, México D. F. 01000, Mexico
†Deceased

Abstract – A test experiment has been performed at the INFN-LNS with the multidetector array CHIMERA with the aim of exploring the feasibility of multi-light-particle correlation analyses on $^{12}C+^{24}Mg$, ^{208}Pb collisions at E=35 AMeV. In particular, inspired by a similar analysis performed with the INDRA detector at GANIL with the same reaction system at E=52 [1] and 95 AMeV, the decay of excited Quasi-Projectile (QP) systems from peripheral reactions into multi-alpha channels is going to be explored. The performed test is preliminary to further studies to be performed with the coupling of FARCOS to CHIMERA.

INTRODUCTION

Multi-particle correlations are a means to study the decay of unbound states produced during nuclear reactions. In this respect invariant-mass spectroscopy has recently become a tool to explore spectroscopic properties such as spins, branching rations and the existence of new states [2,3]. This has been accomplished with direct reactions [2]. However such states are also produced abundantly in heavy-ion collisions during the dynamical evolution of excited and dilute systems [2]. In this spirit multi-particle correlations in heavy-ion collisions are used as a spectroscopic tool that could also provide information on in-medium transport properties and nuclear interaction. This report describes the status of the analysis of a test experiment performed at the INFN-LNS in Catania with the CHIMERA multidetector.

EXPERIMENT AND RESULTS

$^{12}C+ ^{24}Mg$, ^{208}Pb collisions at 35 AMeV incident energy have been studied with beams delivered by the Superconducting Cyclotron in order to test multi light-particle correlation measurements with CHIMERA [4]. In particular the decay of excited quasi-projectiles in peripheral collisions has been reconstructed by means of multiple particle correlations involving only Z=1 and 2 isotopes. For these light particles the energy released in the first silicon detector stage of the telescopes (used as part of event trigger) can be very small. The performed test as aimed at studying the capability of reconstructing events where mostly such light and fast particles were detected.

On Fig. 1 the α−α (top panel) and α−d (bottom panel) coincidence pairs are shown as a function of excitation energy, $E_{star} = E_{tot} - Q$, where E_{tot} is the total kinetic energy in the pairs center of mass frame and Q is the Q-

value for the specific decay channel under study (i.e. ^{8}Be→ α−α and ^{6}Li→ d−α). One may observe that the α−α spectrum shows a narrow peak centred at 0 MeV and a much broader peak centred around 3 MeV. The first peak corresponds to the ground state of ^{8}Be (Q_{value} =−92 keV) and the second one to the first excited state at 3.03 MeV (2^{+}).

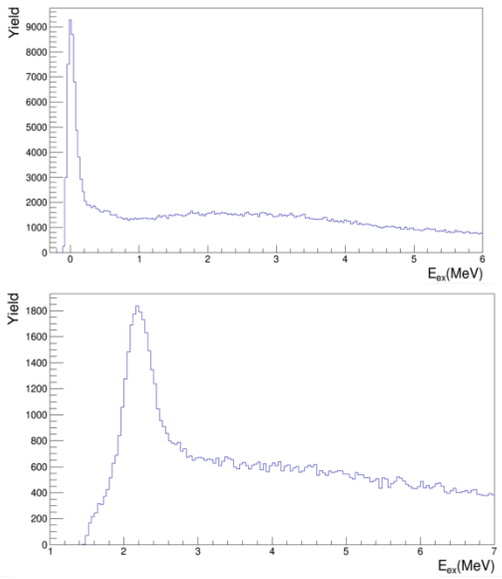

figure 1 : Yield of correlated α-α (top panel) and d-α couples as function of excitation energy.

The d-α spectrum shows a well-shaped peak centred at 2.2 MeV corresponding to the first excited state of ^{6}Li at 2.18 MeV (3^{+}). In both cases, the low energy levels are accurately determined, thus showing a good quality of particle energy calibration and a sufficiently designed angular resolution of the detector array.

Another investigation that represents the aim of the experiment is the decay of excited states of ^{12}C, populated by ^{12}C+ ^{24}Mg at 35 AMeV, into 3 α particles. The plot in Fig. 3 represents 3α correlated spectra as a function of excitation energy.

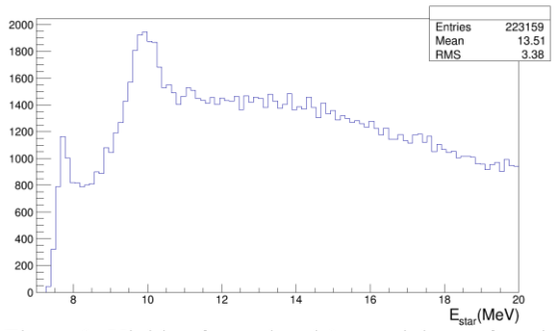

Figure 3: Yields of correlated 3α particles as function of excitation energy.

The spectra shows two peaks centered at E_{star}=7.6 MeV and E_{star}=9.6 MeV. The first peak corresponds to well-known Hoyle state (0^{+}) at E^{th}_{star}=7.65 MeV, while the second one is due to the 3^{-} excited level at E^{th}_{star}=9.64 MeV of ^{12}C. The broader peak centred around 12 MeV could correspond to the overlap of the three states 1^{-} at E^{th}_{star} =10.84 MeV, 2^{-} at E^{th}_{star}=11.82 MeV and 1^{+} at E^{th}_{star} =12.71 MeV.

CONCLUSIONS

These preliminary results show that it is possible to continue this correlations study in order to extract spectroscopic information, such as the competition between sequential and simultaneous decay mode, including links and interplays with the reaction mechanism leading the studied reaction system.. Furthermore we hope to address important physics problems concerning clustering phenomena in nuclei and nuclear matter. For instance the Hoyle state is an excited, resonant state of carbon-12 produced via the triple-alpha process and is characterized by a pronounced molecular-like structure with three alpha particles [5]. The study of the Hoyle state is essential for the nucleosynthesis, but it also represents a clearly isolated state that can be studied as a three-alpha cluster system. Comparisons of its properties measured in reactions performed at different beam energies [2] as well as with different reaction mechanisms (direct reactions, multifragmentation, etc.) may provide information on in-medium nuclear structure representing an important perspective for research on the nuclear interaction itself.

These studies are also preliminary to the development of the FARCOS array specialized in high angular resolution measurements of two- and multi-particle correlations [6,7].

REFERENCES

[1] G. Verde et al., Eur. Phys. J. A 30, 81-108 (2006).

[2] F. Grenier et al., Nucl. Phys. A811, 233 (2008).

[3] R.J. Charity et al., Phys: Rev. C84, 014320 (2011).

[4] A. Pagano, et al. Nucl. Phys. A 734 (2004) 504.

[5] A. Raduta et al., Phys. Lett. B 705, 65 (2011).

[6] G. Verde et al., Jour. of Phys. Conf. Series 420, 012158 (2013).

[7] E.V. Pagano et al., IWM-EC2014, May 6-9, Catania, Italy,https://agenda.infn.it/internalPage.py?pageId=13&confId=6673.

Dipolar degrees of freedom and Isospin equilibration processes in Heavy Ion collisions - I

M.Papa[1], I.Berceanu[2], L.Acosta[3], F.Amorini[3], C.Agodi[3], A.Anzalone[3], L.Auditore[4], G.Cardella[1] M.B.Chatterjee[5], E. De Filippo[1], L.Francalanza[6], E.Geraci[1], L.Grassi[3], B.Gnoffo[1] ,J.Han[3], E.La Guidara[1], G.Lanzalone[7], I.Lombardo[8], C.Maiolino[3], T.Minniti[3], A.Pagano[1], E.V.Pagano[3], S.Pirrone[1], G.Politi[9], F.Porto[9], L.Quattrocchi[10], F.Rizzo[9], P.Russotto[3], A.Trifiro[10], M.Trimarchi[10], G.Verde[1] and M.Vigilante[8]

1) INFN Sezione di Catania, Italy 2) National Institute for Physics, Bucharest, Romania
3) INFN-LNS Catania, Italy 4) INFN Gruppo collegato di Messina, Italy
5) Saha, Institute of Nuclear Physics Kolkata, India 6) INFN Sezione di Napoli, Italy
7) "Kore" Università, Enna, Italy 8)Dipartimento di Fisica, Università Federico II Napoli, Italy
9) Dipartimento di Fisica e Astronomia, Università di Catania, Italy
10) Dipartimento di Fisica Università di Messina, Italy

Abstract - The ^{48}Ca+^{27}Al, ^{27}Al+^{48}Ca, ^{27}Al+^{40}Ca at 40 MeV/nucleon were investigated with the CHIMERA multi-detector. We have determined the time derivative of the total dipole associated to the emitted charged particle using the measured charge and velocity of the multi-detector. This observable is linked in a peculiar way with Isospin equilibration processes.

INTRODUCTION

Global dynamical effects related to Isospin equilibration process can be determined by investigating on the average time derivative of the total dipole $< \vec{D} >$ associated to the fragment production in a nucleus-nucleus collision.

It was also shown in that this quantity is independent on statistical decay processes which are expected to play a role in the final stage of the equilibration process[1,3]. The investigation on this observable therefore allows highlighting the role played by the density dependence of the symmetry energy in the early stage of the interaction. In this stage pre-equilibrium particles emission, IMF production, transfer of mass/charge between the main partners happens just when the largest changes of the density are expected with respect the saturation value.

EXPERIMENTAL PROCEDURE

To investigate on this observable the system ^{48}Ca+^{27}Al at 40 MeV/nucleon was studied with the multi-detector CHIMERA [4] at INFN-LNS Catania. Measurement on the auxiliary system ^{27}Al+^{48}Ca and the reference one ^{27}A+^{40}Ca were also performed in the same experiment :EQUILIBRATION.

The main goal of the measurement was to evaluate the following quantity: $< Dz,c >=< \sum_{i=m} Z_i (V_{Z,i} - V_Z^{cm,d}) >$, it represents (in unit of the elementary charge) the beam axis component of the partial dipole signal related to all the detected charged particles. In the above expression $V_Z^{cm,d}$ is the effective the center of mass (c.m.) velocity associated to the motion of the detected charged particles. It substitutes the c.m. theoretical value appearing in the definition of the total signal **<Dz>** which includes the effect related to the emitted neutron. Even if **.<Dz,c>** represents a partial dipolar signal it is practically insensitive to eventual systematic errors on the velocity determination. The average <,> is taken over ensemble of well reconstructed events ordered according to the charge of the biggest detected fragment Z_b, and to the estimated Total Kinetic Energy Loss TKEL . Only events with a total detected charge equal to 33 (equal to the toal charge of the system) were considered.

The total detected mass was chosen in the interval $62 \leq A_{tot}^{d} \leq 78$. The total measured momentum along the beam axis was selected within 70% of the theoretical value.

By means of the measurements on the auxiliary system ^{27}Al+^{48}Ca and trough a dedicate analysis we have evaluated the effects on possible systematic errors on the indirect charge assignment related to the produced slow fragments in the main investigated system (light partner). In particular, for TKEL<350 MeV, we have compared the charge distribution of TLF fragments as obtained in the main system with the one associated to the PLF in the auxiliary one (direct charge assignment trough ΔE-E technique). The two charge distributions are shown in the inset of Figure 1. The small difference between the two distribution could generate an average systematic errors ΔZ at most equal to 0.5 unit for charge fragments Z<10 . This produces a rather small error on the investigated quantity **Δ<Dz,c>** < 0.2 cm/nsec.

In Figure 1 we show for different Z_b values, the measured **<Dz,c>** values for the system ^{48}Ca+^{27}Al at 40 MeV/nucleon. The ridge in the plot highlights an increasing trend the signal from negative values to almost zero, for decreasing values of Z_b with respect to Z_{PLF}.

We note that in the initial configuration the system should exhibit a limiting value of Dm (grazing collisions)

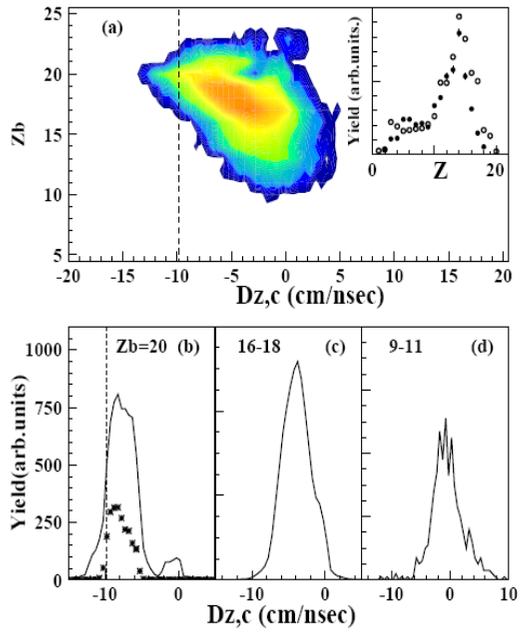

Figure 1: Panel (a): For the system $^{48}Ca+^{27}Al$ at 40 MeV/nucleon, the measured values of **Dz,c** are plotted for different Z_b associated with the selected events (charged multiplicity m≥ 2). The dot-dashed vertical lines indicates the reference limiting values D_m..
Panels (b),(c),(d): **Dz,c** distributions obtained as projections of the above 2-D plot, for different Z_b intervals. In the panel (b) the Dz,c distribution for Z_b=20 and for quasi-elastic events (TKEL < 70 MeV) are plotted with star symbols.

close to about -9.8 cm/nsec.
The decreasing average values of $|< Dz,c >|$ for Z_b different from the projectile atomic number (i.e. less peripheral collisions), represent a clear signature of the evolution towards charge/mass equilibration. This behaviour is in fact related to the production, on average, of more charge/mass symmetric fragments.

The limiting values corresponding to the most peripheral selected collisions D_m are shown in Figure 1 by dot-dashed vertical lines. Panels (b), (c) and (d) show the projections of the 2-D plot for different intervals of Z_b, where we can clearly see the trend. In particular, in panel (b) the spectrum with star symbols is obtained by imposing a cut of TKEL<70 MeV. The large fluctuations of $< Dz,c >$ around the average value are mainly due to physical reasons (the particular "history" of each event) .

Figure 2 shows analogous plots for the reference isospin quasi-symmetric system $^{27}Al+^{40}Ca$ at 40 MeV/nucleon. In this case the limiting value of D_m for "grazing" collisions, is about -2.6 cm/nsec and the data indeed shows values close to zero along with an enhancement near the D_m value (Figure 2b).

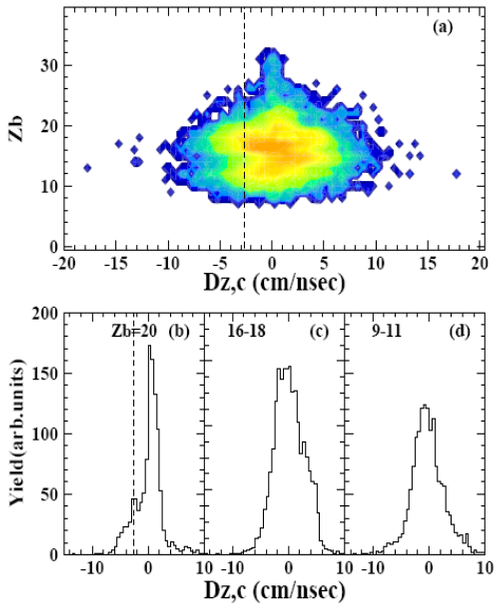

Figure 2: Same as the Figure 1 but for the reference system $^{27}Al+^{40}Ca$.

The comparison between these systems assures us of the good level of confidence in determining $< Dz,c >$.

CONCLUSION

The time derivative of the total dipole associated to all the charged particles produced in the collision $^{48}Ca+^{27}Al$ at 40 MeV/nucleon (TKEL≤350 MeV) has been determined at LNS by means of the multi-detector CHIMERA. The presented results confirm that this observable is able to highlight in a peculiar way the dynamics of the Isospin equilibration[1] processes during the first stage of the nucleus-nucleus collision. The connection between the obtained results and the density dependence of the effective Iso-vectorial interaction are presented in a following (part II) of this report.

REFERENCES

[1] M.Papa et al, to be printed on Phys. Rev. C
[2] M.Papa et al., Phys. Rev. C **72**,064608 (2005) and reference therein (see in particular Appendix D).
[3] M.Papa M and G.Giuliani, Journal of Physics: Conference Series **312** 082034(2011).
[4] A.Pagano et al., Nucl .Phys A**734** 504(2004)

Dipolar degrees of freedom and Isospin equilibration processes in Heavy Ion collisions-II

M.Papa[1], I.Berceanu[2], L.Acosta[3], F.Amorini[3], C.Agodi[3], A.Anzalone[3], L.Auditore[4], G.Cardella[1] M.B.Chatterjee[5], E. De Filippo[1], L.Francalanza[6], E.Geraci[1], L.Grassi[3], B.Gnoffo[1] ,J.Han[3], E.La Guidara[1], G.Lanzalone[7], I.Lombardo[8], C.Maiolino[3], T.Minniti[3], A.Pagano[1], E.V.Pagano[3], S.Pirrone[1], G.Politi[9], F.Porto[9], L.Quattrocchi[10], F.Rizzo[9], P.Russotto[3], A.Trifiro[10], M.Trimarchi[10], G.Verde[1] and M.Vigilante[8]

1) INFN Sezione di Catania, Italy 2) National Institute for Physics, Bucharest, Romania
3) INFN-LNS Catania, Italy 4) INFN Gruppo collegato di Messina, Italy
5) Saha, Institute of Nuclear Physics Kolkata, India 6) INFN Sezione di Napoli, Italy
7) "Kore" Universita', Enna, Italy 8)Dipartimento di Fisica, Università Federico II Napoli, Italy
9) Dipartimento di Fisica e Astronomia, Università di Catania, Italy
10) Dipartimento di Fisica Universita' di Messina, Italy

Abstract - The behaviour of the time derivative of the total dipole measured in the $^{48}Ca+^{27}Al$ system at 40 MeV/nucleon with the CHIMERA multi-detector has been described by means of the CoMD-III model. The comparison of the model calculations with the experimental data allows to extract information on the "stiffness" parameter related to the iso-vectorial interaction in semi-peripheral collisions. Moreover, the same analysis allows for a first estimate of the global effect of the neutron emission on the Isospin equilibration process.

INTRODUCTION

Global dynamical effects related to Isospin equilibration process can be determined by investigating on the average time derivative of the total dipole $\langle \dot{\vec{D}} \rangle$ associated to the fragment production in a nucleus-nucleus collision.

It was also shown that this quantity is independent on statistical decay processes which are expected to play a role in the final stage of the equilibration process[1,3]. The investigation on this observable therefore allows highlighting the role played by the density dependence of the symmetry energy in the early stage of the interaction. In this stage pre-equilibrium particles emission, IMF production, transfer of mass/charge between the main partners happens just when the largest changes of the density with respect the saturation value are expected. In the next section we discuss the comparison of the obtained results on the system $^{8}Ca+^{27}Al$ system at 40 MeV/nucleon[3] with CoMD-III calculations.

COMPARISON WITH COMD-III CALCULATIONS

To obtain information about the behaviour of the iso-vectorial interactions using this experimental data as a starting point [3], we have carried out CoMD-III [4] calculations in the interval of impact parameters b=4-9 fm (the weight of each b is chosen proportionally to b itself). Dynamical calculations have been followed up to about 500fm/c. For each generated event, the second stage of a multi-step statistical decay has been simulated through the Monte Carlo GEMINI code.

The obtained results have been analyzed with an implemented code that takes into account the main filtering effects of the experimental apparatus.

This includes geometrical acceptance for the identified particles and the main selection criteria used in the analysis of experimental data.

The CoMD-III calculations have been performed for stiffness parameter values describing the iso-vectorial interaction, γ=0.8 (L≈ 79 MeV), γ =1 (L ≈ 90 MeV), γ=1.2(L≈100 MeV), γ=1.5(L≈ 114 MeV) and a symmetry energy value of about 32 MeV.

According to previous investigations, the parameters of the effective Skyrme interaction corresponding to a compressibility of about 220 MeV have been chosen following Refs[4].

Figure 1 (panels (a), (b), and (c)) shows the comparison of the calculations with the measured value of **<Dz,c>** (red star points), evaluated from the correlation plot shown in [3]. The values refer to different Z_b windows and TKEL <350 MeV. The vertical bars indicate the statistical uncertainty.

The estimated uncertainties related to the experimental values are in many cases smaller than the plotted symbols. The corresponding theoretical values are plotted in the different panels with black symbols.

The comparison between the calculations and the experimental data is quantified in the figure through the "chi-square" values labelled by χ . According to this parameter, the case where γ=1 gives the best comparison even if it is only slightly better than the case γ=1.2.

The behaviour of **<Dz,c>** can be understood in a qualitative way from the following remarks:

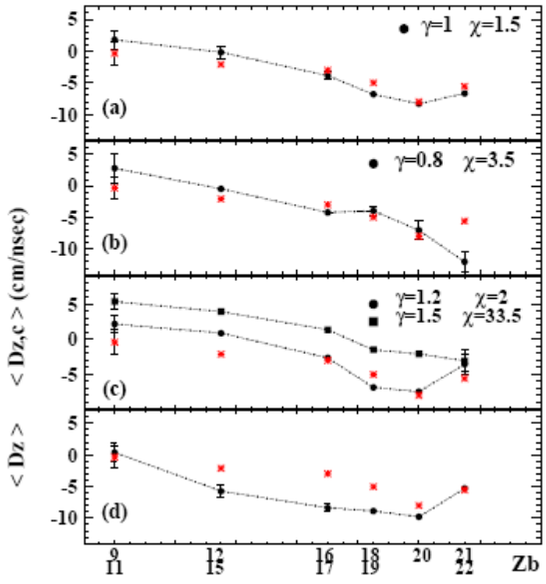

Figure 1. See the text.

as shown in Figure 1 (apart from the case γ=0.8) for $Z_b < Z_{PLF}$ (dominance of mass transfer from PLF to TLF), and for $Z_b > Z_{PLF}$ (onset of fusion and incomplete fusion), **|<Dz,c>|** decreases: this means that on average more charge/mass-symmetric fragments are produced..

In particular it can be shown that in this case center of mass (c.m.) velocity associated to all the charged particles is lower than the global c.m. velocity V_{cm}. Therefore the c.m. velocity of the free neutrons necessarily has to be larger than V_{cm} . This means that, on average, there is more neutron emission from the PLF side (neutron-rich partner).

For γ=0.8 and $Zb > Z_{PLF}$ we instead obtain an opposite behaviour. Therefore in this case the cloud of neutrons has a c.m. velocity smaller than V_{cm}. In this case we have on average more neutron emission from the mid-rapidity and TLF side.

At the present stage of investigation, to recover information about the global degree of dynamical isospin equilibration (including the neutron contribution), we can evaluate **<Dz>** through calculations by using the same set of parameters which "best fit" the experimental value of **<Dz,c>**. In Figure 1 (panel (d)), we compare the calculated values of **<Dz>** for γ=1 , with the experimental values **<Dz,c>**. The difference between these two quantities can therefore represent a first estimation of the global contribution to the dynamical Isospin equilibration associated to the emitted neutrons.

CONCLUSION

The study performed on the behaviour of **<Dz,c>** and **<Dz>** as function of the size of the biggest fragment for TKEL<350 MeV shows a noticeable sensitivity of this observable to the parameters of the microscopic effective interaction.

First attempts to reproduce the experimental values of **<Dz,c>** in essentially binary processes is in overall agreement with CoMD-III calculations using a stiffness parameter for the iso-vectorial interaction γ ≈ 1-1.2 .

More experimental investigation should involve different systems and more central reaction mechanisms.

In particular, a next step forward in this kind of measurements would require a more detailed investigation including a reliable valuation and/or minimizations of possible systematic errors on the velocity of the slow fragments.

This would permit a more reliable experimental estimation of **<Dz>** allowing also for a corresponding experimental valuation of the global effect associated to the dynamically emitted neutrons.

To achieve this goal it would be very useful to use the already extended pulse-shape discrimination technique for slow fragments in the CHIMERA detector and the investigation on systems formed by targets and projectiles having the same mass and charge/mass asymmetry. These systems are in fact associated to vanishing values of **<Dz>** independently from the reaction mechanism .

REFERENCES

[1] M.Papa et al., Phys. Rev. C **72**,064608 (2005) .

[2] M.Papa M and G.Giuliani, Journal of Physics: Conference Series **312** 082034(2011).

[3] M.Papa et al, to be printed on Phys. Rev. C ; LNS-Report 2013-14 "Dipolar degrees of freedom and Isospin equilibration processes in Heavy-Ion collisions-I

[4] M.Papa, Phys. Rev C **87**, 014001(2013)..

Dynamical Dipole mode in heavy-ion fusion reactions in the ^{192}Pb mass region

C. Parascandolo[1], D. Pierroutsakou[1], R. Alba[2], A. Del Zoppo[2], C. Maiolino[2], D. Santonocito[2], C. Agodi[2], V. Baran[3,2], A. Boiano[1], M. Colonna[2], R. Coniglione[2], E. De Filippo[4], M. Di Toro[2,5], U. Emanuele[6], F. Farinon[7], A. Guglielmetti[8], M. La Commara[9,1], B. Martin[9,1], C. Mazzocchi[8], M. Mazzocco[10], C. Rizzo[2,5], M. Romoli[1], M. Sandoli[9,1], C. Signorini[10], R. Silvestri[9,1], F. Soramel[10], E. Strano[10], D. Torresi[10], A.Trifirò[6] and M.Trimarchi[6]

1) INFN - Napoli, Napoli, Italy 2) INFN - Laboratori Nazionali del Sud, Catania, Italy
3) University of Bucharest, Bucharest, Romania and NIPNE-HH, Magurele, Romania
4) INFN - Catania, Catania, Italy 5) Dip. di Fisica e Astronomia, Università di Catania, Catania, Italy
6) INFN - Gruppo Collegato di Messina and Università di Messina, Messina, Italy 7) GSI, Darmstadt, Germany
8) Dip. di Fisica, Università di Milano and INFN - Milano, Milano, Italy
9) Dip. di Scienze Fisiche, Università di Napoli, Napoli, Italy
10) Dip. di Fisica e Astronomia, Università di Padova and INFN, Padova, Italy

Abstract - The dynamical dipole mode was investigated in the mass region of the ^{192}Pb compound nucleus, both in fusion-evaporation and fission events. We present here our results for the fusion-evaporation channel, that prove the dynamical dipole mode excitation also in nuclei much heavier than those studied previously.

INTRODUCTION

In N/Z asymmetric heavy-ion reactions, it is possible to excite a pre-equilibrium collective dipole oscillation that can develop along the symmetry axis of the dinuclear system [1-3]. This oscillation, called "Dynamical Dipole mode" (DD), decays emitting prompt dipole γ-rays, in addition to those coming from the Giant Dipole Resonance (GDR) thermally excited in the hot compound nucleus (CN). The DD radiation presents i) a centroid energy lower than that of a statistical GDR built in a spherical nucleus of similar mass due to the high deformation of the emitting source [2,3] ii) an anisotropic angular distribution with respect to the beam axis because the oscillation is confined in the reaction plane [4] and iii) a γ yield that is predicted to depend on both the beam energy and the reaction dynamics [3]. Experimentally, the DD mode has been investigated in deep inelastic and fusion-evaporation heavy-ion collisions [5-10]. In these measurements, typically in the mass region of Ce, an excess of γ-rays was observed in the GDR energy region for a charge asymmetric reaction, with respect to a more charge symmetric one forming the same CN at identical conditions [6-9] or with respect to statistical model calculations [10]. This γ excess was attributed to the decay of the predicted DD.

The emission of pre-equilibrium DD γ-rays in fusion reactions decreases the excitation energy and hence the initial temperature of the nucleus reaching the statistical phase. This cooling mechanism might be suitable to favour the production of super-heavy elements (SHE) in hot fusion processes. In the above context, in order to verify whether the DD is excited also in systems heavier than those studied before, we decided to study the DD in the region of the ^{192}Pb CN.

EXPERIMENTAL RESULTS

The experiment was performed by using the ^{40}Ca (^{48}Ca) pulsed beam provided by the Superconducting Cyclotron of the LNS, impinging on a 1 mg/cm^2 thick ^{152}Sm (^{144}Sm) target at E_{lab} = 440(485) MeV. Both entrance channels populate the same CN, ^{192}Pb, through a quite different initial dipole moment: 30.6 fm for the ^{40}Ca + ^{152}Sm charge asymmetric reaction and 5.3 fm for the ^{48}Ca + ^{144}Sm more charge symmetric one. The mass asymmetry of the two entrance channels is very similar, namely 0.22 (0.18) for the ^{40}Ca + ^{152}Sm (^{48}Ca + ^{144}Sm) system. Furthermore, according to PACE2 calculations [11], the spin distribution of the CN formed in the two reactions is identical.

Light charged particles and γ-rays were detected by using the MEDEA experimental apparatus [12], made of 180 BaF_2 scintillators, and identified by combining pulse shape analysis and time of flight information. The radiofrequency signal of the Cyclotron was used as time reference.

The fusion-evaporation residues were detected by four position sensitive Parallel Plate Avalanche

Counters (PPACs), subtending 7° in θ, placed symmetrically around the beam direction at θ = 7° polar angle and 70 cm from the target. Down-scaled single events together with coincidence events between at least one fired BaF_2 and a PPAC were collected. By using the above trigger we deduce the γ-ray double differential multiplicity spectra from the ratio of the number of coincidences between γ-rays and evaporation residues and the number of single evaporation events. Details and preliminary results of the experiment can be found in [13].

From the analysis of the energy spectra of the light charged particle in evaporation events we demonstrated that the two reactions lead to the formation of a CN with the same average mass at the same average excitation energy. Therefore, as in our previous works [8,9], all the parameters except the dipole moment were kept identical in the two reactions, so that any difference in their γ-ray spectra and angular distributions can be attributed to the difference in the entrance channel charge asymmetry. By comparing the center-of-mass double differential γ-ray spectra of the two reactions in evaporation events an excess of γ-rays in the more charge asymmetric reaction, concentrated in the energy range E = 8-15 MeV, was observed. This can be seen in Fig.1, where the difference between the spectra of the two systems is shown. This excess is related to the DD γ decay and can be reproduced by means of a lorentzian curve folded by the experimental apparatus response function [14] (line in the figure) with a centroid energy E_{DD} = 11 MeV and a width Γ_{DD} = 3.5 MeV. We observe that E_{DD} is lower than the ground state GDR centroid energy E_{GDR} ~13.5 MeV for a mass in the region of 192, confirming the high deformation of the emitting source, in agreement with expectations for DD emission [2,3] and with our previous works [8,9].

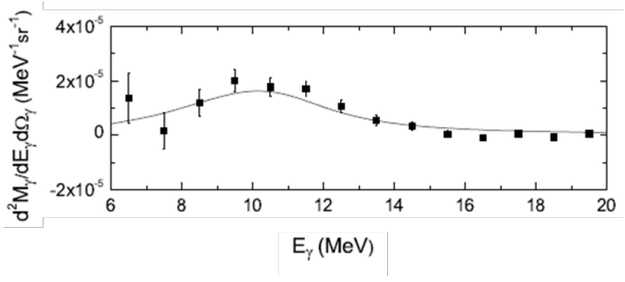

Figure 1: Difference between the charge asymmetric and charge symmetric reaction center-of-mass γ-ray multiplicity spectra. The solid line is described in the text.

In Fig.2 we show the DD γ-ray angular distribution, obtained integrating the observed γ-ray excess in the interval 10 MeV<E_γ<14 MeV, the energy region where the DD γ-ray yield is mostly concentrated. We note that it is anisotropic around 90° with respect to the beam direction. The solid line corresponds to a Legendre polynomial expansion $M_\gamma(\theta_\gamma) = M_0 [1+Q_2 a_2 P_2 \cos(\theta_\gamma)]$, where a_2 is the anisotropy coefficient and Q_2 is an attenuation factor for the finite γ-ray counter, with an a_2 value of -0.84, suggested by BNV theoretical calculations [3]. It reproduces the experimental data quite well, indicating γ emission from a dipole oscillation axis that has performed a small rotation with respect to the beam axis. This is a clear evidence of pre-equilibrium nature of this emission.

All together these findings prove that the DD mode can be excited also in heavy systems.

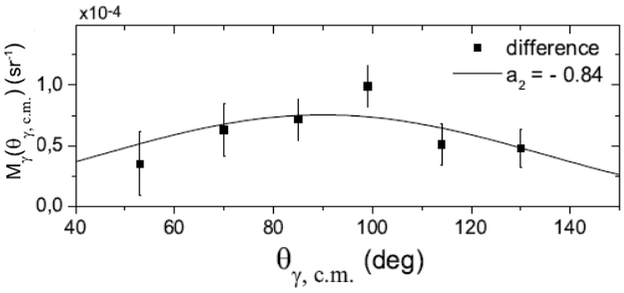

Figure 2: Angular distribution of the difference shown with the symbols in Fig.1, energy-integrated in the interval 10 MeV<E_γ<14 MeV. The solid line is described in the text.

REFERENCES

[1] Chomaz P., Di Toro M. and Smerzi A., Nuc. Phys. A563 (1993) 509

[2] Simenel C., Chomaz P. and de France G., Phys. Rev. Let. 86 (2001) 2971

[3] Baran V. et al., Phys. Rev. Let. 87 (2001) 182501, Nuc. Phys. A679 (2001) 373

[4] Baran V. et al., Phys. Rev. C79 (2009) 021603 (R)

[5] Pierroutsakou D. et al., Eur. Phys. Jour. A16 (2003) 423

[6] Flibotte S. et al., Phys. Rev. Let. 77 (1996) 1448

[7]Amorini F. et al., Phys. Rev. C69 (2004) 014608

[8] Pierroutsakou D. et al., Eur. Phys. Jour. A17 (2003) 71, Phys. Rev. C71 (2005) 054605

[9] Martin B. et al., Phys. Let. B664 (2008) 47; Pierroutsakou D. et al., Phys. Rev. C80 (2009) 024612

[10] Corsi A. et al., 2009 Phys. Let. B679 (2009) 197; Giaz A. et al, Phys. RevC90 (2014) 014609

[11] Gavron A., Phys. Rev. C21 (1980) 230

[12] Migneco E. et al., Nuc. Inst. Meth. A314 (1992) 31

[13] Parascandolo C. et al., Act. Phys. Pol. B42 (2011) 629, Pierroutsakou D. et al., AIP Conf. Proc.1423 (2012) 59-64

[14] Bellia G. et al., Nuc. Inst. Meth. A329 (1993) 173

Hot GDR evolution at high E* in nuclei of mass A ~ 120-132

D. Santonocito[1], Y. Blumenfeld[2], C. Agodi[1], R. Alba[1], G. Bellia[1,3], R. Coniglione[1], F. Delaunay[2], A. Del Zoppo[1], P. Finocchiaro[1], V. Lima[2], C. Maiolino[1], E. Migneco[1,3], P. Piattelli[1], P. Sapienza[1], J. A. Scarpaci[2], O.Wieland[4].

1) INFN-Laboratorio Nazionale del Sud, Via S. Sofia 62, I-95123, Catania, Italy
2) Institut de Physique Nucléaire, IN2P3- CNRS, F-91406 Orsay, France
3) Dipartimento di Fisica e Astronomia dell'Università di Catania, Via S. Sofia 64, I-95123, Catania, Italy
4) INFN - Sezione di Milano, Via Celoria 16, I-20133 Milano, Italy

Abstract – Final results about the evolution of hot Giant Dipole Resonance (GDR) properties with excitation energies in nuclei of mass A = 120 to 132 are presented. Hot nuclei were populated in incomplete fusion reactions in a range of excitation energies 150 MeV ≤E* ≤270 MeV and their decay properties were measured using MEDEA+SOLE+MACISTE setup [1,2]. Evidence of a quenching of the GDR gamma yield was found at 270 MeV excitation energy. The evolution of GDR quenching at higher E* was investigated including data from ^{36}Ar + ^{98}Mo reaction at 37A MeV. A coherent scenario emerges showing the existence of a limiting E*/A ~ 2.1 MeV/A for the collective motion.

INTRODUCTION

The isovector giant dipole resonance (IV-GDR) is a valuable probe of the behavior of nuclei at high temperature, providing unique information on the bulk properties of the nucleus and on the evolution of collective motion under extreme conditions up to its disappearance [3]. While the main decay mode of the GDR is through light-particle emission, its γ decay branch is sufficiently large to probe its characteristics when it is built on highly excited compound nucleus states. Data collected for medium mass nuclei with A ~ 110 to 130 show that below E*= 200 MeV the width progressively increases due to temperature, spin effects and compound nucleus lifetime from 5 MeV up to about 14 MeV and the strength exhausts 100% of the energy-weighted sum rule (EWSR) [4]. Above E*=300 MeV a different scenario emerges and a suppression of the GDR γ ray emission was observed by several authors [5,6]. This phenomenon cannot be explained in terms of standard statistical model which predicts a progressive increase of γ -ray multiplicity with excitation energy due the higher number of steps available for the γ rays to compete with particle emission. However, introducing a sharp suppression of the γ ray emission above a certain excitation energy, the so called sharp cutoff, it was possible to reproduce the data and to deduce the existence of a maximum excitation energy of approximately E*/A ~ 2.0 MeV for the collective motion.

In order to map the excitation energy dependence of the GDR quenching, an experiment was performed to study of γ emission from hot nuclei of mass A ~ 120-132 with excitation energies ranging from 150 to 270 MeV.

EXPERIMENTAL METHOD

The experiment was carried out at the Laboratori Nazionali del Sud in Catania by using ^{116}Sn beams at 17A and 23A MeV delivered by the Superconducting Cyclotron impinging on 1 mg/cm^2 ^{12}C and ^{24}Mg targets. Different projectile-target combinations, namely, ^{116}Sn + ^{12}C at 17A and 23A MeV, and ^{116}Sn + ^{24}Mg at 17A MeV, were used to populate hot nuclei through the mechanism of complete and incomplete fusion. Light charged particles and γ rays were detected in coincidence with evaporation residues by using the MEDEA + SOLE + MACISTE setup [1,2].

HOT NUCLEI CHARACTERIZATION

The excitation energy of the states upon which the GDR is built is a crucial parameter for understanding the experimental results. In this experiment the time of flight (ToF) of the residues was measured in order to characterize the mass transfer for the different reactions. The ToF spectra exhibit distributions indicating the presence of complete and close to complete fusion reactions followed by pre-equilibrium particle emission. In order to select a well-defined excitation energy, only events lying in a region of ±3% of the ToF peak, were retained in the analysis and the study of light-charged-particle and γ -ray spectra was undertaken accordingly. Proton, deuteron, triton and alpha particle energy spectra measured in coincidence with evaporation residues were analyzed in the framework of emission from multiple sources. Spectra were reproduced through a model-fit assuming the emission from isotropic Maxwellian type moving sources. A χ^2 minimization procedure was adopted to extract the fit parameters describing the main features of the emitting sources, namely multiplicities, temperatures and velocities, from the simultaneous fit of the energy spectra measured in MEDEA at different polar angles. This procedure allowed to evaluate the amount of pre-equilibrium emission and to infer, using energy and momentum conservation, the excitation energies and the masses of the hot systems populated in the reactions. In the reactions on ^{12}C target at 17 A and 23 A MeV were populated systems of average mass A=124 and A=123 with E*=150 and 190 MeV respectively. Nuclei with an

average E* = 270 MeV and A=132 were instead reached in the reaction on ^{24}Mg target.

GAMMA SPECTRA ANALYSIS

Gamma spectra were measured in coincidence with the selected fusion events for all the reactions. They display similar features: at low energies an exponentially decreasing component due the statistical emission from the compound nucleus at the end of the decay chain, a bump centred around 14 MeV associated with the GDR decay and above ~ 35 MeV an exponentially decreasing component due to bremsstrahlung emission. The high energy part of the spectra was fitted by an exponential function for energies above 35 MeV, extrapolated down to lower energies and then subtracted from each spectrum in order to obtain only the statistical gamma component.

Gamma-ray spectra were then reproduced using the statistical decay code DCASCADE [7] assuming as initial excitation energy and mass of the systems the values inferred from the procedure described above. A Lorentzian line shape was assumed for the GDR with a strength equal to 100% of the Thomas Reiche Kuhn (TKR) sum rule. For the cases E*=150 and 190 MeV the best fit to the data was obtained assuming E_{GDR} =14.3±0.4 MeV for both reactions while the width increases from 11.0±0.8 MeV to 12.5±1.0 MeV. Ormand parametrization of the level density as a function of the temperature of the system was adopted in the calculations [8].

Statistical model calculations folded with detector response perfectly reproduce the data at 150 and 190 MeV while at E* = 270 MeV it is no longer possible to fit the centroid energy and the width of the GDR because no reasonable parameter set leads to a good data reproduction. The calculation at E*= 270 MeV overshoots the data in the GDR region indicating the onset of the GDR quenching while the low energy region is still well reproduced.

In order to map the progressive evolution of the GDR features as a function of excitation energy we extended the comparison to GDR data extracted in the study of the reaction ^{36}Ar+^{98}Mo at 37A MeV where hot nuclei were populated up to E*=430 MeV. All statistical model calculations applied on this data set overshoot the data in the GDR region, the effect becomes more pronounced with excitation energy. A quantitative evaluation of the experimental GDR yield and the relative statistical model prediction can be found in fig.1a where the experimental GDR γ-ray multiplicities integrated in the region 12-20 MeV and the relative DCASCADE multiplicities are shown for both data sets as a function of the excitation energy per nucleon [9].

The comparison between the GDR yields extracted in different data sets and DCASCADE calculations shows that the absolute values of the multiplicities are well reproduced only at low energy while, above about 2 MeV/A corresponding to data at E*= 270 MeV, the experimental yield falls below the DCASCADE calculations. The break between the two data sets is due, at least in part to the different mass an charge of the nuclei populated in the reactions which influences the values of the decay width for statistical E1 decay.

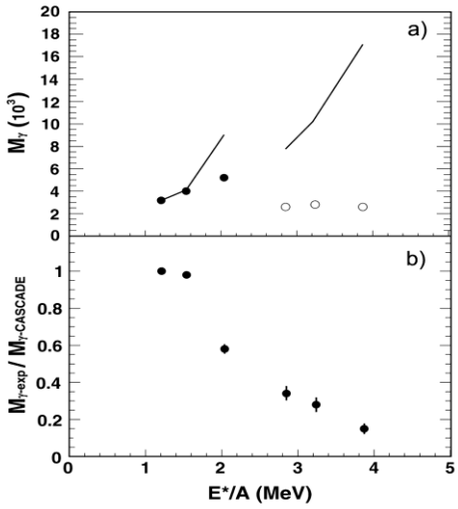

Fig.1 a) GDR γ-multiplicities integrated in the region 12-20 MeV as a function of E*/A. Full symbols show data related to 17*A* and 23*A* MeV reactions while open symbols represent the γ-multiplicities measured in the ^{36}Ar+^{98}Mo reaction. Full lines are associated to the relative DCASCADE calculations. b) ratio of the experimental GDR γ yield to DCASCADE yield.

In the attempt to remove this dependency and make the comparison between the two data sets possible, we have calculated the ratios between experimental and DCASCADE yield for each excitation energy. The results are displayed in fig.1b. A progressive decrease of this quantity is observed starting above 1.5 MeV/A clearly indicating the GDR quenching which seems to set in around 2 MeV/A excitation energy.

CONCLUSIONS

γ-rays and light charged particles were measured in coincidence with evaporation residues of hot nuclei of mass A~120-132 populated, at E* ranging from 150 to 270 MeV. Assuming 100% of the Thomas Reiche Kuhn (TKR) sum rule a clear evidence of a quenching of the GDR γ yield in the data at E* =270 MeV shows up, indicating the existence of a limiting excitation energy for the collective IV motion of about E*/A = 2.1 MeV and suggesting a possible phase transition from ordered to more chaotic motion.

REFERENCES

[1] E. Migneco et al. NIM A314 (1992) 31
[2] G. Bellia et al, IEEE Trans. Nucl. Sci.43 (1996) 1737
[3] D. Santonocito et al., Eur. Phys. J A30 (2006) 183
[4] O.Wieland et al., Phys. Rev. Lett. 97 (2006) 012501
[5] K. Yoshida et al. Phys. Lett. B245 (1990) 7
[6] J.H. Le Faou et al., Phys. Rev. Lett 72 (1994) 3321
[7] I. Dioszegi, Phys. Rev. C64 (2001) 019801
[8] W.E. Ormand et al. , Phys. Rev. C40 (1989) 1510
[9] D. Santonocito et al, Phys. Rev. C90 (2014) 054603

Studying RIB induced fusion reactions with stacked targets

M. Fisichella[1], A.C. Shotter[2], A. Di Pietro[1], P. Figuera[1], M. Lattuada[1,3], V. Privitera[3,4], L.Romano[3,4], C. Ruiz[5], M. Zadro[6]

1) INFN - Laboratori Nazionali del Sud, via S. Sofia 62, I-95125 Catania, Italy
2) School of Physics and Astronomy, JCMB, Mayfield Road, Edinburgh EH9 3JZ, UK
3) Dipartimento di Fisica ed Astronomia, via S. Sofia 64, I-95125 Catania, Italy
4) CNR-IMM MATIS, Catania, Italy
5) TRIUMF 4004 Wesbrook Mall Vancouver BC V6T 2A3 Canada
6) Ruder Boskovic Institute, Bijenicka cesta 54, HR-10000 Zagreb, Croatia

Abstract - For low energy reaction studies involving radioactive ion beams, the experimental reaction yields are generally small due to the low intensity of the beams. For this reason, using the stacked target technique to measure yields offers considerable advantages since several reaction energies may be simultaneously measured. The main disadvantage of the method is the degradation of the beam quality as it passes through the stack due to statistical nature of energy loss processes and any non uniformity of the stacked targets. This degradation can lead to ambiguities of associating effective beam energies to reaction product yields for the targets within the stack. A thorough investigation of these ambiguities has been performed and some of the obtained results are presented.

INTRODUCTION

Over the last decades, different experiments have been performed in order to study fusion excitation functions in collisions induced by weakly bound Radioactive Ion Beams, with typical beam intensities 3 or 4 orders of magnitude lower than the ones of stable beams e.g. [1-5]. In order to compensate for the low RIB currents, the beam is passed through a large number of stacked targets and degrader foils (e.g. ~ 30 foils in [1], up to 24 foils in [2]). The advantage of using such technique is that each target foil in the stack interacts with beam particles having a different average energy; therefore for a fixed beam energy one measures a number of points in the fusion excitation function equal to the number of target foils within the stack. Cross sections are extracted by measuring, off line, the radiation emitted in the decay of the radioactive evaporation residues. In some cases quite thick foils (e.g. 26 mg/cm2 Au targets [2], 10 mg/cm^2 Al degraders [3]) have been used, with corresponding large energy variations between the first and last target of the stack (e.g. ~10 MeV in [1,4], up to ~ 40 MeV in [2]). Due to the large number of used foils and/or their non-uniformities and/or the quality of RIBs used, in many experiments target were irradiated by beams having rather large energy dispersion (e.g. up to ~ 6 MeV FWHM in [4], 1.6 MeV FWHM on the first of 16 foils in [1], ~ 2 MeV FWHM on the first of 3 targets in [5], up to 5-6 MeV FWHM in [2].)

Generally, for these multiple target experiments very limited account is given of how target non-uniformity, straggling effects and incident beam quality can influence the deduced excitation functions due to the potentially large beam energy distribution inside the targets. Indeed, due to the large beam energy distribution and to the strong energy dependence of the fusion excitation functions especially below the barrier, one is measuring a fusion cross section which is an average of the real excitation function $\sigma(E)$ weighted for the beam energy distribution D(E) inside the considered target.

$$\sigma_{mean} = \frac{\int \sigma(E) D(E) dE}{\int D(E) dE}$$

The D(E) probability distribution can be calculated making use of energy loss codes such as SRIM.

The problem is how to relate these measured mean cross-sections to effective beam energies in order to accurately match the actual $\sigma(E)$ function. One way that has been used is to simply relate the measured σ_{mean} to the mean beam energy i.e.

$$\overline{E} = \frac{E_i + E_f}{2}$$

Here, E_i is the mean energy of the beam particles entering the target and E_f the mean energy of the beam particles after completely traversing the target. E_f is usually determined with the aid of simple energy loss calculations. However this takes no account of the beam energy distribution inside the targets. In fact for a stacked target, each target element in the stack experiences a different distribution of beam energies. In addition, the variation across a target of the fusion production cross-section could be very pronounced due to the exponential energy trend of $\sigma(E)$ below the Coulomb barrier. For this reason, an alternative procedure to determine the effective energy has been to use an averaging procedure which weights the beam energy with energy distribution

inside the considered target together and with the trend of the ER production cross section. Thus, for a target of thickness t_0 an effective energy could be associated with the following relation:

$$E_{eff} = \frac{\int_0^\infty E \cdot \sigma(E) \cdot D(E,t_0)dE}{\int_0^\infty \sigma(E) \cdot D(E,t_0)dE}$$

Here $D(E,t_0)$, represents the probability to have a beam particle with energy E inside the considered target of thickness t_0.

DISCUSSION

In all analysis of activation experiments the mean measured cross sections σ_{mean} has been associated either to the mean energy $\bar{E}$ or to the effective energy, E_{eff}. However a simple analysis [6] shows that, in general, none of these two approaches is correct. This can be stated in another way. For the measured cross section σ_{mean}, a reaction energy E_r may be defined such that $\sigma_{mean} = \sigma(E_r)$, where σ(E) is the true cross section function. So the data point (σ_{mean}, E_r) will coincide with the σ(E) curve. Unfortunately, in general neither the data points $(\sigma_{mean}, \bar{E})$ nor (σ_{mean}, E_{eff}) will lie on the curve.

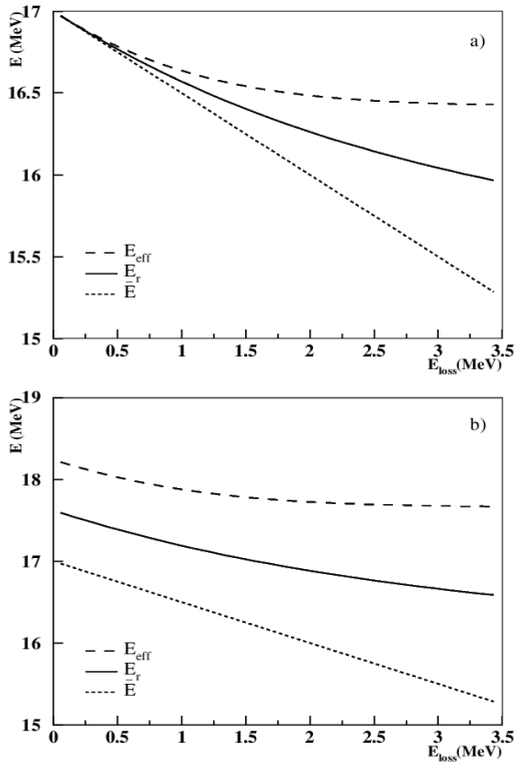

Figure1: $\bar{E}$, E_{eff} and E_r are plotted as a function of the energy loss in the target for an average incident beam energy is 17 MeV a) Delta beam energy distribution; b) Gaussian beam energy distribution with FWHM=2 MeV. See text for details.

To illustrate this important conclusion, the values E_r, E_{eff} and $\bar{E}$ have been calculated using the formulas detailed in [6] for the ^{9}Li + ^{120}Sn reaction. For this calculation it is assumed that the trend of the ^{9}Li + ^{120}Sn sub barrier fusion excitation function has an exponential trend with a slope $\alpha=1.68\ MeV^{-1}$, in agreement with fusion experimental data of ^{6,7}Li on the same target. The values of the three energies have been calculated for a ^{9}Li entrance energy of 17 MeV, and for different energy losses in the target (i.e. targets of different thicknesses). Figure 1a corresponds to an entrance beam energy of zero energy spread, and fig 2b to a Gaussian entrance energy spread of 2 MeV FWHM. As can be seen from fig. 1, only for the ideal case of mono-energetic beam and for very thin targets will the three energies coincide. If the beam energy distribution is large, even in the case of very thin targets, $\bar{E}$ and E_{eff} will differ from E_r. The presence of the energy straggling of the beam and the target non-uniformities will further modify this behaviour, and $\bar{E}$ could even be larger than E_{eff}. This demonstrates that one must be very cautious in assigning an energy to measured mean cross-section especially in the exponential region of the cross-section, if thick targets and/or large beam energy distributions are used.

.

CONCLUSIONS

The main conclusion of our studies, concerning the extraction of fusion excitation functions with multiple targets activation, is the vital importance of target and degrader foil characteristics. This is especially true for experiments where steeply falling cross sections below the Coulomb barrier are to be measured. Therefore the authors strongly recommend that for future publications where such data is presented, enough information should be included concerning the used foil non uniformities, beam energy distribution and their effects on the deduced fusion excitation functions. A complete discussion of the studies we performed on this problem, including complete procedures for studying target non uniformities, calculating D(E,t0) taking such non uniformities into account and to unfold the experimental data is reported in [6]

REFERENCES

[1] P. A. De Young et al., Phys Rev. C58, (1998).
[2] Yu. E. Penionzhkevich et al., Eur. Phys. Jour. A31,185,(2007).
[3] A. Lemasson et al., Phys. Rev. Lett. 103, 232701, (2009).
[4] Yu. E. Penionzhkevich et al., Phys. Rev. Lett. 96,162101, (2006).
[5] C. Signorini et al., Nucl. Phys. A735, 329, (2004).
[6] M. Fisichella et al. to be published

ISTITUTO NAZIONALE DI FISICA NUCLEARE
LABORATORI NAZIONALI DEL SUD
ACTIVITY REPORT 2013/2014

THEORETICAL NUCLEAR PHYSICS

Shear viscosity of the Quark-Gluon Plasma in a Kinetic Theory Approach

A. Puglisi[1,2], S. Plumari[1,2] , F. Scardina[1,2] and V. Greco[1,2]

1) Department of Physics and Astronomy, University of Catania, Via S. Sofia 64, I-95125 Catania (Italy)

2) Laboratorio Nazionale del Sud, INFN-LNS, Via S. Sofia 63, I-95125 Catania (Italy)

Abstract - One of the main results of heavy ions collision (HIC) at relativistic energy experiments is the very small shear viscosity to entropy density ratio of the Quark-Gluon Plasma, close to the conjectured lower bound $\eta/s = 1/4\pi$ for systems in the infinite coupling limit. Transport coefficients like shear viscosity are responsible of non-equilibrium properties of a system: Green-Kubo relations give us an exact expression to compute these coefficients. We compute shear viscosity numerically using Green-Kubo relation in the framework of Kinetic Theory solving the relativistic transport Boltzmann equation in a finite box with periodic boundary conditions. We investigate a system of particles interacting via anisotropic and energy dependent cross-section in the range of temperature of interest for HIC. Green-Kubo results are in agreement with Chapman-Enskog approximation while Relaxation Time approximation can underestimates the viscosity of a factor 2. The correct analytic formula for shear viscosity can be used to develop a transport theory with a fixed η/s and have a comparison with physical observables like elliptic flow.

INTRODUCTION

The main motivation for Heavy Ion Collision (HIC) at relativistic energy experiments was to obtain information about the properties of nuclear matter under extreme conditions of high baryon density or temperature. Relativistic Heavy Ion Collider (RHIC) and Large Hadron Collider (LHC) have produced a transient state of quark-gluon plasma (QGP), the matter that filled the early Universe after the Big-Bang. One of the main discoveries in such experiments is that QGP has a very low shear viscosity to entropy density ratio η/s [1], due to the large anisotropic flows measured [2], close to conjectured lower bound for a strongly interacting system in the limit of infinite coupling, $\eta/s = 1/4\pi$ [3]. This has led more recently to the development of a transport approach at fixed η/s [4] in order to have a comparison with experimental data in the same way of hydrodynamics models. In order to fix η/s one has to know the exact relation between the viscosity and the microscopic details such as cross-section, mean free path and average momentum. In literature there are many approximation schemes that give us different analytical formulas [5][6]. In this work we have computed shear viscosity of a gluon plasma in thermal equilibrium using Green-Kubo relation [7], that is not affected by any kind of approximations, and compared these results with Relaxation Time (RTA) and Chapman-Enskog (CE) approximations. A determination of the viscosity would also allow a better knowledge of the evolution of inhomogeneities and dissipation during the expansion of the QGP matter in the early Universe.

SHEAR VISCOSITY OF GLUON PLASMA

Transport coefficients like heat and electric conductivity, bulk and shear viscosity can be related to the correlation functions of the corresponding flux in thermal equilibrium. Green-Kubo formula for the shear viscosity η assumes the following expression [6]:

$$\eta=\frac{1}{T}\int_0^\infty dt \int_V dx \langle \Pi^{xy}(x,t)\Pi^{xy}(0,0)\rangle \quad (1)$$

where T is the temperature, Π^{xy} is the xy component of energy-momentum tensor, while $\langle . . . \rangle$ is the ensemble average. In this work we calculate numerically the correlation function $C(t)=\langle \Pi^{xy}(x,t)\Pi^{xy}(0,0)\rangle$ solving the relativistic Boltzmann-Vlasov transport equation for a system of massless particles in a static box of volume V in thermal equilibrium:

$$p^\mu \partial_\mu f(x,p)=C(x,p)=\int_2\int_{1'}\int_{2'}(f_{1'}f_{2'}-f_1 f_2) \\ |M_{1'2'\to 12}|^2\delta^4(p_1+p_2-p_1'-p_2') \quad (2)$$

where $f(x, p)$ is the distribution function, C (x, p) is the collision integral written in terms of M , the transition matrix for the elastic process, and $\int d^3p_j/(2\pi)^3 2E_j$. Our aim is to solve numerically the collision integral to evaluate the shear viscosity using Green-Kubo formula and compare this one with analytical approximations of RTA and CE. For a system in thermal equilibrium the correlation function is a decreasing exponential so Green-Kubo formula can be written as $\eta=V/T\langle \Pi^{xy}(0)^2\rangle\tau$ where $\langle \Pi^{xy}(0)^2\rangle$ is the initial value of the correlation function and τ is determined by a fit [8][9]. In Literature there are several methods for the calculation of shear viscosity; one of these is the Chapman-Enskog approach and another is the Relaxation Time Approximation. The difference between these two methods resides in the different way of approximating the collision integral (2). The starting hypothesis of the RTA is that the collision integral can be approximated by $C[f]=-(f-f_{eq})/\tau$, where τ is the so called relaxation time, and one can obtain the following relation:

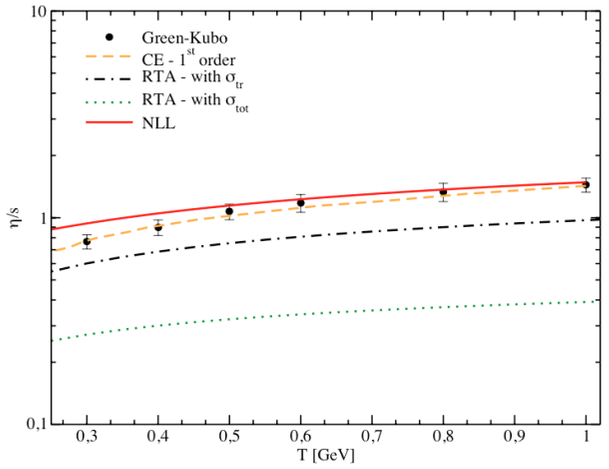

Figure 1: Shear viscosity over entropy density ratio as a function of temperature.

$$\eta_{RTA}=\frac{4}{15}\frac{\langle p\rangle}{\sigma_{tot}},\qquad \eta^{*}_{RTA}=\frac{4}{15}\frac{\langle p\rangle}{\langle h(a)v_{rel}\rangle\sigma_{tot}} \quad (3)$$

where $\langle p\rangle$ is the average momentum, $\sigma_{tr}=h(a)\sigma_{tot}$ the transport cross-section, v_{rel} the relative velocity of incoming particles, $h(a)=4a(1+a)[(2a+1)\log(1+1/a)-2]$ ($a=m2D/s$) and m_D is the Debye mass. The modified RTA η^{*}_{RTA} differs from the simple one only in considering the transport cross-section σ_{tr} instead of the total one. The CE approach is based on a variational approach to the collision integral [10] and one can obtain the following formula:

$$\eta_{CE}=\frac{4}{15}\rho\langle p\rangle\tau_{\eta}=\frac{4}{15}\frac{\langle p\rangle}{g(a)\sigma_{tot}} \quad (4)$$

where

$$g(a)=\frac{1}{50}\int dy\, y^{6}[(y^{2}+\frac{1}{3})K_{3}(2y)-yK_{2}(2y)]h(\frac{a^{2}}{y^{2}})$$

with K_n being the Bessel functions and $a=m_D/2T$. The main difference between the two schemes is that in CE one has to consider in a natural way the transport cross-section. We have considered massless gluons in thermal equilibrium interacting via two-body collisions

$$\frac{d\sigma^{gg\to gg}}{dq^{2}}=\frac{9\pi\alpha_{s}^{2}}{(q^{2}+m_{D}^{2})^{2}},\quad \alpha_{s}(T)=\frac{4\pi}{11\log(\frac{2\pi T}{\Lambda})} \quad (5)$$

where $\Lambda=200\,MeV$, $m_D=T\sqrt{4\pi\alpha_s}$ according to HTL calculations, and αs is the pQCD running coupling constant. The total cross- section in this scheme is energy and temperature dependent: $\sigma_{tot}=9\pi\alpha_{s}^{2}s/m_{D}^{2}(s+m_{D}^{2})$. For this realistic case we computed η/s as a function of temperature in the range $0.2\le T\le 1.0\ GeV$ using Green-Kubo method. The results, shown by black circles Fig. 1, are compared to the CE approximation (orange dashed line), the simple RTA (green dotted line), the modified RTA (black dotted-dashed line) and next-to-leading-log approximation (NLL) from work [11] (red line). We found that CE approximation is in excellent agreement with the Green-Kubo results at accuracy level of 4% while the modified RTA significantly underestimates η/s by about 20%. Green-Kubo results establish that the correct analytical formula describing the shear viscosity of a gluon plasma is just CE approximation. Green-Kubo results and CE prediction are also in agreement with [11].

CONCLUSIONS

Recent developments in the physics of strong interactions at finite T are focusing many efforts on the calculation of transport coefficients and in particular of shear viscosity.We found that, for the realistic case of massless gluons interacting via pQCD-like cross-section, Chapman-Enskog approximation is in agreement with Green-Kubo results at the level of 4% [12]: this agreement supplies an analytical expression that can allow one to develop kinetic transport theory at fixed viscosity with very good precision while Relaxation Time approximation in general underestimates the viscosity even by a factor 2.

REFERENCES

[1] J. L. Nagle et al., New Journal of Physics 13, 075004 (2011)
[2] P. Romatschke et al., Phys. Rev. Lett. 99, 172301 (2007)
[3] P. K. Kovtun et al., Phys. Rev. Lett. 94, 111601 (2005)
[4] G. Ferini et al., Phys. Lett. B 670, 325 (2009)
[5] F. Reif, McGraw-Hill, New York, 1965
[6] S. R. de Groot et al., North-Holland, 1980
[7] M. S. Green, J. chem. Phys. 22, 398 (1954); R. Kubo, J. Phys. Soc. Jpn. 12, 570 (1957)
[8] N. Demir et al., Phys. Rev. Lett. 102, 172302 (2009)
[9] C. Wesp et al., Phys. Rev. C 84, 054911 (2011)
[10] A. Wiranata et al., Phys. Rev. C 85, 054908 (2012)
[11] P. Arnold et al., J. High Energy Phys. 05 (2003) 051
[12] S. Plumari et al., Phys. Rev. C 86, 054902 (2012)
[13] S. Plumari et al., Phys. Rev. D 84, 094004 (2011)

Energy density fluctuation in Early Universe

G.L. Guardo[1,2], V. Greco[1,2] and M. Ruggieri[2]

1) INFN - Laboratori Nazionali del Sud, Catania, Italy
2) Department of Physics and Astronomy, University of Catania, Catania, Italy

Abstract - The primordial nucleosinthesys of the element can be influenced by the transitions of phase that take place after the Big Bang, such as the QCD transition. In order to study the effect of this phase transition, in this work we determine the precise time evolution of the thermodynamic parameters of the early Universe by solving the Friedmann equation for a realistic equation of state (EoS) coming from the heavy ion collision and lattice QCD data of Wuppertal-Budapest. A comparison with the result obtained with simple bag model EoS is made. We also include in the realistic EoS the presence of a strong primordial magnetic field. The realistic equation of state describes a crossover rather than the first-order phase transition between the quark-gluon plasma and hadronic matter. Our numerical calculations of the energy density fluctuations show that small inhomogeneities of strongly interacting matter in the early Universe are moderately damped during the crossover.

INTRODUCTION

The history of the early universe left an imprint on the presently observed cosmos. According to the Friedmann equations the temperature decreases inversely proportional with scale parameter a so that the early universe passes through the electroweak phase transition at $t \approx 10^{-10}$ sec (corresponding to T≈100 GeV), the QCD phase transition at $t \approx 10^{-5}$ sec (T≈ 150 MeV) and the Big Bang Nucleosynthesis (BBN) at t=1 sec-3 min (T =0.1-1 MeV). This BBN plays a crucial role in constraining our views on the universe. It is essentially the only probe of physics in the early radiation dominated epoch during the interval from ≈1-10^4 sec. Moreover, the previously phase transitions could strongly influenced this nucleosynthesis [1]. In this work, we focus the attention on the effect of the QCD phase transition because during this transition the major number of degree of freedom changes and the role of this transition in the initial part of the history of the universe is still under debate. In particular, it was first recognized by Applegate and Hogan [2] that an inhomogeneous distribution of baryons due to a first-order QCD transition could change the primordial abundances of the light elements [3].

EQUATION OF STATE FOR STRONGLY INTERACTING MATTER

One expects that the studies of relativistic heavy-ion collisions may bring us information about the properties of matter in the early Universe by means of the equation of state (EoS) of strongly interacting matter. The use of this EOS in the Friedmann equation allows us to determine the precise time evolution of the thermodynamic parameters in the early Universe.

The simpliest way to take into account the properties of the QGP is the EoS of the MIT Bag Model [4]. It represents the short-distance dynamics by an collisionless gas of massless quarks and gluons and the long-distance confinement effects by a constant negative contribution to the pressure, the bag constant B (in our case B=235 MeV^4). In order to consider a more realistic equation, we use the EoS of 2+1 flavor QCD with physical quark masses presented by the Wuppertal-Budapest collaboration [5]. Moreover, as recently pointed out by the heavy ion collision's data, during the QCD transition should be important to consider also the effect due to the presence of a magnetic fiel. To this idea, we implemented the realistic EoS with a strong primordial magnetic field of about $20m_\pi^2$ that corresponds to a magnetic field of about 10^{15} T, following the model proposed by Gatto and Ruggieri in 2011 [6]. In Figure 1 the equations of state described before are reported with different colored lines. The black dashed line represents the case of ideal gas (the Stefan-Boltzmann limit) that is directly correlated to the degrees of freedom of the system. The difference between the realistic case and the Stefan-Boltzmann limit indicated that the interactions in the plasma are non-negligible at higher temperatures.

Figure 1: Equations of State used in this work..

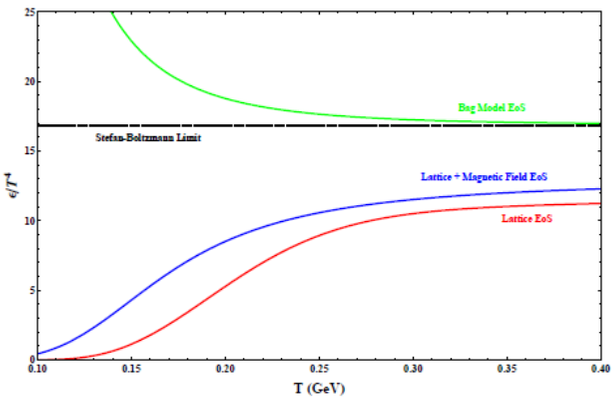

SOLUTION OF THE FRIEDMANN EQUATION

In the energy range considered in the early universe phase transition, it is important to include also the energy density and pressure of the particle from the electro-weak

sector. This particles may be treated as massless, whose effective number of degrees of freedom is g_{ew} =14.45 [1], so we can define the follow quantity that should be added to the previous EoS.

$$\varepsilon_{ew} = g_{ew}\frac{\pi^2}{30}T^4, P_{ew} = g_{ew}\frac{\pi^2}{90}T^4, \sigma_{ew} = \frac{4\varepsilon}{3T} \qquad (1)$$

To determine the precise time evolution of the thermodynamic parameters in the early Universe we should solve the Friedmann equation that, assuming that the expansion of the Universe is isentropic, takes the form:

$$\frac{d\varepsilon}{dt} = -3\sqrt{\frac{8\pi G\varepsilon}{3}}(\varepsilon + P) \qquad (2)$$

The numerical solutions for the three different EoS are reported in Figure 2 that clearly shows the difference between the different approach. The Bag Model (green line) presents a classical plateau during the transition corresponding to the critical temperature of about 170 MeV, on the other hand the use of the realistic lattice calculation (red line) shows a crossover transition in which all thermodynamic parameters change smoothly as functions of the temperature. The effect of the magnetic field (blue line) is to change the critical temperature but the trasition is still a crossover. It is important to stress that the difference between the three cases are strictly confined in the time interval of the transition while for large values of the time the functions became again very similar.

Figure 2: Temperature behavior obtained by solving the Friedmann equation for the three different approach presented in the text.

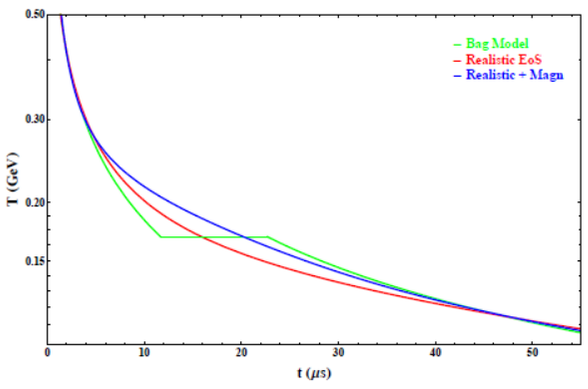

ENERGY DENSITY FLUCTUATIONS

The main goal of this work is to study the effect of the primordial density fluctuations. Indeed, if the QCD phase transition was of the first order, that means that the sound velocity vanishing at critical temperature, the energy density fluctuations would develop large peaks and dips. For crossover transition we do not expect the same behavior but it is interesting to analyze the development of these fluctuations [7]. In order to do this we solved the following system of equation introduced by Schmid, Schwarz and Widerin in 1999 [8].

The numerical resolution of the energy density fluctuation with respect to a function of the time that also consider the time evolution of the scale factor [9] is reported in Figure 3. The starting time t_0 is 1.35ms and is chosen in order to have an initial temperature of 500 MeV, while the final time correspond to 110ms and is well far from the transition so we don't expect to have other effect. The green dashed line correspond to the electro-weak component. It is clear that the difference between the red (realistic lattice QCD EoS) and blue (realistic case with the inclusion of a strong primordial magnetic field) curves and the green one are due only to the QGP and magnetic effect. It is evident that the energy density fluctuations dumping down in the considered time interval in both cases, even if the effect of the magnetic field make the dumping more slowly.

Figure 3: Time evolution of the energy density function with respect to the electro-weak part.

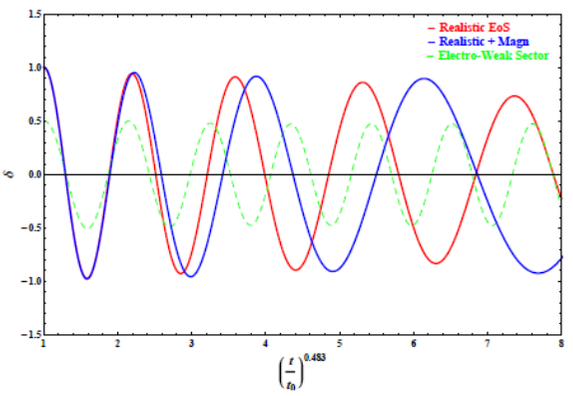

CONCLUSIONS

In conclusion, in this work we studied the effect of the realistic QCD Equation of State on the evolution of the Early Universe solving the Friedmann equation for three different kind of EoS: Bag Model, lattice data and realistic equation with a strong magnetic field. Moreover, we consider the time development of the energy density fluctuation for the realistic cases and we pointed out that the oscillations are dumped during the transition. This imply that there are small chances of inhomogeneities phenomena during the Big Bang nucleosynthesis.

REFERENCES

[1] K. Yagi et al., Quark-Gluon Plasma, Cambridge University Press, Cambridge, 2005.
[2] J.H. Applegate et al., Ap.J., vol. 329, pp. 572 (1988).
[3] T. Kajino et al., NPA, vol. 588, pp. 339c (1995).
[4] A. Chodos et al., PRD, vol. 9, pp. 3471 (1974).
[5] S. Borsanyi et al., JHEP, vol. 1011, pp. 77 (2010).
[6] R. Gatto and M. Ruggieri, PRD, vol. 83, pp. 34016 (2011).
[7] C. Schmid, D. J. Schwarz and P. Widerin, PRL, vol. 78, pp. 791 (1997).
[8] C. Schmid et al., PRD, vol. 59, pp. 43517 (1999).
[9] W. Florkowski, NPA, vol. 853, pp. 173 (2010).

Signals of Bose Einstein condensation and Fermi quenching in the decay of hot nuclear systems

P. Marini[1], H. Zheng[2, 3], G. Verde[4,5], A. Chbihi[6], and A. Bonasera[2, 3]

1) Centre d'Etudes Nucléaires de Bordeaux Gradignan Chemin du Solarium,

Le Haut Vigneau, BP 120, F-33175 GRADIGNAN Cedex

2) Cyclotron Institute, Texas A&M University, College Station, TX 77843, USA

3) Laboratori Nazionali del Sud, INFN, via Santa Sofia, 62, 95123 Catania, Italy

4) Institut de Physique Nucléaire, IN2P3-CNRS, Université Paris-Sud 11, F-91406 Orsay Cedex, France

5) INFN- Sezione di Catania, via Santa Sofia, 62, 95123 Catania, Italy

6) Grand Accélérateur National d'Ions Lourds, Bd Henri Becquerel BP 55027 - 14076 CAEN, France

(For INDRA Collaboration)

Abstract - We report experimental signals of Bose-Einstein condensation in the decay of hot Ca projectile like sources produced in mid-peripheral collisions at sub-Fermi energies [1]. The experimental setup, constituted by the coupling of the INDRA 4π detector array to the forward angle VAMOS magnetic spectrometer, allowed us to reconstruct the mass, charge and excitation energy of the decaying hot projectile-like sources. Furthermore, by means of quantum fluctuation analysis techniques, temperatures and mean volumes per particle as seen by bosons and fermions separately are correlated to the excitation energy of the reconstructed system. The obtained results are consistent with the production of dilute mixed (bosons/fermions) systems, where bosons experience a smaller volume as compared to the surrounding fermionic gas. Our findings recall similar phenomena observed in the study of boson condensates in atomic traps.

DATA SELECTION AND RESULTS

Only peripheral and semi-peripheral collisions, leading to a heavy QP remnant detected in VAMOS with $Z > 5$ have been studied in this work. In order to reconstruct the charge, Z_{QP}, mass, A_{QP}, and momentum vector $\mathbf{p}_{QP}$, of the QP, particles with $Z = 1$, 2 and $Z \geq 3$, detected by INDRA were attributed to QP decay when their longitudinal velocities lay within the range of ±65%, ±60%, ±45%, respectively, of the coincident QP residue velocity. In order to shed more light into these observations, we try to separate bosonic-like events and fermionic-like events by means of the following event-by-event quantity:

$$b_j = \frac{1}{M}\sum_{i=1}^{M}\frac{(-1)^{N_i}+(-1)^{Z_i}}{2}$$

where M is the event multiplicity and Z_i and N_i are the charge and neutron numbers of the ith fragment, respectively. b_j is equal to 1, − 1 and 0 when all fragments emitted in the event are Z even-N even, Z odd N odd, and A-odd, respectively. The temperatures and local volumes of the produced systems can then be estimated by studying the measured particle quadrupole momentum and multiplicity fluctuations, as well as mean multiplicities, according to the quantum fluctuation analysis techniques. In Fig.1, we showed the critical temperature T_0 as function of density for both mixture and boson-like events (the lines indicate the ideal boson gas result). Values of the order of few MeV are obtained for both particles, in agreement with theoretical predictions. The experimentally derived values are systematically higher both for d and α as compared to the ideal case. This is expected because the Coulomb repulsion enhances the condensate. It is important to remark that at high density, and especially for the case (d displays unfortunately large error bars due to poor statistics), the data are closer to the ideal case. This is due to the increased importance of the nuclear force which reduces the Coulomb repulsion.

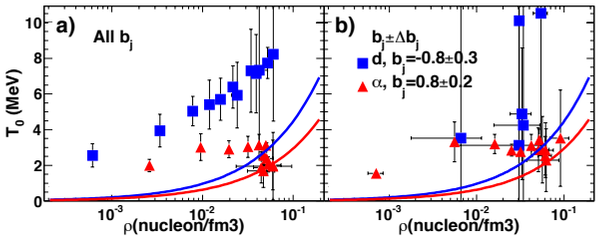

Figure 1: (Color online) Critical temperature vs local density for (a) mixture and (b) boson-like events.

SUMMARY

In summary we have studied the decay of ex-cited quasi-projectile systems produced in mid-peripheral Ca40+Ca40 collisions at E/A = 35 MeV with the INDRA-VAMOS setup. Within the selected events, mean partial volumes per particle and temperatures, probed by bosons (deuterons and alphas) and by fermions (protons) in the low density gas-like phase have been estimated with

quantum fluctuation methods. The observed results show that bosons experience a smaller volume and a higher energy density than fermions. These results may be associated to the presence of boson condensation and fermionic quenching phenomena in nuclear systems. Condensation temperatures are in agreement with theoretical predictions. These phenomena are observed even in events where mixtures of bosons and fermions coexist, suggesting that they are not reduced by boson-fermion interactions. The results of this work recall closely similar phenomena observed in atomic systems where the coexistence of a quasi-pure Bose Einstein condensate of Li7 atoms (bosons) in a Fermi sea of Li6 (fermions) was observed [2]. This interdisciplinary analogy seems to indicate a similar nature for processes occurring in atomic scale and nuclear scale quantum systems, regardless of their different sizes and characteristic interactions. Future investigations on implications of these phenomena on α clustering and symmetry energy at low density also stimulate using particle-particle correlations to estimate emission densities and volumes.

REFERENCES

[1] P. Marini et al., arXiv: 1501.00595.
[2] F. Schreck, L. Khaykovich, K. L. Corwin, G. Ferrari, T. Bourdel, J. Cubizolles, and C. Salomon, Phys. Rev. Lett. 87, 080403 (2001).

Exotic break-up in low energy reactions

M.Colonna[1], V.Baran[2] and C.Rizzo[1]

1) INFN-Laboratori Nazionali del Sud, I-95123, Catania, Italy
2) NIPNE-HH, Bucharest and Bucharest University, Romania

Abstract - We discuss recent studies, within the framework of transport theories, on low-energy heavy ion reactions (E_{beam} ~ 10-30 MeV/nucleon). We concentrate on the analysis of ternary break-up events, of dynamical origin, occurring in semi-central reactions, which have been reported in recent experiments. Interesting perspectives are opening towards the investigation of this mechanism also in neutron-rich (or exotic) systems, with the possibility to access information on the low-density behavior of the nuclear symmetry energy.

INTRODUCTION

A detailed analysis of the mean-field dynamics, and associated shape fluctuations and rotational effects, is crucial to investigate the competition between reaction mechanisms, as well as the nature of new exotic re-separation modes, in low energy dissipative collisions.

We undertake such a study in the framework of the Stochastic Mean Field (SMF) transport model, which has been shown to provide a good description of mean-field dynamics, also incorporating effects of two-body fluctuations and correlations [1].

We will investigate semi-peripheral heavy ion collisions in the beam energy range of 10-30 MeV/nucleon, focusing on the possible occurrence of new breakup modes and on the features of the associated reaction products. This analysis may open a novel understanding of the transition path from deep-inelastic collisions to multi-fragmentation processes and elucidate the nuclear dissipation mechanisms.

TRANSPORT THEORIES AND SYMMETRY ENERGY

Nuclear reactions are modeled by solving transport equations based on mean field theories, with short range (2p-2h) correlations included via hard nucleon-nucleon elastic collisions and via stochastic forces, self - consistently evaluated from the mean phase-space trajectory [1]. In the energy range up to a few hundred MeV/nucleon, the appropriate tool is the so-called Boltzmann-Langevin (BL) equation:

$$\frac{df}{dt} = \frac{\partial f}{\partial t} + \{f, H\} = I_{coll}[f] + \delta I[f] \quad (1)$$

where f (**r**,**p,t)** is the one-body distribution function, the semi-classical analog of the Wigner transform of the one-body density matrix, H(**r**,**p,t**)the mean field Hamiltonian, I_{coll} the two-body collision term incorporating the Fermi statistics of the particles, and $\delta I[f]$ its fluctuating part.

Several approximate treatments of the BL equation have been introduced so far, denoted as one-body (OB) models in the following. For instance, in BUU-like models, the fluctuating term $\delta I[f]$ is neglected, whereas in the Stochastic Mean Field (SMF) model fluctuations are projected onto the coordinate space and are implemented agitating the spatial density profile [1].

In the molecular dynamics (MD) class of models, the many-body state is represented by a product (antisymmetrized or not) of single particle states, which are usually assumed to be gaussians, whose centroids are time dependent. Then the one-body density can be built, which follows a time evolution close to the one expressed by Eq.(1). However, the localization of the nucleon wave packects induces correlations in the propagation in the nuclear mean-field, as well as in the collision integral, which is treated stochastically [2].

Therefore, with respect to OB models, in MD models the fluctuation is expected to have a stronger impact on the collision dynamics, but some genuine ``mean-field'' effects could be missing. Effective interactions (associated with a given Equation of State, EoS) can be considered as an input of all transport codes and from the comparison with experimental data one can finally get some hints on nuclear matter properties.

FRAGMENTATION AT LOW ENERGY: TERNARY BREAKUP

In the framework of an OB model (the SMF model), we discuss semi-peripheral heavy ion collisions in the beam energy range of 10-30 MeV/nucleon, focusing on the possible occurrence of ternary breakup processes and on the features of the associated reaction products.

Recent experimental investigations, performed at LNS, have been concentrated on these exotic separation modes, in the case of Au + Au reactions at 15 and 23 MeV/nucleon [3].

Let us consider first the reaction at 15 MeV/nucleon, b = [4-6] fm. In this case we observe an almost symmetric neck rupture between projectile-like (PLF) and target-like (TLF) fragments, leading to the deformation of both fragments in the majority of the events. Thus important quadrupole and octuple deformations are noticed for the primary PLF/TLF fragments, which may lead to subsequent ruptures (multiple breakup) and, in particular, to ternary breakup events.

An early recognition method is applied to identify the most probable breakup configuration of the PLF (or TLF) fragment.

Figure 1 (top panel) shows the mass distribution of the lightest, A1, and heaviest, A2, fragments, issued from the PLF/TLF breakup, for the impact parameter b = 5 fm.

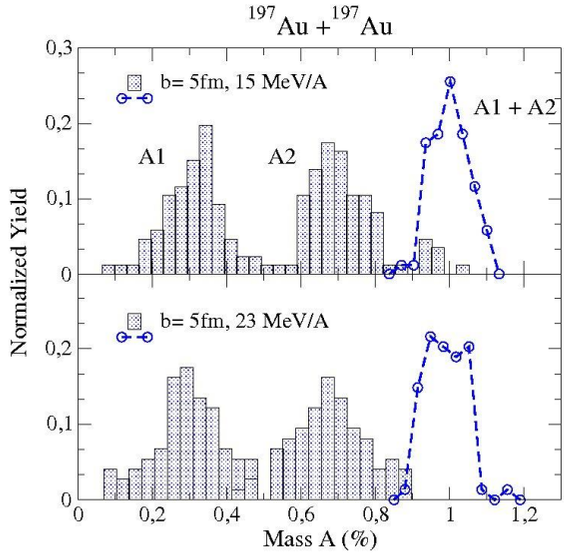

Fig.1: Mass distribution of the fragments A1 and A2, and of their sum, emerging from the breakup of the PLF/TLF fragment, for the reaction ^{197}Au + ^{197}Au at 15 (top) and 23 (bottom) MeV/nucleon. A1 denotes the smallest fragment. Masses are normalized to the average mass of the PLF/TLF fragment.

Once the masses are normalized to the average mass of the PLF (or TLF) fragment, results look in good agreement with experimental data [3]. In particular, the calculations are able to reproduce the distance between the A1 and A2 centroids and the variance of the mass distribution. Similar results have been recently reported in the context of the improved QMD (ImQMD) calculations of ref.[2], where a detailed comparison with the experimental findings of ref.[3] is presented.

Results obtained at the higher bombarding energy of 23 MeV/nucleon are shown in the bottom panel of the figure.

The behavior observed for the mass distribution of fragments A1 and A2 is quite close to the one obtained at 15 MeV/nucleon, however variances are larger, reflecting the more dissipative dynamics. It should be noticed that, in the calculations of ref.[2], as well as in SMF simulations at 15 MeV/nucleon, the lightest fragment (A1) emerges mainly from the neck region, thus being located at mid-velocity. On the other hand, in the data analysis reported in ref.[3], the fragment with the largest parallel velocity (F1) has the smallest mass. In SMF simulations, this feature is present, but at higher energy. Indeed, at 23 MeV/nucleon, owing to increased angular momentum effects, the PLF (or TLF) fragment rotates before it reaches its maximum deformation and a subsequent break-up may take place. As a consequence, in the case of a PLF break-up for instance, the lightest fragment may emerge with large positive parallel velocity.

Thus SMF results point to the occurrence of a reaction mechanism, i.e. neck rupture coupled to angular momentum effects, which could explain the experimental observation. On the other hand, in QMD-like calculations rotational effects could be missing because of the too fast reaction dynamics and the reduced mean-field effects.

In the calculations discussed above, the sensitivity to the ingredients of the EoS has not been explored so far. It would be extremely interesting to extend this kind of investigations to reactions involving neutron-rich (or even exotic) nuclei. Indeed the reaction dynamics could be affected by the neutron-enrichment of the neck region, related to neutron skin effects and/or isospin migration mechanisms [1]. In this case, one would also expect an important sensitivity of the reaction mechanism, and of the features of the emitted fragments, to the isovector terms of the nuclear potential, opening interesting perspectives towards the extraction of new, independent information on the density behavior of the nuclear symmetry energy, which is quite debated nowadays [4].

CONCLUSIONS

We have untertaken an analysis of new fragmentation modes, on which recent experimental investigations have been concentrated, which may develop in low-energy heavy ion collisions. The possibility of observing ternary breakup processes of dynamical origin is explored within the SMF model, looking at the concurrent role of surface mean-field instabilities, dissipative and angular momentum effects. Indeed large quadrupole and octupole deformation is developing in binary exit channels of semi-central reactions, which may lead to a subsequent breakup of the PLF/TLF fragments.

For reactions at ~ 20 MeV/nucleon, SMF calculations are able to explain the main features observed experimentally for ternary breakup events, namely mass partitions (see Fig.1) and the appearance of preferential emission directions. The model also indicates that these features emerge from a delicate balance between the neck dynamics and rotational effects. It would be extremely interesting to extend this kind of investigations to reactions involving neutron-rich (or even exotic) nuclei, where n-skin effects would be expected.

REFERENCES

[1] V. Baran, M. Colonna, V. Greco, M. Di Toro, Phys. Rep. 410 (2005) 335.

[2] Yanjing Li, Shiwei Yan, Xiang Jiang, Lichun Wang, Nucl. Phys. A902 (2013) 1.

[3] J. Wilczynski et al., Phys. Rev. C81 (2010) 024605.

[4] *Topical Issue on Nuclear Symmetry Energy*, Eur. Phys. Jou. {\bf A50} No.2 (2014), edited by Bao-An Li, Angels Ramos,Giuseppe Verde and IsaacVidana.

Heavy Quark Dynamics in QGP:Boltzmann vs Langevin

F.Scardina [1,2], S. K. Das[1], S.Plumari,[1,2],V.Greco,[1,2]
[1] *Department of Physics and Astronomy,University of Catania, Via S.Sofia 64, 95125 Catania,Italy and*
[2] *Laboratori Nazionali del Sud, Via S. Sofia 44, I-95123 Catania, Italy*

Abstract In this review we challenge the assumption of brownian motion for charm quarks and compare the dynamical evolution of charm and bottom quarks in a Fokker-Planck approach and in a Boltzmann Transport one. We show that while for bottom the motion appears quite close to a Brownian one, this does note seems to be the case for charms quarks.

INTRODUCTION

One of the primary aims of the ongoing nuclear collisions at Relativistic Heavy Ion Collider (RHIC) and Large Hadron Collider (LHC) energies is to create a new state of matter where the bulk properties of the matter are governed by the light quarks and gluons. In this context, the heavy quarks (HQ), mainly charm and bottom, play a crucial role since they do not constitute the bulk part of the matter due to their larger mass with respect to the temperature created in ultra-relativistic heavy-ion collisions (uRHIC's) [1]. Due to their large masses HQ can act as a type of external probe to investigate the bulk of the QGP medium and are affected by its density, temperature and collective expansion thereby carrying the information of the created plasma. In the next section, we will focus on the theoretical approaches to describe the dynamical evolution of the HQ comparing the most commonly used Fokker-Planck approach to the Boltzmann transport equation. In section III we discuss the evolution of the HQ spectra in a static medium. Section IV is devoted for single heavy quark diffusion in momentum space. Section IV contain the summary and conclusions.

BOLTZMANN VS LANGEVIN DYNAMICS

The propagation of HQ in QGP has been quite often treated within the framework of Fokker-Planck equation [1, 2]. The main reason is that it was believed that their motion can be assimilated to a Brownian motion due to their perturbative interaction and large mass that should generically lead to collisions sufficiently forward peaked and/or with small momentum transfer. Under such constraints it is known that the Boltzmann transport equation reduces to a Fokker-Planck dynamics, which constitutes a significant simplification of the in medium dynamics. Such a scheme has been very widely employed including some of the authors [2–5, 10, 11] in order to calculate the experimentally observed nuclear suppression factor ($R_{\rm AA}$) [7–9] and their large elliptic flow (v_2) [7] for the non-photonic single electron spectra. Along with the Fokker-Planck approach in some work a description of HQ within a relativistic Boltzmann transport approach has been developed [6, 12–14, 18].

The Boltzmann equation for the HQ distribution function can be written in a compact form as:

$$p^\mu \partial_\mu f_Q(x,p) = \mathcal{C}[f_Q](x,p) \tag{1}$$

where $\mathcal{C}[f_Q](x,p)$ is the relativistic Boltzmann-like collision integral where the phase-space distribution function of the bulk medium appears as an integrated quantity in $\mathcal{C}[f_Q]$, see for example Ref.s [17], while we are interested to the evolution of the heavy quarks distribution function $f_Q(x,p)$.

The Boltzmann equation is solved numerically dividing the space into a three-dimensional lattice and using the test particle method to sample the distributions functions. The collision integral is solved by mean of a stochastic implementation of the collision probability $P = v_{rel}\sigma_{g+Q\to g+Q}\cdot\Delta t/\Delta x$ [16, 17].

The non-linear integro-differential Boltzmann equation can be significantly simplified employing the Landau approximation whose physical relevance can be associated to the dominance of soft scatterings with small momentum transfer $|\mathbf{k}|$ respect to the particle momentum $\mathbf{p}$. Under this assumption the non-linear integro-differential Boltzmann equation reduced to the Fokker-Planck equation (for detail see Ref [15]):

$$\frac{\partial f}{\partial t} = \frac{\partial}{\partial p_i}\left[A_i(\mathbf{p})f + \frac{\partial}{\partial p_j}[B_{ij}(\mathbf{p})]\right] \tag{2}$$

where A_i and B_{ij} are directly related to the so called drag and diffusion coefficient. The Fokker-Planck equation can be solved by a stochastic differential equation i.e the Langevin equation, can be written as [1, 2, 4]:

$$\begin{aligned} dx_i &= \frac{p_i}{E}dt, \\ dp_i &= -Ap_i dt + (\sqrt{2B_0}P^{\perp}_{ij} + \sqrt{2B_1}P^{\parallel}_{ij})\rho_j\sqrt{dt} \end{aligned} \tag{3}$$

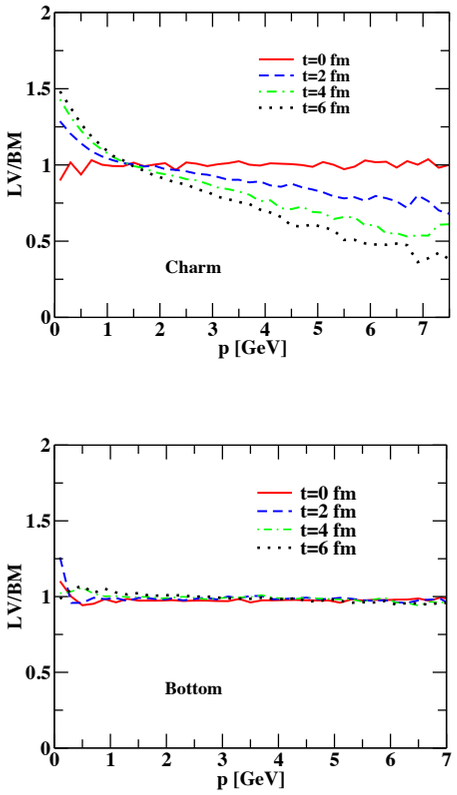

FIG. 1: Ratio between the Langevin (LV) and Boltzmann (BM) spectra as a function of momentum for $m_D = gT$ GeV at different time. Up: charm quarks; Down: bottom quark.

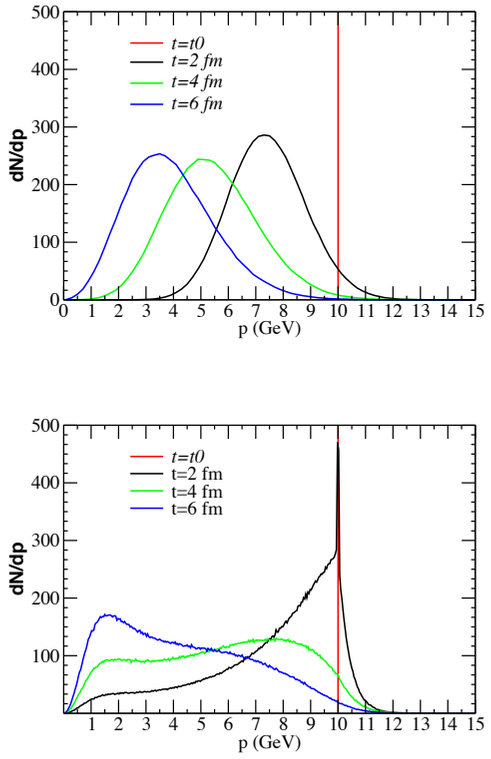

FIG. 2: Evolution of charm quark momentum distribution within Boltzmann equation considering for a charm quark initially at p=10 GeV. Up: Langevin dynamics. Down: Boltzmann dynamics.

where dx_i and dp_i are the coordinate and momentum changes in each time step dt. A is the drag force and B the longitudinal and transverse diffusions, ρ is a stochastic variable Gaussian distributed. in terms of independent Gaussian-normal distributed random variables ρ_j, and

$$P_{ij}^{\perp} = \delta_{ij} - \frac{p_i p_j}{p^2}, P_{ij}^{\parallel} = \frac{p_i p_j}{p^2}. \qquad (4)$$

are the transverse and longitudinal tensor projectors. We will employ the common assumption, $B_0 = B_1 = D$ [2–6, 10].

NUMERICAL RESULTS

We now discuss the evolution of momentum distributions of charm and bottom quarks interacting with a bulk medium at $T = 0.4\,\mathrm{GeV}$ with scattering processes determined by the scattering matrices discussed in the previous section. The initial distribution of heavy quarks are $f(p, t = 0) = (a + b\,p)^{-n}$ with $a = 0.70\,(57.74)$, $b = 0.09\,(1.00)$ and $n = 15.44\,(5.04)$ for charm and bottom quarks respectively. The above function gives a reasonable description of D and B meson spectra in the p-p collision at highest RHIC energy. For the sake of comparison, we solve both the Langevin equation and the Boltzmann equation as described in the above Section. Our purpose is to compare the time evolution starting from the same initial momentum distribution for the both cases. The differential cross section $d\sigma/d\Omega$, main ingredient of the Boltzmann equation, and the drag and diffusion coefficients, key ingredient of the Langevin equation, both originated from the same scattering matrix. The elastic collisions of heavy quarks with gluon has been considered within the pQCD framework to calculate the drag, diffusion coefficients and differential cross section. In the present calculation we used $\alpha_s = g^2/4\pi = 0.35$ and the Debye screening mass as $m_D = gT$.

HEAVY QUARK DIFFUSION IN MOMENTUM SPACE

A more thorough investigation of the heavy quark evolution implied by a Langevin and a Boltzmann approach, we study the heavy quark momentum evolution considering the initial charm quark distribution as a delta distribution at $p = 10$ GeV for the case with $m_D = gT$ GeV. The momentum evolution of the charm quarks are displayed in Fig. 2 (up) within the Langevin dynamics. As known the Langevin dynamics consists of a shift of the average

momenta with a fluctuation around that includes also the possibility to gain energy for the HQ as we see from the tail of the momentum distribution that overshoots the initial momentum $p = 10\,\mathrm{GeV}$ at $t = 2\,\mathrm{fm/c}$, black solid line in Fig.2 (up). In Fig. 2 (down) we present the momentum distribution for charm quark within the Boltzmann equation, is evident a very different evolution of the particles momentum already at $t = 2\,\mathrm{fm/c}$ has a very different spread in momentum with a long tail at low momenta corresponding to some probability to loose a quite large amount of energy and in general a global shape that is not at all of Gaussian form. This essentially indicates that for a particle with $M \sim \langle p \rangle \sim 3T$ as it is for the charm quark at a temperature $T = 0.4\,\mathrm{GeV}$, the evolution is not of Brownian type.

CONCLUSIONS

In this proceeding we have presented a study of the approximations involved by Langevin equation making a direct comparison with the full collisional integral within the framework of Boltzmann transport equation in a box at T=0.4 GeV. We have found that the Langevin approach is a good approximation for bottom quark whereas for charm quark Langevin approach deviates around 40% for the standard pQCD inputs. More specifically, we have found that the underlying dynamics of the single heavy quarks are indeed quite different between the Boltzmann and the Langevin approach and it does not appear to be simply a shift in momentum with a Gaussian fluctuations around it.

[1] R.Rapp and H van Hees, R. C. Hwa, X. N. Wang (Ed.) Quark Gluon Plasma 4, 2010, *World Scientific*, **111**

[2] G. D. Moore, D Teaney, Phys. Rev. C **71**, 064904 (2005)

[3] Hees H van, Greco V and Rapp R 2006 *Phys. Rev.* C **73**, 034913

[4] S. Cao, S. A. Bass, Phys. Rev. C **84**, 064902 (2011)

[5] H. Van Hees, M. Mannarelli, V. Greco and R. Rapp, Phys. Rev. Lett. **100**,192301 (2008)

[6] P. B. Gossiaux, J. Aichelin, Phys. Rev. C **78** 014904 (2008)

[7] A. Adare *et al.* (PHENIX Collaboration), Phys. Rev. Lett. **98**, 172301 (2007).

[8] B. I. Abeleb *et al.* (STAR Collaboration), Phys. Rev. Lett. **98**, 192301 (2007).

[9] B. Abelev *et al.*,(ALICE Collaboration) JHEP **1209** (2012) 112

[10] S. K Das, J. Alam and P. Mohanty, Phys. Rev. C **82**, 014908 (2010)

[11] W. M. Alberico *et al.*, Eur. Phys. J. C, **71** 1666 (2011)

[12] B. Zhang, L. -W. Chen and C. -M. Ko, Phys. Rev. C **72** (2005) 024906

[13] D. Molnar, Eur. Phys. J. C **49** (2007) 181

[14] S. K. Das, F. Scardina, S. Plumari and V. Greco, arXiv:1309.7930 [nucl-th]

[15] S. K. Das, F. Scardina, S. Plumari and V. Greco, Phys.Rev. C **90** 4, 044901 (2014)

[16] G. Ferini, M. Colonna , M. Di Toro and V. Greco, Phys. Lett. B, **670**,325 (2009);

[17] Z. Xu and C. Greiner, Phys. Rev. C **71**, 064901 (2005)

[18] J. Uphoff, O. Fochler, Z. Xu and C. Greiner, Phys. Lett. B **717** (2012) 430

[19] X. Zhu, N. Xu, P. Zhuang, 2008 Phys. Rev. Lett. **100**, 152301 (2008)

[20] M. Nahrgang ,J. Aichelin ,P. B. Gossiaux and K. Werner, arXiv:1305.3823 [hep-ph]

Neutron stars and supernova explosions in the framework of Landau's theory

H. Zheng[1, 2, 3], J. Sahagun[2, 4], A. Bonasera[1, 2]

1) Laboratori Nazionali del Sud, INFN, via Santa Sofia, 62, 95123 Catania, Italy

2) Cyclotron Institute, Texas A&M University, College Station, TX 77843, USA

3) Physics Department, Texas A&M University, College Station, TX 77843, USA

4) Department of Physics, University of California, Berkeley, CA 94720, USA

Abstract - A general formula of the symmetry energy for many-body interaction is proposed and the commonly used two-body interaction symmetry energy is recovered. Within Landau's theory (Lt), we generalize two equations of state (EoS) CCSδ3 and CCSδ5 to asymmetric nuclear matter. We assume that the density and density difference between protons and neutrons divided by their sum are order parameters. We use different EoS to study neutron stars by solving the TOV equations. We demonstrate that different EoS give different mass and radius relation for neutron stars even when they have exactly the same ground state (gs) properties (E/A, ρ_0, K, S, L and K_{sym}). Furthermore, for one EoS we change K_{sym} and fix all the other gs parameters. We find that for some K_{sym} the EoS becomes unstable at high density even for neutron matter. This suggests that a neutron star (NS) can exist below and above the instability region but in different states: a quark gluon plasma (QGP) at high density and baryonic matter at low density. If the star's central density is in the instability region, then we associate these conditions to the occurrence of Supernovae (SN) [1].

THE MAIN RESULTS

We fix incompressibility K=225 MeV, symmetry energy S=28.5 MeV, and the slope of symmetry energy L=73 MeV from Skyrme EoS $CK225_1$ [1]. In this case, EoS $CK225_1$, CK225 and CCSδ3 have the same values for K, S, L and K_{sym}. This motivates us to fix the same values of S, L and K_{sym} for EoS CCSδ5. For the four EoS, $CK225_1$, CK225, CCSδ3 and CCSδ5, we solve the TOV equations for the PNM to obtain the mass-radius relation of neutron stars. The results are shown in Fig. 1. We can see that the mass-radius relations for the neutron stars are different for the four EoS ($CK225_1$ and CK225 are the same in this case) even though they have the same values of K, S, L and K_{sym}. This indicates that the mass-radius relation of the NS is not only determined by K, S, L and K_{sym}, but the high density dependence of the EoS is crucial. We also notice that there are wiggles in the mass-radius relation of PNM NS for CCSδ3 and CCSδ5 rather than $CK225_1$ and CK225 because of a cross-over at high density for the two EoS. Thus, the second order PT assumed in deriving CCSδ3 and CCSδ5 becomes cross-over for these parameters choice. The maximum mass of the NS for CCSδ3 is larger than the one for $CK225_1$ or CK225. The reason for this is because of the higher power of ρ in CCSδ3 compared to CK225. But the maximum mass of the NS for CCSδ5 (which contains even higher power density values) is lower than the one for CCSδ3. The 'missed phase transition' or cross-over softens the EoS and causes the pressure for CCSδ5 to decrease compared to the one for CCSδ3 at the same density.

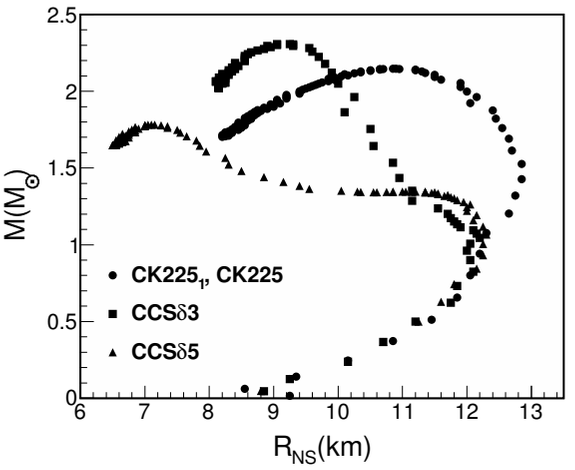

Figure 1: The NS mass-radius relation for $CK225_1$, CK225, CCSδ3 and CCSδ5 with same values of K=225 MeV, S=28.5 MeV, L=73 MeV and K_{sym} = -25 MeV.

The EoS CCSδ5 displays an instability when K_{sym}=-215MeV corresponding to a first order PT. In this case the TOV equations cannot be solved in the instability region. We have used the Maxwell construction to determine the densities where the two phases (which we call phase A and B) are separated. In Fig. 2, we plot the values obtained solving the TOV equations for different initial conditions. The TOV solutions are given by the full lines while the results in the unstable region are given by the dashed lines. The first three panels correspond to central densities above point B. As we see, there is a large part of the star in the unstable region. The stable surface

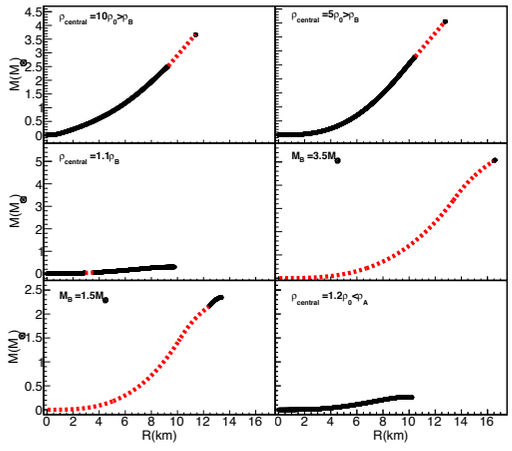

Figure 2: (Color online) The mass versus R for CCSδ5 when K_{sym}=-215 MeV for different central density values indicated in the figure. When $\rho_{central}$ is in the instability region (the fourth and fifth panels) we choose M_B=3.5 $M_\odot$, 1.5$M_\odot$ respectively. The last panel is obtained when the central density is outside the instability region, thus the baryonic phase only.

region becomes bigger and bigger, the closer the central density gets to the critical point B. We can argue that for the latter condition the NS is stable since the gravitational force might be able to constrain the unstable region. However, if the stable surface region is too small, or alternatively the mass contained in the unstable region is too large compared to the total NS mass, then part of the star mass might be 'evaporated' in order to reduce the instability region. Of course, from these estimates we cannot say how much mass will be 'evaporated' and detailed hydrodynamical calculations are needed using these EoS. Since the observations (so far) give a maximum NS of about 2.5±0.5$M_\odot$, we can argue that for the two top panels cases in Fig. 2, the unstable region will be 'evaporated' or 'blown away' which will bring to a rearrangment of the NS with new values of its mass. Of course, these probably are more the conditions for SN explosions.

SUMMARY

In this paper [1], we have shown that two EoS, i.e. $CK225_1$, CK225 obtained from simple Skyrme interactions and other two, i.e. CCSδ3 and CCSδ5 obtained from Lt, with the same values of E/A, ρ_0, K, S, L and K_{sym} at gs density result in different mass-radius relation for neutron stars. We suggest that in order to pin down the EoS we need more constraints at higher densities than the gs one. One constraint might be the critical density (if any) of a first or second order PT. We need to derive the constraints of the EoS from laboratory experiments. We argue that the maximum mass of NS is the results of the competition between the highest power of density in EoS and the PT (if any).

Fixing S=28.5MeV, L=50MeV and changing K_{sym} for CCSδ5, we found that it has an instability region and experiences a PT when K_{sym} =-215MeV. This can be associated to the occurrence of SN phenomena. For this particular choice of the input parameters, stable NS with very small masses are obtained. These small NS masses are indeed found for all the EoS discussed in this work and others. These stars are made of neutrons only (no QGP) and their observation might solve the dark matter 'puzzle'. In particular if the PT (either first or second order) is responsible for the SN explosions, then we expect that the resulting average mass distribution (from many SN events) of NS to follow a power mass-law distribution. It is crucial however, to fix to a better precision the values of S, L and K_{sym} from experiments in laboratories also using radioactive nuclei.

REFERENCES

[1] H. Zheng, J. Sahagun and A. Bonasera, arXiv: 1411.3030.

ISTITUTO NAZIONALE DI FISICA NUCLEARE
LABORATORI NAZIONALI DEL SUD
ACTIVITY REPORT 2013/2014

INSTRUMENTATION AND RELATED TECHNIQUES

4π γ-ray detection with CsI(Tl) scintillators of the CHIMERA array

G. Cardella[1,*], L. Acosta[1], F. Amorini[2], L. Auditore[4], I. Berceanu[8], A. Castoldi[7], E. De Filippo[1], L. Francalanza[2,3], B. Gnoffo[1], C. Guazzoni[7], G. Lanzalone[2,5], I. Lombardo[6], T. Minniti[4], E. Morgana[4], S. Norella[4], A.Pagano[1], E.V. Pagano[2,3], M. Papa[1], S. Pirrone[1], G. Politi[1,3], A. Pop[8], L. Quattrocchi[4], F. Rizzo[2,3], E. Rosato[6,+], P. Russotto[1], A. Trifirò[4], M. Trimarchi[4], G. Verde[1], M. Vigilante[6]

1) INFN - Sezione di Catania, Via S. Sofia, 95123 Catania, Italy

2) INFN - Laboratori Nazionali del Sud, Via S. Sofia, Catania, Italy

3) Dip. di Fisica e Astronomia, Università di Catania, Via S. Sofia, Catania, Italy

4)INFN Gruppo collegato di Messina and Dip. di Fisica e Scienze della Terra, Università di Messina, Italy

5)Facoltà di Ingegneria e Architettura, Università Kore, Enna, Italy

6)Dipartimento di scienze Fisiche, Università Federico II and INFN Sezione di Napoli, Italy

7) INFN Sezione di Milano e Politecnico Milano, Italy

8) Institute for Physics and Nuclear Engineering, Bucharest, Romania

+deceased

Abstract - The γ-decay of the first excited 4.44 MeV 2^+ level of ^{12}C, populated by inelastic scattering of proton and ^{16}O beams at various energies was studied using the CsI(Tl) detectors of the 4π CHIMERA array. A typical pure E2 transition was observed for the γ-rays angular distribution in the case of ^{16}O beam. For the proton beam, a flattening of the angular distribution was observed due to proton spin flip events allowing the population of M=±1 magnetic substates.

INTRODUCTION

This work was aimed to prove the ability of CHIMERA to detect discrete γ-rays and to extract meaningful angular distributions. For this purpose we investigated the test case of the population and decay of ^{12}C (4.44 MeV) first excited level. It is well known that the 4.44 MeV is a 2^+ level decaying to ground state with E2 γ-transition decay [1]. We studied its excitation by inelastic scattering on Carbon target of both proton beams at 12, 15, and 18 MeV incident energy and ^{16}O beams at 10 AMeV. The observed differences between proton and ^{16}O projectiles induced reactions have been understood with respect to the ground state spins of the probes.

We used for the detection of both γ-rays and inelastic scattered beam particles the CHIMERA 4π multidetector [2]. This work is part of our effort to implement a valuable method of γ-rays-particles coincidence measurements, in reaction induced by in flight projectile fragmentation beams as available at Laboratori Nazionali del Sud (LNS) in Catania [3], in order to study the reaction mechanisms and the structure of nuclear systems populated with such exotic beams [4].

EXPERIMENTAL SET-UP

The experiment was performed at LNS in Catania by using the two accelerator facilities of this laboratory, the 13 MV tandem, and the superconducting cyclotron CS, to produce respectively protons and ^{16}O beams. The most useful part of CHIMERA, for γ-ray detection, are the CsI(Tl) belonging to the spherical part of the detector. In fact, due to the larger solid angle coverage of the single detector and the smaller yield of charged particles, we can benefit of a larger signal to noise ratio.

In order to get γ-rays from the 4.44 MeV decay we selected, in the q-value spectrum, from all reactions performed the inelastic scattering (see in fig.1a an example of this spectrum obtained with 18 MeV proton beam). In fig.1b one can see the γ-energy spectrum obtained with such condition adding up all detectors at 58°(empty spectrum). Normalized background was evaluated by looking to events in spurious γ-ray-proton coincidences from elastic scattering (green filled histograms in fig.1a,b).

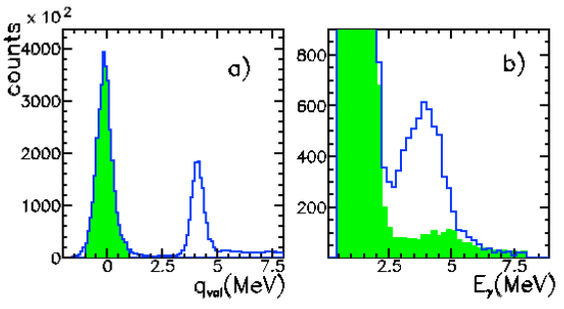

Fig.1 a) q-value spectrum and b) γ-energy spectrum generated in the p+^{12}C reaction at 18 MeV.

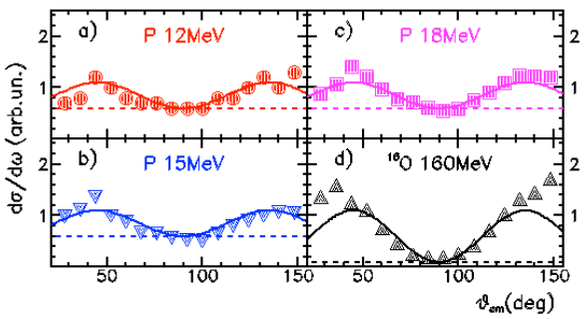

Fig.2 Center of Mass angular distribution of γ-rays detected in the 4 reactions studied.

The angular distribution was evaluated on the ^{12}C reference frame (CM of the recoiling system), choosing as Z axis the ^{12}C recoil direction. This angle was computed, assuming two-body kinematics, from the experimental distribution of scattered protons and ^{16}O. In fig.s 2a,b,c,d the CM γ-ray angular distributions are plotted for the three proton energies and for ^{16}O beam. The distributions are normalized to an average value of 1. As reported in [5] CM angular distributions follow qualitatively the behavior predicted for E2 transition with M=0 (spin projection) $\sin^2(2\theta)$ with a minimum around 90° and maxima around 45° and 135°. Such kind of transition is observed for the ^{16}O beam while to reproduce the experimental behavior (full lines), in the case of proton beams, one has also to include a constant flat distribution (dashed line, approximately of the same order of magnitude). In fact, due to angular conservation law, in case of spin zero beam, as with ^{16}O, only the M=0 projection of the spin is allowed. With proton beams also the population of magnetic subtates M=±1 is allowed. The proton spin flip is responsible of the flattening of the angular distributions.

PERPESCTIVES AND CONCLUSIONS

This work show has shown the capability of the CHIMERA detector to extract meaningful angular distributions from high energy γ-rays. With such a powerful detector a nearly complete spin alignment was observed looking at angular distribution of γ-rays emitted from the decay of the 4.44 MeV first excited state of ^{12}C when populated by inelastic scattering of ^{16}O nuclei. An approximately 50% smaller deepness of minima was observed using proton beams from 12 to 18 MeV. This is due to the population of ^{12}C magnetic substates M=±1, allowed by angular momentum conservation, in case of proton spin flip events. This effect can be used as a complementary way, with respect to elastic scattering, to study the intensity of spin orbit interaction. This interaction is in fact responsible of the proton spin flip process. Often, as in ref. [6-8], this was done in the past using a simple dedicated set-up with detectors for particles and γ-ray detection mounted in both in and out-plane configuration. The 4π geometry used in this work has the advantage to allows the sum of data from all available detectors, irrespective of their detection plane. This can be useful in case of reactions with radioactive beams where, due to scarce statistics, one has to use all possible coincidences data with large solid angle arrays.
We plan to use in future experiments the CsI(tl) of CHIMERA to detect γ-rays in reactions induced by fragmentation radioactive beams at LNS. The γ-ray detection will be useful to disentangle reactions leading to ground state from inelastic channels. We will also try, in selected cases, to extract information on spin flip processes and on the spin orbit interaction with exotic nuclei.

REFERENCES

[1] F. Ajzenberg-Selove Nucl. Phys. A506 (1990) 1; http://www.tunl.duke.edu/nucldata/
[2] A. Pagano, et al., Nuclear Physics A 734 (2004) 504.; A. Pagano, Nuclear Physics News 22 (1) (2012) 25.
[3] I. Lombardo, et al., Nuclear Physics B (Proceedings Supplements) 215 (2011) 272. ; G. Raciti, E. Rapisarda, M. De Napoli, F. Amorini, L. Calabretta, G. Cardella, G. Cosentino,C. Sfienti, V. Shchepunov, Nuclear Instruments and Methods B 266 (2008) 4632.
[4] L. Acosta et al Nuclear Instruments and Methods A 715 (2013) 56; G.Cardella et al EPJ Web 66(2014) 03016
[5] J.R. Beene, F.E. Bertrand, M.L. Halbert, R.L. Auble, D.C. Hensley, D.J. Horen, R.L. Robinson, R.O. Sayer and T.P. Sjoreen; PRC 39(1989)1307.
[6] J.R. Tesmer and F.H. Schmidt; Phys.Rev. C3 (1972) 864.
[7] R. De Leo, G. D'Erasmo, F. Ferrero and A. Pantaleo Nucl. Phys. A212 (1973) 253.
[8] W. Dunnweber, P. D. Bond, C. Chasman, and S. Kubono; PRL 43(1979)1642.

A note on light particle calibration with CsI(Tl) scintillators of the CHIMERA array

L. Acosta[1], F. Amorini[2], L. Auditore[4], I. Berceanu[8], G. Cardella[1], A. Castoldi[7], S. De Luca[4], E. De Filippo[1], L. Francalanza[2,3], B. Gnoffo[1], C. Guazzoni[7], G. Lanzalone[2,5], I. Lombardo[6], N.Martorana[2,3], T. Minniti[4], E. Morgana[4], S. Norella[4], A.Pagano[1], E.V. Pagano[2,3], M. Papa[1], S. Pirrone[1], G. Politi[1,3], A. Pop[8], L. Quattrocchi[4], F. Rizzo[2,3], E. Rosato[6,+], P. Russotto[1], A. Trifirò[4], M. Trimarchi[4], G. Verde[1], M. Vigilante[6]

1) INFN - Sezione di Catania, Via S. Sofia, 95123 Catania, Italy

2) INFN - Laboratori Nazionali del Sud, Via S. Sofia, Catania, Italy

3) Dip. di Fisica e Astronomia, Università di Catania, Via S. Sofia, Catania, Italy

4)INFN Gruppo collegato di Messina and Dip. di Fisica e Scienze della Terra, Università di Messina, Italy

5)Facoltà di Ingegneria e Architettura, Università Kore, Enna, Italy

6)Dipartimento di scienze Fisiche, Università Federico II and INFN Sezione di Napoli, Italy

7) INFN Sezione di Milano e Politecnico Milano, Italy

8) Institute for Physics and Nuclear Engineering, Bucharest, Romania

+deceased

Abstract – Alpha particle energy calibration of CHIMERA CsI(Tl) detector was performed using CS beams. A comparison with proton energy calibration shows unexpected missing quenching effect. This effect is due to a peculiar behaviour of the CHIMERA electronic chain as shown by a comparison performed using digital GET electronics.

INTRODUCTION

It is well known that the light response of scintillators to charged particles is depending from their charge. Heavy Ions with high specific energy loss produce a smaller light output than light particles. This is the so called quenching effect. In order to take into account the charge and mass dependence of the energy-light response function of detectors one can use a formula suggested by Horn [1]

$$L=a_1\{E-a_2AZ^2\ln[(E+a_2AZ^2)/(a_2AZ^2)]\}+a_0$$

where A, Z and E are respectively the mass, charge and energy of the detected fragment, L is the collected light signal, a_0 is a parameter depending on pedestal, a_1 is connected to the electronic gain of the channel and it includes also the scintillation efficiency of the detector, a_2 is related to the Birks quenching factor [2]. This formula is based on the assumption that the quenching of CsI(Tl) light output depends on the specific energy loss of the particle dE/dx (Birks prescription). Using this prescription we find in previous work [3] an average systematic correction of the order of 10% for the energy calibration for proton and alpha particles around 60 MeV. More recently during the INKIISSY campaign we were able to directly compare energy calibration obtained with proton and alpha particle beams delivered at LNS by the superconducting cyclotron, and surprisingly we observed a practically charge-independent energy calibration for the two different particles. This confirms previous observations obtained during the GSI ASYEOS experiment where punching trough proton and alpha particles were found to produce the same energy calibration [4]. In this short report we will explain this effect using results of a recent investigation with the new digital GET electronics [5].

COMPARISON OF ALPHA AND PROTON CALIBRATION

A direct proton and alpha particle calibration was obtained in 2013 during the INKIISSY experimental campaign [6] using proton beams of 62 MeV and alpha particle of 35 AMeV impinging on various targets from gold to proton and using a pulser to verify linearity and determine the pedestal position. In fig. 1 we plot an example of the energy calibration obtained for a CHIMERA CsI(Tl) [7] obtained by a standard peak

sensitive analyzers (se below). The different points are explained in the figure. The data set of the different particles can be practically described by an unique calibration lines. Quenching is not at all observed, on the contrary in this detector, as in many others, alpha particles show tendency to have a larger light response (measured in qdc channels in this picture) than protons. It useful to understand this behaviour that was already noted in a previous experiment performed at GSI always with CHIMERA CsI(Tl). During the ASYEOS [8] experiment in fact a calibration was obtained using punching trough particles relative to Z=1, Z=2 and Z=3 elements with reasonably good linearity results [4].

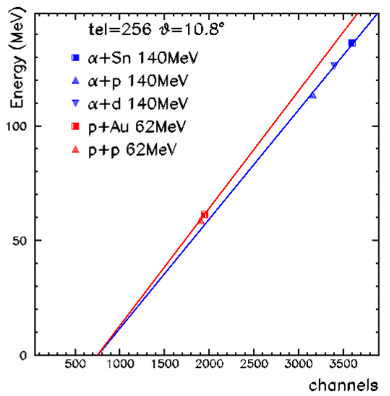

Fig.1 Alpha (triangles) and proton (squares) calibration measurements for one CsI(Tl)

DIGITAL ACQUISITION DATA

During recent tests of the new GET electronics we were able to understand the small light deficit of protons with respect to alphas as due to ballistic effects. The GET electronics will substitute the old (with tendency to be obsolete) electronics of CHIMERA CsI(Tl), and it will be also used for the FARCOS array. It is a digital electronics better described elsewhere in this report [5]. Using this electronics we measured the reactions induced by proton beams at 62 MeV on various targets collecting a variety of particles from different reaction mechanisms. The shape of preamplifier signals was stored for the analysis. Digital filter where used to extract the maximum of the signal (assumed proportional to the energy released by the particle or the light response of the detector) and other information like the rise time of the signal, useful for particle identification. We were able to calibrate data, in proton equivalent energy, using various elastic and inelastic scattering from gold, carbon, proton and deuteron targets. Using such calibrations we selected

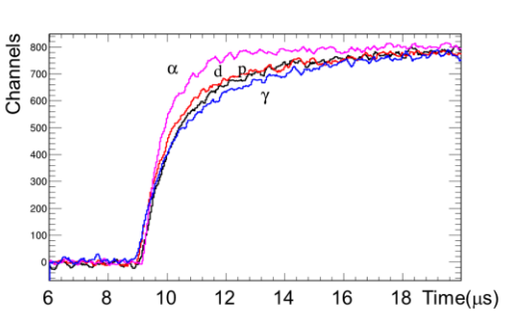

Fig.2 Signals digitized with GET acq.

signals of different identified particles but producing the same light in the scintillator to observe their corresponding rise time. This is shown in fig.2. From the observation of this figure, one immediately note that, the rise time of alpha particle signals is much smaller than the one of proton deuterons and γ-rays. The maximum of the signal with these particles is reached after more than 6 μs. The preamplifier signal in the standard electronics is sent to a SILENA spectroscopy amplifier set with a shaping time of 2 μs. It is clear that the very slow signals produced by proton and γ-rays can produce a ballistic deficit due to 2 μs amplifier filter that was much larger than the one produced by alpha-particles. This effect was responsible of the apparent inverse quenching effect observed in fig.1 from proton and alpha particles. Such limitations will be avoided by digital DAC systems.

REFERENCES

[1] D.Horn et al, NIM A320(1992)273.
[2] J .B . Birks, The Theory and Practice of Scintillation Counting (Pergamon, 1964) 465.
[3] L. Acosta et al Nuclear Instruments and Methods A 715 (2013) 56.
[4] L.Acosta et al IEEE trans.on nucl.sci. 60(2013)284.
[5] S.De Luca et al this report.
[6] P.Russotto et al this report.
[7] A. Pagano, et al., Nuclear Physics A 734 (2004) 504.; A. Pagano, Nuclear Physics News 22 (1) (2012) 25.
[8] P.Russotto et al. this report.

First test with beam of the FARCOS Correlator

E.V. Pagano[1,2], L. Acosta[4], R. Andolina[1], L. Auditore[5], C. Boiano[6], G. Cardella[3], A. Castoldi[7], M. DAndrea[3], E. De Filippo[3], S. De Luca[5], D. Dell'Aquila[8], L. Francalanza[8], E. Geraci[1,3], B. Gnoffo[3], C. Guazzoni[6,7], G. Lanzalone[2,9], I. Lombardo[8], N. Martorana[1,2], T. Minniti[11,12], S. Norella[5], A. Pagano[3], M. Papa[3], S. Pirrone[3], G. Politi[1,3], F. Porto[1,2], L. Quattrocchi[5], F. Rizzo[1,2], P. Russotto[3], G. Sacca'[3], A. Trifiro'[5], M. Trimarchi[5] , G. Verde[3,10], M. Vigilante[8].

1)Università degli studi di Catania, Italy
2)INFN – Laboratori Nazionali del Sud, Catania, Italy
3)INFN – Sezione di Catania, Catania, Italy
4)Istituto de Fisica, Universidad Nacional Autonoma de Mexico, Mexico D.F. 01000, Mexico
5)Università di Messina e INFN – Gruppo collegato di Messina, Messina, Italy
6)INFN – Sezione di Milano, Milano, Italy
7)Politecnico di Milano, Dipartimento di Elettronica, Informazione e Bioingegneria, Milano, Italy
8)INFN – Sezione di Napoli e Dipartimento di Fisica, Università di Napoli Federico II, Napoli, Italy
9)Università Kore Enna, Enna, Italy
10) Institute de Physique Nucleaire d'Orsay, Orsay, France
11)CNR – Istituto per I Processi Chimico-Fisici, Messina, Italy
12)ISIS Facility, Science and Technology Facilities Council, Rutherford Appleton Laboratory, Oxfordshire, UK

Abstract – In this paper, we briefly describe a first test, using a beam, of FARCOS (Femtoscope ARray for COrrelation and Spectroscopy)[1,2]. FARCOS is a new generation detector array mostly devoted on particle correlations that is under construction in Catania.

INTRODUCTION

The study of nuclear dynamic during a Heavy Ion Collision (HIC) is an active field in nuclear physics. In fact, depending on incident energy and impact parameter, one is faced with different time scales and scenarios. In our terrestrial laboratories one can explore nuclear matter in exotic conditions of nuclear density far from the saturation value (0.17 nucleon/fm^3)[3]. With the advent of new-generation radioactive ion-beam facilities, such as FAIR at GSI , FRIB at MSU, SPES at LNL or SPIRAL II at GANIL, these studies assume renewed interest in order to study both the structure of rare isotopes and the property of isospin asymmetric nuclear matter with interesting implications in nuclear astrophysics. From the experimental point of view this studies require more performing detector array in particular having more energy and angular resolution.

FARCOS

FARCOS is a modular array of telescopes each one consisting of three detection stages. The first two stages are Double Sided Silicon Strip Detectors (DSSSD)- 300μm and 1500μm of thicknesses, respectively- with 32 vertical strips in the front side and 32 horizontal strips in the back side. For both the area is 64*x*64 mm^2. The last stage consists of four CsI(Tl) of 6 cm of thickness optically coupled with photodiodes(2×2cm^2) for the read-out. Fig.1 shows the three stages of a single cluster of FARCOS (left side) and their typical close assembling (right side). It is important to note that each cluster is equipped with 132 independent read-out electronics channels (128 for silicon strips and 4 for CsI photodiodes). Particle Discrimination techniques in FARCOS are performed by means of popular ΔE-E technique. The available electronics allows also for pulse shape (PSD) and Time of Light (TOF) methods. Beside the compact design, portability and modularity are important features making an easy coupling of the array to 4π detectors, other correlators and magnetic spectrometers [1]. For the preliminary prototypes, we have used modified versions of CHIMERA-like standard preamplifiers (PAC) for both CsI(Tl) crystals and silicon detectors already developed to match with the necessities of low electronics noise and TOF performance [4]. Starting from these studies, for the read-out of the silicon strips we were testing new pseudo-differential 32-Ch PACs low power consumption (<900 mW for 32 channels) that are very compact (86x80x10) mm^3 NPA-16FL, (98x80x15) mm^3 NPA-16FE. A cooling system is envisaged under vacuum operation.

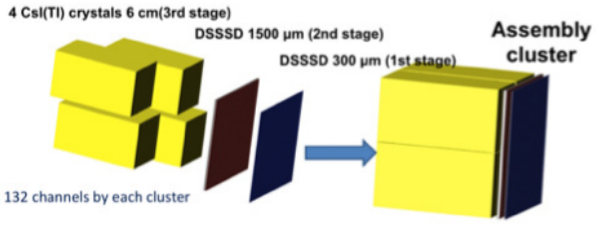

Figure 1: Schematic view of a cluster of FARCOS[2]

FIRST TEST AND CHARACTERIZATION WITH BEAM DURING THE INKIISSY EXPEROMENT AT LNS

FARCOS was tested and coupled with the 4π CHIMERA for the first time during the experiment INKIISSY (INverse KInematic ISobaric System)[5] on April 2013, performed at INFN-LNS of Catania using the K800 Superconducting Cyclotron. The setup consisted of the 4π detector CHIMERA and 4 modules of FARCOS prototype. The experimental configuration FARCOS covered an angular region in the lab frame in the range of polar angles θ_{lab} = 16° −44° and azimuthal opening of value Δφ=75°. The detector was located at a distance of 25 cm far from the target. After a cut in the total strips hits multiplicity (aimed at removing unphysical events) (1≤ multDSSSD≤ 8) good ΔE-E identification matrixes between the first two DSSSD have been obtained.

IDENTIFICATION

For the particle identification in the ΔE-E in Si-Si DSSSD telescope, two procedures were compared. The first one consists in identifying particles in a single-strip – single-strip way, that requires a substantial time consuming for the data analysis. In fact more than 100 identification matrix have to be analysed and the procedure needs high statistic for each strip (see left panel of Fig. 2). The second consists to sum the statistics of more strips, for instance summing 8 strips. In this case the identification work is faster, so improving the statistic for the identification purpose, but it is necessary to perform a strip-by-strip amplitude normalisation (or better an energy calibration), because all the electronic channels are independent (right panel of Fig. 2).

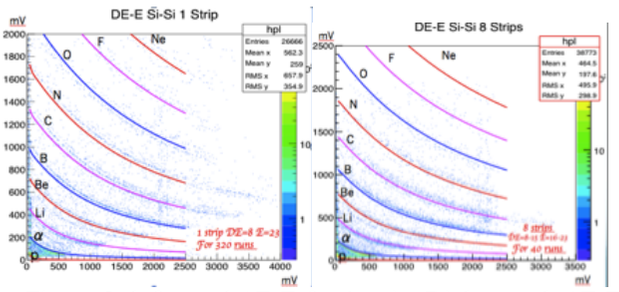

Figure 2: left panel ΔE-E for 1 strip. Right panel: ΔE-E for 8 strips. [1]

The Fig. 2 shows that in FARCOS we have a good separation of elements from protons to Neon in both the two ways. Isotopic identification is also achieved with similar good quality in the two ways, up to charge Z≤ 6. However, for isotopes with larger charge, i.e., 7≤ Z≤ 10, the "single-strip'' procedure allows for a better resolution than the " sum-strip" one (see left and right panels of Fig. 3).

CONCLUSIONS

Tests to extract the performances of four clusters of FARCOS correlator have been performed. The obtained results represent an important step in our experimental R&D work. They are encouraging and indicate that both energy and angular resolutions allow for a satisfactory isotopic identification of light fragments and light charged particles. In order to achieve a more compact electronic configuration, in the next future we will be able to test new ASICs preamplifiers to be coupled with GET electronics and a new DAC system for full digitalization of the signals. In the next five years, we plan to complete the configuration of 20 clusters of FARCOS.

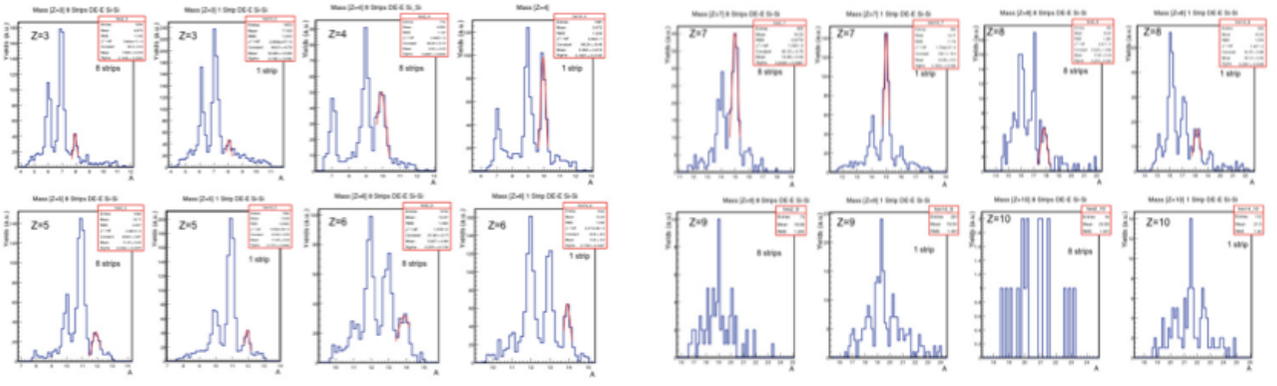

Figure 3: Left panel: Isotopic identification resolution for particle having charge between 3≤ Z≤ 6. Right panel: Isotopic identification resolution for particle having charge between 7≤ Z≤ 10 [1].

REFERENCES

[1] E.V. Pagano et al., EPJ Web of Conferences (2015) in press.
[2] G. Verde et al., Jour. of Phys: Conference Series 420(1), 012158 (2012)
[3] Bao-An Li et al., Phys. Rev. C 71044604 (2005)
[4] C. Boiano, et al., IEEE Trans. On Nucl. Science 51 1931 (2004)
[5] P. Russotto et al., Phys. Rev. C 81, 064605 (2010)

Performance qualification of a FARCOS telescope by means of Digital Data Acquisition

L. Acosta[1,2], L. Auditore[3], C. Boiano[4], G. Cardella[1], A. Castoldi[5,4], E. De Filippo[1], L. Francalanza[1], C. Guazzoni[5,4], G. Lanzalone[1,6], I. Lombardo[7], T. Minniti[1,3], E. Morgana[3], S. Norella[3], A. Pagano[1], E. V. Pagano[1], M. Papa[1], T. Parsani[5,4], S. Pirrone[1], G. Politi[1,8], L. Quattrocchi[3], F. Riccio[5,4], F. Rizzo[8,9], P. Russotto[1], M. Trimarchi[3], A. Trifirò[3], G. Verde[1], P. Zambon[5,4]

1) INFN, Sezione di Catania, Italy
2) Instituto de Física, Universidad Nacional Autónoma de México, Mexico D. F. 01000, Mexico
3) Dipartimento di Fisica, Università degli Studi di Messina, Italy and INFN – Gruppo Collegato di Messina
4) INFN, Sezione di Milano, Italy
5) Politecnico di Milano, Dip. Elettronica, Informazione e Bioingegneria, Milano
6) Università degli Studi di Enna "Kore", 94100 Enna, Italy
7) Università degli Studi di Napoli Federico II, Dip. di Scienze Fisiche Napol an, INFN, Sezione di Napoli, Italy
8) Università degli Studi di Catania, Dipartimento di Fisica e Astronomia, Catania, Italy.
9) INFN – Laboratori Nazionali del Sud, Catania, Italy

Abstract - In this paper we review the measured performance of a novel detection system, named FARCOS (Femtoscopy ARray for COrrelations and Spectroscopy) featuring high angular and energy resolution and able to reconstruct the particles momentum at high precision when readout with a custom versatile high-resolution digital DAQ.

INTRODUCTION

In this paper we present the results of the measurement carried out to assess the ultimate performance of FARCOS at the present stage of development. The key to address the ultimate performance is the use of a dedicated Digital Data Acquisition System able to digitize the full waveform at each channel and to optimize the digital filter to be applied to the different signals. The evaluated prototype telescope features an active area of 6.4 cm × 6.4 cm and is composed of only two detection stages. The first ΔE stage is a Double Sided Silicon Strip Detector (DSSSD), 300 μm thick, featuring 32 × 32 strips. The following stage, acting as calorimeter, is composed by four CsI(Tl) crystals with an active area of 3.2 cm × 3.2 cm and an absorption length of 6 cm.

FRONT-END AND BACK-END ELECTRONICS

The signals coming from the DSSSD are read out by multi-channel charge preamplifiers (CPAs). The CPAs employed in most of the measurements shown in the present paper are an hybrid large bandwidth charge preamplifier with differential output featuring a very simple topology, with a high transconductance JFET as input transistor and an open loop current feedback operational amplifier as gain stage. 32 channels are assembled in a compact module of 8 cm × 10.5 cm. Modules with different sensitivities (10, 20 and 45 mV/MeV) are available. We modified a previously designed custom anti-aliasing filter and amplifier, to receive the differential signals coming from the preamplifiers. A standard single-unit 16-channel NIM module provides in a single device: i) a 2nd order anti-aliasing filter with two programmable cutting frequencies (8 MHz and 40 MHz); ii) a programmable-gain amplifier (gains of 1×, 2×, 4×, 8×) to cope with the full dynamic range of the ADC, able to select the polarity of the output signal; iii) a programmable output offset voltage with AC or DC input coupling selection. Two identical outputs are available one to serve the conventional analog acquisition chain and the other one for the digital DAQ, employed for all the data discussed in the present paper. In order to qualify the performance of a FARCOS telescope, we developed also a custom digital DAQ able to fully digitize the waveforms of the 64 channels of one selected DSSSD and of the 4 corresponding CsI(Tl) scintillators for on-line monitoring, raw waveforms storage, detailed pulse shape analysis, etc. Thanks to the availability of the custom AAA modules it is possible to run the digital DAQ in parallel with the conventional analogue data acquisition chain.

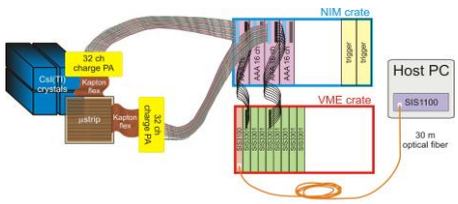

Figure 1. Scheme of principle of the custom digital data acquisition system able to fully digitize the waveforms of the 64 channels of one selected DSSSD and of the 4 corresponding CsI(Tl) scintillators

The simplified schematics of the custom digital DAQ is shown in Figure 1. The signals coming from one of the outputs of the AAA modules are digitized with a set of sampling ADC boards, hosted in a VME crate located in the experimental room. In the present work, we used 8 SIS3301 boards for the 64 channels of the DSSSD, and one SIS3302 board for CsI(Tl) scintillators signals and the external trigger signal from the control electronics. The SIS3301 and the SIS3302 boards are 8-channels, 100MS/s digitizers, with a dynamic range of 5V and a resolution of 14-bits and 16-bits, respectively.

The VME crate is connected to an host PC located in the acquisition room, with a VME-to-PCI bridge, composed of a SIS3100 VME board and a SIS1100 PCI board, linked with a 30 m long optical fiber. The trigger signal is built by exploiting the *auto-trigger* function of the SADC boards. During acquisition, the samples from the SADC are continuously fed to the on-board FPGA, which generates a trigger output signal when the input signal crosses an user-defined threshold. The trigger outputs from all boards are then OR-ed together using a LeCroy 429A logic fan-in fan-out NIM module, and the result is fed back to the STOP input of each board. In this way, we can choose the acquisition channels that generate the global trigger signal and individually configure the threshold level, via software with no need to enter the experimental room, not accessible during measurements.

A dedicated acquisition control software is used to manage the acquisition. It runs on the host PC, under a distribution of Slackware Linux.

MEASURED PERFORMANCE

FARCOS cluster were tested on-beam during a measurement run in July 2012 at Laboratori Nazionali del Sud (INFN, Catania, Italy). The accelerated beams were 62 MeV/u protons and α-particles and 20 MeV/u ^{20}Ne ions on different targets (Au, Al_2O_3, Pb, Al, CD_2). The detectors were placed at polar angle θ=6°. In the experimental chamber there was also a mixed nuclide α-source for calibration purposes. Figure 2a shows an example of the acquired spectrum and Figure 2b and Figure 2c the measured energy resolution at the ^{239}Pu line

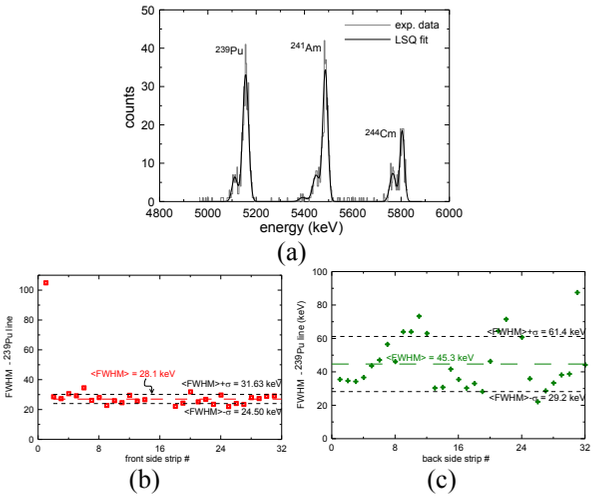

Figure 2. (a) Energy spectrum at one detector channel (junction side) illuminated with a mixed nuclei alpha radioactive source. Measured energy resolution at the ^{239}Pu line for the junction (b) and ohmic (c) side strips of a 300 μm thick DSSSD.

obtained from the spectra collected with the digital DAQ and with a triangular filter with 121 taps kernel for the junction and ohmic side strips, respectively of a 300 μm thick DSSSD. By analyzing the waveforms collected with the digital DAQ we compute the conventional ΔE-E identification matrix, scatter-plotting the maximum of the waveform with respect to its baseline, both for the waveforms coming from the strips of of the 300 μm–thick DSSSD pertaining to telescope T3 and from the corresponding CsI(Tl) scintillator crystal respectively. A triangular digital filter with 201 taps kernel has been applied to the baseline subtracted waveforms for the maximum estimation. The pixelation of the DSSSD allows us to correct for the spatial light yield non-uniformity. Figure 3 shows the obtained corrected scatter plot in the case of the α beam on the Au target together with the energy spectrum (after correction). The measured energy resolution at the elastic scatter peak. The obtained energy resolution is 0.65% FWHM (corresponding to 0.28% r.m.s) to be compared with 0.86% FWHM (0.37% r.m.s.) for the uncorrected spectrum.

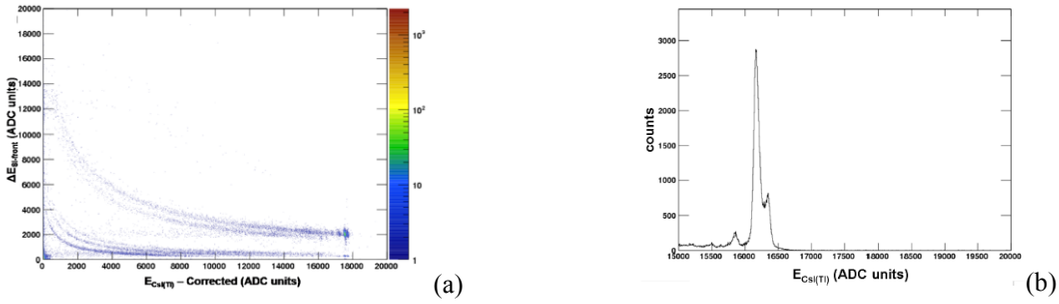

Figure 3. (a) ΔE_{Si}-$E_{CsI(Tl)}$ identification matrix corrected for the CsI(Tl) light yield non-uniformity for the reaction 62 MeV/u α on Au, using a single CsI(Tl) crystal for the E and the sum of the signals of the front strips just in front of the scintillator as ΔE. (b) Energy spectrum collected with one CsI(Tl) crystal after correction for the spatial dependence of the light yield.

FAZIA demonstrator: a significant step forward

S. Barlini[1,2], D. Gruyer[2], N.LeNeindre3, G. Pastore[1,2] , S.Valdrè[1,2] for the FAZIA Collaboration

1) Università di Firenze, via G.Sansone 1, 50019 Sesto Fiorentino (Firenze), Italy
2) INFN Sezione di Firenze, via G.Sansone 1, 50019 Sesto Fiorentino(Firenze), Italy
3) LPC Caen France, F-14050 Caen-Cedex, France

Abstract - The goal of the FAZIA Collaboration is the development of a new-generation detector array for heavy-ion collision studies with stable and radioactive beams. FAZIA telescopes are made of two transmission-mounted silicon detectors (respectively 300µm and 500µm thick), followed by a CsI(Tl) scintillator (10cm thick). During the R&D period, significant improvements in ΔE-E and pulse-shape analysis techniques were obtained by means of a systematic study of silicon detector properties, using dedicated electronics tests. Now, the FAZIA Collaboration has entered the demonstrator phase, aiming at verifying the applicability of the devised solutions for the realization of a larger-scale experimental set-up. The first two FAZIA blocks, equipped with a fully digital electronics, have been tested at LNS in December 2014. Preliminary results are presented in this report.

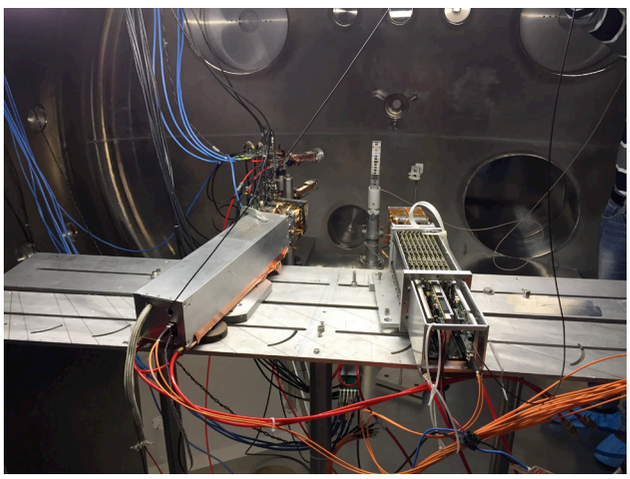

Figure 1: Two FAZIA blocks with embedded electronics disposed inside the Cyclope scattering chamber

INTRODUCTION

The current phase of the European FAZIA project [1] is the commissioning of a demonstrator composed of 12 FAZIA blocks. Two FAZIA blocks, equipped with fully digital electronics, have been tested at the LNS, using a ^{84}Kr beam at 25AMeV impinging on various targets: ^{112,124}Sn, ^{58}Ni, ^{197}Au, and ^{93}Nb

The main objective of this test was to demonstrate that the efficient detection techniques developed during the R&D phase, and their excellent results in terms of ion separation [2-7], are applicable to a block equipped with the final complete FAZIA electronics chain. Coincidence measurement, trigger multiplicity, communication protocols, acquisition and cooling systems have also been tested in real-life experiment conditions.

EXPERIMENTAL SETUP

The two blocks were disposed at about 1m far from the target on both side of the beam axis, covering polar angles between 5.2° and 9.8°. A photo of the set-up is presented in Fig. 1. Each block contains 16 detection telescopes, consisting of a 20x20mm^2 active area Si-Si-CsI(Tl) telescopes, thus exploiting both the standard ΔE-E identification technique for particles punching through the first layer and the pulse-shape analysis (PSA) approach for particles stopped inside it. During this demonstrator phase, both charge and current signals in silicon detectors are digitized and acquired. It is seen on Fig. 1 that, for each block, the eight front-end cards (FEE) are just next to the detectors, in the scattering chamber, to reduce electronic noise contributions and disturbs before the digitalization process. The distance from Si pads and the preamplifiers is less than 15cm. Each FEE handles six channels from the preamplifiers to the digital stages and is equipped with two FPGAs. Each FPGA processes the six signals of a single telescope: current (250MHz, 14 bit), charge high gain (250MHz, 14 bit, 350MeV full scale), and charge low gain (100MHz, 14 bit, 4GeV full scale) of the first silicon; current (250MHz, 14 bit), and charge (100MHz, 14 bit, 4GeV full scale) of the second silicon; and charge signal of the CsI(Tl) scintillator (100MHz, 14 bit, 400MeV silicon-equivalent full scale). The two gains used for the charge signal of the first Si detector are meant to improve the isotopic identification by PSA. Only a pair of optical fibres is used to communicate with each block, and to extract data towards the acquisition system. This is a particularly innovative and challenging solution.

VERY PRELIMINARY RESULTS

The first objective of this commissioning was to check the operation of a complete FAZIA block under beam and to control the effective identification capability.

Fig. 2 shows, for one of the 32 telescopes, the ΔE-E correlation for particles stopped in the second Si detector. Charge identification for all reaction products, from hydrogen to krypton, are clearly visible. In addition, isotopic resolution is achieved up to Z~20, in qualitative agreement with previously published results using single telescopes [2]. The inset of Fig. 2 shows the particle identification (PID) spectrum for Z=13-15 particles, integrated over the whole energy range. A clear mass identification was obtained for such particles.

The "energy *vs.* current maximum" PSA [7] correlation for particles stopped in the first Si layer is presented in Fig. 3 showing that fragments are resolved in charge over the whole Z range. In addition, isotopes are separated up to Z~15 (see inset of Fig. 3). We would like to stress that it is the first time that isotopic resolution is achieved in PSA with such a low gain pre-amplifier [6].

The second objective of this commissioning was to test the coupling of two FAZIA blocks. Since the electronics of one block has been strongly damaged at the beginning of the test, probably due to an abrupt vacuum leakage in the scattering chamber, coincidences between the two blocks have been only partially observed. However, coincidences between particles detected in the working block were measured, allowing us to successfully test the trigger multiplicity.

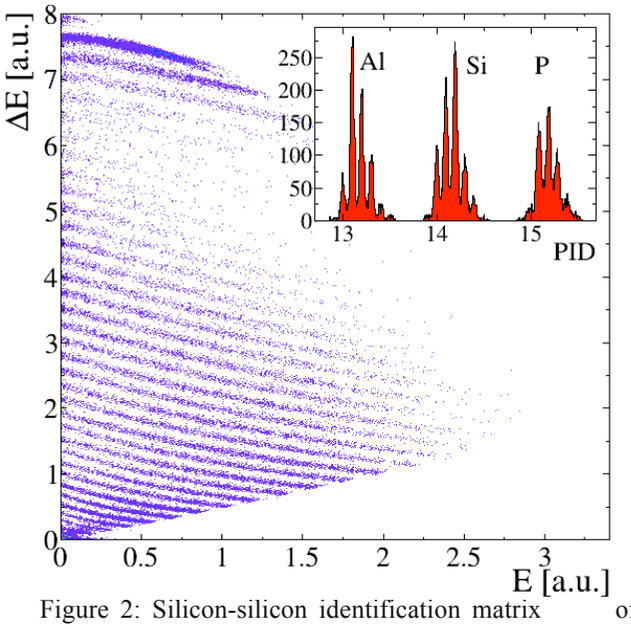

Figure 2: Silicon-silicon identification matrix of particles stopped in the second silicon detector. The Z lines are distinguishable starting from Z=1 up to Z=36. Mass identification is achieved up to Z~20

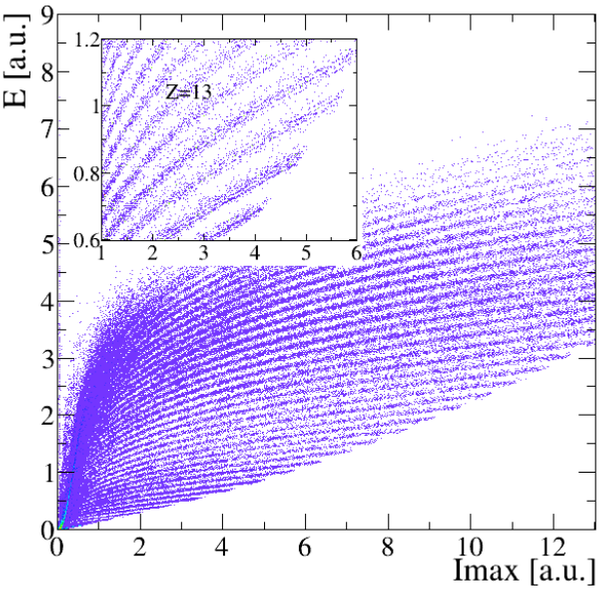

Figure 3: Correlation between energy and current maximum of particles stopped in the first silicon detector. Charge identification is achieved up to Kr and mass identification up to Z~15

CONCLUSION

This test has demonstrated that the excellent identification capabilities obtained with single FAZIA telescopes are practically reproduced in the FAZIA block, equipped with the definitive electronics chain. Multi-particle coincidences were also verifyied, allowing us to run in trigger multiplicity higher than 1. This is mandatory for accomplishing the two experiments using 4 FAZIA blocks that are scheduled in 2015 at the LNS, and represents a significant step toward the FAZIA demonstrator.

REFERENCES

[1] R. Bougault et al., Eur. Phys. J. A (2014) 50: 47
[2] S. Carboni et al., NIMA 664, 251 (2012).
[3] N. Le Neindre et al., NIMA 701, 145 (2013).
[4] L. Bardelli et al., NIMA 605, 353 (2009).
[5] L. Bardelli et al., NIMA 602, 501 (2009).
[6] L. Bardelli et al., NIMA 654, 272 (2011).
[7] S. Barlini et al., NIMA 600, 644 (2009).

THE ELI-NP FACILITY: DESIGN OF A LARGE AREA SILICON ARRAY DETECTOR AND OF THE VACUUM CHAMBER FOR NUCLEAR ASTROPHYSICS AT ELI-NP

V. Crucillà[1], A. Anzalone[1], M. La Cognata[1], D. Lattuada[1,2], C. Spitaleri[1,3], A. Taffara[3]

1) Laboratori Nazionali del Sud – Instituto Nazionale di Fisica Nucleare, Catania, Italy
2) Kore University, Enna, Italy
3) Dipartimento di Fisica & Astronomia, University of Catania, Catania, Italy

Abstract – This paper is concerned with the first phase of conceptual design of a Silicon Strip Detector (SSD) array and of the related vacuum vessel.

The SSD, the scattering chamber and the ancillary equipment will fit in the gamma ray beam line of the new ELI-NP facility, to be used in measurements utilizing intense gamma ray beams.

This phase will be followed by the detailed design and manufacturing of the system.

SILICON STRIP DETECTOR ARRAY (SSD)

Silicon detectors represent one of the best solution for their detection for a number of reasons: (i) they guarantee exceptional energy resolution, (ii) they have almost 100% efficiency in charged particle detection, (iii) thresholds can be set to very small values, (iv) they are not sensitive or very little sensitive to neutrons, gamma rays and electrons, which would constitute the beam induced background [1].

Excitation functions and angular distributions can be measured over a wide range allowing for a better understating of reaction mechanism.

The proposed system is made of n. 3 rows per n. 12 X3 (SS) PSD detectors produced by Micron Semiconductor Ltd., to form a barrel. X3 (SS) PSD detectors are 4-strip detectors 4.36 cm wide 7.69 cm long, position sensitive along the longitudinal axis. The total number of PSD detector is 35 (the central ring contains n. 11 detector to permit the positioning of the target in the middle of the detector holder). The total angular coverage in the laboratory system is 100°.

The angular coverage is extended down to about 20° (160° at backward angles) by using end cap detectors such as the assembly of four QQQ3 segmented detectors by Micron Semiconductor Ltd. Each quadrant of the QQQ3 is segmented into 16 radial segments (3 mm pitch) and 16 angular segments, with inner and outer radii of 4.91 and 10 cm.

To hold the detectors, a cylindrical stainless steel holder (diameter 30.6 cm, length 34.1 cm) has been designed. This one will be fixed inside the scattering chamber by an apposite flange. The detectors are individually removable from the holder for maintenance or replacement. The shielded cases for preamps (N. 5 MSI-8 preamps by Mesytec for each X3(SS) detector and N. 1 MPRS-16 channel preamps by Mesytec for each QQQ3 detector) can be arranged on the external surface of the detector holder.

This system set-up is very compact with a minimum death angle due to the detector frame and to the detector holder. Since position is determined by charged partition, the number of electronic channels is 303 for the whole barrel.

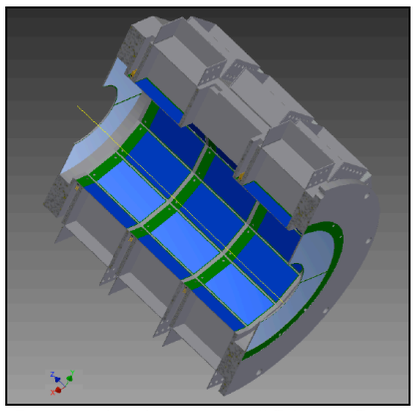

Figure 1: Longitudinal section of Silicon Strip Detector array SSD assembly and detector holder composed of N. 35 X3 SS Micron Semiconductor detectors and N 8 QQQ3 Micron Semiconductor detectors.

DESIGN OF THE VACUUM CHAMBER

Geometry

The vacuum chamber which accommodate the detector holder is horizontally placed, has a cylindrical geometry and is composed of two parts: a first part in built with the beam line, to which are connected the pumping station, the vacuum measurement devices, the gate valves and the target ladder, and a second part which support the detector holder. This can be moved by an apposite actuator in order to completely extract the detector holder.

Legislation and codes

It's quite difficult to define a clear basis for the regulation to be applied to the design and construction of the vacuum chamber [8].

The common practice is to treat the vacuum vessels as a pressure vessel with some arrangements. In this case, European legislation is at now based upon directive

97/23/EC of the European Parliament and of the Council of 29 May 1997 on the approximation of the laws of the Member States concerning pressure equipments.

The safety code for pressure vessel and pressurized pipelines of CERN [3] has been taken into account.

Boundary Conditions

Environmental constrains taking into account in this phase are the weight of the material and of the ancillary equipments, the differential pressure on the vacuum chamber (1 bar during operation), operating temperature (room temperature, is not considered baking out of the vessel).

Material

Stainless steel is chosen as material for the realization of the vacuum vessel.

In particular 1.4301 chromium-nickel steel is one of the most used materials for the construction of chamber and components in vacuum technology because has excellent cold forming, welding and polishing properties and sufficient corrosion resistance [9].

Design

Stresses generated by loads (external pressure, weight etc) should remain in the elastic range. This means that the equivalent stress according to Von Mises criterion should not exceed the elastic limit anywhere in the structure. Since the pressure act on the external surface, the resulting stresses on the walls of the vessel are compressive leading to the buckling effect. Buckling is a non-linear phenomenon and it could be strongly influenced by manufacturing defects. For this reason a safety factor must be applied (EN 13458 quotes 2.0 for outer jackets) [8].

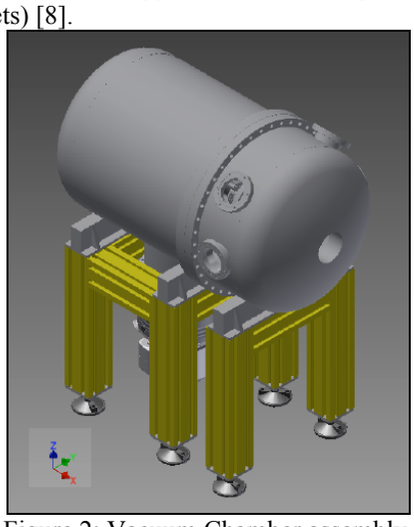

Figure 2: Vacuum Chamber assembly.

In this pre-design phase, simple analytical methods have been used for to calculate the stresses and to taking into account the mains geometrical parameters [8].

The results of the calculation are shown in the following table.

Table 1: Dimension and main characteristics of vacuum chamber

Parameter	**Range**
Pressure range	up to 10^{-7} Pa UHV
Diameter	62,3 cm
Lenght	117,6 cm
Flange	Wire seal flange 27” with copper gasket DN200 CF-F Flange for turbomolecular pump
Feedthrougs	N 4 100CF flanges seal: glass ceramic – N. of pins 2xD50 – cont current 3A per pin – test voltage 500 V DC
Pumping station	Pfeiffer C 40 CV version lubricant free root pump Pfeiffer Hi Pace 1200 turbomolecular pump

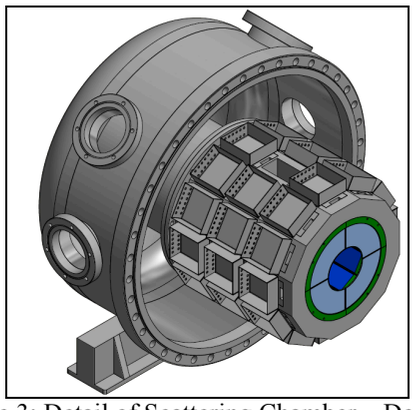

Figure 3: Detail of Scattering Chamber – Detector Holder Assemmbly.

REFERENCES

[1] ELI — Extreme Light Infrastructure Science and Technology with Ultra-Intense Lasers Whitebook, eds. G.A. Mourou et al., THOSS Media, 2011.

[2] Antonello Anzalone, Moshe Gai, Chiara Mazzocchi, Ovidiu Tesileanu, Claudio Ugalde - ELI-NP — Charged Particle Detection at ELI-NP, Technical Design Report RA4 – TDR 4.

[3] CERN — Pressure Equipment – Safety Code D2 – Rev.2.

[4] C. Hauviller – Design of Vacuum Chambers for Experimental Regions of Colliding Beam Machines.

[5] O. Gröbner and C. Hauviller – Design Aspects of LEP Experimental Vacuum Chambers.

[6] M. Steffensen and P.M. Srubin – Database Requirements for the Vacuum Systems of LHC.

[7] J.C. Brunet, J.C. Godot, C. Hauviller, W. Jeker, A. Poncet, I. Wilson - The Design and Construction of a Transparent Vacuum Chamber for Interaction Areas of Colliding Beam Machines.

[8] C. Hauviller – Design Rules for Vacuum Chambers.

[9] Pfeiffer Vacuum – The vacuum Technology Book Volume II.

The ELI-NP facility: Electronic readout of silicon strip detector

A. Taffara[1], A. Anzalone[2], V. Crucillà[2], M. La Cognata[2], D. Lattuada[2,3], C. Spitaleri[1,2]

1) Dipartimento di Fisica & Astronomia, University of Catania, Catania, Italy
2) Laboratori Nazionali del Sud – Instituto Nazionale di Fisica Nucleare, Catania, Italy
3) Kore University, Enna, Italy

Abstract – This report describes the readout electronics that will be used for the silicon strip detector array to be installed at the ELI-NP facility.

ELECTRONIC CASE

The readout of the silicon strip detector array will performed by using the Generic Electronics for TPCs (GET).

This would ensure high resolution keeping costs low and strongly reducing the bulk of the front end electronics.

Research and development activity would be necessary to adapt the GET electronics to X3 and QQQ3 silicon strip detectors. In particular, external preamplifiers have to be implemented to guarantee the best energy and position resolution and proper coupling with the GET readout.

An additional advantage of the adoption of a GET systems is the possibility to have common electronics and DAQ systems with other experiments to be installed at the ELI-NP facility, leading to a standardization of the readout systems strongly enhancing the efficiency of the setups.

GET ELECTRONICS

The GET project is an international collaborative effort to investigate a novel approach towards building medium sized scalable system with a presently maximum of 30k channels having multiple possible applications with comparatively high throughput capabilities and resolution. The choice of new technological solutions allows a reduction in the number of point-to-point connections in the system and should therefore provide for a more reliable system. A fully computerized and distributed control approach will give fast calibration and significant reduction in the set-up time of the system [1].

The core component of the GET electronics is a custom-made 64-channel ASIC chip called AGET (*ASIC for GET*) that employs Switched Capacitor Array (SCA) fast analog memory. The block diagram of the AGET chip is displayed in Fig.1.

Four AGET chips are mounted on a single front-end AsAd card (*ASIC and ADC*). Its main features are the following:

- up to 256 channels in a single board;
- charge preamplifiers with 4 programmable gains per channel (120 fC –10 pC);
- shaping amplifiers with 16 programmable time constants per channel (50 ns – 1 µs),
- SCA analog, circular buffers with 512 cells (sampling points) per channel;
- adjustable sampling frequency of SCA buffers (1 – 100 MHz);
- 12-bit ADC with dynamic range of 2 V_{p-p} and with fixed sampling frequency of 25 MHz for reading SCA memories (one ADC channel per AGET chip);
- possibility to bypass charge- and/or shaping amplifier;
- self- and external triggering, hit counting and test pulse injecting capabilities.

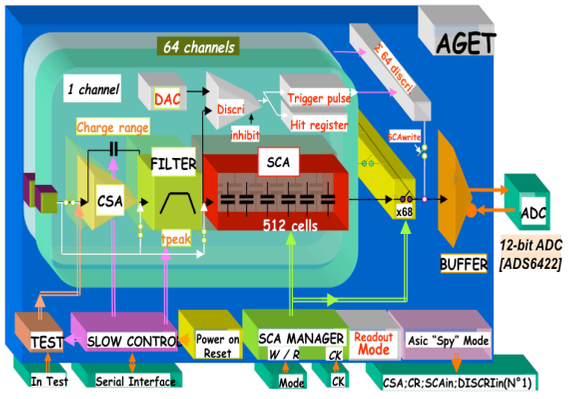

Figure 1: Block diagram of the AGET chip

The global view of the GET electronic is displayed in fig. 2 .

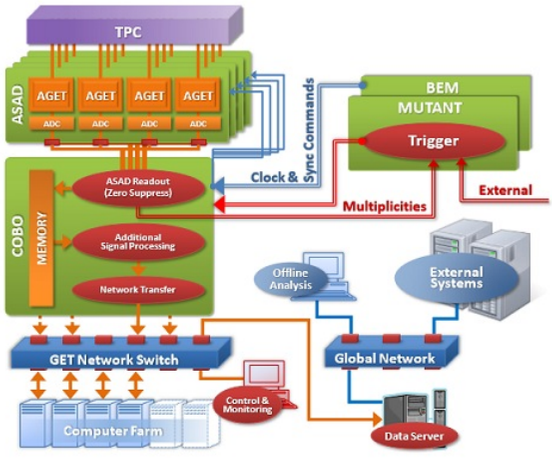

Figure 2: Global view of the GET electronic

The digital outputs of the 4 ADCs are transmitted by 8 differential lines with a maximum speed of 1.2 Gbit/s to the CoBo board.

The CoBo (Concentration Board) board is responsible for applying a time stamp, zero suppression and compression algorithms to the data. It will also serve as a communication intermediary between the AsAd and the outside world. The slow control signals and commands to the AsAd will be transmitted via the CoBo (four AsAD per CoBo).

The Mutant (Multiplicity Trigger And Time) card manages the multiplicity, the conditions for the trigger, and the distribution of the clock on the whole system. The global data is transmitting through network switch to computer farm.

CoBo and MuTanT are set in microTCA crate [2]. Data are transmitted through a 10 Gb-Ethernet network to the computer farm. A μTCA chassis can houses ten CoBos and a MUTANT.

The BEM (Back-End Module) card must ensure the interface between the GET electronics and other ancillary equipment used in nuclear physics experiments.

Taking into account that the use to charge-partition silicon strip detectors, proposed for ELI-NP facility, allows us to reduce to 311 the number of channels to be instrumented, it means that two boards would be necessary to handle the whole detector readout. R&D activity is presently ongoing to achieve high position and energy resolution using X3 and QQQ3 detectors, with respect to preamplifiers and readout software. A major aim is to achieve pulse shape discrimination in the case of charge partition position sensitive silicon detectors.

REFERENCES

[1] E. Pollacco et al., Physics Procedia 37 (2012) 1799-1804

[2] MicroTCA, PICMG http://www.picmg.org/index.htm

Thomson Spectrometer for ionic acceleration study

C. Altana[1,2], G. Lanzalone[1,4], A. Muoio[1,3] S. Tudisco[1],

A. Anzalone[1], GAP Cirrone[1], F. Musumeci[1,2], F. Schillaci[1], M. Castro[1], S. Salamone[1]

1) INFN-LNS, Via S. Sofia 62, 95123 Catania, Italy

2) DFA-Univ. degli Studi di Catania, Via S. Sofia 64, 95123 Catania Italy

3) DFST-Univ. degli Studi di Messina Viale F.S. D'Alcontres 31, 98166 Messina, Italy

4)Univ. degli Studi di Enna "Kore", Via delle Olimpiadi, 94100 Enna, Italy

Abstract - This report describes the development of a powerful and self-consistent technique to be used as a diagnostic tool for the ionic acceleration study in laser-generated-plasmas.

INTRODUCTION

Recent developments in laser technology allow to generate high-density and high-temperature plasmas by means of laser-matter interaction, therefore it is possible to produce and accelerate ion beams in the multi-MeV energy range [1], [2]. An important diagnostic for analysing these ion beams is the Thomson Parabola Spectrometer (TPS) [3]. This is used to measure the energy spectra of different ion species in a given solid angle. Magnetic and electric fields are used to detect ions according to their velocity and charge-to-mass ratio. It is a particularly useful diagnostic of laser-plasma interactions in which a range of ion species are accelerated. This spectrometers are usually equipped with CR-39 or radiochromic films as the position-sensitive ion detector, which allows to obtain information on energy, number of ions, etc., but do not show the image instantly. Otherwise, with a microchannel plate coupled to a phosphor screen (MCP-PH) and a conventional reflex camera it is possible to observe online the spectrogram and in single shot measurements. Moreover, MCPs allow to detect even low number of ions with a spatial resolution of some tens of microns. The spectrogram analysis is difficult because is necessary determine the spectrogram origin location and the spatial resolution depending on the trace width. For this reason TPS are often used in series with time-of-flight detectors. By means of the calibration of TPS we have developed a powerful and self-consistent technique for spectrogram analysis [3]. In this contribution we report on the results of an experimental measurement performed with a TPS developed at INFN-LNS [4].

EXPERIMENTAL SET-UP

Different measurements were carried out at INFN–LNS and at CNR–INO. At LENS laboratory (Laser Energy for Nuclear Sciences) in Catania a Q-switched Nd:YAG laser with 10^{12} W/cm^2 laser intensity, 1064 nm fundamental wavelengths, 6 ns pulse duration, operating in single shot mode, was employed to ablate a 2 mm thick aluminum target in order to produce the plasma.

At ILIL (Intense Laser Irradiation Laboratory) in Pisa a femto-source Ti:SA oscillator with a 200nm bandwidth and 20fs pulse duration was used. The laser beam irradiates solid thin foils in Target Normal Sheath Acceleration (TNSA) regime in order to generate non-equilibrium plasma in forward direction i.e. in the rear side of the target. Ion acceleration emitted from plasma was monitored employing the TPS. It is composed by two pinholes to collimate the ions; the first is 1 mm in diameter and the second, 10 cm distant, is 100 μm in diameter. Later, a deflection sector composed by an electric and a magnetic field partially overlapping with each other is placed. The applied magnetic fields and an electric voltage was applied across two deflecting plates, producing an electric field orthogonal to the direction of the incident ions. After passing the drift region, which allows to increase the particles deflection and separation among different traces, the ions position is detected using a imaging system. A microchannel plate coupled to a phosphor screen 2 cm in diameter and a reflex camera is used to acquire the produced light [4].

Working principle

The resulting ion dispersion, assuming uniform magnetic (B) and electric (E) fields, can be calculated using the follows equations [5]:

$$x_m = \frac{QeBL_m\left(Dm+\frac{L_m}{2}\right)}{\sqrt{2mE_{kin}}} \qquad y_e = \frac{QeEL_e\left(D_e+\frac{L_e}{2}\right)}{2E_{kin}} \tag{1}$$

where x_m and y_e are the deflection measured with respect the origin, Q is the charge state of the ion, e is the charge of the electron, m is the ions mass, E_{kin} is the kinetic energy, B and E are the applied magnetic and electric fields, L_m and L_e are the geometric length of the magnet and the electrodes, D_m and D_e are the drift between the end respectively of the magnet or of the electrodes and the detector.

Combining the equation of magnetic and electric deflections it get the parabolic equation:

$$y_e = \frac{mEL_e\left(D_e+\frac{L_e}{2}\right)}{QeB^2L_m^2\left(D_m+\frac{L_m}{2}\right)^2}x_m^2 \qquad (2)$$

which means that ions with the same charge-to-ratio and different energies are deflected on a parabolic trace on the detector screen. Because the magnetic and electric deflections have a hyperbolic dependence on the energy, it is possible, note the deflection, to derive the kinetic ions energy from the equations (1) and (2) as follows:

$$E_{kin} = \frac{A_m}{x_m^2} \quad or \quad E_{kin} = \frac{A_e}{y_e} \qquad (3)$$

RESULTS

In this section, analysis of spectrograms is described.

The spectra contain a bright halo, which constitutes the origin of the parabolic ion traces, due to x-radiation and neutral particle produced by the laser-plasma interaction propagating straight through the electromagnetic field and parabolic traces associated to protons and other ions outgoing from the bright region.

Along a parabola, the energy gradually decreases from the origin towards the edge of the detector. In the spectrograms, the electrical and magnetic deflections are normalized to the respective fields in order to no have dependence from the spectrometer geometry. In particular, the image shown in Fig. 1 represents a typical TPS spectrum obtained by irradiating a 2 mm thick Al target.

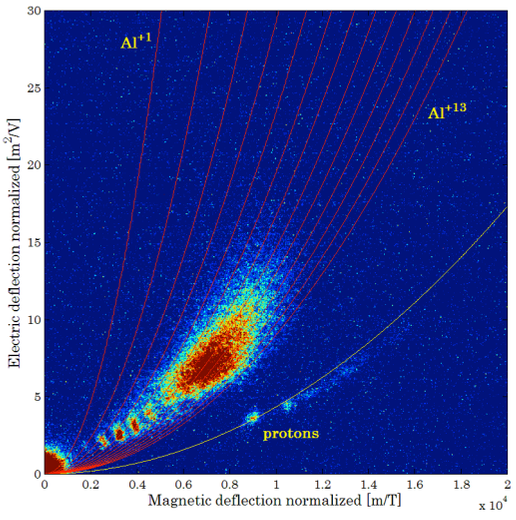

Figure 1: Spectrograms from a 2 mm thick Al target at LENS laboratory.

Protons and ions aluminium are observed: the proton maximum energy is 5 keV, while the Al ions have a maximum energy of 35 keV.

It is no possible to well-spatially resolve the aluminium charge states because the TPS is optimized for higher energy. In Fig. 2 is shown the spectrogram obtained irradiating a Mylar thin target at intensity of 10^{19} W/cm^2 (TNSA regime).

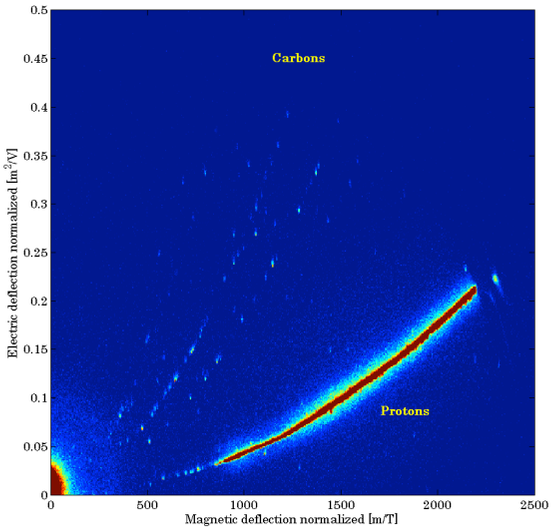

Figure 2: Spectrograms from a Mylar thin target at ILIL.

The maximum kinetic energy of the protons emitted from laser-produced plasma in the forward direction is 2 MeV.

CONCLUSION

Thomson Parabola spectrometer can provide useful detailed information on physical processes, ion species and charge states generated in single-shot laser experiments. Moreover, the use of MCP as the position-sensitive detector gives us the ability to measure the ion image online, immediately after the laser shot.

By means of the calibration of TPS it was possible obtain the kinetic energy of different ion species with a self-consistent technique.

REFERENCES

[1] E. L. Clark et al., Phys. Rev. Lett. 85 (2000) 1654.

[2] M. Hegelich et al., Phys. Rev. Lett. 89 (2002) 085002.

[3] W. Mrozet al., 2000 Rev. Sci. Instr.7 (2000) 1417.

[4] F. Schillaci et al., Acta Polytechnica 54(4) (2014) 285.

[5] M. J. Rhee, Rev. Sci. Instr. 55 (1984) 1229.

Calibration and characteriation of a Thomson Parabola Spectrometer

F. Schillaci[a,b], G.A.P. Cirrone[a,b], G. Cuttone[a], M. Maggiore[c], D. Margarone[b], G. Parasiliti Palumbo[d], P. Pisciotta[a], D. Rifuggiato[a], F. Romano[a],G. Russo[d,e], V. Scuderi[a,b], A. Tramontana[a,d], A. Velyhan[b,], A. Amato[a], G.F. Caruso[a], S. Salamone[a]

[a]*Istituto Nazionale di Fisica, Laboratori Nazionali del Sud*
[b]*Institute of Physics of the ASCR, ELI-Beamlines Project*
[c]*Istituto Nazionale di Fisica Nucleare, Laboratori Nazionali di Legnaro*
[d]*Physics Department, University of Catania*
[e]*INFN Section of Catania, c/o Physics Deparment, Catania University*

Abstract - A high energy resolution, high dispersive power Thomson Parabola Spectrometer has been developed at INFN-LNS in order to characterize laser-driven beams up to 30–40MeV for protons. This device has parallel electric and magnetic field to deflect particles of a certain charge-to-mass ratio onto parabolic traces on the detection plane. Calibration of the deflection sector is crucial for data analysis, namely energy determination of analysed beam, and to evaluate the effective energy limit and resolution. This work reports the study of monochromatic proton beams delivered by the TANDEM accelerator at LNS (Catania) in the energy range between 6 and 12.5MeV analysed with our spectrometer which allows a precise characterization of the electric and magnetic deflections. Also the energy and the *Q*/*A* resolutions and the energy limits have been evaluated proposing a mathematical model that can be used for data analysis, for the experimental set up and for the device scalability for higher energy.

Introduction

Thomson Parabola Spectrometers (TPS) is a device used to measure charge-to-mass and energy of charged ions. In recent years it has found applications in the diagnostics of laser accelerated ions. In the TPS set-up, the particles are dispersed in the direction perpendicular to the magnetic field according to their charge-to-momentum ratio and the electric field deflects the particles in its direction and the deflection is proportional to the charge-to-energy ratio. The distances of the deflected beam spot form the reference point, usually due to neutral radiation produced in laser-target interaction, can be used to characterize the beam in terms of energy, momentum and q-over-m ratio, which allows the analysis of the ion source properties as well. An efficient TPS have been realized at INFN-LNS within the ELIMED project. Here we shortly report the results obtained during the TPS calibration with INFN-LNS Tandem proton beams in the energy range between 6 and 12,5MeV [1]. Tandem allows to vary the energy of accelerated particles with a great precision and in a very narrow energy spread ($\Delta E=E<0,1\%$). During the experiment the deflection sector have been calibrated and also the energy resolution and the energy limit of the device have been evaluated.

TPS description and experimental procedure

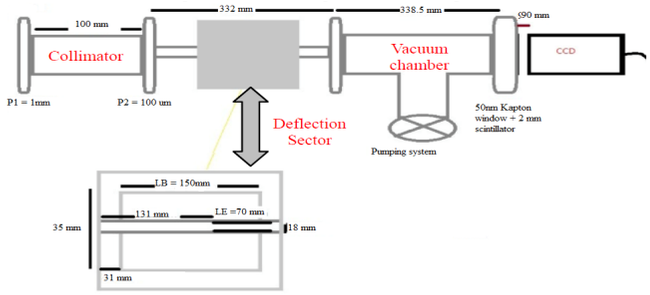

Figure 1: Layout of spectrometers

A TPS has been designed and realized at INFN-LNS for the characterization of ion beams up to 30-40MeV protons with an high energy resolution (some percent for higher energy). The device has been tested in different experimental runs at PALS laboratory and some results have been already reported. The TPS shows in fig.1 consists of four parts: the collimation system, the deflection section, the magnification drift and the imaging system. The whole system must operate under vacuum at the ideal pressure value of 10^{-5} mbar. The magnetic field is produced by an electromagnet made of two resistive coils and a H-shaped iron yoke ensuring good field uniformity along the particles trajectories. The field can be tuned up to 0,25T, corresponding to a measured coil current of 86,2A; for B > 0,2T a cooling system is required. The electric field is generated by two copper electrodes, 7 cm long, with a gap of 18 mm. A map of the electric field has been simulated and it can be assumed uniform along particles trajectory. It can be tuned up to 30 kV of electrical potential difference over the electrodes gap. Effective field lengths, used to treat magnetic and electric field in hard-edge approximation, are 18,82 cm and 8,04 cm, respectively. After passing the deflection and drift region, which allows to increase both particles deflections and separation among different traces, an imaging system is used as a detector. In this case it is a 2mm thick BC408 squared plastic scintillator with a side of 50 mm. It was set outside the spectrometer and the produced light was acquired with a CCD camera CHROMA C4-DSP, exposition time have been set to 10 sec. The vacuum chamber has been closed with a 50 nm thick kapton window. The electric and magnetic dispersion of the spectrometer have been calibrated using monochromatic proton beams produced by the INFN-

LNS Tandem. The TPS has been set at the 80° experimental hall of LNS laboratory. It was aligned using a laser directed down the beamline and its position within the pipe have been verified at three different points over a 5m length. Just before the spectrometer entrance was set a quartz beam viewer to check the beam profile. We have selected two different values of the magnetic field (0,09T and 0,07T) in order to not lose the low energy spot outside the detector surface. For the electric field we have selected the following values of potentials: 12 kV, 20 kV and 24 kV. For each beam energy the deflection section has been mapped combining all the acquired spots in a single image, the code used for this process is GIMP2. The overall image includes the cases of zero magnetic and electric fields, representing the origin of the spectrogram and it is a crucial point for data analysis. Points obtained with zero electric or magnetic field are the y and x axes of the reference frame respectively. The beam spot size have been evaluated to be 4 pixel = 340 μm, which means that the beam divergence is less than 0,18 mrad. This values have been evaluated from geometric consideration and without taking in account scattering effects on the pinholes and on the kapton window and scintillator. This is an important datum as such a small angle means that the system was very well aligned with the beamline.Infact Tandem delivers an almost parallel beam with a gaussian angular distribution and the above value is due to the fact that the beam portion entering the spectrometer is very close to the beam centroid.

Analysis of experimental data

The full procedure for carrying out the calibration of the deflection sector is reported in [1] and it is briefly described below. The ion beam profile on the quartz was inspected visually using a camera mounted on a view port perpendicular to the quartz viewer. The electric field calibration measurements are performed without magnetic field and viceversa. An example is in Figure 2. The equation describing the electric calibration hiperbola is:

$$E_{kin} = \frac{A_e}{y} \qquad (1)$$

where *Ae* is a factor taking in account the geometry of the system and the characteristic of the ion species. A similar equation can be evaluated for the magnetic field. The agreement between experimental calibration hyperbolas and theoretical equation is within the 7%. Combining the equation of an electric and a magnetic hyperbolas it is possible to have the equation of a parabolic trace on the detector screen. For different combinations of electric and magnetic fields, it was observed that the theoretical coefficient and the experimental coefficient result to be in agreement within the 10The energy resolution can be expressed as a function of the energy and of the field (electric or magnetic) by the derivative of the calibration hyperbolas.

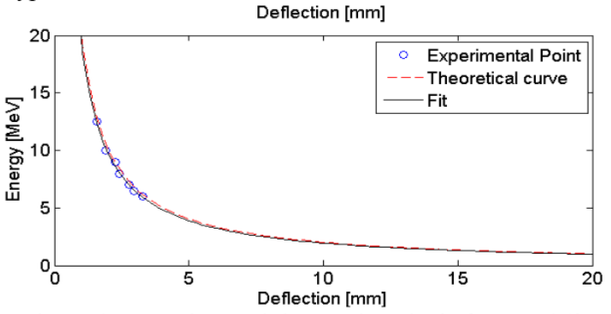

Figure 2: Experimental data and analysis for V = 24kV

Data analysis shows that protons with an energy of 40MeV can be resolved; the same resolution can be obtained for other ion species with maximum energy of (4**Q*) AMeV. However, energy resolution is strictly related to the Q/A resolving power strongly dependent on the electric deflection and on the beam spot size on the detector screen, which is δ =340 μm for the in exam. It can be evaluated calculating the smaller distance from the spectrogram center at which it is necessary to set two energy point of ions with close Q/A ratio in order to have them resolved. Hence their distance, in the vertical, or y axes, direction have to be bigger than δ. Calculations show that the energy limit for carbon ions is actually (1,2**Q*) AMeV and all six charge states are fully resolved at distance of 23,2 mm from the spectrogram origin. In this conditions protons are not affected and their energy limit remains of 40 MeV.

Conclusions

Thomson parabola ion spectrometer has been designed to study ions accelerated from the rear side of laser illuminated targets. The magnetic and electric deflection of the device has been calibrated using ions of well-known energy from the LNS Tandem accelerator in Catania, allowing the absolute energy of studied ions to be determined. Furthermore, the energy limit and the energy and Q/A resolutions have been determined. Calibration of the deflection sector is crucial for this kind of device, as it is affected by several error source such as the position of the spectrogram origin, presence of parasitic field etc. Once the deflection sector is calibrated data analysis of laser-accelerated ions can be performed in a more precise and robust way. Moreover the proposed model, results useful for setting up the TPS and to study its scalability for realize devices suitable for higher energy. The proposed study on energy limit and energy resolution is also crucial for the scalability of the system and the realization of a more performing device with very high-energy resolution suitable for the ion beams that will be produced at ELI-beamlines.

References

[1] Schillaci et al, 2014 *JINST* **9** T10003 doi:10.1088/1748-0221/9/10/T10003.

Medium Resolution Mass Separator for SPES Project at LNL

A. D. Russo[1], L. Calabretta[1] , M. Comunian[2] , L. Bellan[2]

1) INFN Laboratori Nazionali del Sud, Catania, Italy

2) INFN Laboratori Nazionali di Legnaro, Padova, Italy

Abstract -The SPES facility need a High resolution Mass Separator (HRMS) and also a Medium Resolution Mass Separator (MRMS) to remove the isobar beams produced in the production target and the isobar contaminant introduced by the charge breeder. The description of the MRMS and its characteristics are here presented.

INTRODUCTION

The goal of SPES project is to provide, to the LNL users, radioactive beams having mass between 210 and 80 amu with high state of charge. Unfortunately, in this range the mass differences between nuclei that have the same number of nucleons (A) but different atomic number (Z) are very small.

The SPES facility uses a HRMS to obtain the ions of interest and to remove isobar ions contaminant produced inside the target. After the HRMS, the beam is send at a charge breeder to increase its charge state. To clean the radioactive beam from contaminants produced by the charge breeder a MRMS is mandatory.

The layout of SPES project at LNL is shown in Fig. 1.

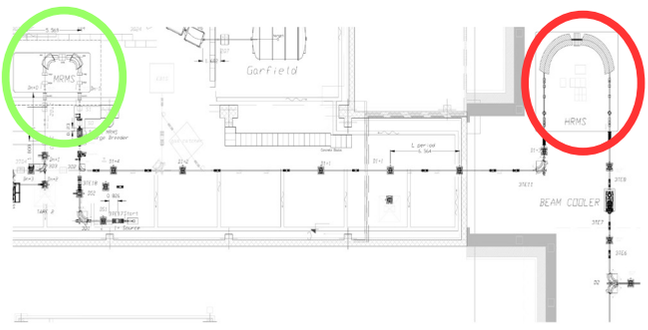

Figure 1: The SPES layout: the red circle show the 1+ separator, the green circle show the 19+ separator.

To study of MRMS was optimised for the most interesting radioactive to be delivered by SPES project, this is the Tin 132 (^{132}Sn), with charge states 19+ and with energy of 3.04 MeV. The MRMS is placed on a high voltage platform (120kV), how shown in Fig. 2.

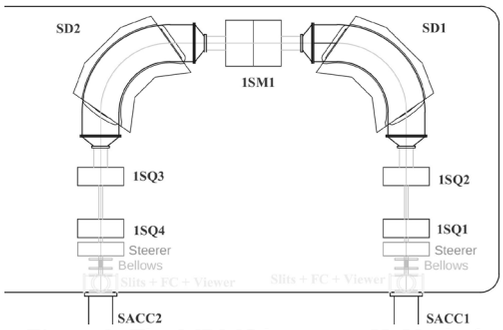

Figure 2: The MRMS layout on H. V. platform.

According to the study of the charge breeder [1], it was estimated that a mass resolution of 0.1% should be sufficient to clean up the beam from the majority of the contaminants introduced by the charge breeder.

The goal of MRMS is to obtain a mass resolving power equal to 1000.

The general specifications of the reference beam are summarized in Table 1.

Table1: Beam reference specifications

Beam charge	19+
Beam energy	3.04 MeV
RMS Normalized Beam emittance in both planes	0.1 π mm mrad
Twiss parameters in both planes	α=0 β=0.5
X_{RMS}	2.66 mm
X'_{RMS}	5.33 mrad
Y_{RMS}	2.66 mm
Y'_{RMS}	5.33 mrad

OPTICS DESIGN AND THE PROPOSED LAYOUT

We performed the optical design for the beam reference using the TraceWin code [2], a computer program that solves beam transport problems at first order using the matrix formalism and the high order using multiparticle dynamics.

The Fig. 2 shows the MRMS layout in the last configuration. In this configuration there are four electrostatic quadrupole (ISQ), two magnetic dipole (SD), one multipole (SM1), two steerers and many diagnostic devices.

The beam line study

The layout of the MRMS is symmetric in order to reduce the optical high order aberrations.

IFig. 3 shows the beam envelope along the MRMS. It is parallel at the symmetric plane, in x and y direction.

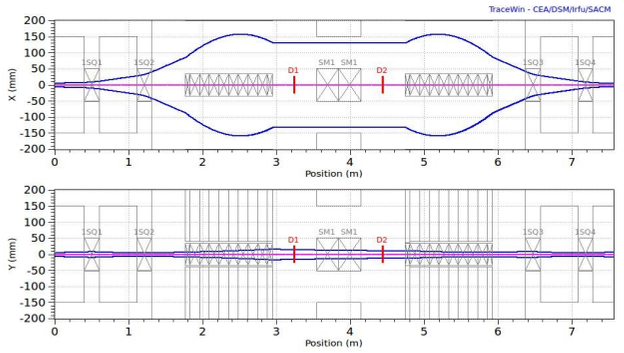

Figure 3: The MRMS envelope.

Resolving Power calculation

From the first order matrix is possible to obtain the first order Resolving Power [3] at the RMS value (1).

It is

$$RP = \frac{m}{\Delta m} = \frac{M_{16}}{4 \cdot X_0 \cdot M_{11}} = 6489 \qquad (1)$$

To optimize the system is necessary to introduce one multipole at the symmetry plane of separator. Moreover curvature radii on the pole faces of both the two dipoles are necessary in order to reduce the high order aberration of the system.

The features of Quadrupoles and Dipoles are in table 2.

Table 2: Elements general characteristics

Quadrupoles	**ISQ1 - ISQ2**	**ISQ3 - ISQ4**
Voltage at the pole tip [V]	-4710	-3892.5
Length [mm]	200	200
Aperture radius [mm]	50	50
Dipoles	**SD1 - SD2**	
Faces edge β_{in} and β_{out} [°]	33.35	
Faces radius edge curvature R_{in} and R_{out} [mm]	950 - 750	
Bending Radius [mm]	750	
Vertical aperture [mm]	35	
Horizontal aperture [mm]	200	
Magnetic Field [T]	0.20238	

The voltage component of multipole has been optimized by TraceWin code, but their values are not presented because further detailed studies must be performed.

To verify the effective resolving power of the system, three different beam with 0.1% mass difference are simulated by TraceWin code representative of the MRMS, Fig 4.

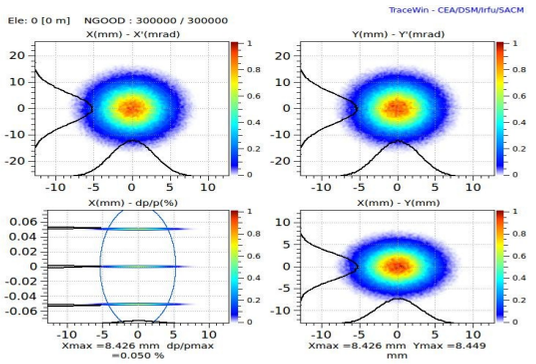

Figure 4: The beam at the MRMS entrance.

The Fig. 4 is the output of TraceWin. It is quite clear how well we can distinguish the three peaks related to three mass values with difference of 0.1% Fig. 5 .

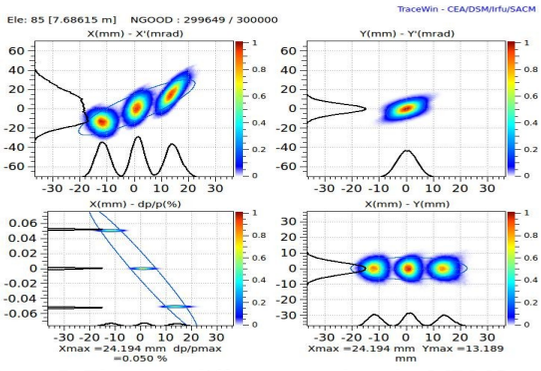

Figure 5: The three difference peak at the MRMS exit.

CONCLUSION

According to the proposed resolving power goal in the premise, the MRMS line has been designed to purify a 3.04 MeV $^{132}Sn^{19+}$ beam from contaminant with a mass difference equal to 0.1%. The design, including optics study and devices arrangements, provides a good compactness of the separator, which can be placed on a H.V. platform. More studies on multipole voltage correction component are necessary because the performance on MRMS depend strongly on these.

REFERENCES

[1] A. Galatà, *private communication*

[2] TraceWin manual http://irfu.cea.fr/Sacm/logiciels/index3.php.

[3] K. L. Brown et al., TRANSPORT, a computer program for designing charged particle beam system, SLAC-91 (1997).

HELNED: Helium-3-free low-cost neutron detectors

Massimo Barbagallo[1], Luigi Cosentino[2], Carmelo Marchetta[2], Alfio Pappalardo[2], Carlotta Scirè[2], Sergio Scirè[2], Gianfranco Vecchio[2] and Paolo Finocchiaro[2]

1) INFN Sezione di Bari, via Orabona 4, 70126 Bari, Italy
2) INFN Laboratori Nazionali del Sud, via S.Sofia 62, 95125 Catania, Italy

Abstract - We developed a technique for thermal neutron detection not making use of ^{3}He. As a neutron converter we used ^{6}LiF, being the neutron capture cross section of ^{6}Li very well known and with only an alpha and a triton in the exit channel. We can deposit thin layers of converter onto several different substrates, to be placed on top of solid state detectors capable of efficiently detecting the decay products.

INTRODUCTION

For the detection of thermal or low energy neutrons, as a viable alternative to ^{3}He tubes [1,2], semiconductor-based detectors can be used in combination with a neutron reactive film, usually called neutron converter, which converts neutrons into charged particles. The two nuclear species commonly considered suitable neutron converters are ^{6}Li (natural abundance ≈7%, thermal neutron cross section ≈940b) and ^{10}B (natural abundance ≈20%, thermal neutron cross section ≈3840b). The corresponding neutron capture reactions involved are:

$$^6Li + n \rightarrow {}^3H\ (2.73\ MeV) + \alpha\ (2.05\ MeV)$$

and

$$^{10}B + n \rightarrow {}^7Li\,(1.01\,MeV) + \alpha\,(1.78\,MeV)$$

$$^{10}B + n \rightarrow {}^7Li\,(0.84\,MeV) + \alpha\,(1.47\,MeV) + \gamma(0.48\,\mathrm{MeV})$$

We decided to choose ^{6}Li because after capturing a neutron it has a unique decay channel, with no gamma rays, with a higher available kinetic energy and with lighter particles produced, therefore easier to detect than in the case of ^{10}B. We use it in form of LiF, enriched at 95% in ^{6}Li, that is a very stable and no expensive salt which we can deposit uniformly as very thin layers onto rather large substrates up to several hundreds of cm^2. Based on these assumptions in this paper we will show that cheap solid state neutron detectors with good n/gamma discrimination can be built, even though having a low intrinsic efficiency.

A SILICON PAD FOR NEUTRON DETECTION

The charged particles lose some of their energy passing through the converter; the energy loss depends on the converter material itself, the particle type and its energy, and therefore the choice of film thickness that can be practically used is limited. Moreover, the reaction products entering the detector must have sufficient energy in order to produce signals large enough for particle discrimination from the gamma background.

In Figure 1 we sketched the conversion mechanism of a neutron inside the ^{6}LiF layer. As the two reaction products are emitted in opposite directions, only one of them may enter the sensitive layer and be detected. The case shown makes use of a double-sided silicon pad detector, 3 cm x 3 cm, 300 µm thick, with a neutron converter on each face. In our tests, in view of investigating different configurations, we employed two slightly different converter thicknesses and substrates, namely 1.8 µm on glass and 1.5 µm on plastic.

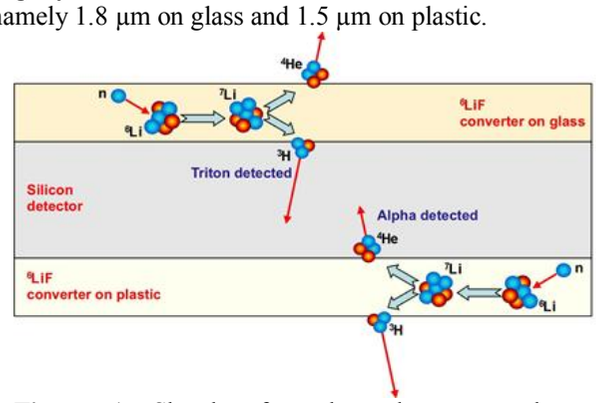

Figure 1. Sketch of a thermal neutron detector consisting of a double-sided silicon detector coupled with two ^{6}LiF neutron converters. As the neutron energy is very low, the reaction products are emitted in opposite directions in the laboratory frame, and only one is detected.

The ^{6}LiF depositions on the substrates were done in house, using an evaporator complex, and the choice of having the converter independent of the detector allows an efficient modularity and operation.

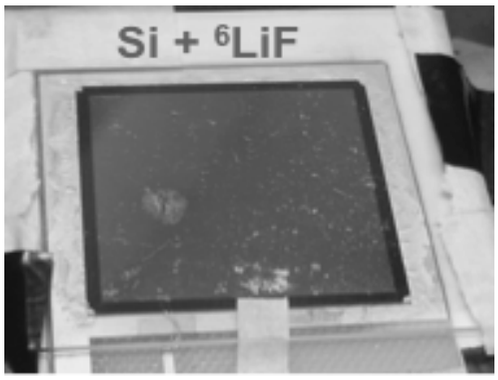

Figure 2. The silicon detector sandwiched between two ^{6}LiF neutron converters.

In figure 2 we show a picture of a detector prototype, which was sandwiched between the two converters and then placed inside a neutron moderator made from

polyethylene blocks (Figure 3), in order to be tested with an AmBe neutron source.

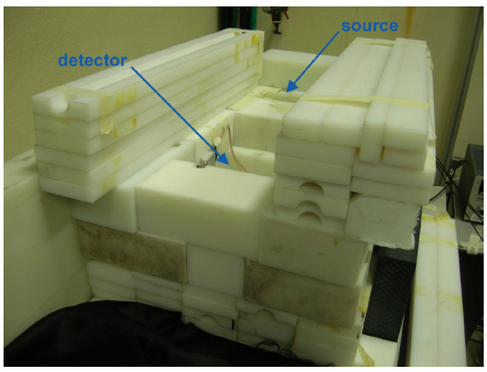

Figure 3. The neutron moderator made from polyethylene blocks.

We remark that such a source, besides producing neutrons with a broad spectrum centered around 4-5 MeV, produces also as many high energy gamma rays (≈ 4.4 MeV) as well as a huge amount of ≈59 KeV low energy gamma rays. We performed such a test, under different configurations, in order to disentangle the detector behavior. In Figure 4 we superimposed three typical spectra obtained with the detector under the following respective conditions: no neutron source (area 1), converters installed; with neutron source but no converter (area 2); with neutron source, converters installed (area 3). What immediately sticks out is that the spectrum without source, only due to background gamma (and cosmic) rays, lays entirely below about 0.3 MeV.

When exposing the detector without neutron converters to the AmBe source, the only contribution to the spectrum comes from gamma rays. In this case we can see that such a contribution lays below ≈ 0.5 - 0.6 MeV. Conversely, when installing the two converters and exposing the sandwich to the neutron source, we see a totally different spectrum shape, due to the detection of alpha and triton particles, coming from the neutron capture on ^{6}Li followed by the decay of ^{7}Li into alpha and triton. The alpha contribution in the spectrum is between 0.6 MeV and 1.7 MeV, whereas the triton contribution is between 1.7 MeV and 2.7 MeV, exactly as expected from calculations and simulations, and both represent a perfect signature of a neutron detection.

The macroscopic cross section of ^{6}LiF (enriched in ^{6}Li at 95% as it is our case) for thermal neutron capture is 57 cm^{-1}, which for our converters 1.8 µm and 1.5 µm thick corresponds to intrinsic efficiency of respectively ≈1% and ≈0.85%. In case of two identical 1.8 µm converters the intrinsic efficiency would be 2%. As for the detection efficiency, it depends on the energy loss of the two reaction products inside the converter itself and in the dead layer of the silicon detector, and on the electronic threshold. An accurate calculation was performed, giving a value around 75%. Under the described configuration a thermal neutron impinging on the detector will have a ≈1.5% probability of being detected. In order to increase this probability one will have to increase the overall active area, either tiling or stacking several identical detector sandwich assemblies.

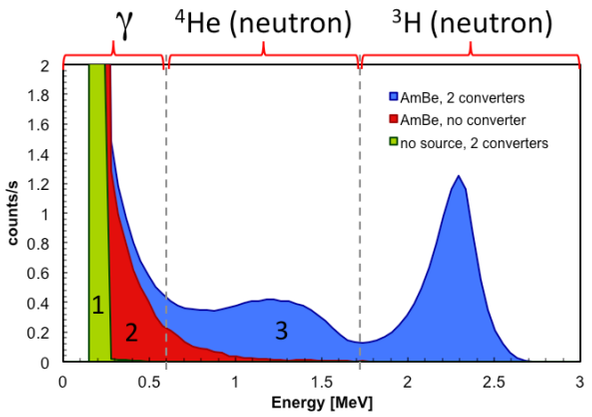

Figure 4. Three typical spectra obtained with the detector under the respective conditions: no neutron source, converters installed (area 1); with neutron source but no converter (area 2); with neutron source, converters installed (area 3). The gamma contribution to the spectrum is roughly below 0.6 MeV; the alpha contribution between 0.6 MeV and 1.7 MeV; the triton contribution between 1.7 MeV and 2.7 MeV.

CONCLUSION

We have developed a low-cost technique to build thermal neutron detectors, based on ^{6}LiF converters coupled to particle detectors, likely useful in several applications as a replacement of the traditional ^{3}He tubes. We are actively working on further improvements, in particular making use of scintillators, in order to increase the intrinsic (several layers) and the geometrical (wider area) efficiency.

ACKNOWLEDGMENTS

We are indebted to Paolo Peerani and Vittorio Forcina of the European Commission, Joint Research Centre, Institute of Transuranium Elements, Ispra, Italy, for making available the AmBe neutron source and the moderator. Apart from that, their advice and suggestions were invaluable.

REFERENCES

[1] 1. C. Manfredotti, A. Lo Giudice, F. Fasolo, E. Vittone, C. Paolini, F. Fizzotti, A. Zanini, G. Wagner, C. Lanzieri, Nucl. Instr. And Meth. A552, 131-137 (2005)

[2] 2. R. J. Nikolic, C. L. Cheung, C. E. Reinhardt, T. F. Wang, Nanotech 2006 Boston United State, UCRL-PROC-219274 (2006).

[3] 3. D.S. McGregor, M. D. Hammig, Y. H. Yang, H. K. Gersch, R.T. Klann, Nucl. Instr. And Meth. A500, 272-308 (2003)

Mapping the inter-strip response of the Silicon layers of the FARCOS telescopes

L. Acosta[1,2], L. Auditore[3], C. Boiano[4], G. Cardella[1], L. Carraresi[5,6], A. Castoldi[7,4], E. De Filippo[1], L. Francalanza[1], C. Guazzoni[7,4], G. Lanzalone[1,8], I. Lombardo[9], T. Minniti[1,3], E. Morgana[3], S. Norella[3], A. Pagano[1], E. V. Pagano[1], M. Papa[1], T. Parsani[7,4], S. Pirrone[1], G. Politi[1,10], L. Quattrocchi[3], F. Riccio[7,4], F. Rizzo[10,11], P. Russotto[1], F. Taccetti[6], M. Trimarchi[3], A. Trifirò[3], G. Verde[1], P. Zambon[7,4]

1) INFN, Sezione di Catania, Italy
2) Instituto de Física, Universidad Nacional Autónoma de México, Mexico D. F. 01000, Mexico
3) Dipartimento di Fisica, Università degli Studi di Messina, Italy and INFN – Gruppo Collegato di Messina
4) INFN, Sezione di Milano, Italy
5)Dip. di Fisica e Astronomia, Univ. degli Studi di Firenze
6) INFN, Sezione di Firenze
7) Politecnico di Milano, Dip. Elettronica, Informazione e Bioingegneria, Milano
8) Università degli Studi di Enna "Kore", 94100 Enna, Italy
9) Università degli Studi di Napoli Federico II, Dip. di Scienze Fisiche Napoli and INFN, Sezione di Napoli, Italy
10) Università degli Studi di Catania, Dipartimento di Fisica e Astronomia, Catania, Italy.
11) INFN – Laboratori Nazionali del Sud, Catania, Italy

Abstract – In the framework of the qualification of the response matrix of the Silicon layers of the FARCOS telescopes we performed a systematic investigation of the impact of particle interaction in the inter-strip region on the induced signal shape.

INTRODUCTION

Differently from existing correlator systems, such as MUST2 and HiRA, FARCOS aims also at identifying in charge and mass even particles stopping in the first detection layer. This is made possible by performing pulse shape analysis of the induced current (mapped in the preamplifier output waveform profile). To this aim it is crucial to perform thorough characterizations of the silicon detector layers in terms of both the linearity of the amplitude response and of the efficiency and collection properties as a function of the point of incidence. We have experimental evidence – and was also observed in the literature for other strip detectors [1], [2], [3], [4], [5], [6] – that inter-strip incidence (i.e. the incidence in the gap between two strips) not only causes trivial charge division but also alters the shape of the induced signal. The phenomenon is more pronounced depending on the energy and ion type.

We performed a systematic investigation of the impact of particle interaction in the inter-strip region on the induced signal shape. The approach we chose in order to guarantee the systematicity is the use of a pulsed monochromatic ion beam – featuring an average number of particles per pulse well below one particle per bunch – with high energy and spatial resolution as probing tool, in addition we decided to digitize the whole output waveform at all strips for each acquisition. As a precious guide for the interpretation of the experimental results we performed an accompanying set of simulations by means of a custom semi-analytical code [7] able to compute the 3D electron-hole transport and therefore calculate the induced charges and currents at any electrode by means of the Ramo Theorem [8].

EXPERIMENTAL SETUP

The pulsed monoenergetic proton beam coming from the DEFEL beam-line [9] of the 3MV Tandetron accelerator of the LaBeC (Laboratorio di Tecniche Nucleari per i Beni Culturali) [10], located in Sesto Fiorentino (FI), Italy, is an attractive tool to probe the response of the detector-frontend system at different levels of charge injection. At DEFEL the continuous beam coming from the accelerator is deflected transversally across a slit allowing a bunch of protons (or ions) to proceed downstream through an aperture only during a very short time interval of the order of 1 ns. The adjustment of the size of the aperture with a motorized slit, and of the intensity of the continuous beam, is the key feature to create a pulsed beam with a variable and finely controllable number of particles in each pulse (down to an average value much below 1 proton per trigger and with a position of interaction in a defined area of down to better than 40 μm × 40 μm) [11]. We probed the detector response matrix of DSSSDs of the two thicknesses used in the FARCOS telescopes. The detectors have been characterized both in front injection (protons incident on

the junction side) and in back injection (protons incident on the ohmic side). Different beams were accelerated: 1 MeV (16.6 µm projected range, 0.8 µm straggling), 3 MeV (92 µm projected range, 4 µm straggling) and 5 MeV (216 µm projected range, 9.5 µm straggling) protons and 7.5 MeV Li ions (17.7 µm projected range, 0.6 µm straggling) to explore the impact of different ions and different ionization profiles. For sake of clarity we discuss in the present paper only data relative to front injection and to the 300 µm thick detectors. The vacuum level in the experimental chamber is kept below 1×10^{-4} mbar during all the measurements. The pulsed beam repetition rate is kept constant for all the measurements and equal to 100 Hz. The horizontal and vertical slits opening that defines the beam spot size was 200 µm. The DSSSD was biased at 5 V over-depletion in all the measurements.

PHENOMENOLOGY OF INTER-STRIP EVENTS

Profiting of the high spatial resolution of the beam we performed several scans across the strips to record the waveform response and to investigate their shape as a function of the position of interaction. Considering the single-proton peak, it is possible to derive the strip profile and evaluate the amount of sharing events between neighbor strips. In the following we report the results of the irradiation of the inter-strip region in the case of 1 MeV and 3 MeV protons.

Figure 1 shows the scatter plot of the amplitude of the output waveforms measured at two neighbor junction-side strips. The waveforms have been baseline-subtracted and digitally filtered with a 201—taps-wide triangular filter. In the case of the deep ionization caused by 3 MeV protons we apparently observe a "conventional" charge sharing phenomenon, as demonstrated by the straight lines on which the experimental data gather. Each line corresponds to the interaction with the detector of bunches composed by an increasing number of protons.

If we lower the energy of the impinging protons to 1 MeV, so that we have a shallower ionization profile, the scatter plot will be drastically changed, as shown in Figure 2a. Once again the two clusters marked with A and C correspond to the full collection of a single proton at one of the two neighbour strips. However shared events – giving a signal on both strips – do not lie on the line connecting the two clusters –corresponding to fixed sum of the two amplitudes, i.e. complete charge collection – but feature a lower total amplitude, due to a charge loss. The same phenomenon is "shadowed" on the scatter plot relative to the ohmic side strips, shown in Figure 2b, where we notice that sharing events gather on two parallel lines. The line joining the two clusters pertaining to full collection are events featuring a full collection on one of the two junction-side strips and suffering sharing between the two ohmic-side strips. The line at lower amplitudes is due to events suffering sharing both on the junction-side strips and on the ohmic-side strips.

REFERENCES

[1] J. Yorkston et al., NIMA 262 (1987) 353.
[2] S. Takeda et al., NIMA 579 (2007) 859.
[3] Y. Blumenfeld, NIMA 421 (1999) 471.
[4] J. Hayward et al., NIMA 586 (2008) 215.
[5] D. Torresi et al., NIMA 713 (2013) 11.
[6] L. Grassi et al., AIP Conf. Proc. 1491(2012).
[7] A. Castoldi et al., 2012 IEEE Nuclear Science Symposium and Medical Imaging Conference Records (2012) 961.
[8] S.Ramo, Proc. IRE, vol. 27, pp. 584-585, 1939.
[9] F. A. Mirto et al., NIMB 266 (2008) 2113.
[10] P.A. Mando', Nuclear Physics News 19 (2009) 5.
[11] A. Castoldi et al., 2013 IEEE Nuclear Science Symposium and Medical Imaging Conference Records, 2013.

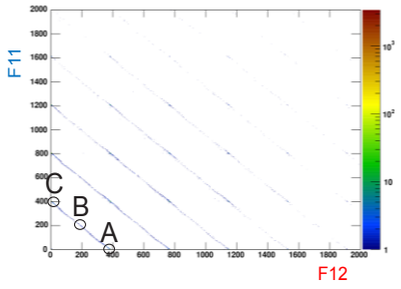

Figure 1. Scatter plot of the amplitudes of the signals measured at two neighbour junction-side strips in the case of 3 MeV protons impinging on the junction-side in the inter-strip region.

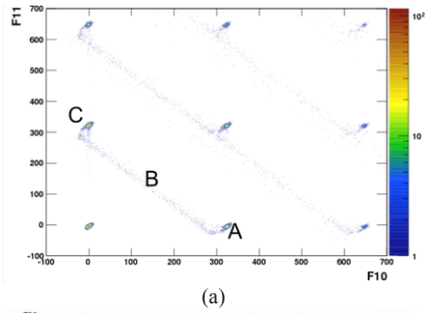

(a)

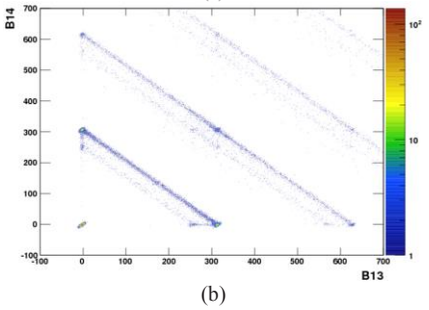

(b)

Figure 2. Scatter plot of the amplitudes of the signals measured at two neighbor (a) junction-side strips, (b) ohmic-side strips in the case of 1 MeV protons impinging on the junction-side in the inter-strip region.

New spectrometer for cluster ion beam induced luminescence

H. Ryuto,[1)] F. Musumeci,[2,3)] A. Sakata,[1)] M. Takeuchi,[1)] G. H. Takaoka[1)]

[1] *Photonics and Electronics Science and Engineering Center, Kyoto University, Kyoto 615-8510, Japan*
[2] *Department of Physics and Astronomy, Catania University, Catania, Italy*
[3] *INFN Laboratori Nazionali del Sud, Catania, Italy*

Abstract A new spectrometer to detect the luminescence originated by the collision of cluster ions on solid materials is presented. Eleven photomultipliers (PMT) with band-pass interference filters allowed us to detect the luminescence within the wavelength range from 300 to 700 nm. Experiments confirm the presence, foreseen by molecular dynamic (MD) simulation, of high temperatures and pressure during the collision.

INTRODUCTION

Ion beams are widely employed in the semiconductor industry for processing. The luminescence induced by irradiation of ion beams at MeV energy can be used to obtain information on the impurities and imperfections within the near surface region [1,2]. Even the irradiation effects of cluster ion beams have been studied [3,4]. The clusters are aggregates of atoms or molecules bound by intermolecular forces. They have often very large mass-to-charge ratio. So, cluster ions accelerated with several kV voltages are relatively slow and the lattice disorder, induced by the irradiation by a cluster ion beam, is small even for large sputtering yields [4]. According to the MD calculations the effective temperature of the clusters could reach some tens of thousand K and the pressure some GPa [5]. This should enhance the chemical interactions between the molecules composing the clusters and the target. Moreover, the high temperature suggests the possibility of some photonic emission during the collision process. Indeed, previously we reported the detection of photons during the irradiation of silicon and gold targets by water cluster ions accelerated at 9 kV [6].

We called such an emission “cluster ion beam induced luminescence” (CIBIL). To achieve spectral information, useful to better understand the phenomenon, the cluster irradiation system in Kyoto University has been improved and a single photon spectrometer has been developed at LNS and mounted and used in Kyoto.

MATERIAL AND METHODS

A full description of the set up used was reported elsewhere [7]. Here we resume the essential information. Figure 1 shows a sketch of the apparatus and an enlarged view of the photon detectors. The set up consists of three vacuum chambers. Water and argon cluster ion beams were produced by the adiabatic expansion method [8], were injected, at 0.30 and 0.45 MPa respectively, into the vacuum chamber to produce clusters. The clusters were ionized by electron ionization, using a special oxide filament cathode. Small clusters were eliminated from the beam applying a retarding voltage of 9 V. The applied

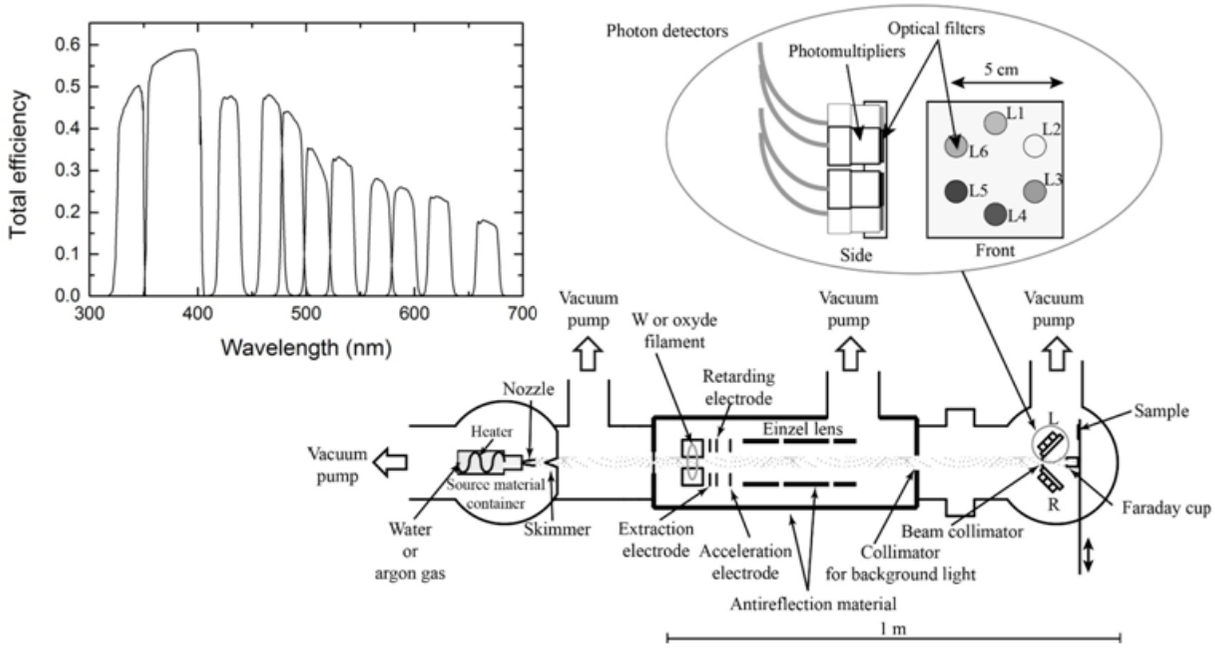

Figure 1: Experimental set up and filter+PMT efficiency.

acceleration voltage ranged between 3 and 9 kV. The beam was focused using an einzel lens. The sample and a Faraday cup, able to measure the beam intensity, were attached on a linear motion feedthrough. The photons detection system, consists of 12 PMTs put on 2 holders placed at left and right side of the beam axis, upstream of the sample, their windows being on a vertical plane (see fig. 1). This compact geometry increases the collection efficiency of the PMTs. Eleven band-pass filters with central wavelengths from 340 to 670 nm, were attached in front of the PTMs. To maximize the efficiency of the system and suppress the infrared leakage of the band-pass filters, two types of PMTs, the multialkali R7400P-01 and the bialkali R7400P, both produced by Hamamatsu Photonics, were used. The global efficiency of the system, which includes the filters transmission spectrum and the PMT quantum efficiency, is shown in the plot of figure 1. The whole spectrometric system has a sensitivity four order of magnitude higher than that of ordinary CCD spectrometers.

Materials are chosen to compare the obtained results with the forecast of some simulations available in the literature, mainly based on the use of MD [5]. For this purpose we used argon and water as cluster beams and five different targets. Argon and water clusters are very different both for the chemical reactivity and for the bonding forces between the components of cluster. Moreover, the emission spectrum in the optical range of water is very low compared with that of Argon. As target three metals (Au, Fe, Al) a semiconductor (Si) and a dielectric (SiO_2) are chosen.

RESULTS AND DISCUSSION

In the case of water clusters we obtained an unexpected result: CIBIL is anisotropic in the case of metallic targets. Figure 2 shows the intensities measured without filters, in the different positions of the holders for an Au target. In this figure an isotropic (Lambertian) source should correspond to the same value of the intensity measured in the different positions. It is possible to see that the emission is strongly anisotropic. On the other hand the luminescence of SiO_2 is isotropic.

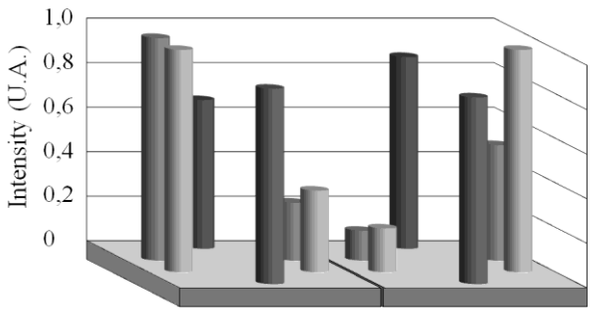

Figure 2: Evidence of strong anisotropy in the CIBIL of water on Au target.

To explain this behavior we are preparing a system able to give complete information on the spatial distribution of the emitted radiation and to measure the various spectral components under the same angle.

Ar clusters produce, with all targets, an isotropic CIBIL always characterized by a maximum corresponding to the blue maximum of the Ar I spectrum [9]. This maximum, if seen with our spectral system, should be very thin: the calculated values for the two filters at the two wavelength around the maximum are about an order of magnitude lower of the measured ones. This discrepancy can be overcome considering a broadening of the argon spectrum lines due to the high temperature and pressure, foreseen by MD simulations (see figure 3).

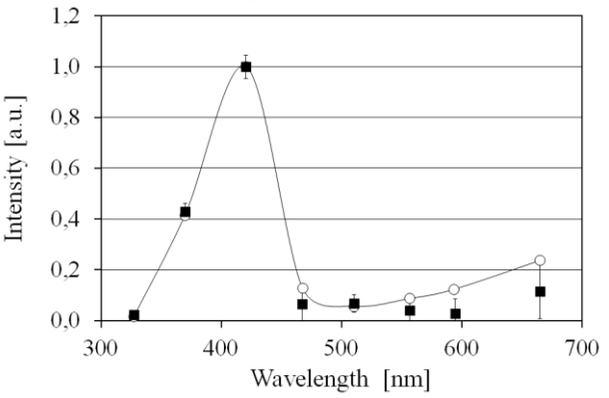

Figure 3: ■ Experimental spectrum of CIBIL of Ar on Al target. ○ Spectrum calculated assuming a maximum temperature of 20000 K and a pressure of few GPa.

Summarizing our experiment have shown that clusters are nanostructures very interesting both from the fundamental and from the applicative point of view because are able to give information on the behaviour of matter in very extreme conditions.

REFERENCES

[1] P. D. Townsend, P. J. Chandler, L. Zhang, Optical Effects of Ion Implantation, Cambridge University Press, Cambridge, 1994, chapter 4

[2] R. J. Brooks, D. E. Hole, P. D. Townsend, Nucl. Instrum. Meth. B190, 136 (2002)

[3] I. Yamada, Nucl. Instrum. Meth. B148, 1 (1999).

[4] G. H. Takaoka, H. Ryuto, M. Takeuchi, J. Mater. Res. 27, 806 (2012).

[5] H.-P. Chen, U. Landman, Science 260, 1304 (1993).

[6] H. Ryuto, F. Musumeci, A. Sakata, M. Takeuchi, G.H. Takaoka, Rev. Sci. Instrum. 85, 02C303 (2014).

[7] H. Ryuto, F. Musumeci, A. Sakata, M. Takeuchi, and G. H. Takaoka, Rev. Sci. Instrum. 86, 023106 (2015).

[8] O. F. Hagena, W. Obert, J. Chem. Phys. 56, 1793 (1972).

[9] NIST Atomic Spectroscopy Databases, http://www.nist.gov/pml/data/atomspec.cfm..

A Multiaxis Motion Control System based on an Fpga

G. De Luca[1], G. Limoli[1,2]

1) INFN Istituto Nazionale di Fisica Nucleare - Laboratori Nazionali del Sud
2) DIEEI Dipartimento di Ingegneria Elettrica, Elettronica ed Informatica - Università degli Studi di Catania

Abstract - The main purpose of this project is the realization of an embedded system based on an FPGA in which a multiaxis motion control system is implemented. The aim is to obtain a device independent of architecture and FPGA producer companies in which a modular hardware is installed, able to guarantee exportability, computational speed, accuracy, power efficiency, compactness and especially lower cost.

INTRODUCTION

Most mechanical systems used at INFN-LNS, like robotic arms, real-time diagnostic beams, x-ray scanners, etc., in which DC motors with incremental encoders are used, need dedicated motion control systems. The use of an FPGA to realize this kind of control is due to the advantage over other technologies like MCU and ASIC. Compound to the MCU, it provides better performance, taking advantage of hardware parallelism that allows, in this case, control of a certain number N of axis, according to the amount of logical elements and multipliers present in the model of FPGA adopted. Besides, it takes advantage of the MCU in terms of bit resolution and system-clock frequency. On the other hand, the use of an FPGA in instead of ASIC reduces the time to market and allows the realization of reconfigurable and reprogrammable devices. An FPGA offers also significant economic and versatility advantages over COTS. VHDL language is used to describe hardware in modules, compatible in different IDEs. These modules are easily adaptable on different applications and can be resynthesized in different FPGAs with few changes.

SYSTEM OVERVIEW

The realized system consists of an FPGA development board, a RISK-based MCU, a personal computer, a motor driver and N motors (Figure 1). It can control N axis in speed and position. The number N depends on the total number of logical elements and multipliers available on the FPGA used. In this case, a DE0-Nano board has been used. It embeds Altera's Cyclone® IV FPGA and contains the modular hardware description in VHDL code (look the next paragraph). The ATmega2561 microcontroller communicates with the Fpga using SPI and with Computer through SI. In the MCU a firmware is implemented to manage the setting of parameters in VHDL-modules and the reading of position/speed values. The computer is used as a GUI. The L-6203-based motor driver can support up to four motors. Finally, Faulhaber motors are equipped with HEDS-5400 encoders that have 100 lines per revolution.

FPGA SYSTEM OVERVIEW

The hardware description, developed using Quartus II web edition, consists of different modules apt to elaborate signals that come from the incremental encoders. The main modules, written in VHDL, are: Encoder Reader, Profile Generator, PID and PWM generator (Figure 2 in the next page).

- The **encoder reader** module includes a digital filter (reduces glitches and noises originating from the encoder), a quadrature decoder (achieves higher resolution quadrupling the number of impulses per revolution), a position-counter and a speed-meter.

- The **profile generator** module includes a ramp generator used in speed control and a trapezoidal generator used in position control. It allows smooth speed profiles and preserve mechanical parts of the system. A finite state machine is implemented in the programmable logic device to describe the trapezoidal generator (Figure 3 in the next page).

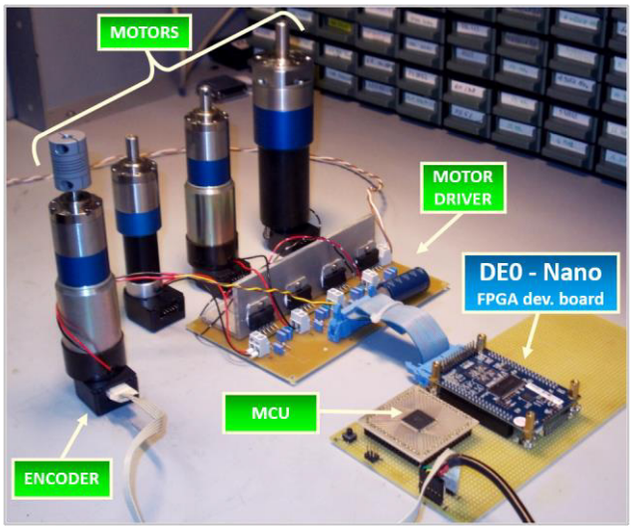

Figure 1: Photograph of the realized system.

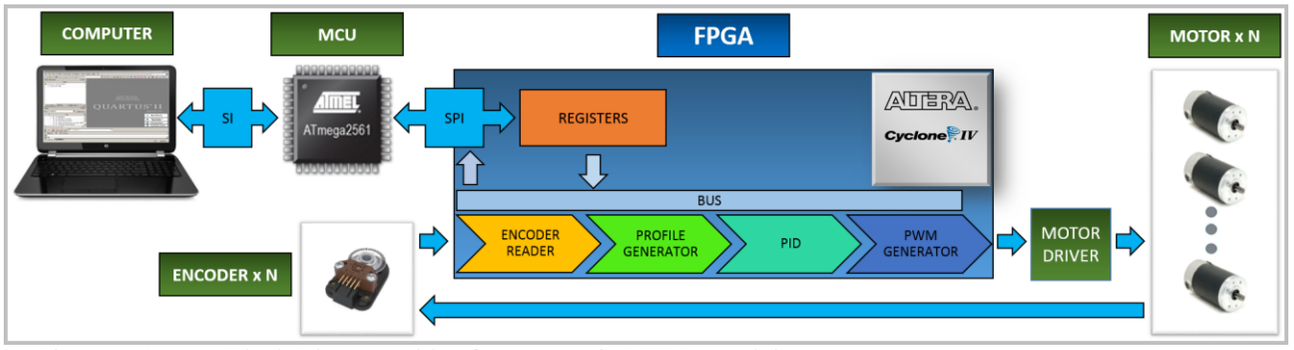

Figure 2: System Block Diagram with a focus on main VHDL-Modules.

- The **PID** module attempts to minimize the error between the required and detected (by the encoder reader) speed or position.

- The **PWM generator** module encodes the signal that comes from PID into a modulated pulsing signal, used as input by motor-drive.

.

Each module contains modifiable parameters that can be set to fulfill the requirements of the motors, encoders and mechanical system used. It is possible, for example, to modify bit-resolution, PWM-resolution, PID parameters, the acceleration step of the profile generator or of the ramp generator and so on.

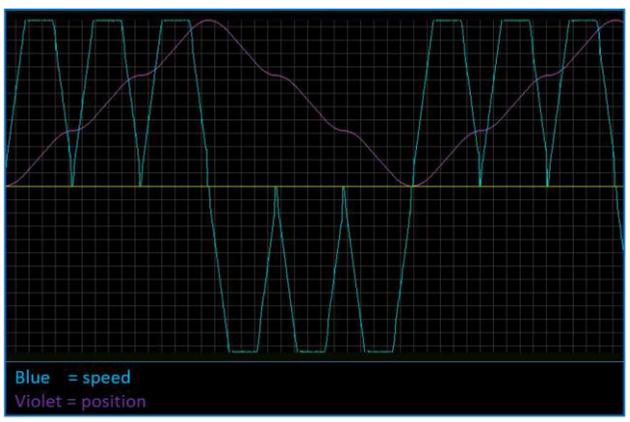

Figure 3: Simulation Chart - The screenshot shows an example of trapezoidal profile.

CONCLUSIONS

The code portability, the possibility to extend the number of axis and configure a large amount of parameters, the capacity to use high resolution encoders up to 4096 steps for revolution are the strong point of this system. The future development of this project is the realization of a SOC in which FPGA, firmware and interfaces are totally embedded.

Acronyms used – Field Programmable Gate Array (FPGA), Direct Current (DC), Micro Controller Unit (MCU), Application Specific Integrated Circuit (ASIC), Commercial Off-the-Shelf Component (COTS), Very High Speed Integrated Circuits Hardware Description Language (VHDL), Integrated Development Environment (IDE), Reduced Instruction Set Computing (RISK), Serial Peripheral Interface (SPI), Serial Interface (SI), Graphical User Interface (GUI), Proportional Integral Derivative (PID), Pulse Width Modulation (PWM), System on Chip (SOC).

REFERENCES

- G. De Luca et al., INFN-LNS Activity Report 2010, p.253-256.
- Altera “Quartus II Handbook” Version 14.1.0
- M. Mouse & D.V. Lettnin, “Synthesyzable VHDL Design for FPGAs” (2014).
- B. Mealy & F.Tappero, “Free Range VHDL”, RLS 1.17 (2013).
- W. Kleitz, “Digital Electronics – A digital approach with VHDL”, 9th ed. (2012).
- R.S. Sandige and M.L. Sandige, “Fundamentals of Digital and Computer Design with VHDL” (2012).

ISTITUTO NAZIONALE DI FISICA NUCLEARE

LABORATORI NAZIONALI DEL SUD

ACTIVITY REPORT 2013/2014

ASTROPARTICLE PHYSICS

The acoustic detectors network in the Central Mediterranean Sea

G. Larosa[1], S. Viola (for the KM3NeT-Italia, EMSO-Italia and SMO Teams)

1) *INFN – LNS (Istituto Nazionale di Fisica Nucleare – Laboratori Nazionali del Sud) via Santa Sofia 62, 95125 Catania, Italia.*

Abstract - The study and acoustic monitoring of the underwater environment is become of fundamental importance in the last decades for a plethora of scientific disciplines as astroparticle physics, geophysics and underwater acoustic.

Since 2005 INFN and INGV jointly operate submarine observatories in the Western Sicily EMSO (European Multidisciplinary Seafloor Observatory) node [1]. The collaboration, has promoted the installation and operation of two cabled deep-sea infrastructures: the Catania node (N 37°30' E 015°23"), 2100 m depth, 25 km offshore the harbour of Catania and the Capo Passero node (N 36°17', E 015°59'), 3500 m depth 100 km offshore Portopalo di Capo Passero, Sicily. Both infrastructures are fully operational and they are the first cabled facilities available for EMSO and KM3NeT.

Passive acoustic monitoring in deep sea represents a field of common interest for both institutes and projects. Acoustic detectors are sampled underwater and send continuously data to shore providing real-time acoustic monitoring of the deep-sea environment.

This is at present the largest acoustic infrastructure in the Mediterranean Sea with application in different research fields.

CATANIA NODE

The Catania node was located at 25 km East offshore the harbour of Catania to 2100 m depth. It was equipped with 28 km of underwater electro-optical cable split in two branch both of 5 km hosted two different terminations and named Test Site North (TSN) e Test Site South (TSS). Both terminations are connected to shore through the underwater electro-optical cable that permit transmission data in real-time on optical fiber and power through conductors. Thanks to this connection the acquired data can be analysed in real-time 24h/24 and stored in dedicated repository to be investigated offline.

Several underwater observatories were connected in both terminations.

In TSN, NEMO-SN1 (Submarine Network 1) observatory was operated from 2005 to 2008. This station was equipped with geophysics and oceanographic sensors aiming at geophysical and environmental monitoring on underwater depth environment within the Europeo GMES (Global Monitoring for Environment and Security) program.

In TSS, O*v*DE (Ocean noise Detection Experiment [2], Fig. 1) was installed from 2005 to 2006 and funded under the activities of the NEMO (NEutrino Mediterranean Observatory) project. It was the first real-time station to monitor the underwater acoustic background at large depth. O*v*DE was equipped with four large bandwidth hydrophones (30 Hz – 50 kHz), placed in a tetrahedral framework of ~1 m side. It acquired data from January 2005 to November 2006 and provided the first long-term data on the underwater noise in the Ionian Sea and also a unique opportunity to study the acoustic emissions of marine mammals living in the area or transiting during their movements within the Mediterranean basin.

From June 2012 to May 2013 EMSO-SN1 observatory operated in the TSN node. It was equipped with several probes and sensors to allow a real-time and long-term monitoring of the site performing: seismological, geomagnetic, gravimetric, accelero-metric, physico-oceanographic, hydroacoustic, and bioacoustic measurements (Fig. 1) [3].

From June 2013 the EMSO-SMO acoustic observatory has been deployed and connected in the TSS node. It was provided of four hydrophones large bandwidth to be able to acquire acoustic data synchronous in real-time (Fig. 1). This permits also correlations of acoustics events acquired from different station located a large distance apart.

The shore station is located at Catania harbour and hosts power supply and data acquisition systems. This is connected to the Laboratori Nazionali del Sud, Istituto Nazionale di Fisica Nucleare (LNS-INFN) to center of Catania through 660Mbps Internet Radio Link. This link

Figure 1: From left to right: 1) EMSO-SN1 observatory; 2) O*v*DE observatory; 3) EMSO-SMO observatory.

permits data storage in a central database hosted at LNS and, from there, the connection to the GARR network, making data available to a large scientific community.

The shore station is also equipped with a Global Positioning System (GPS) that permits the time synchronization of the data both on-shore and off-shore.

Moreover an AIS (Automatic Identification System) antenna is installed at LNS-INFN. It provides ship-traffic information used in correlation to acoustic data.

CAPO PASSERO NODE

Since 2007 the INFN has developed a new large scale cabled abyssal infrastructure off Capo Passero (Sicily). The infrastructure consists of a shore laboratory in the port area of Portopalo di Capo Passero and a sea infrastructure connected through a deep-sea cable of 100 km at 3500 m depth.

This infrastructure will host a future underwater neutrino telescope high energy KM3NeT [4]. The activity started in 1998 within the framework of the INFN NEMO (Neutrino Multidisciplinary Observatory) project.

KM3NeT will be a neutrino telescope hosting several thousand optical sensors displaced in volume of water of few km^3. A prototype detector (named KM3NeT-Italia prototype or NEMO-Phase2) was deployed on March 2013 and shut down in August 2014 (Fig. 2) [5]. The prototype hosts 32 optical modules to able to detect light signals emitted by subatomic particles (muons and electrons) originated by cosmic rays and cosmic neutrinos. The detector hosts also the SMO (Submarine Multidisciplinary Observatory) underwater observatory: an array of 10 SMID TR-401V1 hydrophones, forming a vertical 3D antenna 300 m high [6]. Whose data were continuously sampled underwater at 192kHz /24 bit, and transmitted to shore. All SMO receivers are phased and synchronized by a common master clock and data are time-stamped underwater with GPS time [7]. The acoustic system SMO is a multi-purpose detector that: 1) provided, acoustically, the position of the mechanical unit underwater using references acoustic signals emitted by a Long Base Line (LBL) of acoustic beacons anchored on sea-floor at about 400 m from the tower; 2) identified and tracked biological acoustic sources, with focus on sperm-whales detection; 3) measured the acoustic noise in deep sea aiming both at environmental monitoring and future acoustic neutrino detection. Oceanographic probes (CTDs and currente meters) were also installed to monitor the seawater column. Within 2016 will be deployed about 30 sea structures that will host hundreds of acoustic sensors. So the Capo Passero Node will host the largest acoustic detector for scientific use in the Mediterranean Sea.

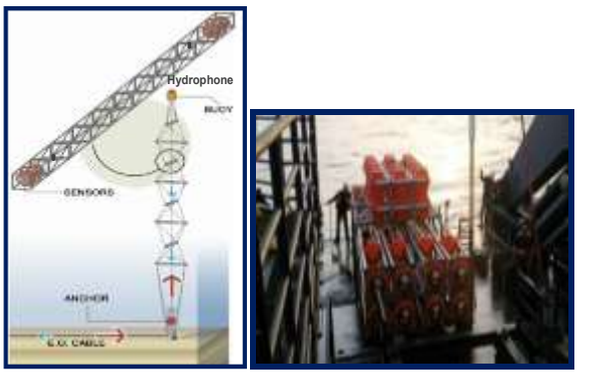

Figure 2: Scenic view of KM3NeT prototype (on the left). The KM3NeT-Italia prototype on the "Nautical Tide" deployed in March 2013 (on the right).

CONCLUSIONS

The technology solution developed by INFN and INGV to underwater applications are a huge opportunity to study in astroparticle physic, geophysics and acoustic underwater. The acoustic observatories deployed offshore Catania and Capo Passero are the largest infrastructures of acoustic research in the Mediterranean Sea.

ACKNOLEDGEMENT

This work was supported by the FIRB 2008 (RBFR08NRZE) project.

REFERENCES

[1] http://www.emso-eu.org.
[2] G. Riccobene et al., NIM A604 (2009) 149–157.
[3] P. Favali et al., *Peer-Reviewed Technical Comunication,* IEEE Journal of Oceanic Engineering, vol.38, n. 2, aprile 2013.
[4] http://www.km3net.org/
[5] Aiello et al., Astroparticle Physics 66 (2015) 1–7.
[6] https://web2.infn.it/smo/
[7] S.Viola et al., NIM A725 (2013) 207–210.

First results on underwater acoustic background in Capo Passero: towards monitoring station for the European Marine Strategy

R. Grasso[1], G. Larosa[1] for SMO, KM3NeT Italia and EMSO Collaborations.

1) INFN-LNS, via Santa Sofia 62, 95125 Catania, Italy

Abstract - In recent years the Italian legislation is supporting the conservation of marine ecosystems. The conservation actions require the propaedeutic study and monitoring of the physical and chemical characteristics of the underwater environment that is influenced by the increase of human activities [1].

The European Marine Strategy [2, 3] and the Italian legislation establish criteria and methodological standard to identify and analyse the underwater sounds introduced by anthropogenic activities. In particular they define criterions and indicators concerning: i) the distribution in time and place of intermittent sounds of high, medium and low frequency (such as airguns, piles, sonars, explosions); ii) continuous low frequency sounds (such as vessels).

The Submarine Multidisciplinary Observatory (SMO) is an underwater acoustic antenna installed on board the NEMO-KM3NeT tower, that is a prototype of a high-energy neutrino detector deployed at 3500 m water depth, 100 km offshore Capo Passero (Sicily).

We present preliminary results of the analysis of underwater acoustic data recorded by the SMO antenna, operating since 23 March 2013 until August 2014.

DATA SET AND ANALYSIS PROCEDURE

The SMO antenna consists of 10 high sensitivity and broadband (10Hz÷70kHz) acoustic sensors (hydrophones) and environmental probes (two Conductivity-Temperature-Depth probes to measure sound velocity at the site and one Doppler Current Sensor) [4-9].

Hydrophone signals were sampled underwater at 192 kHz/24 bit. The continuous stream of acoustic data from the hydrophones (6.2 Mbps per hydrophone) was analysed in real time on shore, only the recording of the first five minutes of every hour are stored on a digital library.

Fig. 1 displays the power spectral density as function of frequency, of a typical five minutes recording. This file was divided into slices of 2^{16} samples (341 ms), using an overlap of 50% and Hanning windowing, for each slice the periodograms were calculated (nfft = 2^{16}) as shown by grey area. The figure also shows the mean value of the power spectral density and different percentiles of the distribution. Fig. 2 displays the spectrogram of the same recording using nfft=2^{16}. The beacon pulses, shown in this figure, are signals emitted by acoustic emitters used for positioning purposes.

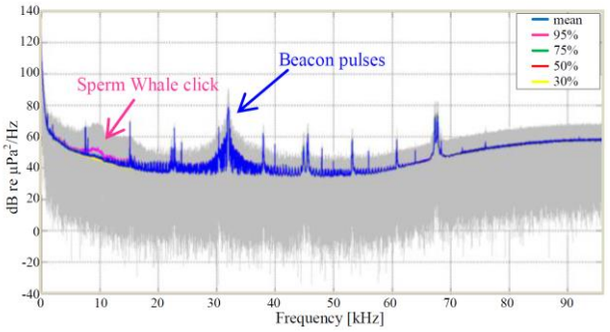

Figure 1: Periodogram of a 5 minutes recording (27 March 2013 – time 11:00): the grey area represents the PSD calculated every 341 ms time-slice. The average value and percentiles of the distribution are shown.

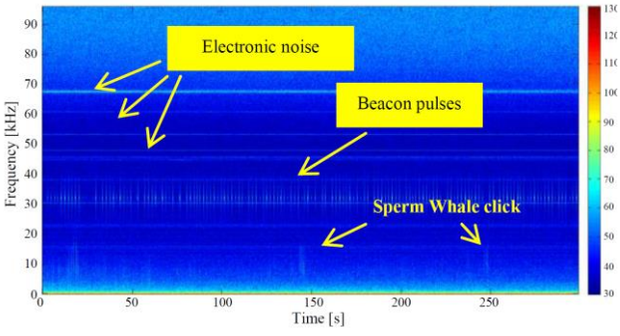

Figure 2: Spectrogram of a 5 minutes recording (27 March 2013 – time 11:00). Mean value of the power spectral density (dB re µPa^2/Hz) as a function of frequency and time.

The data analysis of the recordings of the first five minutes every hour of April 2013 point out the presence of continuous and impulsive underwater acoustic signals. The analysed data set consists of 673 files over 720 recordings scheduled; missing recordings were due to detector commissioning issues.

CONTINUOUS LOW FREQUENCY SOUND

The analysis of continuous low frequency sounds have been carried out following the requests of the European Marine Strategy [2,3], that suggests to evaluate the trends in the ambient noise level within the 1/3 octave bands 63 and 125 Hz central frequencies.

Fig. 3 shows an example of the power spectral densities in 1/3 octave bands recorded in the period 13-20 April 2013. Shipping noise (high, medium and low) and noise introduced by wind speed (black lines) from Urik [10] are also shown for comparison. Fig. 4 displays the average noise level in 1/3 octave bands centered at 63Hz and 125 Hz in April 2013.

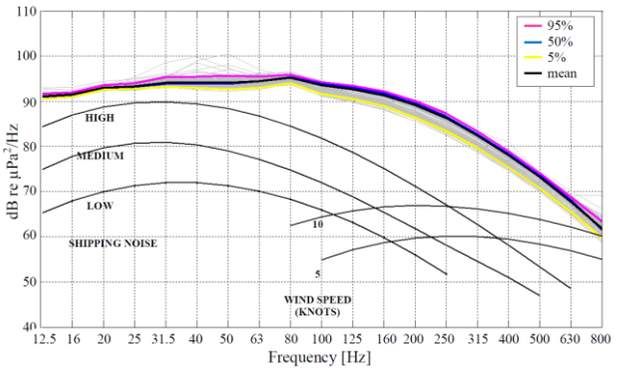

Figure 3: Recordings from 13-20 April 2013 (192 files). Measured noise level in 1/3 octave bands of five minutes recording (light-grey lines), percentiles P5, P50, P95 and mean value (see legend).

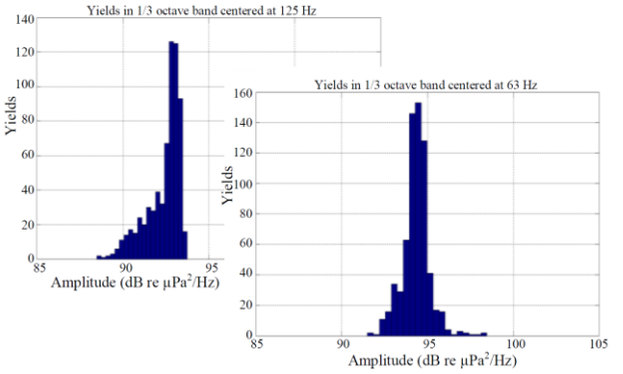

Figure 4: Average noise level in 1/3 octave bands centered at 63Hz and 125Hz in April 2013.

IMPULSIVE SOUNDS

In April 2013 anthropogenic impulsive sounds at high frequency (such as sonar) were not found in the data set. At mid and low frequency (10 Hz ÷ 10 kHz) noise produced by ships in transit was detected (see fig. 5). The KM3NeT positioning beacon pulses (frequency of 32 kHz, time duration of 5 ms and power of 180 dB re 1µPa@1m) were identified and used as calibration source.

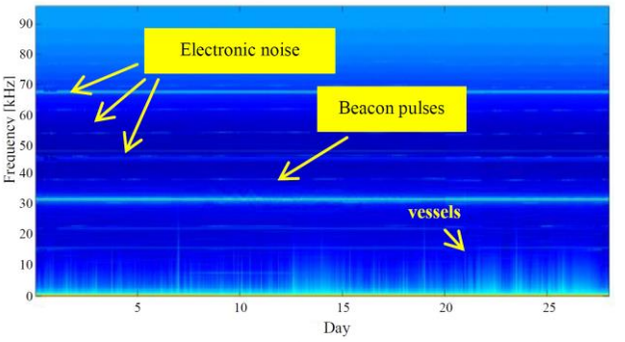

Figure 5: Spectrogram of the average value of power spectral density (April 2013 – 673 recordings).

CONCLUSION

The SMO antenna has been operating for more than seventeen months, at 3500 m depth off Capo Passero (Sicily). Data from the 10 hydrophones were continuously sent to shore and analysed in real time. An unbiased sample of data (5 minutes every hour) was stored on hour disk.

The presented results show that SMO acoustic antenna has optimal performances in terms of frequency and time resolution. Preliminary analysis of the data in accordance with the requirements of Italian and European legislation points out the potential impact of the used technique and of the SMO detector.

ACKNOWLEDGEMENT

This work was supported by the FIRB 2008 (RBFR08NRZE) project.

REFERENCES

[1] Decreto Legislativo 13 ottobre 2010, n.190
[2] Marine Strategy Framework Directive, Task Group 11 Report, April 2010
[3] European Marine Strategy Framework Directive Good Environmental Status (MSFD-GES), Final Report, February 2012
[4] http://web.infn.it/smo
[5] F. Simeone et al., NIM A 662 (2012) S246–S248.
[6] S. Viola et al., NIM A 725 (2013) 207-210
[7] F. Ameli et al., NIM A 626-627 (2011) S211-S213
[8] S. Aiello et al., Astroparticle Physics 66 (2015) 1-7
[9] S. Viola., Ph.D. Thesis in Physics - Catania University (2012)
[10] Knudsen et al., 1948; Wenz, 1962; reviewed in Urik, 1983

Deep-Sea multidisciplinary observatories: SMO & EMSO infrastructures for the long term acoustic monitoring of cetaceans

V. Sciacca[1,2*], F. Caruso[1,2], E. De Domenico[2] G. Bellia[1], G. Larosa[1], G. Pavan[3], E. Papale[4], C. Pellegrino[5] S. Pulvirenti[1], G. Riccobene[1], F. Simeone[6], S. Viola[1]
for the SN1, EMSO and SMO Collaborations.

1) INFN – LNS, Catania, Italy
2) DiSBA, University of Messina, Italy
3) CIBRA, University of Pavia
4) CNR – IAMC, Torretta Granitola (TP)
(5) INAF, Bologna.
(6) INFN, Università di Roma 1, Roma.
**Corresponding author, e-mail: sciaccav@lns.infn.it*

Abstract – Since 2005, the deep sea multidisciplinary observatories installed offshore Eastern Sicily allow to obtain important information on the presence of several cetacean species, in an area where there was no previous information available. Among these, the fin whale (*Balaenoptera physalus*) and the sperm whale (*Physeter microcephalus*) are considered legally protected by IUCN (International Union for the Conservation of Nature and Natural Resources). Results showed here are referred to the acoustic data acquired through the deep sea stations NEMO – OvDE and EMSO – SN1. Both observatories have been deployed in the Gulf of Catania - in different years - 25 km off the city port, at a depth of 2100 m.

INTRODUCTION

Since 2005, the INFN operates submarine observatories offshore Eastern Sicily, Ionian Sea, in collaboration with INGV (Italian National Institute for Geophysics and Volcanology) and CIBRA (Centro Interdisciplinare Bioacustica e Ricerche Ambientali, University of Pavia). The collaboration, signed at a regional, national and European level, has promoted the installation of two cabled deep-sea infrastructures: the Catania node, 2100 m depth, 25 km offshore the harbour of Catania, and the Capo Passero node, 3500 m depth, 100 km offshore Portopalo di Capo Passero. The first results on cetacean acoustics were obtained through the INFN NEMO – OvDE (Ocean Noise Detection Experiment) station, which has been operational between 2005 and 2006 [1,2,3]. Since 2012, the sensors installed within the EMSO (European Multidisciplinary Seafloor and Water Column Observatory) [2] and SMO (Submarine Multidisciplinary Observatory) projects [4] enable a detailed investigation of habitat usage, migration patterns and vocal behaviour of several cetaceans species offshore Eastern Sicily [5,6]. Among these, new information on the occurrence in the area of dolphins, fin whales (*Balaenoptera physalus*) and sperm whales (*Physeter microcephalus*) were obtained. Moreover, the acoustic arrays deployed within the SMO and EMSO experiments allowed for the first time the long term monitoring of underwater noise in relation to cetaceans biodiversity. These represent fundamental steps in providing feedbacks for cetacean species conservation policies.

PASSIVE ACOUSTIC MONITORING

Thanks to the acoustic data acquired through the large bandwidth hydrophones installed aboard the NEMO – OvDE (2005-2006) and the EMSO-SN1 (2012-2013) stations, it was possible to monitor the presence of the odontocete species (dolphins and sperm whales) within the Gulf of Catania [6]. Acoustic data, sampled at 96 kHz and saved at a rate of 5min/h, were analysed through the visual investigation of the spectrograms and the simultaneous listening of the recordings (*SeaPro Software* - CIBRA). Additionally, the development of automatic detection algorithms allowed to reveal sperm whales "clicks" and to measure their typical stable *Inter Pulse Interval* (IPI) [6]. This value represents a useful indicator of the specimens' size and sex, allowing to carry on population studies [7]. Furthermore, in 2012, a seismic hydrophone with a flat frequency response and a reliable calibration curve, in the range from 15 Hz to 1 kHz, has been installed on board the EMSO – SN1 platform. This sensor acquired continuously (24/7) acoustic data, allowing to monitor the presence of fin whales "20 Hz calls" [8]. Thanks to this data set, the first long term measures on the levels of noise within the fin whales communication frequency band (15-30 Hz) have been also carried out in the area.

Sperm whale

The data analyzed from the year 2005 to the 2012 revealed new information on the presence of sperm whales offshore Catania. The comparison among different recording years showed a clear decrease, from 2005-06 to 2012, in the acoustic presence of sperm whales (5 min/h). Furthermore, an algorithm developed allowed to measure automatically the stable IPI values of the detected clicks. Thus, it has been possible to observe that the animals

identified for the year 2005 were well-distributed in size, sex and sexual maturity [7] (Fig. 1).

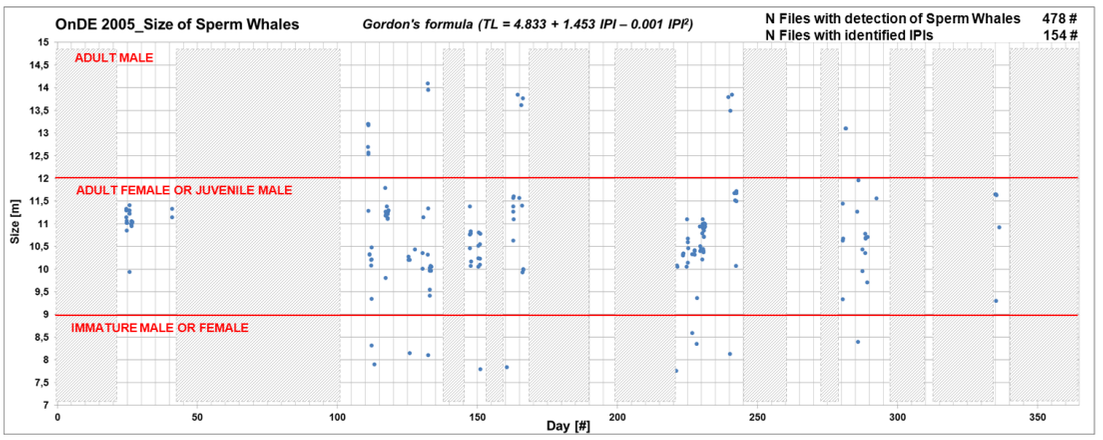

Figure 1. Distribution in size of the sperm whales recorded in 2005 by the NEMO-OvDE station [8].

Fin whale

By using the low frequency seismic hydrophone installed aboard the EMSO-SN1 platform it has been possible to monitor for the first time fin whales acoustic activity in the area. From June 2012 to May 2013, acoustic data were continuously acquired and stored in 10 minutes long files. The acquired data were analyzed by means of a proprietary code developed in MATLAB® environment, which calculates the spectrogram of each record in the band of frequencies between 1 and 50 Hz (8192 points FFT, 50% overlap, Hamming window). This analysis allowed the identification of the Mediterranean fin whale vocalizations [8] (Fig. 2).

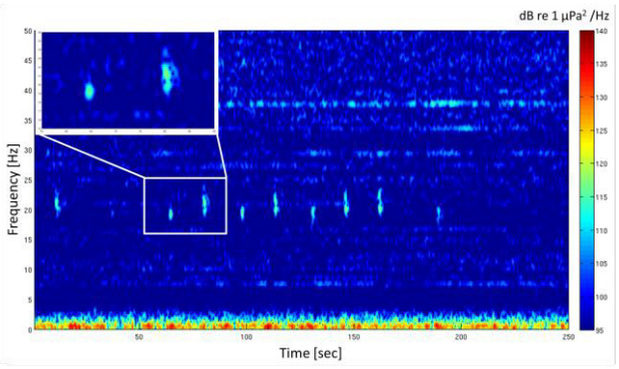

Figure 2. Spectrogram (250 sec, 1 - 50 Hz) of a recording acquired by the SN1 low frequency hydrophone. The figure shows a sequence of the Mediterranean fin whale calls (type A and B zoomed in the box).

About 7.000 hours of acoustic recordings have been investigated through spectrograms analysis and the typical Mediterranean fin whale calls were detected in different months of the year [6,8].

DISCUSSION

The deep-sea Passive Acoustic Monitoring carried out revealed a decreased acoustic detection rate, in 2012, of odontocete species sounds. The algorithm developed allowed the automatic detection of sperm whales' clicks, together with the related measure of the size. New ecological information on the observed population was examined (characterization of age, sex and sexual maturity). Furthermore, the first deep-sea recordings of fin whales offshore Catania strengthen the hypothesis that the Ionian Sea represents an important route through a seasonal migration of the species. The long term activities of the KM3NeT and EMSO projects will provide a better understanding of the cetaceans' occurrence in the Western Ionian Sea, thanks to the investigation of their acoustic behaviour and population ecology.

REFERENCES

[1] Pavan G., et al. (2008). Federal Agency for Nature Conservation, Bonn, Germany: 7-14.

[2] Favali P. et al. (2013). IEEE Journal of Oceanic Engineering 01/2013 38(2): 358 – 374.

[3] Riccobene et al. (2007). Journal of Physics: Conference Series. Vol. 81. No. 1. IOP Publishing.

[4] Simeone F., Viola S. (2011). Mobile Adhoc and Sensor Systems (MASS), IEEE 8th International Conference, 898-903, 17-22 Oct. 2011– doi:10.1109/MASS.2011.107.

[5] Nosengo N., Pavan G. and Riccobene G. (2009). Nature 462 - 3:560-561

[6] Caruso et al. (2014). Biol. Mar. Mediterr. (2014), 21 (1): 393-394.

[7] Goold J.C. (1996). J. Acoust. Soc. Am. 100(5): 3431–3441.

[8] Sciacca et al. (2015). Geophysical Research Abstracts Vol. 17, EGU2015-13117-4, 2015. EGU General Assembly 2015.

Hydrophone Calibration of the SMO acoustic antenna

R. Grasso[1], S. Viola[1] for SMO, KM3NeT Italia and EMSO Collaborations.

1) INFN – LNS, via Santa Sofia 62, 95125 Catania, Italia.

.

Abstract - Within the activities of KM3NeT Italia, a prototype neutrino detector was deployed the 23rd March 2013 and operated until August 2014. The prototype is a three dimensional "tower-like" mechanical structure, made of 8 stories (8 m horizontal length) interconnected by ropes, anchored on the sea bed (3500 m depth) and kept in tension by appropriate buoy, reaching a vertical extension of about 500 m above the seabed. The prototype tower hosts 4 optical modules and 2 hydrophones at each storey, two CTDs and one Doppler current sensor. All sensors are digitized underwater and data are sent continuously to shore via a vertical backbone and a 100 km-long electro optical cable, used also to provide power to the detector from the shore laboratory, in the harbour of Capo Passero (South East Sicily).

The hydrophones form an acoustic antenna designed, built and installed within the SMO (Submarine Multidisciplinary Observatory) project. Innovative read-out electronics was developed to obtain underwater GPS time stamping of hydrophone data with accuracy better than 1μs. The SMO hydrophones fulfill three tasks: provide acoustic positioning to the detector, monitor the acoustic noise in the aim of searching for acoustic neutrino signals and detect biological signals of cetaceans. In this contribution, we present the calibrations of these acoustic sensors made through calibrated emitters.

THE SMO ACOUSTIC SENSORS

The SMO antenna is a 3D array of 10 high sensitivity and broadband (10Hz÷70kHz) acoustic sensors (hydrophones) [1-6]. Couples of acoustic sensors were placed, at a distance of about 7 m, on floors #1, #2, #3, #4 and #6. Hydrophone signals were sampled underwater at 192 kHz/24 bit and analyzed in real-time on shore. Raw data were recorded every hour for five minutes and stored on a digital library. A successful R&D activity was carried out to select and test large-bandwidth hydrophones for 4000 m depth application, with optimal and constant sensitivity as a function of depth. Hydrophones (TR-401 (V) -1, produced by the company SMID of La Spezia, Italy) was selected for SMO antenna [7].

Calibration in laboratory

All hydrophones were calibrated and certified at different pressures (up to 400 bars) at NATO - URC (NATO Undersea Research Center). The sensitivity of all hydrophone + preamplifier assemblies was measured. As shown in Fig.2 it is almost constant in the whole frequency band, about -171 dB re 1V/uPa for all hydrophones).

Each hydrophone shows isotropic radiation pattern in the whole bandwidth and a relative sensitivity variation with hydrostatic pressure ≤ 1dB (see Fig. 1). Sensitivity calibration was also carried out at low frequency, this allowed us to extend the hydrophone operational range at lower frequencies (250 Hz).

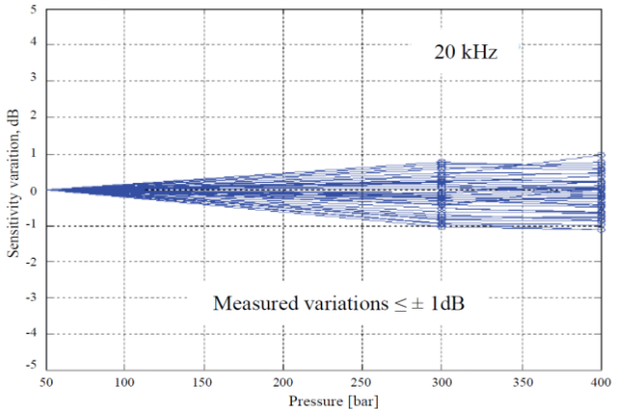

Figure 1: Relative hydrophones sensitivity variations with hydrostatic pressure

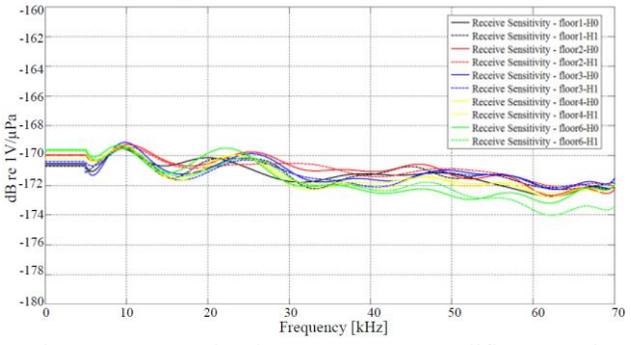

Figure 2: Hydrophones + preamplifier receive sensitivity

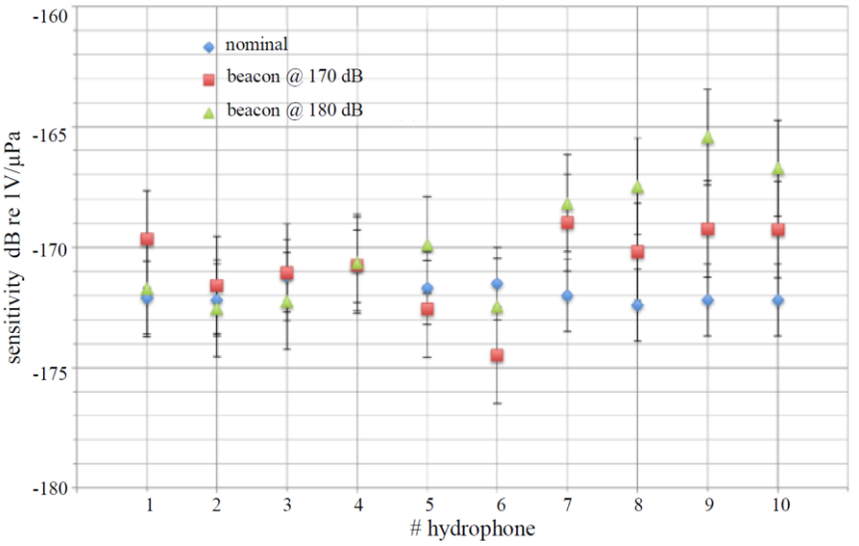

Figure 3: Sensitivity of antenna Km3NeT Italia – SMO hydrophones evaluated in laboratory and in situ

Calibration in situ

At sea, the hydrophones of the SMO antenna were tested and calibrated using a Long Baseline (LBL) of beacons anchored on floor in known positions. The LBL beacons emit pulses with a frequency of 32 kHz, time duration of about 5ms, emission power between 170 and 180 dB re 1µPa @ 1m with specific radiation patterns.

For the purpose to calibrate hydrophones in situ, exposed in this work, we have performed a dedicated data analysis. We have used signals from two acoustic emitters positioned respectively at the base of the tower and about 400 m away. Taking into account the wave attenuation and dispersion of geometrical absorption during propagation, we calculated the theoretical sound pressure received by each sensor. This value was compared with the signal measured on the hydrophones. In this way, the experimental sensitivity of hydrophones were evaluated in working conditions. The results obtained for a generic file of 5 minutes of acquisition are shown in Figure 3 by way of example. Figure 4 shows the mean value of power spectral density (dB re µPa^2/Hz) of the sound acquired by all the hydrophones of the Km3NeT Italia - SMO antenna during a generic five minutes acquisition.

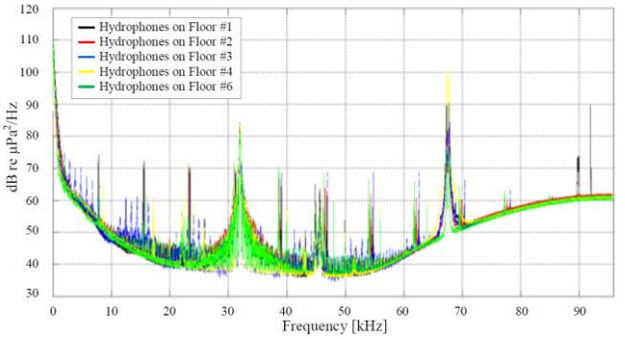

Figure 14: Mean value of the PSD of the acoustic signal acquired by all hydrophones of the antenna Km3NeT Italia- SMO (five minutes acquisition, 18 April 2013, starting time 00:00)

CONCLUSIONS

The analysis of data show a good agreement between the calibration data provided by NATO and those measured in situ and indicates a good functioning of hydrophones at a depth of 3500m. The hydrophones of the detector SMO are therefore useful for a correct measure of the noise in situ in a very wide frequency band.

ACKNOWLEDGEMENT

This work was supported by the FIRB 2008 (RBFR08NRZE) project.

REFERENCES

[1] http://web.infn.it/smo
[2] F. Simeone et al., NIM A 662 (2012) S246–S248.
[3] S. Viola et al., NIM A 725 (2013) 207-210
[4] F. Ameli et al., NIM A 626-627 (2011) S211-S213.
[5] S. Aiello et al., Astroparticle Physics 66 (2015) 1-7
[6] S. Viola, Ph.D. Thesis in Physics - Catania University (2012)
[7] A. Sapienza et al., Technical report NURC (2009) 1-44

ISTITUTO NAZIONALE DI FISICA NUCLEARE
LABORATORI NAZIONALI DEL SUD
ACTIVITY REPORT 2013/2014

ION SOURCES AND ACCELERATORS

Accelerators status and developments

D. Rifuggiato on behalf of the Accelerator Division

INFN LNS

Abstract - In 2013 and 2014 both the LNS accelerators were switched off for several months. This time was taken to upgrade some fundamental components of the two accelerators: the helium liquefier for the Superconducting Cyclotron and the charging system and the first accelerating tube for the Tandem. The aim was to restore the reliability level of both the accelerators, and in the Tandem case the performance level that recently were decreasing.

At the end of 2014 most of this upgrade phase was finished.

SUPERCONDUCTING CYCLOTRON

At the beginning of 2013 a failure of the helium liquefier occurred: the cold turbine was found to be broken and was replaced with a new one. The Cyclotron operation restarted on January 25. Beams were delivered to users until May 2 2013, when another failure occurred, again on the turbine. Therefore, in May 2013 a review of the liquefier was done in order to find out the reasons of these serious failure events, and to evaluate the general conditions of the system. As a result of this review, it was decided to accomplish what is called revamping of the liquefier, i.e. extraordinary maintenance and upgrade, which was going to take more than 6 months. In particular: a) the PLC Telemecanique TSX17 to be replaced with a new generation Siemens PLC, b) the complex of the warm section to be revamped including seals and piping replacement, c) filters and seals of the main compressor to be replaced. At the same time, most of the Liquid Nitrogen circuit will be renovated.

The helium liquefier has been working with no long interruption for more than twenty years with an outstanding reliability level. The revamping operation was intended to restore the past level of reliability.

As a matter of facts the Superconducting Cyclotron was not operating until September 2014 because of the revamping of the Helium liquefier. This extraordinary maintenance was committed to Air Liquide, France, being the manufacturer company. The whole operation, not considering the time necessary to get the order ready, took 1 year, the starting time being October 2013, while the expected time interval, as indicated by Air Liquide, was approximately 6 months. This delay was mainly caused by Air Liquide, in particular by problems of manpower and underestimation of the time needed to get the software for the new PLC ready. A minor delay, partially recovered, was caused by an unexpected breakdown of the cooling circuit of the helium compressor. The compressor was repaired in about 1 month during the accomplishment of many other maintenance operations regarding the warm section and the new PLC.

At the end of September 2014, the cryostat of the Cyclotron was full of liquid helium. The first tests were made at the beginning of October for 3 weeks. On October 20 the experimental program started. Experiments with high priority, since they had been cancelled in 2013, were performed first, according to the availability of users. In particular, the experiments with the ENSAR TNA03 support were scheduled before the end of 2014. Protons were sent to the proton-therapy hall in view of a session of patient treatment, scheduled in November 2014 and then postponed to the beginning of 2015 upon decision of the Policlinico Hospital. Experiments were performed with the MAGNEX spectrometer and tests were made at the FAZIA detector. Applied physics experiments in the field of radiobiology, dosimetry and radiation hardness were also performed in the beam line dedicated to Applications.

When the Cyclotron was stopped in May 2013, around 5 months of experiments had been scheduled. Moreover, in June 2013 the PAC approved new experiments for approximately 1 more year. Therefore no new call for experiments will be sent before the end of 2015.

ECR SOURCES

The upgrade operation on both the ECR sources is going on. In particular the superconducting source Serse is being provided with an autonomous cryogenic system, so as to be independent from the main helium liquefier, since in the most recent years it has been suffering from the supply priority of the main helium liquefier given to the Cyclotron. The new system is based on two commercial cryo-coolers, which have already been purchased, and on the replacement of the present current leads with high T_c ones. The two cryo-coolers of this new system have been delivered and tested at LNS, while their installation and commissioning, together with the replacement of the present current leads with high Tc ones will be done in 2015.

Concerning the room temperature source Caesar, its control system has been completely renovated during the long stop of the Cyclotron, therefore its reliability has now increased. Also, in the new configuration an oven is installed for production of metallic beams. All in all the operating conditions of the two ECR sources should be improved.

TANDEM

During the years 2013 and 2014 the Tandem was partially available for users.

Since HVEC belts have not been available for many years, several attempts were done to get operative conditions by using belts produced by an Italian company, but no satisfactory solution was found: the belt must have electrical and mechanical characteristics similar to the original one made by HVEC, therefore a heavy R&D program would be necessary to produce a suitable belt, but no company is available to do that due to the poor commercial interest. Then it was decided to replace the belt with the Pelletron system, provided by the NEC company, who declared that the Pelletron would have been available at the beginning of 2015. The cost for this big upgrade was covered by the "premiale" project "LNS Astrofisica Nucleare".

The problems of bad residual pressure in the Low Energy section, occurred at the end of 2011, forced to dedicate time and resources to find a solution. At the end of 2013, several months were dedicated to an extensive campaign of search for vacuum losses in the Low Energy section, i.e. the first accelerating tubes. After many attempts to detect and fix the leaks, it was decided to replace the first and eight tubes, quite evidently damaged by mechanical and electrostatic stress.

While waiting for the upgrade to be possible, some experiments approved by the Scientific Committee, not requiring a high performance of the Tandem, were performed in 2013 and 2014. The tube n. 1 was fixed with a special vacuum sealant, and an old belt, not too much damaged, was reused. Light beams at low energy, requiring a terminal voltage of no more than 7 MV, were delivered.

In the first months of 2014, from January to April, beams were delivered to users. A big fraction of the total beam time was dedicated to nuclear astrophysics and nuclear structure experiments.

In May 2014 the new accelerating tube n. 1 was delivered by Vivirad, France, see Fig. 1. After site acceptance tests, the old accelerating tube n. 1 was replaced by the new one. Vacuum tests followed until the end of September 2014. From October to December 2014 general tests of the Tandem were accomplished, including beam tests, in order to prepare the machine to the MP-Pelletron conversion, which was scheduled in January 2015: the charging system, up to now based on the use of belts, was going to be based on the so-called “Pelletron” system, designed and constructed by NEC, USA. The Pelletron was agreed to be shipped at the beginning of January 2015 and installed soon after its arrival at LNS.

Therefore, in 2015 a remarkable upgrade phase of the Tandem, intended to restore a high level of reliability and performance, will be completed.

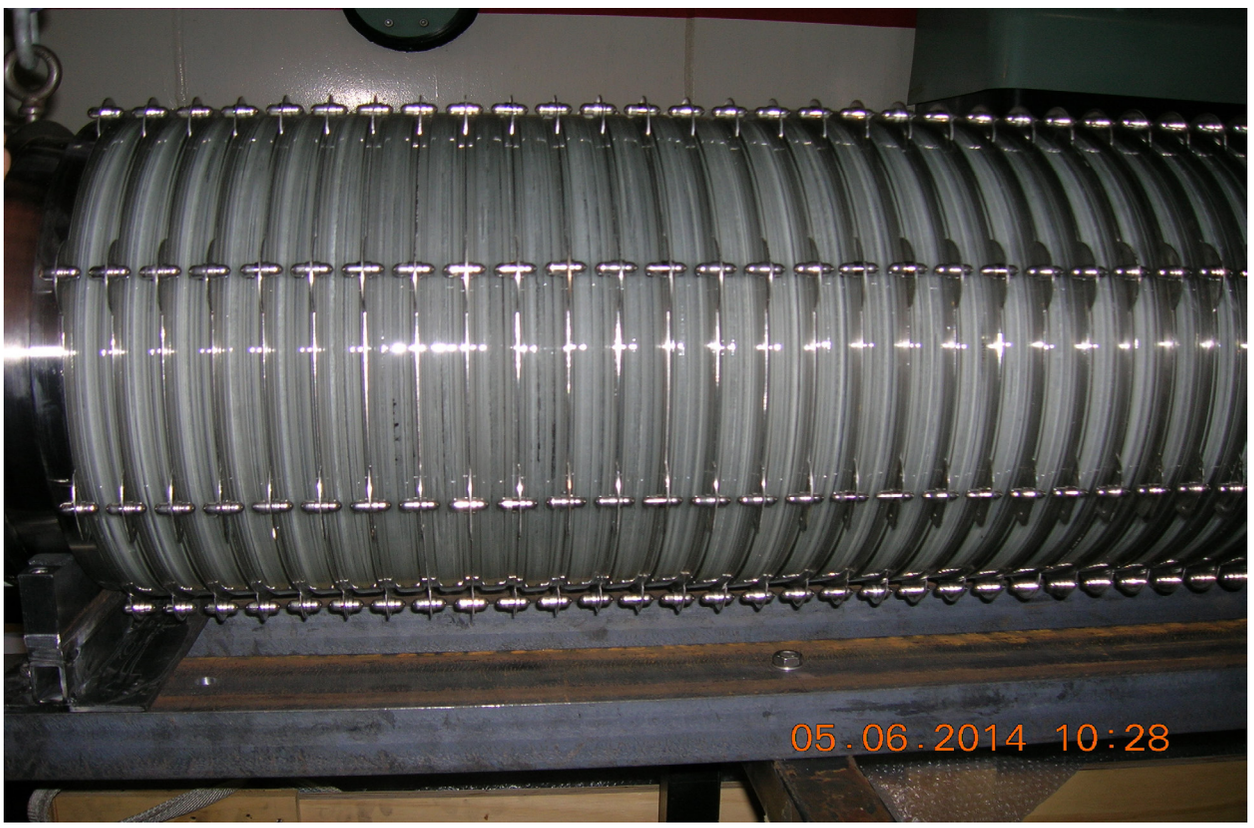

Figure 1: the new accelerating tube delivered by Vivirad

Proposal to upgrade the LNS Superconducting Cyclotron

A. Calanna[1], L. Calabretta[1], D. Rifuggiato[1], G. Cuttone[1], G. D'Agostino[1],
M. Maggiore[2], A. Radovinsky[3]
1) INFN-LNS, Catania, Italy
2) INFN-LNL, Legnaro, Italy
3)PSFC T&ED MIT, Cambridge, MA 02139, USA

Abstract – To increase the beam current delivered by the LNS superconducting Cyclotron we recommend to use the stripping extraction. A conceptual design of a new superconducting magnet and a new cryostat is here presented. Beam dynamics simulations along the new extraction trajectories are also presented.

INTRODUCTION

A new experiment, called NUMEN, proposes to measure the element of nuclear matrix using double charge exchange experiments [1, 2]. This measure is of interest also for the double beta decay neutrino-less experiment. The main request for our existing superconducting cyclotron (CS) is to increase the beam current. A higher beam current is also useful for many other experiments that use radioactive ions beam produced with in-flight technique [3] and also for the production of radioisotope of medical interest.

In particular, the aim of present study is to ascertain the feasibility of extraction by stripping from the CS, for the energy and mass range of interest of the NUMEN experiment. The investigated energy range is 15- 60 AMeV and the ions investigated are ^{12}C, ^{18}O and ^{20}Ne to span a reasonably wide mass range.

The LNS CS is a three sector compact machine with a wide operating range, being able to accelerate heavy ions with values of q/A ranging from 0.1 to 0.5 to energy from 2 to 100 AMeV. The CS was designed as an accelerator to perform nuclear physics experiments, which require low intensity beams.

The main limitations to extract high beam power are the two electrostatic deflectors. In fact, due to the compactness of the accelerator the last accelerated orbit is not fully separated from the previous one, which implies a extraction efficiency lower than 60%. The lost beam, dissipated mainly in the septum of the first electrostatic deflector, causes serious damages to the device that is not able to hold the high voltage.

The goal of the proposed modification is to make extraction by stripping possible in the CS to achieve high power beams for the set of beams of interest. At the same time the versatility of the CS is to be maintained, since there is a consistent demand of beam types in a wide mass and energy range. For this reason the CS will be equipped with two extraction modes: extraction by stripping and extraction by electrostatic deflectors. The feasibility of extraction by stripping through the existing extraction channel with an increased transversal section has been studied.

In addition, a new extraction channel has been designed to increase as much as possible the number of the extracted ions and energies.

TECHNICAL APPROCH

The code EXTRAZ has been mainly used for the beam simulations: this is the code currently used for determination of the Cyclotron extraction parameters starting from the measured field maps. The procedure consists of few steps. At first, the Eigen-ellipse at the equilibrium orbit at the proper extraction energy and angle is computed by using the code GENSPE. Then a change in the ratio of the charge over the mass simulates the stripping process. For instance, a carbon ion is accelerated with a charge state of 4+, after the stripper its charge state will be 6+. We assume that the entire medium-light ions here considered have a charge state equal at their Z after the stripping, which means they are fully stripped of their electrons. After the change in the charge state, the beam trajectory is strongly perturbed and the three-fold symmetry is lost. The particles orbit generally around the centre of the cyclotron if the ratio between the final charge state over the accelerating charge state, Q_f / Q_{acc}, is smaller than 1.5.

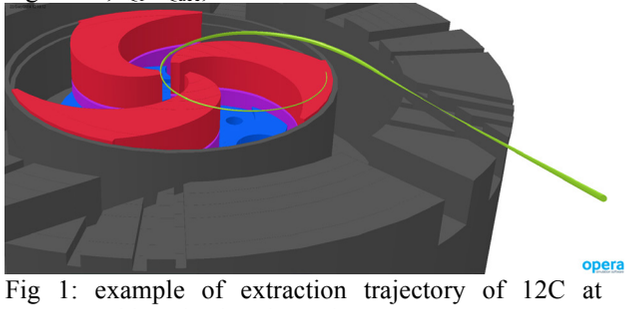

Fig 1: example of extraction trajectory of 12C at 45 AMeV achieved using the code OPERA.

The extraction trajectories that do not rotate around the centre of cyclotron cannot be simulated by the code ESTRAZ. In these cases, we use an OPERA 3D model to track the reference particle and the particles that describe the contour of the radial and vertical beam emittance through the cyclotron up to the extraction channels (see Fig.1). The last part of the extraction trajectories has been evaluated using the code EXTRAZ to compute the magnetic gradients needed to deliver the beam outside the cyclotron yoke. An example of the outcome is in Fig.1 that represents the trajectory of the stripped beam inside the cyclotron. Fig. 2) shows the radial and axial beam envelope computed with Estraz code.

The beam dynamics simulations were made chosen a value of the normalized emittance of 1 π mm.mrad, which is about twice larger than the expected. The 3 magnetic channels, MC, and their angular positions are shown too. These pictures are just for sake of clearness of the explanation.

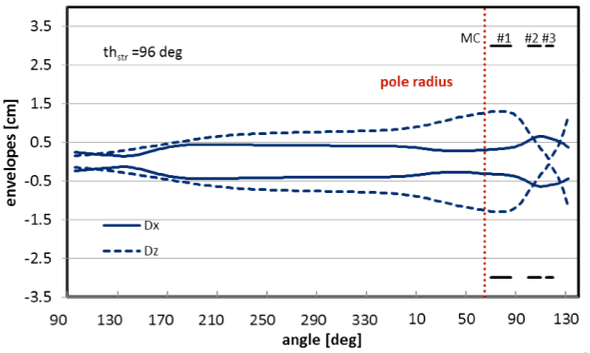

Fig 2: Beam envelope along extraction trajectory of ^{12}C at 45 AMeV

A substantial work has been done to transform the usual measured bi-dimensional B(R,θ) magnetic field map into a 3D magnetic field map, that is possible to import in to an OPERA model to evaluate also the particle trajectories off the median plane. The beam dynamics parameters describing the Eigen-ellipse of the last closed orbits are achieved by the program GENSPE, than they are transformed into geometrical parameters that can be used as input to track the both the closed orbits and the extraction orbits when the ratio q/A is opportunely changed. Of course, when it possible to use both methods, manipulations from OPERA results and ESTRAZ, the results are the same.

In Fig.3 there is sketch of all the ions studied. An internal document has been submitted to INFN board for evaluation. It contains all the details and considerations done on the emittance values, the stripper positions, the evolution of the two envelopes, as well as the needed gradients of the MC for both cases: extraction through the existing or new channel.

NEW CRYOSTAT AND SUPERCONDUCTING MAGNET

The design of the two extraction channels requires to build a new cryostat, including a new set of superconducting coils. In particular, it requires a stress analysis of the cryostat structure to evaluate the maximum size of each penetration across the cryostat.

A study report for the "New superconducting magnet for the LNS Cyclotron" has been prepared by the Plasma Science and Fusion Center of MIT (Boston)[4].

Here we recall shortly the main results of this study.

- The form factors of the new coils are very similar to the previous coils;
- The new cryostat fits the same outer size of the previous cryostat;
- The new Liquid helium vessel is radially smaller than the previous;
- There is more room for the liquid nitrogen shields;
- The new magnet can be operated also with a 5 W of nuclear heating due to the 200 W beam losses;
- Hoop stress analyses in the coils shows that the proposed solution is quite safe;
- The size of the Liquid Helium Vessel allow to drill in the mid-plane of the LHe vessel extraction channels with a vertical gap of the room temperature wall larger than 60 mm (+/-30 mm) and the radial width of the extraction channel larger than +/- 100 mm around the reference trajectory (20 cm total width), without significant effects on the safety of the superconducting coil;
- The expected liquid helium consumption will be <20lt/hour (at 4 K) and the Liquid nitrogen consumption <18 lt/hour (at 77 k).

CONCLUSIONS

The present study demonstrates that it is possible to achieve the required beam power with good focusing properties to respond to the LNS experiment demands.

REFERENCES

[1] M. Cavallaro et al. [2] C. Agodi et al.:present report
[3] Raciti G. et al. Nuclear Physics; Sec A; Vol834; Issue: 1-4; March 1; 2010; pp. 780c-783c
[4] A. Radovinsky et al. TBP Magnet Technology 2015

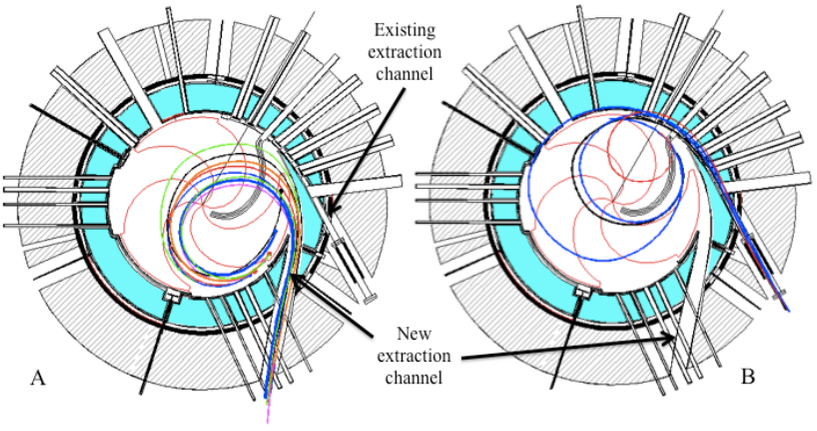

Fig 3: The extraction trajectories produced by stripper foils extracted through the new (A) and the existing (B) channels.

Injection tests of high-intensity H_2^+ beam for IsoDAR cyclotron

J. R. Alonso[1], S. Axani[1], L. Calabretta[2], L. Celona[2], D. Campo[2], G. Castro[2], J. M. Conrad[1], F. Labrecque[3], R. Gutierrez-Martinez[4], G. Messina[2], B.F. Milton[3], M. Sedita[2], D. Winklener[1], L. Winslow[4] , E. Zappalà[2]

1) MIT, Cambridge, MA 02139, USA
2) INFN-LNS, Catania, Italy
3) BCSI,Vancouver, BC V6P 6T3, Canada
4) UCLA, Los Angeles, CA 90095, USA

Abstract - A test stand cyclotron designed to accelerate high-intensity q/a = 0.5 beams up to 1 AMeV has been assembled at the development labs of Best Cyclotron Systems, Inc. (BSCI) in Vancouver, Canada. The Versatile Ion Source (VIS) from LNS-INFN Catania has been coupled to this test stand cyclotron to perform preliminary injection tests. Some results of the experimental activity are here summarised.

INTRODUCTION

The IsoDAR and DAEδALUS experiments to search for sterile neutrinos and CP violation in the neutrino sectors have been proposed [1,2,3]. These experiments require cyclotrons able to supply 10 mA proton beams. In particular, IsoDAR needs a compact cyclotron [4] able to accelerate H_2^+ up to 60 AMeV, while DAEδALUS [5] will use a Superconducting Ring Cyclotron Booster to increase the energy of the H_2^+ beam up to 800 AMeV. The acceleration of the H_2^+ ions is advantageous to reduce the space-charge effects at injection and allowing stripping extraction at the top 800 AMeV energy.

Injection efficiency in a compact cyclotron has a value typically 10% that can be increased up to 15-20% with the help of a buncher device. Ion source current around 25 to 50 mA are request. We plan to experimental investigate the effect of the space charge at these current.

An experimental program to test injection of high-intensity H_2^+ beams was performed by the collaboration among MIT, LNS-INFN (Catania), and BCSI. The experimental program was serious delayed by the interference with the commercial program of BCSI. For this reason the experimental program despite it was done in a period of just 5 months, it was spread along the spring 2013 to fall 2014.

THE EXPERIMENTAL SETUP

Fig. 1 shows the layout of the test stand. The VIS source [6] at LNS-INFN (Catania) was able to deliver up to 15 mA of H_2^+. Similar results were achieved at BCSI. To increase this current value new ionization vacuum chambers with smaller size were built and tested but unfortunately without significant improving. A big solenoid is located 50 cm ahead the extraction point of the source. It provides primary focusing, and also allows separating protons from H_2^+ ions. An emittance meter was installed in a 6-way iso-160 vacuum T, located about 1.5 m after the solenoid. A Bergoz 100 mm bore DCCT was used as a primary current monitor, but only for the first part of experiment just to check the beam current measured by the Faraday cups and the beam stopper installed along the beam line. After this device another 6-way iso-160 vacuum T houses a collimator and movable beam stop. Two magnetic quadrupoles, which can be rotated around the beam axis, and another solenoid, complete the injection line. These allow flexible adjustment of beam focus and shape at the entrance of the spiral inflector inside the cyclotron magnet.

CENTRAL REGION

The final injection system consists of a Spiral Inflector (SI) to bend the beam onto the median plane and properly shaped electrodes of the two RF cavities that drive the beam along the first acceleration turns. The design of this system was a compromise between the characteristics of the IsoDAR cyclotron and the properties of the small cyclotron developed by BCSI[6]. The SI was designed to inject the 60 keV beam of H_2^+ into the cyclotron median plane. The gap between the electrodes is 15 mm to ensure sufficient space for the high-intensity beam. The inner surfaces of the electrodes have a "V" shape to improve the beam focusing. The maximum voltage request at the SI is ±10.2 KV. A tilt angle of 21° was also introduced to place the beam along a suitable injection trajectory for

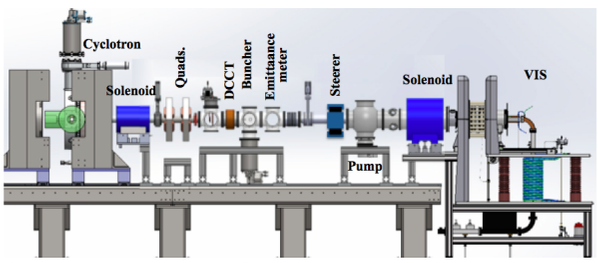

Figure 1: Layout of the test stand at the BCSI development lab in Vancouver, Canada. The ion source is in a high-voltage cage at far right; the test cyclotron is on the left. Total length of test stand is about 5 meters.

matching with the acceleration orbit. The simulations, without space-charge effects, show good beam transport efficiency through the device.

The cyclotron central region was designed with two RF-cavities instead of the four planned for the IsoDAR cyclotron. The working frequency is the 6th harmonics to stay near the operating frequency range of the RF cavities of BCSI cyclotron. Due to the high harmonic (6th) and frequency of 49.2 MHz, the focusing action of only two cavities is not enough, so less than 50% of the beam injected, in the acceptance phase, it is expected to reaches the final energy of 1 MeV. As a result of the simulations done, we strongly suggest reducing the operating frequency of the IsoDAR cyclotron to the 4th harmonic. Indeed, simulations of the central region with four RF cavities operated in 4th harmonic show a larger phase acceptance and a better beam transmission, near 90%.

EXPERIMENTAL RESULTS

The ion source from LNS-Catania arrived in Vancouver in April 2013. A team from LNS, MIT, and UCLA throughout the spring and summer 2013 conducted tests with the H_2^+ beam. The tests included optimization of the H_2^+ beam current, H_2^+ /proton ratio, removal of protons from the H_2^+ beam by solenoid focusing, and performing emittance measurements. The RF cavities of cyclotron had been completed in the 2014, so the injection and acceleration tests were performed on summer/fall 2014.

Different experimental set-up of the VIS source were tested, also changing the plasma chamber, but the maximum H_2^+ current measured was around 10 to 12 mA, with a 8 mm extraction hole. Scanning the current on the beam stop vs. solenoid current, we are able to achieve a good, but not perfect, separation of protons from H_2^+.

The collecting surfaces, collimator and beam stop, just downstream of the DCCT are not magnetically suppressed, so there is no control over secondary electron current is lacking. To try to make the sum of currents on the collimator and beam stop equal to the DCCT reading, a 50 V bias was placed on both collimator and beam stop. This lead to consistent current readings, however did have a significant effect on the beam size, indicate that the 50 V bias is enough to draw the neutralizing electrons away from the beam. The effect is repeatable and instantaneous with application or removal of the bias.

A series of photographs taken through a window, like fig.2 (Left), shows a clear tight beam at 235 amps, and another one at 330 amps supplied by the solenoid, corresponding to protons and H_2^+ focus respectively (Source extraction voltage 60 kV). With a collimator aperture of 8 mm, 100% of the H_2^+ can be transmitted, but protons are over focused and about 5% are estimated to pass through the collimator. However, an unforeseen issue is that the proton beam is over focused substantially upstream, and propagates beyond the focus at a divergence such that it is lost on the walls of the vacuum chamber, producing heating of the chamber itself and of the O'ring Viton made. Fig. 2 left shows the photo of H_2^+ beam focused. The photo was taken through a quartz window placed directly below the emittance scanner (fig.1). On fig.2 (right) the beam emittance achieved with an Allison scanner [7] is shown. Both the figures where performed with microwave power levels of 380 W, corresponding to a 50% of H_2^+ and 50% of proton, and with solenoid feed with 340 A. Evaluation of emittance indicate our measured values are about two times higher than previous VIS emittance values measured for the proton beam. Further details on these tests have been presented [8,9].

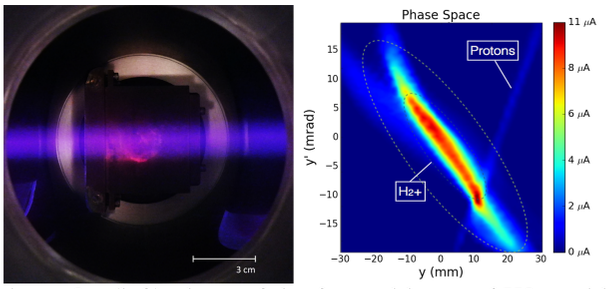

Figure 2: (left) photo of the focused beam of H2+, with solenoid supplied with 340 A. (Right) Emittance plots for H_2^+ and a contaminant proton beam. The blue and green dotted ellipse represent the ellipse boundaries of 1 rms and 4 rms emittance respectively.

The measured injection efficiency of the H_2^+ beam across the spiral inflector is higher than 90% when the data are correct for the proton beam contamination. Another very important test is the maximum voltage applied on the electrodes of the Spiral inflector that was in excess of 13.5 kV vs. the nominal 10.2 kV value request for the injection of the 60 keV H2+. This means that we have about 35% of margin. This will be useful to inject beam with 70 keV and to use larger gap between the electrodes.

ACKNOWLEDGEMENTS

We thank the 5th National Committee of INFN for its precious support. Support from MIT and UCLA, and National Science Foundation Grants NSF-PHY-1148134 and NSF-PHY-1205175 is also gratefully acknowledged.

REFERENCES

[1] J.M. Conrad and M.H. Shaevitz, Phys.Rev.Lett. 104, 141802 (2010).
[2] J. Alonso et al. [The DAEdALUS Collaboration], arXiv:1006.0260 [physics.ins-det] (2010)
[3] A. Bungau, et al, Phys. Rev. Lett. 109, 141802 (2012)
[4] D. Campo et Al., Study for Isodar Cyclotron, Report LNS 2013/14
[5] A. Calanna et Al., Study for a Superconducting Ring Cyclotron for DAEdALUS, Report LNS 2013/14
[6] R. Miracoli et al. Rev. Sci Instrum. 83, 02!305 (2012)
[7] P.W Allison, J.D. Sherman, D.B. Holtkamp, IEEE Trans. Nucl. Sci. NS-30, 2204 (1983)
[8] J. Alonso et al., ThuP53, ICIS 2013
[9] F. Labrecque et Al, Int. Cyc. Conf. and App., Vancouver 2013, JACOW web site

Superconducting Ring Cyclotron for DAEdALUS experiment

A. Calanna[1], J. R. Alonso[2], L. Calabretta[1], J. M. Conrad[2], F. Meot[3], M. Haj Tahar[3], J. Minervini[4]

1) INFN-LNS, Catania, Italy
2) MIT, Cambridge, MA 02139, USA
3) BNL, Upton, Long Island, New York, USA
4) PSFC T&ED MIT, Cambridge, MA 02139, USA

Abstract - A superconducting Ring Cyclotron to deliver 800AMeV H_2^+ beam at high power has been studied. The technical solution and the update results are presented.

INTRODUCTION

The cyclotron complex for the DAEδALUS CP-violation neutrino experiment [1,2,3] consists of a compact cyclotron able to accelerate H_2^+ beams up to 60AMeV, and a superconducting ring cyclotron (DSRC) able to accelerate the beam up to 800 AMeV. An efficient extraction is performed by H_2^+ dissociation with thin stripping foils.

The DSRC, accelerates H_2^+ up to energies of 800 AMeV to deliver a proton beam power of 1.6MW on target. The extracted proton beam is then delivered on a megawatt-class target for neutrino production.

Space-charge dominated beam dynamics simulations using OPAL have been performed for an eight-sector geometry, and indicate acceptable transmission and low beam losses. Subsequent engineering magnet design studies [4.5] pointed to a six-sector configuration as more practical. A short summary of the process that led us to a six-sector-cyclotron is published in [5]. In that paper, it is explained why and in what way a six-sector machine is the best solution in terms of injection and extraction systems, of RF-cavity-design, of winding of the coils, and, not negligible, in terms of costs. Results on the magnetic field, acceleration and focalization are reported and they are very close to the state-of-art. In this document, some details and pictures will be included for a summary description of the model.

THE NEW MAGNETIC SECTOR

Fig.1 shows the new design of the DSRC, which is a six-sector cyclotron. Few considerations:

- The gap between the poles is 8 cm, which is a safe value considering the dimensions of the vacuum chamber, which thickness will be in the order of 0.5- 1 cm (respectively at the inner and outer radii);
- In the hill there is a 20 cm gap (in the z direction) to host a tie-plate that has to connect the longest arms of the coil to contain the huge azimuthal force. The tie-plate is inside the cryostat and at 4.2 K. The Technology and Engineering Division (T&ED) of the MIT Plasma Science and Fusion developed the magnet conceptual design to provide very preliminary cost estimates to fabricate a single magnet sector [6]. The conceptual design includes solid modelling and analyses for the conductor and winding pack design, high temperature superconductor and copper current leads for the magnet, structural design of the magnet cold mass, cryostat and warm-to-cold supports, cryogenic design of the magnet cooling system, and magnet power supply sizing. T&ED estimated the thickness of this plate to 6.5 cm, so 20 cm is a safe value taking into account the cryostat size;
- The iron is spiralled at outer radii to assure the vertical focusing. In the middle of the hill there is a big hole, the iron around this hole, for an height of 5 cm, was used to fine tune the magnetic field to achieve the isochronism along the acceleration path;
- The shape of the coil was decided after few interactions with T&ED's group. The cross-section is constant at 31x16 cm^2. The current density is 34 A/mm^2. The distance between the iron and the internal face of the coil is 10 cm (in [6] this value is accepted, but the possibility to be increased at 11cm has to be investigated). Moreover, in contrast with the previous design, the coil is everywhere parallel to the median plan, from which the distance is 12 cm.

Fig.1 shows a sketch of the bottom half of the machine. The space between the sectors is enough to accommodate the structural coil case and the cryostat, which had been studied by PSFC. Moreover, there is enough space for the beam injection and extraction systems. A sketch of injection and extraction lines studied so far, are reported in Fig.1 too. For more details see [7].

The valleys will host 4 PSI-like cavities (in blue in Fig.1), which are able to achieve 1MV of acceleration voltage and are the best performing between the existing ones. Beam dynamics along the acceleration path was evaluated with the code SPIRAL GAP, which is a code that still does not take into account the space-charge effects. This evaluation highlighted an issue we have to take into account. Our configuration has symmetry six in the iron, but we forecast 4 PSI-like RF-cavities, this means that the acceleration has a symmetry two component. The coupling effect of this symmetry when the resonance $\nu_r=2$ is crossed at 670 AMeV broadens the beam radially. Consequently, when the beam crosses the Walkinshaw resonance at 780 AMeV, we see a broadened vertical beam.

Results of simulations of the beam acceleration show the problem disappears when a 6-sector-cyclotron with 6 acceleration cavities (with the same energy gain per turn as in the case with 4 cavities) are used. We did the same calculation using 3 or 5 cavities and always the same energy gain per turn and the result was similar [5].

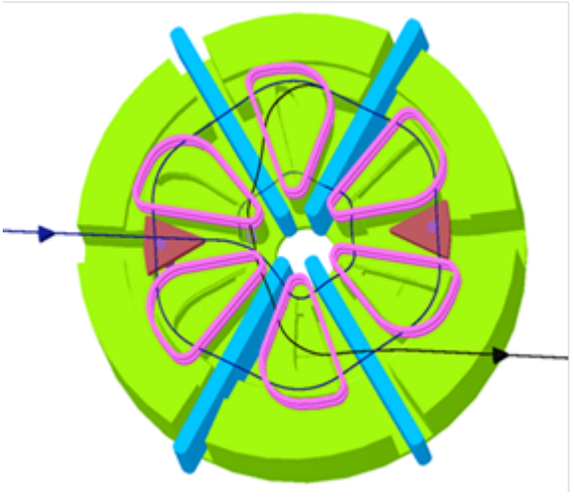

Figure 1: Bottom half of the DSRC.

Unfortunately, we can install only 4 PSI-like resonators because the electrostatic deflector for the beam injection and the correcting magnet along the extraction trajectory, are both located in the central region of the DSRC. We are evaluating to install two additional double gap resonators starting at the average radius of 380 cm (in red in Fig.1). These two additional cavities could be similar to the new double gap cavities designed by PSI for the upgrading of the Injector II. Alternative solution to solve this problem is to change the magnetic field configuration at outer radii to move the Walkinshaw resonance out of the acceleration region, which is not trivial neither quick.

In addition to all considerations done up to now, the following Table1 contains additional design parameters that describe the iron and coil structure and forces.

The values are reported in comparison with the RIKEN Super-Conducting Cyclotron in RIKEN Nishina Center. SRC is the world's first ring cyclotron that uses superconducting magnets, and has the strongest beam bending force among the cyclotrons. It can boost the ion beam energy up to 440 AMeV for light ions and 350 AMeV for very heavy ions such as uranium nuclei to produce intense radioactive beams. For all these reasons we consider Riken SRC as our reference cyclotron. The code Genspe has been used to study beam dynamics. The isochronism, which represents the difference between the ideal field and the calculated field, is everywhere less than +/-1‰, in particular, at the outer radii, which is the most critical part, it is even better in the order of +/-0.5‰ [5]. The 2 vital parameters responsible of the focusing of the beam in the radial, vr, and vertical, ν_z directions have a good behaviour along the whole acceleration path [5].

Table 1: Margin Specifications

Basic	**DSRC**	**Riken-SRC**	**units**
Max field on hill	4.72	3.8	T
Max field on coil	4.27	4.2	T
Stored energy	166	235	MJ
Coil size	31x16	21x28	cm^2
Coil length	10.82	10.86	m
Current density	34	34	A/mm2
Expansion force	1.8	2.6	MN/m
Radial shifting	2.05	0.36	MN
Vertical force	7.07	3.3	MN
Cyclotron Height	6	6	m
Outer radius	7.3	7.2	m
Weight/sector	830	800	tons
SC trim coil	None	4	Sets
Extraction method	Stripper foil	El. Def.	

CONCLUSIONS

The present study demonstrates that it is possible to achieve the required isochronous field with good focusing properties to produce a H_2^+ beam at 800 AMeV. In a further step of the study some parameters have to be fine adjusted to achieve a more reliable solution. In the next future simulations using the OPAL code will be performed to confirm the space-charge effects do not jeopardize the acceleration.

AKNOWLEDGEMENTS

Support from MIT and UCLA, and National Science Foundation Grants NSF-PHY-1148134

REFERENCES

[1] J.M. Conrad and M.H. Shaevitz, Phys.Rev.Lett. 104, 141802 (2010).
[2] J. Alonso et al. [The DAEδALUS Collaboration], arXiv:1006.0260 [physics.ins-det] (2010)
[3] A. Bungau, et al, Phys. Rev. Lett. 109, 141802 (2012)
[4] A. Calanna et al., IPAC2012, USA, MOPPD026.
[5] A. Calanna et al., Cyclotrons'13, Canada, WEPPT029.
[6] J. Minervini et al., "Engineering Study of Sector Magnet for the Daedalus Experiment", arXiv:1209.4886.
[7] A. Calanna et Al. "Injection and extraction from the Superconducting Ring Cyclotron", present report

Injection and extraction from the superconducting ring cyclotron for DAEδALUS experiment

A. Calanna[1], J. R. Alonso[2], L. Calabretta[1], J. M. Conrad[2], F. Meot[3], M. Haj Tahar[3], M.Shaevitz[4]

1) INFN-LNS, Catania, Italy
2) MIT, Cambridge, MA 02139, USA
3) BNL, Upton, Long Island, New York, USA
4) Columbia University, New York, USA

Abstract - The preliminary study of the injection line into the 6 sectors Superconducting Ring cyclotron is here reported. The injected beam is a molecular beam of H_2^+ at energy of 60 MeV/amu. We simulated the injection path of the H_2^+ and evaluated radial injection scheme, the parameters of the necessary element and the beam envelope beam along the injection line are presented.

The beam extraction is performed by H_2^+ dissociation crossing a thin stripping foil. The simulated extraction trajectories, the proposed solutions and the related problem are also presented.

INTRODUCTION

The Superconducting Ring Cyclotrons (SRC) has been studied in the past years to perform the DAEδALUS experiment [1,2]. This cyclotron has to deliver an average beam power of about 2 MW with a duty cycle of 20%. This means that the peak power of the cyclotron is about 10 MW. So this accelerator could be usable also to drive sub-critical Thorium reactor or waste transmutation reactor. After some preliminary study [3,4] with 8 sectors, the design has significantly evolved in a 6 sectors to reduce costs and complexity. The maximum magnetic field was also reduced from the early value of 6 T to 4.5 T and consequently, the radial magnetic forces on the sectors are significantly decreased [5,6,7].

The cyclotron complex consists of an injector cyclotron accelerating H_2^+ molecules up to 60 MeV/amu and then the beam is injected into the 6-sectors cyclotron by means of electrostatic and magnetic elements, and accelerated up to 800 AMeV. The acceleration is performed by 6 RF cavities, 4 single gap, PSI-like, and 2 double-gap. A plot of the OPERA magnetic field map in the median plane including the injection trajectory and the equilibrium orbit at the injection energy are shown in Fig. 1. The study of the injection beam line and the evaluation of the equilibrium orbit were performed using the ZGOUBI [8] code that confirmed the previous study performed the code developed at MSU (SPIRALGAP, GENSPE) and used by the Catania group.

Here the preliminary study of beam injection line and the solutions how to perform an efficient 100% beam extraction are described.

THE INJECTION BEAM LINE

The injection system needs to transport the beam from a point outside the cyclotron ring to the first orbit suitable for acceleration. The main constraints of the design are:

- The beam has to match the equilibrium orbit;
- The beam envelope has to be kept small (<4 cm) along the injection trajectory;
- Mechanical compatibility with the magnet and RF cavities of the SRC.

An usual easy and straightforward solution to study and describe the injection problem is to track backwards (clockwise) starting from the matching point. The matching point is where the injection trajectory match the equilibrium orbit that is at the exit of ED1 un Fig. 1).

The elements of the injection line are two electrostatic deflectors ED1 and ED2 and two magnetic channels B1 and B2. ED1 and ED2 are placed inside an empty valley they are independent to simplify alignment to the injected beam. The magnetic channel B1 is installed inside the gap of a sector magnet, while the B2 channel is in the transition region between a sector magnet and the empty valley. Then, to simulate the injection elements, the magnetic and the electrostatic field of each device used along the injection line were added to the original magnetic field map and imported in ZGOUBI. To focus the beam it was necessary introduce a focusing gradient field of 0.68 kGauss/cm just inside the B2 magnet. The parameters of the injection devices are shown in table 1.

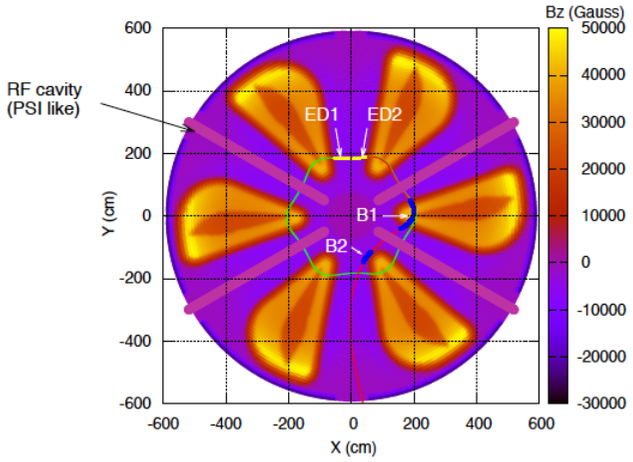

Figure 1: Layout of the injection system for the SRC

Table 1: Electrostatic and magnetic channel parameters

Label Device	Type	Strength	Effective Length
ED1	Electrostatic	50 kV/cm	0.55 m
ED2	Electrostatic	50 kV/cm	0.39 m
B1	Magnetic	9 kGauss	1.13 m
B2	Magnetic	18 kGauss	0.42 m

The axial beam envelope along the injection channel is shown in fig. 2). The red trajectories are obtained with the B2 magnet channel without focusing gradient; while the green trajectories are achieved applying a 0.68 kGauss/cm gradient only at magnet channel B2. The maximum vertical size of the beam envelope reaches the 4 cm just at outer radii outside the cyclotron magnet. The radial size of the beam is a bit larger than 4 cm at outer radii and matches the equilibrium orbit with a size <1.6 cm. The emittance value used in our simulation is13.5 π mm.mrad, that is a very large value, just to take account of transport non-linearity and beam halo.

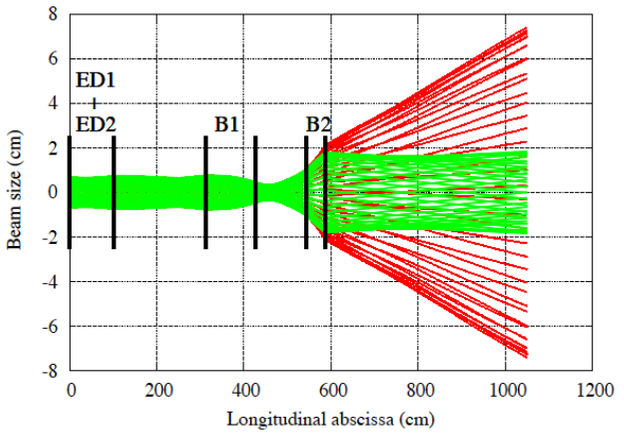

Figure 2: Axial beam envelope along the injection line. Red trajectories are achieved without focusing gradient. Green trajectories with a focusing gradient applied on B2.

BEAM EXTRACTION BY STRIPPING

The extraction by stripping is used in many commercial cyclotrons to extract beam current of 1 mA and more. The stripper is also used at SNS (Oak Ridge) to inject the 1 GeV H^- beam into the accumulator ring. So this technique is chosen to extract the H_2^+ beam from the DSRC. The DSRC will be operate with a pulse width around 1 - 2 msec. to ensure the foil temperature stay below 2000 K. according on the experience of SNS foil lifetime of several months is expected. In fig. 3) two extraction trajectories of the proton beam generates from the H_2^+ beam crossing the stripper foil are shown. The slow extraction (Blue line) cross the center of the DSRC while the Fast Extraction (Red line) is more attractive. To achieve the slow extraction, the stripper is placed at entrance of the sector, while for the fast extraction the stripper is placed at the exit side of the sector. Anyway, the stripper has to stay in a region where the magnetic field has the polarity of the hill and a value lower than 2 kGauss. Indeed, in these regions the electrons stripped from the H_2^+ are bend towards the outer radius and can be removed easily, avoiding to heating of the stripper foil. Unfortunately, the present magnetic configuration produces a separation of only 3÷4 cm between the accelerated orbit and the fast extraction trajectory. A magnetic configuration with higher reversed field in the valley can increase this separation. The use of permanent magnet placed in the valley to increase locally the field and then the separation between the extracted trajectory and the last accelerated orbit will be also investigated.

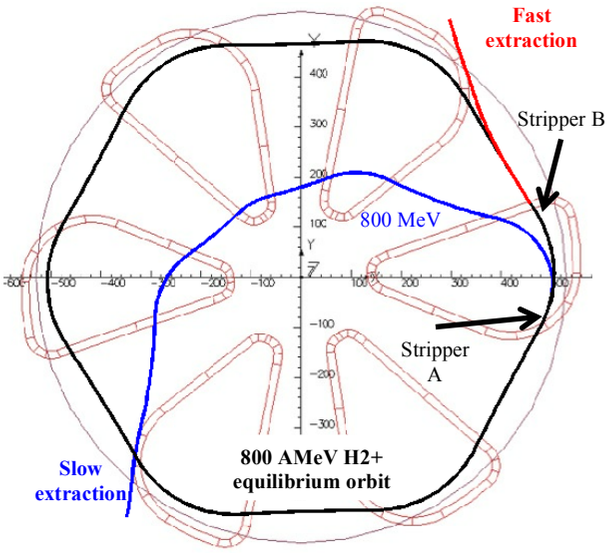

Figure 3: Trajectories of proton produced by H_2^+ dissociation in a localized position go away from the booster cyclotron.

CONCLUSIONS

The present study demonstrates that it is possible to inject the 60 AMeV H_2^+ into the DSRC using just two magnetic channel and electrostatic deflectors. The two possible extraction lines (slow and fast) have not interference with the main components of the cyclotron.

REFERENCES

[1] J.M. Conrad and M.H. Shaevitz, Phys.Rev.Lett. 104, 141802 (2010).

[2] J. Alonso et al., "Expression of Interest for a Novel Search for CP Violation in the Neutrino Sector: DAEδALUS", Jun 2010. e-Print: arXiv:1006.0260.

[3] L. Calabretta et al., Int. Conf. on Cycl. and their App. Lanzhou 2010; TUA1CIO01 http://www.JACoW.org

[4] A. Calanna et al., PAC New York (USA) 2011, http://www.JACoW.org

[5] A. Calanna et al, Int. Cycl. Conf. App., Vancouver (C) 2013, http://www.JACoW.org

[6] J. Minervini et al., "Engineering Study of Sector Magnet for the DAEδALUS Experiment", arXiv:1209.4886.

[7] D.Campo et Al., IPAC, Hamburg (D) 2014, http://www.JACoW.org

[8] F. Meot, "ZGOUBI users' guide", BNL (USA)

Update of the ECR ion sources

S. Marletta[1], M. Castro[1], M. Cafici[1], F. Chines[1], F. Speziale[1], S. Vinciguerra[1], L. Andò[1], G. Castro[1], L. Celona[1], L. G. Cosentino, S. Gammino[1], O. Leonardi[1], D. Mascali[1], D. Nicolosi[1], S. Pulvirenti[1], F. Noto[1], G. Torrisi[1,2]

1) INFN-LNS Catania, Italy
2) Univ. Reggio Calabria, Italy

Abstract
At INFN-LNS two Electron Cyclotron Resonance Ion Sources (ECRIS) have been used to produce highly charged ion beams to be accelerated by the K-800 Superconducting Cyclotron (CS) since the end of '90s. In the recent years the LHe shortage limited the SERSE availability to few weeks only and an improvement of the CAESAR performance was requested at the same time. Therefore it was decided to start a series of improvements to the two sources, and at the same time to consider the possibility to add a third ECRIS to the injection line or to replace CAESAR with a new ECRIS. The latter option is the most convenient when looking to the future upgrade of the CS and it is coherent with the developments ongoing in different European laboratories, which requested the INFN-LNS collaboration in order to upgrade their injectors.

SERSE CRYOSTAT AND OVEN UPGRADE

The recent SERSE availability has been unsatisfactory because of some intrinsic drawbacks coming from the transfer line of the LHe and from the cryogenic plant, so the proposal to modify the cryostat to operate in stand-alone mode, over the table since twelve years, was finalized. Costs and risks (non reliable technology was available years ago for this kind of applications) were the limiting factors that suggested to postpone this modification, but in 2013 a study carried out by a consultant demonstrated that the use of Pulse Tubes (which have no parts needing any maintenance at LHe temperature) and a different design of the cryocooler mechanics may limit any risk and at the same time it may allow a reasonably short time for the modifications (few weeks). In 2014 the technical proposal of a company confirmed the considerations above and an order was issued for the "turret" construction (i.e. all the cryogenic element to provide Helium recondensation along with the current leads of HT-superconductors), while the procurement of two 1.5 W cryocoolers was carried out.
The two cryocoolers will be integrated in the SERSE cryostat in place of the LHe transfer line (in the design one cryocooler instead of siphon, while the other will be used for the HTS thermalization and recondensation); the existing current leads, responsible of the major thermal load, will be replaced by properly designed HTS.
The method of cooling the current leads is quite modular so that it can be thoroughly tested in the factory before it goes to INFN-LNS.
This design is based on a cryocooler placed in vacuum (continuously with the cryostat main vacuum space), while the current leads (and other services like level gauges and voltage taps) run down inside the neck. The neck diameter is not changed (approximately 100mm).
In the 4K volume, there will be a finned copper heat exchanger which will be used to recondense the helium gas in the neck. The cryocooler will be connected to the neck to the HTS adductors by flexible copper links at 50K and 4K, and care is done to avoid thermal stress and to give some margin for alignment during installation.
It will be possible to remove the cryocooler for servicing or exchange without dismounting the current leads, and to remove the current lead insert without interaction with the cryocoolers. The turret's mechanics construction is under way and the factory tests will be carried out in July 2015, to start the warm-up of the cryostat at the same time. In August-September 2015 the modified turret will replace the old one, so that extensive test may be carried out before delivering beams to users. A long run test with plasma in the worst condition as for X-ray production rate will conclude the site acceptance test.
The upgrade of the cryostat is the most important upgrade of the SERSE source under way, but the implementation of a new high temperature oven is to be mentioned, which already permitted the production of gold beams for the users. In fig. 1 a picture of this oven, able to run up to 1800 K, is shown.

Fig. 1 – A picture of the oven for the SERSE source.

CAESAR MODIFICATIONS

The path towards the improvement of CAESAR performances is based on two key points: i) magnetic field enhancement to operate from 14 GHz to 18 GHz; ii) redesign of a new microwave injection system.

The first point has been obtained by adding a plug at injection side to increase the injection mirror (see fig. 2); after that some iron of the yoke was removed for mechanical reasons; recently tests have been carried out to optimize its position, according to fig. 2.

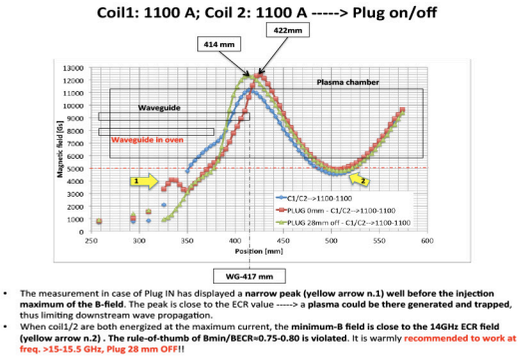

Fig. 2 – Magnetic values for the injection side field of the CAESAR trap in three different configurations (without plug and with the plug in two positions, 28 mm apart).

It can be observed that the magnetic measurements are in agreement with the OPERA calculations and the presence of the plug has the effect to increase the injection maximum field of 20% approximately. Since the B-min field of CAESAR is produced by two coils only, the plug also boosts the minimum value B_0; this way, the "rule of thumb" of $0.7<B_0/B_{ECR}<0.8$ is violated in most of cases when the frequency is <14.5 GHz. The optimum operative frequency seems to be in the range between 15 and 16 GHz, and specific experimental tests are expected within May 2015, to test the CAESAR performances in terms of the frequency scaling when using a broadband (8-18 GHz) TWT microwave generator. During the preliminary tests at higher frequency, i.e. 18 GHz, in 2014, the source produced beam currents about 20 to 40% larger than they did with the 14 GHz generator in the same conditions. The new measurements of the magnetic field profile have also permitted to explore the optimal position of the waveguide at the injection endplate, as highlighted in fig. 2.

CONSIDERATIONS ABOUT NEW SOURCES

The best ion sources' choice for the K-800 SC upgrade has been considered in 2014 and different solutions are in ballot. Two new designs of ion sources have been preliminarily studied, i.e.: ASIA (Advanced Source for Ion Accelerators, a 3rd generation ECRIS following a "conservative" approach) and HIBLAS (Heavy Ions Beams pLAsma Source, following a more challenging approach). The option ASIA is somehow more conservative since this source is based on a mature magnetic field technology. The description of the specific operating parameters of ASIA and HIBLAs is given in table 1. A third proposal (more conservative than ASIA, but characterized by a good compromise between robustness and versatility) is the AISHa source, currently under construction at INFN-LNS [1], which can be easily adapted to the Nuclear Physics demands. With respect to the ASIA and HIBLAs, AISHA works at lower magnetic field and plasma energy content, then the maximum performance in terms of high intensity heavy ion beams shall be less impressive with respect to the sources described in table. In case of CS upgrading, AISHa would permit to operate with larger currents for the light ions during the commissioning phase. In the case of a further need to upgrade the beam current, a decision between ASIA and HIBLAs may be taken, as the limitation of magnetic field and the smaller size of the plasma chamber (Φ = 92 mm) will not permit to AISHA to fulfil all the expectations, even if a possible upgrading to 21 or 24 GHz is envisaged.

Parameter	ASIA	HIBLAs
Frequency	24 GHz + 28 GHz	28 GHz + 35 GHz
Max power	3+1 kW	5+5 kW
Radial field (chamber wall)	1.6 – 2.0 T	2.7 T
Axial field	3.0/0.5/2.0 T	4.5/0.7/3.2 T
Voltage	20 – 40 kV	40 – 60 kV
Plasma ch. ϕ	≈ 150 mm	180 mm
Plasma ch. length	≈ 550 mm	700 mm

Table 1: Design parameters of the two sources proposed for the upgrading of the K-800 SC.

The increase of the operating voltage for any source is one of the main conditions to fulfil for different reasons:

a) the extracted current increases as $V^{3/2}$;
b) beam losses in the LEBT are smaller;
c) matching to the cyclotron acceptance is improved.

Higher currents for heavy ions may be also obtained by means of an upgrading of the SERSE source plasma chamber in order to operate at higher voltages, up to 35 kV, and with a larger power than 4 kW. This change has been studied from the mechanical point of view but a complete thermomechanical analysis is to be carried out, in order to allow also its effective upgrade to 21-24 GHz operating frequency.

In order to improve the beam transport efficiency and minimize current losses, a better beam diagnostics has been built and will be tested in 2015, with a cheap and reliable system, easy to use and control. It consists of a high sensitivity CCD camera detecting the light produced by an ion beam hitting the surface of a scintillating screen and of a frame grabber for image acquisition. Several screens can be used, like LYSO, CaF2 and KBr. In particular, a homemade scintillating screen was developed. The scintillating material, BaF2, was evaporated on a 2 mm thick aluminium plate. At the end of the evaporation process, a 2 μm thick BaF2 layer was created on the aluminium background.

REFERENCES

[1] L. Celona et al., this report

Plasma heating studies in Electron Cyclotron Resonance Ion Sources in the framework of the ENSAR-ARES activities

D. Mascali[1], S. Biri[2], R. Racz[2], C. Caliri[1,3], G. Castro[1], L. Celona[1], L. Neri[1], G. Torrisi, C. Altana, G. Sorbello, A. Galatà, S. Gammino[1] and G. Ciavola[1]

1) INFN - Laboratori Nazionali del Sud,Via S. Sofia 62, 95125 Catania, Italy
2) Institute for Nuclear Research, Hungarian Academy of Sciences, H-4026 Debrecen, Bem tér 18/c, Hungary
3) Università degli Studi di Catania, Dip.to di Fisica e Astronomia, via S. Sofia, 64, 95125 Catania, Italy
4) Università Mediterranea di Reggio Calabria, DIIIES, Via Graziella, 89100 Reggio Calabria, Italy;
5) CNR-Istituto per i Beni Archeologici e Monumentali, Via Biblioteca 4, 95124 Catania, Italy
6) Università degli Studi di Catania, DIIT, Viale A. Doria 6, 95125 Catania, Italy

Abstract - The ENSAR/ARES team continued the exploration of plasma X-ray emission properties with a focus onto the correlation of the produced charge states and the charge state distribution. The outputs of the GSI experiment in 2013 [1] have shown that the frequency affects the plasma heating (and in turns the buildup of the warm electrons population) as a consequence of the wave-to-plasma coupling mediated by the resonator nature of the plasma chamber. The following idea was that – conversely to the traditional road followed so far, consisting in "volumetric" measurements of plasma radiation – space resolved X-ray measurements would be necessary in order to investigate how the plasma structure in the "warm electrons" domain changes with the resonant modes. Results of the experimental and theoretical activities will be illustrated in the following.

INTRODUCTION

A new setup based on a CCD camera coupled to a small pin-hole for X-ray imaging and space resolved spectroscopy has been designed, assembled and tested in November 2014 at ATOMKI – Debrecen (Hungary).

As propaedeutic stage to CCD setu-up [2], SDD and HpGe detectors were used to characterize the volumetric plasma emission. The SDD detector has been placed on the injection side of the ATOMKI ECRIS in order to allow X-ray measurements and beam extraction (including CSD determination) at the same time, thus providing a direct relationship between the CSD and the plasma spectrum.

EXPERIMENTAL SETUP

The overall setups used during the experimental campaign, as well as the simplified sketches of the experimental apparatus are shown in figures 1 and 2. Figure 2 shows the two different setups used for the measurements of the emission at intermediate energies (2-30 keV). The short collimator configuration – estimating the total flux coming both from the plasma and the chamber - was useful for making possible CCD camera measurements ensuring safe operations below the critical photon flux. For the same reason a HpGe detector was also used for monitoring the high energy part of the plasma spectrum. The "long collimator" configuration was instead very useful for evaluating plasma density and temperature. The collimator length, in fact, was calculated in order to avoid any interception of the cone of view with the extraction endplate (the cone lies exactly within the extraction hole). In this way, the detected X-rays can be considered as solely emitted by the plasma bulk itself, allowing the plasma density and temperature calculation along the line of sight. After the SDD measurements, the CCD (made by 256x1024 pixels and with a sensitivity range 400 eV – 10 keV, approximately) was coupled to a lead pin-hole and placed along the axis, facing the chamber from the injection flange. The plasma chamber inspection was possible through a metalling mesh covering about the 60% of the injection endplate.

EXPERIMENTAL RESULTS

Results collected during the experimental campaign are illustrated in figures 3 and 4. Figure 3 shows the trend of the <q> as a function of plasma energy content. Each point corresponds to a different frequency, in the range 12.8-13.5 GHz, with steps of 40 MHz each. <q> clearly grows with the energy content, but the scattered points demonstrate that it is not strictly a matter of density or temperature (or the product between them) being each <q> obtainable by different combinations of energy contents, depending on the pumping wave frequency. We expect it is the shape of the plasma density, which plays a fundamental role, that gives the explanation to these data, and not only the global energy deposited into the warm electrons population, as detectable by the SDD.

This motivated the X-ray imaging and space resolved spectroscopy (XSRS). Hereby we will show just imaging for a single excitation frequency (figure 4). Color scale refers to the number of photoelectrons produced in each pixel (therefore related to the flux of X-rays impinging on it). The general structure of the plasma is clearly visible, with an hollow profile of the emission intensity (less intensity in the near-axis region), the branches due to the electrons escaping from the confinement volume, and the hot spots due to lost electrons producing bremsstrahlung radiation when impinging on the chamber walls.

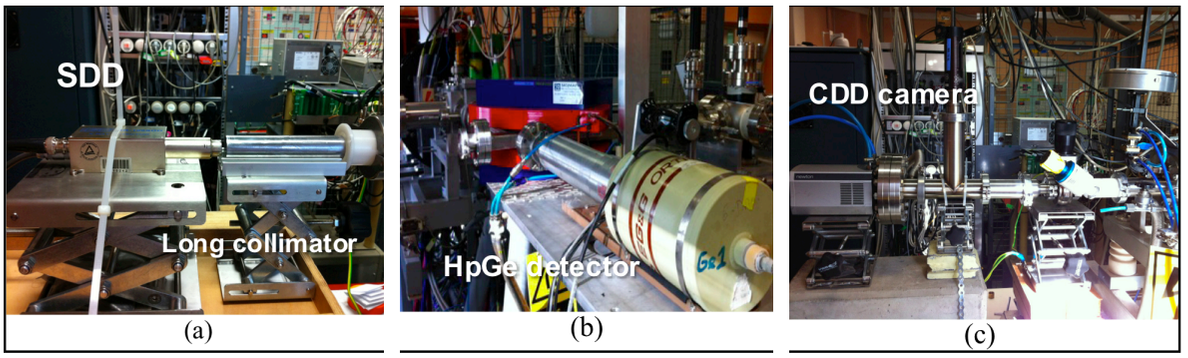

Figure 1: (from left to right) - a) long collimator setup for the Silicon Drift Detector; b) HpGe detector for the characterization of the X-ray emission at high energy (E>40 keV); c) CCD camera coupled to a lead pin-hole for X-ray imaging of the plasma.

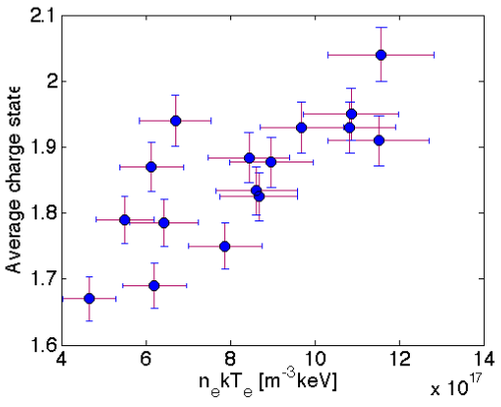

Figure 2: average charge state as a function of the plasma energy content as measured by SDD spectra. Points refer to different RF frequencies.

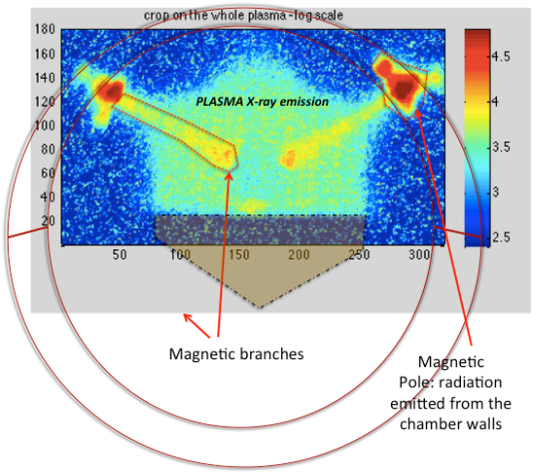

Figure 3: Imaging of the plasma obtained by the CCD camera pin-hole method.

This motivated the X-ray imaging and space resolved spectroscopy (XSRS). Hereby we will show just imaging for a single excitation frequency (figure 4). Color scale refers to the number of photoelectrons produced in each pixel (therefore related to the flux of X-rays impinging on it). It is clearly visible the general structure of the plasma, the hole in the near axis region, the branches due to the electrons escaping from the confinement and the hot spots due to lost electrons producing bremsstrahlung radiation when impinging on the chamber walls.

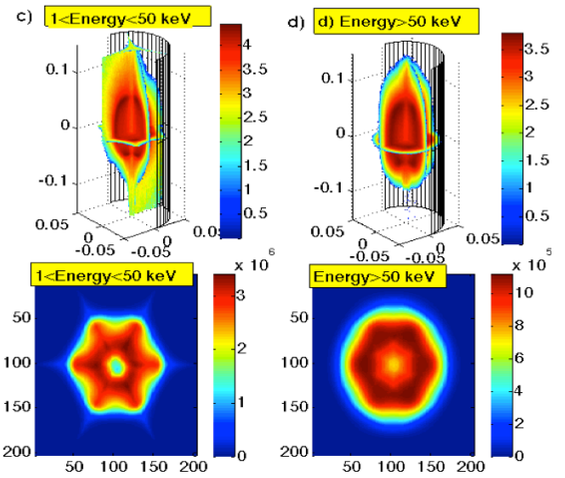

Figure 4: Upper row: Simualated 3D density distribution [a.u] at different energy ranges (a.u. in log scale); Lower row: integrated density distribution in a 2D transversal view (a.u. in linear scale).

Several features of the plasma structure are already clear from this picture, and can be better explained looking to the simulations [3], that are now in very nice agreement with the experimental data. Figure 4 shows them: i) simulation reproduce the feature of the plasma as a dense plasmoid surrounded by a rarefied halo; ii) electrons at different energies distribute differently in the space: cold electrons in the core, hot ones in near ECR regions, leaving a hollow profile in the near axis region; this impacts on ion dynamics and ion beam shape, which strongly depends on electron/ion distribution on the plasmoid surface. Therefore, the optimization of the ion beam formation will be possible in future by optimizing the scheme of the wave launching, with a more efficient deposition of energy in the near axis region.

REFERENCES

[1] D. Mascali et al. Rev. Sci. Instrum. **85** , 02A956 (2014); http://dx.doi.org/10.1063/1.4858115
[2] S. Biri et al., Rev. Sci. Instrum. 75, 1420 (2004);
[3] D. Mascali et al. Eur. Phys. J. D (2015) 69: 27
DOI: 10.1140/epjd/e2014-50168-5,

Test of the first equipment developed for the ESS accelerator

S. Gammino, L. Celona, L. Neri, D. Mascali, G. Castro, G. Torrisi, L. Andò, O. Leonardi, D. Nicolosi, L. Allegra, N. Amato, A. Caruso, F. Chines, G. Gallo, A. Longhitano, G. Manno, S. Marletta, E.G. Messina, S.M. Passarello, E. Zappalà,

INFN-LNS, Catania, Italy

Abstract - The design update of the European Spallation Source accelerator has been carried out in the previous years and the construction of the prototype of the microwave discharge ion source able to provide a proton beam current larger than 74 mA to the 3.6 MeV RFQ started. Different new requests was inserted during the already started design phase, the increase of the current, the increase of the source stability and the possibility to vary the proton current without changing the current of the source. The new requests obliged to redesign some parts of PS-ESS and of the LEBT introducing new components (such as iris), and forced the design to a flexible strategy merging conservative solutions with innovative solutions. Different parts of PS-ESS and the LEBT will be able to provide, with an intrinsic flexibility, the standard configuration and new solution that will be tested to increase the performance or to reduce the balance the negative effects of other borderline solutions. One of the most critical point of the LNS in-kind contribution is developing of the right chopper strategy able to perform fast rise and fall time of an intense beam transported in high Space Charge Compensation (SCC) regime. The construction of the chopper, of the LEBT collimator and of the fast current measurement was done with high priority to perform test at LNS and at the BETSI setup of CEA-Saclay in advance with respect the design of all the others LEBT elements.

DEFOCUSING CHOPPER TEST

The chopper was designed in order to reduce the heating problem due to a focused chopped beam in the LEBT collimator and to speed up the beam pulse rise and fall time in presence of an high SCC degree. The scape of the electrodes was chosen to be able to provide two electric field components, one for the deflection of the beam and the latter for the defocusing of the beam[1].The recent collaboration between LNS and Ganil, in the frame of the Spiral 2 project, was a good starting point in the design of the ESS LEBT chopper electronics. The position and the scope of the two choppers developed for the two project are the same and also the time response request is practically the same. The chopper electronic works up to 10 kV, 14 Hz repetition frequency rate, with a rise and fall time of 15 nanosecond and it was designed to be as reliable as possible because it is part of the beam stop chain of the machine protection system.

Different tests have been carried out with the aim to measure the beam pulse rise time dependence from the chopper voltage, the LEBT pressure, the LEBT gas composition and other optical parameters. BETSI test bench was composed by the source, two solenoids like for IFMIF, an emittance measurement unit (EMU), a beam dump, a residual gas analyzer and vacuum ancillaries.

The LNS team also prepared a dedicated setup for low impedance measurements of the current impinging on the LEBT collimator and on the beam-stop located behind it. At first we measured the current transported in the LEBT when the chopper is turned on and the current of H2+ and of the focused H+ when the chopper is turned off. In the latter case, since beam stop was placed after the LEBT collimator, the beam transmitted through the hole has been measured. With such configuration we double-checked the rise and the fall time of the produced beam pulse. The extremely low impedance (5.8 ohm) current readout, allowed fast current measurement ($3 * \tau = 3 *$ 534 pF * 5.8 ohm = 9.3 ns) despite the high capacitance of the LEBT collimator (534 pF).

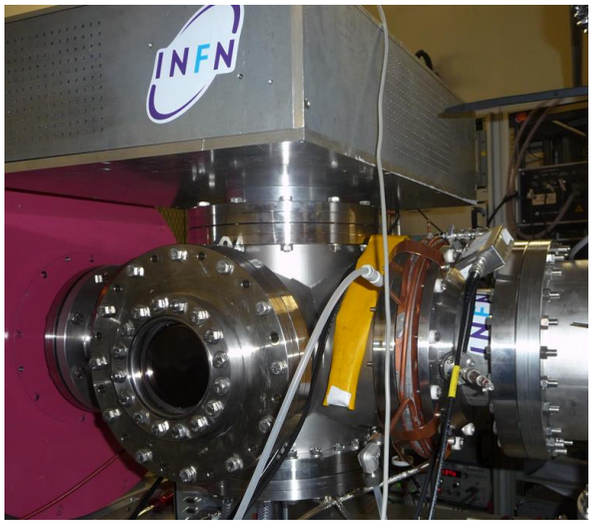

Figure 1: Defocusing chopper with high voltage electronics box and LEBT collimator installed on the BETSI setup.

EXPERIMENTAL RESULTS

There was different troubles and mismatches between the experimental setup used and what planned for the ESS accelerator, the result are not conclusive but the

measurements campaign allowed to estimate rise and fall times and give to us the possibility to try to understand the involved phenomena.

The beam pulse fall time is the simplest to understand because is not sensitive to the SCC effects. We measured a fall time of 50 ns, and we observed that this value is not sensitive to the condition of the LEBT and of the chopper. We estimated that this amount of time is due to the time needed to switch on the voltage on the chopper electrode (15 ns) and the time needed for the beam to pass through the electric field region of the chopper. When the chopper is switched on the beam after the electric field region of the chopper is not deflected, the beam that is at the center is half deflected and only the beam that is at the beginning of the electric field region is fully deflected. The shape of the transmitted beam is composed by all this parts so the fall time is sensitive to the length of the electric field region that in our case produce 35 ns time lapse. For the understanding of the fall time measurement, shown in the next figure, it is important to notice the delay due to the location of the different measurement points with respect to the position of the chopper. In the figure below it is possible to see a very big electromagnetic interference due to the fast chopper transition. This effect cannot be avoided and must be taken into account for the design of all the equipment will be used in the ESS accelerator.

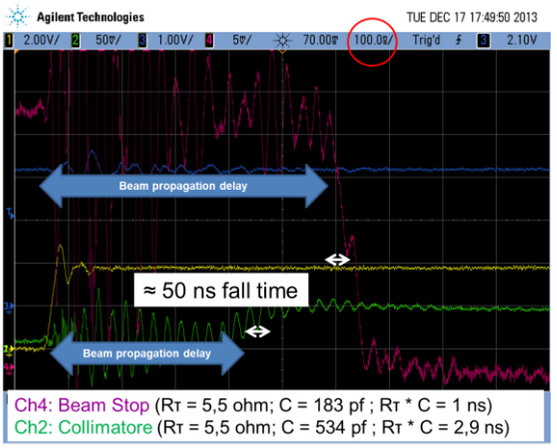

Figure 2: Beam pulse fall time.

The beam pulse rise time is observed when the chopper is switched off and the beam start to travel along the axis. After the voltage chopper transition (15 ns) and the beam propagation delay due to the trip along the electric field region (35 ns) we observed a slow transition of the beam pulse current that is due to the reconstruction of the SCC. When the chopper is on the electric field destroy the SCC at least in the region close to the chopper. When the beam is suddenly switched from the deflected trajectory to the straightway trajectory a part of the electron cloud is probably lost so the SCC of the beam after the chopper transition start from a value different from 100%. After the chopper transition the beam is completely not compensated close to the chopper and is partially compensated from the copper to the LEBT collimator. After the chopper transition the beam need time to reconstruct the SCC lost. By changing the pressure inside LEBT, the magnetic configuration of the two solenoids or the voltage of the chopper, we observed changes in these slopes. In the figure below the a slow transition of 250 ns is reported for the configuration chosen like the most opportune for the ESS setup.

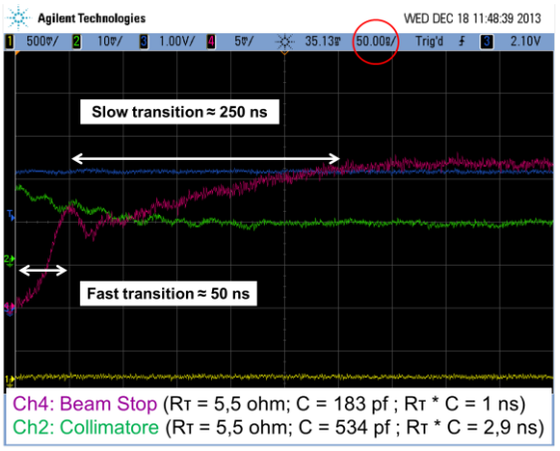

Figure 3: Beam pulse rise time.

UPGRADES

Using the knowledge gained during this test we was able to design a completely new chopper that merge the faster beam chopping strategy, the needed compactness (157 mm flange length along the beam direction), the increased shielding (to protect the power electronics) and the presence of the feedback antenna and the water-cooling need.

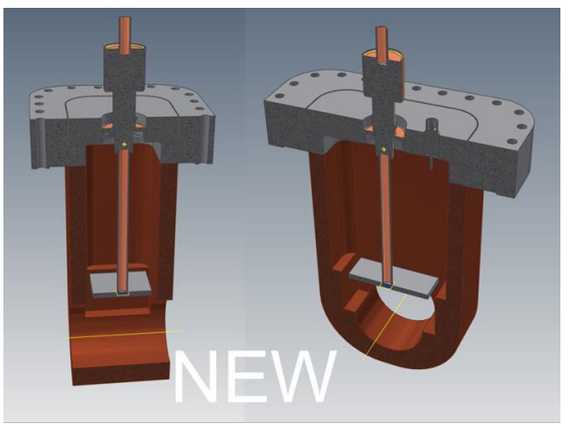

Figure 4: New design for the defocusing chopper.

ACHNOULEDGEMENTS

The collaboration of the CEA-IRFU team, for the measurement on the BETSI setup is warmly acknowledged. The authors wish to thanks the Technical Services, Workshop, Administrative Staff of LNS for the support to the ESS project and the comprehension of its challenges.

REFERENCES

[1] L. Neri et al., R.S.I 85, 02A723 (2014)

Design of the AISHa Ion source for hadrontherapy facilities

L. Celona[1], L. Allegra[1], G. Castro[1], G. Costa[1], F. Chines[1], G.Cuttone[1], G. Gallo[1],S. Gammino[1], O. Leonardi[1], S. Marletta[1], D. Mascali[1], L Neri[1], D. Nicolosi[1], F. Noto[1], G. Torrisi[1,2], , G. Ciavola[1,3], L. Andò[1], F. Romano[1], G. Costa[1], A. Galatà[1,4]

1) INFN - Laboratori Nazionali del Sud,Via S. Sofia 62, 95125 Catania, Italy
2) Università Mediterranea di Reggio Calabria, Dipartimento di Ingegneria dell'Informazione, delle Infrastrutture e dell'Energia Sostenibile, Via Graziella, 89100 Reggio Calabria, Italy;
3) CNAO Foundation, Strada Campeggi, 53, Pavia PV, Italia
4) INFN - Laboratori Nazionali di Legnaro, Viale dell'Università, 2, 35020 Legnaro PD, Italia

Abstract - Different facilities for hadrontherapy have been built or designed in the recent past and Italy is present in the field either with synchrotron-based and with cyclotron-based facilities. For both types of accelerators the availability of high brightness multiply charged ion beams is essential and R&D efforts in this subject has already started within the frame of a collaboration between the Sicilian Authority and INFN. The construction of a new ECR ion source operating at 18 GHz, named AISHa, is under way.

INTRODUCTION

The AISHa ion source has been designed by keeping in mind the typical requirements of hospital-based facilities, where the minimization of the mean time between failures (MTBF) is a key point together with the maintenance operations which should be fast and easy. Therefore, a so called 3rd generation ECR ion source is not suitable, being quite complex for unskilled operators.
The new AISHa source is designed to be an intermediate step between the 2nd generation ECRIS (unable to provide the requested current and/or brightness) and the 3rd generation ECRIS (too complex and expensive). It is intended to be a multipurpose device, operating at 18 GHz, in order to achieve higher plasma densities. It should provide enough versatility for future needs of the hadron therapy, including the ability to run at larger microwave power to produce different species and highly charged ion beams. At the same time, the electrical power to be installed for its operation will be kept below 50 kW. This demand implies also the simplification of all ancillary systems including an oven for metallic ion beams, which permits the production of new beam for hadrontherapy and for other applications. The AISHa source is funded within the framework of the program of Sicilian Government named PO FESR 2007-2013 and a pool of Sicilian SME is associated with INFN for this project. The source is potentially interesting for any hadrontheraphy center using heavy ions.

MECHANICAL DESIGN AND BEAMLINE

The plasma chamber will be stainless steel made and it is designed to operate at a maximum power rate of 2 kW by using a multi-channel water-cooling system. The insulation will be adapted to 40 kV operation by means of a 20 mm thick Glass Fiber/Carbon fiber tube surrounding the hexapole, keeping magnets and yoke at ground potential. The movable extraction system will permit to adapt the AISHa source to other facilities (e.g. the high voltage platform for INFN-LNL). A new type of dc break has been designed to permit reliable operation even at 40 kV. The layout of the source is shown in Fig. 1.

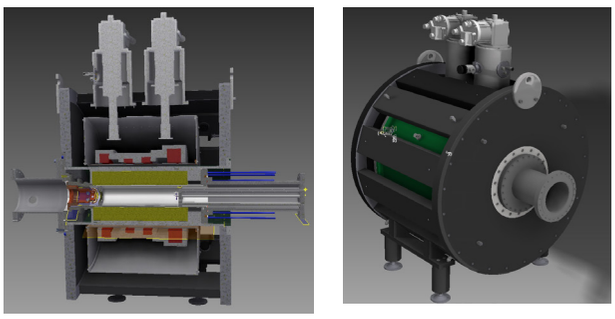

Figure 1: AISHa The layout of the source

In the development of this new source some improvements of mechanical and structural type have been introduced, in particular the optimization has involved two important parts of the source: the hexapole containment chamber and the plasma chamber. The optimization of these components has focused on two aspects: structural mechanics and fluid dynamics; both of these aspects have been optimized by using the COMSOL simulator. Permanent water flow in the plasma chamber is required to provide the expected low temperature. Therefore, the goal of our study was to optimize the design of the grooves.

The results obtained in the case of aluminum 3003-H18 in terms of temperature are satisfactory, as we are able to keep the maximum temperature on the outer surface of the plasma chamber in the order of almost 30°C thus avoiding any permanent damage to the magnets that are in contact with it. The flow obtained is substantially laminar.

MAGNETIC SYSTEM DESIGN

The AISHa source will be based on a hybrid magnetic system able to confine the plasma radially by means of a permanent magnet hexapole, providing a maximum field of 1.3 T in the plasma chamber; the axial confinement will be given by a set of superconducting solenoids, enclosed in a compact cryostat. The cryostat will include two cryocoolers that permit to the equipment to run in He-free configuration. Studies have been carried out for two different configurations, with 3 or 4 solenoids to generate the mirror field, but the solution with 4 solenoids was chosen for its versatility, even if it increases slightly the construction cost. The use of two middle coils instead of one may allow to finely tune the mirror ratio that is deemed to improve the ECR heating process according to recent achievements [1]. The hexapole demagnetization due to the superconducting solenoidal field has been carefully taken into account in the OPERA calculations to check where and if the demagnetization vector is greater than the coercitivity; such calculations permitted to appropriately choose the permanent magnet materials and to define the final hexapole structure. The magnetic field values obey to the so-called ECRIS standard model for the operational frequency of 18 GHz. The peak field at the injection sides will be around 2.6 T and at the extraction side it will be about 1.7 T, with a minimum value so low as 0.4 T, about 60% of the ECR resonance field. This design should maximize the plasma density with a moderate microwave power and with a set of magnets that do not present any criticality. The cryostat has quite compact dimensions (its total length is 620 mm and its diameter 550 mm); the ECR region may be sufficiently long to facilitate the production of multiply charged ions; by changing the current in the two middle coils the ECR region may extend it up to 100 mm. The tunable magnetic profile allows to improve the heating efficiency, suppressing the production of quasi-collisionless high energy electrons.

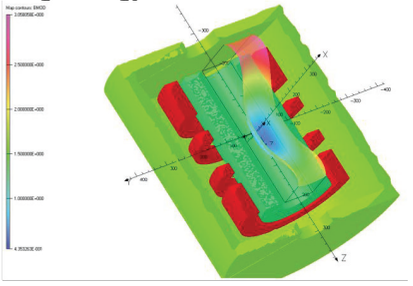

Figure 2: A 3D view of the entire magnetic system

The permanent magnet hexapole is made of NdFeB and it has a total length of 440 mm, slightly longer than the plasma chamber, which length is 360 mm, roughly corresponding to the distance between the two maxima of the mirror field. The superconducting solenoids are NbTi made and they are surrounded by an iron yoke, 50 mm thick, with 50 mm thick end plates on both sides. The current density in the four coils is 145, 121,120 and 121 A/mm^2 respectively, with the second and third coil current running in opposite direction with respect to the injection and extraction coil. The maximum axial gradients is about 13 T/m, enough to run the plasma in "strong gradient regime" [1,2] even for moderate microwave power (500 W to 1 kW).

MICROWAVE SETUP

The microwave injection system is the key element of the AISHa source design, according to our recent studies [1-2]. The source will use a configuration with two amplifiers at high frequency (around 18 GHz) that inject separately the two frequencies in the chamber where the plasma is produced. The new generation klystron allows to change the frequency of about one GHz to exploit the mechanisms of Two Frequency Heating (TFH) and Two Close Frequency Heating (TCFH).

The position of the input waveguides (WR62 type) was determined on the basis of the field pattern for the different modes. An estimation was performed on the maximum intensity of the modal electric fields excited in a vacuum filled cylindrical cavity, representing the plasma chamber. Simple considerations indicated that a position close to the value of 0.6r is the best choice. The two frequency heating has been largely used to generate moderate currents of the highest charge states, but it has never been used to optimize the beam brightness. It may be helpful whether both the frequencies would be separately tuneable. In this way the electron energy distribution function may be optimized for the ionization of a definite charge state.

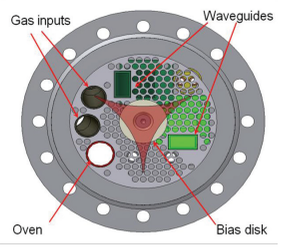

Figure 3: The injection flange

REFERENCES

[1] S. Gammino et al, Plasma Source Sci.&Tech. 18 (2009) 045016.

[2] S. Gammino, et al., IEEE Trans. on Plasma Science, (2008) vol. 36, 4 part II, 1552.

3D-full wave and kinetics numerical modelling of Electron Cyclotron Resonance Ion Sources plasma

G. Torrisi[1,2], D. Mascali[1], L. Neri[1], G. Sorbello[1,3], L. Celona[1], G. Castro[1], L. Di Donato[1,3], T. Isernia[2] and S. Gammino[1]

1) INFN - Laboratori Nazionali del Sud,Via S. Sofia 62, 95125 Catania, Italy
2) Università Mediterranea di Reggio Calabria, Dipartimento di Ingegneria dell'Informazione, delle Infrastrutture e dell'Energia Sostenibile, Via Graziella, 89100 Reggio Calabria, Italy;
3) Università degli Studi di Catania, Dipartimento di Ingegneria Elettrica Elettronica ed Informatica, Viale Andrea Doria 6, 95125 Catania, Italy

Abstract - We present a numerical approach to solve the 3D Maxwell-Lorentz system with the aim of investigating the interaction of the electromagnetic waves with the magnetized non-homogeneous plasma produced inside Electron Cyclotron Resonance Ion Sources. The FEM COMSOL Multiphysics® software was used to compute the electromagnetic field in a cavity filled by the anisotropic-inhomogeneous plasma, described by a full non-uniform dielectric tensor in "cold plasma" approximation. The full-wave solution is then coupled to an "in-Matlab" developed kinetic code based on a PIC – Particle-In-Cell strategy, solving the Newton-Lorentz equation of motion for plasma electrons. Our model explains the experimentally observed frequency sensitivity and gives a relevant contribution to the challenging goal of predicting the electron/ion dynamics in ECR plasmas

INTRODUCTION

Wave propagation modelling in magnetized plasma – including the coupling with the Newton-Lorentz equations of motion – represents a powerful tool for a better understanding of the physical phenomena occurring in the ECRIS plasma-filled resonant cavity, and a necessary step towards future developments and further optimization of advanced ECRIS.

COUPLED ELECTROMAGNETIC AND PARTICLE MOTION MODEL

Considering the plasma as a dispersive medium modelled as a cold magneto-fluid with collisions, in the Maxwell's equations appears a tensorial relation $\overline{\overline{\varepsilon}}(\vec{r})\cdot\vec{E}(\vec{r})$ that describes the field-plasma interaction.

According to the the "cold plasma" approximation, considering the actual magneto-static structure of an ECRIS (minimum-B configuration, see [1] for $B_{x,y,z}$ components) that is not uniform nor axis-symmetric, $\overline{\overline{\varepsilon}}(\vec{r})$ depends in a complex way from the magnetostatic field and the local electron density $n_e(x,y,z)$, (details in [1]). Full wave simulations are carried out, through the COMSOL Multiphysics FEM solver, considering the geometry shown in Fig. 1 (a) with an initial electron density $n_e(x,y,z)$ and the above described "cold plasma" model. Since nearby the resonance surface, individuated from the iso-surface $|\vec{B}_0| = B_{ecr} = \frac{m_e}{e}\omega$, the permittivity $\overline{\overline{\varepsilon}}(\vec{r})$ varies widely, in such narrow region the mesh needs to be finer and to achieve this, the ECR iso-surface has been used also to start the mesh construction and growth (Fig 1)).

Figure 1: on the left, the simulated geometry: Cavity and waveguide; on the right, the non-uniform mesh density: it is finer nearby the ECR layer .

FULL-WAVE AND PARTICLES MOTION 3D SIMULATION SETUP

The electromagnetic field $\{\boldsymbol{E}(\boldsymbol{r}), \boldsymbol{H}(\boldsymbol{r})\}$ solution is coupled to a 3D kinetic Matlab® code that is based on a numerical particles-in-cell method that simulates a plasma as a collection of N macro-particles, (being N much smaller than real plasma particles), with corresponding spatial coordinates and momenta described by the functions $\boldsymbol{r}_i(t)$ and $\boldsymbol{p}_i(t)$ for i^{th} particle. We considered a plasma consisting of a single species only (electrons), whose trajectories obey the Lorentz single particle equation of motion, considering electro-static (Spitzer) collisions at 90°:

$$\frac{d\,\boldsymbol{p}_i(t)}{dt} = q[\boldsymbol{E}(\boldsymbol{r}_i(t)\,, + \boldsymbol{v}_i(t \times \boldsymbol{B}(\boldsymbol{r}_i(t), t)] \qquad (1)$$

The kinetic code, following the relativistic Boris scheme, solves the equation of motion (1) of each single macroparticle for its entire life (i.e. until they impinge on the chamber walls), accumulating the electron density in a 3D grid; the output of the kinetic code is a new map for the local electron density n_e (x,y,z) to be used for computing $\bar{\bar{\varepsilon}}(\boldsymbol{r})$ and the electromagnetic field $\{\boldsymbol{E}(\boldsymbol{r}), \boldsymbol{H}(\boldsymbol{r})\}$. This loop should run until a convergence is reached. Hereby we show results up to step 1, i.e. after the evaluation of the magnetized plasma action on RF and vice-versa.

NUMERICAL RESULTS AND DISCUSSION

Figures 2 illustrate the COMSOL outputs for the power dissipation $\frac{1}{2}\vec{E}\cdot\vec{J}$ into the cavity (and the plasma in particular), assuming, at step 0, a preformed plasma with a maximum density of $0.7n_{cutoff}$ inside the volume embedded by the ECR surface. This field was used to calculate the electron motion.

In Figure 2, we show the dissipated power density by multislice, representation (3D): it is evident that the most part of the power is absorbed at the ECR layer. In Fig. 3 the electron density distribution is represented over the ECR isomagnetic surface as well as over planar sections.

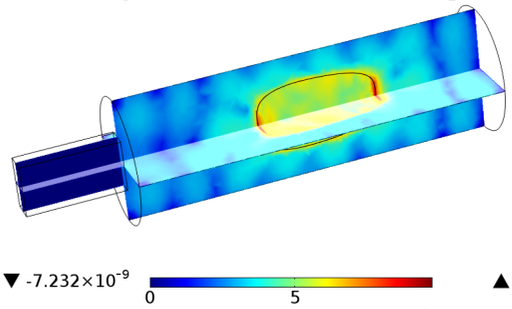

Figure 2: RF power loss density [W/m^{-3}] into the plasma plasma filled cavity (log scale)

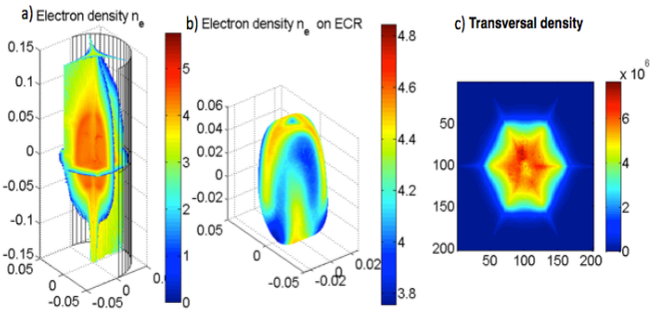

Figure 3: Total electron density n_e

This results highlight very interesting effects: i) the overall structure of the plasma assumes an hexagonal shape in agreement with the few available imaging results [2]; ii) the electrons (see fig. 3) accumulate mostly inside the volume limited by the ECR surface, forming a high density plasma core that can be named as "plasmoid", surrounded by a rarefied halo; iii) a density depletion region appears in the quasi-axial region, and it may be the responsible of hollow shapes in the transversal ion beam intensity plots, often observed in ion transport beam lines; iv) although the modal field distribution is perturbed by the medium, a standing wave pattern still persists in the plasma filled cavity as we can see in Fig. 2, and this may explain the sensitivity to the frequency tuning [3] manifested by many ECRIS.

PERSPECTIVES

The synergic (full wave plus kinetic) approach represents a considerable step forward with respect to other approaches already attempted in the past, when oversimplified models (assuming single mode refractive indexes, e.g. of R-waves [4] have been adopted. Additional steps will be needed to exhaustively model the plasma dynamics until the ion beam formation, which is the final goal of our activity.

ACKNOWLEDGEMENTS

The authors are warmly grateful to the INFN V Nat. Sci. commission funding the RDH-UTOPIA and ARES project

REFERENCES

[1] G. Torrisi et al., J. Electromagn, Waves Appl. 28, 1085 (2014)
[2] S. Biri et al., Rev. Sci. Instrum. 75, 1420, (2004).
[3] L. Celona et al., Rev. Sci. Instrum. 79, 023305, (2008).
[4] E. G. Evstatiev, et al., *Rev. Sci. Instrum*. 85, 02A503 (2014).

The Flexible Plasma Trap (FPT) for the production of overdense plasmas

S. Gammino[1], L. Celona[1], D. Mascali[1], G. Castro[1], L. Neri[1], G. Torrisi[1,2], G. Sorbello[1,3], O. Leonardi[3], C. Altana[1], C. Caliri[1], L. Allegra[1], F. Chines[1], L. D'Antoni[1], S. Di Modica[1], G. Gallo[1], G. Manno[1], S. Marletta[1], A. Maugeri[1], E. Messina[1], A. Seminara[1], B. Trovato[1], M. Tringale[1], G. Vasta[1], E. Zappalà[1]

[1] *Istituto Nazionale di Fisica Nucleare – Laboratori Nazionali del Sud, Via S. Sofia 62, 95123 Catania, Italy*
[2] *Università Mediterranea di Reggio Calabria, DIIES, Reggio Calabria (Italy)*
[3] *Università degli Studi di Catania, D. I.E.E.I., viale A. Doria, 6 - 95125 Catania, Italy*

Abstract

Electron Cyclotron Resonance Ion Sources (ECRIS) are currently the most efficient ion sources among those used in facilities dedicated to nuclear physics with stable and exotic beams, because of their ability to generate intense beams of medium charge state ions, or moderate intensities at high and very high state of charge (even 0.5 emA of U^{33+} o Xe^{34+}) [1].

The experience gained over the last four years at INFN-LNS allowed to understand new mechanisms of production of the plasma, highlighting the main weaknesses of the previous ECR ion sources modelling. The tests have been carried out on a fixed field plasma reactor with interesting results described in ref. [2,3] but the needs of a more flexible magnetic field led to a different type of plasma trap, named Flexible Plasma Trap, now ready to operate at INFN-LNS.

OVERDENSE PLASMAS

Very detailed models concerning the generation, propagation and absorption of electrostatic waves in plasmas (BW type) have been proposed by many theoretical physicists working in the field of controlled nuclear fusion by magnetic confinement [4]. In this context, the magnetic structure is mainly characterized by toroidal symmetries.

In the case of the ECR ion sources, the magnetic field has a clear axial development, although it differs from the purely axial symmetry typical of the devices like the Simple Mirror (magnetic bottle) due to the hexapolar contribution. Therefore the design of a source designed for the possible excitation of BW would allow to study their properties in an unexplored physical context, allowing the extension of the theoretical modelling of the phenomenon to plasmas confined by magnetic configurations of B-min type.

Preliminary studies were carried out on that effect in the early 90's by Golovanivski [5] who demonstrated the possibility to achieve a direct XB modal conversion [5], i.e. from the electromagnetic wave to wave of Bernstein (electrostatic), in a multipolar magnetic field configuration.

The BW are then absorbed to the harmonics of the cyclotron frequency.

Such expertise is deemed to be very useful, because the ability to optimize the main plasma parameters in ECRIS is considered as an unique tool to improve the beam quality, not only the beam intensity, that in turns permits a better matching to the following accelerator.

The availability of a compact plasma trap with flexible magnetic field, able to excite either the ECR and off-resonance plasmas, should allow to obtain a high plasma energy content in absence of radial confinement by means of a hexapole.

The study of a possible alternative mechanism of plasma excitation will be performed through the transmission of electromagnetic waves which should be absorbed at the second harmonic cyclotron (i.e. at values of magnetic field equal to half of the field at ECR resonance). This mechanism should allow to extend the region of "active" plasma (i.e. the one characterized by high electron densities), to cover the entire volume of the chamber.

Additionally, the study of the frequency tuning by means of the use of a broadband microwave generator (TWT), besides allowing to test the plasma heating in the second harmonic, permits to verify the effectiveness of the frequency tuning of the electromagnetic wave on increasing the electron density, as already observed with denser, energetic plasmas as those produced in High B mode plasma traps.

MAGNETIC FIELD PROFILES

The investigation of EBW-heating under different magnetic field configurations will be carried out by means of a plasma trap made of three solenoids which allow the tuning of the magnetic field profile. They will be studied with plasma and RF diagnostics placed parallel and perpendicularly to the B axis.

The overdense plasma is accessible only to plasma waves, that can be excited by pumping electromagnetic waves under proper injection properties. New injection schemes must be designed, considering alternative magnetic field profiles, tuning of frequency in the range between 3 and 7 GHz, and using sophisticated modelling and diagnostics tools, like the pinhole camera and CCD [6].

In particular we have considered three magnetic field profiles:

1. "Off-Resonance configuration", that permits the studies on plasma dynamics in case of parallel/perpendicular launching in a B field configuration like that of MDIS (fig. 3). The typical shape of the magnetic field for MDIS machines is a quasi-flat profile everywhere above the resonance value. This ensures electron densities around the cutoff at 2.45 GHz or slightly larger ($n \approx 10^{11}$ cm^{-3}), temperatures sufficient for hydrogen ionization (T=15-20 eV) and H_2 molecule lifetimes long enough for their ionization and proton generation [7].
2. "Simple mirror" for multiply charged ions production (like the one described in fig. 3). Studies about balance equations [8] of the different species living into the plasma for proton beams production (H_2, H_2^+, H^+) or for multicharged ions from light elements like Li or C, reveal that the reciprocal abundance is regulated by the relative lifetimes. The prolongation of low charge ions' lifetime, obtained when using the simple-mirror configuration, will increase the ionization efficiency thus boosting the production of 2^+ or 3^+ ions already at moderate RF power, while improving also the reliability of the source [8].
3. "Magnetic Beach" for exploiting mode conversion at UHR and EBW absorption in higher harmonics (fig. 1); to be converted into a BW, the X mode requires a rapidly dropping magnetic field which makes possible either UHR and second harmonic absorption. This configuration is sometime called "magnetic beach" [3].

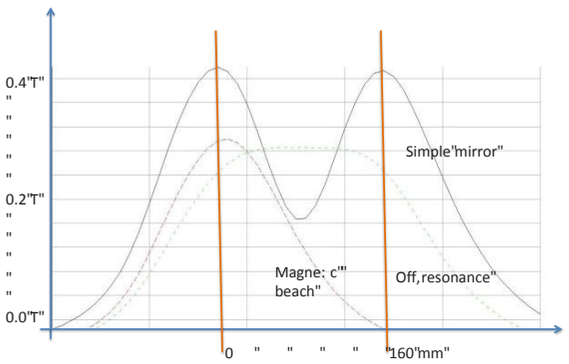

Fig. 1: Off-resonance, simple mirror and magnetic beach field profiles.

PLASMA CHAMBER

A particular attention was paid to the design of the plasma chamber which should take into account the ability to couple different waveguide inputs, including the possibility to have contemporary input of microwaves in two directions one perpendicular to the other, in order to have an adequate water cooling in the microwave windows location, and to permit at the same time to host different type of diagnostics, either optical and X-ray diagnostics in the first series of experiments, then also microwave interferometry and RF analysers able to span all the frequency range of the used microwaves and the first few harmonics.

The FPT setup has been installed at INFN-LNS and the commissioning and first tests are foreseen to be carried in spring 2015. A view of the FPT is shown in figure 2.

The design of FPT is optimized for plasma studies but with some modifications an extraction system may be installed, so that it may be transformed in an ion source and be coupled to a Low Energy Beam Transfer line, thus comparing the results of plasma studies with the output of the beam diagnostics.

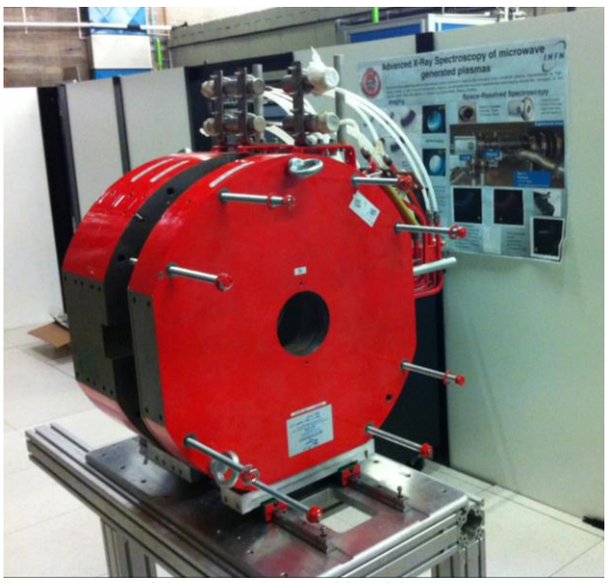

Fig. 2**:** *A view of the general ensemble of the FPT setup, including the RF system.*

ACKNOWLEDGEMENTS

The support of the 5th National Committee of INFN through the RDH-UTOPIA experiment is gratefully acknowledged.

REFERENCES

[1] B. Wolf. Handbook of Ion Source. FL: CRC Press, Boca Raton, 1995.
[2] D. Mascali et al., *Nuclear Instr. & and Meth.* A653 (2011)
[3] G. Castro et al., Applied Surface Science 272, 59-64 (2013)
[4] H. P. Laqua, *Plasma Phys. Control. Fusion* 49 (2007) 49:R1, (2007)
[5] K.S. Golovanivsky el al. *Physical Review* E, vol. 52, n.3 (1995)
[6] D. Mascali et al, *Rev. Sci. Instr*. 85, 02A956 (2014)
[7] T. Taylor and J. S. C. Wills, Nucl. Instrum. Methods Phys. Res. A 309, 37 (1991).
[8] H. Zhang. Ion Sources. Science Press Beijing and Springer, 1999.
[9] F. F. Chen. Introduction to the Plasma Physics and Controlled Fusion: Plasma Physics. U.K.:London Press, London, 1986.

Conceptual design and simulation of a microwave interferometer for plasma density measurements in ion sources

G. Torrisi[1,2], V. Finocchiaro[1], D. Mascali[1], G. Sorbello[1,3] , R. Agnello[1], G. Castro[1], L. Celona[1], L. Neri[1] and S. Gammino[1]

1) INFN - Laboratori Nazionali del Sud,Via S. Sofia 62, 95125 Catania, Italy
2) Università Mediterranea di Reggio Calabria, Dipartimento di Ingegneria dell'Informazione, delle Infrastrutture e dell'Energia Sostenibile, Via Graziella, 89100 Reggio Calabria, Italy;
3) Università degli Studi di Catania, Dipartimento di Ingegneria Elettrica Elettronica ed Informatica, Viale Andrea Doria 6, 95125 Catania, Italy

Abstract - Electron Cyclotron Resonance Ion Sources (ECRIS) further development is related to the availability of new diagnostic tools, nowadays consisting of few types only of devices designed on purpose for such compact machines. Microwave Interferometry is a non-invasive method for plasma diagnostics and represents the best candidate for the whole plasma density measurements. Interferometry in ECR Ion Sources is a challenging task due to their compact size. The typical density range of ECR plasmas (10^{11}-10^{12} cm^{-3}) causes the probing beam wavelength to be in the order of few centimetres, which is comparable to the chamber radius. The paper describes the design of a new microwave interferometer based on the so-called "frequency sweep" method

INTRODUCTION AND MOTIVATION

The development of microwave diagnostics is a fruitful strategy because microwaves crossing the plasma are sensitive to the entire energetic spectrum of the plasma, allowing global evaluation of the average density.
In the classical scheme of a microwave interferometry a microwave signal at frequency larger than any cutoff/resonance frequency of the plasma under investigation is splitted into two different branches: the first one is launched into the plasma, the second one is used as reference signal, propagating into a waveguide of calibrated length.
The basic idea is that the density comes out from phase shift which explicitly depends on the natural plasma oscillation ω_p, i.e. the electron density, as depicted by the mathematical relations below:

$$\Delta\varphi = \frac{\omega}{c}\left[1-\left(1-\frac{\omega_p^2}{\omega^2}\right)^{1/2}\right]L, \qquad \omega_p^2 = \frac{n_e e^2}{m\varepsilon_0}$$

where L is the plasma length, c the speed of light, ω the probing microwave pulsation and the other quantities are the standard fundamental physical constants.
In ECRIS the measurement is greatly complicated by the mechanical constraints, which limit considerably the ratio L/λ, where L is the characteristic length of the plasma chamber, and λ is the wavelength.

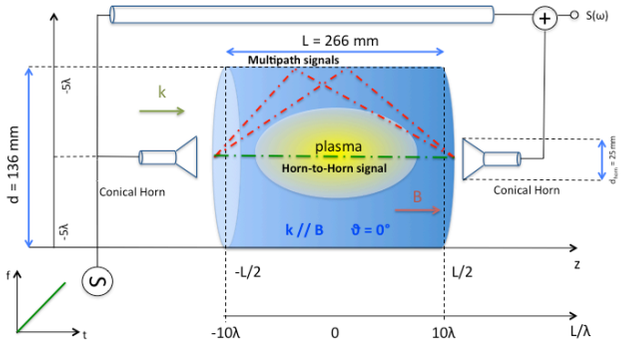

Figure 1: *Sketch of the microwave interferometer design, with particular emphasis on the dimensions of the plasma chamber and their relationship with the wavelength.*

Figure 1 highlights the conceptual layout of an interferometer setup applied to small-size plasma chambers like in case of ECR ion sources. The main problem consists in the multipath given by probing signal reflections at the chamber walls (reflecting surfaces). To be significant, the measurement must be depurated by spurious components, and this can be done only applying a more sophisticated experimental strategy.

EXPERIMENTAL STRATEGY

The proposed methodology moves from the one described in [1-2] but it needs to be specifically developed for ECR ion source devices. In order to suppress multipath signal we have to follow two main directions: first we need to use a frequency swept method, where the density is derived by the frequency shift of a beating signal obtained during the fast sweep of both probing and reference microwave signals:

$$M(t) = A\sin\left(\omega_{\text{int}}t + \phi_2 + \phi_{plasma}\right) + B\sin\left(\omega_{\text{int}}t + \phi_1\right)$$

where A and B are the amplitudes of the plasma and reference leg signals respectively, ω_{int} is the microwave source frequency, ϕ_1 is the phase shift due to dispersion

in waveguide in the reference leg, ϕ_2 is the phase shift due to dispersion in waveguide in the plasma leg, and ϕ_{plasma} is the phase shift due to dispersion in the plasma; the inner cavity multipaths contributions (the lower amplitude spectral components of Fig. 2) can thereby be suppressed by cleaning the spurious frequencies from the beating signal spectrum component (the fundamental first frequency component of Fig. 2).

This depuration of the spectrum (a sort of "instrument calibration" to be carried out without the plasma) is possible because we are able to perform spectral analysis of the beating signal: FFT of the receiving horn collecting signal has been done, displaying the quasi-monocromatic beating that it is evident in case of "in-vacuum" propagation (see Fig. 3).

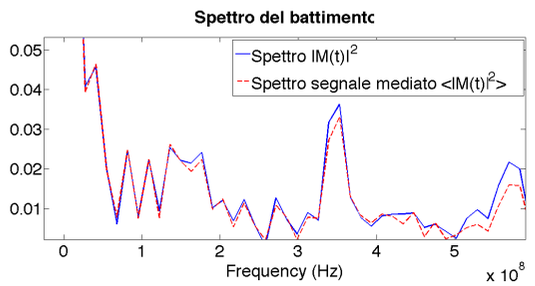

Figure 2: Spectrum of the beating signal in case of "in-cavity" horn-to-horn propagation

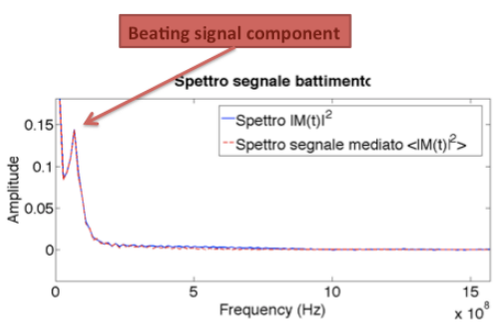

Figure 3: Spectrum of the beating signal in case of "in-vacuum" horn-to-horn propagation.

Concerning this antenna design, since the characteristic densities of our plasmas lie in the range n_e= 5*10^{17} - 5*10^{18} e / m^3, the frequencies suitable for high sensitivity "beating shift" detection lie in the range 20-25 GHz.

This second (not mandatory but very useful) part of the interferometer design, concerned the optimization of an high-directivity horn antenna carried out through CST EM and RF COMSOL simulations at high frequency (see Fig. 4). Further optimisation of the antennas should additionally improve the aspect ratio between the main spectral component and the multipath peaks.

In a practical way, the measurement consists in the evaluation of the beating signal shift

$$S(\omega) = 2A^2 \cos^2\left[\frac{1}{2}\left(\int_L k_{plasma}\, dl + \int_{\delta L} k_{guida}\, dl\right)\right],$$ as depicted in figure 5 (simulation).

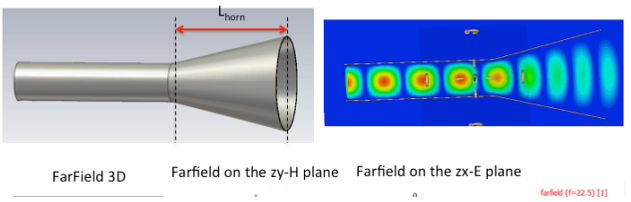

Figure 4: Preliminary design of the launching/receiving antennas for the proposed interferometry setup (simulations performed in COMSOL Multiphysics)

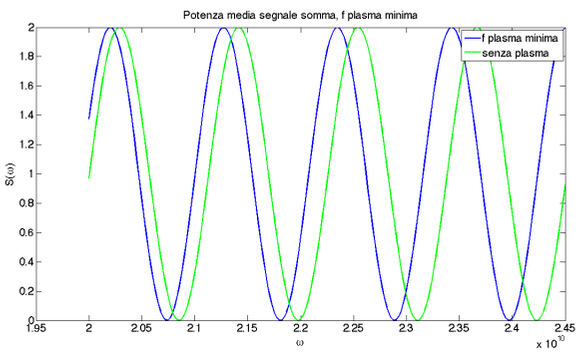

Figure 5: Simulation of the beating signal frequency shift due to the plasma. The simulation has been done for a plasma of density: n_e= 5*10^{17} m^{-3}.

Although some details have still to be fixed by improving the modelling and the numerical simulations, the overall layout of the experimental setup is already defined, and can be depicted as in figure 6.

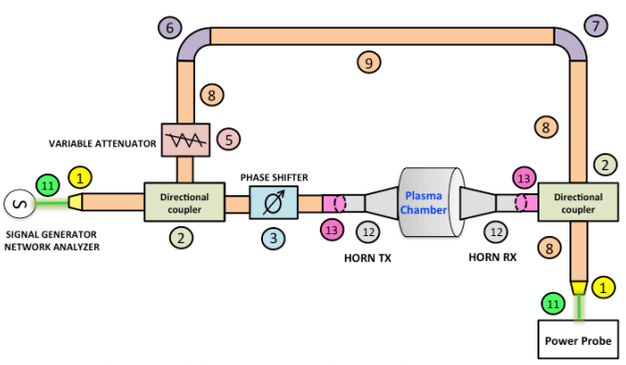

Figure 6: Scheme of the proposed experimental setup

REFERENCES

[1] Scime E., et al. , Rev. Sci. Instrum. 72, 1672 (2000)

[2] Howard J. et al., Appl Opt. 2006 Dec 1; 45(34): 861-30

Upgrade of the Versatile Ion Source for H_2^+ generation at the BEST test-stand

L. Celona[1], G. Castro[1], S. Gammino[1], D. Mascali[1], L. Neri[1], G. Torrisi[1,2], G. Castorina[3], O. Leonardi[1], G. Patti[1,4], L. Allegra[1], G. Gallo[1], E. Zappalà[1], G. Messina[1], A. Maugeri[1], A. Seminara[1]

[1] *Istituto Nazionale di Fisica Nucleare – Laboratori Nazionali del Sud, Via S. Sofia 62, 95123 Catania, Italy*
[2] *Università Mediterranea di Reggio Calabria, DIIES, Reggio Calabria (Italy)*
[3] *Università degli Studi di Catania, D. I.E.E.I., viale A. Doria, 6 - 95125 Catania, Italy*
[4] *INFN – LNL Viale dell'Università, 2 35020 Legnaro (Padua) Italy*

Abstract

DAEδALUS and IsoDAR experiments require high intensity H_2^+ beams to be accelerated by high power cyclotrons for neutrinos generation. The Catania Versatile Ion Source (VIS) has been moved and installed on a test stand at the Best Cyclotron Systems (Vancouver, Canada) for injection and acceleration proof of principle tests. VIS has been developed for proton generation, so a new plasma chamber and injection system has been designed for increasing the H_2^+ beam intensity. In this report the optimization for H_2^+/p ratio and emittance measurements will be shown and discussed.

INTRODUCTION

The DAEδALUS and IsoDAR experiments require high-current beams for studies about the neutrino physics [1-3] DAEδALUS needs 800 MeV protons at a peak current of 10 mA, while IsoDAR will use 60 MeV protons also at 10 mA. The needed current of 10 mA is a factor of five greater than the highest currents currently delivered by a cyclotron (PSI 590 MeV cyclotron delivers ~2 mA). To overcome this limitation, H_2^+ ions can be used instead of protons. Perveance arguments [4] indicate that space-charge effects for 5 mA of H_2^+ (equivalent to 10 mA of protons) at 70 keV injection energy are equivalent to those of 2 mA of protons at the typical 30 keV injection energy. Since the acceleration efficiency expected is about 10%, 50 mA of H_2^+ should be produced. In case of effective pre-bunching of the beam a factor of two improvement could be obtained, dropping the current requirement to 25 mA. The VIS source [5] has many advantages in terms of compactness, high reliability, capability to operate in CW mode or in pulsed mode, reproducibility, and low maintenance. Because of its compactness and reliability it has been moved and installed at the BEST test stand of Vancouver to produce the H_2^+ beam for inflection and acceleration tests.

As the VIS source has been optimized for proton production, some changes have been carried out to increase H_2^+ fraction.

Atomic physics arguments show that the H_2^+/p ratio is strongly affected by electron density n_e and ion lifetime in plasma τ_i [6]. In particular the decrease of τ_i favors H_2^+ generation since it decreases the probability that H_2^+ collide with electrons leading to the molecule break. The simplest way to decrease τ_i is to decrease the plasma chamber dimensions, since τ_i is proportional to the average ion path within the plasma.

THE NEW PLASMA CHAMBER AND INJECTION SYSTEM

A series of studies [7] have been carried out to define the dimensions of the new plasma chamber for replacing the standard VIS plasma chamber (10 cm long and 5 cm in radius), as shown in figure 1a. In order to maintain the fundamental mode at VIS operating frequency (2.45 GHz), the electric field propagation in different chambers layouts has been simulated in COMSOL and tested at INFN-LNS.

The chosen solution was a 10 x 2.5 cm chamber, shown in figure 1b. A new waveguide has been designed to match 2.45 GHz microwaves with a smaller plasma chamber, in order to restore the wave propagation at 2.45 GHz with very low losses.

EXPERIMENTAL RESULTS

The new plasma chambers and injection system has been mounted and tested on the BEST Test-stand.

Work pressure, measured in the LEBT, was in the range $1 \cdot 10^{-5}$ – $1.8 \cdot 10^{-5}$ mbar. For values lower than $1 \cdot 10^{-5}$ mbar, the extracted beam was unstable, while at higher pressure

than $1.8 \cdot 10^{-5}$ mbar some discharge occurred. Finally microwave power ranged from 100 W (ignition power) to 500 W. The tests hereby presented have been carried out with the extraction potential of 62.700 kV and the negative electrode biased at 3 kV. The aperture of the extraction hole has been fixed at 8 mm.

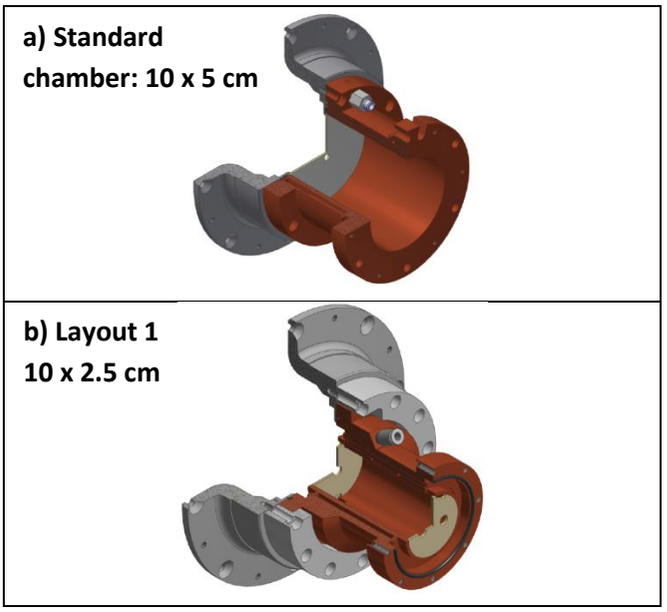

Figure 1: a) the standard chamber of VIS; b) new layout: 10 x 2.5 cm chamber;

The new plasma chamber has been characterized by modifying the position Δz of the permanent magnets, and then adjusting the neutrals pressure and the RF power. For shifts lower than 4 mm the plasma is not ignited and no beam was extracted. Best results in terms of H_2^+ fraction are obtained when Δz=4 mm and for $1.4 \cdot 10^{-5}$ mbar background pressure. For microwaves' power lower than 250 W, H_2^+ fraction is in the range 40-50%. Maximum H_2^+ current to the Faraday cup, 12.2 mA, has been obtained with a microwave power of 250 W and $1.6 \cdot 10^{-5}$ mbar pressure (figure 2).

Standard layout in the same experimental conditions [8] allowed to extract just 35 mA total current with 25% H_2^+ fraction (figure 7). Only 9 mA were carried to the faraday cup. The new VIS set-up enabled to increase H_2^+ fraction up to 40-45% and transmitted H_2^+ current from 9 mA to 12.2 mA.

Normalized emittance was ever lower than 0.2 π mm mrad, but an hollow beam was observed.

The experiments carried out at BEST permitted to collect important information for the design of a more performant ion source with an improved optics. New tests with the new plasma chambers are foreseen at LNS with the possibility to change the magnetic field profile and microwave frequency.

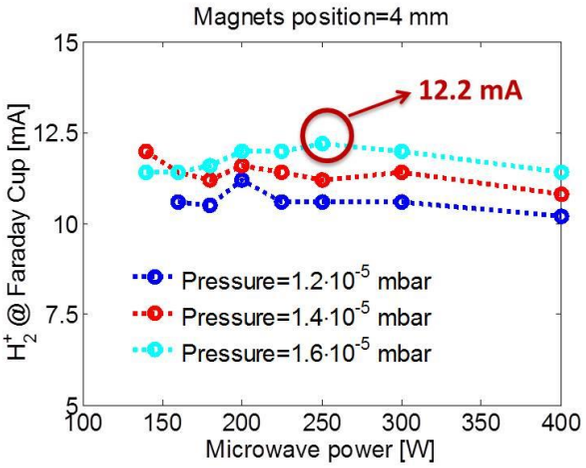

Figure 2: H_2^+ current at faraday cup against microwaves power for different pressures.

ACKNOWLEDGEMENTS

The authors are warmly grateful to the INFN V Nat. Sci. Committee funding the RDH-UTOPIA project.

REFERENCES

[1] J. M. Conrad and M. H. Shaevitz, Phys. Rev. Lett. **104**, 141802 (2010).

[2] J. Alonso *et al.* (the DAEδALUS Collaboration), e-print arXiv:1006.0260 [physics.ins-det].

[3] A. Bungau *et al.*, Phys. Rev. Lett. **109**, 141802 (2012).

[4] J. Alonso et al. Review of Scientific Instruments **85**, 02A742 (2014);

[5] R. Miracoli et al. Review of Scientific Instruments **83**, 02A305 (2012)

[6] H. Zhang, *Ion Sources* (Science Press Beijing and Springer, 1999).

[7] Celona et al, Proc.of Cyclotrons 2013, Vancouver, BC, Canada TUPPT014

[8] R. Miracoli, Characterization Of Microwave Discharge Ion Source For High Proton Beam Production In Cw And Pulsed Mode, PhD thesis, 2010

WAVEGUIDE DC-BREAK DESIGN AT 2.45 GHz

O. Leonardi[1], L. Celona[1], G. Torrisi[1,2], L. Allegra[1], S. Gammino[1]

[1] *Istituto Nazionale di Fisica Nucleare – Laboratori Nazionali del Sud, Via S. Sofia 62, 95123 Catania, Italy*
[2] *Università Mediterranea di Reggio Calabria, DIIES, Reggio Calabria (Italy)*

Abstract
2.45 GHz microwave ion sources are frequently used for proton beam production. Usually, they are located on high voltage platform to allow the beam extraction but they are connected to devices placed at ground as the RF generator [1]. Indeed, a waveguide electric insulator placed between the high voltage region and the ground is needed.
Two basic aspects should be considered in the design: the microwave should be transferred from the RF generator to the ion source with minimum reflection and minimum radiation losses, furthermore the electrostatic field has to be maintained under the dielectric strength using materials with costs as low as possible.

INTRODUCTION

This document presents the study and design of a 2.45 GHz waveguide DC-Break to fulfill an insulation requirement of 100 kV.

In particular, it was designed to achieve a microwave insertion loss as low as possible and radiation losses lower than 5% when it handles a maximum microwave power of 1.5 kW.

The structure is composed by several steps of WR340 standard waveguide interlinked by several dielectric gaps that fill only partially the internal cross-section of the waveguide. Several insulating materials have been considered taking into account the mechanical, thermal, chemical and electrical features.

The layout has been designed and optimized by means of frequency domain electromagnetic simulators.

DC-BREAK DESIGN

The proposed structure is composed by 11 aluminium sections (9 of 41 mm length and the two with the input/output flanges of 47.5 mm length), with a cross section of 86.36 x 43.18 mm and thickness of 2 mm separated by 10 gaps of dielectric insulators whose layout is shown in Fig. 1.

The dielectric goes inside the waveguide cross section for 3 mm through a T-shaped insert with a base of 5 mm. The particular shape of the dielectric window allows the structure to be mechanically self-sustained and easily changeable as needed. The overall length of the waveguide DC-Break is 484 mm, including the flanges.

The final choice of the used dielectrics material, MACOR®[2], results from a preliminary study carried out by simulations in which the electrical features such as dielectric permittivity and loss tangent have been the main sweet parameters.

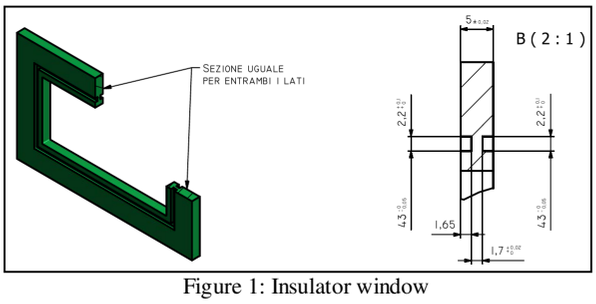

Figure 1: Insulator window

MACOR is an excellent insulator at high voltage: it has a dielectric constant ε_r= 5.67 and loss tangent tanδ=7.1x10^{-3}, it can insulate up to about 62 kV/mm; it is a good thermal insulator and is stable up to temperatures of 1000 °C with very little thermal expansion or outgassing. It can be machined into any shape and precision part by using ordinary metal working tools and it requires no post firing after machining.

The configuration with 10 dielectric gaps results from the need to operate routinely at 100 kV and to achieve an insulation not lower than 10 kV between two adjacent gaps. In order to fix the total resistance of the whole structures, metal pipes are soldered around alternating steps of metal part interlinked by super PFA tubes in which demineralized water flowing at 20 °C with electrical conductivity of 2 µS at a pressure of 5 bar. The dielectric has been extended of 10.2 mm in the outer region of waveguide in order to shield metal pipes and to prevent electrostatic discharges. The arrangement of soldered metal pipes along the longer side of waveguide allows to keep the temperature low when the fundamental mode TE_{10} is propagating inside the structure.

The whole layout will be held on by 4 rods of KETRON PEEK threaded and tightened on the waveguide flanges. Figure 2 shows a render view of the whole DC-Break assembly.

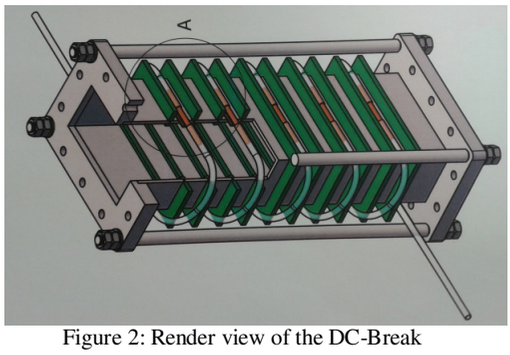
Figure 2: Render view of the DC-Break

SIMULATION RESULTS

The following simulated results have been achieved by simulations where each insulator domain is meshed with about 18500 tetrahedrons having an average edge length smaller than 1 mm in order to obtain a good numerical accuracy.

Although the MACOR is a very hard material, it is also very fragile, therefore several simulations have been carried out to increase the thickness of the insulator windows in order to make them more robust keeping at the same time the radiation losses below ~3%. For this reason a good tradeoff was a thickness of the inner groove equal to 1.7 mm and the height of T-shape inserts equal to 3 mm. Fig. 3 shows the Net Power Flow outgoing by output port of DC-Break for a linear increase of the inner groove thickness into 1.5-1.8 mm range. It is evident that the losses not exceed 4% over the entire frequency band.

Fig. 4 shows the simulated $|S_{21}|$ for the final layout of DC-Break: the estimated losses for 1.5 kW operational power at 2.45 GHz are about 45 W.

The following pictures show a detail of the Electric Field Amplitude and the Real Poynting Vector along two longitudinal cut-planes in the waveguide for a TE_{10} excitation at 2.45 GHz and 1.5 kW power.

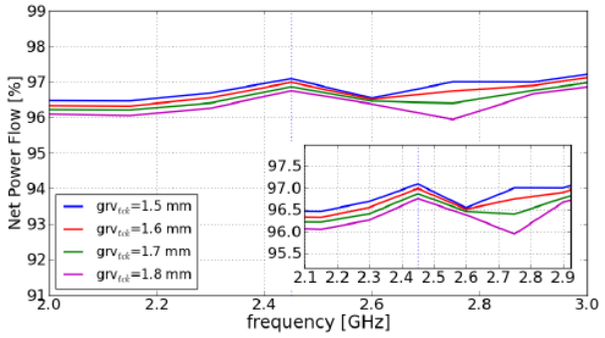

Figure 3: Net Power Flow outgoing by output-port of DC-Break for a linear increase of inner groove thickness.

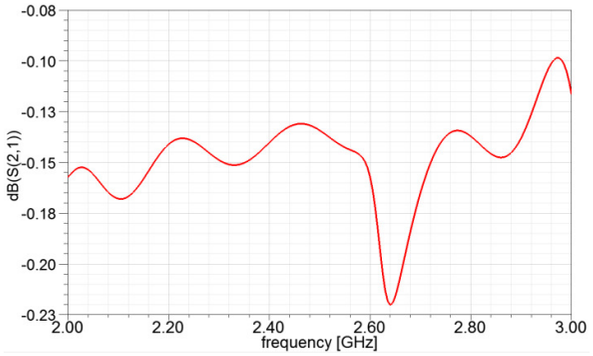

Figure 4: $|S_{21}|$ of final layout of DC-Break

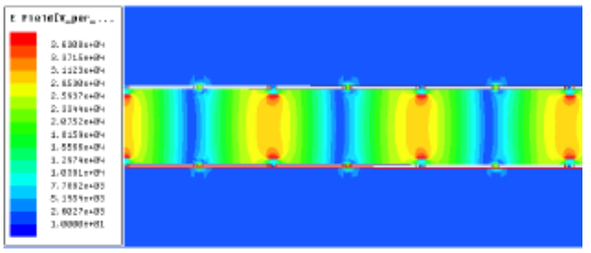

Fig. 5: Electric Field Amplitude for TE 10 excitation at 2.45 GHz and 1.5 kW

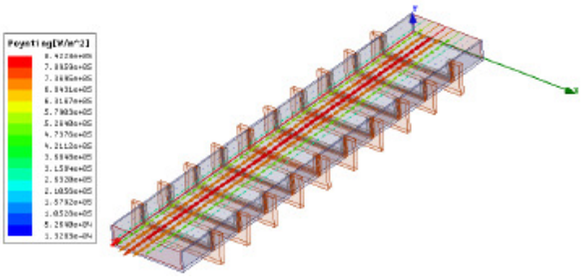

Fig. 6: Poynting Vector for TE 10 excitation at 2.45 GHz and 1.5 kW.

CONCLUSIONS

A compact and relatively cheap waveguide DC-Break operating at 2.45 GHz has been designed and simulated to fulfill an insulation requirement up to 100 kV.

The modular solution and the particular shape of insulator windows provides a mechanical self-sustainability and versatility for eventual further modifications.

The device will be assembled and tested at INFN_LNS during the 2nd quarter 2015.

REFERENCES

[1] Ian G. Brown, *The physics and technology of ion sources* (John Wiley & Sons, 2006).

[2] www.corning.com/specialtymaterials/advanced_optics/specialty_glass_ceramics/products/macor/index.aspx

The New Axial Buncher at INFN-LNS

A. Caruso[1], G. Gallo[1], A. Longhitano[1], A. Spartà[1], E. Zappalà[1], G. F. Caruso[1], G. Manno[1], E.G. Messina[1], J. Sura[2], F. Consoli[3], Li Pengzhan[4]

1) INFN-LNS, Catania, Italy
2) Warsaw University, Warsaw, Poland
3) Associazione Euratom-ENEA sulla Fusione, Frascati, Italy
4) China Institute of Atomic Energy, Beijing, China

Abstract - A new axial buncher for the K-800 superconducting cyclotron is going to be installed at LNS [1]. This new device will replace the present buncher placed along the vertical beam line, inside the yoke of the cyclotron at about half a meter from the medium plane. Maintenance and technical inspection are very difficult to carry out in this situation. The new buncher will still be placed along the axial beam line, just before the bottom side of the cyclotron yoke. It consists of a drift tube driven by a sinusoidal RF signal in the range of 15-50 MHz, a matching box, an amplifier, and an electronic control system. A more accurate mechanical design of the beam line portion will allow for the direct electric connection of the matching box to the ceramic feed-through and drift tube. This particular design avoid, any connection through coaxial transmission line. It will reduce the entire geometry, the total RF power and the maintenance. In brief, the new axial buncher is a compact system including beam line portion, drift tube, ceramic feed-through, matching box, amplifier and control system interface in a single structure.

STUDY AND DESIGN

The basic two-gap buncher structure [4] is shown in Fig.1, between the SERSE ion source [5] and the K-800 superconducting cyclotron.

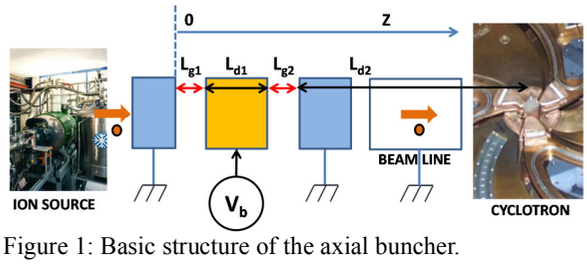

Figure 1: Basic structure of the axial buncher.

It is a drift tube, fed by the sinusoidal voltage $V_B = V_{MB}\sin(\omega t + \varphi_0)$, and placed between two grounded tube electrodes. L_{g1} and L_{g2} are the two gaps of 5 mm length. The distance between the Buncher and the inflector at the cyclotron central region is 3011 mm, and it is imposed by mechanical constraints. Particles generated by the ion source have $v_{z0} = \sqrt{2q_iV_s/m_i}$ velocity, being q_i and m_i their charge and mass, and V_s the voltage of the source output electrode. The drift tube length L_{d1} is 83.5 mm. This length is chosen so that L_{d1}+L_{g1} is an odd integer multiple of the $\beta\lambda/2$ quantity. In particular, $\beta\lambda = v_{z0}/f$ (with f cyclotron frequency) is the path of the particles in one period and, because of the fixed geometry of the cyclotron central region, has to be constant.

The basic theoretical study of the bunching effect in the present structure has been analytically performed by considering a time-varying and spatially uniform electric field within the two L_{g1} and L_{g2} gaps. Here particles undergo a time varying acceleration, whereas they will move in uniform linear motion within the following drift tubes. For example, for α particle the calculated particle trajectories are shown in Fig. 2a-2b in the Applegate diagrams, referred to one period. The trajectories grouping is apparent. The time instants when they reach the cyclotron inflector is t_{d2}. In Fig 2c-2d the plot of t_{d2} versus t_0/T is shown. The V_{MB} voltage has been tailored to optimize the particle transmission within the cyclotron acceptance time, referred to the 35° phase. This is clearly shown in Fig 2c-2d, where the curve is tangent to the dotted boundaries.

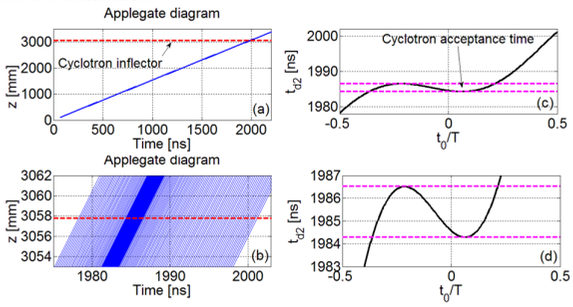

Figure 2: (a) and (b): Applegate diagrams with different scales; (c) and (d) t_{d2} versus t_0/T.

Under these conditions the particle transmission to the cyclotron is TR = 57.6%, and the energy spread is $\Delta E/E$ = 1.15%.

The mechanics (see Fig. 3) include the drift tube (c) and the ground electrodes (b) inside a four-gate beam line section (a) already installed along the beam line. A standard vacuum ceramic feed-through connects the drift tube with the external RF signal. Fig. 3d shows the position of the buncher along the axial beam line - the human body on the reference plane gives a rough scale factor of the full size dimension. The distance between the

centre of the drift tube and time focus is about 3m. The beam line section dimensions are 403 and 176 mm, in length and width respectively. The upper and lower flanges, in/out beam, are DN100CF. The horizontal central orthogonal flanges are two standard DN160CF.

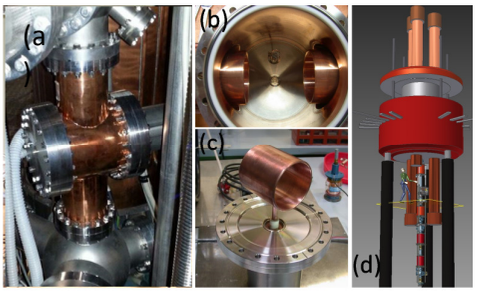

Figure 3: Buncher mechanic (a,b,c) and cyclotron (d).

The Fig. 3c shows the ceramic feed-through connected to the drift tube assembled on one of the two DN160CF. The other DN160CF hosts a pair of RF pick-ups, see Fig. 3b. The drift tube is copper made, while a galvanic deposition of copper of a few hundred µm (well above the skin effect) has been placed on the ground electrodes and the standard steel cross section beam line. In this way all the surfaces are in copper, except the flanges relative to the feed-through and pick-up. The copper deposition has increased the total Q factor of the system which prevents and/or minimizes any copper surface facing a steel surface under high vacuum. The length, the inner diameter and the thickness of the drift tube are 83.5, 75 and 2.5 mm respectively.

From the electrical point of view the drift tube can be seen as a capacitance of about 27pF with a self-resonance frequency of 352,75 MHz. The frequency range of the axial buncher is identical to the cyclotron's, between 15 and 50 MHz. A matching circuit has been developed to adapt the drift tube capacitive impedance to the standard 50 Ω for all the bandwidths. The matching box schematic is shown in Fig. 6.

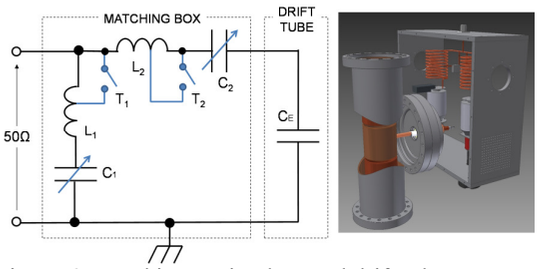

Figure 6: Matching-tuning box and drift tube.

C1 and C_2 are two vacuum multi-turn variable capacitors from 5 to 500 pF and L_1 and L_2 are two 'selectable' inductors. The range 15-50 MHz, too large for two fixed inductors, has been divided in two bandwidths, the lower (L_1=L_2=4.2µH) and the upper (L_1=L_2=1.3µH). The bandwidth is selectable, from low to high, by the commutation of a double relay contact, T_1 and T_2. The schematic of Fig. 6 is an impedance transformer, from Z_0=50Ω to Z_b, where Z_b is the impedance seen at the input of the feedthrough. A specific design of the beam line portion will allow for the direct electrical connection of the matching box to the drift tube, see Fig.7. This particular design prevents any connection through coaxial transmission line. It reduces the entire geometry, the connection losses, the total RF power and the maintenance.

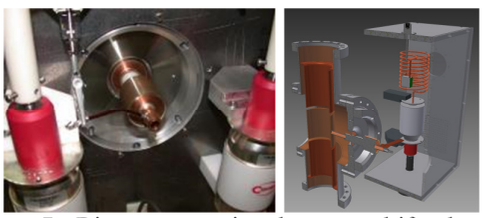

Figure 7: Direct connection between drift-tube and matching box.

Some numerical simulations have been developed to calculate, for all the operative frequencies, the capacitance values of C_1 and C_2, the buncher voltage, V_{MB}, at the drift tube and the relative RF power applied at the matching box. V_{MB} will be between 64 and 110 V, for an RF power of 1-2 W, only. The main components and the block diagram of the test bench are: RF synthesizer, power amplifier, directional coupler, matching-box and drift tube inside the beam line section under vacuum ($2.8x10^{-6}$mbar). See Fig. 8.

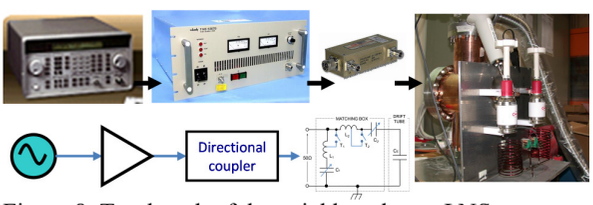

Figure 8: Test bench of the axial buncher at LNS.

The whole frequency bandwidth has been accomplished in terms of impedance matching and drift tube voltages. Scattering parameter, Q-factor measurements and drift tube voltage measurements are shown in Fig 9.

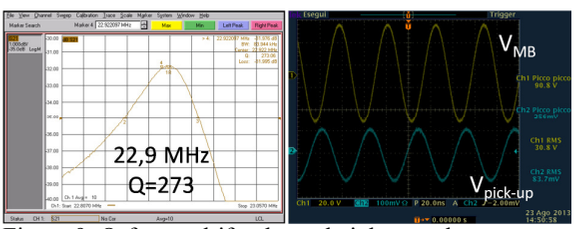

Figure 9: Q-factor, drift tube and pick-up voltages.

A 5 mm thickness iron shield panelling, covers the inside surface of the matching box, to prevent the cyclotron strong magnetic field inside the box. We believe we can produce a first test on the beam with this new buncher during the 2015.

REFERENCES

[1] A. Caruso et al, The New Axial Buncher at INFN-LNS, CANADA, CYCLOTRONS 2015.

Management software for the INFN-LNS accelerators beamlines

G. Vecchio[1], L. Cosentino[1], S. Pulvirenti[1], E. Furia[1], S. Cavallaro[1], B. Diana[1]

1) INFN Laboratori Nazionali del Sud, via S. Sofia 62, 95135 Catania

Abstract – This paper describes design and development of an online console for the management of the accelerators beamlines at INFN-LNS. We illustrate the software functionality and the hardware and software architecture.

INTRODUCTION

This paper presents the software platform aiming to control all the transport elements that constitute the LNS beamlines. A complex and highly ergonomic Graphic User Interface (GUI) allows to control all the parameters with a user-friendly interactive approach, ensuring high functionality so that **the beam operator can visually work in a realistic environment through the beamlines**. The modular approach of this platform allows to build and modify all the beamlines, just including/removing all the elements (dipole, quadrupoles, faraday cups, quartz, etc..), that can be managed individually.

The users that transport the beam can therefore set and read all the setting parameters, thanks to a continuous communication with the field level. All the information related to the beamline elements involved in the beam transport, included the beam intensities measured by the faraday cups and the beam spot images acquired by the quartz, can be stored in a centralized database, with suitable criteria to have a historical archive, that can be exploited during the beam tuning operation.

All this software platform has been built by using JavaFX, a new java-based software platform for creating rich internet applications and advanced graphics user-interfaces [1].

FUNCTIONAL REQUIREMENTS

The functional requirements of the system is illustrated in Fig. 1.

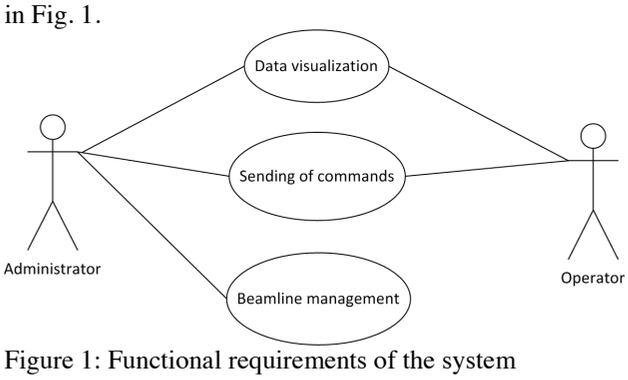

Figure 1: Functional requirements of the system

Thanks to the initial login, the application can switch among administrator or operator's mode and makes available the features for the user logged in.

HARDWARE - SOFTWARE ARCHITECTURE

The system hardware and software architecture is shown in Fig. 2. The field elements network is connected to Redis, a centralized and in memory persistent database [2].

The local accelerator console, queries the database through a polling procedure and gets the data coming from the field. The communication between Redis and the local console is done by a TCP connection through a proprietary protocol called RESP.

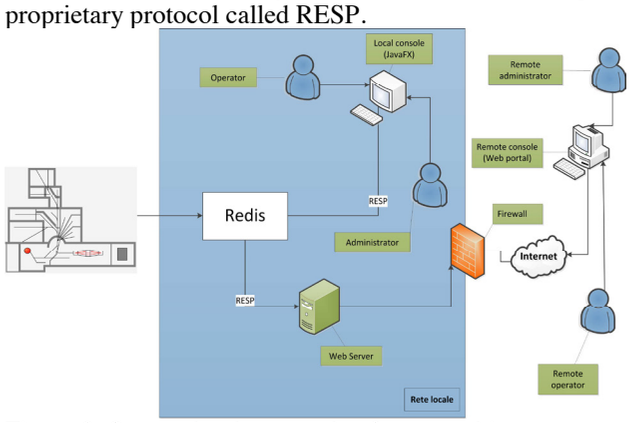

Figure 2: System hardware and software architecture

Moreover, a web server expose, through a web portal, the console on internet for remote control.

Console Software Architecture

The software architecture adopted on the local console is three-tier with the use of the architectural pattern Model-View-Controller (**MVC**), which separates the presentation layer from business logic and data storage [3].

The **view** shows the data provided by the **model** that is directly connected to the database, whereas the **controller** accepts inputs and converts it to commands for the model or view, as shown on Fig. 3.

Moreover, in the model layer, we have used Java Persistence API (JPA), a Java specification for the access, the persistence and the management of data between Java objects and relational databases [4].

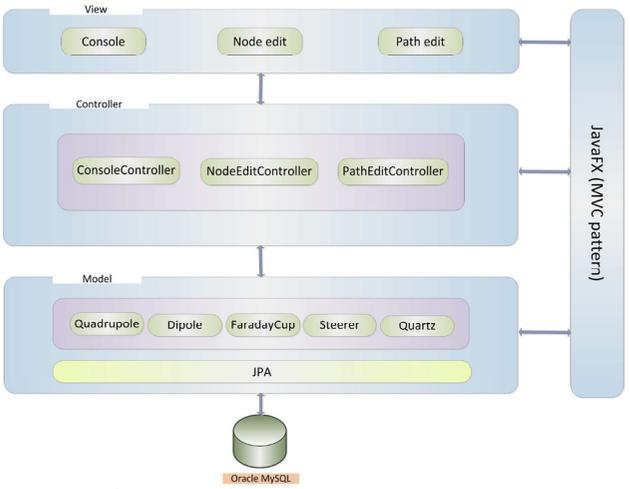

Figure 3: Console software architecture

The main advantages of JPA rather than a database driver connector is that in JPA data is represented by classes and objects rather than by tables and records.

USER INTERFACE

The initial login screen allows the differentiation of the two user roles: administrator and operator. The synoptic for the control of beamline elements was obtained with the tools provided by the JavaFX framework. In this panel, that contains the plant of the building, we can navigate easily by mouse and we can do zoom in and zoom out to see some place in detail.

Console

The control panel of the beamline is shown in Fig. 4. It allows to the operators to send all the commands and to receive instant feedbacks from the beamline elements. Moreover the operator can handle possible alarm conditions and can see graphically beamline status changes.

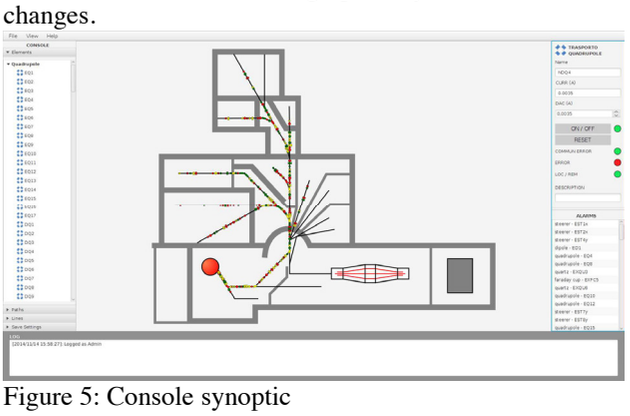

Figure 5: Console synoptic

Configurations save and reload

A great advantage of this software platform is represented by the availability of a database to save and recall a specific system configuration. Fig. 6 shows the particular ergonomic design of the panel for the configuration finding, that can be done by element, mass number (A), state of charge (Q), energy (E), date and name of the experiment.

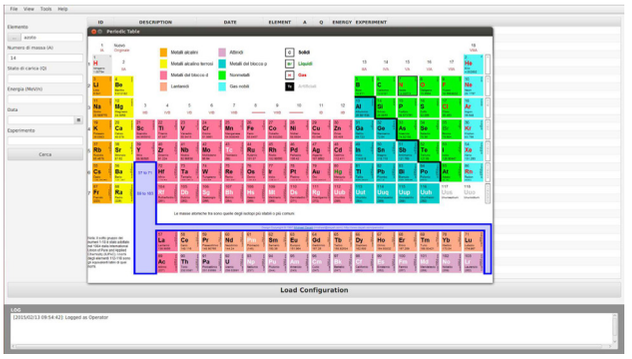

Figure 6: Load of configurations by setting some parameter

TESTS

The tests carried out on the system showed the excellent management of the resources as CPU and memory. Fig. 7 represents the optimal CPU time consumption and the memory handling by the garbage collector, with high rate of throughput.

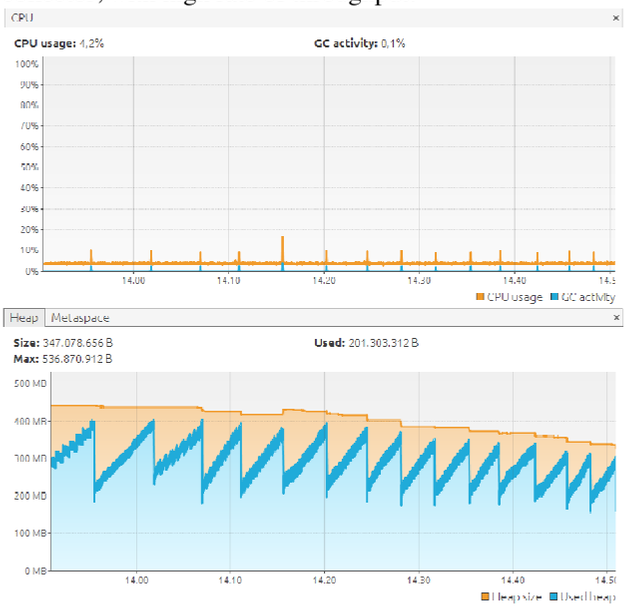

Figure 7: CPU and memory usage with an high throughput

CONCLUSIONS

In this paper we presented a system for the management of the LNS accelerators beamline. The synoptic meets the initial requirements and provides to operators a more simple and interactive control.

REFERENCES

[1] James Weaver et al., Pro JavaFX 2: A definitive guide to rich clients with Java Technology, 2012.
[2] Josiah L. Carlson, Redis in Action, 2013.
[3] Scott Hommel, Implementing JavaFX Best Practices, 2014.
[4] John O'Conner, Using the Java Persistence API in Desktop Applications, 2007.

Data exchange protocol for the INFN-LNS accelerators beamlines

G. Vecchio[1], L. Cosentino[1], S. Pulvirenti[1], E. Furia[1], S. Cavallaro[1], B. Diana[1]

1) INFN Laboratori Nazionali del Sud, via S. Sofia 62, 95135 Catania

Abstract – This paper describes design and development of a data exchange protocol for the management of the INFN-LNS accelerators beamlines. We illustrate the data structure server adopted, Redis, and the hardware and software architecture of the whole system.

INTRODUCTION

This paper presents the software platform aiming to store, send and manage all the data coming from and to the field devices. The beamline is composed by different devices from different vendors and for this reason a standard protocol for data exchange is strongly required.

Compared to traditional data acquisition systems, we developed a new concept of control system and data acquisition framework, based on a data structures server which so far had never been used for supervisory control.

We have chosen Redis [1] as a highly scalable data store, shared by multiple and different processes and applications [2]. This system easily allows cross-platform, cross-server and cross-application communication, using extremely lightweight libraries.

REDIS OVERVIEW

Redis is part of the NoSQL databases, efficient and powerful tools for storing and manipulating large quantities of data [3].

In particular, Redis is a data structures server supporting different kind of values, unlike traditional key-value stores that only associate string keys to string values. In Redis values are not limited to strings, but can also hold more complex data structures like lists, sets and hashes.

Redis stores everything in primary memory which is very fast in read and write of data. For this reason it is perfectly suited to store small information which needs to be accessed, modified and inserted at a very fast rate.

REDIS ARCHITECTURE

Redis architecture contains two main processes: Redis client and Redis server. Redis server is responsible for storing data in memory. It handles all kinds of management and forms the major part of architecture.

Clients are available for the most popular programming languages, and a command line tool is also available to directly send queries to the server.

Since Redis stores everything in RAM, depending on the user requirements it might be needed to put data on a non-volatile storage media. There are three ways to make the in-memory database persistent: RDB mechanism, AOF and SAVE command.

RDB makes a copy of all the data in memory and stores it in a permanent storage when certain criteria are met. AOF logs all the write operations received by the server and therefore can be used to reconstruct the entire dataset. Finally, SAVE command can force Redis server to create a RDB snapshot anytime using the client [4].

Redis Replication

Replication is a technique involving many computers to enable fault-tolerance and data accessibility. In a replication environment many computers share the same data with each other so that even if some computer goes down, all the data will be available.

Redis replication is very simple to use and to configure master-slave replication, that allows slave Redis servers to be exact copies of master servers (Fig. 1).

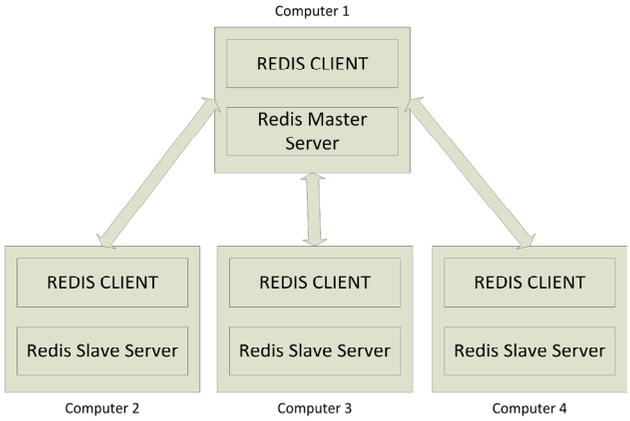

Figure 1: Redis replication

When a new slave is added to the environment, the master automatically synchronizes all data with the slave. In master-slave configurations the master should have persistence turned off, so that in case of a server crash a slave is usually promoted to master role. This is meant to prevent data loss, since setting up a brand new master would start with its own dataset.

Redis Clustering

Clustering is a technique by which data can be shared among many computers. The main advantage is that more data can be stored in a cluster because it's a combination of computers. Redis Cluster provides a way to run a Redis installation where data is automatically shared across multiple Redis nodes, as shown in Fig. 2.

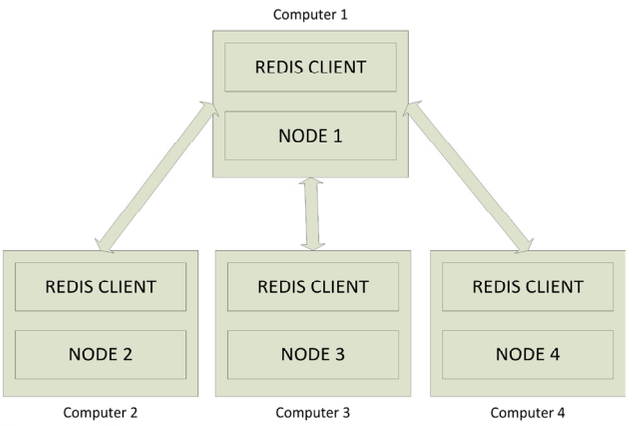

Figure 2: Redis clustering

Redis Protocol

Redis clients communicate with the Redis server using a protocol called **RESP** (REdis Serialization Protocol), that is simple to implement, fast to parse and human readable.

RESP can serialize different data types like integers, strings, arrays. There is also a specific type for errors. Requests are sent from the client to the Redis server as arrays of strings representing the arguments of the command to execute. Redis replies with a command-specific data type.

RESP is binary-safe and does not require processing of bulk data transferred from one process to another, because it uses prefixed-length to transfer bulk data.

A client connects to a Redis server creating a TCP connection to the port 6379. While RESP is technically non-TCP specific, in the context of Redis the protocol is only used with TCP connections (or equivalent stream oriented connections like Unix sockets).

HARDWARE - SOFTWARE ARCHITECTURE

The system hardware and software architecture is shown in Fig. 3.

It is a typical star-topology network, where both console-level and field-level computers are connected via Ethernet to a central Redis server. We are also planning a web server to allow remote monitoring of the beam data.

Early tests have shown very promising results in term of read and write operations throughput.

This approach obviously has a very critical element, the failure of the server. For this reason we are planning solutions to provide high availability and realiability for the control system.

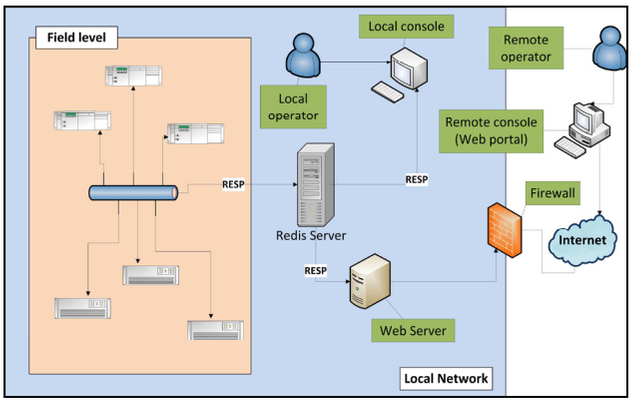

Figure 3: System hardware and software architecture

LNS Beamline: Redis configuration

The keys used on our Redis server have this format:

StationName_DeviceName:Attribute|Type

This kind of attribute separation ensures a more efficient use of network bandwidth, in addition to a logical separation of attributes for each device.

Moreover, every station has a variable that contains a timestamp for all of the values associated to the keys, useful for the graphic representation of the data.

If a field-level computer hangs up or loses connectivity with the server, its variables are deleted from Redis after a certain timeout, so that every client trying to read that data can properly handle this situation.

We tested our system with a polling time of 100 ms and a data exchange of tens of kiloBytes, and we have observed an excellent management of CPU and memory.

CONCLUSIONS

In this paper we presented a data exchange protocol for the management of the INFN-LNS accelerators beamlines.

We explored a new way to exchange data between devices and computers inside special environments, where high performance and reliability are needed.

After some early tests, we can say that the whole system is very efficient with a fast data exchange and Redis is an excellent solution even for industrial applications.

REFERENCES

[1] Salvatore Sanfilippo, http://redis.io/documentation
[2] Josiah L. Carlson, Redis in Action, 2013.
[3] Shashank Tiwari, Professional NoSQL, 2011.
[4] Matt Palmer, Instant Redis Persistence.

ISTITUTO NAZIONALE DI FISICA NUCLEARE

LABORATORI NAZIONALI DEL SUD

ACTIVITY REPORT 2013/2014

INTERDISCIPLINARY PHYSICS

Transport and dosimetry solutions for laser driven beams: the ELIMED beam line

G.A.P. Cirrone[1], G. Cuttone[1] , F. Romano[1], V. Scuderi[1,2], A. Amato[1], L. Andò[1], A. Attili[5], M. Borghesi[6], G. Candiano[1], L. Cosentino[1], M. Costa[1], F. Costanzo[1], C. D'Amato[1], G. De Luca[1], D.Doria[6], G.Gallo[1], S.Gammino[1], G. Korn[2], T. Germek[1] ,G. La Rosa[1], R. Leanza[1,3], R. Manna[1], M. Maggiore[4], V. Marchese[1], D. Margarone[2], A. Maugeri[1], G. Milluzzo[1,3], A. Musumarra[1], L. Pandola[1], G. Petringa[1,3], S. Pulvirenti[1], D. Rifuggiato[1], D. Rizzo[1], R. Sacchi[1], S. Salamone[1], F. Schillaci[1], M. Sedita[1], A. Tramontana[1,3] , B. Trovato[1], C. Vaglianisi[1]

1) INFN-LNS, Via S. Sofia 62 - 95125 Catania, Italy

2) Institute of Physics ASCR, v.v.i. (FZU), ELI-Beamlines Project, Na Slovance 2, 182 21 Prague, Czech Republic

3) Universita´ degli Studi di Catania, Dipartimento di Fisica e Astronomia, Via S. Sofia 64, Catania, Italy

4)INFN-LNL,Viale dell'Universit´a 2 - 35020 Legnaro (PD), Italy

5) Istituto Nazionale di Fisica Nucleare, Sezione di Torino, Via P. Giuria 1, Torino, Italy

6) *Centre of Plasma Physics, School of Mathematics and Physics, The Queen's University of Belfast, United Kindom of Great Britain*

Abstract - Within 2017, the ELIMED (ELI-Beamlines MEDical applications) transport beam-line and dosimetric systems for laser-generated beams, will be installed at the ELI-Beamlines facility in Prague (CZ), inside the ELIMAIA (ELI Multidisciplinary Applications of laser-Ion Acceleration) experimental hall. The beam-line will be composed by two sections: one in vacuum, devoted to the collecting, focusing and energy selection of the primary beam and the second in air, where the dosimetric devices will be installed.

THE ELIMED APPROACH FOR THE ELIMAIA BEAM LINE

Nowadays, the innovative high power laser-based particle acceleration technique can represent a concrete future alternative in the field of particle acceleration [1]. Several experimental investigations as well as theoretical studies, allowed discovering the potentialities of the laser-target acceleration mechanisms, as regard the applicability in different fields of physics.

The non-conventional features of laser-driven particle beams in the so called Target Normal Sheath Acceleration regime, as for instance the wide energy and angular distributions, the high dose rate and the low reproducibility [2], make necessary the study and the development of appropriate transport and diagnostic devices in order to make the optically accelerated particles suitable for multidisciplinary applications, like medical physics and, in particular, the hadrotherapy.

Laser-based accelerators could significantly increase the availability of high-energy ion beams and induce a wider spread of particle therapy based facilities around the world. The demonstration of the real applicability of these innovative particle beams in multidisciplinary applications, with particular care to hadrontherapy, is the main aim of the ELIMED project, born in 2012 from a collaboration between the INFN-LNS (Nuclear Physics Laboratory, Catania, Italy) and ASCR-FZU (Institute of Physics of the Czech Academy of Science) in charge of the ELI-Beamlines facility.

The project foresees the development and the realization of a complete transport beam line, including diagnostics and dosimetric devices accurately designed for optically accelerated beams.

At the end of 2012, the ELIMED initiative was presented at the ISAC (International Scientific Advisory Committee) of ELI-Beamlines and finally accepted at the end of 2013 [3]. In 2013 the ELI-Beamlines Institute officially started the development of the ELIMAIA experimental hall, representing the ELI-Beamlines facility area specifically dedicated to the ion acceleration and their applications. Finally, as result of a public tender, launched in 2014 by the FZU (ELI-Beamlines), the INFN-LNS has been officially appointed to realize the beam transport and the dosimetric and irradiation section for ELIMAIA .

A three years contract has been signed between the INFN and the ELI-Beamlines for the realization of the laser-accelerated ion transport beam-line .

The ELIMED project represents the part of the ELIMAIA activities addressed to transport, handling and dosimetry of the laser-driven beams and to the achievement of stable, controlled and reproducible beams that will be in future available to all the users interested in the multidisciplinary and medical applications of such innovative technology. The preliminary design of the interaction chamber that will be installed in the ELIMAIA hall and the ELIMED beam line are shown in figure 1.

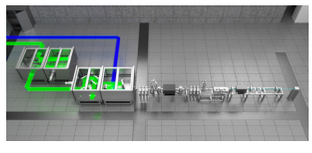

Figure 1: Layout of ELIMAIA experimental hall.

The contract foresees, also, tests of the operational functioning of each beam-line element, using both conventional and laser-driven ion beams.

With this aim, all the developed devices will be tested at the LNS, using proton beams delivered by the Tandem and the superconducting cyclotron (CS), in an experimental hall entirely dedicated to the ELIMED project. A picture of the LNS beam-line is shown in fig. 2.

Figure 2. The beam line under construction at the LNS for the ELIMED tests with conventional proton beams.

The project is mainly divided in three working packages, concerning the study and the development of the transport elements, diagnostic and dosimetric devices and the realization of the Geant4 simulation of the entire ELIMED line, which will be available at the end of 2017.

Beam transport solution

Ions accelerated by laser-matter interaction are characterized by high intensities, multiple species and charge states, a wide energy spectrum and a large energy-dependent angular distribution. Therefore, in order to make these non-conventional beams suitable for multidisciplinary applications, the design of specific beam line transport elements is mandatory. The main aim of the transport elements will be the control of the beam final energy and angular distributions, the beam-line reliability as well as the flexibility and reproducibility of the final beam spot size and the final dose distribution.
The first element placed few cm downstream the target, collects, focuses in angle and pre-selects in energy, the accelerated particle beam. It will be constituted by a set of permanent quadrupoles; their displacement along the beam line direction will be provided by independent motors remotely controlled. In particular, a quadrupole system prototype, already realized at the LNS, with magnetic field gradient of 110 T/ m and 114 T/ m, 20 mm bore and respectively with lengths of 40 and 80 mm, will be adopted to efficiently collect and focus ion beams up to 30 MeV. The final beam energy refinement will be performed by means of a second transport device prototype: an energy selection system (ESS), able to select particles with energy up to 100 MeV. The ESS will be based on a conductor resistive coil that will allow varying the magnetic field according to the particle energy of interest.
Some prototypes of the transport beam-line, useful for a first characterization, have been already developed, tested and, simulated (using both analytical and Monte Carlo approaches) [4],[5],[6].

Beam diagnostics elements

In order to control the beam along the entire beam line, different diagnostics detectors have been considered. The diagnostics will be based on beam emittance meter devices to measure the emittance along the whole beam-line and Silicon Carbide and CVD diamond detectors or secondary particle emission detectors (SEM) for the particle energy spectrum measurement in Time Of Flight (TOF) mode.

Dosimetric solutions for ELIMED

A precise knowledge of the absolute dose, released by the incoming radiation, is essential in many applications, like radiotherapy or nuclear medicine, where the dosimetric accuracy is a crucial prerequisite. It is in fact demonstrated that an uncertainty higher than 5% in the absorbed dose evaluation can compromise the effectiveness of a radiation treatment as well as the patient health. Dosimetric international protocols have been already established since 2000 for conventional clinical ion beams [7]. On the other hand, due to their peculiarities (very high dose rate, very low reproducibility) no recommendations are available today for dose evaluation using laser-driven ion beams. Nevertheless, during the last decade many researchers started several investigations on targets, detectors and procedures, in order to achieve an accurate evaluation of the dose released by such kind of beams.
Currently, different kind of dosimeters are under investigation for laser-driven beams: solid state detectors such as nuclear-track detectors, CR39, radiochromic films, termoluminescent dosimeters (TLD), ionimetric detectors like Faraday Cups (FC) and ionization transmission chambers for high dose-rate beams.
Indeed, due to the high dose-rate and low reproducibility of laser-driven beams, the use of dose-rate independent dosimeters is crucial. With this aim, an innovative Faraday Cup (FC) for the absolute dosimetry has been recently designed and realized within the ELIMED collaboration. Its technical design was inspired to similar detectors already developed for ion-beam dosimetry [8, 9], but innovative geometrical solutions have been adopted in order to further improve the overall charge collection efficiency [10].

References

[1] G. Mourou et al., Rev. Mod. Phys 78 (2006) 309.
[2] A. Macchi et al., Rev. Mod. Phys. 85, (2013) 751
[3] D. Margarone, G.A.P. Cirrone, G. Cuttone, G. Korn, AIP Conf. Proc. 306 1546, 1-1.
[4] M. Maggiore et al., in: II ELIMEDWorkshop and Panel, AIP Conference Proceedings 1546, (2013) 34-43.
[5] F. Romano et al., in: II ELIMED Workshop and Panel, AIP Conference Proceedings 1546, (2013) 63-69 .
[6] V. Scuderi et al., NIMA740 (2014) 87-93.
[7] IAEA, Absorbed Dose Determination in External Beam Radiotherapy: An International Code of Practice for Dosimetry Based on Standards of Absorbed Dose to Water, Pub. by IAEA(Vienna), (2000).
[8] R. Cambria et al., Phys. Med. Biol. 42 (1997) 1185-1196.
[9] G. Cuttone et al., Physica Medica - Vol. XV, N.3 (1999)
[10] J.D. Thomas et al., NIM A536 (2005) 11-21.

Geant4 Monte Carlo simulations and applications in medical physics

F. Romano[1], R. Calcagno[1], G. A. P. Cirrone[1], G. Cuttone[1], S. E. Mazzaglia[1], G. Milluzzo[1,2], M. G. Sabini[3], V. Scuderi[1,4], A. Tramontana[1,2], A. Varisano[1]

1) INFN-LNS, Via S. Sofia 62 - 95125 Catania, Italy
2) University of Catania,Via S. Sofia 64 - 95125 Catania, Italy
3) Dipartimento di Diagnostica per Immagini, Azienda Ospedaliera "Cannizzaro", Catania, Italy
4) Institute of Physics of the ASCR, ELI-Beamlines Project, Harfa Office Park Ceskomoravská- 2420/15a CZ 190 93 Prague, Czech Republic

Abstract – Monte Carlo (MC) methods are currently considered the most powerful approaches in the medical physics field, from the absolute and relative dose calculation to the verification of the Treatment Planning Systems. MC approaches are also useful for the simulation of transport beam lines, in order to predict the output beam characteristics also for non-conventional accelerated input. In this report, MC applications developed at LNS with the GEANT4 toolkit are presented.

INTRODUCTION

The GEANT4 (GEometry ANd Tracking) MC toolkit is one of the most versatile and widespread codes used today for particle tracking and largely employed in many kinds of applications [1, 2]. It is a C++ object-oriented toolkit permitting the simulation of particle interactions with matter and providing advanced functionalities for all typical domains of simulation. Initially developed for High Energy Physics Experiments simulation, it is now widely used also for low-energy medical physics applications. Some of the authors of this work are currently members of the official GEANT4 collaboration, contributing to the maintenance of the *advanced examples*, and developing two examples currently distributed in the public release of the code, named *hadrontherapy* and *gammaknife*.

GEANT4 APPLICATIONS IN THE MEDICAL FIELD

Several applications in the medical physics domain have been developed using the GEANT4 toolkit. An advanced example simulating a Gamma Knife device for Stereotactic Radiosurgery has been recently included in the public release. It reproduces in details the cobalt sources displacement inside the unit and allows a comparison with the Treatment Planning System used for the dose computation. The PRIMA (Proton IMAging) prototype for proton Computer Tomography (pCT) has been also fully simulated to investigate the reconstruction methods and study the path of the proton beams. Moreover, the fragmentation of carbon ion beams on thick and thin targets (FRATT and FRAG experiments) has been studied in order to validate the GEANT4 nuclear for beams of interest in hadrontherapy. As concern the use of proton and ion beams for therapeutic purposes, the *hadrontherapy* advanced example is developed and maintained for several years. In the application, the CATANA beam line for eye melanoma treatment is fully simulated and, recently, a module dedicated to the computation of the dose-average linear energy transfer has been included [3, 4]. During the last year, a new module has been also implemented, reproducing a typical beam line for the transport and handling of laser-driven beams.

The CATANA beam line and the average linear energy transfer calculation

The *Hadrontherapy* example simulates a typical proton/ion therapy beam line, including all the necessary elements, from the diffusion and modulation system to the detectors for relative and absolute dosimetry. The application offers also the possibility to change many beam line parameters without modifying the source code, i. e. run-time by means of several idle commands. Moreover, a module dedicated to the calculation of the average 3-dimentional Linear Energy Transfer (LET) for proton and carbon ion beams has been recently added. For instance in Figure 1 the total and primary LET-dose distributions for a 62 MeV proton beam in PMMA are shown. The dose curve is compared with experimental data, normalized at the entrance [5].

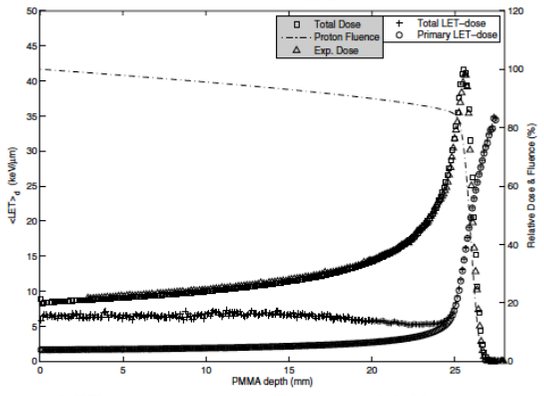

Figure 1. LET-dose distributions for a 62 MeV proton beam in PMMA. The relative dose distributions and primary protons fluence are given in arbitrary units.

A module dedicated to the computation of the Relative Biological Effect (RBE) has been also developed and it will be soon included in the public release of the example.

The laser-driven beam line

During the last years, the interest in particle acceleration driven from ultra intense lasers is strongly growing, thanks to the huge number of potential applications and to the possibility to investigate new physics regimes. It could bring to more compact and less expensive acceleration systems and, consequently, to a larger availability of radiation beams around the world. However, current available laser-driven charged particle beams are characterised by non-conventional and sometimes extreme features, such as a wide divergence and a 100% energy spread. In this framework the capability to accelerate laser-driven beams in a controlled and reproducible manner for their use in any potential downstream applications, like linac injection, isotope production, imaging or radiobiology, represents one of the main objective for many worldwide researchers.

In this background, the ELIMED (MEDical and multisciplinary application at ELI-beamlines) project was born and a transport beam line dedicated to laser-driven beams has been recently realized. This beamline has been simulated with Geant4 and it has been also added as optional choice to the *hadrontherapy example*. The Monte Carlo approach has allowed, indeed, to optimize the beam line elements design and to study the output beam features modifying the input characteristics. As shown in figure 2 two main devices compose the beam line: a collecting focusing system and an energy selector. The first element, placed few cm downstream the source point, collects, focuses and pre-selects in angle and energy the accelerated particles. The final beam energy refinement is obtained by means of the energy selection system (ESS), composed of two collimators, four permanent dipole magnets with alternating polarity and a central slit [6,7]. Each element has been simulated in details, and several idle commands have been implemented in order to change run-time some geometrical parameters, as necessary [8]. Regarding the magnetic fields, they have been treated using a grid map with a 2 mm step and a linear interpolation. The grids have been obtained by OPERA simulations and read by a dedicated new class.

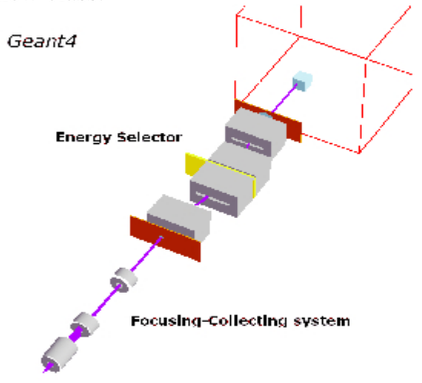

Figure 2. The transport beam line for laser-driven charged particles, implemented in the *hadrontherapy* advanced example.

The new dosimetric detector

There are many suitable applications for the optically accelerated beams, but we have focused our attention on the possibility to irradiate cell samples with controlled dose distributions. However the ultra-short duration of laser-driven multi-MeV ion bursts offers dose rates of about 10^9 Gy/min, very far from the conventional values. In this background and considering the saturation effects of dosimetric detectors typically used for conventional beams, an alternative detector has been proposed: a Faraday Cup, well know dose rate independent detector, has been recently realized at LNS at this aim.

Several preliminary studies have been performed in order to optimise shape, dimensions, materials and electric field features, by means of COMSOL, Simion and Geant4 simulations. The final configuration, reported in figure 3 and described in [9], represents the final prototype and it has been implemented in the public *hadrontherapy* application.

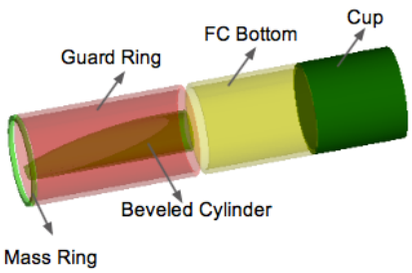

Figure 3. Schematic layout of the innovative Faraday Cup, simulated as default detector in the *hadrontherapy* advanced example.

CONCLUSIONS

MC methods can be considered one of the most powerful approaches in the medical field. Geant4 is an open source MC toolkit, widely used for several applications. Our group is part of the official collaboration and has gained a long and consolidated experience. Beyond the daily working on physics model validation and advanced example development, a constant activity of dissemination is carried out, with the organization of national and international courses.

REFERENCES

[1] S. Agostinelli *et al.*, Nucl. Instr. and Meth. in Phys. Res. A, Vol. 536, Issue 3, 250-303 (2003)
[2] J.Allison et al., Nuclear Physics News Vol. 17, 2, 20-24 (2007)
[3] G.A.P.Cirrone et al., NUCLEAR SCIENCE and TECHNOLOGY Vol. 2, pp.207-212 (2011)
[4] Cuttone G *et al.*, THE EUROPEAN PHYSICAL JOURNAL PLUS vol. 126, 65 (2011)
[5] F. Romano *et al.*, Phys. Med. Biol. 59, 2863-2882 (2014)
[6] M.Maggiore *et al.*, AIP Conf. Proc.1546, 34-43 (2013)
[7] V. Scuderi *et al.*, NIM A 740, 87-93 (2014)
[8] F. Romano et al., AIP Conf. Proc. 1546, 63-69 (2013)
[9] G.A.P. Cirrone *et al.*, NIM A, in press

Dosimetric approaches for laser-driven ion beams: an innovative Faraday Cup

V. Scuderi[1,2], G.A.P. Cirrone[1], F. Romano[1], A. Amato[1], G. Candiano[1], G. Cuttone[1], R. Leanza[1,3], R. Manna[1], V. Marchese[1], G. Milluzzo[1,3], G. Petringa[1,3], F. Schillaci[1] , A. Tramontana[1,3]

1) INFN-LNS, Via S. Sofia 62 - 95125 Catania, Italy
2) Institute of Physics ASCR, v.v.i. (FZU), ELI-Beamlines Project, Na Slovance 2, 182 21 Prague, Czech Republic
3) Universita´ degli Studi di Catania, Dipartimento di Fisica e Astronomia, Via S. Sofia 64, Catania, Italy

Abstract – An innovative Faraday Cup (FC), optimized for high pulsed ion beams, has been designed and realized at INFN-LNS, within the ELIMED project. The FC has been tested with the 62 MeV proton beams delivered by the superconducting cyclotron (CS) at the CATANA protontherapy facility (LNS), in order to investigate the device charge response as a function of the applied bias. Moreover, the electromagnetic pulse (EMP) produced by the laser-matter interaction and its propagation inside the FC has been studied in order to disentangle the real ion signal from the electromagnetic noise and obtain a correct dose evaluation.

ABSOLUTE DOSIMETRY OF LASER DRIVEN ION BEAM

Due to the unconventional features of the optically accelerated ion beams, such as the broad energy and angular distributions [1], the high dose-rate (about 10^9 Gy/s [2]), the poor reproducibility and stability of the beams, no dosimetric international protocol has been established, so far.
The high dose rate characterizing these new particle beams and the poor stability makes, indeed, necessary the development of appropriate dose-rate independent dosimetric systems, as for instance the Faraday Cup.

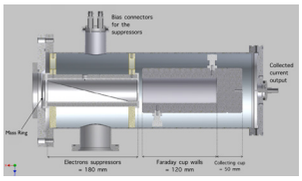

Figure1. Schematic layout of the FC developed at the LNS.

The FC realization at LNS has been possible thanks to several preliminary studies performed in order to optimize shape, sizes, materials and electric field features, using the COMSOL FEM (Finite Element Method) software, the Simion FEA (Finite Element Analyze) software and the Monte Carlo Geant4 [19] simulation toolkit.
Figure 1 shows the final FC geometry in details. The FC prototype is about 400 mm long with an internal radius of 20 mm. It consists of a 25 um kapton window, a 5 mm thin mass ring, a 180 mm steel suppressor and a 50 mm aluminum cup.
Since the ionization of the residual gas could affect the charge measurements, a vacuum of about 10^5 mbar is required as working condition.
A FC allows the extraction of the absolute dose [Gy] released in water (D_w) from a proton beam, according to the expression:

$$D = \frac{1}{A}\frac{\int S(E)N(E)dE}{\int N(E)dE}\frac{Q}{e}1.602\ 10^{-10}\ [Gy]$$

where A [cm^2] is the effective beam area, $S(E)_w$ the mass stopping power in water [MeV/cm^2 g] at a given energy E, Q[C] is the measured charge and e is the elementary charge. As it is well known [4], the value of total collected charge Q can be strongly affected by both the secondary electrons generated at the entrance window by the beam-kapton interaction and the ones produced by the beam within the cup material. The former, if able to reach the cup, lead to an underestimation of the total charge while the latter, if generated with sufficient energy to leave the collecting cup, may cause a charge overestimation. In order to improve the charge collection accuracy, following the work presented by Thomas et al. in ref. [5], a peculiar electric field has been designed. The electric field results from the combined effect produced by two coaxial electrodes. The external electrode is a metallic hollow cylinder whereas the internal one is a peculiar beveled cylinder.
The cylindrical symmetry of the electric field provided by the external electrode is broken due to the presence of the internal one. The resulting effect is a strongly asymmetric electric field, characterized by a significant transversal component able to maximize the deflection of the secondary electrons generated by both the entrance window and the cup [6].

Test with conventional proton beams

In order to investigate the FC prototype response, a charge measurement characterization as a function of the applied bias has been performed using the 62 MeV proton beams delivered by the superconducting cyclotron (CS) at the CATANA protontherapy facility at the INFN-LNS.

The FC prototype has been placed along the beam-line at about 9 cm downstream the last collimator, a 20 mm diameter collimator has been used for the characterization. The FC operating vacuum was 10^{-5} mbar. The FC current signal as a function of the collecting time was measured by means of an electrometer Keithley (Model 6517A). Such preliminary characterization of the FC prototype charge collection as a function of the voltage applied to the secondary electron suppressor has been performed using, uniquely, the external cylindrical electrode. In order to check the suppression efficiency the applied voltage has been varied from -2400 Volt to 2400 Volt. Each charge measurement has been performed for a fixed delivered dose of 15 Gy. The dose released has been controlled using the online transmission monitor chambers, calibrated with respect to the Markus ionization chamber, i.e. the absolute dosimeter. The collected charge, obtained integrating the current signal for the time interval required to deliver 15 Gy, vs the applied voltage is shown in figure 2.

As one can see, a typical flat voltage response plateau in the negative voltage range between -2400 V and -400 V can be observed; on the other hand, for positive voltages a collected charge dependence increasing with the voltage applied is evident. The charge collection response observed in the FC prototype is in quite well agreement with the typical behavior of standard FCs used for absolute dosimetry [4,7]. A complete characterization of the FC prototype suppression efficiency using the internal beveled cylinder, in order to identify the most suitable operating suppressor configuration, is foreseen at the INFN-LNS.

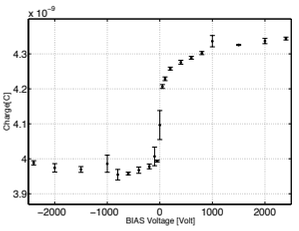

Figure2. Charge collected by the FC as a function of the bias applied to the external suppressor

Study of the electromagnetic pulse (EMP)

A typical high power laser-matter interaction, and the subsequent plasma production is accompanied by the emission of an intense electromagnetic pulse (EMP) which propagates inside and outside the interaction chamber [8], interfering with the diagnostics devices and affecting their response. Therefore, in the case of a dosimeter, it is crucial to perform a systematic study, in terms of frequency and amplitude of the not-negligible electromagnetic noise due to the laser pulse, before to proceed to the dose evaluation [9].

The developed FC has been preliminary tested in an experimental campaign, at the PALS laboratory (Prague, CZ), where a 2TW laser system (about 1KJ of energy delivered on target and a time duration of 300 ps), is available. The FC was mounted on the interaction chamber at 30◦ with respect to the target normal axes in the backward direction. The signal was registered with a 2 GHz Le Croy Digital Oscilloscope.

Figure 3 (left) shows a typical FC signal registered during the laser shot.

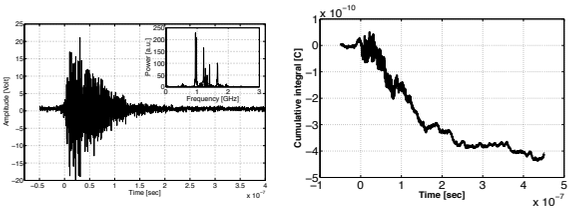

Figure3. A typical FC signal during the laser shot (left). The inset shows the correspondent Fourier transformation. The cumulative integration of the signal (right).

As one can clearly see, the electromagnetic noise is characterized by high frequency components from few hundreds of MHz up to1 GHz.

Based on the frequency analysis, the significant noise signal results from the EMP propagation inside the interaction chamber [8,9,10] and seems to be predominant with respect to the charge signal, affecting the measurement of the total collected charge. Nevertheless, the cumulative integration of the whole signal, shown in Figure 3 (right), reveals the presence of a charge contribution that, although very small, can be separated by the huge EMP noise contribution [6]. This result indicates the necessity to perform a thorough study to allow the separation of the noise contribution from the physical signal. The use of appropriate electronic circuits, as filters or amplifiers, might allow removing or reducing the higher frequency contributions related to the EMP.

References

[1] A. Macchi et al., Rev. Mod. Phys. 85, (2013) 751

[2] Doria D at al., American Institute of Physics AIP Advances, 2 (1), pp.011209-011215 (2012).

[3] J.Allison et al., Nuclear Science, IEEE Transactions on, 53, 1, (2006) 270-278

[4] R Cambria et al., Phys. Med. Biol. 42 (1997) 1185-1196.

[5] J.D. Thomas et al., Nuclear Instruments andMethods in Physics Research A 536 (2005) 11-21.

[6] G.A.P. Cirrone, et al., Nuclear Instruments & Methods in Physics Research A (2015), http://dx.doi.org/10.1016/j. nima.2015.02.019i

[7] G. Cuttone et al., Physica Medica - Vol. XV, N.3 (1999).

[8] M.J. Mead, at al., Rev. Sci. Instrum. 75 (2004) 4225-4227.

[9] Seong Hee Park et al., Journal of the Korean Physical Society, Vol. 49, No. 1, (2006)

[10] M. De Marco et al., Journal of Physics: Conference Series 508 (2014) 012007

Monte Carlo simulation of neutrons flux and ambient dose equivalent in 0° experimental room at Laboratori Nazionali del Sud.

S. Russo[1], R. Leanza[1], G. Russo [1,2],G.A.P. Cirrone [1], G. Cuttone [1],

1) INFN-LNS
2) IBFM-CNR

Abstract - The characterization of environmental radiation fields around the particle accelerators, in terms of dosimetric and spectrometric quantity, is essential for the protection of workers and population.

In this work we estimate, with FLUKA code [2], the neutron ambient dose equivalent H*(10), produced by 62 MeV protons beam on two different targets, carbon and silicon, as well as the flow of neutrons and their energy spectra, resulting from a change in experimental conditions in a 0° beam line of the LNS. The simulations have also allowed us to design a modification of the shielding of the room in order to reduce the doses.

INTRODUCTION

At LNS, until now, cyclotron proton beams were accelerated with energies with maximum currents of about 10 nAe, but new experimental demand [1] require higher currents, about 100 nAe. In the new experimental conditions, the preliminary assessments of neutrons ambient dose, deduced by extrapolating past measured values, involving to the need of detailed evaluation, in order to ensure compliance with the dose limits and the general principles of radiation protection (ALARA).

GEOMETRY AND METHODS

In the room geometry, visible in Figure 1, we have taken into account the concrete parts (walls, roof, floor) and air, omitting the other materials which contribution on the diffusion and absorption of neutrons is negligible.

In this study we haven't taken into account the contribution due to gamma radiation, because it is more than an order of magnitude lower, compared to the neutrons contribution.

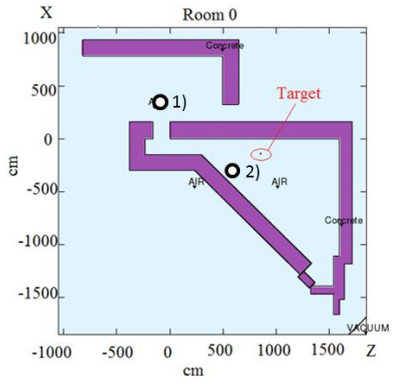

Figure 1: top view of geometry of the 0° room.

Three studies were performed. The first to simulate the present distribution of the ambient dose generated by a 10nAe current protons beam, impinging in a carbon target. The second to estimate the ambient dose for the future experimental configuration: protons beam with the same energy on silicon target, but current of 100nAe. The third simulation to modify the entrance maze in order to to reduce the dose outside the hall.

We calculated H*(10) and the flow (n/cm2/s) in all areas and the energy spectra outside the entrance door.

The validity of the simulations was verified with experimental measurements made with two portable detectors: a rem counter LB6411 [7] calibrated at a centre of metrology, and a BTI N-PROBE [6]. Both provides information in terms of H*(10) and the BTI one also gives energy spectrum and flow. The measuring points are visible in Figure 1), point 1) and 2).

A further validation was conducted by comparing the results with analytical models reported in NCRP publications [4,5].

RESULTS

simulation 1.

The plot of H*(10) in the first experimental setup, (62 MeV protons, 10 nAe, on carbon target) is shown in Figure 2. The simulated values are similar to those measured by the rem counter, reported in Table 1.

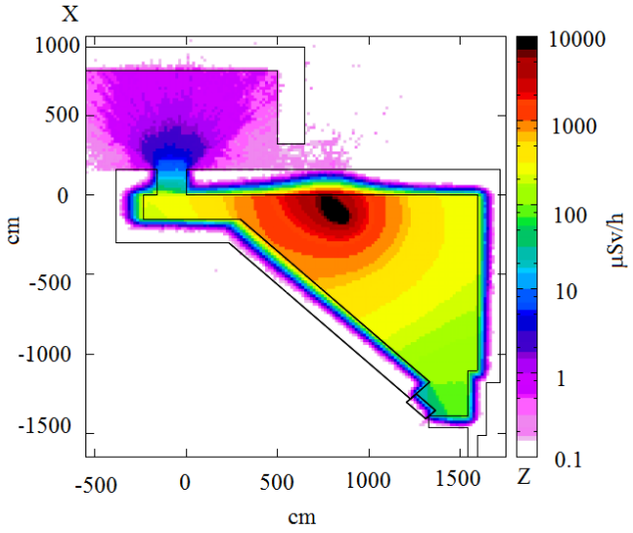

Figure 2: simulation in the first experimental setup.

point	H*(10) [µSv/h]
1)	5.8
2)	4000

Table 1: Measurements of H*(10), in the first experimental setup in point 1) and 2).

The neutron flux, simulated with a detector in the point 1), is reported in Figure 3. The measured value, at the same point, is shown in Table 2. The simulation is in agreement with the measured data for the component of high energy, while we can notice an underestimation of thermal component by the detector.

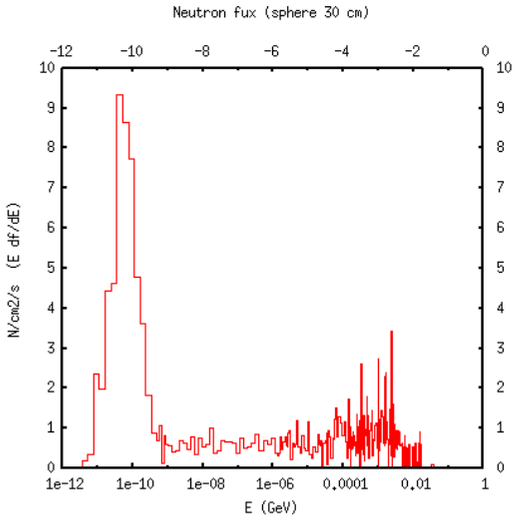

Figure 3: simulation of neutron flux in the first experimental setup in point 1).

	flux	H*(10)	rate
MeV	n/cm2/s	uSv	mSv/h
<0.01	4.6e+000	1.0e-001	1.9e-004
.01-.5	1.3e+000	3.0e-001	5.7e-004
>0.5	3.0e+000	2.7e+000	5.0e-003
total	8.8e+000	3.1e+000	5.8e-003

Table 2: flow and dose measurements in the first experimental setup in point 1).

This values were also compared, in good agreements, with measures made with Bonner sphere spectrometers [3] in the same hall, beam and irradiation condition.

simulation 2

The simulation in the future experimental configuration (62 MeV proton, 100 nAe, on silicon target), give as the information that doses are about 20 times higher than those in the first experimental configuration and values higher than 50-100 µSv/h are expected near the door where the worker stay to collect data. This confirm the necessity to revise the entrance maze in order to reduce the dose outside the hall.

simulation 3

The third study consisted of several geometry simulations of the labyrinth in order to find the best logistics solution to reduce the impact of new shielding in an experimental hall that is already in use. The best solution was to insert two arms of ordinary concrete, one inside and one outside the room, both with a thickness of 50 cm, that can reduce the ambient dose equivalent outside the door to less than 1 µSv/h, which are compatible with the permanence of staff, see Figure 4.

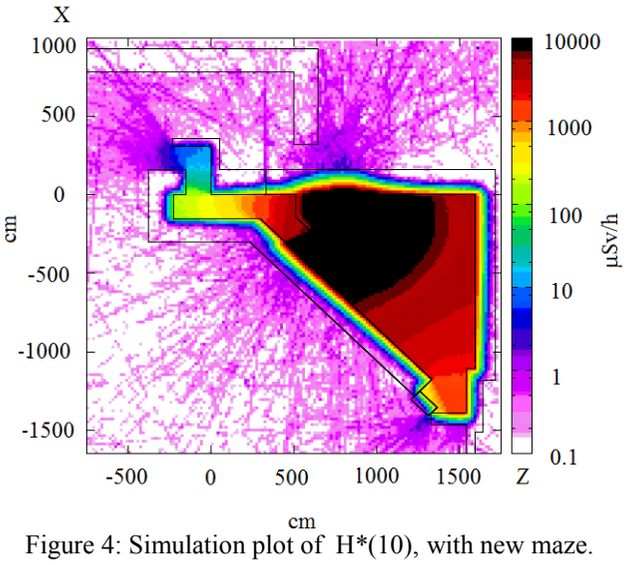

Figure 4: Simulation plot of H*(10), with new maze.

CONCLUSIONS

Monte Carlo simulations with the Fluka code, used for the first time at LNS for radioprotection purposes, allowed us to make very reliable estimations for the ambient dose equivalent and for the neutrons flows. The simulations are in good agreement with measurements and with the analytical estimates derived from NCRP publications.

Furthermore, by simulating different geometries in changing the maze, it was possible to find the best design of the shielding and reduce the impact on the logistics of the room, still ensuring the ALARA principles for the protection of people.

REFERENCES

[1] E. Alemanno, et al "Radiation damage of polycrystalline diamond exposed to 62 MeV protons". Nucl. Instrum. & Meth. (NIM-A), Volume 730, 1 December 2013.

[2] http://www.fluka.org/

[3] K. Amgarou, et al. "Measurement of the neutron fields produced by a 62 MeV proton beam on a PMMA phantom using extended range Bonner sphere spectrometers", Nucl. Instrum. & Meth. in Physics Research Section A (NIM-A), July 2011.

[4] NCRP Report n.144 "Radiation protection for particle accelerator facilities", December 31-2003.

[5] NCRP Report n.38 "Protection against Neutron radiation", October 15-1991.

[6] H.Ing et al. "Portable spectroscopic Neutron Probe", Radiation protection dosimetry vol.126 n.1-4 2007.

[7] A. Klet et al. "The New Remcounter LB6411", IEEE transactions on Nuclear Science, Vol. 44, N. 3, June 1997, 757-759.

LENS - Laser Energy for Nuclear Science

G. Lanzalone[1,2], S. Tudisco[1], A. Anzalone[1], C. Altana[1,3], A. Muoio[1,4], F. Musumeci[1,3], C. Caliri[1,3], G.A.P. Cirrone[1], D. Mascali[1], F.P. Romano[1,5], G. De Luca[1], S. Salamone[1], F. Schillaci[1], A. Scordino[1,3]

1) INFN-LNS, Via S. Sofia 62, 95123 Catania, Italy
2) Univ. degli Studi di Enna "Kore", Via delle Olimpiadi, 94100 Enna, Italy
3) DFA-Univ. degli Studi di Catania, Via S. Sofia 64, 95123 Catania Italy
4) DFST-Univ. degli Studi di Messina Viale F.S. D'Alcontres 31, 98166 Messina, Italy
5) CNR, Sezione di Catania dell'IBAM, Via A.Ddi Sangiuliano 262, 95100 Catania, Italy

Abstract – In this contribution we describe status and perspectives of the new facility at LNS: the LENS laboratory, Laser Energy for Nuclear Science.

INTRODUCTION

Plasma is by far the most common form of matter known. Plasma in the stars and in the tenuous space between them makes up over 99% of the visible universe and perhaps most of that which is not visible. Given its nature, the plasma state is characterized by a complexity that exceeds that exhibited in the ordinary states, solid, liquid, and gaseous. Correspondingly, the physical properties of nuclear matter, e.g. structure, life times, reaction mechanisms etc., could be changed inside the plasma. These studies represent then one of the most far ranging, difficult and challenging research areas today, and their implications could potentially cover others fields, from quantum physics to cosmology, astrophysics etc.

The future availability of high-intensity laser facilities (e.g. the European infrastructure ELI-NP), capable of delivering tens of peta-watts of power into small volumes of matter at high repetition rates, will give the unique opportunity to investigate nuclear reactions and fundamental interactions under extreme plasma conditions. In this context, one of the most crucial aspects concerns the nuclear fusion mechanism and in particular the role played by the electron screening. Direct measurements using accelerated beams show that, at very low energies, the electrons in the target's atoms partially screen the Coulomb barrier between the projectile and the target [1], resulting in an enhancement of the measured cross section compared with the bare nucleus one.
The electron screening effects are significantly affected by the target conditions and composition [2]; it thereby results of particular importance the measurement of cross-sections at extremely low energetic domains, including plasmas effect, i.e. in an environment that under some circumstances and assumptions can be considered as "stellar-like" (for example, for the study of the role played by free/bounded electrons on the Coulombian screening can be done in dense and warm plasmas).
Usually, astrophysically relevant reactions are performed in the laboratories with both target and projectile in their ground state. However, in high temperatures plasmas (10^8 K), an important role can be also played by the excited states, as already deeply discussed in the pioneering theoretical work of Bahcall and Fowler [3]. Thus determining the appropriate experimental conditions that allow evaluating the role of the excited states in the stellar environment could strongly contribute to the development of nuclear astrophysics.
The direct measurements of reaction rates in plasma offers this chance. In addition, other new topics can be conveniently explored such as three body fusion reactions as those predicted by Hoyle [4], lifetime changes of unstable elements [5] or nuclear and atomic levels [6] in different plasma environments; other fundamental physics aspects like non-extensive statistical thermodynamics [7] can be investigated in order to validate/confute the general assumption of local thermal equilibrium that is traditionally done for plasmas. Our collaboration is proposing the study of these research topics at the future facility ELI-NP which is being built in Romania; in particular, the implementation of general-purpose experimental set-up for the conduction of these experiments. In this context at LNS, we realised a new test laboratory for the issues related to this activity.

We are developing several plasma diagnostics, optical time resolved imaging, optical spatially resolved spectroscopy, X-ray imaging, X-ray spectroscopy, Thomson parabola spectrometer for ions detection.

EXPERIMENTAL SET-UP

The laboratory is equipped with two Nd:YAG laser of 2,2 and 0,7 Joule of energy, at fundamental wavelength of 1064 nm with a duration of 6 ns and a rep. rate of 10 Hz. The 2,2 J laser beam was focused through, fused silica, plano-convex lens (one inch of diameter) on target at an angle of about 30°, with respect the target normal, and

placed inside an interaction circular vacuum chamber (of about 1m of diameter). The target is equipped with some micrometric remote motion devices, which allows movements along three directions.

Two Ions Collectors-ToF (IC) are placed at different angles, in order to reconstruct the ions or electrons energies distribution.

A Thomson Parabola (TP) spectrometer is used because it is considered the elected detector for laser-driven beams characterization. Its working principle is widely described in literature [8] and it is based on the effect of mutually parallel electric and magnetic field acting on a charged particle.

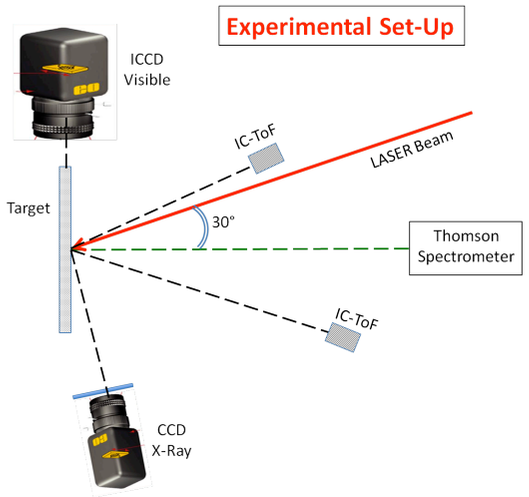

Figure 1: Sketch of the experimental set-up of LENS laboratory.

One of the fastest optical shutters available is an image intensifier. An ICCD (Intensified CCD) is a device where the image intensifier is coupled with a CCD in a way to amplify its sensitivity and give the possibility to acquire images in a small time widows (at list about 2 ns). This devices is extremely useful to study the time evolution of laser generated plasmas. Fig. 2 shows some results of our set-up irradiating on aluminum thick target.

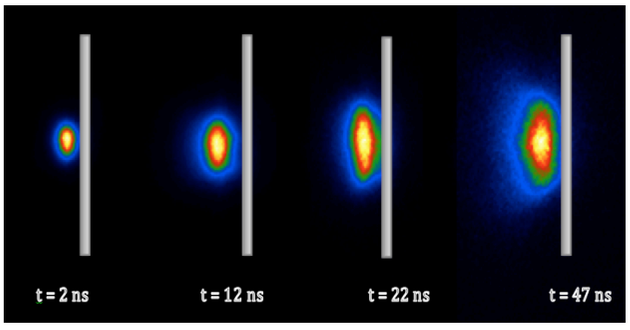

Figure 2 : ICCD images of spatial distributions of the expanding plasma after 2ns, 12ns, 22ns and 47ns, displayed as a "false colour" image

The set up is also equipped with a cooled CCD for X-ray detection, in order to perform X-ray imaging (through the pinhole technique) and space-resolved X-ray spectroscopy (by using gratings). Preliminary tests of the CCD camera were done with the use of our laser source on aluminum target. Figure 3 shows X-ray imaging obtained with laser-plasma source by X-ray CCD camera equipped with a pinhole. The performance and results related to the TP spectrometer are widely discussed in C. Altana et al. contribution on this LNS-report book.

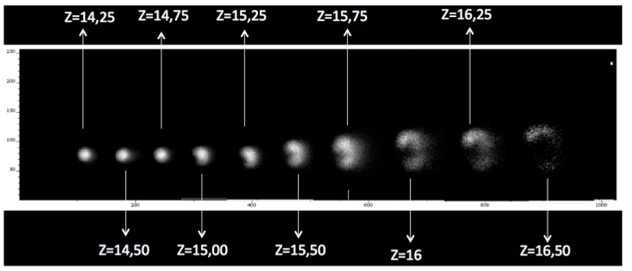

Figure 3: Exemplary images for different target position (Z) obtained with X-ray CCD camera with laser-plasma source. The Z positions is related to the different positions of the focusing lens of laser beam.

CONCLUSION

A novel laboratory has been developed at INFN-LNS. It has been designed in order to investigate the laser-generated plasmas and on nuclear physics inside the plasma. At the present time we are performing experiments with one laser beam.

We plane to use the second laser to realize further diagnostic (like plasma density measurements through the shadowgraph or interferometry technique), but we have in program to use also the second laser pulse to generate a second plasma in order to perform experiments with colliding plasmas, which are very attractive for investigating nuclear reactions under these conditions.

REFERENCES

[1] E.E. Salpeter, Australian Journal of Physics 7(3) (1954) 373
[2] M. Lipoglavsek et al., Eur. Phys. Jou. A 44 (2010) 71, and ref. there in
[3] N.A. Bahcall and W.A. Fowler Astrophysical Journal 157 (1969) 645
[4] F. Hoyle, Monthly Notices of the Royal Astronomical Society 106 (1946) 343
[5] B.N. Limata, Eur. Phys. J. A 27, s01, (2006) 193
[6] F. Hannachi et al., 2007 Plasma Phys. Control. Fusion 49 B79
[7] C. Tsallis, "Introduction to Nonextensive Statistical Mechanics…", Springer 2009
[8] G A P Cirrone et al 2014 JINST 9 T08001 doi:10.1088/1748-0221/9/08/T08001

Test at ENEA ABC laser to study some nuclear fusion reactions in plasma

A. Anzalone[1], A.Bonasera[1,2], P. L. Andreoli[4], M. Cipriani[4], F. Consoli[4], V. Crucillà[1], R. De Angelis[4], G. Di Giorgio[4], F. Ingenito[4], M. La Cognata[1], D. Lattuada[1,5], R. Manna[1], S. Romano[1,3], V. Scuderi[1], A. Spitaleri[1], C. Spitaleri[1,3], S. Tudisco[1], A. Tumino[1,5]

1) Laboratori Nazionali del Sud – Instituto Nazionale di Fisica Nucleare, Catania, Italy
2) Cyclotron Institute, Texas A&M University, College Station, TX, USA
3) Dipartimento di Fisica & Astronomia, University of Catania, Catania, Italy
4) Associazione Euratom – ENEA sulla fusione, via E.Fermi 45.6500044, Frascati, Italy
5) Facoltà di Ingegneria ed Architettura, Università degli studi di Enna Kore, Enna, Italy

Abstract - We have performed experiments at the ENEA ABC laser facility (two beams of 50 J each 3 ns wide). The goal of these experiments is the study of the $p+^{11}B$, $^{6}Li+^{6}Li$ reactions and others [1,2], in the context of the emerging partnership between the Enea Fusion group and the LNS ASFIN group.

The plasma generated by laser-target interaction will give us the possibility of testing screening effects in fusion reactions, which are very relevant for nuclear astrophysics.

MEASURING S-FACTORS IN HOT AND DENSE PLASMA

The astrophysical S-factor is the main parameter of any thermonuclear reaction. The S-factor determines the reaction cross-section. In the Sun and stars of our Universe, it defines the probability of reaction at very low energies. The S-factor may be obtained experimentally, but for the majority of interacting light nuclei, which take part in the thermonuclear processes, it can be done in the energy range 100 keV÷1 MeV only; and the errors of its measurement may reach 100% and more, more often than not.

In the extrapolation of the cross section σ(E) of a charged-particle induced nuclear reaction to astrophysical energies one uses the equation

$$\sigma(E) = S(E)E^{-1} \exp[-2\pi\eta(E)]$$

where η(E) is the Sommerfeld parameter and S(E) the astrophysical S-factor [3]. The equation assumes that the Coulomb potential of the target nucleus and projectile is that resulting from bare nuclei. However, for nuclear reactions studied in the laboratory, the target nuclei and the projectiles are usually in the form of neutral atoms or molecules and ions, respectively. The electron clouds surrounding the interacting nuclides act as a screening potential: the projectile effectively sees a reduced Coulomb barrier, both in height and radial extension. This, in turn, leads to a higher cross section for the screened nuclei [4].

The Trojan horse method (THM) allows us to study a nuclear reaction of astrophysical importance free of Coulomb suppression and electron screening with no need of extrapolation (see [5] for a review on the method). In the THM, the low-energy cross section of a *A(x,c)C* reaction is obtained by extracting the quasi-free (QF) contribution to a suitable *A(a,cC)s* reaction. Particle *x* is virtual so the *A(x,c)C* THM cross section is half-off-energy-shell (HOES) and cannot be right juxtaposed to the direct (on-energy-shell, OES) cross section. However, it has been proved [5] that HOES effects can be corrected for, essentially, by introducing the penetration of the Coulomb barrier. In fact, since the QF reaction is induced at energies well above the Coulomb barrier, the participant *x* is brought inside the nuclear field of *A* with no Coulomb repulsion.

Besides making it possible to reach very low energies, an additional advantage is possibility to access bare nuclei astrophysical factors, as the measurements are performed at energies larger than coulomb barrier where the shielding by electron clouds is negligible. High intensity laser-solid interactions produce plasmas in which the nuclei are free of electrons and therefore give us the opportunity of studying screening factor and fusion rate in an unexplored low energy range. Therefore, these synergic studies can allow us to achieve an unprecedented accuracy in nuclear astrophysics.

DIAGNOSTICS

A Faraday cup has been realized at LNS and tested at ABC Laser with very good results. CR-39 foils were used as detectors of charge particles around the irradiated target. The analysis of these detectors will be made to the LNS where it was developed an automatic trace analysis. However, the most diagnostic used was the one in their laser ABC [6].

The analysis of the acquired data are in progress.

We ackwonledge MIUR for partly supporting our work through the grant “Premiale Astrofisica Nucleare”

REFERENCES

[1] A. Bonasera et al. (LAPLAFUS coll.) *Measuring the astrophysical S-factors in plasmas*, 4 Int. Conf. on Fission and properties of neutron rich nuclei-Sanibel Is. Nov. 2007, J. Hamilton et al. eds., p. 541

[2] S. Kimura, A. Anzalone, A. Bonasera A, Phys. Rev. E 79 (2009) 038401

[3] C. Rolfs & W. Rodney, Cauldrons in the Cosmos, The University of Chicago Press, Chicago, 1988

[4] K. Czerski, A. Hulke, A. Biller, P. Heide, M. Hoeft, G. Ruprecht, Eur. Phys. Lett. 54 (2001) 449

[5] R.E. Tribble et al., Rep. Prog. Phys. 77 (2014) 106901.

[6] F. Consoli et al., Nucl. Instr. Meth. B 720 (2013) 149

Advanced targets preparation for Proton Acceleration by Laser-Plasma using TNSA regime

L. Torrisi[1,2], M. Cutroneo[3], L. Calcagno[4], P. Musumeci[4], G. Ceccio[1], A. Cannavò[1], A. Italiano[5], S. Cavallaro[2], C. Marchetta[2], J. Ullschmied[6], J. Wolowski[7], J. Badziak[7], A. Torrisi[8]

[1]*Dipartimento di Fisica e SdT, Università di Messina, Italy*
[2] *INFN-Laboratori Nazionali del Sud, Catania, Italy*
[3]*Institute of Nuclear Physics, ASCR, Rez, Czech Republic*
[4]*Dipartimento di Fisica ed Astronomia, Università di Catania, Italy*
[5]*INFN-Sez. CT, Gruppo Collegato di Messina, Italy*
[6]*Institute of Physics, ASCR-PALS, Prague, Czech Republic*
[7]*Institute of Plasma Physics and Laser Microfusion, Warsaw, Poland*
[8]*Institute of Optoelectronics, Military University of Technology, Warsaw, Poland*

Abstract – Advanced targets are prepared as thin foils to be irradiated, in TNSA regime, in vacuum by high laser intensity.

Hydrogenated materials containing nanostructures enhance the laser absorption at the laser wavelength decreasing the reflections and transmissions inducing high electron temperature and density of the non-equilibrium plasma. Optical measurements, compositional analysis, electron microscopy and laser irradiation at low intensity permit to characterize the different thin targets.

Their composition, geometry and sub-microscopic structure is optimized as a function of the laser intensity, pulse energy and pulse duration that will be used in order to accelerate high energy proton beams.

INTRODUCTION

The proton beam production using high intensity laser-matter interaction, instead that traditional ion accelerators, is undergoing a growth of interest due to many application fields, from protontherapy to laser ion sources and from Astrophysics to Nuclear fusion studies.

In order to accelerate protons at energies above 1 MeV and at bunches above 10^{10} particles/cm^2, Target-Normal-Sheath-Acceleration (TNSA) regime can be employed using laser intensity above 10^{15} W/cm^2 [1]. Fig. 1 shows a scheme of the laser irradiating in TNSA regime.

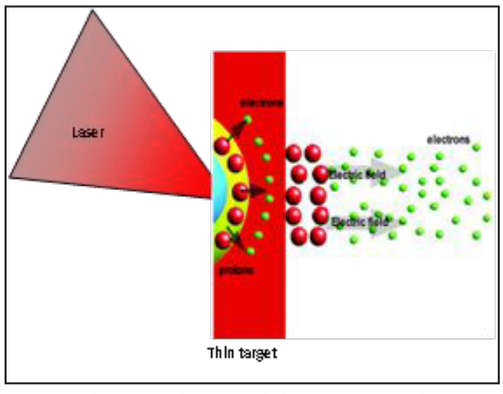

Fig. 1: Scheme of the TNSA regime.

The high proton acceleration and yield is sought not only using high $I\lambda^2$ parameters, being I the laser intensity and λ the laser wavelength, but also using particular conditions of laser irradiations and using peculiar targets in composition and geometry. The laser pulse energy and pulse duration, for example, permit to control the relativistic electron acceleration at the target surface producing in the rear side of the target a controllable electron density responsible of the high electric field driving the ion acceleration. The use of optimal focal position permits to control preplasma effects on the self-focusing conditions [2]. The use of polarized laser light may be employed to induce plasma wave excitations enhancing the plasma temperature and the plasma particle acceleration [3].

In order to obtain high proton yield the target must contain high hydrogen content, such as in polymers, while to obtain high proton energy the target must contain high Z elements potentially capable of generating high electronic density and temperature plasmas. Advanced targets may be prepared and tested before to be submitted to the high intensity lasers by measuring their absorption and reflection at the used wavelength. Their preparation, permits to reduce the reflection and back-scattering light at the critical density surface and to optimize the composition, thickness and geometry in order to enhance the proton yield and proton energy emission. In this sense at LNS and Physics Department of Messina University highly equipped laboratories with spectroscopic state-of-the-art diagnostics are allowing the realization of advanced targets that promise to accelerate protons above 10 MeV of energy with low energy straggling.

EXPERIMENTAL SET-UPS

Targets are prepared using different hydrogenated polymers, hydrides and hydrogen absorbent nanostructures or containing metallic multilayers or nanoparticles. Surface plasmon resonance (SPR) is achieved embedding conductive nanoparticles in the polymers or depositing nano-isles on the surfaces or at the

interfaces of multilayered targets. Moreover, low density foams may be employed to reduce reflections and to produce underdense plasmas and preplasmas enhancing ion acceleration. Optical spectroscopy permits to control the absorption bands of the advanced targets, mass quadrupole spectroscopy the relative amount of emitted atoms, electron and X-ray microscopy the target uniformity and morphology, surface profiler measures the surface roughness. The preliminary measurements of target characterization are performed using Nd:YAg laser operating at 1064 nm, with 9 - 3 ns pulse duration and intensities of the order of 10^{11} W/cm^2 [4].

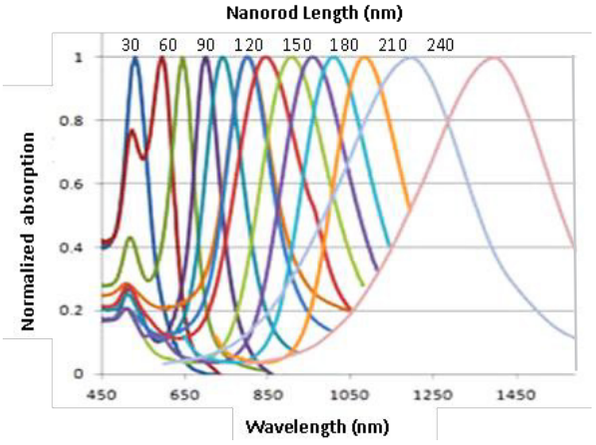

Fig. 1: SPR absorption bands of Au nanorods as a function of their dimension.

The targets are prepared to be irradiated in three European Laboratory facilities that have accepted the Prof. Torrisi's proposals:

The PALS laboratory of ASCR, in Prague, using a Iodine Laser at 1315 nm wavelength, 10^{16} W/cm^2 intensity and 300 ps pulse duration. In this laboratory recently advanced targets have permitted to accelerate protons at energies higher that 5 MeV with a Boltzmann-like distribution [5].

The IPPLM laboratory in Warsaw, using a Ti sapphire laser operating at 800 nm wavelength, 10^{19} W/cm^2 intensity and 40 *fs* pulse duration. In this laboratory advanced targets have been investigated to accelerate MeV protons in order to check their uniformity in composition, thickness and roughness using focal spot dimension of 10 microns and different target geometries employed to produce jet plasma emissions [6].

The Centre Lasers Intenses et Applications (CELIA) of the University of Bordeaux, using a Ti sapphire laser operating at 100 mJ, 800 nm, 35 fs at 10 Hz repetition rate to study of relevant physics on laser-plasma coupling in the shock-ignition intensity regime. In this last case the interest is devoted mainly to the preparation of advanced deutered targets for Fusion studies [7].

Fast diagnostics to measure the proton energy is based mainly on the use of Thomson parabola spectrometry, semiconductor detectors, ion collectors, plastic scintillators, X-ray CCD streak camera imaging and different kind of track detectors.

RESULTS

The use of advanced targets has permitted to enhance significantly the proton acceleration in TNSA regime at PALS, as reported in literature and represented in the summary plot of Fig. 2. The maximum proton energy is here represented as a function of the $I\lambda^2$ parameter comparing many measurements obtained in different laboratories in the word with our data. The prevision of the 0.5 MeV protons at 10^{16} W/cm^2 has been largely surpassed thanks to the use of our "advanced targets" that permitted to obtain more than 5 MeV at PALS [5].

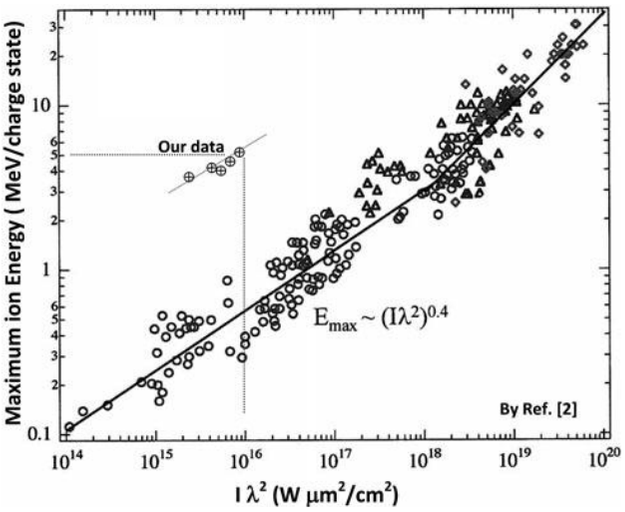

Fig. 2: Comparison of our data with the maximum ion energy as a function of the $I\lambda^2$ parameters

The inners structure of the thin targets and the target thickness can be optimized to generate an electron and ion emission at high density with high sheath acceleration along the normal to the target surface and simultaneously to control the ion energy distributions enhancing the yield of the more energetic particles.

High pressure and density gas-puff targets are also in preparation and under study, following the experience of many laboratories in the word [8], in order to use repetitive lasers permitting to generate continuum accelerated proton beams. The laser parameters, irradiation conditions and the use of advanced target are permitting also to reduce the proton energy straggling doing to predict that in the not too distant future can arise beams of protons almost mono-energetic.

REFERENCES

[1] L Torrisi et al., *J. of Physics: Conf. Series* 508 (2014) 012002-1-7.
[2] L. Torrisi et al., *Laser and Part. Beams* 26 (2008) 379.
[3] L. Torrisi et al., *Nucl. Instr. & Meth.B*, in press 2015.
[4] L Torrisi et al., *Phys. Scripta* 9 (2015) 015603,1-9.
[5] L. Torrisi, *Laser and Part. Beams* 32(03) (2014)383.
[6] J. Badziak et al., *App. Phys. Letters* 103 (2013), 124104
[7] L. Antonelli et al., *Acta Technica* 56 (2011) T57-T69.
[8] P. W. Wachulak et al., *Appl. Physics* B, in press. 2015.

Stabilisation/solidification of radionuclide-polluted soils: application of a performance testing protocol and assessment of γ-radiation shielding index as a function of emission energy

P.P. Falciglia[1,2], S. Romano[2,3], V. Puccio[1,2], F.G.A. Vagliasindi[1]

1) Department of Civil Engineering and Architecture, University of Catania, Viale A. Doria, 6, 95125 Catania, Italy
2) Laboratori Nazionali del Sud - INFN, Via S. Sofia, 62, 95125 Catania, Italy
3) Department of Physics and Astronomy, University of Catania, Viale A. Doria, 6, 95125 Catania, Italy

Abstract - This work focuses on the stabilisation/solidification (S/S) of radionuclide-polluted soils at different ^{232}Th levels using Portland cement alone and with barite aggregates. The potential of S/S was assessed applying a full testing protocol and calculating γ-radiation shielding (γRS) index. The results indicate that the addition of barite aggregates to the cement gout leads to a slight improvement of the S/S performance in terms of durability and contaminant leaching but reduces the mechanical resistance of the treated soils samples. Barite addition also causes an increase in the γ-rays shielding properties of the S/S treatment up to about 20%. Results allow the calculated γRS values and those available from other experiments to be applied to hazard radioactive soil contaminations.

INTRODUCTION

Environmental contamination by radionuclides is a serious problem worldwide. Artificial radionuclides or Naturally Occurring Radioactive Material (NORM) are introduced into the environment following several anthropogenic causes, such as nuclear power production, military, medical, research or industrial applications [1]. As a result of the penetrating power of γ-rays, radionuclides able to generate this form of radiation represent a long term hazard to environment and human health [2]. Thorium (^{232}Th) is a γ-ray emitter NORM that presents present both a chemical and radiological hazard, representing a permanent problem [3].

In situ cement based-stabilisation/solidification (S/S) is a technique aimed at both converting contaminants into their less mobile forms and encapsulating them into a solid monolithic structure [4]. The commonly used cement is Portland cement (PC), however, PC can be mixed with other materials, in order to give specific properties or to reduce the amount of cement and consequently costs. PC based S/S techniques have been documented as appropriate for several heavy metal contaminated soils and they could represent an optimal choice for the treatment of radionuclide polluted soils, due also to the possibility of using specific materials such as PC and barite aggregate, in order to achieve a contaminant radiation shielding. However, the possibility of treating radionuclide polluted soil by PC based S/S has never been investigated. The main aims of the work are: (i) to investigate the potential of PC/barite-based S/S technique for radionuclide-polluted soil treatment applying a full testing protocol; (ii) to assess the γ-radiation shielding feature of the tested S/S treatments as a function of the radiation emission energy and the soil contamination level.

MATERIALS AND METHODS

Contamination procedure and testing protocol

A sandy soil was artificially contaminated with ThO_2 at levels in the range of 0.2 - 15.0%. Two types of Portland cement (32.5 Rck and 42.5 Rck) (PC) were selected as primary binders. Barite powder (B) was also employed. The S/S treatment was performed by mixing contaminated soil samples with wet PC or with PC and B at two different soil:grout ratios in order to obtain 28 d-cured S/S cylindrical samples (Table 1).

Table 1: Experimental matrix

Treatment	C32.5: C42.5: Barite	Water: Dry Grout	Soil: Grout	^{232}Th (%)	Test/ measures
A	1:0:0	0.42:1	4:1	2.0	Testing protocol + γRS calculation
B	0:1:0		4:1		
C	1:0:0		3:1		
D	0:1:0		3:1		
E	0:1:1		3:1		
E	0:1:1		3:1	5.0	γRS calculation
E	0:1:1		3:1	8.0	
E	0:1:1		3:1	15.0	

Experimental protocol on S/S samples included the following tests: setting time, unconfined compressive strength (UCS), freeze and thaw and leaching tests.

γ-ray measurement and γRS index calculation

When the radioactive source and the shielding elements are mixed together, as in the case of radionuclide-polluted soils treated by S/S, the shielding effects of the treatment are difficult to assess only knowing the linear attenuation coefficient (μ) [4]. In order to overcome this limitation, a novel experimental index defined as Gamma Radiation Shielding (γRS) of S/S monolithic samples was chosen as representative parameter to assess the effectiveness of the

treatment in terms of limitation of the radioactivity effects. γRS index is defined in Eq 1:

$$\gamma RS = \frac{I_{Soil} - I_{SS}}{I_{Soil}} \cdot 100 \quad (1)$$

where I_{Soil} is the γ-ray counting rate of the contaminated soil sample (CPS) measured before the treatment and I_{SS} is the one corresponding to the treated soil sample. I_{Soil} and I_{SS} were measured and γRS was calculated for all contaminations levels (treatment E) and for all the treatments (contamination level of 2.0%). The γ-ray counting rate was measured at *Radioactivity Laboratory* of the *INFN-Laboratori Nazionali del Sud*, Catania (Italy) using a High Purity Germanium (HPGe) Gamma ray spectrometer. Measurements were carried out for a detection period of 86400 s.

RESULTS AND DISCUSSION

Results showed that the different S/S treatments and the contamination level significantly influence the performance of the treated samples in terms of setting time, compressive strength, durability and leaching. The addition of barite aggregates into the cement gout leads to a slight improvement of the S/S performance in terms of durability and contaminant leaching but reduces the mechanical resistance of the treated soils samples. γRS values calculated as a function of the emission energy for the investigated treatment (^{232}Th contamination level 2.0%) are reported in Table 2. The lowest γRS average value of 5.7% was observed for the treatment A, while a γRS increase up to 11.52% occurred using a higher percentage of grout or the Rck 42.5 cement (treatments B, C and D), but the highest γRS was reached only for the treatment E where barite was employed. A marked increase up to 20.38% is in fact achievable only when adding barite into the grout. Furthermore, a marked variation of γRS was observed with energy changing, the lowest values being observed for energies higher than 861.11 keV. The increased γ-ray shielding properties observed for the treatment E, are due to the increase in the density of the mix obtained by replacing cement with high-density material such as barite. In addition it was found that shielding properties of the treatment do not depend on the concentration of the radionuclide present into the soil. This aspect is fundamental since it allows to shift all the γRS values obtained as a function of the energy to a different radioactivity of the soil samples and thus to any contamination level different from that used in the experiment.

Table 2: γRS (%) index as a function of the emission energy (E) calculated for all the investigated treatments.

	Treatments				
E (kev)	**A**	**B**	**C**	**D**	**E**
74.81	6.40±3.8	25.85±2.9	13.97±3.5	15.15±3.3	51.22±2.3
87.20	9.21±4.3	8.02±4.3	15.23±3.8	19.51±3.7	31.36±3.9
89.80	4.13±6.2	5.14±6.5	17.97±4.7	10.00±5.1	37.11±4.4
238.63	3.85±1.3	12.87±1.1	11.44±1.1	6.94±1.2	16.89±1.2
241.00	2.57±4.1	8.23±3.7	9.96±3.7	11.26±3.7	17.01±4.0
277.73	17.19±5.0	23.55±4.4	1.24±5.5	31.05±4.3	-0.87±6.4
300.09	15.84±4.4	16.91±4.3	7.73±4.8	-1.59±5.2	33.87±3.9
338.32	8.17±3.4	9.26±3.2	6.96±3.3	-2.53±3.8	1.33±3.6
583.02	9.66±2.0	15.02±1.8	9.40±2.0	11.88±1.9	15.66±2.1
726.84	0.87±4.6	13.16±4.1	9.32±4.5	14.78±3.9	18.23±4.1
861.11	3.71±6.2	15.60±5.2	17.79±5.2	10.46±5.7	16.17±5.6
910.40	0.47±3.4	1.98±3.3	4.17±3.2	4.00±3.2	10.89±3.1
968.94	1.04±4.5	4.48±4.2	2.33±4.5	5.22±4.2	16.07±4.0
Average	5.69	11.52	9.45	10.47	20.38

CONCLUSIONS

Results showed the best mechanical and durability performance for the S/S treatment with the highest cement amounts and in absence of barite, while, in terms of radioprotection and contaminant leaching, the addition of barite significantly improved the S/S performance. Therefore, because the cement-barite based S/S completely respect the official regulatory limits, it must be considered as the overall best choice. Data obtained are of scientific and practical interest and may be used for further research representing a suitable tool to optimize the S/S treatment and cost assessment of full-scale remediation activities. Knowing the γRS values of a selected S/S treatment as a function of the emission energy allows the calculation of the radioactivity of an S/S treated soil also in the presence of high-level radioactive contaminants.

REFERENCES

[1] M.D. Siegel et al., Environmental Geochemistry 11 (2014) 191-256.

[2] A. Kumar et al., International Journal of Radiation Biology 85-4 (2009) 338-347.

[3] W.M. Abdellah and M.S. Al-Masri, Journal of Environmental Radioactivity 129 (2014) 63-67.

[4] P.P. Falciglia et al., Journal of Geochemical Exploration 142 (2014) 104-111.

PIXE-alpha non destructive and in situ compositional investigation of black gloss on ancient pottery

L. Pappalardo[1,2], S. Barresi[3], G. Biondi[1], C. Caliri[2], F. Caruso[1], R. Catalano[2,4], G. Lamagna[5], A. Manenti[5], A. Orlando[2,6], F. Rizzo[2], F. P. Romano[1,2], H.C. Santos[2,7]

1) IBAM-CNR, Via Biblioteca 4, 95124, Catania, Italy
2) LNS-INFN, Via Santa Sofia 62, 95123, Catania, Italy
3) Miur
4) INFN, Sezione di Catania, Via S. Sofia 64, 95123, Catania, Italy
5) Museo Archeologico Regionale "Paolo Orsi", Via Teocrito 66, Siracusa
6) INAF-OACT, Via S. Sofia 78, 95123, Catania, Italy
7) Instituto de Fisica – Universidade de Sao Paulo – SP - Brasil

Abstract - At the LANDIS laboratory of IBAM/CNR-INFN/LNS of Catania, a systematic study on the chemical composition of ancient black gloss present on the surfaces of attic vases and of the ones exhibiting typologies belonging to different archaeological periods has been carried out by means of the PIXE-alpha (Particle-Induced X-ray Emission) portable system. The use of the PIXE-alpha spectrometer is particularly suited for the black gloss characterization because the analysis is confined into the first 10-20 microns of the surface due to the sharp range of the alpha particles in a silicate matrix. The low and medium atomic number elements are well evidenced (from Na to Zn) and detected.
The composition of the analyzed surfaces has been investigated and a chemical-based discrimination between attic and other typologies of black gloss has been proposed.

INRODUCTION

Different studies [1-4] have been, in the last years, carried out on attic black gloss characterization, by the use of various techniques both non destructive (PIXE, XRF and by the use of Synchrotron Radiation) and destructive (ICPP, SEM, etc.) with the aim of studying the production technologies and of finding new tools, whenever the observation is not sufficient, for the discrimination between attic black gloss (whose chemical composition is well known) and other typologies of black gloss related to archaeological periods who overlap or are very close to the attic one and so, stylistically, do not present sometimes a well appreciable difference. Quantitative, non destructive and in situ determination of the constituents is mandatory [4] if a large number of precious artifacts, generally preserved at the museums, are to be examined.
The non-destructive analyses have been carried out in our laboratory on same few sherds of local ceramics [5] and in-situ at the "Paolo Orsi" Archaeological Museum in Syracuse (Sicily) and at the Archaeological Museum of Catania [6]. Results are presented and discussed.

THE MEASUREMENTS

The portable PIXE-alpha spectrometer developed at LNS/INFN-CNR/IBAM has been used [7]. As it is known, it make use, as charged particle emitter, of an annular ^{210}Po radioactive alpha (of about 5 MeV energy) source, realized in the LNS Alpha-laboratory. The energy resolution of the PIXE-alpha spectrometer is 122eV and an He flux between the source and the sample is assured in order to reduce the absorption of the alpha particles and of the low energy X-rays so allowing the analysis of light atoms like Na.
Figure 1 shows the spectrometer during a measurement. at the Archaeological Museum of Catania. Figure 2 shows an X-ray energy spectrum taken on a black gloss of an attic Greek vase. The X-lines corresponding to the characteristic chemical elements (from Na to Fe) are well visible. The quantitative analysis has been carried out by the use of the GUPIX software [8] in the matrix iteration option.

Figure 1: *The PIXE-alpha spectrometer during a measurement on the black gloss of an ancient vase.*

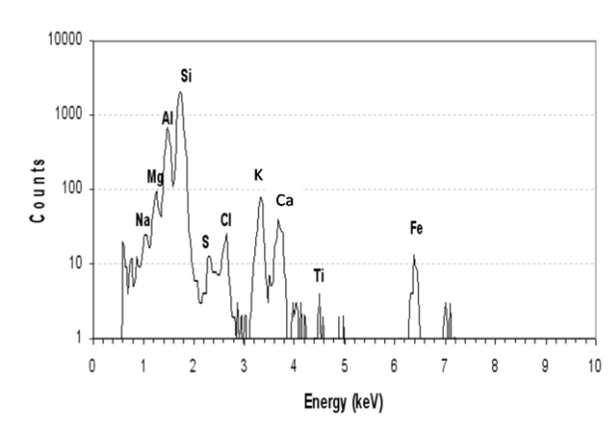

Figure 2: X-ray energy spectrum taken on a black gloss of an attic vase. Note the high intensity of the Si, K, Fe X-lines characteristic of attic black gloss.

In figure 3 the ratio K_2O/CaO vs. CaO concentration values is plotted for the black gloss measured in various vases surfaces. Attic glazes are all characterized by a high-from 2 to 4 value of the above ratio due to the use of an important quantity of fusing agent mixed to illitic well refined clay and associated with low value of CaO, whereas local and siceliote potters data show larger concentration of CaO and lower K_2O/CaO ratio probably corresponding to less refined clay.

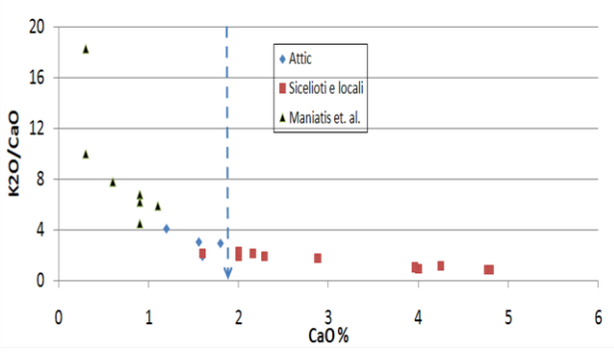

Figure 3: K_2O/CaO ratio vs. CaO. All the analyzed attic black gloss results (red) lies on the left part of the dashed line. Siceliote (blue) and local data on the right part. However, some of the late (VI-V B.C.) siceliote data are non distinguishable from the attic ones. Destructive results on Attic vases from ref.2 are also presented (black). Errors on the K_2O/CaO and CaO are 20% and 10% respectively.

CONCLUSIONS

The use of PIXE-alpha non destructive and portable spectrometer has allowed the quantitative analysis, in situ, of the black glaze of several ancient pottery surfaces. The data on attic ceramics agree, within the errors, with the destructive results of ref. [2] so, giving a sufficient confidence to our method. As general result it could be noted that the present chemical data confirm the use of an elaborated technology in producing the attic glaze surface; very similar chemical data are found in the analysis of late (VI-V B.C.) siceliote artefacts. This could suggest that they were produced in Greece and explicitly destined to exportation or produced in Sicily by using the imported material and technology as suggested by ref. [1]. The most recent (V-IV B.C.) siceliote and local ceramics show, on the contrary, a more variable recipe suggesting a less controlled process of production.

REFERENCES

[1] J.V. Noble, *The Technique of Attic Vase–Painting,* American Journal of Archaeology, 64,4 (1960) 307-318.

[2] Maniatis et al., *New evidence for the nature of the attic black gloss.* Archaeometry 35 (1993) 23-24.

[3] C. C. Tang, E. J. MacLean, M. A. Roberts, D. T. Clarke and E. Pantos, *The Study of Attic Black Gloss Sherds using Synchrotron X-ray Diffraction.* Journal of Archaeological Science (2001) **28,** 1015–1024

[4] L. Pappalardo J. De Sanoit, F.P. Romano, *Black gloss characterisation of greek attic pottery carried out by means of the new non-destructive PIXE-alpha portable system*. Proceedings of the 2nd International Congress on "Science and Technology for the Safeguard of Cultural Heritage in the Mediterranean Basin", July 5-6, Paris, France, Elsevier (1999) 661-663.

[5] L. Pappalardo, G. Pappalardo, F. Rizzo, F.P. Romano *Analisi non distruttive di pigmenti ceramici, dipinti e pitture murali* - Il Dialogo dei Saperi, metodologie Integrate per i Beni Culturali Edizioni Scientifiche Italiane, Tomo II, (2010) 707-716.

[6] L.Pappalardo F.P.Romano FRizzo (2015) - *Caratterizzazione non-distruttiva ed in-situ della composizione di vernici nere di vasi sicelioti e presunti attici appartenenti alla Collezione Libertini, mediante la tecnica portatile PIXE-alfa dell'IBAM/CNR – LNS/INFN di Catania.* In: "Il Museo di Archeologica dell'Università di Catania", Bonanno Editore, ISBN 978-88-6318-006-0, 230-232. (2015) 230.

[7] L. Pappalardo, F.P. Romano, S. Garraffo, J. de Sanoit, C. Marchetta, G. Pappalardo - *The improved LNS PIXE-alpha portable system: archaeometric applications.* Archaeometry 45, 2 (2003), 333-339.

[8] T.L. Hopman Z.Nejedl, J.A.Maxwell, J.L.Campbell, Nucl. Instrum. and Methods 2002; B89: 138.

ACKNOWLEDGEMENTS

The Authors aknowledge Prof. E. Tortorici and Prof. G. Pappalardo for useful suggestions and comments.

The improved XPIXE-α spectrometer: calibration of the system by using fused petrological standard materials

L. Pappalardo[1,2*], R. Catalano[1,2], C. Caliri[1], A. Orlando[1,3], F. Rizzo[1], H.C. Santos[1,4] and F.P. Romano[1,2]

1) INFN-LNS Via S:Sofia, 62, Catania
2) IBAM-CNR Via Biblioteca, 4, Catania
3) INAF-OACT, Via S. Sofia 78, 95123 Catania, Italy
4) Instituto de Fisica, Universidade de Sao Paulo, SP, Brasil

L. Miraglia
INGV-Catania, Piazza Roma,2

Abstract – The improved XPIXE-α spectrometer (XPIXE2) is described. The calibration of the system, carried out by using a set of fused and diluted petrological certified samples, is presented and the limits of application are discussed.

INTRODUCTION

The XPIXE-α spectrometer has been designed and realized in 2004 by LNS-INFN in collaboration with the CEA laboratory of Saclay (France) [1]. It is based on the use of a 1 mCi annular radioactive ^{244}Cm source (emitting alpha particles of about 5.1 MeV energy and X-rays mainly from 16 to 23 keV) sealed in a massive Mylar container whose confinement is obtained by a thin window realized as a sandwich of Kapton (8μm thick) and a diamond-like carbon (DLC) 0.2 μm thick obtained by a sputtering procedure by Galileo Avionic. This window, being constituted of light elements, avoids the contamination of the spectra due to the presence of medium weight elements (like Ti) in the windows material. Our ^{244}Cm based portable system is similar to the one, not portable, used by the NASA [2, 3] in the Mars exploration; this latter spectrometer making use of 30 mCi radioactive sources.

Due to the simultaneous emission of alpha particles and X-rays the XPIXE-α spectrometer is particularly suited for the analysis of light elements through the PIXE mechanism, and of medium elements, through the XRF mechanism. Homogeneous samples (like glasses) are the best candidates for successful quantitative analysis by the use of this system.

The main scope of the present work is to describe the upgraded XPIXE2 spectrometer and to illustrate the method of calibration based on the use of fused and diluted certified international standards. Due to the dilution , we expect that the matrix effects are negligible so, the regression curves – cunts vs concentration- for the analyzed chemical elements will approach to straight lines.

THE XPIXE-α UPGRADED VERSION (XPIXE2)

Fig. 1 shows the XPIXE2 upgraded version. On the left, the case containing the electronics followed by the detector is shown. This latter is inserted on the source holder followed by the ^{244}Cm source container. In the picture is evident the small white diameter tube in which a He flux flows; this allows the inhibition of the Ar presence in the spectrum and a better resolution for the low Z chemical element. The tube is connected to the source container. On the right, the system of micrometric positioning of the sample, which assures the geometrical reproducibility, is shown. During the measurement the sample is approached in contact to the source container.

The new Amptec SDD detector 20mm^2 active area and 133 eV energy resolution allowed a gain of a factor two on the efficiency. In Fig. 2 a schematic view of the detector, the ^{244}Cm source and the head measurement hole is shown.

CALIBRATION WITH FUSED AND DILUTED PETROLOGICAL REFERENCE STANDARDS

Due to the presence of both PIXE and XRF mechanisms it is not possible to use, for the quantitative analysis, the fundamental parameters software GUPIX [4, 5] and AXIL/QXAS [6, 7] both taking into account correctly the matrix effects. Some attempts [8] have been made in a simpler case in which the geometry of the apparatus is better defined. In the present case the very compact geometry makes it difficult to develop a software based on the fundamental parameters analytical approach.

For the above reasons we decided to test the feasibility of quantitative analysis by calibrating the system trough the use of a set of fused and diluted reference standards. The dilution should reduce the matrix effect: in this case a linear correlation between intensity and concentration is

expected. Also, the fused samples should eliminate the effects due to in homogeneity of the material under analysis.

The reference samples were prepared at the Istituto di Geofisica e Vulcanologia, Osservatorio Etneo (INGV-OE) of Catania. They were fused using a Claisse FLUXY 30 system. The dilution was 6:1 and Litium Tetraborate ($Li_2B_4O_7$) was used as fusing agent [9].

The following petrologic standards: BR; BX-N; DR-N; GA; GSP-1; JA-2; MA-N; Mica-Fe; Mica-Mg; UB-N and PM- S were used [10]. The acquisition of the XPIXE spectra were made by approaching each sample in contact to the opening of the spectrometer head. Measurement times were 7200 sec .For the extraction of the peak intensities (peak areas of Na, Mg, Al, Si, K, Ca, Ti, Fe) the deconvolution software of AXIL / QXAS was used.

The experimental intensities (counts) were compared to the certified concentration values in order to verify the linearity between intensity and concentration. As expected if the matrix effects (absorption, self-absorption, etc.) are negligible due to the strong dilution. The precision of the system was estimated by a repeatability procedure and was found to be better than 3% (with counting statistic less than 1%).

Figure 1: The XPIXE2 spectrometer.

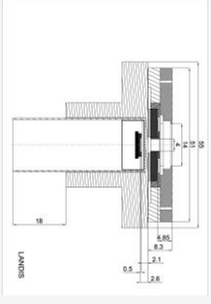

Figure 2: The measurement head.

The analytical results were plotted in a diagram concentration vs intensity for all elements (we express the elements as oxides due the igneous nature of the reference standards). Fig. 3 shows the linear regression data between concentration and intensity for some typical cases. In all the analyzed cases the R^2 values are close to the unity.

CONCLUSIONS

The obtained values of the R^2 index, which are close to unity, evidence a generally good linearity between intensity and concentration . This can be considered as an indication that matrix effects are negligible. Consequently the data can be used as calibration for the apparatus and can allow to deduce concentration values of unknown fused and diluted samples whose intensities lie into the working limits evidenced by the regression curves.

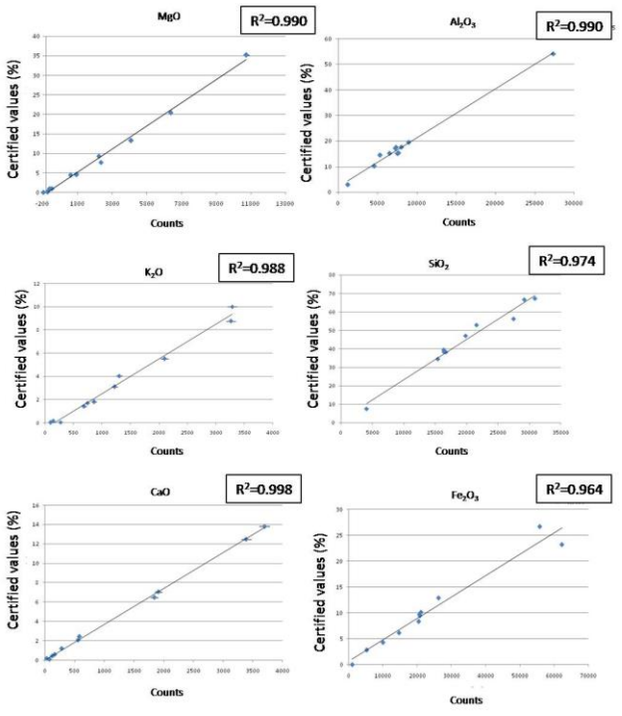

Figure 3: Linear correlation between concentration and intensity.

REFERENCES

[1] J. Pappalardo et al., X.Ray Spectrometry 36 (2007), pp. 310-31

[2] R. Rieder et al., Geophys. Res. 108 (2003) doi:10.1029/2003/JE002150

[3] R. Gellert et al., J. Geophis. Res. 111 E02S05, doi: 10.1029/2055JE002555, 2006

[4] J. A. Maxwell et al., NIM-B 95 (1995), pp. 407-421

[5] M. Omand et al., NIM-B (2005), pp. 123-136

[6] F. He et al., Analiical Chemistry 63 (1991) 2237

[7] F. He et al., NIM-B 299 (1990), pp. 580

[8] J.L. Campbell et al., J. Geophys. Res., 114, E04009 doi:10.1029/2009/E003481, 2010

[9] Miraglia L., Rapporti Tecnici INGV.235 (2012), pp. 5-8.

[10] Govindaraju K. (1994), Geostandards Newsletter, Vol. XVIII. Special Issue.

AKNOWLEDGEMENTS

We aknowledge Prof G. Pappalardo for the useful suggestions and Dott. A. Massimino for elaboration of the data.

Elemental and imaging X-ray based techniques for the investigation of Attic black gloss and its imitation in the Mediterranean area

C. Caliri[1], R. Catalano[1,2], A. Orlando[1,3], L. Pappalardo[1,4], F. Rizzo[1], H.C. Santos[1,5] and F.P. Romano[1,4]

1) LNS, INFN, Via S. Sofia 62, 95123 Catania, Italy
2) INFN, Sezione di Catania, Via S. Sofia 64, 95123 Catania, Italy
3) INAF-OACT, Via S. Sofia 78, 95123 Catania, Italy
4) IBAM-CNR, Via Biblioteca 4. 95124 Catania, Italy
5) Instituto de Fisica, Universidade de Sao Paulo, SP, Brasil

Abstract – Black gloss decoration of the Attic pottery is considered an interesting case study in different disciplines; mainly for its special manufacturing process and its technological features, but also for the aesthetic characteristics and historical value.

In this work, we report the Attic black gloss compositional investigation by combining different elemental and imaging X-ray based techniques developed at LANDIS laboratory of INFN-LNS and IBAM-CNR. The aim of the experimental activity is to discriminate among different manufacturing workshops and to distinguish original Attic pottery from imitations manufactured in the Mediterranean area (Sicily and South Italy) during the classical period.

INTRODUCTION

Attic black gloss (BG) was produced in Athens for several centuries; the manufacturing technique reached its perfection in the classical period (VI–IV century BC), in which the firing procedure and the kiln technology exhibited an extraordinary level of sophistication. For these aspects, Attic pottery (and in particular the BG layer) have been largely investigated. The previous studies [1-2] indicate that the BG is manufactured by a fine suspension of an illitic clay (enriched in iron and potassium), applied directly to the porous ceramic surface.

Attic pottery is fired under a three-step oxidizing–reducing–oxidizing process at 800–950 °C; the Fe oxides composing the Fe-rich slip, undergo in a phase transformation resulting in the formation of the black gloss layer. Simultaneously, the aluminium-silicate minerals in the slip matrix, transform the black layer into a vitrified surface. This glazing process protects the ferrous minerals from re-oxidation in the final oxidation and cooling stages.

During the classical period, Attic black gloss composition as well as the firing process have been largely imitated in the Greek colonies, especially in southern Italy. The possibility to discriminate among the various production workshops and to establish the provenance of artworks is still an opened question.

In this work we present the results of the investigation of 26 fragments belonging to the collection of the Archaeological Museum of Taranto. They consisted of 3 original Attic fragments and of 23 samples attributed to workshops operating in South Italy during the Classical period. Figure 1 shows some of the investigated samples. The analyses was performed by combining non-destructive X-ray based methods, namely low energy XRF, micro-XRF and XRF imaging. They were aimed to: i) quantify the major elements in the BG and Red slip (RS) layers (low energy XRF); ii) provide provenance information based on the qualitative trace elements composition (punctual micro-XRF analyses); iii) investigate the painting technique by performing a two-dimensional elemental mapping (XRF imaging).

Figure 1: a) an Attic fragment manufactured during 480-460 BC; b) an Apulo sample manufactured in south Italy during 440-410 BC.

EXPERIMENTALS

The quantitative determination of major elements in the BG and RS layers was performed by using a low energy (LE) XRF spectrometer. It consists of a 100 W X-ray tube coupled to a large area SDD detector. The compact geometry and a helium flux allow the detection of X-rays down to 1 keV energy. The application of a low potential and a high current (8 kV and 1.5 mA) to the special HV installed on the spectrometer, enables the possibility to work in the low energy domain, with a low penetrating X-ray beam. This is optimal for the case of samples of limited thickness like the BG layer in Attic pottery (typically 10-20 micron thick). In order to perform the quantitative analysis, the LE-XRF system was calibrated by means of 26 Reference Samples. Since the LOD is in

the range of 0.1-1 weight %, only major elements can be quantified by the use of the LE-XRF.

The qualitative trace elements analysis is performed by the use of a micro-XRF spectrometer consisting of a Rh microfocus tube coupled to a polycapillary mini-lens focusing the beam down to a spot of 40 µm. A 130 eV energy resolution and 50 mm^2 active area SDD is placed in a 90° geometry with respect to the beam. The micro-XRF spectrometer presents a LOD in the ppm range and allows the trace element determination with high chemical sensitivity.

In the case of the pottery samples, the punctual micro-XRF measurements were performed at 38 kV and 100 µA and they lasted 300 seconds. Different points in the BG and RS surfaces were analyzed in order to take into consideration local in homogeneities of the samples.

Additionally, the micro-XRF system is equipped with motorized and fully programmable 3-axes (with a 10 cm travel range) that allows performing the elemental mapping of the samples. Step size and dwell time in the scansions are selected depending on the dimensions of samples being investigated and on the spatial resolution to be obtained in the final images.

RESULTS

As an example of the XRF imaging, Figure 2 shows the elemental imaging of one of the investigated samples (2.5×2.7 cm). It was scanned at 150 µm step-size an 1 second dwell time. The elemental maps depict the distribution for some major elements (Fe, Ca, K) that characterize the Attic pottery and its imitations. Moreover, some adjustments performed by painter during the painting process can be unearthed observing the elemental maps.

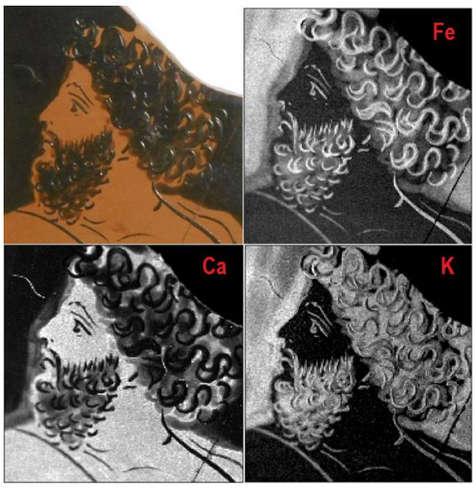

Figure 2: Example of a two dimensional elemental mapping of a sample

Useful information on the production technology and on the provenance of samples are determined by the LE-XRF and micro-XRF analyses. Table 1 summarize a comparison of the average composition of the Attic BG obtained during the investigation versus the one published in the literature.

Al_2O_3 [%]	SiO_2 [%]	K_2O [%]	
30.0±2.0	46.1±1.8	7.0±1.6	**IMITATION**
31.1± 0.2	45.0±1.0	6.9±1.3	**ATTIC**
30.0±1.1	46.2±1.6	5.4±1.1	**Published data**
CaO [%]	**TiO_2** [%]	**FeO** [%]	
1.9±0.8	0.7±0.1	14.2±1.7	**IMITATION**
1.3±0.9	0.8±0.3	14.8±1.2	**ATTIC**
0.8±0.3	0.6±0.3	14.5±1.6	**Published data**

Table 1: Quantitative data of the Attic and imitations BG

Provenance studies were performed on the basis on the trace elements composition. The method is qualitative Results (Figure 3) show a clear separation in the Cr and Ni patterns suggesting their use to discriminate among different production workshops in different geographic areas.

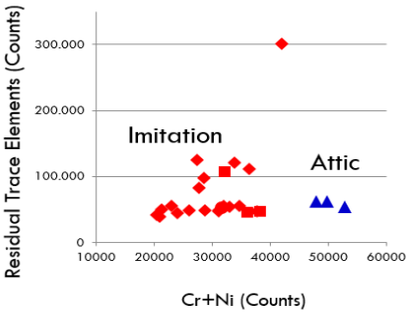

Figure 3: Trace elements analysis

CONCLUSIONS

This work was focused on the characterization of Attic black gloss pottery and its imitation in the Mediterranean area. The main aim was to establish a completely non-invasive method to be applied in-situ by combining different analytical techniques in order to obtain information on the production technology and to discriminate between the Attic production workshops and those operating in South Italy during the classical period.

The analyses were performed by combining the low energy XRF, the micro-XRF and XRF scanner developed at the LANDIS laboratory of the LNS-INFN and IBAM-CNR .

REFERENCES

[1] Y. Maniatis, E. Aloupi, A.D. Stalios, New Evidence For The Nature Of The Attic Black Gloss. Archaeometry, 35 (1993) 23–34.

[2] C.C. Tang, E.J. MacLean, M.A. Roberts, D.T. Clarke, E. Pantos, A.J.N.W. Prag, The Study of Attic Black Gloss Sherds using Synchrotron X-ray Diffraction, Journal of Archaeological Science, 28 (2001) 1015-1024.

In-situ compositional investigation of silver coins by means of X-ray fluorescence portable technique

R. Catalano[1,2], R. Amato[3], C. Caliri[1], G. Lamagna[3], A.M. Manenti[3], A. Orlando[1,4], L. Pappalardo[1,5], F. Rizzo[1], S. Santangelo[5], H.C. Santos[1,6] and F.P. Romano[1,5]

1) LNS, INFN, Via S. Sofia 62, 95123 Catania, Italy
2) INFN, Sezione di Catania, Via S. Sofia 64, 95123 Catania, Italy
3) Museo Archeologico Regionale "Paolo Orsi", Via Teocrito 66, 96100 Siracusa, Italy
4) INAF-OACT, Via S. Sofia 78, 95123 Catania, Italy
5) IBAM-CNR, Via Biblioteca 4. 95124 Catania, Italy
6) Instituto de Fisica, Universidade de Sao Paulo, SP, Brasil

Abstract - X-ray based analytical techniques are particularly suited for the non-destructive investigations of Cultural Heritage. An interesting case concerns the compositional determination of archaeological coins by means of X-ray Fluorescence. Recently, the use of such technique was applied in a systematic survey aimed to investigate the silver coin production, during the Greek period, in the Mediterranean area.

In this paper, we report the results of the investigation of the silver coins belonging to the collection of the "Paolo Orsi" Archaeological Museum in Syracuse. The Museum present one of the richest collection of Greek coins, which circulated in Sicily during the fourth and the third centuries BC. Such coins were manufactured in Syracuse and in other mints from Greece (i.e. Lefkada and Corinth) and they are particularly important since their investigation can support the knowledge on the commercial, political and social relations between Sicily and Greece in that historical period.

INTRODUCTION

The growing interest in the archaeological research techniques is important to obtain detailed evidence of the history and culture of the past. In particular, the compositional analysis of silver coins performed with X-ray Fluorescence technique (XRF) provides information on ancient technology [1,2].

One of the most interesting question deals with the classification of the coins into originals, copies and imitations, according to their provenance and to their silver content. The archaeological challenge arises from the need to explain the diversification of these coins as well as the differences in composition, weight and physical aspect [3,4].

In this study, 114 Hellenistic silver coins were analyzed by means of a portable XRF spectrometer. The coins are part of the collection of the "Paolo Orsi" Museum in Syracuse, which consists of nearly 9,000 coins circulated through Southern Italy from the Greek period to the Italian unification in 1861. The *Pegasus* (figure 1), in particular, were manufactured by the mints of Corinth, Lefkada and Syracuse, while the *Philistis* were produced by the mints of Syracuse for local circulation only. The samples originate from the fourth and third centuries BC, coming from different excavations in Sicily and acquisitions from private collections. Comparison of the compositional data of such a large number of silver coins from the different mints is expected to shed some light on the silver sources available in the Hellenistic Mediterranean and on the production techniques.

Figure 1: Pegasus from the Syracuse mint

EXPERIMENTALS

The analysis were carried out by the use of a X-ray Fluorescence portable spectrometer developed at the LANDIS laboratory of the LNS-INFN.

It consists of a tungsten anode X-ray tube (mod. Neptune produced by the OXFORD INSTRUMENTS) operating at 38 kV and 0.3 mA, coupled to a straight shaped 3 mm lead collimator to focus the beam on the samples (small noise contribution in Pb-L line).

The detection of X-rays induced on the samples was performed by a 80 mm^2 SDD detector (Mod. AXAS-M1 produced by the KETEK) with an energy resolution of 138 eV at 5.9 keV.

The X-ray source and the detector were placed in a compact 90° geometry, with source-sample and sample-detector distances equal to 20 mm and 10 mm respectively.

The acquisition time was set at 100 seconds in order to detect enough statistics even for trace elements analysis.

Two laser spots coupled on the spectrometer head were aligned in such a way to ensure the placement of the analyzed area on the reference plane. The quantification was based on the fundamental parameter (FP) method by means of Axil software.

According to the experimental set-up and procedure a wide range of elements can be detected. Limit of detection depend upon the specific element and is typically of the order of μgr/gr.

RESULTS

We have analyzed 114 ancient Greek coins, of which 84 *Pegasus* (distributed as 19, 50 and 15 from the mints of Syracuse, Corinth and Lefkada respectively) and 50 *Philistis* from the mint of Syracuse.

A characteristic XRF spectrum of analyzed coins, showing dominance of Ag, is shown in figure 2. Spectrum show minor elements that include Pb, Cu and Au, while trace elements of Br, Bi, Fe and Sn where identified based on their weaker K and L lines.

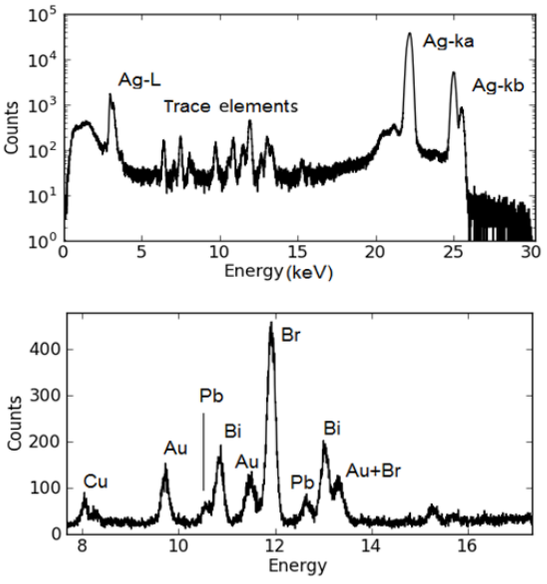

Figure 2: XRF spectrum with trace elements

The coins have been found to have a purity of 91 to 97% Ag. This study also revealed that the sum of concentrations of trace elements was never greater than 1%. No significant variations were found between the Ag content of the coins of the different mints. Nevertheless, some outliers can be found. The production of the mint of Syracuse is less homogeneous than that of Corinth and Lefkada; in particular, the production of Syracuse is characterized by higher content of Cu and smaller amount of Ag. Moreover, the mint of Corinth and Lefkada seems to be characterized by a more established production technique. With regard to *Philistis*, they are characterized by greater fineness of the alloy than *Pegasus*; their compositional homogeneity also suggests a well-defined production technology.

In order to reduce the number of the variables, the principal component analysis (PCA) was also performed (figure 3), showing that the elements that explain the highest variance of the data are Ag, Cu and Au.

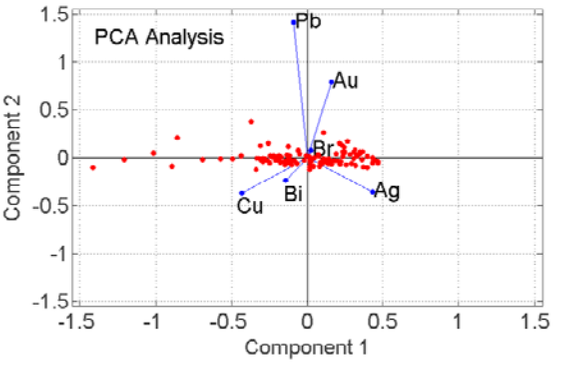

0

Figure 3: Principal component analysis

CONCLUSIONS

The use of high-energy XRF portable system developed at the LANDIS laboratory of the LNS-INFN was applied to the non-destructive investigation of the silvering technology used to manufacture the *Pegasus* and the *Philistis* coins by the mints of Corinth, Lefkada and Syracuse during the fourth and third centuries BC. The issue represents an interesting and still opened question concerning Greek coinage.

In the present contribution, the results obtained indicate that the coins consist of a silver/copper alloy with a very high purity between 91 and 97%. The outcomes have supported the existence of some differences between the three mints, being the Corinth and Lefkada productions characterized by a higher compositional homogeneity, thus showing a more established production technology.

The statistical evaluation of the data by PCA has yielded that the elements that have the highest variance are Ag, Cu and Au.

As final remark we can say that this portable system has proved to be a reliable technique in the study of ancient coins. Its most important advantage is the fact that *in situ* measurements can be carried out with a relatively high analytical speed without moving the object from the museum to the laboratory

REFERENCES

[1] V. Kantarelou et al., Spectrochimica Acta Part B: Atomic Spectroscopy, 66 (2011) 681-690.
[2] C. Zarkadas et al., Spectrochimica Acta Part B: Atomic Spectroscopy, 59 (2004) 1611-1618.
[3] F. Rizzo et al., Microchemical Journal, 97, 2, (2011) 286-290.
[4] L. Torrisi et al., Eur. Phys. J. D, 54 (2009) 225-232.

Non-destructive compositional investigation of historical enamels by using XRF imaging techniques

H.C. Santos[(1,2)], C. Caliri[(1)], R. Catalano[(1,3)], G. Mascali[(1,6)], A. Orlando[(1,4)], L. Pappalardo[(1,5)]

F. Rizzo [(1,6)], and F.P. Romano[(1,5)]

(1) INFN-LNS, Via Santa Sofia 62, 95123, Catania
(2) Instituto de Física – Universidade de São Paulo – SP – Brasil
(3) INFN-Sez. di Catania, Via Santa Sofia 64, 95123, Catania
(4) INAF-OACT, Via Santa Sofia 78, 95123, Catania
(5) IBAM-CNR, Via Biblioteca 4, 95124 Catania
(6) Università di Catania, Dipartimento di Fisica e Astronomia, Via Santa Sofia 64, 95123, Catania

Introduction

Historical enamels can be analyzed with success by the XRF method. The XRF allows the detection with a high chemical sensitivity of medium- and high-Z elements composing colorants and opacifiers.
Enamel compositions changed during the time based on the raw materials available for their production. Consequently, the determination of the chemical composition of the enameled artworks could serve as a tool for identifying their typology, provenance and for discriminating among genuine, restored and fakes objects. In this work, we present the results of the nondestructive investigation of some historical enamels belonging to a private collection by combining the compositional results obtained with the XRF modular scanner installed at the LANDIS laboratory of the LNS-INFN and IBAM-CNR in Catania. The system presents a compact dimension and low weight and can be used in-situ. The investigated artworks consisted of silver objects of different shapes and dimensions (in the range of 10-20 cm), decorated with enamels presenting various hues of colors (white, red, yellow, green, blue, brown) and with dimensions down to the mm scale. They date back to the XII-XIII century even if their authenticity was never verified. The XRF scanner, thanks to the use of interchangeable polycapillary optics can be used both for the macro- and for the micro-XRF imaging. The macro-XRF scansion allowed obtaining a global image of the elemental distribution on the investigated artworks. A micro-XRF scansion was used for studying with high resolution the spatial distribution of some elements non-compatible with the historical period dating the artworks under study. Results presented in this work are limited to the macro-XRF investigation. Micro-XRF combined with a NNMA (Non Negative Multivariate Analysis) analysis is in progress

Experimental

The XRF scanner consists of an X-rays microfocus tube coupled to a strongly focusing polycapillary optic producing an X-ray beam of 25 μm spot size. The detection of the X-ray fluorescence induced on the sample, is obtained by a SDD detector placed in a compact 90 degree geometry. The detector presents a large active area and a 133 eV energy resolution at 5.9 keV. The scansion of samples is performed by a motorized and programmable 3-axes system with a travel range of 75 cm x 75 cm x 10 cm.
The minimum step size during the scansion is 1 μm and the dwell time can be reduced down to 50 ms. To adjust the correct position of the sample on the focus, there is an optical camera with magnifying optic and two laser.
Figure 1 shows the experimental set-up.

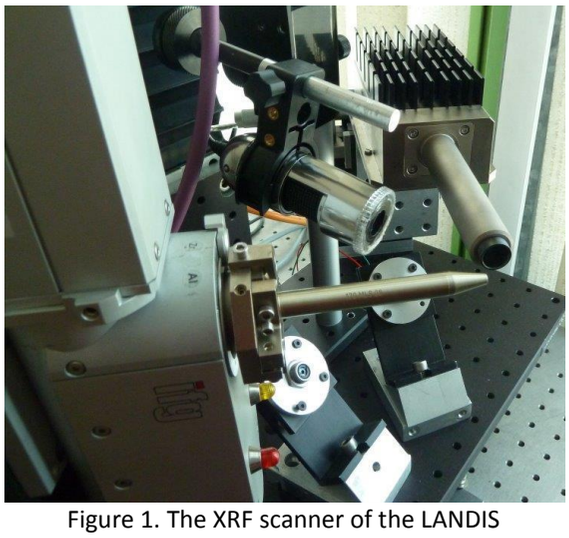

Figure 1. The XRF scanner of the LANDIS laboratory.

Analyses of the enameled objects

The two dimensional elemental distribution of the enameled surfaces were obtained applying the XRF investigation in the scansion mode; the scansions step size was determined in order to get a high quality image of the elemental distribution.
The images from the scansion of the objects under investigation are shown in the Figures 2-4. The raw data were processed by using the PyMca software developed at the ESFR [1].
Figure 2 show the elemental images obtained from an enameled silver plate artwork representing a Christ. All the enamels in the plate, with the exception of the red one, are composed by an high content of lead.
In the white pigments Pb and As is always present. The lead arsenate was introduced during the XVIII century as opacifier; it has been used in the white enamels since that time [2].
Fe and Mn characterize the brownish pigments. The blue in the Christ mantle present a Co-based colorant agent, while the yellow pigment is characterized by Cr [3]. Zn and Cr was detected in the hair and in the beard of Christ, in combination of Fe. Finally, the red pigment present Zn, and the μ-XRF revealed Se and Cd. The use of these elements to produce red enamels was introduced at the beginning of the XIX century [4].

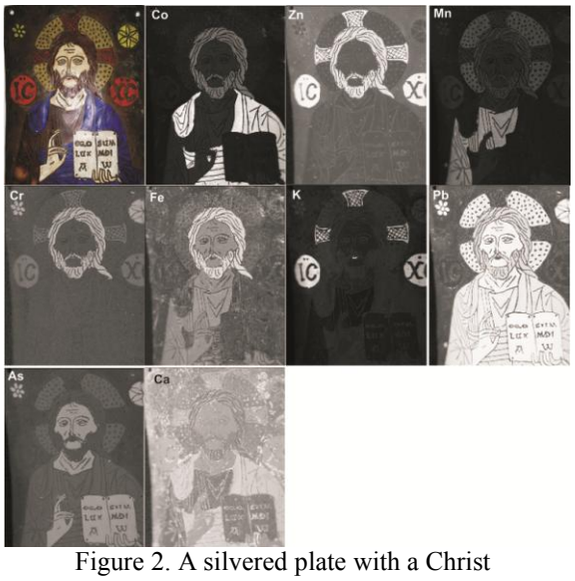

Figure 2. A silvered plate with a Christ representation.

The second object investigated by the macro-XRF scansion was a pot used to keep the Ostia.
This object presents only a white pigment. The analyses (Figure 3) evidenced that the white enamel is obtained by combining Pb and As.
As in the previous case, the use of a lead arsenate was probable for the manufacturing of the white. The alloy in the object resulted composed of Ag and Cu as main components.

Figure 3. The pot picture and the elemental imaging of the selected area in the yellow square.

Finally, a bottle made of a silvered alloy and presenting green and blue enamels in an Arab decorative motif, was investigated by the XRF scansion technique. The green was characterized by Cr (i.e. chromium green used since 1850) [3] and the blue by K.
The alloy composition was obtained from a μ-XRF analysis. In the alloy was detected Ag as the main element and Fe, Ni, Cu.

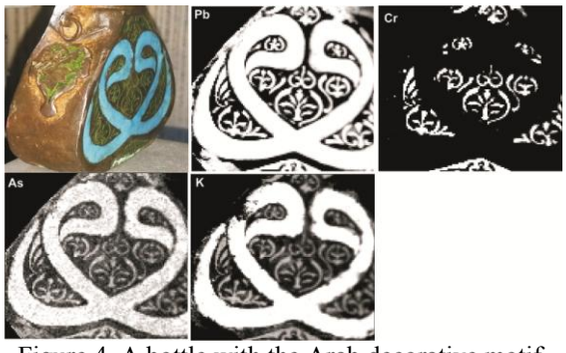

Figure 4. A bottle with the Arab decorative motif and the elemental distributions of the main components.

Conclusions

The portable XRF scanner of the LANDIS laboratory at the LNS-INFN and IBAM-CNR has been used for the elemental mapping of enamelled artefacts from a private collector. The images distribution allows correlating the elements with the precursor pigments. Results suggest that these objects were manufactured in XIX century.

References

[1] V.A. Solé, E. Papillon, M. Cotte, Ph. Walter, J. Susini, Spectrochim. Acta Part B 62 (2007) 63-68.
[2] Kırmızı, B., Colomban, P. and Blanc, M., J. Raman Spectrosc., 41, 2010, 1240–1247.
[3]Publicação Técnica PT Vol 15, 01/2011 - Laboratório de Física Nuclear Aplicada. Depto. de Física – Universidade Estadual de Londrina. www.uel.br_grupos_gfna_padroesdepigmentos.pdf
[4] Weyl, W.A., *Colored glasses*. 1953, Society of Glass Technology.

On-line remote monitoring of radioactive waste repositories

Claudio Calì[1], Luigi Cosentino[1], Pietro Litrico[1], Alfio Pappalardo[1,2], Giuseppe Passaro, Carlotta Scirè[1], Sergio Scirè[1], Gianfranco Vecchio[1] and Paolo Finocchiaro[1]

1) Laboratori Nazionali del Sud, INFN, via S.Sofia 62, Catania, Italy
2) SOGIN S.p.A, via Torino 6, Roma Italy

Abstract - A low-cost array of modular sensors for online monitoring of radioactive waste was developed at INFN-LNS. We implemented a new kind of gamma counter, based on Silicon PhotoMultipliers and scintillating fibers, that behaves like a cheap scintillating Geiger-Muller counter. It can be placed in shape of a fine grid around each single waste drum in a repository. Front-end electronics and an FPGA-based counting system were developed to handle the field data, also implementing data transmission, a graphical user interface and a data storage system. A test of four sensors in a real radwaste storage site was performed with promising results.

INTRODUCTION

Among the many issues associated to the disposal of short and medium term radioactive waste worldwide produced, there is the storage inside suitable sites where a high level of safety must be guaranteed. In order to detect possible leaks of radioactive material and to efficiently reduce the risks of contamination for the operators and for the environment.

Detector Mesh for Nuclear Repositories (DMNR) is a project for a prototype demonstrator of the online monitoring of short-medium term radioactive waste, currently under development at INFN-LNS Catania. Such a system is planned to be distributed, fine-grained, robust, reliable, and based on low-cost components, providing a 3-dimensional map of the radioactivity produced by the waste inside the storage area. We have suggested to adopt a mesh of low cost radiation detectors, namely scintillating fibres, arranged as a grid of sensors around each waste drum (Fig. 1), readout by means of SiPM (Silicon PhotoMultiplier) photosensors capable of detecting the tiny light signals of few photons ([1], [2]). These allow to record continuously the measured activity, in order to check the instant rate and also the counting history around each drum. This system could also open new perspectives on the modality of waste packaging and storage.

Front-end electronics and an FPGA-based counting system were developed, in order to handle the data flow coming from the field sensors. Such a system also deals with the redundant data transmission toward a console with a graphical user interface and a data storage system (fig.2)

THE EXPERIMENTAL APPARATUS

The mesh of detectors has to be properly distributed, fine-grained, robust, reliable, and should be based on low-cost components. In addition, the sensors have to be operated in Geiger mode (on/off), since they are just needed to count the ionizing radiation events.

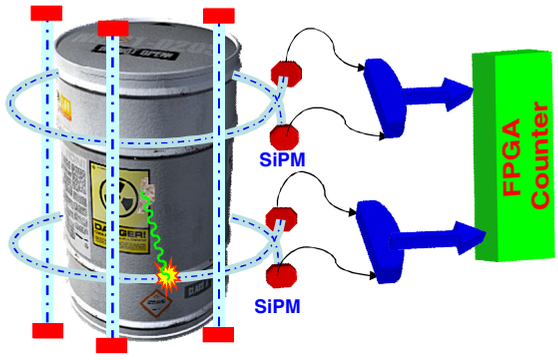

Figure 1. A possible layout of the fibres around the drum.

Each detector consists of a scintillating optical fibre, 1 m long. The fibre is a plastic one made of a scintillating core of polystyrene and a PMMA cladding, manufactured by Saint-Gobain Crystals.

The fibers are arranged around each drum in longitudinal and/or ring geometry, as in figure 1. Both geometries can be adopted, as the most likely leak position has to be determined. Each fibre can intercept radiation coming out of the drum wall, mostly gamma rays, so that the energy released inside its active volume is converted into scintillation light, that propagates to both ends of the fibre itself to be detected by the photosensor.

The output signal of a SiPM is generally small and needs further amplification. So we have used an innovative amplifier developed from our electronic department featuring a linear gain around 200 and a bandwidth of 4GHz. Each of the two SiPM outputs from a fiber is fed to an amplifier, whose output goes into a discriminator. The outputs of the two discriminators are combined by the coincidence unit, that will thus produce an output pulse only when a predefined amount of light is detected at both fiber ends.

The figure 3, shows a sketch of the front-end electronics architecture for one fiber. The digital output signals are represented near each component. It is worth to remark that a single FPGA can handle many fibers at once.

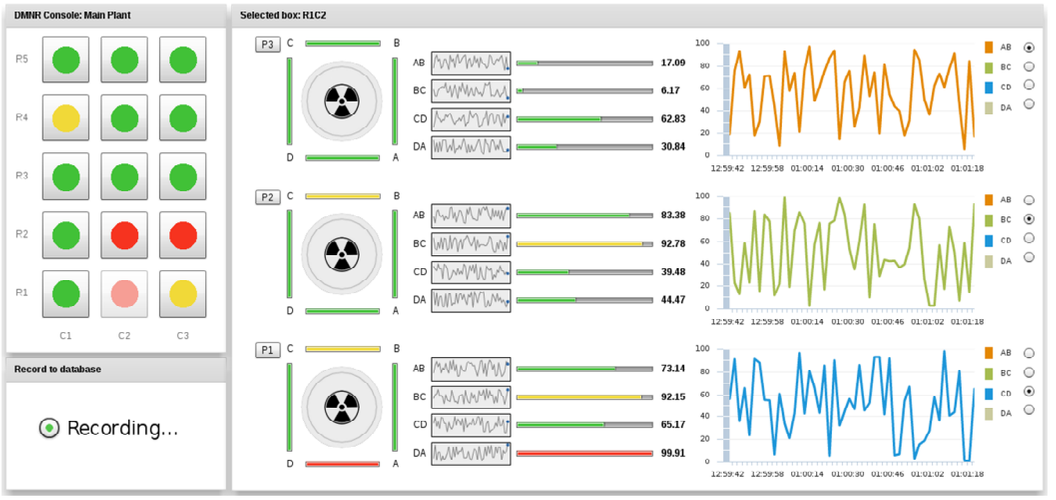

Figure 2. Graphical user interface

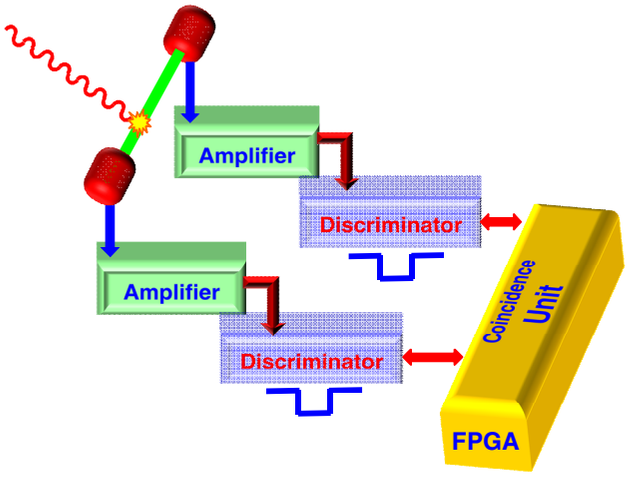

Figure 3. Scheme of the front-end electronics for one fiber.

Several tests were performed with the fiber sensors on the bench with and without laboratory sources, in order to verify the capability of gamma detection, the sensitivity, the stability, to measure the noise level and the ambient radiation count rate. But the most important test, was to be performed in a real environment of radwaste. This is why we decided to perform a measurement inside a temporary storage site at a Sogin installation in Sessa Aurunca (CE) Italy.

For this purpose we installed four of our fiber sensors onto a trolley. The same trolley also hosted the front-end electronics, whereas the output digital pulses travelled on long cables towards the FPGA data acquisition system, placed outside, in order to be counted and recorded. The measurements were done in seven positions from the P0 position, outside the storage site, to the P6 positions inside the storage close to a rows of drums. On the left of the plot is shown how the counting rates change while the operator move the trolley inside the storage (Fig 4).

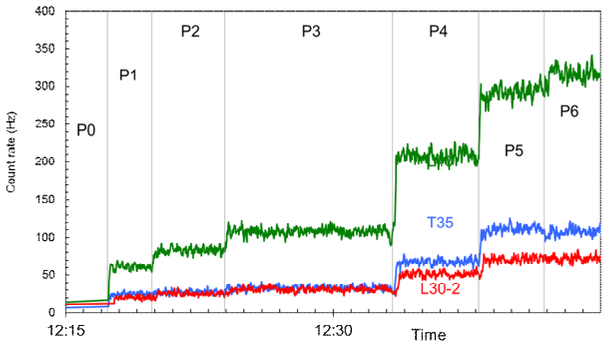

Figure 4. Counting rates as a function of time. First phase when the operator move the trolley along the seven positions.

CONCLUSIONS

The DMNR project has shown that a real time online monitoring system for radioactive waste is feasible. The test performed inside a storage site has shown performance beyond the expectation.

After the agreement between INFN and Sogin S.p.A signed on November 2012, was installed (June 2014) a pilot demonstrator system inside a Radwaste storage site (Garigliano Nuclear plant, Sessa Aurunca (CE)) for an extended period of time.

REFERENCES

[1] P.Finocchiaro, "DMNR: a new concept for real-time online monitoring of short and medium term radioactive waste" in Radioactive Waste: Sources, Types and Management, Nova Science Publishers, 2012

[2] P. Finocchiaro, et al., "Characterization of a Novel 100-Channel Silicon Photomultiplier - Part I: Noise", IEEE Transactions on Electron Devices, Vol.55, No.10, 2757-2764, October 2008

The DMNR system hardware setup

S. Scirè[1], G. Vecchio[1], C.Scirè[1], S. Grillo[1], C. Greco[1], A. Pappalardo[1],

L. Cosentino[1], C. Calì[1], P. Litrico[1], G. Passaro[1], P. Finocchiaro[1]

1) Istituto Nazionale di Fisica Nucleare – Laboratori Nazionali del Sud

Abstract - Detector Mesh for Nuclear Repositories (DMNR) is a real-time monitoring system, developed at INFN-LNS, able to collect and store information necessary for the purpose of knowledge, protection and safety of the public. This paper shows the skeleton architecture of the readout solution we have adopted, focusing on the Field Programmable Gate Array (FPGA) based high performance data acquisition system.

INTRODUCTION

A wide range of nuclear power facilities have been decommissioned so far and many of them will be dismantled worldwide over the next years. If we add the hospital and industrial radwaste, we understand that decommissioning has become a profitable business, being a sector which by 2050 will develop global revenues of 165 billion euro. The greater radioactive waste production increases, the greater need to increase the security and transparency of its management is required.

DMNR is an innovative system that allows continuously monitoring and recording the radioactive activity that comes out from radioactive waste drums, in particular it is capable of detecting gamma rays emission.

The use of collected data is intended for radioactive security operators, the regulatory body, local national and international interested groups, such as Civil Defence, Fire Departments, Ministries, environmental organizations (such as Italian organizations ENEA, ISPRA, ARPA, etc.) and peaceful nuclear energy promoter organization, such as IAEA.

The allowed data network topologies are point to point and multidrop with industrial serial bus, it is possible to implement an additional (or exclusive) wireless protocol, to benefit the advantage of redundancy and replication of data path and avoid single point of failures in network.

THE SYSTEM

The overall system is assembled by robust and cheap items: each sensor is composed by a scintillating fiber optic, optically coupled at both ends to two Silicon Photo Multipliers (SiPMs) [1]. Each sensor is connected to a Eurocard PCB module design board that performs power supply, signal amplification and voltage level discrimination, by means of I^2C remotely programmable DAC. To suppress the random noise of SiPMs, a tunable time coincidence logic has been implemented on the same board. The output digital signal, that represents a radiation event, is generated at LVDS voltage specifications.

Figure 1: Amplification board schematic.

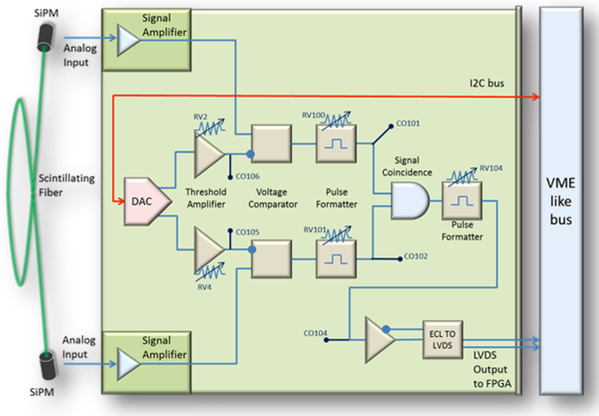

12 sensor boards are connected, by a VME like bus, to another board hosting the FPGA witch records the radiation events and packs data, then transmits to the monitoring software by serial line. The combinational logic is able to work in parallel to collect data from sensors, record timestamp and exchange information with the soft microprocessor implemented in the same chip. An array of 12 independent high speed 32 bit wide counters, able to collect up to 25 MHz input frequency, stores data from each sensor connected.

Figure 2: Connection bus schematic.

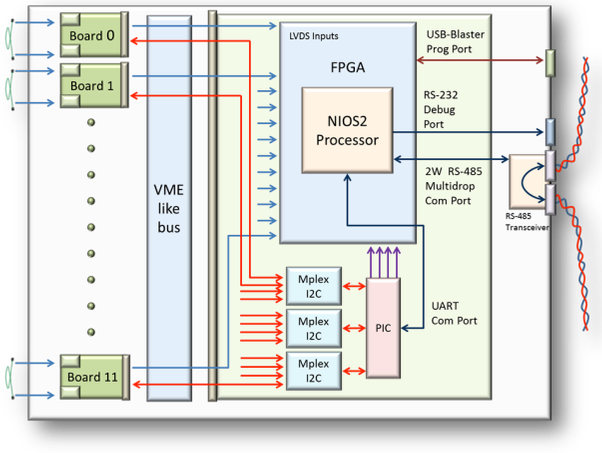

The FPGA is configured to host an ALTERA NIOSII soft microprocessor [2], an hardware specific firmware was developed to allow a remote operator to

communicate with the system. It is possible to change internal parameters and registers values to tune the sensitivity of each sensor by programming the DAC voltage output in each sensor board.

The whole electronic assembly is packed inside a 3U 19'' rack system, containing also a ± 12 V linear power supply, a 5 V and a 30 V switching power supply.

Figure 3: The DMNR rack station.

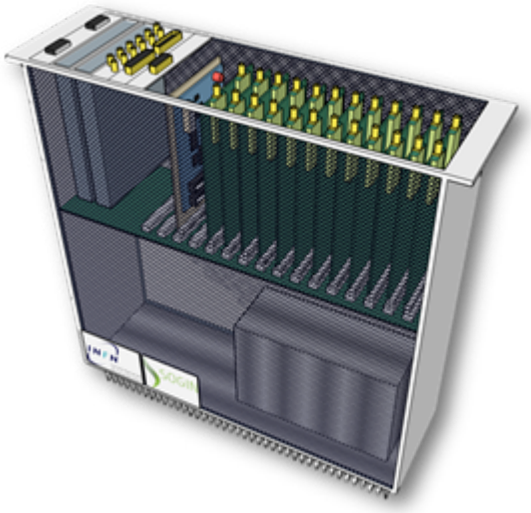

To verify the full functionality of the remote system some automatic supervision features have been implemented, like an internal watchdog to force the reboot of the whole system if a freeze status is detected and a running time counter that reports the time period passed since the last system start-up.

Transmission Protocol

Message exchange occurs through a multidrop 2 wire RS-485 serial line network; to manage the medium access we decided to use polling technique: the remote operator station is configured as master and all the rack stations as slaves. Every station has an univocal assigned address so it answers only to commands sent to itself. Every time the receiving routine sends a command to the detector station it receives an handshake answer, to state the correct receiving and execution of it; broadcast messages instead are received and eventually executed from all stations but there is no answer to avoid collision in the shared medium.

Every message is sent using ASCII printable characters, to simplify the protocol message analysis.

Remote consolle

Once the data arrive at the higher level section a robust and reliable software component sends them to an online console for real-time monitoring and to a database system for historical archive. The Graphical User Interface shows the data carried out from the sensor network and permits to set many parameters in the electronic devices, such as sensor's sensitivity and the time period between two consecutive data acquisitions [3]. Inside the database, the stored information includes the daily average activity reported by each sensor, any displacement of elements inside the radwaste storage and any warning raised by the system.

REFERENCES

[1] Pappalardo et al., Optical Engineering Vol. 53 (2014), issue 4, 047102

[2] Nios II Processor www.altera.com/devices/processor/nios2/ni2-index.html

[3] Vecchio et al., IJNESE Vol. 3 (2013), issue 3, pp. 64-71

Functional characterization of mitochondrial respiratory complex I by delayed luminescence spectroscopy

I. Baran[1,*], A. Scordino[2,3], D. Ionescu[1], S. Privitera[2], R. Grasso[2], M. Gulino[2,4], F. Musumeci[2,3], I.T. Tofolean[1], C. Ganea[1]

1) "Carol Davila" University of Medicine and Pharmacy, Dept. of Biophysics, 8 Eroii Sanitari, 050474 Bucharest, Romania

2) Istituto Nazionale di Fisica Nucleare - Laboratori Nazionali del Sud, 62 S. Sofia, Catania, Italy

3) Dipartimento di Fisica e Astronomia, Università di Catania, 6 v.le Andrea Doria, I-95125 Catania, Italy

4) Università degli Studi di Enna "Kore", Facoltà di Ingegneria, Architettura e delle Scienze Motorie, Cittadella Universitaria, 94100 Enna, Italia

Abstract - Delayed luminescence (DL) spectroscopy proved successful in several clinical applications, but its cellular origin is still unclear. Our results obtained with human leukemia Jurkat T cells challenged with Complex I targeting agents like rotenone, menadione and quercetin support the notion that DL is produced primarily within the mitochondrial electron transfer system at the level of Complex I. The data provide novel insights into the structural and functional organization of respiratory Complex I, which appears to function predominantly as a dimer and less frequently as a tetramer in this cell type. States emitting blue or green/yellow light are most likely excited states of Complex I-associated NADH or FMN, respectively, which are produced after a series of forward and backward electron transfer steps involving inner Fe/S clusters of Complex I. Furthermore, the timescales of various electron transfer steps involving the formation of flavin and ubisemiquinone radicals with subsequent production of superoxide can be estimated from delayed red-light emission.

INTRODUCTION

Complex I (NADH:ubiquinone oxidoreductase), the largest enzyme of the mitochondrial respiratory chain, catalyzes the transfer of two electrons from NADH, the reduced form of nicotinamide adenine dinucleotide (NAD^+), to ubiquinone (Q), in a process coupled to the translocation of four protons to the intermembrane space. The first stage in the overall enzymatic reaction is a one-step transfer of two electrons from NADH to the prosthetic group of the complex, flavine mononucleotide (FMN), situated in the remotest hydrophilic subunit, denoted as FMN-b. Subsequently, reduced FMN-b transfers individually the two electrons to a wire of eight consecutive iron-sulfur (Fe/S) clusters which span the extramembranous domain of the complex. The reduction of Complex I-associated ubiquinone by the first electron from the terminal Fe/S cluster (N2) produces the ubisemiquinone radical ($Q^{\bullet}$) which can then receive the second incoming electron to become fully reduced ubiquinone (ubiquinol, QH_2). It is currently considered that Q reduction by N2 occurs in a large cleft formed by the two subunits that contact the first subunit (ND1) of the membranous domain of Complex I. This wide hydrophobic cavity formed at the junction between the two arms of Complex I is also the place where hydrophobic inhibitors of Complex I like rotenone (ROT) or artificial electron acceptors like menadione (vitamin K_3; MD) also appear to bind.

Here we performed a detailed analysis of the properties of ultra-weak photon-induced delayed photon emission (Delayed Luminescence, DL) of Jurkat cells by employing treatments with rotenone, as well as with menadione and quercetin (QC). All the three drugs share net structural similarities with ubiquinone and therefore can bind Complex I, inside or close to the Q-binding pocket. In view of the common effects of these drugs at the level of Complex I, we could investigate in more detail the connection between delayed luminescence and the mitochondrial metabolism. At present, despite the fact that DL spectroscopy proved successful in some clinical applications, the origin of delayed luminescence of living cells is still under debate [1-6]. DL, also called "delayed fluorescence", represents a very weak light emission elicited upon light- or UV-irradiation, which differs from ordinary ("prompt") fluorescence by an unusual long decay time. Our current results demonstrate that the ultra-weak photon-induced delayed photon emission of Jurkat cells is quantitatively related to the mitochondrial level of NADH and that of oxidized FMN, supporting the notion that DL is mainly produced within the mitochondrial electron transfer system at the level of Complex I.

MATERIALS AND METHODS

Human leukemia Jurkat lymphoblasts were cultured in MegaCell RPMI 1640 medium as described [1,2]. Cell density and viability were examined by microscopy. For *Delayed Luminescence spectroscopy*, an improved version of the ARETUSA set-up was used [6]. Cell samples were excited by a Nitrogen Laser source (Laser

Photonics LN 230C; wavelength 337 nm, pulse-width 5 ns, energy 100±5 µJ/pulse). A multi-alkali photomultiplier tube (Hamamatsu R-7602-1/Q) was used as a detector. The detected signals were acquired by a Multi-channel Scaler (Ortec MCS PCI) with a minimum dwell-time of 200 ns. DL measurements were done on at least 3 different drops from each cell sample (drop volume 15-25 µl) at room temperature (20±1ºC). For s*pectrofluorimetry*, cells were washed and resuspended in a standard saline solution. Fluorescence was recorded at 37ºC in a Horiba Jobin Yvon spectrofluorimeter [1,2]. The cell sample was excited sequentially at 360 and 400 nm and emission was collected at 600 nm and 435 nm. The level of NADH and FMN was estimated as the fluorescence intensity at Ex. 360/Em. 435 and Ex. 450/Em. 510, respectively.

RESULTS AND DISCUSSION

DL spectroscopy and NADH/FMN_{ox} fluorimetric data were collected after treatments with ROT, QC, MD and H_2O_2, or QC in combination with MD or H_2O_2. Consistent with our previous reports [1,2], QC and MD inhibited DL significantly, in a dose-dependent manner. H_2O_2 elicited as well an inhibitory effect on DL, but to a much lesser extent. Combination of QC and MD at high dose also decreased consistently the VIS-DL yield, whereas combination of quercetin with a high dose of H_2O_2 exerted a more reduced effect. The DL yield in the visible domain depended in a Hill-like fashion on the level of NADH as well as that of oxidized flavine mononucleotide (FMN_{ox}), with apparent Hill coefficients of 4.3 (Fig. 1). In addition, spectral DL analysis indicated different degrees of cooperativity of both NADH and FMN_{ox}, reflected in differing Hill coefficients associated with blue, green/yellow and red light emission (3.9, 7.2 and 2.8, respectively). In addition, measurements of NADH and FMN_{ox} levels indicated that ROT binding exhibits an apparent Hill coefficient of 2.0-2.4, suggesting that Complex I functions mainly as a dimer in intact Jurkat cells. Based on these findings, we propose that blue and red DL is produced predominantly by dimeric Complex I, whereas green/yellow DL arises mainly from tetrameric Complex I. Thus, the DL data indicate that green/yellow light emission (presumably associated with tetrameric Complex I) contributes 39%, whereas blue- and red-light emission (associated with dimeric Complex I) contributes 61% to total DL. So, our results suggest that about 60% and 40% of Complex I oligomers in Jurkat cells are in dimeric and tetrameric form, respectively. In conclusion, based on the main findings that: 1) DL is closely related to the level of oxidized FMN, which is found primarily in the mitochondria, 2) DL is also linked to the level of NADH, the substrate of mitochondrial Complex I, 3) ROT, a specific inhibitor of Complex I, affected DL considerably, and 4) MD and QC, which interact robustly with Complex I, also affected DL significantly, all our results reinforce the idea [1] that mitochondrial Complex I plays a major role in delayed luminescence.

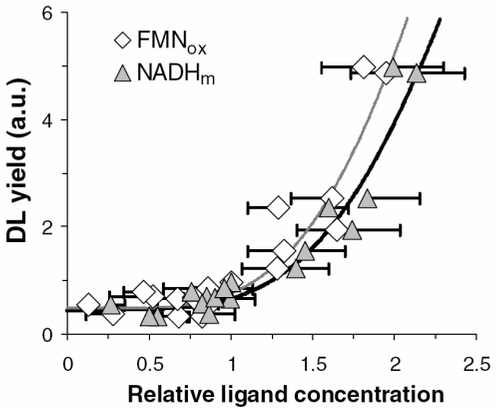

Figure 1: The dependence of the VIS total DL yield on the relative concentration of NADH or FMN_{ox}, obtained after treatments of Jurkat cells with ROT, MD, QC or H_2O_2. Data were fitted to a Hill-type equation.

To summarize, our studies provide evidence that the ultra-weak photon-induced delayed photoemission of intact Jurkat cells originates mainly from mitochondrial Complex I, which appears to function predominantly as a dimer and less frequently as a tetramer in this cell type. Complex I oligomers appear to exhibit cooperative interaction between monomers at the level of the rotenone site 1, NADH/NADPH sites and both FMN sites. Moreover, in individual monomers, both pairs of pyridine nucleotide (NADH/NADPH) binding sites and flavin (FMN-b/FMN-a) binding sites, which are situated at the two extremities of the extramembranous domain of Complex I, display strong cooperativity in the binding of their specific ligands. In addition, the timescales of various electron transfer steps involving the formation of flavin and ubisemiquinone radicals with subsequent production of superoxide can be estimated from delayed red-light emission. All these findings raise the attractive possibility that DL spectroscopy could be used as a reliable, sensitive and robust technique to probe electron flow within Complex I and gain valuable insights into the structural and functional organization of this respiratory complex in situ.

ACKNOWLEDGEMENTS

This work was supported by a grant of the Romanian National Authority for Scientific Research, CNCS - UEFISCDI, project number PN-II-ID-PCE-2011-3-0800.

REFERENCES

[1] Baran I. et al. 2010. *Cell Biochem Biophys* 58: 169-179
[2] Baran I. et al. 2013. *J Biomed Optics* 18: 127006
[3] Musumeci F. et al. 2005. *J Photochem Photobiol B*. 79: 93-99
[4] Kim H.W. et al. 2005. *Cancer Lett*. 229: 283-289
[5] Mik E.G. et al. 2008. *Biophys J*. 95: 3977-3990
[6] Tudisco S et al., 2004. *Nucl Instr Meth Phys Res A* 518: 463-464

Apoptotic pathway induced by Berberine on thyroid cancer cell lines monitored by Delayed Luminescence

A. Scordino[1,2,*], A. Campisi[3], R. Grasso[2], R. Bonfanti[3], M. Gulino[4,2], R. Parenti[5], F. Musumeci[1,2]

1) Department of Physics and Astronomy, University of Catania, Catania, Italy
2) Southern National Laboratories of National Institute for Nuclear Physics, Catania, Italy
3) Department of Drugs Science, University of Catania, Catania, Italy
4) Faculty of Engineering, Architecture, University of Enna Kore, Enna, Italy
5) Department of Bio-Medical Science, University of Catania, Catania, Italy
**corresponding author, e-mail :scordino@lns.infn.it*

Abstract - We explored the possibility to monitor, by means of Delayed Luminescence measurements, the effect of Berberine on thyroid cancer cells. Delayed Luminescence changes correlate with immunoblotting analysis and may be a hallmark of induced apoptosis.

INTRODUCTION

Recent advances in detection of the ultra-weak Delayed Luminescence (DL) after photo-induction of human cells [1] have shown the possibility of using DL measurements as a non-invasive diagnostic tools in clinical survey, and cancer in particular .

Thyroid cancer is the most common endocrine malignancy and incidence is steadily increasing.

Berberine is a natural compound known to have significant anti-inflammatory activities, and recently reported to have a broad anticancer effects, by exerting several effects on mitochondria, causing cell proliferation arrest, mitochondrial fragmentation and depolarization, oxidative stress and decrease in ATP levels, and increasing level of apoptosis.

After the investigation of the relationship between apoptosis and DL of leukemia Jurkat T-cells [2], herein, we assessed the correlation between apoptosis and UVA induced ultra-weak photon emission (DL) in two different human thyroid cancer cell lines, the Follicular FTC-133 and the Anaplastic 8305C cell lines. The Follicular thyroid carcinoma (FTC-133) is one of the most common type of differentiated thyroid carcinoma and may be overtly or minimally invasive. On the other hand the poorly differentiated Anaplastic thyroid cancer (8305C) is the least common type of thyroid cells but shows rapid progression and a very poor prognosis due to its aggressive behaviour and resistance to cancer treatments.

MATERIALS AND METHODS

Follicular FTC-133 and Anaplastic 8305C human thyroid cancer cell cultures (Cell Bank Interlab Cell Line Collection, Genoa, Italy) were suspended in an appropriate medium and incubated at 37°C in humidified 5% CO_2–95% air mixture, The medium was replaced every 2 or 3 days.

For the treatment the cells were incubated with Berberine hydrochloride (Sigma-Aldrich, Milan, Italy) at different concentrations (5, 10, 25, 50, 100 μg/ml) for 12, 24, 48 h.

To verify the involvement of the apoptotic pathway induced by the treatment with Berberine, we assessed DNA fragmentation by TUNEL test (terminal deoxynucleotidyl-transferase mediated dUTP nick-end-labeling test), effector Caspase-3 cleavage and p53, p27 protein expression by Western blot analysis. Densitometric analysis was performed after normalization with anti-mouse β-tubulin.

In order to perform DL measurements on untreated (control) and Berberine hydrochloride treated cells the medium was removed, and after centrifugation the pellets were suspended in PBS at room temperature (20°C) (cell concentration about 10^6 cells/mL). DL measurements were performed with the ARETUSA set-up developed at LNS-INFN [3], and improved with a novel sample holder realized [1] in order to perform measurements on small quantity of cell cultures and reduce possible unwanted background signals. In addition to the DL intensity emitted in the total wavelength range of the detection apparatus (400-800 nm), we measured only two spectral components, the Blue component (460 nm) and the Red component (650 nm), in order to shorten the duration of each measurement so preventing cell stress.

RESULTS AND DISCUSSION

After a preliminary test by using different concentrations and incubation intervals with Berberine, we performed comparison in DL measurements for the treatment with a dose of 50 μg/ml berberine at 24h incubation time, because for this treatment we get the smallest difference between cell survival for the two cell types.

The results show that the Berberine is able to activate the apoptotic pathway, increases the tumour suppressor protein p53 expression levels and induces DNA fragmentation in both human thyroid cancer cell lines, even if the effect appears more evident in follicular cell lines.

Moreover immunoblot assay shows that the overexpression of the cell cycle inhibitor p27 protein is greater in follicular cells than in the anaplastic ones. It is known that increased level of p27 protein typically cause cells to arrest or slow down the cell division cycle. Our result allows supposing a greater contribution of cell cycle arrest in growth inhibition in the follicular thyroid cells than in the anaplastic ones.

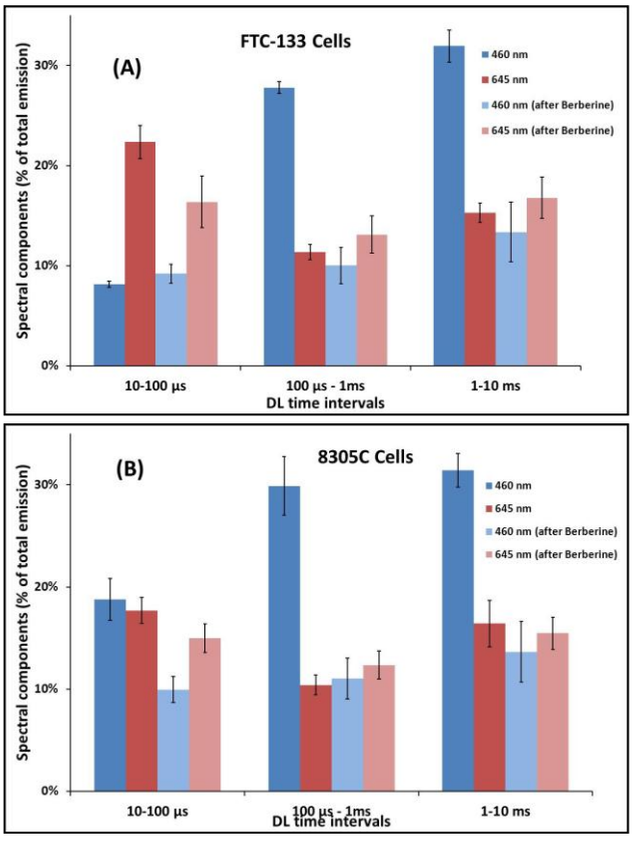

Figure 1: Blue (λ_{em} = 460 nm) and Red component (λ_{em} = 645 nm) percentage of DL emission from untreated and Berberine treated cell lines in different time intervals of the temporal decay. (A) Follicular FTC-133 cell line, (B) Anaplastic 8305C cell line. Results are expressed as average ± SE values of three different experiments in quintuplicate.

After the Berberine treatment DL emission from the two cell types decreases with respect the control, but the spectral response of the two cell types is different. Moreover, as observed in other cells [2], DL temporal trends denote a multimodal behaviour that can be accorded to the sum of at least three exponential decays with decay times in the time intervals 10-100 µs, 100 µs - 1 ms and 1-10 ms respectively. To compare the DL response we used the fraction of the spectral components with respect the total emission, in order to have dimensionless functions independent of experimental parameters that can change from one run to the other, as for instance cell density. Results are reported in Figure 1. In the anaplastic 8305C cells the Blue component is the largest fraction of the total emission and there is a strong reduction of this component all over the time course of the decay, while differences in the Red component after Berberine treatment are inside the errors. In the well differentiated follicular FTC-133 cells the pronounced decrease of the Blue components after Berberine treatment occurs only at long time, but in the short time region the Red component, that is the largest one, decreases after Berberine treatment, while changes in the Blue component are inside the error in this time interval.

Likely candidate for the Blue and Red spectral emission are reduced nicotinamide adenine dinucleotide (NADH) and protoporphyrin IX (PpIX), respectively, whose concentrations were estimated to increase in cancerous tissues as compared to normal ones.

The behaviour of the Blue components, especially at longer time, could be linked to NADH oxidation and an irreversible decrease of intra-mitochondrial NADH pool, Caspase activation of the apoptotic pathway (with consequent ATP decrease) through the release of cytochrome *c* as a result of the outer mitochondrial membrane becoming permeable.

The different contribution of the Red components could be ascribed to a different iron homeostasis in the two cell lines. In Literature an inverse relationship was found between PpIX and iron, so as a consequence different level of PpIX could be present in the two types of cells. It is likely that in the anaplastic 8305C cells increased iron requirement are related to the intensive angionesis. On the other hand a relevant iron uptake is required for aerobic mitochondrial respiration in the differentiated FTC-133 cells. So the increased PpIX emission in such cells could be interpreted according to an inability to complete the heme synthesis in mitochondria because of iron shortage and the reduction of the Red component in the short time region could be related to the antioxidant effect of Berberine that enhances the quenching of DL from PpIX.

CONCLUSIONS

The reported results support the hypothesis that DL from human cells originates mainly from mitochondria and suggest that DL is able to reveal the activation of the apoptotic pathway.

Moreover, these findings suggest that DL may not be cell-type specific and encourage further studies toward the use of DL spectroscopy in investigating mitochondrial dysfunctions in various diseases or in cancer diagnosis.

Our results lend further support for the development of this methodology in clinical applications, as a valuable tool of investigation in a multiparameter approach to diagnosis of cancer and monitoring of therapeutic treatments.

REFERENCES

[1] A.Scordino et al., J. Photochem. Photobiol. B- Biol 139, (2014) 76
[2] I.Baran et al., Oxidative Medicine and Cellular Longevity 2012 (2012) 498914
[3] S.Tudisco et al., NIM A 518, (2004) 463

Radiobiological analysis of human lung adenocarcinoma cells after irradiations with protons and carbon ions

O. Keta[1], T. Bulat[1], D. Todorović[2], V. Petković[1], G.A.P. Cirrone[3], F. Romano[3], V. Marchese[3], G. Cuttone[3], A. Ristić-Fira[1], I. Petrović[1]

1) Vinča Institute of Nuclear Sciences, University of Belgrade, Belgrade, Serbia
2) Faculty of Medical Sciences, University of Kragujevac, Kragujevac, Serbia
3) Istituto Nazionale di Fisica Nucleare, Laboratori Nazionali del Sud, Catania, Italy

Abstract - The aim of this *in vitro* study was to analyse effects of protons and carbon ions on survival and level of phosphorylation of histone H2AX (γ-H2AX) in CRL-5876 human lung adenocarcinoma cells. Irradiations with protons and carbon ions were performed with single doses ranging from 1 to 8 Gy. Irradiation effects on cell survival were analysed after seven days using clonogenic assay. Induction of γ-H2AX was followed by Western blot 30 min, 2, 6 and 24 h after irradiation. It has been shown that carbon ions are superior in cell killing than protons and that the level of phosphorylated histone H2AX is time and dose-dependent.

INTRODUCTION

Lung cancer is an aggressive disease and includes small-cell lung carcinoma (SCLC) and non-small-cell lung carcinoma (NSCLC) [1]. Radiation therapy of tumor is important therapeutic approach [2]. Due to high linear energy transfer (LET), protons and carbon ions have radiobiological advantages over conventional radiotherapy with X- and γ-rays. Relative biological effectiveness (RBE) strongly depends on LET and represents a measure of effectiveness of specific type of radiation in comparison with conventional radiation [3].

In this work inactivation effects of protons and carbon ions on NSCLC CRL-5876 lung adenocarcinoma cells were examined using clonogenic assay. It has been reported that retention of γ-H2AX foci 24 h after treatment could be an indicator of the loss of clonogenic potential [4]. In order to investigate the dynamics of induction and disappearance of γ-H2AX foci, the dose of 4 Gy was chosen from a range of irradiation doses tested by clonogenic assay. Since high irradiation doses can lead to foci overlapping, thus to underestimation of their number, when immunocytochemical methods are involved, γ-H2AX expression was monitored using Western blot. Kinetics data are used to identify time point of maximal γ-H2AX expression. At this time point the dose-dependency of γ-H2AX induction after irradiation was tested.

MATERIALS AND METHODS

Cell Culture and Experimental Conditions

Human CRL-5876 lung adenocarcinoma cells were obtained from the American Tissue Culture Collection (ATCC, Rockville, MD, USA) and cultured in the RPMI 1640 cell culture medium supplemented with 10% foetal bovine serum (FBS, Sigma-Aldrich Chemie GmbH, Steinheim, Germany) and penicillin/streptomycin (Sigma-Aldrich Chemie GmbH), in a humidified atmosphere of 5% CO_2 at 37°C (Heraeus, Hanau, Germany).

Irradiations with 62 MeV/u mid SOBP protons and pristine carbon ions were carried out at INFN-LNS, Italy with doses ranging from 1 to 8 Gy, at the dose rate of ~12 Gy/min. Relative dose for protons was 100.0±1.6% with corresponding LET value of 4.7±0.2 keV/μM. For carbon ions, relative dose was 49.2±3.8% with corresponding LET of 198.2±1.8 keV/μM.

Clonogenic Assay

After irradiation, cells were seeded at a suitable number into the 6-well plates and incubated for 7 days. The cells were then fixed with methanol (Zorka Pharma, Šabac, Serbia) and stained with 10% Giemsa solution (Alkaloid A.D., Skopje, Macedonia). Groups of more than 50 cells were scored as colonies. Survival was defined as number of colonies in irradiated samples compared with control.

Western Blot Analysis

Western blot analysis was performed as previously described [5]. Briefly, after blocking, membranes were incubated at 4ºC overnight with 1:1000 dilution of the primary anti-γ-H2AX antibody (BioLegend, San Diego, USA) in PBST (PBS-Tween20)/BSA and anti-β-actin antibody (Sigma-Aldrich Chemie GmbH) diluted 1:1000 in PBST/non-fat dry milk. After washings in PBST, the membranes were incubated with horseradish peroxidase-conjugated antibody (HRP, Cell Signalling) diluted 1:5000 in PBST/BSA. Densitometric analysis was performed using Image J Analysis PC software.

Statistical Analysis

Analysis of variance (ANOVA) followed by Tukey's post hoc test was used to calculate statistical differences using Graphpad Prism statistical software (San Diego, CA, USA). The results are presented as means±SEM and the level of significance was set at $p<0.05$.

RESULTS AND DISCUSSION

Effects of Protons and Carbon Ions on CRL5876 Cell Survival

It has been shown that CRL-5876 cells are radioresistant with SF2 value of 0.61 for γ-rays [6]. According to the survival data shown in Table 1, carbon ions have better inactivation effects on CRL-5876 cells compared to protons. This is reflected in much lower SF2 and thus higher RBE values.

Table 1: SF2 and RBE for CRL5876 cells

Irrad. type	SF2	RBE(2Gy, γ)
γ-rays	0.61±0.01	1.00
$^{1}H_{SOBP}$	0.49±0.01	1.33±0.33
$^{12}C_{FULL}$	0.05±0.01	5.55±0.65

Effects of Protons and Carbon Ions on γ-H2AX Expression in CRL-5876 Cells

Similar expression profiles of γ-H2AX after irradiations with protons and carbon ions were obtained by Western blot. Maximum level of γ-H2AX expression was detected 2 h post-irradiation (Fig. 1). Dose-dependent increase in γ-H2AX expression both for protons and carbon ions was found in this time point. Nevertheless, slightly higher increase in γ-H2AX level is found after irradiations with carbon ions compared to protons, especially for higher doses, i.e., 4, 6, and 8 Gy (Fig. 2A, B).

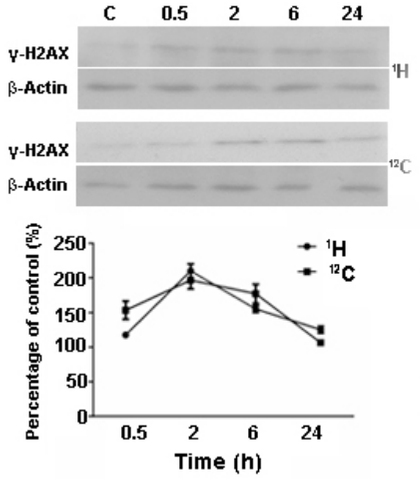

Figure 1: γ-H2AX levels in CRL-5876 cells 30 min, 2, 6 and 24 h after irradiation with 4 Gy of protons and carbon ions. β-Actin was used as loading control. Results are presented as Mean±SEM.

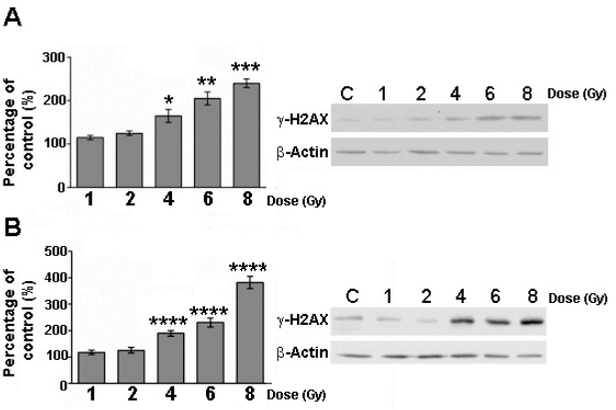

Figure 2: γ-H2AX levels in CRL-5876 2 h after irradiation with 1, 2, 4, 6 and 8 Gy of protons (A) and carbon ions (B). β-Actin was used as loading control. Results are presented as Mean±SEM.

* - 0.01< p<0.05; ** - 0.001< p<0.01; *** - 0.0001< p<0.001; **** - p<0.0001.

CONCLUSIONS

Carbon ions have better inactivation effects on radioresistant CRL-5876 cells compared to protons. The level of phosphorylated histone H2AX is time and dose-dependent.

ACKNOWLEDGEMENT

The research leading to these results has received funding from the European Union Seventh Framework Programme FP7/2007- 2013 under Grant Agreement nÂ°262010 - ENSAR. The EC is not liable for any use that can be made on the information contained herein. This work was also financially supported by the Ministry of Education, Science and Technological Development of Serbia (grants 173046 and 171019) and by Istituto Nazionale di Fisica Nucleare, Laboratori Nazionali del Sud, Italy.

REFERENCES

[1] R. A. Vescio et al., Cancer Research 50(18) (1990) 6095.
[2] R. Baskar et al., Int J Med Sci 9(3) (2012) 193.
[3] J. S. Loeffler, M. Durante, Nat Rev Clin Oncol 10(7) (2013) 411.
[4] J. P. Banath et al., BMC Cancer 10 (2010) 4.
[5] T. Bulat et al., INFN-LNS Activity Report 2011 (2012) 310.
[6] O. Keta et al., Nuclear Technology and Radiation Protection 29 (3) (2014) 233.

Analyses of apoptotic and cell cycle protein expression in non-small lung cancer cells: effects of proton and carbon ion irradiations

V. Petković[1], O. Keta[1], T. Bulat[1], D. Todorović[2], G.A.P. Cirrone[3], F. Romano[3], V. Marchese[3], G. Cuttone[3], I. Petrović[1], A. Ristić-Fira[1]

1) Vinča Institute of Nuclear Sciences, University of Belgrade, Belgrade, Serbia
2) Faculty of Medical Sciences, University of Kragujevac, Kragujevac, Serbia
3) Istituto Nazionale di Fisica Nucleare, Laboratori Nazionali del Sud, Catania, Italy

Abstract – The goal of this study was to examine p53 and p21 protein expression in non-small lung cancer cells irradiated with therapeutic protons and carbon ions. Single doses of 1 and 3 Gy were applied and the effects of irradiations were analyzed by Western blot at 48 h and 7 days after treatment. p53 and p21 have dose and time dependent profile, while carbon ions caused significant elevation of p53 comparing to protons. These results indicate that carbon ions induce more severe DNA damage, thus trigger DNA repair and subsequently apoptosis which is to be further analysed.

INTRODUCTION

Lung cancer has two morphological types: small cell lung cancer (SCLC) and non-small cell lung cancer (NSCLC). Around 80% of all lung cancer patients are diagnosed with NSCLC. Medical treatment of this type of cancer involves both proton and carbon ion therapy [1]. Carbon ions are classified as high LET (linear energy transfer) radiation with high ionization density and relative biological effectiveness (RBE). Protons are classified as lower LET radiation and have RBE around 1.2 to 3.5 times smaller than carbon ions [2]. In order to cover tumor tissue with high accuracy the method of spread out Bragg peak (SOBP) is used in both proton and carbon ion therapy [2, 3].

In response to cellular stress and DNA damage, expression of pro-apoptotic protein p53 is activated [4]. Besides its role in apoptosis and DNA repair, p53 mediates cell cycle arrest by stimulating expression of cyclin-dependent kinase inhibitor p21. p21 protein regulates progression through cell cycle checkpoints in late G1, S, G2 and M phase [5]. As previously shown, ionizing radiation causes DNA damage and triggers expression of both p53 and p21, where p53 expression could be elevated for days or weeks after treatment [4]. In this study the effect of SOBP proton and carbon ion irradiations on p53 and p21 expression were analyzed in the functions of time and dose. We followed the effect of chosen single doses (1 and 3 Gy) 48 h and 7 days after treatment.

MATHERIALS AND METHODS

Cell culture

Human NSCLC CRL-5876 cells were purchased from the American Type Culture Collection (ATCC, Manassas, Va, USA) and cultured in the RPMI 1640 cell culture medium supplemented with 10% foetal bovine serum (FBS, Sigma-Aldrich Chemie GmbH, Steinheim, Germany) and penicillin/streptomycin (Sigma-Aldrich Chemie GmbH) in a humidified atmosphere of 5% CO_2 at 37°C (Heraeus, Hanau, Germany).

Irradiation procedure

Cells were irradiated with 62 MeV/u mid-SOBP protons and pristine carbon ions with the single doses of 1 and 3 Gy respectively at the dose rate ~12 Gy/min, in air at room temperature. Relative dose for protons was 100.0±1.6% with corresponding LET value of 4.7±0.2 keV/µM and for carbon ions 49.2±3.8% with corresponding LET of 198.2±1.8 keV/µM. The whole procedure was carried out in INFN-LNS, Italy.

Western blot

48 h and 7 days from irradiation, CRL-5876 cells were collected and analysed using Western blot [6]. Primary anti-p53 and p21 antibodies were used in 1:1000 dilutions (Cell Signaling Technology, Massachusetts, USA). For normalization purposes, immunoblots were incubated overnight at 4ºC with rabbit polyclonal anti-β-actin antibody (Sigma-Aldrich Chemie GmbH). After washing, membranes were incubated with horseradish peroxidase-conjugated anti-mouse antibody (HRP, Cell Signaling) diluted 1:5000 in PBST/BSA. Densitometry was performed using ImageJ Analysis PC software.

Statistical analyses

Calculation of statistical differences was determined by analysis of variance (ANOVA) and post hoc Tukey's test in Graphpad Prism statistical software (San Diego, CA, USA). The results are presented as means±SEM and the level of significance was set at $p<0.05$.

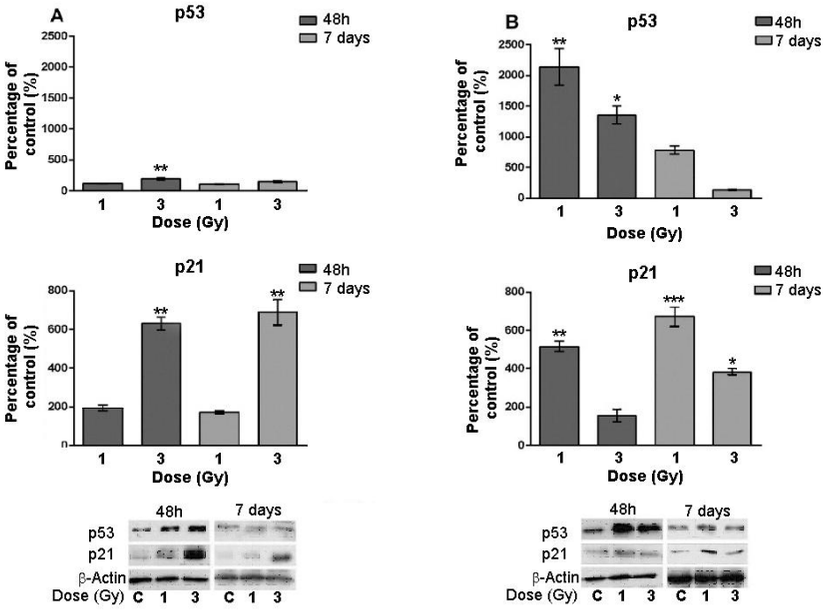

Figure 1: Western blot detection of p53 and p21 protein expression in CRL-5876 cells 48 h and 7 days after irradiation with SOBP protons (A) and carbon ions (B). β-actin was used as loading control. Results are shown as mean±SEM.

* - 0.01< p<0.05; ** - 0.001< p<0.01; *** - 0.0001< p<0.001.

RESULTS AND DISCUSSION

Effect of SOBP protons on p53 and p21 expression profile

Treatment with SOBP protons triggered significantly higher expression of p53 protein at dose of 3 Gy compared to control ($p<0.01$) after 48 h, while after 7 days the expression was slightly elevated. Expression of p21 at both time points was statistically higher at 3 Gy ($p<0.01$) compared to control (as shown in Figure 1A).

Effect of carbon ion on p53 and p21 expression profile

Significant rise of p53 expression was present at 1 ($p<0.01$) and 3 Gy ($p<0.05$) compared to control, 48 h following irradiation. After 7 days this significance was not detected. The p21 expression after 48 h was significantly higher only in cells irradiated with 1Gy compared to control ($p<0.01$). After 7 days the level of p21 was higher at both doses of 1 Gy ($p<0.001$). and 3 Gy ($p<0.01$) compared to control (results shown in Figure 1B).

CONCLUSIONS

Expression of p53 and p21 in CRL-5876 cells irradiated with SOBP protons shows that possible mechanism of cell response to DNA damage 48 h and 7 days after irradiation could be cell cycle arrest and repair rather than apoptosis. However, carbon ions induced apparently higher amount of DNA damage which resulted in high level of p53 protein. Expression profiles of both p53 and p21 may indicate that apoptosis was the fast cell response to DNA damage at selected doses, while the late response could be cell cycle arrest. In CRL-5876 cells carbon ions induced more DNA damage than SOBP protons for the same dose levels and time points.

ACKNOWLEDGEMENT

This research was carried out under Grant Agreement nÂ°262010 - ENSAR funded by the European Union Seventh Framework Programme FP7/2007-2013. The EC is not liable for any use that can be made on the information contained herein. Also, this work was financially supported by the Ministry of Education, Science and Technological Development of Serbia (grants 173046 and 171019) and Istituto Nazionale di Fisica Nucleare, Laboratori Nazionali del Sud, Italy.

REFERENCES

[1] M. L. Haas, Contemporary issues in lung cancer: a nursing perspective, 2nd ed. Boston: Jones and Bartlett (2010) 17.
[2] Y. Demizu et al., BioMed Res Int 2014 (2014) 1.
[3] W. C. Schlegel et al., New Technologies in Radiation Oncology, 1st ed. Springer-Verlag Berlin Heidelberg (2006) 345.
[4] R. A. Weinberg, The Biology of Cancer, 2nd ed. New York: Garland Science (2014) 335.
[5] T. Abbas and A. Dutta, Nat Rev Cancer, 9 (2009) 400.
[6] X. Yu et al., J Natl Cancer Ins, 94 (2002) 504.

ISTITUTO NAZIONALE DI FISICA NUCLEARE
LABORATORI NAZIONALI DEL SUD
ACTIVITY REPORT 2013/2014

GENERAL INFORMATION

Organization and Personnel

Director: G. Cuttone

Research Coordinators
Astroparticle Physics: P. Sapienza
Experimental Nuclear Physics: C. Agodi
Theorical Physics: V. Greco
Interdisciplinary Physics and Technological Developments: G.A.P. Cirrone

Division Heads
Research: L. Calabretta
Accelerators: D. Rifuggiato
Technical and General Service: G. Schillaci

International Scientific Committee
R. Bougault (Laboratoire de Physique Corpusculaire de Caen ENSICAEN, France) - Chairman
T. Aumann (Technical University – Darmstadt, Germany)
M. J. G. Borge (Istituto de Estructura de la Materia, Spain)
P. Descouvemont (Universitè Libre de Bruxelles, Belgium)
F. Gramegna (INFN - LNL, Italy)
A. Kacperek (Douglas Cyclotron Clatterbridge Centre for Oncology, UK)
R. E. Tribble (Texas A&M University Cyclotron Institute, USA)

Administration Service Unit
S. Cesare

Users Committee
Coordinator: E. De Filippo

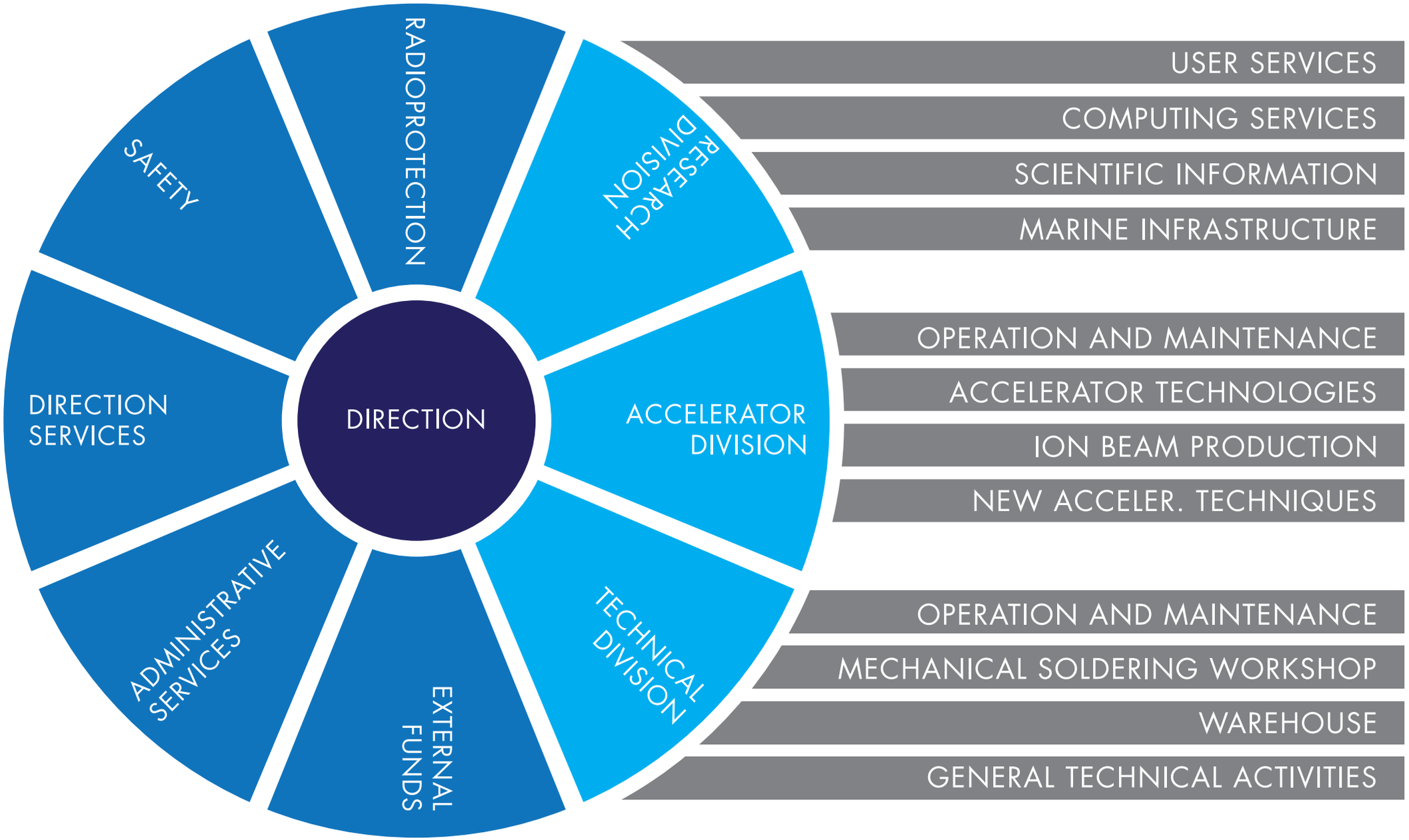
DIRECTION
RADIOPROTECTION
SAFETY
DIRECTION SERVICES
ADMINISTRATIVE SERVICES
EXTERNAL FUNDS
RESEARCH DIVISION
ACCELERATOR DIVISION
TECHNICAL DIVISION
USER SERVICES
COMPUTING SERVICES
SCIENTIFIC INFORMATION
MARINE INFRASTRUCTURE
OPERATION AND MAINTENANCE
ACCELERATOR TECHNOLOGIES
ION BEAM PRODUCTION
NEW ACCELER. TECHNIQUES
OPERATION AND MAINTENANCE
MECHANICAL SOLDERING WORKSHOP
WAREHOUSE
GENERAL TECHNICAL ACTIVITIES

LNS PERSONNEL	2013	2014
Permanent Research staff	21	22
Temporary Research staff	2	2
Permanent Technological staff	9	9
Temporary Technological staff	6	10
Permanent Administrative staff	13	13
Temporary Administrative staff	6	6
Permanent Technical staff	68	68
Temporary Technical staff	4	5
Scientific and Technological Associates	12	12
Retired Associates	6	5
Coordinated and Continous Collaborations	2	5
INFN research fellows - grants	42	43
PhD Students	21	24
Other Institutions research grants	7	7
Specialization School Students	8	6
Personnel other institutions	24	27
Undergraduate Students fellow	14	4
Undergraduate Students	13	12

Scientific Guests and Users 2013

Delor Antdine	*Belgium*
Brandao de Oliveira J. Roberto	*Brazil*
Medina Heber Nilberto	*Brazil*
Rodrigues Marcia Regina Dias	*Brazil*
Bao Xiaojun	*China*
Sun Baoyuan	*China*
Zadro Mile	*Croatia*
Ademard Guilain	*France*
Bonnet Eric	*France*
Borderie Bernard	*France*
Bougault Remi	*France*
Brulin Gwnail	*France*
Edelbruck Pierre	*France*
Frankland John	*France*
Gruyer Diego	*France*
Hugon Christophe	*France*
Lacroix Denis	*France*
Le Neindre Nicolas	*France*
Lopez Olivier	*France*
Lucaroni Andrea	*France*
Marino Michele	*France*
Rivet Marie-France	*France*
Rossomme Severine	*France*
Salomon Franck	*France*
Salomone Vincenzo	*France*
St-Onge Patric	*France*
Stancampiano Elisa	*France*
Vient Emmanuel	*France*
Viti Vincenza	*France*
Pakou Athena	*Greece*
Papa Massimo	*Greece*
Sgouros Onoufrios	*Greece*
Simeone Francesco	*Greece*
Soukeras Vasileios	*Greece*
Spadaccini Giulio	*Greece*
Styliaris Efstathlos	*Greece*
Santosh Kumar Das	*India*
Chaudhary Pankaj	*Ireland*
Prise Kevin	*Ireland*
Schettino Giuseppe	*Ireland*
Adrini Oscar	*Italy*
Aiello Sebastiano	*Italy*
Allegra Luciano	*Italy*
Aloisio Alberto	*Italy*
Alpat Behcet	*Italy*
Altana Carmen	*Italy*
Ameli Fabrizio	*Italy*
Andolina Rosatio	*Italy*
Anghinolfi Marco	*Italy*
Auditore Lucrezia	*Italy*
Babini Gabriele	*Italy*
Balduzzi Maria	*Italy*
Barbagallo Massimo	*Italy*
Barbato Felicia Carla Tiziana	*Italy*
Barlini Sandro	*Italy*
Battiato Mario	*Italy*
Battistoni Giuseppe	*Italy*
Beverini Nicolo'	*Italy*

Delor Antdine	*Belgium*
Brandao de Oliveira J. Roberto	*Brazil*
Medina Heber Nilberto	*Brazil*
Rodrigues Marcia Regina Dias	*Brazil*
Bao Xiaojun	*China*
Sun Baoyuan	*China*
Zadro Mile	*Croatia*
Ademard Guilain	*France*
Bonnet Eric	*France*
Borderie Bernard	*France*
Bougault Remi	*France*
Brulin Gwnail	*France*
Edelbruck Pierre	*France*
Frankland John	*France*
Gruyer Diego	*France*
Hugon Christophe	*France*
Lacroix Denis	*France*
Le Neindre Nicolas	*France*
Lopez Olivier	*France*
Lucaroni Andrea	*France*
Marino Michele	*France*
Rivet Marie-France	*France*
Rossomme Severine	*France*
Salomon Franck	*France*
Salomone Vincenzo	*France*
St-Onge Patric	*France*
Stancampiano Elisa	*France*
Vient Emmanuel	*France*
Viti Vincenza	*France*
Pakou Athena	*Greece*
Papa Massimo	*Greece*
Sgouros Onoufrios	*Greece*
Simeone Francesco	*Greece*
Soukeras Vasileios	*Greece*
Spadaccini Giulio	*Greece*
Styliaris Efstathlos	*Greece*
Santosh Kumar Das	*India*
Chaudhary Pankaj	*Ireland*
Prise Kevin	*Ireland*
Schettino Giuseppe	*Ireland*
Adrini Oscar	*Italy*
Aiello Sebastiano	*Italy*
Allegra Luciano	*Italy*
Aloisio Alberto	*Italy*
Alpat Behcet	*Italy*
Altana Carmen	*Italy*
Ameli Fabrizio	*Italy*
Andolina Rosatio	*Italy*
Anghinolfi Marco	*Italy*
Auditore Lucrezia	*Italy*
Babini Gabriele	*Italy*
Balduzzi Maria	*Italy*
Barbagallo Massimo	*Italy*
Barbato Felicia Carla Tiziana	*Italy*
Barlini Sandro	*Italy*
Battiato Mario	*Italy*
Battistoni Giuseppe	*Italy*
Beverini Nicolo'	*Italy*

Delor Antdine	*Belgium*
Brandao de Oliveira J. Roberto	*Brazil*
Medina Heber Nilberto	*Brazil*
Rodrigues Marcia Regina Dias	*Brazil*
Bao Xiaojun	*China*
Sun Baoyuan	*China*
Zadro Mile	*Croatia*
Ademard Guilain	*France*
Bonnet Eric	*France*
Borderie Bernard	*France*
Bougault Remi	*France*
Brulin Gwnail	*France*
Edelbruck Pierre	*France*
Frankland John	*France*
Gruyer Diego	*France*
Hugon Christophe	*France*
Lacroix Denis	*France*
Le Neindre Nicolas	*France*
Lopez Olivier	*France*
Lucaroni Andrea	*France*
Marino Michele	*France*
Rivet Marie-France	*France*
Rossomme Severine	*France*
Salomon Franck	*France*
Salomone Vincenzo	*France*
St-Onge Patric	*France*
Stancampiano Elisa	*France*
Vient Emmanuel	*France*
Viti Vincenza	*France*
Pakou Athena	*Greece*
Papa Massimo	*Greece*
Sgouros Onoufrios	*Greece*
Simeone Francesco	*Greece*
Soukeras Vasileios	*Greece*
Spadaccini Giulio	*Greece*
Styliaris Efstathlos	*Greece*
Santosh Kumar Das	*India*
Chaudhary Pankaj	*Ireland*
Prise Kevin	*Ireland*
Schettino Giuseppe	*Ireland*
Adrini Oscar	*Italy*
Aiello Sebastiano	*Italy*
Allegra Luciano	*Italy*
Aloisio Alberto	*Italy*
Alpat Behcet	*Italy*
Altana Carmen	*Italy*
Ameli Fabrizio	*Italy*
Andolina Rosatio	*Italy*

Scientific Guests and Users 2014

Janssens Koen	*Belgium*
Bocaline Zagatto Vinicius Antonio	*Brazil*
Borello Lewin Thereza	*Brazil*
Brandao De Oliveira J. Roberto	*Brazil*
Rodrigues Marcia Regina Dias	*Brazil*
Roman Padilla Alvarez	*Brazil*
Torrieri Giorgio	*Brazil*
Godoy Rojias Rodrigo A.	*Chile*
Hua Zheng	*China*
Ming-Hua Weng	*China*
Zadro Mile	*Croatia*
Cechak Tomas	*Czech Republic*
Hanusova Tereza	*Czech Republic*
Kracmerova Tereza	*Czech Republic*
Lenka Thinova	*Czech Republic*
Pastykova Veronika	*Czech Republic*
Ademard Guilain	*France*
Augey Lou	*France*
Bonnet Eric	*France*
Chbihi Abdou	*France*
Fable Quentin	*France*
Frankland John	*France*
Le Neindre Nicolas	*France*
Lopez Oliver	*France*
Vient Emmanuel	*France*
Burkhay Volodymyr	*Germany*
Schulte Kathrine	*Germany*
Pakou Athina	*Greece*
Pierroutsakou Dimitra	*Greece*
Sagia Eleni	*Greece*
Sgouros Onoufrios	*Greece*
Borghesi Marco	*India*
Chatterjee Mihir	*India*
Chaudhary Pankaj	*India*
Chibihi Abdelouahad	*India*
Doria Domenico	*Ireland*
Marshal Thomas	*Ireland*
Ademard Guilain	*Italy*
Adriani Oscar	*Italy*
Aiello Sebastiano	*Italy*
Albergo Sebastiano	*Italy*
Alimonti Gianluca	*Italy*
Alpat Behcet	*Italy*
Altana Carmen	*Italy*
Anghidolfi Marco	*Italy*
Anirban Saha	*Italy*
Auditore Lucrezia	*Italy*
Badalà Angela	*Italy*
Balduzzi Maria	*Italy*
Barbato Felicia	*Italy*
Barlini Sandro	*Italy*
Battiato Mario	*Italy*
Bechet Alpat	*Italy*
Bellini Vincenzo	*Italy*
Bertulani Carlos	*Italy*
Biagi Simone	*Italy*
Bicchieri Marina	*Italy*
Bini Maurizio	*Italy*
Bisogni Maria Giuseppina	*Italy*
Bissi Luisa	*Italy*
Blasi Nives	*Italy*
Boiano Alfonso	*Italy*
Bonechi Lorenzo	*Italy*
Bongi Massimo	*Italy*
Broglia Riccardo Amerigo	*Italy*
Bruzzi Mara	*Italy*
Bucciolini Marta	*Italy*
Cabibbo Maurizio	*Italy*
Caliri Claudia	*Italy*
Campajola Luigi	*Italy*
Canella Stefania	*Italy*
Cannizzo Fabrizio	*Italy*
Capone Antonio	*Italy*
Cardella Giuseppe	*Italy*
Caruso Anna	*Italy*
Casini Giovanni	*Italy*
Catalano Roberto	*Italy*
Cavallaro Salvatore	*Italy*
Chatterjee Suparna	*Italy*
Chiodini Gabriele	*Italy*
Cinarelli Davide	*Italy*
Cinausero Marco	*Italy*
Civinini Carlo	*Italy*
Colilli Stefano	*Italy*
Costa Caterina	*Italy*
Costa Giuseppe	*Italy*
Costa Salvatore	*Italy*
Cuppari Carlo	*Italy*
Curciarello Francesca	*Italy*
Cutroneo Maria	*Italy*
D'agata Giuseppe	*Italy*
D'alessandro Rafaello	*Italy*
D'amico Salvatore	*Italy*
D'andrea Murizio	*Italy*
De Filippo Enrico	*Italy*
De Leo Veronica	*Italy*
De Napoli Marzio	*Italy*
De Prete Marina	*Italy*
Deniskina Natalia	*Italy*
Di Blasi Francesco	*Italy*
Di Capua Francesco	*Italy*
Di Toro Massimo	*Italy*
Dini Valentina	*Italy*
Esposito Giuseppe	*Italy*
Fabris Daniela	*Italy*
Farina Edoardo	*Italy*
Fazzi Alberto	*Italy*
Feng Zhaoqing	*Italy*
Fermani Paolo	*Italy*

Ferroni Matteo	*Italy*
Ferroni Matteo Alberto	*Italy*
Fichera Filippo	*Italy*
Foti Antonino	*Italy*
Francesca Perozziello	*Italy*
Frankland John	*Italy*
Geraci Elena	*Italy*
Giardina Giorgio	*Italy*
Giordano Valentina	*Italy*
Giove Dario	*Italy*
Giudice Nunzio	*Italy*
Giuliani Fausto	*Italy*
Giusa Antonio	*Italy*
Gramegna Fabiana	*Italy*
Grande Sveva	*Italy*
Grandemange Pierre	*Italy*
Grimaldi Antonio	*Italy*
Gruyer Diego	*Italy*
Guardone Nunzio	*Italy*
Gueli Anna Maria	*Italy*
Immè Giuseppina	*Italy*
Italiano Antonio	*Italy*
Keta Otilija	*Italy*
Kordyasz Andrzej	*Italy*
Kroha Vaclav	*Italy*
Kubono Shigeru	*Italy*
La Guidara Elena	*Italy*
Lamia Debora	*Italy*
Lamia Sergio	*Italy*
Landolina Beatrice	*Italy*
Lanza Agostino	*Italy*
Leonora Emanuele	*Italy*
Librizzi Francesco	*Italy*
Livanou Anastasia	*Italy*
Lo Nigro Salvatore	*Italy*
Lo Presti Domenico	*Italy*
Lombardo Ivano	*Italy*
Longhitano Fabio	*Italy*
Lucaroni Andrea	*Italy*
Luciani Annamaria	*Italy*
Luongo Orlando	*Italy*
Maccioni Giorgia	*Italy*
Magistrati Giorgio	*Italy*
Mammoliti Francesco	*Italy*
Mandaglio Giuseppe	*Italy*
Manti Lorenzo	*Italy*
Marco Sessa	*Italy*
Mazzocco Marco	*Italy*
Melon Barbara	*Italy*
Menichelli Mauro	*Italy*
Minniti Triestino	*Italy*
Moscato Ivo	*Italy*
Mostacci Domiziano	*Italy*
Nannini Adriana	*Italy*
Olmi Alessandro	*Italy*
Pagano Angelo	*Italy*
Pallotta Stefania	*Italy*
Palma Alessandra	*Italy*
Palmerini Armando	*Italy*
Papa Massimo	*Italy*
Papadionisiou Marianna	*Italy*
Pappalardo Giuseppe Salvatore	*Italy*
Parasiliti Palumbo Gianluca	*Italy*
Pasquali Gabriele	*Italy*
Perricone Dario	*Italy*
Perrina Chiara	*Italy*
Piantelli Silvia	*Italy*
Pirrone Sara	*Italy*
Poggi Giacomo	*Italy*
Politi Giuseppe	*Italy*
Pugliatti Cristina	*Italy*
Quattrocchi Lucia	*Italy*
Randazzo Nunzio	*Italy*
Reito Santo	*Italy*
Riggi Francesco	*Italy*
Romaniuk Mariia	*Italy*
Rosi Antonella	*Italy*
Russo Andrea	*Italy*
Russo Giuseppe	*Italy*
Russotto Paolo	*Italy*
Saccà Gaspare	*Italy*
Salemi Giuseppe	*Italy*
Salvatore Iacono	*Italy*
Sanfilippo Simone	*Italy*
Santini Catia	*Italy*
Santoro Simone	*Italy*
Scandurra Anastasia	*Italy*
Scarlini Enrico	*Italy*
Servioli Leonello	*Italy*
Sinatra Donatella	*Italy*
Sipala Valeria	*Italy*
Sperduto M. Leda	*Italy*
Stefanini Andrea	*Italy*
Strano Emanuele	*Italy*
Sutera Concetta Maria	*Italy*
Tabocchini Maria Antonella	*Italy*
Talamonti Cinzia	*Italy*
Tobia Giampaolo	*Italy*
Tomarchio Elio A.G.	*Italy*
Torresi Domenico	*Italy*
Tricomi Alessia	*Italy*
Trifirò Antonio	*Italy*
Trimarchi Marina	*Italy*
Troja Sebastiano Olindo	*Italy*
Tuvè Cristina	*Italy*
Valdrè Simone	*Italy*
Ventura Carlo	*Italy*

Verde Giuseppe	*Italy*
Zani Margherita	*Italy*
Fujita Yoshitaka	*Japan*
Hayakawa Seiya	*Japan*
Kubono Shigeru	*Japan*
Sashala Naik Alvin	*Mauritius*
Kupny Sebastian	*Poland*
Soukeras Vasileios	*Poland*
Keta Otilija	*Republic of Serbia*
Petkovic Vladana	*Republic of Serbia*
Petrovic Ivan	*Republic of Serbia*
Ristic-Fira Aleksandra	*Republic of Serbia*
Betsis Dariya	*Russia*
Kulikovskiy Vladimir	*Russia*
Kuznetsov Slava	*Russia*
Conradie Lowry	*South Africa*
Cetinkaya Hakan	*Turkey*
Hakan Cetinkaya	*Turkey*
Sogukpinar Haci	*Turkey*
Kres Evgenii	*Ukraine*
March Norman Henri	*United Kingdom*
Bonasera Aldo	*Usa*
Desiati Paolo	*Usa*
Formaggio Joseph	*Usa*
Iachello Francesco	*Usa*
Kopper Claudio	*Usa*
Radovinsky Alexey	*Usa*
Volpe Francesco A.	*Usa*
Yeck James H.	*Usa*
Avsar Deniz	
Haab Patrick	
Hoyler Friedrich	
Miabala Justin	
Saha Anirban	
Zadeh Ali	

SEMINARS

Fri 11-Jan-2013
Santosh Kumar Das
Heavy Quark dynamics in the QGP

Abstract

We will discuss the dynamics of Heavy Quarks during the evolution of the Quark-gluon Plasma created at both RHIC and LHC energy. Heavy Quarks show a strong interaction in the hot QGP and the first studies indicated large non perturbative contribution to their interaction with the medium.

Thu 24-Jan-2013
J.R.B. Oliveira
Rainbow pattern in 16O+27Al and the influence of channel coupling on the far-side nuclear scattering and Short review of semi-classical approach to nuclear rainbow scattering

Abstract

1- Recent data on the elastic scattering of $^{16}O+^{27}Al$ at 100 MeV confirm, up to ~75 degrees in the center of mass, the Sao Paulo Potential Coupled Channel calculations. These calculations predict a nuclear rainbow pattern in the far-side component of the nuclear scattering, which is not expected for such heavy-ion system, since internal trajectories become strongly absorbed, as inferred from standard optical model calculations. The classical trajectories and the polarization potentials for this system are studied in order to help to understand the phenomenon.
2- 2- Stimulated by the predictions and first experimental results of a nuclear rainbow pattern in the elastic scattering of relatively heavy ions, some of the semi-classical approaches to this phenomenon are reviewed, including the WKB approximation with extension to complex trajectories and complex angular momenta.

Mon 11-Mar-2013
S.Gammino
Presentazione dei nuovi progetti ESS e AISHA

Thu 18-Apr-2013
A.Sarti
12C ions fragmentation measurements with the FIRST experiment at GSI

Thu 30-May-2013
G.Foti
Città della Scienza: una vetrina della creatività

Wed 19-Jun-2013
J.Strait
Science opportunities with long baseline neutrino

Mon 8-Jul-2013
D.Montanari
The LBNE Cryostat and Cryogenic Systems

Abstract:

The Long-Baseline Neutrino Experiment (LBNE) is a broad scientific program being developed in the United States as an international partnership. LBNE consists of an intense neutrino beam produced at Fermi National Accelerator Laboratory (Fermilab), a highly capable set of neutrino detectors on the Fermilab campus (Near Detector), and a large underground liquid argon Far Detector at Sanford Underground Research Facility (SURF) in the state of South Dakota. LBNE will make detailed studies of neutrino oscillations including measurements of the mass hierarchy and CP violation that take advantage of the 1300 km baseline. At the far site, the large underground detector will open a new window to the search for nucleon decay, supernova neutrinos, and interesting astrophysical phenomena. This talk will describe the plans for the LBNE Far Detector Cryostat and Cryogenic Systems and their current status. The LBNE 35 ton prototype will also be presented: it is the LBNE prototype that we have built at Fermilab to test the purity in a membrane cryostat and the deployment of TPCs. Long term plans and current status will be detailed.

Thu 11-Jul-2013
M.Barbagallo
n_TOF: misure di sezioni d'urto neutroniche per astrofisica e tecnologie nucleari

Fri 19-Jul-2013
V.N.Kondratyev
Ukraine: Creation and transmutation of magnetized nuclei at explosively dense matter

SEMINARS

Thu 25-Jul-2013
A.Moro
Application of the CDCC method to the understanding

Abstract:

Nuclei in the proximity of the proton and neutron drip-lines are often weakly bound, or even unbound, and hence their properties are influenced by positive-energy states. Collisions of these weakly-bound systems by stable nuclei will be also influenced by the coupling to the unbound states. This effect was first noticed in deuteron-induced reactions, and later observed in the scattering of other loosely bound nuclei, such as halo nuclei. Inclusion of the positive-energy part of the spectrum in reaction calculations is not straightforward, because these states constitute a continuous and hence infinite. In addition, the wave-functions associated to positive states are non-normalizable, making also difficult its inclusion coupled-channels formalisms. A practical way of taking into account these states is using a discrete representation of the continuum, for which a variety of methods have been envisaged. The combination of this discretization method with the coupled-channels formalism gives rise to the so-called Continuum-Discretized Coupled-Channels (CDCC) method. In this seminar, we review the CDCC formalism, starting from its original formulation in the context of deuteron scattering, and including some recent advances, such as it extension to three-body projectiles or its application in transfer reactions. As an example, we present recent applications of the method to the scattering of two- and three-body halo nuclei at energies around the Coulomb barrier, underlining the physical information that has been extracted from these analyses.

Fri 26-Jul-2013
A.Moro
Core excitation effects in structure and reactions

Abstract

Breakup experiments provide useful spectroscopic information of weakly-bound exotic nuclei. The extraction of structure information from these experiments is done by comparing the data with some reaction model, such as semiclassical, adiabatic, DWBA or CDCC, among others. Many of these methods make use of few-body picture of the weakly-bound system. The validity of this picture relies on the assumption that the reaction dynamics is dictated by the degrees of freedom corresponding to the relative motion between the constituents, which are considered inert themselves.Consequently, these methods ignore possible excitations of the clusters constituents. For example, within this picture, the breakup of a halo nucleus is described in terms of excitations of the valence particle(s) outside an inert core, thus ignoring transitions between different core states during the collision as well as admixtures of core excited components in the states of the weakly-bound nucleus. These simplifying assumptions are not expected to be accurate when the clusters are deformed. In this case, in addition to the valence excitation, the interaction with the target can induce the dynamic excitation of the core. Moreover, the core-excited admixtures are important to describe the structure of the states of these systems and, therefore, it is not obvious that a simple single-particle model will be able to account properly for the transitions what will occur among these states during the collision. In this seminar, we discuss the role of core excitation in the scattering of halo nuclei and present new theoretical developments to account for these effects, from a simple no-recoil DWBA model to the more sophisticated continuum-discretized coupled-channels method. The models are applied to several breakup reactions induced by ^{11}Be and ^{19}C nuclei and compared with available data. The calculations evidence very clearly the importance of core excitation in the scattering of halo nuclei.

Mon 16-Sep-2013
S.Adrian
Acoustics Activities in Spain for the KM3NeT

Fri 20-Sep-2013
G.Battistoni
Il codice di simulazione Monte Carlo FLUKA e le sue applicazioni in Adroterapia

Tue 24-Sep-2013
L.Trache
Scientific director IFIN-HH - Presentation of IFIN-HH, Bucharest: past, present and mostly future

Abstract

I am going to present the "Horia Hulubei" National Institute for Physics and Nuclear Engineering (IFIN-HH in Romanian), the largest and most powerful research institution in Romania. I will tell briefly about its past, then talk about the present facilities and research. We have a broad range of activities, from those specific to a national nuclear physics laboratory, to theoretical physics and fundamental and applicative nuclear physics research. While the tandem accelerator of 9 MV is older and known to some of you at LNS for its research program in nuclear structure and reactions, two newer tandetrons, of maximum voltage 3 MV and 1 MV respectively, may be less known. These are meant for applications in Ion Beam Analysis and AMS forusers in Romania and South-Eastern Europe. Two cyclotrons, a strong gamma irradiator are used for applications, including studies of medical radioisotopes, the study and preservation of cultural heritage and environmental studies.The future is in the use of the current facilities, but also in ELI-NP, an European facility built in the back of our institute. I will present it shortly and talk about some of its challenges. Throughout the presentation I will insist on the possibilities to enlargeand strengthen the collaboration between LNS and IFIN-HH.

Tue 15-Oct-2013
M.Colonna
Reazioni nucleari dalla barriera Coulombiana alle energie di Fermi: sinergia tra teoria ed esperimento

SEMINARS

Abstract

Verranno discussi alcuni approcci teorici che consentono di descrivere le proprieta' di sistemi complessi a molti corpi, quali i nuclei, e le reazioni che li coinvolgono. Da questo studio, a partire dal confronto frateoria ed esperimenti di reazioni fra ioni pesanti, emergono informazioni su proprieta' fondamentali dell'interazione nucleare, in varie condizioni di densita', temperatura, asimmetria di carica. Questi ingredienti sono alla base della comprensione di alcune caratteristiche dei nuclei esotici e del comportamento delle stelle compatte, dove si trova materia nucleare in condizioni estreme

Tue 22-Oct-2013
G.Pappalardo
I ruggenti anni 50 della Fisica catanese

Tue 22-Oct-2013
D. Lacroix
Pairing effects on nuclear dynamics: illustration on collective motion, transfer and fusion reactions.

Abstract

The effect of pairing on small and large amplitude dynamics is discussed using a fully microscopic theory based on a simplified BCS version of the Time-Dependent Hartree-Fock Bogolyubov (TDHFB) theory [1]. This approach is rather versatile and allows describing both the collective vibrations of a single nuclei or the collision between two heavy ions partners. The isoscalar and isovector Giant Quadrupole Resonance (GQR) is systematically investigated in spherical nuclei. Around 300 nuclei have been considered over the nuclear charts. This study provides a benchmark for the time-dependent approach and shows that it is able to properly describe the energy of both low lying and high-lying states but misses the description of the damping effect, similarly to QRPA [2]. We will see how the simultaneous measurement of isoscalar and isovector GQR can be used as a tool to get the density dependence of the symmetry energy. The time-dependent approach is also used to describe nuclear reactions near the Coulomb barrier. The influence of pairing correlations on multi-nucleon transfer is studied for reactions around the Coulomb barrier energy [3].The analysis of small and large amplitude dynamics demonstrates that the present description of a many-body system with pairing, similarly to the original TDHF can describe mean properties in collective space but underestimate quantum fluctuations. We have recently shown that a stochastic mean-field (SMF) approach where the TDHFB evolution is generalized to include initial fluctuations in collective space can provide a practical solution to this problem in superfluid systems [4]. This approach will be illustrated.

Thu 5-Dec-2013
Ferenc Nagy
Need for speed. The picoSEC project for Ultra Fast Photon Detection

Thu 5-Dec-2013
L.Pandola
Search for neutrinoless double beta decay of 76Ge with the GERDA experiment at LNGS

Abstract

The GERmanium Detector Array (GERDA) experiment at the Gran Sasso Laboratory (LNGS) of INFN is searching for the neutrinoless double beta decay of 76Ge, i.e. 76Ge → 76Se + 2e-. The neutrinoless double beta decay has been searched for in many nuclei, and the lower limits of the half-lives are of the order of 1024-1025 yr. While the neutrino-accompanied version of the double beta decay is an allowed (and rare) process in the Standard Model of particle physics, the neutrinoless double beta decay is forbidden because of the violation of the lepton number conservation. The observation of this nuclear process, which is predicted by models beyond the Standard Model, would imply that neutrinos have a Majorana mass component. Provided that the exchange of light Majorana neutrinos is the leading mechanism of neutrino-less double beta decay, measuring or constraining the half-life sheds also light on the absolute neutrino mass scale.The experiment makes use of high-purity Germanium (HPGe) made of material isotopically enriched in 76Ge. The detectors are operated naked in liquid argon, which serves as cooling medium and as passive shielding against the external radiation. The GERDA setup is complemented by a 5m-thick water buffer, which is equipped with photo-multipliers and operated as a Cherenkov muon veto. The experimental signature for the neutrinoless double beta decay is a mono-energetic peak at the Qββ-value of the 76Ge decay (2039 keV).The first phase of the experiment was recently completed and the upgrade to the second phase, with increased detector mass and reduced background, is ongoing at LNGS.The Phase I data used for the analysis for the search of neutrinoless double beta decay was collected between November 2011 and May 2013 with a total exposure of 21.6 kg·yr. A blind analysis has been performed and all calibrations and event selection criteria had been finalized before the data were processed in the blinded 10 keV window around the Qββ-value of the 76Ge decay. A new measurement of the half-life of the neutrino-accompanied double beta decay of 76Ge is presented. Comments will be made about the possible synergies with nuclear physics experiments, to improve the knowledge of the nuclear matrix elements and to provide data to benchmark theoretical calculations.

Wed 15-Jan-2014
F.A. Volpe
Introduzione alle onde di Bernstein

Thu 16-Jan-2014
F.A. Volpe
Ricerca su plasmi magnetizzati e fusione controllata alla Columbia University

SEMINARS

Abstract

Con la costruzione del tokamak internazionale ITER ormai ben avviata, è quanto mai importante dirimere gli ultimi nodi che ne possano prevenire il successo, cosí com'è importante discutere il passo seguente, che potrebbe essere un reattore dimostrativo di tipo stellarator. Per tali ragioni, Columbia University conduce esperimenti di controllo di instabilitá magnetoidrodinamiche sia presso il tokamak HBT-EP da essa operato, sia presso il DIII-D National Fusion Facility. La Columbia opera inoltre uno stellarator (CNT) ed ha recentemente ultimato la costruzione di un ibrido tokamak-stellarator (CIRCUS). Una macchina lineare (CLM) e due dipoli magnetici (CTX e LDX, quest'ultimo sito presso il MIT) completano il quadro delle attivitá sperimentali presenti che verranno passate in rassegna in questo seminario. Si accennerá anche a sviluppi futuri, in particolar modo alla prima Electron Cyclotron Resonance Ion Source (ECRIS) toroidale.

Fri 7-Feb-2014
F. Cappuzzello
Reazioni nucleari come strumento per la determinazione della massa del neutrino
L. Calabretta Parte1
Ciclotrone di alta intensità per radioisotopi e fisica fondamentale
L. Calabretta Parte 2
Possibili scenari di potenziamento degli acceleratori dei LNS

Wed 12-Feb-2014
Hakan Cetinkaya
Turkish Accelerator Center – Proton Accelerator project

Fri 14-Feb-2014
S.Sanfilippo
Presentazione software della tecnologia open-source Redis

Fri 21-Mar-2014
M.Bicchieri
Ospiti inattesi all'interno dei materiali librari e loro riconoscimento non distruttivo

Thu 17-Apr-2014
J.Formaggio
The Quest for Neutrino Masses" Part I: Cosmology, Oscillations and Direct Neutrino Mass Measurements.

Abstract

Neutrino mass has been a perplexing and subtle puzzle in our understanding of the Standard Model of particle physics. In this talk, I will review the various ways physicists have tackled the question of neutrino mass, with particular emphasis on the role that cosmology and nuclear physics have played in this quest

Fri 18-Apr-2014
J.Formaggio
The Quest for Neutrino Masses. Part II: The Future of Neutrino Mass Measurements

Abstract

The shape of the beta decay energy distribution is sensitive to the mass of the electron neutrino. Attempts to measure the endpoint shape of tritium decay have so far seen no distortion from the zero-mass form, thus placing an upper limit. Here we show that a new type of electron energy spectroscopy could improve future measurements of this spectrum and therefore of the neutrino mass. We propose to detect the coherent cyclotron radiation emitted by an energetic electron in a magnetic field. For mildly relativistic electrons, like those in tritium decay, the relativistic shift of the cyclotron frequency allows us to extract the electron energy from the emitted radiation. As the technique inherently involves the measurement of a frequency in a non-destructive manner, it can achieve a high degree of precision. In this talk, we present the status of the first prototype and discuss the long-term plans of the experimental program.

Mon 5-May-2014
M.Di Toro
Reazioni fra ioni pesanti ed Equazione di Stato nucleare: The Catania Mean Field Road Map

Mon 5-May-2014
S.Cavallaro
Rivelazione dei neutroni emessi nella fusione prodotta nei plasmi-laser

SEMINARS

Thu 15-May-2014
P.Desiati
High energy neutrinos and cosmic rays with the IceCube Observatory at the South Pole

Abstract

IceCube is currently the largest observatory dedicated to the detection of high energy neutrinos. It is located at the Geographic South Pole and it is buried under the antarctic ice between 1400 and 2400 meters depth. It consists of over 5000 optical sensors, optimized to detect Cherenkov light emitted by charged particles produced by neutrino interactions. In combination with other cosmic messengers, such as gamma rays, neutrinos can unravel one of the greatest mysteries of astrophysics: the origin of cosmic rays, still a mystery after 100 years after their discovery. IceCube has also a km2 surface array dedicated to the indirect detection of primary cosmic rays at the knee and above. I will talk about the most recent results on the detection of high energy neutrinos and about the exciting birth of neutrino astrophysics we are witnessing. I will also show the results on cosmic ray spectrum, composition and anisotropy, and discuss what they can possibly mean in the context of cosmic ray origin and propagation

Tue 20-May-2014
F.Iachello
The double beta decay

Tue 20-May-2014
J.Yeck
The ESS project : status and perspectives

Wed 4-Jun-2014
G.Torrieri
Event by Event fluctuating initial conditions on the collective dynamics observed in heavy-ion collisions

Fri 4-Jul-2014
L.Conradie
New developments at iThemba LABS

Abstract

The main activities of iThemba LABS, a multi-disciplinary research centre situated near Cape Town in South Africa, are provision of beams of accelerated charged particles, using three cyclotrons and two Van de Graaff accelerators, for nuclear physics research, neutron therapy, proton therapy and the production of radionuclides for hospitals and industry. An overview of the accelerator facilities will be given and new developments at the laboratory will be discussed. The status of the newly developed low-level RF control system, the construction of a new ECR ion source, a beam phase measuring system, comprising of 21 fixed probes, for the separated-sector cyclotron and an RF amplitude and phase monitoring system for 16 RF systems are some of the developments that will be covered. Plans for a radioactive ion beam facility and the upgrading of the two electrostatic accelerators will also be discussed.

Mon 7-Jul-2014
R.A. Broglia
Pairing in nuclei

Thu 10-Jul-2014
M.Borghesi, D.DoriaIon
Ion acceleration by high power lasers: state of the art and experimental progress

Tue 15-Jul-2014
S.Kubono
Development of AVF cyclotron, RI beam separator and astrophysics experiments in RIKEN

Tue 9-Sep-2014
C.Kopper
The IceCube Detector and its Future High- and Low-Energy Extensions

Fri 12-Sep-2014
C.Kopper
Recent results from IceCube

Mon 22-Sep-2014
K.Janssens
New (X-ray based) ways of elemental and chemical imaging of cultural heritage artefacts

SEMINARS

Tue 23-Sep-2014
K.Janssens
Alteration and degradation of artists' pigments and related archaeological materials

Wed 24-Sep-2014
Ming-Hua Weng
Vacuum fluctuation effects on asymmetric nuclear matter

Thu 16-Oct-2014
Hua Zheng
Density and temperature from quantum fluctuation

Mon 20-Oct-2014
A.Radovinsky
New Magnet for the LNS Superconducting Cyclotron

Wed 10-Dec-2014
A.Bonasera
Dalla dinamica delle stelle alle centrali nucleari a fusione

Abstract

Utilizzando laser di alta potenza e' possibile riprodurre condizioni tipiche delle stelle ed, in alcuni casi, nella nucleosintesi del Big Bang. Per primi abbiamo dimostrato che e' possibile misurare le probabilità di fusione direttamente in tali sistemi complessi. La comprensione dettagliata dei vari meccanismi in gioco permette non solo di fare ricerca di base ma anche applicazioni di interesse generale come per esempio le centrali nucleari a fusione ed altro in particolare in medicina. I nostri risultati sperimentali e teorici possono essere realizzati alla National Ignition Facility (NIF) in California, il più' grande laboratorio di laser al mondo con circa 200 laser per una energia totale superiore a 1.6 MegaJoule (MJ) in 3 nanosecondi (ns).

Wed 17-Dec-2014
K.Schulte
Studies on electron cloud dynamics for an optimized space charge lens performance

DEGREES THESES

Carmen Loredana Altana
Title: Spettroscopia X ad alta risoluzione spaziale ed energetica di plasmi eccitati da microonde.
Tutors: A. Musumarra, S. Gammino, D. Mascali, F.P. Romano
University of Catania 2013

Stefano Burrello
Title: Effetti del Pairing sull'Instabilità Spinodale in Materia Nucleare Asimmetrica
Tutors: V. Greco, M. Colonna, F. Matera
University of Catania 2013

Brunilde Gnoffo
Title: Studio delle reazioni 78,86 Kr+ 40,48Ca a 10 AMeV con il multirivelatore CHIMERA ai Laboratori Nazionali del Sud
Tutors: G. Politi, S. Pirrone
University of Catania 2013

Valentina Marchese
Title: Sviluppo e implementazione di sistemi dosimetrici per l'analisi di effetti radiobiologici indotti da adroni su cellule neoplastiche
Tutors: L. Calabretta, G.Cuttone, G.A.P. Cirrone, A. Ristic Fira, I. Pedrovic
University of Catania 2013

Eugenia Naselli
Tittle: I reattori nucleari: dal reattore termico ai sistemi ADS
Tutors: F. Rizzo, R. Alba
University of Catania 2013

Dario Nicolosi
Title: Evidence of Nuclear Rainbow in the 16O + 27Al elastic scattering @ 280 MeV"
Tutors: F. Riggi, F. Cappuzzello, D. Carbone
University of Catania 2013

Lucia Oliva
Title: Termodinamica del Quark-Gluon Plasma in un Modello a Quasiparticelle Accoppiate al Polyakov Loop
Tutors: V. Greco, M. Ruggieri
University of Catania 2013

Pietro Pisciotta
Title: Tecniche dosimetriche per fasci di protoni accelerati tramite interazione laser-target
Relatore: L. Calabretta Correlatori: G.A.P. Cirrone e F. Romano
University of Catania 2013

Claudia Rocca
Title: Approccio multidisciplinare per lo studio della presenza dei delfinidi nel golfo di Catania
Tutors: G. Bellia, C. Giacoma, F. Caruso, E. Papale, G. Riccobene
University of Catania 2013

Danila Scandura
Title: Rilevazione di presenze di capodogli (Physeter Macrocephalus L. 1758) nel mar Ionio
Tutors: G. Bellia, G. Riccobene
University of Catania 2013

Agata Trovato
Title: Development of reconstruction algorithms for large volume neutrino telescopes and their application to the KM3NeT detector
Tutors: A. insolia, R. Coniglione, P. Sapienza;
University of Catania - PhD 2013

Rosario Andolina
Title: Simulazione di Rivelatori a strip di Silicio per studi di correlazioni particella-particella.
Tutors: F.Rizzo, G.Verde
University of Catania 2014

From left to right: Carmen Loredana Altana, Vanessa Brio, Stefano Burrello, Carlo Cuppari, Giuseppe D'Agata, Daniele Dell'Aquila, Andrea Gagliano, Brunilde Gnoffo, Valentina Marchese, Giuliana Giuseppina Milluzzo, Eugenia Naselli, Dario Nicolosi, Lucia Oliva, Pietro Pisciotta, Chiara Platania, Donatella Sinatra, Agata Trovato.

Mario Battiato
Title: Descrizione della fase progettuale della nuova sorgente di ioni AISHa per adroterapia oncologica. -
Tutors: A. Musumarra, L. G. Celona, D. Mascali
University of Catania 2014

Vanessa Brio
Title: Sistema ottico di osservazione e analisi delle distribuzioni spaziali di un fascio di protoni per radioterapia oculare
Tutors: F. Rizzo, F. Romano
University of Catania 2014

Mario Bruno
Title: Studio della correlazione gamma-particelle con il Multirivelatore CHIMERA ai Laboratori Nazionali del Sud
Tutors: F. Rizzo, G. Cardella
University of Catania 2014

Carlo Cuppari
Title: Progettazione di una linea per il trasporto e la dosimetria di fasci di protoni accelerati attraverso interazione laser-materia
Tutors: A. Musumarra, F. Romano
University of Catania 2014

Giovanni D'Agata
Title: Simulazione termomeccanica tramite codice fem della camera del plasma di una sorgente di protoni
Tutors: A. Musumarra, D. Mascali, L. Neri
University of Catania 2014

Giuseppe D'Agata
Title: Misura della sezione d'urto 19F(α, p)22Ne con il metodo del Cavallo di Troia nel contesto astrofisico
Tutors: C. Spitaleri, R. G. Pizzone
University of Catania 2014

Daniele Dell'Aquila
Title: Studio della struttura a cluster di 16C e 10Be tramite break–up indotto su target CH2 /CD2 ai LNS
Tutors: F. Rizzo, G. Cardella, I. Lombardo
University of Catania 2014

Francesco Di Blasi
Title: Progettazione meccanica preliminare di un ciclotrone per la produzione di radioisotopi
Tutors: A. Musumarra, D. Cittadino
University of Catania 2014

Andrea Gagliano
Title: Progettazione di un sistema di raffreddamento per le cavità RF di un ciclotrone per la produzione di radioisotopi
Tutors: A. Musumarra, M. Costa
University of Catania 2014

Federico La Paglia
Title: Gui and real-time analysis of undersea acoustic data for the european multidisciplinary seafloor observatory and km3 neutrino telescope projects
Tutors: A. Musumarra, G. Riccobene, C. Pellegrino
University of Catania 2014

Giuliana Giuseppina Milluzzo
Title: Monte Carlo simulation and experimental tests of a Faraday Cup for absolute dosimetry with high pulsed ion beams
Tutors: F. Rizzo, G.A.P. Cirrone, F. Romano, V. Scuderi
University of Catania 2014

Chiara Platania
Title: Il Multi-Threading nel codice di simulazione Montecarlo Geant4
Tutors: A. Musumarra, F. Romano
University of Catania 2014

Donatella Sinatra
Title: Fem thermomechanical simulation of a metal vaporizing equipment embedded in an ion source
Tutors: A. Musumarra, L. Neri, D. Mascali, S. Gammino
University of Catania – PhD 2014

Maria Fisichella
Title: The development of experimental techniques to investigate sub-barrier fusion reactions induced by weakly bound nuclear beams
Tutors: L. Torrisi, M. Lattuada
University of Messina 2014

Laura Francalanza
Title: Exploring Central Collisions in the Reaction 58Ni+48Ca at 25 AMeV with CHIMERA
Tutors: A.Pagano, F.Rizzo
University of Catania - PhD 2014

Events

Tue 29-Jan-2013
ESS Warm linac meeting

Tue 19-Feb-2013
Olimpiadi di fisica

Tue 5-10 Mar-2013
Mostra interattiva di scienze, sperimentare giocando-conoscere sperimentando "Il mondo dei Suoni"

Sun 10-Mar-2013
Inquinamento ambientale da radon

Mon 18-22 Mar-2013
Settimana della Cultura Scientifica e Tecnologica

Wed 10-Apr-2013
Workshop NI: Build Your Own Embedded System per la progettazione embedded basata su FPGA con l'utilizzo di hardware NI RIO (Reconfigurable I/O)

Mon 13 May 2013
Meeting progetto !CHAOS

Mon 27-31 May 2013
Final technical meeting on "Microanalytical Techniques based on Nuclear Spectrometry for environmental monitoring and material studies" (IAEA coordinated research project 1576)

Thu 30-May-2013
Città della Scienza: una vetrina della creatività

Wed 5-Jun-2013
Il Corso AIFM - Modelli predittivi degli effetti della radioterapia con fasci esterni

Wed 19-21 Jun-2013
LNS PAC Meeting

Mon 24-Jun-2013
KM3Net collaboration meeting

Thu 27-Jun-2013
Meeting on the ESS Ion Source and LEBT: Integration 2

Fri 12-Jul-2013
I progetti Europei KM3NeT ed EMSO

Fri 19-Jul-2013
User Selection Panel di ENSAR

Wed 4-Sep-2013
XXXIII Convegno Nazionale SISFA

Sun 15-27 Sep-2013
7th European Summer School on Experimental Nuclear

Tue 8-Oct-2013
SPES- oneday workshop "Isospin on reaction mechanism with

Events

Tue 8-Oct-2013
ENSAR

Fri 18-Oct-2013
"E. Majorana" International workshop on underwater acoustic

Tue 22-Oct-2013
“I ruggenti anni ’50 della Fisica Catanese”

Tue 5-Nov-2013
WPCF 2013 - IX Workshop on Particle Correlations and

Thu 14-Nov-2013
Il nuovo programma HORIZON 2020

Fri 22-Nov-2013
Conferenza Nazionale delle Infrastrutture di Ricerca

Mon 25-Nov-2013
Meeting WG-KM3NeT di acustica

Fri 6-Dec-2013
LNS Users Meeting

Thu 12-Dec-2013
Elimed meeting

Wed 15-Jan-2014
INFN-Energia e Industria verso Horizon 2020 e nuovi mercati

Tue 18-Feb-2014
Olimpiadi di fisica

Wed 5/10 - Mar-2014
Mostra Sperimentare giocando conoscere sperimentando il mondo dei suoni

Wed 19-Mar-2014
LabView FPGA

Mon 31-Mar-2014 - Mon 7-Apr-2014
Settimana Cultura Scientifica e Tecnologica

Mon 31-Mar-2014
Erasmus Intensive Programm MANTRA

Tue 15-Apr-2014
Riunione Comitato Trasferimento Tecnologico INFN

Wed 16-Apr-2014
Tavola Rotonda Trasferimento Tecnologico INFN

Tue 6 / 9-May-2014
IWM-EC 2014 International Workshop on Multi facets of Eos and Clustering

Events

Tue 27-May-2014 - Fri 30-May-2014
Workshop della Commissione Calcolo e Reti dell'INFN

Wed 23-Jul-2014
Riunione Nazionale Gruppo 5

Mon 28-Jul-2014
Sicily-East Asia Workshop - Low Energy Nuclear Physics

Tue 16-Sep-2014
Presentazione annullo filatelico speciale infn "Le eccellenze del Sapere"

Fri 26-Sep-2014
Notte Europea dei Ricercatori

Tue 30-Sep-2014
RICAP-14

Mon 20-Oct-2014
Riunione CVI

Mon 10 / 14-Nov-2014
IV Seminario Nazionale Rivelatori Innovativi

Mon 17-Nov-2014
2nd GEANT4 international school and ROOT analysis concepts

Mon 24-Nov-2014
n-tof meeting

Wed 26-Nov-2014
Km3Net collaboration meeting

Tue 2-Dec-2014
LNS users meeting

Sat 13-Dec-2014
Il Mediterraneo e la Sicilia: un laboratorio di accoglienza e scienza

ISTITUTO NAZIONALE DI FISICA NUCLEARE
LABORATORI NAZIONALI DEL SUD
ACTIVITY REPORT 2013/2014

LNS ACTIVITY PHOTO GALLERY

3,6 MeV
90 MeV
2000 MeV
ESS - The INFN contribution
INFN has been involved in the Design Update phase (2011-12), for several components of the LINAC, and it is involved in the next phase, aimed to the construction of prototypes
The Proton source
The LEBT
The Drift Tube Linac
The Superconducting elliptical cavity @ high energy section
INFN

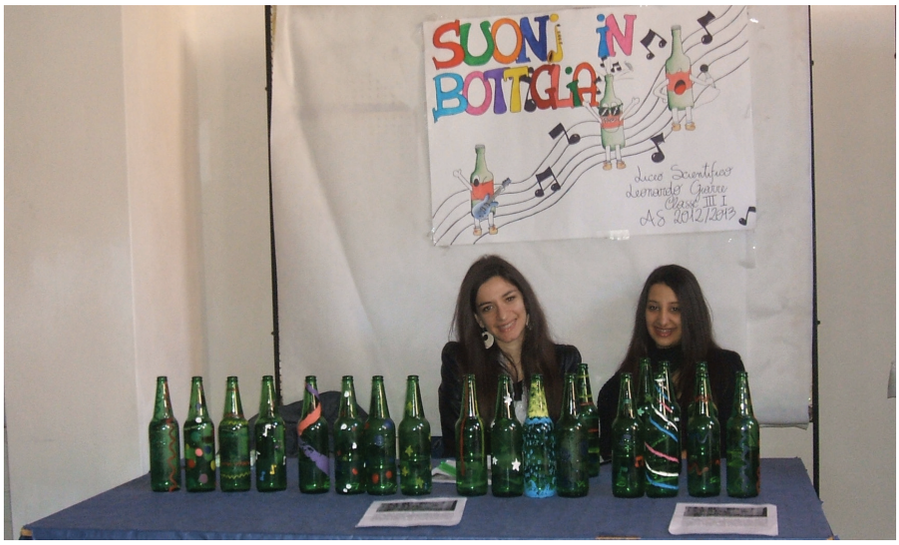

Tue 5-10 Mar-2013 Mostra interattiva di scienze,
sperimentare giocando-conoscere sperimentando "Il mondo dei Suoni"

Il Radon è un gas radioattivo più pesante dell'aria, incolore, inodore, chimicamente inerte, praticamente impercettibile senza adeguati sistemi di rilevamento. Proviene prevalentemente da terreni con un elevato contenuto di Uranio/Radio quali tufi, pozzolane, alcuni graniti e rocce di origine vulcanica. Il Radon 222, il principale isotopo di questo gas, è il prodotto del decadimento dell'Uranio 238. Mentre gli altri elementi della serie radioattiva sono solidi, il Radon è un gas e, in quanto tale, può infiltrarsi attraverso fessure e crepe, attraversare materiali porosi, dissolversi nell'acqua e penetrare così negli edifici anche attraverso le condutture idriche.
Una volta accumulatosi, il Radon può essere respirato e continuare la serie radioattiva all'interno dell'organismo, con grande danno alla salute, aumentando il rischio di sviluppare neoplasie polmonari. Studi epidemiologici diffusi dall'Organizzazione Mondiale della Sanità (OMS) e dall'Agenzia Internazionale per la Ricerca sul Cancro (IARC) hanno, infatti, ormai scientificamente stabilito la cancerogenicità di questo gas.
Sul territorio nazionale, si stima che circa il 10%-30% dei carcinomi polmonari sia imputabile al Radon che risulta essere la seconda causa di tumore al polmone dopo il tabacco.

La permeabilità del suolo, la struttura geomorfologica del terreno e le caratteristiche costruttive dell'edificio determinano la quantità di Radon che giunge in superficie e che si annida nei fabbricati. Il Radon rappresenta un fattore di rischio rilevante per circa 1 milione di edifici in tutta Italia.
Anche i materiali per l'edilizia emettono diverse quantità di radiazioni, a seconda della zona di provenienza. Alcuni materiali da costruzione (granito, tufo, porfido, basalto, cementi pozzolanici ecc.) contengono più radiazioni di altri. Pertanto la scelta dei materiali edilizi più idonei andrebbe effettuata solo dopo la valutazione di un esperto dotato di specifiche apparecchiature. Una volta accertata la sua eventuale presenza nell'edificio e la sua concentrazione media annuale, è possibile diminuire la sua pericolosità con una serie di accorgimenti tecnici adottati nelle metodiche di bonifica.

Radioattività da Gas Radon (Bq/mc)

THE INTERNATIONAL ASSOCIATION OF LIONS CLUBS
DISTRETTO 108 Yb Sicilia
IV e V Circoscrizione
Anno sociale 2012-2013
Governatore: dott. Antonio Pogliese
"Dall'Associazionismo alla Società Civile: dalle analisi alle proposte"

SERVICE INTERCLUB
"EDUCAZIONE ALL'AMBIENTE E ALLA SOSTENIBILITA'"

LIONS CLUBS:

CATANIA HOST
PATERNO'
ADRANO – BRONTE - BIANCAVILLA
CATANIA ETNA
RANDAZZO
CATANIA NORD
CATANIA BELLINI
CATANIA GIOENI
CATANIA STESICORO CENTRUM
CATANIA RIVIERA DELLO IONIO N. C.
CATANIA FARO BISCARI
CATANIA AGORA'
CATANIA MEDITERRANEO

INQUINAMENTO AMBIENTALE DA RADON
RISCHIO PER LA SALUTE: PREVENZIONE E BONIFICA

I.N.F.N – Laboratori Nazionali del Sud
Catania – Via Santa Sofia, 62
Domenica, 10 Marzo 2013 – Ore 09,15

PROGRAMMA DEI LAVORI

Ore 09,15 - ACCOGLIENZA

Ore 09,45 – APERTURA DEI LAVORI E INDIRIZZI DI SALUTO:

Notaio Maria Grazia Tomasello
Presidente IV Circoscrizione -Distretto Lions 108 Yb

Dott. Giuseppe Spampinato
Presidente V Circoscrizione - Distretto Lions 108 Yb

Dott. Giacomo Cuttone
Direttore Laboratori Nazionali del Sud–INFN – Catania

Ing. Carmelo Maria Grasso
Presidente Ordine Ingegneri Provincia di Catania

Avv. Raffaele Stancanelli
Sindaco di Catania

INTRODUCE E MODERA

Dott. Luigi Savarino
Biologo - Consulente del Distretto Lions 108 Yb
per l'Area "Ecologia – Ambiente – Energia"

RELATORI

Prof. Claudio Spitaleri
Ordinario di Fisica Nucleare – Università di Catania
Ricercatore INFN - Laboratori Nazionali del Sud

Prof. Michelangelo Maria Di Salvo
Direttore U. O. C. Angiologia Med.- Az. Policlinico CT
Specialista in Medicina del Lavoro
Coord. Area Sanità Pubblica Distretto Lions 108 Yb

Architetto Anna Carulli
Coordinatore INBAR – Sicilia
INBAR – Istituto Nazionale di BioArchitettura

INTERVENTI PROGRAMMATI

Prof. Massimo Carpinelli
Presidente Comm. Scientifica Nazionale V° INFN
Ordinario di Fisica Applicata Università di Sassari

Dott.ssa Maria Cristina Reitano
Dirigente Fisico ARPA Sicilia – S.T. Catania

Ing. Biagio Ciarcià
Ingegnere civile edile – Libero professionista

Ore 12,45 Dibattito

Ore *13,00 Conclusioni*

Prof. ing. Santi Cascone
Assessore mobilita' e viabilità del Comune di Catania.

Dott Antonio Pogliese
Governatore del Distretto Lions 108 Yb - Sicilia

Ore *13,30 Cocktail*

R.S.V.P.
Luigi Savarino – Cell. 339 7595452
Silvana Grasso – Cell. 360 3077101

Ci è gradito invitare
la S.V. e gentile Consorte
al convegno
nell'ambito del Service Interclub
"Educazione all'Ambiente e alla Sostenibilità"
sul tema:

INQUINAMENTO AMBIENTALE DA RADON
RISCHIO PER LA SALUTE: PREVENZIONE E BONIFICA

I Presidenti

CATANIA HOST	*Ettore Toscano*
PATERNO'	*Placido Distefano*
ADRANO-BRONTE-BIANCAVILLA	*Alfio Platania*
CATANIA ETNA	*Paolo Amato*
RANDAZZO	*Giuseppe D'Amico*
CATANIA NORD	*Mario Distefano*
CATANIA BELLINI	*Ciro Mosca*
CATANIA GIOENI	*Francesco Pezzella*
CATANIA STESICORO C.	*Alessandro Pittari*
CATANIA RIVIERA IONIO	*Francesco Noto*
CATANIA FARO BISCARI	*Alberto Rovelli*
CATANIA AGORA'	*Luigi Savarino*
CATANIA MEDITERRANEO	*Francesca Dionisi*

LNS ACTIVITY PHOTO GALLERY

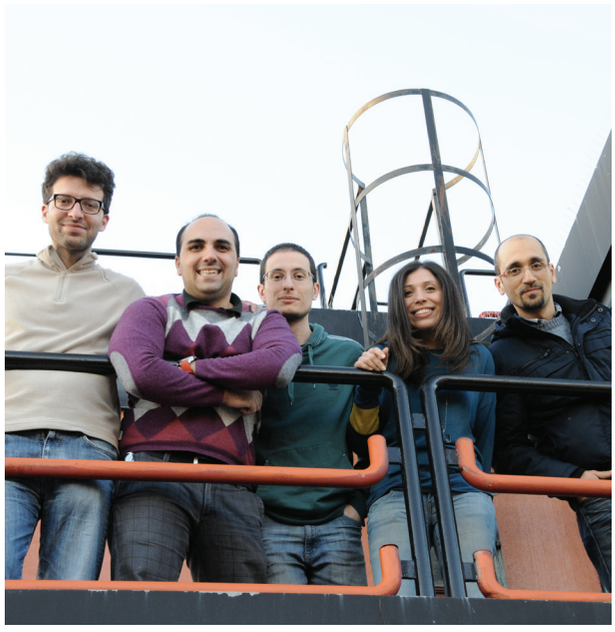

LNS ACTIVITY PHOTO GALLERY

Laboratori Nazionali del Sud, Istituto Nazionale di Fisica Nucleare

27 – 31 May 2013

IAEA

Third Research Co-ordination Meeting (RCM)
of the Co-ordinated Research Project (CRP)

Micro-analytical Techniques Based on Nuclear Spectrometry for Environmental Monitoring and Material Studies

Aifm
Associazione Italiana di Fisica Medica

Associazione Italiana di Fisica Medica

MODELLI PREDITTIVI DEGLI EFFETTI DELLA RADIOTERAPIA
CON FASCI ESTERNI - II ED

INFN-LNS, 5-6-7 giugno 2013

Finalità del corso

Le innovazioni tecnologiche introdotte negli ultimi anni nella Radioterapia a fasci esterni, sia dal punto di vista della erogazione della dose (IMRT, IGRT) che dal punto di vista della definizione dei volumi,, hanno stimolato la tendenza ad alterare gli schemi di frazionamento convenzionali, innalzando la dose totale e/o variando la dose per frazione e/o il tempo totale di trattamento.
Le variabili in gioco nella scelta della strategia terapeutica sono aumentate e non è più possibile prescindere dall'applicazione di modelli radiobiologici per predirne l'efficacia.
L'obiettivo di questo corso è quello di fornire le basi per comprendere lo scopo, le applicazioni e le limitazioni della modellizzazione e ottimizzazione radiobiologica dei trattamenti radioterapici.
Il primo giorno sarà focalizzato sulla risposta cellulare alle radiazioni e sui modelli di probabilità di controllo tumorale, incluso gli ultimi avanzamenti in campo modellistico e nella caratterizzazione genetica della radiosensibilità e della radioresistenza.
Nella seconda giornata saranno approfonditi i modelli predittivi della tossicità dei trattamenti per i tessuti sani, incluso gli ultimi avanzamenti nel campo degli effetti dose-volume, nell'impatto di variabili cliniche e genetiche e negli approcci statistici avanzati di "data mining"..
Nella giornata conclusiva saranno illustrati i principi dell'ottimizzazione radiobiologica dei trattamenti e gli approcci più avanzati della radioterapia a fasci esterni, basati appunto sui modelli predittivi, con particolare enfasi alle applicazioni nel campo della radioterapia adattiva.
Il corso è rivolto ai Fisici Medici e ai Medici Radioterapisti chiamati a raccogliere, in stretta collaborazione, la sfida della Radioterapia Moderna. Anche i tecnici TSRM possono sicuramente beneficiare dei contenuti del corso.

PROGRAMMA

Mercoledì 5 Giugno 2013
Introduzione e modelli degli effetti sul tumore

8:15 Registrazione Partecipanti
8:45 Presentazione del Corso
9:00 Radiobiology models in the era of High-Tech RT and genomics *A. Nahum (Clatterbridge, UK)*
9:45 Effetti dell'irraggiamento sui sistemi cellulari *F. Ballarini (Pavia)*
10:45 Coffee Break
11:15 Irraggiamento e crescita tumorale: riparo, ripopolamento, riossigenazione, radiosensibilità *A.Nahum (Clatterbridge, UK)*
12:15 Modello Lineare-Quadratico: applicazione pratica *M. Schwarz (Trento)*
13:00 Lunch
14:30 Modellizzazione della Tumor Control Probability *A.Nahum (Clatterbridge, UK)*
15:15 Caratterizzazione genetica di radiosensibilità e radio resistenza *M. Mangoni (Firenze)*
16:00 Coffee Break
16:30 Radiobiologia degli adroni per radioterapia *M. Durante (Darmstad DE)*
17:30 Modellizzazione della risposta tumorale in ipo-frazionamento spinto *G. Gagliardi (Stoccolma, SE)*
18.15 Fine lavori

Giovedì 6 Giugno 2013
Modelli della tossicità per i tessuti sani

8:30 Modelli predittivi della tossicità: una visione integrata *T. Rancati (Milano)*
9:10 Effetti dose-volume: metodi statistici per l'analisi dei dati clinici *L. Strigari (Roma)*
9:50 Modelli predittivi di rischio di tossicità: selezione delle variabili e stima della robustezza di un modello *M. Carrara, T. Rancati (Milano)*
10:30 Coffee Break
11:00 Modellizzazione della Normal Tissue Complication Probability *L. Strigari (Roma)*
11:45 Modelli avanzati di predizione delle tossicità a reti neurali *M. Carrara (Milano)*
12:30 Predittori genetici-molecolari delle tossicità e combinazione con parametri dosimetrici e clinici *T. Rancati (Milano)*
13:15 Lunch
14:30 Problematiche nella pianificazione e gestione di studi di tossicità con grandi popolazioni di pazienti *C. Fiorino (Milano)*
15:15 Revisione critica delle relazioni dose-volume: Testa-collo *S. Broggi (Milano)*
15:45 Revisione critica delle relazioni dose-volume: Torace-addome *G. Gagliardi (Stoccolma, SE)*
16:15 Coffee Break
16:45 Revisione critica delle relazioni dose-volume: Pelvi *C. Fiorino (Milano)*
17:30 Tossicità e frazionamenti alterati *G. Sanguinetti (Negrar, VR)*
18:00 Fine lavori

Venerdì 7 Giugno 2013
Modelli predittivi e ottimizzazione del trattamento

8:30 Modelli predittivi & Adaptive RT: una introduzione *V. Valentini (Roma)*
9:15 Imaging funzionale e "dose painting" *M. Brambilla (Novara)*
10:00 Coffee Break
10:30 Ottimizzazione radiobiologica dei trattamenti radioterapici *M. Schwarz (Trento)*
11:15 ART strategies to increase the local tumor control *J.J. Sonke (Amsterdam, NL)*
12:00 Modificazioni anatomiche per predire e misurare le tossicità in radioterapia ed implicazioni in ART *G. Sanguinetti (Negrar, VR)*
12:45 Lunch
14:15 Techniques of elastic registration and dose tracking: applications in the field of outcome prediction models *J.J. Sonke (Amsterdam, NL)*
15:00 "Molecular targeting": definizione di categorie di pazienti in base alla risposta predetta ed ottimizzazione del trattamento *M. Mangoni (Firenze)*
16:00 Discussione/dibattito
16:30 Test finale e chiusura del corso
17:00 Fine lavori

SI RINGRAZIA

TECNOLOGIE AVANZATE · tema SINERGIE · ELEKTA · ELSE · VARIAN medical systems

Portopalo 12 luglio 2013:
I progetti Europei Km3NeT ed EMSO. Gli osservatori abissali
al largo della Sicilia nuova frontiera per la ricerca e la tecnologia:
sinergie tra Enti di Ricerca, Università e Autorità Marittime"

The 7th European Summer School on Experimental Nuclear Astrophysics
September 15-27, 2013
Santa Tecla Palace Hotel, Sicily, Italy
Primordial Universe, Stellar Evolution and Nucleosynthesis, Direct and Indirect Measurements, Underground Experiments, Radioactive Ion Beams
Directors of the School
C. Rolfs (Bochum), C. Spitaleri (Catania)
Scientific Committee
M. Aliotta (Edinburgh)
M. Busso (Perugia)
A. Coc (Orsay)
M. El Eid (Beirut)
T. Kajino (Tokyo)
K.L. Kratz (Mainz)
S. Kubono (Tokyo)
K. Langanke (GSI)
J. José (Barcelona)
T. Motobayashi (RIKEN)
A. Mukhamedzhanov (TAMU)
E. Nappi (Bari)
O. Straniero (Teramo)
G. Rogachev (FSU)
L. Trache (Bucharest)
R. Tribble (TAMU)
M. Wiescher (Notre Dame)
Local Committee
R.G. Pizzone (chair)
G. Agnello
S. Hayakawa
V. Potenza
G.G. Rapisarda
M.L. Sergi
astro2013@lns.infn.it
agenda.infn.it/conferenceDisplay.pyconfid=5302
Scientific Secretary:
L. Lamia

2013

Experimental Nuclear Astrophysics
September 15-27, 2013
Santa Tecla Palace Hotel, Sicily, Italy
Primordial Universe, Stellar Evolution and Nucleosynthesis, Direct and Indirect Measurements, Underground Experiments, Radioactive Ion Beams
Local Committee
Scientific Secretary:

3° SPES ONE-DAY WORKSHOP
Isospin on reaction mechanism with RIBs
Catania 8-9 October 2013 *INFN-LNS*

Scientific Commitee

A. Covello	INFN-Sez. & Univ. Napoli
E. De Filippo	INFN-Sez. di Catania
F. Gramegna	INFN-LNL
G. La Rana	INFN-Sez. & Univ. Napoli
A. Pagano	INFN-Sez. di Catania
S. P.	INFN-Sez. di Catania
F. Rizzo	INFN-LNS & Univ. di Catania

Local Organizing Commitee

C. Agodi	INFN-LNS
G. Lanzalone	INFN-LNS & Univ. di Enna
S. P.	INFN-Sez. di Catania
G. Politi	INFN-Sez. & Univ. di Catania
P. Russotto	INFN-Sez. di Catania

Secretary

G. Agnello INFN-LNS - V.Potenza INFN-LNS

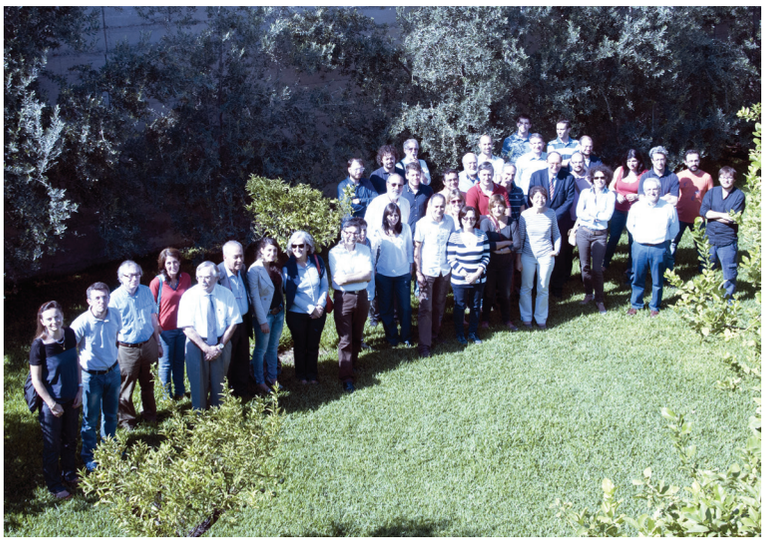

LNS ACTIVITY PHOTO GALLERY

Martedì 22 Ottobre 2013 ore 10:30
Sala Conferenze LNS
Prof.Giuseppe Pappalardo
"I ruggenti anni '50 della Fisica Catanese"

Cippitani
Di Gioacchino
Iozzolino
Studio Legale e Commerciale

EU CORE

Horizon 2020

Catania, 14-15 novembre 2013
Roberto Di Gioacchino & Irene Liverani

© EU CORE Consulting & Studio Cippitani Di Gioacchino Iozzolino
Diritti riservati e riproduzione vietata.
È inoltre vietato diffondere queste dispense attraverso la pubblicazione su siti internet

LNS Status in the National & International framework
WHAT NEXT@LNS?
Giacomo Cuttone
INFN – Laboratori Nazionali del Sud, Catania, Italy
INFN
LNS

NEC

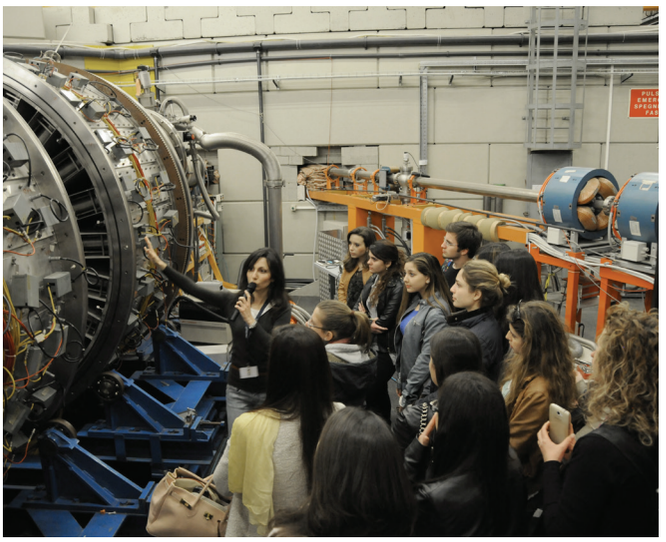

LNS ACTIVITY PHOTO GALLERY

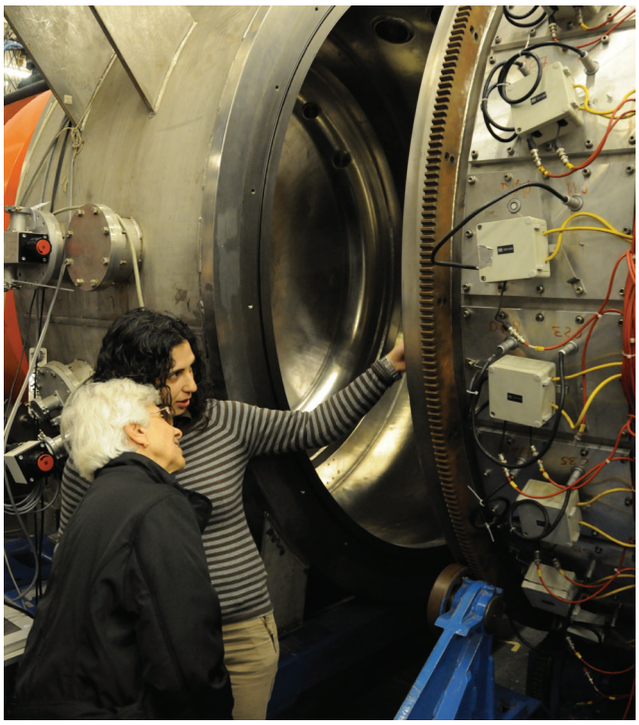

INFN
Istituto Nazionale di Fisica Nucleare

CICLOTRONE SUPERCONDUTTORE
Risultati CHIMERA

INFN
Istituto Nazionale di Fisica Nucleare

LNS ACTIVITY PHOTO GALLERY

Comune di Misterbianco
Assessorato Sviluppo Economico e delle Attività' produttive
Presidenza Consiglio Comunale
Promuove
Misterbianco
#fiera
EXPO INNOVATION
Ecosostenibilità - Energia rinnovabile - Tecno innovation
Game online - App online - E-commerce - Artigianato tecnologico
DAL 15 AL 18 MAGGIO 2014
Centro Storico, ingresso fiera: Via Gramsci
Notte Bianca
SABATO 17
dalle 20 alle 00
PRIMO
"RADUNO MUSICI DA STRADA"
Notte di musica, shopping e divertimento
MAKÉ TERRA
DOMENICA 18
piazza Mazzini
dalle 8 alle 20
Esposizione e degustazioni di prodotti biologici e naturalmente sani

Venus
Virtual Ambity Neural Unit System

ARIES
venus

LNS ACTIVITY PHOTO GALLERY

Ministero
dello Sviluppo Economico
Francobolli serie tematica
"le Eccellenze del sapere"
dedicati ai laboratori nazionali di
fisica nucleare facenti capo all'istituto
Nazionale di Fisica Nucleare:
Frascati - Gran Sasso - Legnaro
Laboratori del Sud.

LNS ACTIVITY PHOTO GALLERY

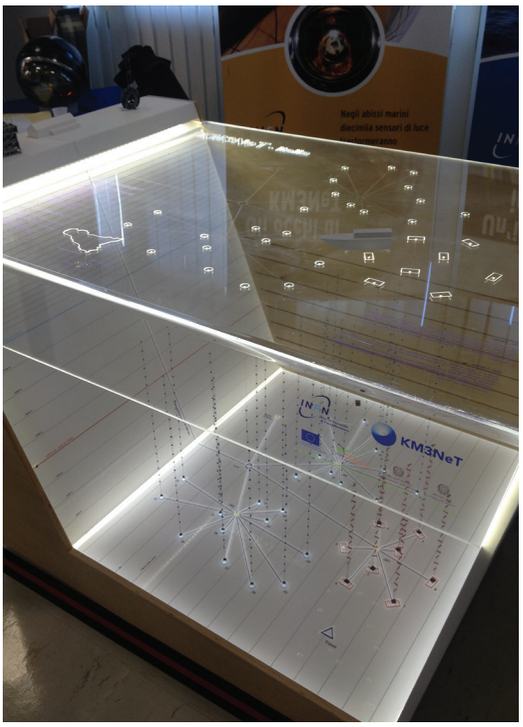
Negli abissi marini
decimila sensori di luce
KM3NeT

Notte Europea
dei Ricercatori
DREAMS European
Researchers' Night
Horizon 2020
INFN
Laboratori Nazionali del Sud
Catania 26 Settembre 2014 ore 18.00
INGRESSO LIBERO
Ospiti della manifestazione:
Beans
Liar Queen Tribute Band
Mario Tozzi
Gino Astorina
Trio Anima Mundi
Orchestra Falcone Borsellino
della Città Invisibile
Presenta: Ruggero Sardo
L'apprendista
Stregone
Fisica
Musica
Dibattito
Spettacolo
Esperimenti live
Annullo filatelico
Concorso artistico
foto poesia prosa
27/28 Settembre
Visite guidate
INFO
Laboratori Nazionali del Sud
Via S. Sofia, 62 - Catania
Tel. 095 542301
E-mail: nottericercatori@lns.infn.it
www.lns.infn.it
Seguici
anche su

LNS ACTIVITY PHOTO GALLERY

LNS ACTIVITY PHOTO GALLERY

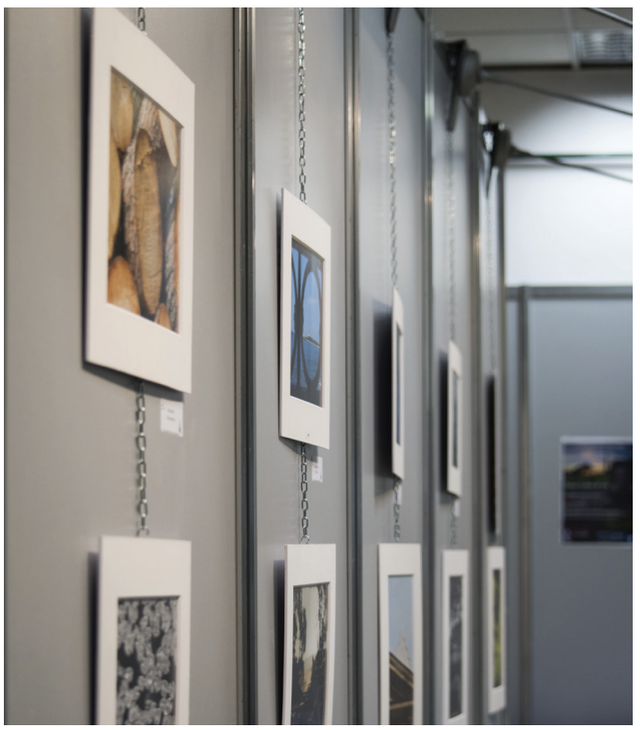

LNS
ACTIVITY
PHOTO
GALLERY

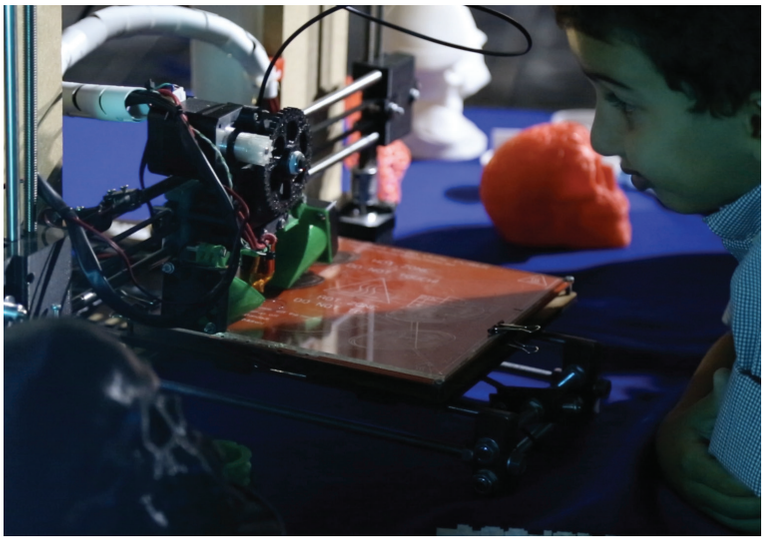

ORCA
INFN

Contest "InCantami, Galileo!": Scienza: la poesia nel reale

Concorso artistico (fotografia, poesia, prosa) organizzato dai Laboratori Nazionali del Sud per l'evento Notte dei Ricercatori. Sono stati invitati i partecipanti a mettere al centro il fascino della Scienza, intesa come strumento che l'uomo possiede per indagare la suggestiva armonia della Natura. I partecipanti sono quindi stati invitati a lasciarsi incantare da "Galileo" – che qui è metafora di Scienza – che fu protagonista dello straordinario cammino che ha portato la Fisica Sperimentale a scrutare l'infinitamente piccolo e l'infinitamente grande, disvelandone segrete simmetrie e mirabili strutture.

PER LA PARTE LETTERARIA:

Giuria:

- Margherita Verdirame, professoressa di Lettere all'Università di Catania
- Riccardo Orioles, giornalista e direttore de "I Siciliani giovani"
- Sergio Collura, critico letterario e docente di estetica

Primo Premio:

alle opere di **Gianluca Furnari**, nato il 23/03/1993, laureando in Lettere classiche, appassionato di poesia contemporanea sin dall'adolescenza già vincitore di borsa di studio al concorso di scrittura indetto dal Comune di Adrano in occasione del 150° anniversario dell'Unità d'Italia nel 2011, partecipa al Contest "InCantami Galileo" quale autore di due componimenti poetici dal titolo **"Avevamo abitato le scogliere"** e **"Il cammino (ovvero della conoscenza)"**, Queste due poesie spiccano per la loro forma simbolicamente suggestiva e per il contenuto di notevole profondità e rilevanza.

Avevamo abitato le scogliere

Avevamo abitato le scogliere
organogene, in forma di coralli,
ed i fondali, lungo le *rift valley*,
raccolti intorno a fumarole nere;

avevamo trasceso le frontiere
del mondo: correvamo gli intervalli
da stella a stella, eravamo nei metalli
di supernove, nelle nane nere;

ma vegliavamo immoti al capezzale
dell'astro tramontante, Omicron Ceti
(quattrocento anni luce di distanza),

persuasi che in questo esserci carnale
e nel nucleo scomposto dei pianeti
era un solo deserto, una sostanza.

Il cammino (ovvero Della conoscenza)

Di quel cammino che imboccammo
ricordi che alla vista
replicava i paesaggi, razionale:
ricordi le radure, gli infrangibili
assetti, quelle bocche febbricose
di fiumi che chiudevano città,
cimiteri impazienti

(noi duravamo) e me, che pedinavo
l'etimo della pietra,
che decrittavo il gergo delle luci,
nella speranza che ogni cosa a un tratto
ritornasse al suo posto.

«Ma questa terra simula alfabeti, –
dicevi – tesaurizza i proprî sensi.»
E mi indicavi sui sentieri spenti
quasi un residuo avaro
del mondo, fluttuante in superficie,
come la penna atrofizzata, infranta
di un lirico dimentico di sé.

Eppure sugli stagni
dove ci fermavamo nei mattini
intesi al freddo delle rive
qualcosa insorgeva, quasi un'anima
improvvisa, sommersa:

giustificava tutto.

Secondo classificato ex aequo:
all'opera **senza titolo** di **Flavia Maria Chiara Toscano**, Classe 1992. Laureanda in Lettere Classiche all'università di Catania, ha iniziato a coltivare la passione per la scrittura e la letteratura da bambina partecipando a concorsi di poesia scolastici e collaborando alla gestione di un giornale durante il liceo. Appassionata ad ogni genere di arte, spera di poter intraprendere un percorso lavorativo nel campo dell'Editoria.

Esempio di divulgazione per l'infanzia, godibile per la scorrevolezza della lingua e l'estrosità dello stile;

Avvicinate i polpastrelli del pollice e dell'indice di una stessa mano fino a farli sfiorare.
Quando Giove era piccolo così trascorreva intere giornate steso sul manto erboso del giardino di casa sua tentando di guardare il cielo sopra di lui… peccato, però, che il suo nome equivaleva alla disgrazia di un intero paese confinato ai confini d'Europa.
Infatti tutti gli abitanti di quel piccolo e caotico villaggio erano stati condannati da Giove stesso – non il bambino! La grande divinità dell'olimpo – a trascorrere i loro anni sulla terra senza poter mai alzare la testa verso l'alto. Per nessun motivo e in nessuna occasione. I più anziani, quelli che dovrebbero essere anche i più saggi, vivevano con la convinzione che tale misfatto funesto fosse stato mandato proprio a loro a causa di Giove – stavolta si parla del ragazzo! – perché portando, con quella poca grazia di cui era dotato, il nome del signore degli dei aveva arrecato una grande offesa a tutte le divinità.
Ma Giove, incurante di tutte le voci da villaggio, cresceva felice nella sua casetta arancione e quando ebbe conosciuto una bella donna, all'età giusta, si sposò e insieme ebbero cinque figli intelligenti, diligenti, alcuni un po' pigri ed uno in particolare troppo curioso. I loro nomi erano: Io, Europa, Ganimede, Callisto e Galileo.
Purtroppo quando la madre morì per cause misteriose, come succedeva in quel luogo e in quel tempo per le persone che in vita avevano goduto di una certa fama, sparivano al tramonto del loro ultimo sospiro e la moglie di Giove era stata famosa per la sua raffinata bellezza. E così anche lei sparì.
Su questo fenomeno nemmeno i più anziani osavano pronunciarsi e per lungo tempo rimase un mistero irrisolto. La vita nel villaggio però, immutabile di fronte a tutto, continuava e ormai più nessuno parlava del cielo sopra le loro teste. Nessuno più si chiedeva cosa ci fosse lassù dove non potevano guardare.
Solo Galileo, il più piccolo figlio di Giove, non smise di incuriosirsi e per non dimenticare ogni sua immaginazione, ogni sua idea, annotava tutti i suoi pensieri su dei quaderni logori con delle copertine rilegate in pelle.
-Ma tu hai mai visto il cielo?- chiedeva con innocenza al padre tutte le sere davanti al camino.
-Ti ricordi del profumo della mamma? E pensa anche al sapore della cosa più buona che hai mai assaggiato. E rifletti sui litigi coi tuoi fratelli. Pensa ai tuoi sogni. E chiudi anche gli occhi figlio mio: cosa riesci a vedere? Virgilio e Omero li ricordi?- rispondeva entusiasta, ma prima che il figlio potesse pronunciarsi nuovamente aggiungeva:
-Ecco, ragazzo. Tutto quello che sai e che ricordi, tutto quello che immagini e che ritieni impossibile è il cielo – Galileo però non capiva mai il significato di quelle parole, ma gli servivano giorno dopo giorno per riaccendere la fiammella della curiosità che ardeva sempre più prepotentemente.
-Io un giorno guarderò il cielo- affermava con impertinenza.
Il padre si preoccupava amaramente perché sapeva che nel villaggio nessuno avrebbe mai accettato che qualcun altro sfidasse il divino Giove, ma non riusciva a dire parole dure al figlio per ammonirlo severamente.
Così Galileo continuò a crescere, e ogni anno i suoi quaderni raddoppiavano.
Nel frattempo un'altra grande tragedia stava per abbattersi sulla famiglia di Giove.
Io, Ganimede, Europa e Callisto avevano contratto la stessa malattia della madre che lentamente, senza che nessuno se ne potesse accorgere prima, li stava portando alla morte.
-Giove salvali- invocava il pover'uomo, padre dei figli, disperato -Oppure uccidi pure me e la tua più grande offesa sarà estirpata-
E Giove, che a quel tempo tutti ascoltava e tutti esaudiva, concesse ai quattro ragazzi e al padre un ultimo respiro poco prima del tramonto.
Galileo aveva da poco intrapreso brevi viaggi oltre i confini del paese conosciuto alla ricerca di nuove risposte ai suoi innumerevoli interrogativi e quella sera, quando rientrò in casa subito dopo il tramonto, i corpi dei fratelli e di Giove erano già spariti.
Pianse per ore, poi giorni. Al compimento della prima settimana smise di piangere e ricominciò a scrivere.
Credeva che la condanna del paese sarebbe stata ritirata con la morte del padre ma non fu così e quindi per raggiungere l'obbiettivo che inseguiva da una vita era necessario continuare a porsi delle domande. "L'uomo Interrogativo" lo chiamavano in quel paese alla periferia d'Europa. Girovagava per il villaggio, fra la gente comune, con una piuma fra le dita e un quadernetto logoro aperto malamente sull'altra mano.
-Galileo perché domandi ancora? Non troverai nulla di diverso- gli dicevano i più anziani.
Ma Galileo non era pronto a rassegnarsi. Solo e solitario, senza famiglia, in compagnia della sua curiosità e sete di conoscenza si rinchiuse nella sua casetta arancione col camino sempre acceso e mai più nessuno lo vide.
Questa potrebbe essere la fine. Niente gloria, niente meraviglia o sorpresa. Nessuna risposta.
Galileo però visse tanti altri anni e scrisse tanti altri quaderni.
Un giorno io stesso, che provenivo dal centro d'Europa,

finii in periferia ed entrai in quella casa arancione per proteggermi dall'intemperie. La mia curiosità, solo simile a quella di Galileo, mi spinse a frugare in quella casetta e su un tavolo trovai migliaia di lettere e centinai di quaderni logori.
Di un uomo chiamato Galileo nemmeno l'ombra.
La signorotta grassoccia ma gentile che mi aveva accompagnato fin lì mi disse che accadeva sempre così in quel paese: la gente spariva quando giungeva la sua ora e che potevo prendere tutti i quaderni di Galileo se volevo.
E vi dirò una cosa: li presi davvero perché erano scritti in maniera così disordinata che ne rimasi affascinato.
Scarabocchi, disegni e note prive si senso logico riempivano quelle pagine. Vi erano descritti sogni impossibili, immagini di mondi che potevo vedere solo ad occhi chiusi ma la mia pagina preferita è rimasta, fino ad oggi, quella recante il disegno di un grosso Telescopio. Così lo chiamava il signor Galileo, figlio di Giove, fratello di Europa, Io, Callisto e Ganimede.
Era un oggetto così strano che non saprei descriverlo ma so che lui lo riteneva la sua più grande scoperta.
Ma soprattutto era riuscito a scoprire il cielo grazie al Telescopio, l'aveva veramente guardato e non alzando la testa verso l'alto.
Non so come fece, non so se a causa di questo Giove il divino, nuovamente infurio tao, lo fece sparire prima del suo tempo ma una sua annotazione a piè di pagina diceva: "Papà si scordò di aggiungere una cosa riguardo al cielo: in quel mondo ci sarebbe finito anche lui. Ogni sera, infatti, lo saluto e insieme a lui do un'occhiata a Io, Ganimede, Callisto ed Europa. Non ho ancora trovato mamma, però."
Credo che Galileo fosse riuscito a trovare tutte le risposte che aveva sempre richiesto. C'era riuscito perché non riusciva ad accontentarsi di quell'immutabilità in cui viveva un intero paese, c'era riuscito perché si era posto le domande giusto. Ci era riuscito perché aveva trovato un modo per guardare sopra la sua testa.
E forse, oggi, anche Galileo si trova lì. Con Giove e i suoi figli. Dove tutti gli impossibili dovrebbero stare. Dove chi ha il coraggio di guardare in alto, oltre le condanne e le maledizioni immutabili, dovrebbe sempre stare.
Di certo non è dove sarò io.
Non mi sono mai posto le domande, io trascrivo solamente quello che vedo, mai quello che mi chiedo.
"Proibire la teoria copernicana vorrebbe dire vietar agli uomini guardar verso il cielo" [Galileo Galilei, Lettere Copernicane]

Secondo classificato ex aequo:

E all'opera, di **Roberto Fiorenza**, dal titolo **"Una vita imbottigliata"**, narrazione incentrata su una tematica tecnologica, la cui originalità fa dimenticare qualche occasionale caduta formale. L'autore ventiquattrenne vive a Centuripe (En). Lo scorso 25 Luglio ha completato gli studi universitari con la laurea magistrale conseguita con lode presso l'Università di Catania in chimica dei materiali. Nel 2012 ha conseguito nello stesso ateneo la laurea triennale in chimica industriale. Da sempre appassionato di libri e di letteratura, è fermamente convinto della necessità di un'unione fra le due culture, quella scientifica e quella letteraria, in quanto espressioni dello stesso concetto di natura, di vita, visti sotto due prospettive diverse ma allo stesso tempo uniche e complementari.

Una vita imbottigliata

PiETro era stanco, eppure era solo lunedì. Un'altra settimana di un altro mese di un altro anno di lavoro, in fabbrica. Ormai da quasi trenta anni lui e tutta la sua famiglia ripetevano quegli stessi processi, con un'attività frenetica soprattutto negli ultimi tempi. Il lavoro tuttavia non era certo noioso, almeno nella prima parte. Innanzitutto, presentarsi al lavoro richiedeva un duro impegno in palestra, seguito da una tremenda seduta in sauna. Il personal trainer dell'azienda infatti seguendo le rigide direttive impostagli dalla direzione pretendeva per tutti una forma fisica perfetta e la sauna non era vista come un attività rilassante, tutt'altro, le temperature alte e i tempi di permanenza abbastanza lunghi e obbligatori erano volti al raggiungimento della perfezione, più che dimagrire gli impiegati non facevano altre che essiccare. PiETro però quel giorno era inquieto. Si era svegliato così, eppure per lui quel lunedì era speciale, era arrivato finalmente il giorno della promozione. Altri suoi (numerosi) fratelli avevano vissuto con trepidazione quel giorno, ma, in famiglia erano tutti abbastanza schivi, nessuno ne parlava più di tanto, né soprattutto si aveva idea di cosa succedesse dopo la promozione; infatti nessuno dei suoi parenti era stato visto dopo il passaggio. Circolavano in merito alcune voci che PiETro non sapeva se considerare veritiere o leggende metropolitane: c'era chi sosteneva che fosse una passeggiata: dopo i primi mesi di ambientazione seguiva subito la pensione, chi sosteneva invece che il lavoro era lunghissimo e ripetitivo, altri affermavano che i più fortunati diventano importanti, preziosi. Ma le voci che più spaventano PiETro erano quelle del pericolo del lavoro stesso: si vociferava che dopo alcuni mesi si subiva, senza la possibilità di opporsi un processo terribile, che sconvolgeva completamente il fisico per poi ritornare al lavoro con un'altra mansione più bassa essendo cambiati internamente. Forse per tutti questi motivi PiETro non si dava pace ma ormai l'ora era arrivata, era pronto

per varcare la soglia del grande capannone il cui accesso era precluso solo ai meritevoli di promozione. Appena entrato sentì subito un'ondata di calore, la temperatura era così alta che PiETro quasi svenne, si sentiva mollo, quasi come se fosse stato fuso. Mentre provava queste sensazioni si sentì spinto da dietro: gli altri che come lui venivano quel giorno promossi erano smaniosi di uscire da quella zona viste le temperature
proibitive, l'effetto fu che PiETro si ritrovò come schiacciato contro qualcosa, la forza di compressione era inesorabile e mostruosa, egli ebbe la sensazione di essere come la sabbia bagnata usata dai bambini e pressata sugli stampi colorati in spiaggia per creare quelle forme geometriche precarie sulla monotona battigia. Finalmente la temperatura si abbassò improvvisamente e un vento fortissimo e leggero quasi come fosse soffiato da Eolo stesso lo attraversò completamente. Si sentiva strano come se il suo corpo fosse mutato. Quando vide la sua immagine riflessa su un bancone metallico PiETro realizzò di essere cambiato. Il suo fisico si era trasformato, era diventato sottilissimo nella parte superiore mentre era bombato, quasi ingrassato nella parte inferiore. A quel punto lui e gli altri "promossi" venivano divisi: una parte incluso PiEtro andò nel corridoio a destra mentre gli altri (PiETro poté spiarli grazie al suo nuovissimo collo pronunciato) andavano in altri corridoi, curiosamente, quelli che erano con lui avevano il suo stesso fisico mentre gli altri che erano stati separati erano diversi: c'erano quelli che erano uguali a lui con un uniforme diversa, colorata, altri invece erano ingrassati moltissimo nella parte centrale, altri ancora erano invece magrissimi, sottilissimi e stavano per qualche ragione, incomprensibile per PiETro , attaccati fra loro. A tutti quelli che erano con lui era stata consegnata la stessa uniforme bianca trasparente con una striscia colorata orizzontale in mezzo in cui era indicata il nome dell'azienda. Cosa ancor più strana era che adesso si avviavano verso la doccia. PiETro era sbalordito; non avrebbero inesorabilmente macchiato le nuovissime uniformi? Invece con sua grande sorpresa la sua divisa rimase immacolata, si sentiva solamente un po' più gonfio, pesante come se fosse staro riempito di qualcosa. Ma le bizzarrie non erano finite. Adesso a tutti venivano consegnati e obbligati a indossarli dei cappelli inusuali. Erano anch'essi trasparenti ma più opachi rispetto all'uniforme inoltre avevano un'insolita peculiarità: non potevano essere tolti da chi li indossava diventando a tutti gli effetti come una parte del corpo, anche se qualcuno, dall'esterno, poteva toglierli. Preso atto di tutto ciò PiETro e i suoi colleghi uscirono finalmente dal capannone per dirigersi verso gli enormi tir. Sapeva, dai racconti che si inseguivano in fabbrica, che non sarebbe più tornato indietro e pieno di dubbi e timoroso partì suo malgrado, d'altronde non aveva scelta. Il viaggio fu lungo almeno uno o due giorni secondo PiETro, alla fine dell'odissea il tir arrestò la sua corsa. Come prigionieri in gabbia lui e i suoi compagni non vedevano l'ora di riabbracciare finalmente il sole, tuttavia furono costretti ad ammassarsi l'uno accanto all'altro, gli fu detto che finalmente erano giunti alla loro nuova collocazione. Quella era un'ennesima novità per Pietro. Era molto più
piccola rispetto alla prima, e (cosa che fece sobbalzare PieTRo) strettissima. Inoltre ad ulteriore aumento del suo disagio gli era stato posta una fascia di metallo a cingere il suo nuovo ventre bombato, a impedimento di qualsiasi movimento. Ma dove erano i sindacati? Quale promozione era mai questa? PiETro si sentiva disperato, il clima era inoltre abbastanza rigido. Smaltita la rabbia e la frustrazione iniziò a dare un'occhiata al quel luogo abietto. A causa della cintura metallica poteva solo vedere i suoi vicini di posto, tutti compagni che avevano compiuto con lui il viaggio, sopra di lui invece c'erano altri "stranieri". Avevano un'uniforme completamente diversa, con vari colori inoltre non sembravano per nulla suoi colleghi. Mentre cercava di capire chi o cosa fossero i suoi nuovi vicini, tutto il locale all'improvviso iniziò a vibrare. Quello che a PiETro sembrava il pavimento della stanza era in realtà un ascensore. Questo salì superando il posto dove egli era collocato, tanto che non vide più che cosa succedeva. Sentì solamente un frastuono come di qualcuno che cadeva rovinosamente. Subito dopo l'ascensore si abbassò e un suo collega straniero veniva tirato fuori dal locale, successivamente ritornò la pace. Cosa era successo? Che fine aveva fatto il suo collega? L'inquietudine aumentava e si trasformò in paura quando rivide dopo molto tempo l'uniforme del suo collega che aveva subito il processo di spostamento. Era di fronte a lui ma tutta strappata e vuota come se lo stesso dipendente l'avesse gettata via, scomparendo lui stesso. Negli attimi successivi vide ripetere gli stessi procedimenti di spostamento, a intervalli irregolari. Mentre rifletteva su tutto ciò si chiese cosa sarebbe successo se l'ascensore si fosse fermato sul suo posto: avrebbe subito altri processi restrittivi o avrebbe recuperato almeno in parte la sua libertà? Non dovette attendere molto per soddisfare tutte le sue curiosità. Il diabolico marchingegno infatti si mise di nuovo in moto e stavolta si fermò proprio sul ripiano in cui soggiornava PiETro. Sentì che i suoi colleghi erano in fermento qualcosa stava succedendo, infatti non passò molto che l'agitazione divenne panico, e tutti iniziarono a spingersi. Sfortunatamente PiETro era di fronte all'ascensore e lo spintone di un suo collega non fece altro che indirizzarlo proprio all'interno del temuto aggeggio. Fu rovesciato e inclinato fino a quando non sentì una morsa stringersi attorno al suo largo ventre, stava uscendo dal nuovo luogo di lavoro per esplorare l'ignoto. La prima sensazione che ebbe oltre alla paura e all'inquietudine di fondo fu inusuale (come tutto in quella giornata); dall'esterno, infatti, stavano per toglierli quel cappello che mai da solo sarebbe riuscito a estrarre. Si sentì completamente indifeso e in balia degli eventi, sperduto. Il suo capo nudo veniva adesso avvicinato (sempre stringendo il suo ventre) a qualcosa di secco e allo

stesso tempo morbido che PiETro non riuscì a individuare e quasi immediatamente si sentì svuotato almeno in parte. Quella sensazione duro poco, fu quasi istantanea, poco dopo infatti si ritrovò di nuovo con il cappello e più leggero sopra un piano orizzontale marrone, ben arredato con tanti fogli,carpette e uno schermo gigante. Da lì si accorse di essere entrato in nuovo mondo, la luce della stanza che proveniva dallo splendido sole che soggiornava all'esterno irradiava il tutto e per la prima volta in tutta la giornata PiETro si sentì un po' sollevato, vedere il sole, la luce, lo tranquillizzava in qualche modo. Negli attimi successivi si ripeté a volte in maniera regolare, altre volte in maniera irregolare quella strana situazione verificata precedentemente con il senso di leggerezza che man mano diventava sempre maggiore. Era come se ad ogni "estrazione forzata" del cappello divenisse più leggero. Il processo continuò fino a quando si sentì completamente vuoto, neanche il tempo di familiarizzare con questa ennesima modifica che PiETro fu catapultato nei peggiori istanti della sua vita. Si sentì scacciare da una forza inarrestabile a cui non poté in nessuno modo opporsi privo del suo cappello e completamente alleggerito. Quando il suo ventre fu così ridotto da rasentare il piano orizzontale dove era posto gli fu collocato nuovamente il cappello e fu sbalzato, come una palla, in un altro ennesimo luogo scuro e silenzioso. PiETro era sconvolto. La sua nuova siluette era stata irreversibilmente modificata: il suo collo pronunciato esile e elegante non esisteva più, il suo ventre era praticamente un tutt'uno con la parte inferiore del suo corpo, si sentiva male, si sentiva spazzatura. Diede un'occhiata intorno c'erano altri come lui, alcuni colleghi altri no, tutti ammassati e tutti maltrattati. Alcuni avevano ancora l'uniforme, altri c'è l'avevano malridotta, altri ancora non l'avevano totalmente. Aveva capito. Era lì, di fronte al luogo in cui era collocato l'ascensore infernale, il luogo dove aveva visto lo straniero scomparire. Stava iniziando a razionalizzare tutto. Ecco perché nessuno dei colleghi ne parlava, ecco perché nessuno dei suoi familiari era tornato. Quella non era una promozione era la morte. Ma che senso aveva? Si chiedeva PiETro incredulo, tutte quelle ore in palestra, tutta quella preparazione a che giovavano se era quella la fine di tutto, se la sua "promozione" durava così poco? Non riusciva a darsi pace e nessuno dei suoi sventurati compagni era in grado di rispondergli, anche perché nessuno di loro voleva o poteva parlare. Trascorse molto tempo dentro quel luogo cosi triste, così oscuro. Il sole, la luce l'avevano sedotto e abbondato. Come avrebbe voluto rivederlo, almeno una volta... non era però più il tempo di pensare a queste utopie, un ennesimo spostamento lo attendeva. Finalmente dopo un periodo imprecisato, lunghissimo per PiETro, sentì che qualcosa si muoveva. Quel luogo triste veniva scosso, come se ci fosse un terremoto e si ritrovò catapultato insieme con gli altri all'interno di un altro tir. Un altro viaggio? E per dove? Si chiese PiETro, tuttavia quel tir, quel viaggio erano in qualche modo familiari come se stesse ritornando al luogo di partenza. Non era possibile ripeteva dentro di sé, non lo avrebbero accettato così come era ridotto, altro che palestra...Tutti quei dubbi furono spazzati via poco dopo. Il viaggio era terminato, finalmente erano arrivati quel parcheggio, quell'albero, quella casetta, PiETro era sicuro, era ritornato a "casa". Ma come si poteva facilmente immaginare non rientrava da vincente, dal portone principale, veniva dirottato verso una zona oscura della fabbrica, al di là del familiare capannone dove aveva passato tutti quei giorni monotoni. Andava verso un'ala della fabbrica misteriosa sulla quale, come al solito, circolavano voci e leggende. Si raccontava che solo quelli non adatti, fisicamente imperfetti andassero verso quel locale e il loro destino era ignoto, oppure altri narravano di trattamenti strani e pericolosi. Come ormai aveva imparato a fare PiETro si era convinto che doveva sperimentare e non doveva fidarsi delle voci che lo perseguitavano. Di certo il suo umore, come il suo fisico, erano a terra. Non pensava a nessuna mansione che sarebbe andata bene per il suo nuovo "io" e il pessimismo iniziava a pervaderlo. Entrato nel famoso capannone dovette subire uno strano e allo stesso tempo particolare trattamento. Inizialmente lui e gli altri suoi colleghi furono posti all'interno di un enorme cilindro che ruotava con un foro centrale, tanti risero e si divertivano sembrava che fossero stati mandati al parco giochi. PiETro da buon spirito scientifico osservava: la maggioranza di loro è vero si divertiva, ma i più piccoli o i troppo grandi o grossi venivano spazzati via dal cilindro attraverso quel foro centrale, per loro il divertimento era già terminato. Successivamente furono avviati alle docce, anche se non si sentiva a proprio agio con quel suo nuovo "fisico" dopo tutte quelle emozioni quella doccia ci voleva proprio. Si accorse che durante il lavaggio la sua uniforme ormai lacerata, andò via definitivamente. Ma quello che per PiETro sembrava un piccolo sollievo si trasformò presto nell'ultimo momento piacevole di quella giornata. Non passo molto infatti che lui e gli altri furono trascinati quasi a forza in una zona che non avrebbero mai voluto vedere. La paura, i dubbi si trasformarono in consapevolezza. PiETro solo in parte risollevato dalla doccia appena fatta, vide i suoi colleghi che lo precedevano scomparire dietro grida strazianti e terribili. Purtroppo per lui sperimentò su di sé che cosa stava accadendo. Il suo fisico gobbo, veniva smembrato, distrutto, macinato. Nonostante il dolore estremo PiETro pensò che in fini dei conti quello che stava subendo era un ritorno si sentiva come se fosse ritornato bambino dove non aveva bisogno di un fisico perfetto, né di subire trattamenti particolari. Ritornato "embrione" dopo aver sopportato notati sempre in fabbrica e ne parlavano spesso i suoi cugini stranieri e in particolare seBUSTiAno. Comunque una cosa era certa un ennesimo sconvolgimento lo aspettava. Il nuovo posto era però almeno all'inizio del tutto simile al precedente. Certo la mensola era più piccola

e meno spaziosa ma pur sempre comoda. Non poteva lamentarsi. Accadeva però a intervalli regolari che veniva spostato per essere completamente dispiegato e messo in movimento, come se fosse stato indossato. Quello era il momento prediletto di PiETro perché poteva finalmente esplorare, guardare, sperimentare. Oltre al sole, poteva analizzare la bellezza della natura, la diversità delle persone, degli animali, delle piante, della vita, insomma. Ogni volta che quel gesto si ripeteva egli era al settimo cielo e si rasserenava, quella sì che era una promozione con i fiocchi. Certo, doveva subirsi delle lavate tremende all'interno di un luogo angusto e a temperature abbastanza alte, veniva centrifugato, bagnato, asciugato e infine doveva subire la scottante superficie di un ferro, ma quelle sofferenza erano un prezzo ragionevole da pagare per quello che in quei giorni aveva visto e appresso: la sperimentazione attraverso l'osservazione della natura, la forma più elementare e pura di scienza. In un giorno di esplorazione la sua sorpresa, la sua sete di sapere si tramutò in paura. Notò su un tavolo un oggetto familiare. Era trasparente, con una fascia colorata in mezzo, un ventre bombato, un collo pronunciato e un cappello anch'esso bianco ma più scuro. Non c'erano dubbi, quello era LUI o perlomeno qualcuno che come lui aveva subito la prima promozione. Da novello sperimentatore lo analizzò per bene, e notò che il simbolo della sua uniforme era identico a quello che lui adesso aveva stampato su di sé, inoltre notò uno stano simbolo: tre frecce che formavano un cerchio e al cui interno era disegnato un numero. La sua curiosità era diventata sete di sapere cercò in tutti i modi di comunicare con quel suo "simile" per metterlo in guardia della sventure che da lì a poco avrebbe dovuto sopportare ma non ci riuscì. Dovette andare via con l'amaro in bocca e con una domanda che lo perseguitava cosa era quel simbolo? Sentiva dentro di sé che era la chiave di tutto, della comprensione, della spiegazione. Sperò con tutto il cuore di poter rincontrare quel suo simile ma il giorno dopo non lo vide. Come un segugio cercò di analizzare tutti i possibili luoghi dove avrebbe potuto trovarlo, ma niente, era scomparso. Prendendo la sua esperienza come punto in comune guardò, per quello che il suo "fisico" permetteva dentro quei contenitori rettangolari bui e puzzolenti a cui tutti associavano un nome: spazzatura. Anche in quei posti per qualche ragione familiari a PiETro non trovò nessuna traccia del suo sventurato collega. Tuttavia quel giorno non era stato infruttuoso aveva notato che tanti cappelli opachi erano raccolti insieme e accatastati in un contenitore, dove era impresso in una sorte di gigantografia quel simbolo con le frecce. Il suo "amico" non poteva essere lontano. Infatti il giorno successivo finalmente lo riviste. Era all'interno di un altro contenitore e già aveva assunto quella forma orrenda tutta schiacciata. Provò pena per lui, ricordando le sofferenze che dovette sopportare anche lui, ma cosa che più lo inquietava e che stavolta insieme al simbolo era indicato un parola che subito lo segnò nel profondo e gli aprì le porte della comprensione. Quella parola era RICICLO. Aveva capito tutto: tutte quelle sofferenze erano per un motivo: PiETro era stata riciclato.

Nota dell'autore
(da leggere categoricamente alla fine del racconto).

La laurea è troppo fresca per non raccontare qualcosa di "materiale". In questo breve racconto ho voluto raccontare il punto di vista inusuale di una bottiglia in PET (il nostro protagonista è in fatti PiETro) che partendo da materia prima (polimero) diventa prima bottiglia e poi attraverso il processo di riciclo diventa un tessuto e quindi una t-shirt. Ho scelto questo inusuale argomento perché ho voluto mettere in risalto, o almeno ci ho provato, sperando di esserci riuscito, il concetto stesso di RICICLO. Dal mio punto di vista questo processo è la naturale evoluzione del rapporto uomo-scienza-natura. Galileo ci ha dato il mezzo per studiare e per stupirci di fronte alla natura, poi l'uomo è riuscita in minima parte a comprenderla e a sfruttare le sue enormi potenzialità insieme al progresso tecnologico. Lo sfruttamento eccessivo però ci ha posto di fronte a un bivio: rispettare la natura o andare incontro alla sua distruzione. Pian piano stiamo cercando di chiedere "scusa" alla natura sviluppando processi sempre più green e volti appunto al riciclo. Questo è il punto di incontro dell'uomo, della scienza e della tecnologia odierni con la natura che in fin dei conti rimane speciale semplicemente cosi come è, osservandola e stupendoci del suo quotidiano, cosi come PiETro ha fatto. In particolare le fasi di lavorazione del PET sono messe in evidenza dai termini in corsivo. Inizialmente la forma fisica perfetta e le saune esprimono il processo di essiccamento del polimero di base .Il PET fuso viene poi iniettato su uno stampo. Segue poi la fase di soffiaggio. Il fisico bombato nel ventre e allungato nella parte superiore esprime la forma della bottiglietta mentre i colleghi con forme diverse esprimono le moltitudini di contenitori bianchi o colorati che si possono fabbricare in PET in cui l'uniforme rappresenta l'etichetta. La doccia successiva rappresenta il riempimento con acqua, e il cappello non è altro che il tappo.

PER LA PARTE FOTOGRAFICA:
Giuria:
- Dottore Domenico Santonocito, ricercatore INFN e critico fotografico
- Avvocato Giuseppe Pappalardo, critico fotografico

Primo Premio
All'opera di **Nunzio Santisi**, **senza titolo**, per la buona illustrazione del tema assegnato risolto dall'autore nell'individuazione della poetica macrofotografica come strumento idoneo ed opportuno per dare visibilità a quanto in natura può apparire infinitamente piccolo ma infinitamente interessante. L'autore privilegia un'accurata visione di un insetto raccolto nella sua quotidianità e dentro il suo ambiente naturale. Senza turbare tale ambiente rispetta le luci naturali e l'atmosfera dell'insieme che si risolvono, per chi guarda, in maggiore conoscenza.

Secondo classificato
Opera di **Giacomo Piccioni** dal titolo **"Acqua"** per la ritrovata ricerca all'interno della fotografia in bianconero di una nuova forma capace di rendersi espressiva all'interno di grigi e di una precisa plasticità.

Terzo classificato
Opera di **Gianluca Pizzone** dal titolo **"A sea of blue"** per un atteggiamento di scoperta caratterizzato da una semplicità coniugata con la volontà di trovare elementi (la macchia del papavero, il filo d'erba) di sorpresa e musicalità.

Quarto classificato:
Opera di **Vinicio Tullio** dal titolo **"Impressionismo 1"** per la risoluta volontà di rintracciare nel mondo naturale l'immagine che altri artisti hanno saputo formulare con diversa iconicità. Si apprezza inoltre la compattezza della raffigurazione.

Primo Classificato | Nunzio Santisi

Secondo Classificato | Giacomo Piccioni

LNS ACTIVITY PHOTO GALLERY

Terzo Classificato | Gianluca Pizzone

Quarto Classificato | Vinicio Tullio

LNS ACTIVITY PHOTO GALLERY

Dichiarazione di Messina 2.0:
La via italiana all'Open Access

Messina 4 novembre 2014 - La firma della Road Map.
Il Direttore dei LNS Dott. Giacomo Cuttone
delegato dal Presidente dell'INFN Prof. Fernando Ferroni
firma l'accordo a nome dell'INFN.

INFN
LNS

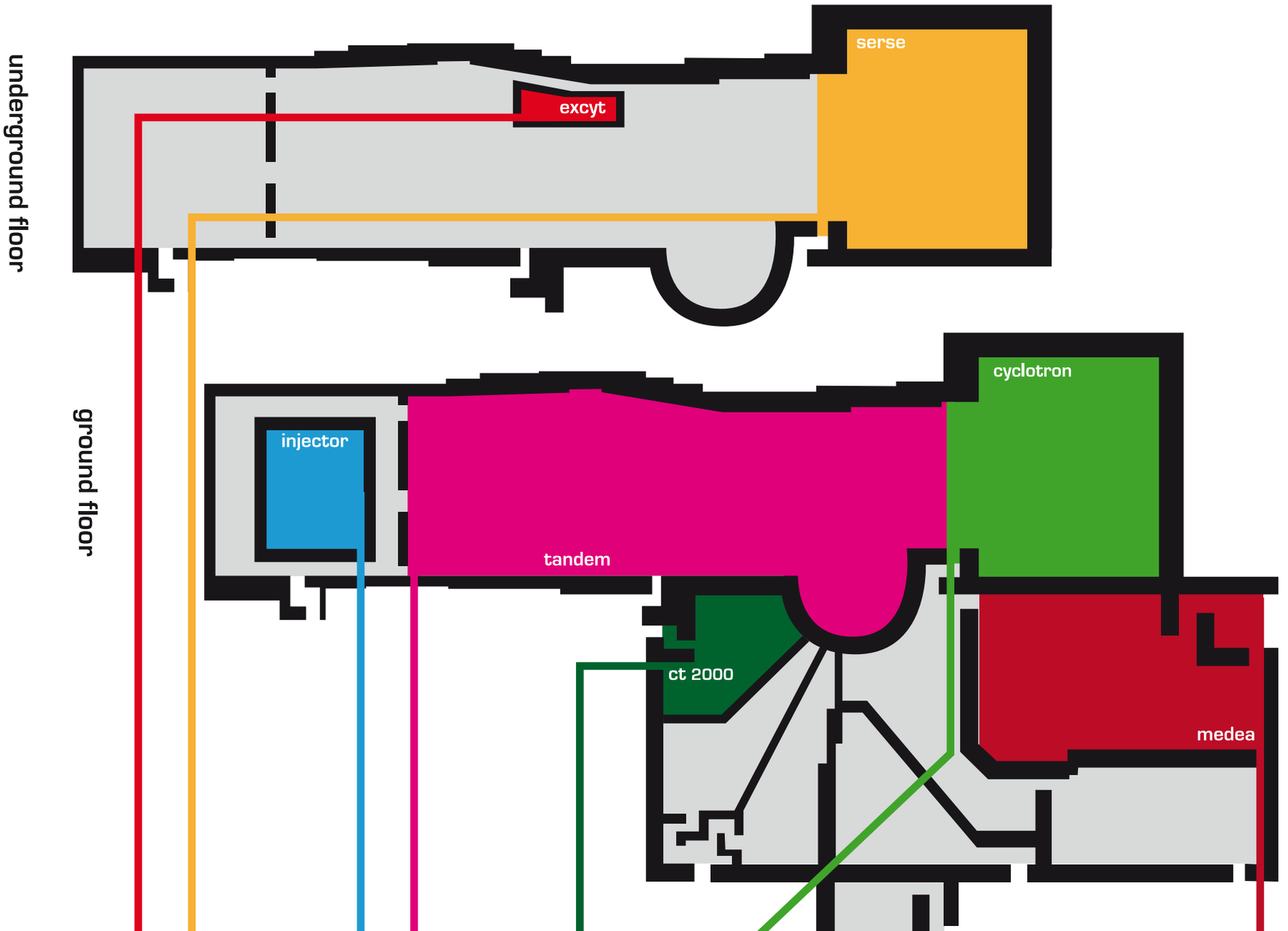
underground floor
ground floor
serse
excyt
cyclotron
injector
tandem
ct 2000
medea

ISTITUTO NAZIONALE DI FISICA NUCLEARE

LABORATORI NAZIONALI DEL SUD

ACTIVITY REPORT 2013/2014

LNS EXPERIMENTAL HALLS

chimera

medea

catana

magnex

ct 2000

cyclotron

injector

tandem

excyt

serse

EXPERIMENTAL NUCLEAR PHYSICS AND ASTROPHYSICS
THEORETICAL NUCLEAR PHYSICS
INSTRUMENTATION AND RELATED TECHNIQUES
ASTROPARTICLE PHYSICS
ION SOURCES AND ACCELERATORS
INTERDISCIPLINARY PHYSICS
GENERAL INFORMATION
LNS ACTIVITY PHOTO GALLERY

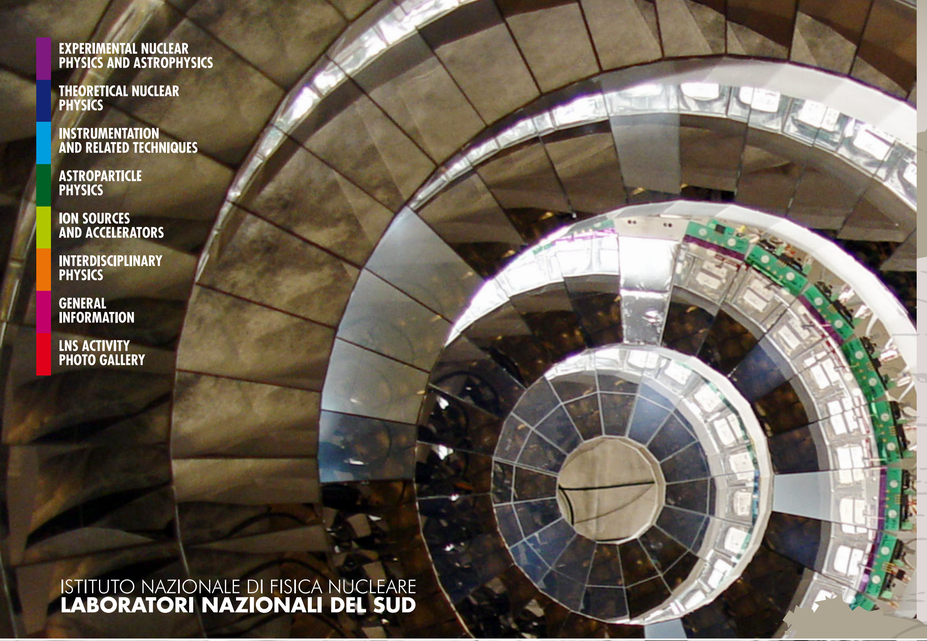

ISTITUTO NAZIONALE DI FISICA NUCLEARE
LABORATORI NAZIONALI DEL SUD

ACTIVITY REPORT 2013/2014

Via Santa Sofia 62 Catania – Italy
phone +39 095 542111
e-mail: direzione@lns.infn.it
info: sis@lns.infn.it
www.facebook.com/infn.lns
www.lns.infn.it

ISSN 1827-1561

INFN-LNS

ISTITUTO NAZIONALE DI FISICA NUCLEARE
LABORATORI NAZIONALI DEL SUD

ACTIVITY REPORT 2013/2014

INFN-LNS

INFN LNS

ISTITUTO NAZIONALE DI FISICA NUCLEARE
LABORATORI NAZIONALI DEL SUD

ACTIVITY REPORT 2013/2014

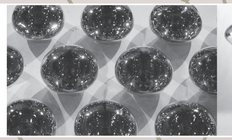

LNS and the European Research Infrastructures

The ESS project
The European Spallation Source (ESS) is one of the largest science infrastructure projects being built in Europe. The ESS facility will be the world's leading neutron source for the study of life and materials sciences, soft condensed matter, magnetic and electronic phenomena, energy, engineering materials and geo-sciences, archaeology and heritage conservation and fundamental and particle physics. ESS will be constructed in Lund, but realized by at least 17 European countries.

ELI-BEAMS and ELIMED
ELI-Beamlines is one of the pillars of the pan-European project ELI (Extreme Light Infrastructure) based in the Czech Republic and Rumenia. It will be an ultra high-intensity, high repetition-rate, femtosecond laser facility whose main goal is generation and applications of high-brightness X-ray sources and accelerated charged particles in different fields. ELIMED (MEDical and multidisciplinary applications at ELI) is a project based on laser-driven proton sources for clinical application in the field of hadrontherapy.

KM3NeT is the next generation neutrino telescope. Located in the deepest seas of the Mediterranean, it will open a new window on our Universe. With the telescope scientists will search for neutrinos from distant astrophysical sources such as supernovae, gamma ray bursters or colliding stars. An array of thousands of optical sensors will detect the faint light in the deep sea from charged particles originating from collisions of the neutrinos and the Earth. The facility will also house instrumentation for Earth and Sea sciences for long term and on-line monitoring of the deep sea environment and the sea bottom at depth of several kilometers.

EMSO
The European Multidisciplinary Seafloor and water-column Observatory has the basic scientific objective of monitoring of environmental processes related to the interaction between the geosphere, biosphere, and hydrosphere, including natural hazards. It is composed of several deep-seafloor and water column observatories. One of these is located in the Mediterranean sea.